

HIGH-STRENGTH STEEL BARS IN EARTHQUAKE-RESISTANT T-SHAPED CONCRETE WALLS

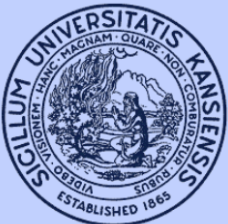
By

Mohammad Sajedul Huq
Alexander S. Weber-Kamin
Shahedreen Ameen
Rémy D. Lequesne
Andrés Lepage

A Report on Research Sponsored by

Charles Pankow Foundation
ACI Foundation's Concrete Research Council

Structural Engineering and Engineering Materials
SM Report No. 128
September 2018



THE UNIVERSITY OF KANSAS CENTER FOR RESEARCH, INC.
2385 Irving Hill Road, Lawrence, Kansas 66045-7563

**HIGH-STRENGTH STEEL BARS IN
EARTHQUAKE-RESISTANT
T-SHAPED CONCRETE WALLS**

By

Mohammad Sajedul Huq
Alexander S. Weber-Kamin
Shahedreen Ameen
Rémy D. Lequesne
Andrés Lepage

A Report on Research Sponsored by

Charles Pankow Foundation
ACI Foundation's Concrete Research Council

Structural Engineering and Engineering Materials
SM Report No. 128
THE UNIVERSITY OF KANSAS CENTER FOR RESEARCH, INC.
LAWRENCE, KANSAS
September 2018

ABSTRACT

The object of this study was to determine experimentally the influence of selected reinforcing steel mechanical properties on wall deformation capacity. Four large-scale T-shaped reinforced concrete wall specimens with different types of reinforcement were subjected to reversed cyclic displacements. The primary variables were the yield strength (f_y) and the tensile-to-yield strength ratio (f_t/f_y) of the reinforcing bars. The study also aimed to identify the minimum uniform elongation (ϵ_{su}) and fracture elongation (ϵ_{sf}) required of high-strength reinforcement for use in earthquake-resistant concrete structures.

Test data are presented from four walls, T1 with conventional Grade 60 (420) reinforcement and T2, T3, and T4 with high-strength Grade 100 (690) reinforcement. The flexural reinforcement consisted of No. 6 (19) bars inside confined boundary elements and No. 4 (13) bars elsewhere. Confining reinforcement in boundary elements consisted of No. 3 (10) hoops and crossies of the same grade as the flexural reinforcement. Wall T1 had f_t/f_y of 1.34 and 1.39 for the No. 6 (19) and No. 4 (13) bars, respectively. Walls with Grade 100 (690) reinforcement had f_t/f_y of 1.15 and 1.10 for T2, 1.23 and 1.21 for T3, and 1.36 and 1.20 for T4. All walls were loaded with a shear span-to-depth ratio of 3 and had the same nominal dimensions and concrete compressive strength (8 ksi or 55 MPa). Axial load was limited to the self-weight of the wall and testing apparatus. The walls were designed to have nearly the same nominal flexural strength. Flexural yielding controlled the lateral strength of the walls, inducing an average shear stress up to $3.5\sqrt{f'_c}$, psi ($0.29\sqrt{f'_c}$, MPa). To ensure large tensile strain demands in one of the loading directions, the neutral axis depth at nominal flexural strength did not exceed the thickness of the flange. Design of the walls complied with ACI Building Code (ACI 318-14) requirements for special structural walls with additional detailing requirements applied based on ATC 115.

Walls designed for a target flexural strength using Grade 60 (420) or Grade 100 (690) reinforcement, with similar f_t/f_y for the primary flexural reinforcement, had similar strength and deformation capacity (defined as the drift cycle completed before a 20% loss of lateral strength). The limited test data indicate that walls with low axial force and reinforcement that satisfies tensile-to-yield strength ratio ($f_t/f_y \geq 1.2$), uniform elongation ($\epsilon_{su} \geq 6\%$), and fracture elongation ($\epsilon_{sf} \geq 10\%$) exhibit a minimum drift ratio capacity of 3%. Walls T1, T2, T3, and T4 exhibited drift ratio capacities of 3.7, 1.8, 3.0, and 3.9%, respectively.

Moment-curvature analyses were conducted to evaluate the use of the plastic hinge model for estimating the deformation capacity of the walls and the maximum strain demands. The use of the plastic hinge model was conservative for estimating wall deformation capacity with simple rules for the plastic hinge length depending on whether deformations due to shear and strain penetration are considered. However, the plastic hinge model did not consistently provide conservative estimates of the maximum strain demands.

ACKNOWLEDGMENTS

This report was prepared as a doctoral dissertation by M. S. Huq under the direction of Professors Andrés Lepage (Chair) and Rémy Lequesne (Co-Chair).

Primary financial support was provided by the Charles Pankow Foundation and the Concrete Research Council of the ACI Foundation, under grant RGA #06-14. Additional support was provided by Commercial Metals Company, Concrete Reinforcing Steel Institute, Harris Rebar, Midwest Concrete Materials, Nucor Corporation, and The University of Kansas through the Department of Civil, Environmental & Architectural Engineering and the School of Engineering.

Grateful acknowledgment is made to the Industry Champions, David Fields (principal of MKA, Seattle) and Ramón Gilsanz (partner of GMS, New York), and Advisory Panel, Dominic Kelly (principal of SGH, Boston) and Conrad Paulson (principal of WJE, Los Angeles), for their ideas and constructive criticism.

Appreciation is due to a number of dedicated students and technicians who were involved in the construction of specimens and test programs.

TABLE OF CONTENTS

ABSTRACT	i
ACKNOWLEDGMENTS	iii
LIST OF TABLES.....	vii
LIST OF FIGURES	viii
1 INTRODUCTION	1
1.1 Motivation	1
1.2 Objective and Scope	1
1.3 Research Significance.....	1
2 BACKGROUND	3
2.1 Advanced High-Strength Steel (AHSS)	3
2.2 Deformation Capacity of Slender Walls	4
2.3 Strength of Slender Walls.....	6
2.4 Tests of Slender Walls Reinforced with AHSS.....	7
3 EXPERIMENTAL PROGRAM	10
3.1 Specimen Design	10
3.2 Materials	13
3.3 Specimen Construction.....	15
3.4 Test Setup and Procedure	16
3.4.1 Description of Setup.....	16
3.4.2 Instrumentation.....	16
3.4.3 Loading Protocol.....	18
4 EXPERIMENTAL RESULTS AND ANALYSIS	19
4.1 Measured Shear versus Drift Ratio	19

4.2	Progression of Damage.....	23
4.3	Measured Reinforcement Strains	25
4.3.1	Wall Stem Longitudinal Reinforcement	25
4.3.2	Wall Flange Longitudinal Reinforcement.....	27
4.3.3	Wall Transverse Reinforcement.....	28
4.3.4	Comparisons.....	29
4.4	Concrete Strain Profile.....	30
4.4.1	Wall Stem Concrete Strains	31
4.4.2	Wall Flange Concrete Strains	35
4.4.3	Comparisons.....	37
4.5	Components of Drifts	38
4.5.1	Shear	38
4.5.2	Base Shearing.....	43
4.5.3	Flexure	43
4.5.4	Opening at the Base of the Wall	46
4.5.5	Comparisons.....	48
4.6	Crack Widths.....	51
4.7	Wall Elongation.....	53
4.8	Stiffness	55
4.8.1	Effective Initial Stiffness.....	55
4.8.2	Unloading Stiffness	58
4.9	Hysteresis	59
4.9.1	Takeda Model.....	59
4.9.2	Energy Dissipation.....	60
4.9.3	Modeling Parameters	61
5	Calculation of Force-Deformation Relationships.....	63
5.1	Material Models	63

5.1.1	Stress-strain Relationships for Concrete in Compression	63
5.1.2	Stress-Strain Relationships for Reinforcing Steel	64
5.2	Moment-Curvature Relationships	64
5.2.1	Assumptions	64
5.2.2	Moment-Curvature Relationships for Walls with Grade 60 (420) Reinforcement.....	65
5.2.3	Moment-Curvature Relationships for Walls with Grade 100 (690) Reinforcement	66
5.2.4	Comparisons.....	66
5.3	Deformation Capacity	68
5.3.1	Assumptions	68
5.3.2	Deformation Capacity of T-Shaped Walls.....	71
5.3.3	Comparisons.....	72
5.4	Strain-Drift Relationships	72
5.4.1	Assumptions	72
5.4.2	Strain-Drift Relationships of T-shaped Walls.....	73
6	CONCLUDING REMARKS	75
7	REFERENCES	79
	TABLES	85
	FIGURES.....	106
	APPENDIX A: NOTATION.....	360
	APPENDIX B: POST-YIELD STRAIN PENETRATION	366

LIST OF TABLES

Table 1 – Summary of test program (1 ksi = 6.89 MPa).....	86
Table 2 – Loading protocol	87
Table 3 – Data associated with computed nominal flexural strength (1 in. = 25.4 mm, 1 ft = 305 mm, 1 kip = 4.45 kN)	88
Table 4 – Key dates for specimen casting and testing	89
Table 5 – Batched proportions for concrete mixture (1 gal = 3.79 liters, 1 oz = 0.278 N, 1 lb = 4.45 N, 1 in. = 25.4 mm)	90
Table 6 – Measured concrete strength at test day (1 ksi = 6.89 MPa).....	91
Table 7 – Reinforcing steel properties (1 in. = 25.4 mm, 1 ksi = 6.89 MPa).....	92
Table 8 – Chemical composition of reinforcing bars	93
Table 9 – Maximum measured shear force and drift ratio (1 kip = 4.45 kN, 1 psi = 0.00689 MPa).....	94
Table 10 – Drift cycle and bar location where bar buckling or bar fracture first occurred	95
Table 11 – Secant stiffness from measured shear-drift envelope (1 in. = 25.4 mm, 1 kip = 4.45 kN).....	96
Table 12 – Wall data for cracked stiffness calculation (1 in. = 25.4 mm, 1 kip = 4.45 kN).....	97
Table 13 – Unloading stiffness derived from measured shear versus drift ratio (1 in. = 25.4 mm, 1 kip = 4.45 kN)	98
Table 14 – Modeling parameters for nonlinear seismic analysis	99
Table 15 – Stress-strain parameters for concrete (1 ksi = 6.89 MPa)	100
Table 16 – Stress-strain parameters for reinforcing steel bars (1 ksi = 6.89 MPa).....	101
Table 17 – Moment-curvature data (1 in. = 25.4 mm, 1 ft = 305 mm, 1 kip = 4.45 kN).....	102
Table 18 – Calculated deformation capacity due to flexure only (for a maximum compressive strain of 0.015 in the confined stem) (1 in. = 25.4 mm)	103
Table 19 – Calculated deformation capacity due to flexure, shear, and strain penetration (for a maximum compressive strain of 0.015 in the confined stem) (1 in. = 25.4 mm, 1 kip = 4.45 kN)	104
Table 20 – Maximum drift cycle completed without bar fracture and comparison with bar elongation properties	105
Table B.1 – Strain penetration amplification factor α_{sp} based on Eq. B.12 ^a	371

LIST OF FIGURES

Figure 1 – Base of walls with Grade 60 (420) reinforcement in Western United States	107
Figure 2 – Elongation and strength for conventional and advanced high-strength steels, adapted from Zuidema et al. ^[90]	108
Figure 3 – Stress-strain curves representative of conventional steel and advanced high-strength steel reinforcement, adapted from Lepage et al. ^[46] (1 ksi = 6.89 MPa)	108
Figure 4 – Test setup and specimen details used by Kimura and Ishikawa ^[44]	109
Figure 5 – Shear force versus drift ratio response reported by Kimura and Ishikawa ^[44] for specimen with axial load of $0.10Agfc'$, where $fc' = 15$ ksi (105 MPa) and $fy = 100$ ksi (690)	109
Figure 6 – Reinforcement layout for T1 (1 in. = 25.4 mm)	110
Figure 7 – Reinforcement layout for T2 and T3 (1 in. = 25.4 mm)	111
Figure 8 – Reinforcement layout for T4 (1 in. = 25.4 mm)	112
Figure 9 – Confined boundary element in stem of T1 (1 in. = 25.4 mm)	113
Figure 10 – Confined boundary element in stem of T2, T3, and T4 (1 in. = 25.4 mm)	113
Figure 11 – Confined boundary element in flange of T1 (1 in. = 25.4 mm)	114
Figure 12 – Confined boundary element in flange of T2, T3, and T4 (1 in. = 25.4 mm)	114
Figure 13 – Reinforcement data and wall section properties (1 in. = 25.4 mm)	115
Figure 14 – Typical wall elevation (1 in. = 25.4 mm)	116
Figure 15 – Illustration of loading protocol described in Table 2	117
Figure 16 – Measured stress versus strain for No. 6 (19) bars (1 ksi = 6.89 MPa)	118
Figure 17 – Measured stress versus strain for No. 4 (13) bars (1 ksi = 6.89 MPa)	119
Figure 18 – Fractured No. 4 (13) bar from T2 after tensile test	120
Figure 19 – Bar deformation details for No. 4 (13) bar in T2	120
Figure 20 – Casting of base block for T1	121
Figure 21 – Preparing concrete cylinders and in-situ tests during casting	121
Figure 22 – Lift 1 reinforcement assembly (T2)	122
Figure 23 – Lift 1 formwork assembly (T1)	122
Figure 24 – Lift 2 casting (T3)	122
Figure 25 – Top block formwork assembly (T1)	122
Figure 26 – Test setup	123
Figure 27 – Steel spreader beams below laboratory strong floor for base block hold-downs	124
Figure 28 – Wall instrumentation (elevation view of wall stem) (1 in. = 25.4 mm)	125
Figure 29 – Wall instrumentation (elevation view of wall flange) (1 in. = 25.4 mm)	126
Figure 30 – Locations of optical markers on wall stem (1 in. = 25.4 mm)	127
Figure 31 – Locations of optical markers on wall flange (1 in. = 25.4 mm)	127
Figure 32 – Plan view of base block indicating locations of optical markers (1 in. = 25.4 mm)	128

Figure 33 – Wall T1 strain gauge locations (1 in. = 25.4 mm).....	129
Figure 34 – Wall T2 strain gauge locations (1 in. = 25.4 mm).....	130
Figure 35 – Wall T3 strain gauge locations (1 in. = 25.4 mm).....	131
Figure 36 – Wall T4 strain gauge locations (1 in. = 25.4 mm).....	132
Figure 37 – Shear versus drift ratio for T1 (1 in. = 25.4 mm, 1 kip = 4.45 kN).....	133
Figure 38 – Shear versus drift ratio for T2 (1 in. = 25.4 mm, 1 kip = 4.45 kN).....	133
Figure 39 – Shear versus drift ratio for T3 (1 in. = 25.4 mm, 1 kip = 4.45 kN).....	134
Figure 40 – Shear versus drift ratio for T4 (1 in. = 25.4 mm, 1 kip = 4.45 kN).....	134
Figure 41 – Shear versus drift ratio for T1 indicating fracture of longitudinal bars.....	135
Figure 42 – Shear versus drift ratio for T2 indicating fracture of longitudinal bars.....	135
Figure 43 – Shear versus drift ratio for T3 indicating fracture of longitudinal bars.....	136
Figure 44 – Shear versus drift ratio for T4 indicating fracture of longitudinal bars.....	136
Figure 45 – Map of fractured bars	137
Figure 46 – Wall drift ratio capacity versus uniform elongation of longitudinal reinforcing bars, based on data from Table 7	138
Figure 47 – Wall drift ratio capacity versus fracture elongation of longitudinal reinforcing bars, based on data from Table 7	138
Figure 48 – Wall T1 at 1% drift ratio.....	139
Figure 49 – Wall T2 at 1% drift ratio.....	139
Figure 50 – Wall T3 at 1% drift ratio.....	140
Figure 51 – Wall T4 at 1% drift ratio.....	140
Figure 52 – Wall T1 at 2% drift ratio.....	141
Figure 53 – Wall T2 at 2% drift ratio.....	141
Figure 54 – Wall T3 at 2% drift ratio.....	142
Figure 55 – Wall T4 at 2% drift ratio.....	142
Figure 56 – Wall T1 at 3% drift ratio.....	143
Figure 57 – Wall T2 at 3% drift ratio.....	143
Figure 58 – Wall T3 at 3% drift ratio.....	144
Figure 59 – Wall T4 at 3% drift ratio.....	144
Figure 60 – Wall T1 at 4% drift ratio.....	145
Figure 61 – Wall T2 at 4% drift ratio.....	145
Figure 62 – Wall T3 at 4% drift ratio.....	146
Figure 63 – Wall T4 at 4% drift ratio.....	146
Figure 64 – Wall T1 with bar buckling in unconfined flange during first cycle to 2% drift ratio (stem in tension).....	147
Figure 65 – Wall T2 with bar fracture in unconfined flange at base during first cycle to 2% drift ratio (stem in compression)	147

Figure 66 – Wall T3 with bar buckling in unconfined stem during second cycle to 2% drift ratio (stem in tension).....	148
Figure 67 – Wall T4 without bar buckling or fracture in unconfined flange during second cycle to 2% drift ratio (stem in compression).....	148
Figure 68 – Wall T1 with additional bar buckling in unconfined flange during second cycle to 3% drift ratio (stem in tension)	149
Figure 69 – Wall T2 with bar fracture in confined flange at base during first cycle to 3% drift ratio (stem in compression)	149
Figure 70 – Wall T3 without bar buckling or fracture in unconfined flange during second cycle to 3% drift ratio (stem in compression)	150
Figure 71 – Wall T4 with bar buckling in unconfined flange during second cycle to 3% drift ratio (stem in tension).....	150
Figure 72 – Wall T1 with bar buckling in unconfined stem during first cycle to 4% drift ratio (stem in tension)	151
Figure 73 – Wall T1 with bar fracture in confined stem during first cycle to 4% drift ratio (stem in tension)	151
Figure 74 – Wall T2 at 4% drift ratio.....	152
Figure 75 – Wall T2 at 4% drift ratio.....	152
Figure 76 – Wall T3 with bar buckling in unconfined flange during first cycle to 4% drift ratio (stem in tension).....	153
Figure 77 – Wall T3 with bar fracture in confined stem during first cycle to 4% drift ratio (stem in tension)	153
Figure 78 – Wall T4 with bar fracture in unconfined flange during first cycle to 4% drift ratio (stem in compression)	154
Figure 79 – Wall T4 with bar fracture in confined stem during second cycle to 4% drift ratio (stem in tension)	154
Figure 80 – Condition of confined stem in compression leading to bar buckling before bar fracture in T1	155
Figure 81 – Condition of confined stem in T2	155
Figure 82 – Condition of confined stem in compression leading to bar buckling before bar fracture in T3	156
Figure 83 – Condition of confined stem in compression leading to bar buckling before bar fracture in T4	156
Figure 84 – Condition of stem in T1 at peak of second cycle to 2% drift ratio.....	157
Figure 85 – Condition of stem in T2 at peak of second cycle to 1.5% drift ratio	158
Figure 86 – Condition of stem in T3 at peak of second cycle to 2% drift ratio.....	159
Figure 87 – Condition of stem in T4 at peak of second cycle to 2% drift ratio.....	160
Figure 88 – Top block damage in T1 at 2% drift.....	161
Figure 89 – Measured strain in longitudinal bar at confined stem 18 in. (457 mm) below base of T1.....	162
Figure 90 – Measured strain in longitudinal bar at confined stem 18 in. (457 mm) below base of T2.....	162

Figure 199 – Measured strain in longitudinal bar at unconfined flange 100 in. (2540 mm) above base of T3	217
Figure 200 – Measured strain in longitudinal bar at unconfined flange 100 in. (2540 mm) above base of T4	217
Figure 201 – Measured strain in hoop at confined stem 3 in. (76 mm) above base of T1	218
Figure 202 – Measured strain in hoop at confined stem 3 in. (76 mm) above base of T2	218
Figure 203 – Measured strain in hoop at confined stem 3 in. (76 mm) above base of T3	219
Figure 204 – Measured strain in hoop at confined stem 3 in. (76 mm) above base of T4	219
Figure 205 – Measured strain in hoop at confined stem 3 in. (76 mm) above base of T1	220
Figure 206 – Measured strain in hoop at confined stem 3 in. (76 mm) above base of T2	220
Figure 207 – Measured strain in hoop at confined stem 3 in. (76 mm) above base of T3	221
Figure 208 – Measured strain in hoop at confined stem 3 in. (76 mm) above base of T4	221
Figure 209 – Measured strain in hoop at confined stem 6 in. (152 mm) above base of T1	222
Figure 210 – Measured strain in hoop at confined stem 6 in. (152 mm) above base of T2	222
Figure 211 – Measured strain in hoop at confined stem 6 in. (152 mm) above base of T3	223
Figure 212 – Measured strain in hoop at confined stem 6 in. (152 mm) above base of T4	223
Figure 213 – Measured strain in horizontal bar at unconfined stem 22.5 in. (572 mm) above base of T1	224
Figure 214 – Measured strain in horizontal bar at unconfined stem 22.5 in. (572 mm) above base of T2	224
Figure 215 – Measured strain in horizontal bar at unconfined stem 22.5 in. (572 mm) above base of T3	225
Figure 216 – Measured strain in horizontal bar at unconfined stem 22.5 in. (572 mm) above base of T4	225
Figure 217 – Measured strain in horizontal bar at unconfined stem 52.5 in. (1330 mm) above base of T1	226
Figure 218 – Measured strain in horizontal bar at unconfined stem 52.5 in. (1330 mm) above base of T2	226
Figure 219 – Measured strain in horizontal bar at unconfined stem 52.5 in. (1330 mm) above base of T3	227
Figure 220 – Measured strain in horizontal bar at unconfined stem 52.5 in. (1330 mm) above base of T4	227
Figure 221 – Envelope of measured strain in longitudinal bars at confined stem for 1.5% drift ratio (1 in. = 25.4 mm)	228
Figure 222 – Envelope of measured strain in longitudinal bars at confined stem for 2% drift ratio (1 in. = 25.4 mm)	229
Figure 223 – Envelope of measured strain in longitudinal bars at confined flange for 1.5% drift ratio (1 in. = 25.4 mm)	230
Figure 224 – Envelope of measured strain in longitudinal bars at confined flange for 2% drift ratio (1 in. = 25.4 mm)	231
Figure 225 – Envelope of measured strain in longitudinal bars at unconfined flange for 1.5% drift ratio (1 in. = 25.4 mm)	232
Figure 226 – Envelope of measured strain in longitudinal bars at unconfined flange for 2% drift ratio (1 in. = 25.4 mm)	233
Figure 227 – Calculated concrete strain along Column 1 for stem of T1 (1 in. = 25.4 mm)	234

Figure 265 – Calculated concrete strain in Layer 1 for flange of T2 (1 in. = 25.4 mm).....	272
Figure 266 – Calculated concrete strain in Layer 2 for flange of T2 (1 in. = 25.4 mm).....	273
Figure 267 – Calculated concrete strain in Layer 3 for flange of T2 (1 in. = 25.4 mm).....	274
Figure 268 – Calculated concrete strain in Layer 4 for flange of T2 (1 in. = 25.4 mm).....	275
Figure 269 – Calculated concrete strain in Layer 5 for flange of T2 (1 in. = 25.4 mm).....	276
Figure 270 – Calculated concrete strain in Layer 6 for flange of T2 (1 in. = 25.4 mm).....	277
Figure 271 – Calculated concrete strain in Layer 1 for flange of T3 (1 in. = 25.4 mm).....	278
Figure 272 – Calculated concrete strain in Layer 2 for flange of T3 (1 in. = 25.4 mm).....	279
Figure 273 – Calculated concrete strain in Layer 3 for flange of T3 (1 in. = 25.4 mm).....	280
Figure 274 – Calculated concrete strain in Layer 4 for flange of T3 (1 in. = 25.4 mm).....	281
Figure 275 – Calculated concrete strain in Layer 5 for flange of T3 (1 in. = 25.4 mm).....	282
Figure 276 – Calculated concrete strain in Layer 6 for flange of T3 (1 in. = 25.4 mm).....	283
Figure 277 – Calculated concrete strain in Layer 1 for flange of T4 (1 in. = 25.4 mm).....	284
Figure 278 – Calculated concrete strain in Layer 2 for flange of T4 (1 in. = 25.4 mm).....	285
Figure 279 – Calculated concrete strain in Layer 3 for flange of T4 (1 in. = 25.4 mm).....	286
Figure 280 – Calculated concrete strain in Layer 4 for flange of T4 (1 in. = 25.4 mm).....	287
Figure 281 – Calculated concrete strain in Layer 5 for flange of T4 (1 in. = 25.4 mm).....	288
Figure 282 – Calculated concrete strain in Layer 6 for flange of T4 (1 in. = 25.4 mm).....	289
Figure 283 – Envelope of concrete strain for confined stem at 1.5% drift ratio (data from optical markers along Columns 1 and 2) (1 in. = 25.4 mm).....	290
Figure 284 – Envelope of concrete strain for confined stem at 2% drift ratio (data from optical markers along Columns 1 and 2) (1 in. = 25.4 mm).....	291
Figure 285 – Envelope of concrete strain for confined flange at 1.5% drift ratio (data from optical markers along Column 11) (1 in. = 25.4 mm).....	292
Figure 286 – Envelope of concrete strain for confined flange at 2% drift ratio (data from optical markers along Column 11) (1 in. = 25.4 mm).....	293
Figure 287 – Envelope of concrete strain for unconfined flange at 1.5% drift ratio (data from optical markers along Columns 8, 9, and 10) (1 in. = 25.4 mm).....	294
Figure 288 – Envelope of concrete strain for unconfined flange at 2% drift ratio (data from optical markers along Columns 8, 9, and 10) (1 in. = 25.4 mm).....	295
Figure 289 – Displacement Δ_{shear} due to shear distortion of Layer 2 (1 in. = 25.4 mm).....	296
Figure 290 – General deformed shape of a station.....	296
Figure 291 – Components of angular change for a station.....	296
Figure 292 – Calculated shear distortion for T1 (data from optical markers, Columns 1 through 8) (1 in. = 25.4 mm).....	297
Figure 293 – Calculated shear distortion for T2 (data from optical markers, Columns 1 through 8) (1 in. = 25.4 mm).....	298

Figure 294 – Calculated shear distortion for T3 (data from optical markers, Columns 1 through 8) (1 in. = 25.4 mm)	299
Figure 295 – Calculated shear distortion for T4 (data from optical markers, Columns 1 through 8) (1 in. = 25.4 mm)	300
Figure 296 – Base shearing displacement of T1 based on data from optical markers, see Eq. 18 (1 in. = 25.4 mm)	301
Figure 297 – Base shearing displacement of T2 based on data from optical markers, see Eq. 18 (1 in. = 25.4 mm)	301
Figure 298 – Base shearing displacement of T3 based on data from optical markers, see Eq. 18 (1 in. = 25.4 mm)	302
Figure 299 – Base shearing displacement of T4 based on data from optical markers, see Eq. 18 (1 in. = 25.4 mm)	302
Figure 300 – Calculated flexural rotation for T1 (data from optical markers, Columns 1 and 8) (1 in. = 25.4 mm)	303
Figure 301 – Calculated flexural rotation for T2 (data from optical markers, Columns 1 and 8) (1 in. = 25.4 mm)	304
Figure 302 – Calculated flexural rotation for T3 (data from optical markers, Columns 1 and 8) (1 in. = 25.4 mm)	305
Figure 303 – Calculated flexural rotation for T4 (data from optical markers, Columns 1 and 8) (1 in. = 25.4 mm)	306
Figure 304 – Rotation due to base opening versus drift ratio for T1 (data from optical markers, see Eq. 16)	307
Figure 305 – Rotation due to base opening versus drift ratio for T2 (data from optical markers, see Eq. 16)	307
Figure 306 – Rotation due to base opening versus drift ratio for T3 (data from optical markers, see Eq. 16)	308
Figure 307 – Rotation due to base opening versus drift ratio for T4 (data from optical markers, see Eq. 16)	308
Figure 308 – Contribution of deformation components from bottom 87 in. (2210 mm) for T1	309
Figure 309 – Contribution of deformation components from bottom 87 in. (2210 mm) for T2	310
Figure 310 – Contribution of deformation components from bottom 87 in. (2210 mm) for T3	311
Figure 311 – Contribution of deformation components from bottom 87 in. (2210 mm) for T4	312
Figure 312 – Cumulative contribution of deformation components from bottom 87 in. (2210 mm) for T1 ...	313
Figure 313 – Cumulative contribution of deformation components from bottom 87 in. (2210 mm) for T2 ...	314
Figure 314 – Cumulative contribution of deformation components from bottom 87 in. (2210 mm) for T3 ...	315
Figure 315 – Cumulative contribution of deformation components from bottom 87 in. (2210 mm) for T4 ...	316
Figure 316 – Calculated shear distortion within top 200 in. (5080 mm) for T4 (data from potentiometers).....	317
Figure 317 – Calculated flexural rotation within top 200 in. (5080 mm) for T4 (data from potentiometers)	317
Figure 318 – Measured crack width at peak positive drift (stem in compression) versus drift ratio	318
Figure 319 – Measured crack width at zero shear versus peak positive drift ratio attained (stem in compression) (1 in. = 25.4 mm)	319

Figure 320 – Measured crack width at peak negative drift (stem in tension) versus drift ratio	320
Figure 321 – Measured crack width at zero shear versus peak negative drift ratio attained (stem in tension) (1 in. = 25.4 mm)	321
Figure 322 – Crack width ratio (w_{zero}/w_{peak}) versus drift ratio for positive loading direction (stem in compression)	322
Figure 323 – Crack width ratio (w_{zero}/w_{peak}) versus drift ratio for negative loading direction (stem in tension)	323
Figure 324 – Calculated elongation at zero shear for T1 (data from optical markers, Columns 1 through 8) (1 in. = 25.4 mm)	324
Figure 325 – Calculated elongation at zero shear for T2 (data from optical markers, Columns 1 through 8) (1 in. = 25.4 mm)	324
Figure 326 – Calculated elongation at zero shear for T3 (data from optical markers, Columns 1 through 8) (1 in. = 25.4 mm)	325
Figure 327 – Calculated elongation at zero shear for T4 (data from optical markers, Columns 1 through 8) (1 in. = 25.4 mm)	325
Figure 328 – Idealized force-displacement curve and hysteresis model	326
Figure 329 – Envelope of shear versus drift ratio for T1 (1 in. = 25.4 mm, 1 kip = 4.45 kN)	327
Figure 330 – Envelope of shear versus drift ratio for T2 (1 in. = 25.4 mm, 1 kip = 4.45 kN)	327
Figure 331 – Envelope of shear versus drift ratio for T3 (1 in. = 25.4 mm, 1 kip = 4.45 kN)	328
Figure 332 – Envelope of shear versus drift ratio for T4 (1 in. = 25.4 mm, 1 kip = 4.45 kN)	328
Figure 333 – Envelope of shear versus drift ratio (1 in. = 25.4 mm, 1 kip = 4.45 kN)	329
Figure 334 – Effective initial stiffness K_e normalized by flexural stiffness based on gross moment of inertia I_g	330
Figure 335 – Cracked moment of inertia I_{cr} normalized by gross moment of inertia I_g	330
Figure 336 – Unloading stiffness versus drift ratio (1 in. = 25.4 mm, 1 kip = 4.45 kN)	331
Figure 337 – Normalized unloading stiffness versus drift ratio	331
Figure 338 – Stiffness reducing exponent versus normalized displacement	332
Figure 339 – Shear versus drift ratio for T1, Takeda hysteresis model vs. measured response (1 in. = 25.4 mm, 1 kip = 4.45 kN)	333
Figure 340 – Shear versus drift ratio for T2, Takeda hysteresis model vs. measured response (1 in. = 25.4 mm, 1 kip = 4.45 kN)	333
Figure 341 – Shear versus drift ratio for T3, Takeda hysteresis model vs. measured response (1 in. = 25.4 mm, 1 kip = 4.45 kN)	334
Figure 342 – Shear versus drift ratio for T4, Takeda hysteresis model vs. measured response (1 in. = 25.4 mm, 1 kip = 4.45 kN)	334
Figure 343 – Shear versus drift ratio during second cycle to 1% drift ratio (1 in. = 25.4 mm, 1 kip = 4.45 kN)	335

Figure 344 – Shear versus drift ratio during second cycle to 1.5% drift ratio (1 in. = 25.4 mm, 1 kip = 4.45 kN)	335
Figure 345 – Shear versus drift ratio during second cycle to 2% drift ratio (1 in. = 25.4 mm, 1 kip = 4.45 kN)	336
Figure 346 – Shear versus drift ratio during second cycle to 3% drift ratio (1 in. = 25.4 mm, 1 kip = 4.45 kN)	336
Figure 347 – Hysteretic energy dissipation index E_h	337
Figure 348 – Hysteretic energy dissipation index versus drift ratio	338
Figure 349 – Measured shear versus drift ratio compared with modeling parameters from Table 14 (1 kip = 4.45 kN)	339
Figure 350 – Stress-strain relationships for concrete in compression	340
Figure 351 – Stress-strain relationships for confined and unconfined concrete in compression using parameter values from Table 15	341
Figure 352 – Stress-strain relationships for steel	342
Figure 353 – Comparison of measured steel stress-strain relationships for No. 6 (19) bars with the calibrated strain-hardening model using parameter values from Table 16 (1ksi = 6.89 MPa)	343
Figure 354 – Moment-curvature relationships for T1 (1 in. = 25.4 mm, 1 ft-kips = 1.36 m-kN)	344
Figure 355 – Moment-curvature relationships for T2 (1 in. = 25.4 mm, 1 ft-kips = 1.36 m-kN)	345
Figure 356 – Moment-curvature relationships for T3 (1 in. = 25.4 mm, 1 ft-kips = 1.36 m-kN)	346
Figure 357 – Moment-curvature relationships for T4 (1 in. = 25.4 mm, 1 ft-kips = 1.36 m-kN)	347
Figure 358 – Moment-curvature relationships for all walls (1 in. = 25.4 mm, 1 ft-kips = 1.36 m-kN)	348
Figure 359 – Ratio of test to calculated maximum moment	349
Figure 360 – Ratio of maximum moment from test to calculated nominal moment	349
Figure 361 – Curvature comparisons at relevant events for all walls (1 in. = 25.4 mm)	350
Figure 362 – Idealized curvature distribution for plastic hinge model	351
Figure 363 – Inverse of ϕ_K versus drift ratio for bottom 50 in. (1270 mm) of wall based on data from optical markers	352
Figure 364 – Simplified trend for inverse of ϕ_K versus drift ratio for bottom 50 in. (1270 mm) of wall (data from Figure 363)	353
Figure 365 – Measured and calculated deformation capacities	354
Figure 366 – Calculated deformation capacity for T2 using different values of ℓ_p	355
Figure 367 – Measured and calculated maximum tensile strain of reinforcement	356
Figure 368 – Measured and calculated maximum tensile strain of concrete surface, 14-in. (356-mm) gauge length	356
Figure 369 – Measured and calculated maximum compressive strain of concrete surface, 14-in. (356-mm) gauge length	357
Figure 370 – Average of measured-to-calculated maximum tensile strain of reinforcement	358

Figure 371 – Average of measured-to-calculated maximum tensile strain of concrete surface	358
Figure 372 – Average of measured-to-calculated maximum compressive strain of concrete surface	359
Figure B.1 – Post-yield strain penetration assumptions	372
Figure B.2 – Influence of β_u and β_y on β_ℓ	373
Figure B.3 – Strain penetration amplification factor α_{sp} versus drift ratio, based on Table B.1	373

1 INTRODUCTION

1.1 Motivation

For many years, U.S. building codes for structural concrete^[2,3,4,5,6] have not permitted the use of high-strength reinforcing bars with a nominal yield strength greater than 80 ksi (550 MPa) for purposes other than as transverse reinforcement for confinement. Increased understanding and acceptance of high-strength steel bars would allow designers to reduce the amount of reinforcement used in structural members, resulting in less reinforcement congestion, simpler construction, and reduced cost.

1.2 Objective and Scope

The main objective of this study is to determine experimentally the influence of the tensile-to-yield strength ratio of high-strength reinforcing bars on longitudinal reinforcement strain demands and on the overall behavior of slender T-shaped reinforced concrete walls, including deformation capacity. This investigation also aims to determine the minimum uniform elongation required of high-strength reinforcement used in earthquake-resistant structures. The study of T-shaped walls is important because the shape of the cross-section results in larger longitudinal reinforcement tensile strain demands than in most other members. The effect of replacing conventional Grade 60 (420) reinforcement with a reduced amount of high-strength Grade 100 (690) reinforcement (with nominal yield strength of 100 ksi, or 690 MPa) is evaluated in this study using data from tests of large-scale reinforced concrete walls subjected to reversed cyclic displacements.

1.3 Research Significance

The available literature on the use of high-strength steel bars as concrete reinforcement has focused predominantly on beams and columns. Previous studies have not investigated the cyclic

response of asymmetric concrete walls reinforced with Grade 100 (690) steel bars available in the U.S. The present experimental study seeks to address this knowledge gap.

This research provides test data essential for evaluating the use of high-strength reinforcement in slender concrete walls and for studying the effects of reinforcement mechanical properties on wall deformation capacity, mainly the uniform elongation (strain at peak stress) and tensile-to-yield strength ratio. The study was identified as a high-priority item by ATC 115 in the “Roadmap for the Use of High-Strength Reinforcement in Reinforced Concrete Design”^[19]. The ATC 115 document outlines the research effort needed to incorporate the use of high-strength reinforcement into building design and construction practice. Results of this study are expected to influence proposed changes to the ACI Building Code and ASTM A706^[14], including recommendations for new limits on tensile-to-yield strength ratio, minimum uniform elongation, and minimum fracture elongation of Grade 100 (690) reinforcing bars.

2 BACKGROUND

Reinforced concrete (RC) walls are commonly used as the primary lateral-force-resisting system for buildings in regions of high-seismicity due to their high lateral strength and stiffness. However, construction can be difficult in structures designed for earthquake resistance because of the heavy longitudinal and transverse reinforcement required to ensure adequate deformation capacity and strength (Figure 1). The reinforcement congestion can limit design options and, as a result, performance objectives^[51] are constrained by the materials currently available to engineers.

High-performance structural materials, such as advanced high-strength steel (AHSS)^[90], have the potential to impact the design and construction of RC walls. Metallurgical advances have led to the development of AHSS, a class of steels with yield strengths exceeding 80 ksi (550 MPa) and fracture elongations exceeding 10% (Figure 2), at competitive cost. Use of these materials may lead to significantly reduced reinforcement congestion without compromised performance.

The following is a summary of pertinent literature available on AHSS, the deformation capacity and strength of slender RC walls, and findings from very limited tests of RC walls reinforced with AHSS reinforcement under reversed cyclic displacement demands.

2.1 Advanced High-Strength Steel (AHSS)

Stress-strain curves representative of conventional and high-strength reinforcement are shown in Figure 3 for steel bars readily available in the U.S. and other countries. Reinforcing bars produced in the U.S. generally conform to ASTM specifications A615^[13], A706^[14], or A1035^[15].

Leading design and construction firms have recently moved in the direction of adopting high-strength steel for use in place of conventional Grade 60 (420) reinforcement^[65,66,77]. However, these efforts have been limited by U.S. building codes^[6,10,11,41], which allow only Grade 60 (420) reinforcement for resisting shear, flexure, and axial loads in structures with moderate to high seismic

hazard (although yield stresses up to 100 ksi (690 MPa) are permitted as transverse reinforcement for concrete confinement since the 2008 edition of ACI 318^[4]). The limitations in U.S. building codes reflect a lack of comprehensive research on the use of AHSS in structural elements constructed in accordance with U.S. practice and subjected to seismic-type demands.

Confronted by the limits of conventional construction materials, the U.S. structural engineering community has proposed design guidelines^[1,53] for the use of AHSS in concrete structures. Although this effort has been supported by the research community, significant gaps in the research remain^[19,53]. The focus of this research is on the use of AHSS in reinforced concrete slender walls dominated by flexure, where the term “slender” refers to a wall with a height-to-length ratio equal to or greater than 2.

2.2 Deformation Capacity of Slender Walls

Ensuring adequate deformation capacity is a primary design objective when slender walls participate in the lateral-force-resisting system of structures in areas of high seismic hazard. Early work demonstrated that the deformation capacity of RC walls subjected to inelastic displacement reversals depends on several factors, including cross-section geometry, arrangement of longitudinal and transverse reinforcement in the boundary elements, axial compressive stress, confinement, and shear stress^[26,59,61,68].

The important role of transverse reinforcement (confinement) in improving deformation capacity, through both delayed reinforcement buckling and increased concrete compressive strain capacity, was emphasized by research conducted in the late 1970s^[21,54,55,62,72,80]. Stringent confining reinforcement requirements at wall boundaries were subsequently adopted in the ACI Building Code^[2] in 1983. Although special detailing requirements at wall boundaries aimed at improving deformation capacity, construction of walls conforming to the new provisions was onerous due to the excessive amounts of transverse reinforcement required in boundary elements. Observations

following the 1985 earthquake in Viña del Mar, Chile, coupled with a series of subsequent studies, indicated that the need for confining reinforcement in wall boundary elements is a function of deformation demand^[8,56,63,64,73,89] (i.e., for walls with low axial compressive stress, adequate performance can be obtained with reduced confining reinforcement in stiffer structures). Considerable effort was dedicated to refining confining reinforcement requirements in the ACI Building Code^[3], resulting in new provisions that relate the need for boundary element confining reinforcement to compressive strain demands associated with the design displacement^[78,81,82,83,84,85,87,89]. It is not known to what extent the use of high yield stresses in the design of compression and tension reinforcement affects concrete compressive strain demands and thus, the need for confining reinforcement.

The importance of preventing or delaying shear strength degradation in reinforced concrete members under reversed cyclic loads was shown by research in the 1970s^[20,24,54,56,69,72,86]. Through studies of beams and columns subjected to inelastic displacement reversals^[20,24,69,86], it has been shown that degradation of shear strength is better controlled in members with closely spaced transverse reinforcement, longitudinal reinforcement distributed throughout the depth of the member, lower shear demand, and presence of moderate axial load. Tests of slender wall specimens have shown that walls under high shear stress exhibit diminished deformation capacity when shear-resisting mechanisms degrade under load reversals^[54,56,72]. More recently, it has also been shown^[23,33] that shear-related degradation in walls is a function of longitudinal elongation resulting from cracking and yielding. It is therefore not clear whether the use of AHSS will impact shear strength and stiffness degradation in walls in relation to walls reinforced with conventional steel. This ambiguity results from two conflicting observations: 1) shear strength degradation may be more severe in AHSS reinforced walls because of the lower post-cracking stiffness that is expected when less reinforcement is provided (due to higher yield stress), and 2) AHSS may delay shear strength

degradation because the greater elastic strain (due to higher yield stress) may reduce member elongation at a given drift.

Finally, there is a risk that deformation capacity will be limited by fracture of tensile reinforcement in flanged and lightly reinforced walls^[88]. Although the tensile strain capacity of AHSS is less than conventional Grade 60 (420) steel, it has been shown that high-strength steels exhibit a modulus of toughness and low-cycle fatigue life similar to conventional strength steel in response to axial-strain-controlled reversed cyclic tests with strain amplitudes representative of demands expected in large seismic events^[48]. It is therefore unknown whether fracture of AHSS reinforcement will limit the deformation capacity of slender shear walls. It is important to note that in ACI 318-11^[5] and earlier versions, ASTM A615^[13] Grade 60 (420) reinforcement (with fracture elongations as low as 6%) has been allowed in high seismic regions provided the actual yield strength (f_y) does not exceed the specified yield strength by more than 30%, and that the tensile strength exceeds $1.25f_y$.

2.3 Strength of Slender Walls

Early research indicated that the behavior of slender walls subjected to lateral loads is analogous to the behavior of cantilevered beams^[37,59,60]. Accordingly, provisions in the ACI Building Code^[6] for calculating the strength of walls closely parallel those of frame members.

First principles govern the flexural design of walls, in which a nominal moment is calculated and required to exceed demand by a code-specified margin. In practice, the amount of longitudinal steel required to resist demand is often large, with longitudinal boundary element reinforcement ratios typically between 3 and 5%. Such high reinforcement ratios result in heavily congested reinforcement cages (Figure 1). With AHSS use, reinforcement congestion could be significantly reduced.

The ACI Building Code^[6] equation for calculating the nominal shear stress capacity, v_n , of walls is based on the sum of independent contributions from concrete and transverse reinforcement ($v_n = v_c + v_s$). The contribution of the concrete is $v_c = 2\sqrt{f'_c}$, psi ($0.17\sqrt{f'_c}$ MPa) in walls with a minimum height-to-length ratio of 2.0 (slender walls). It is not known whether the higher longitudinal and transverse strains expected with AHSS reinforcement will affect the capacity of the concrete to resist shear stress in slender walls subjected to inelastic cyclic loading. The contribution of web reinforcement to shear, v_s , is calculated as the product of the horizontal web reinforcement ratio and the yield stress of the reinforcement, $\rho_t f_y$, where ρ_t cannot be less than 0.0025 in walls designed to resist seismic loads, and f_y cannot be taken greater than 60 ksi (420 MPa). The 0.0025 limit is intended to ensure $\rho_t f_y \geq v_c$ ^[26,60], but this condition is only satisfied for concrete strengths up to 5.6 ksi (39 MPa) when $f_y = 60$ ksi (420 MPa). The upper limit of 60 ksi (420 MPa) is imposed because slender walls constructed with AHSS reinforcement have not been tested in the United States. Tests of squat walls^[27] reinforced with Grade 100 (690) steel bars and with transverse reinforcement ratios as low as 0.0015 (but proportioned so that $\rho_t f_y \geq v_c$) showed similar strength and deformation capacity to those of squat walls reinforced with conventional Grade 60 (420) reinforcement.

ACI 318 Building Code^[6] provisions require that the shear strength assigned to an individual wall does not exceed $10\sqrt{f'_c}$, psi ($0.83\sqrt{f'_c}$, MPa). The Code imposes this upper limit because research^[25,26,54,55] has shown that higher shear stresses lead to a higher risk of web-compression failures and reduced deformation capacity. The present study does not address walls with shear stress approaching this upper limit.

2.4 Tests of Slender Walls Reinforced with AHSS

Few tests of AHSS reinforced slender walls are reported in the literature. Tests conducted in Japan^[9,43,44] of walls reinforced with Grade 100 (690) reinforcement generally demonstrated that

AHSS reinforced walls exhibit acceptable strength and deformability. However, the dimensions and reinforcement details used in construction of the specimens do not allow evaluation of critical variables and are not closely representative of U.S. practice. Tests of AHSS reinforced squat walls have been recently reported^[27] and support the use of high-strength reinforcement.

The most relevant tests were reported by Kimura and Ishikawa in 2008^[44]. The specimens were rectangular in cross-section, had a height-to-length ratio of 2, and were subjected to reversed cyclic displacements of increasing magnitude (Figure 4). The specimens were reinforced with Grade 100 (690) reinforcement and subjected to axial loads of either 10 or 15% of $A_g f'_c$. Figure 5 shows the measured shear force versus drift response for the specimen constructed with 15 ksi (105 MPa) concrete and subjected to an axial load of 0.10 $A_g f'_c$. The specimens exhibited drift ratio capacities of 2.0 and 1.5% at axial load levels of 10 and 15% of $A_g f'_c$, respectively, which are consistent with drift capacities exhibited by well detailed wall specimens constructed with Grade 60 (420) reinforcement^[45,78]. These tests demonstrate the utility of AHSS reinforcement in earthquake-resistant concrete walls. In all cases, the drift capacity was limited by compression zone failure characterized by cover spalling, damage to the core, and reinforcement buckling.

Unfortunately, these test results are of limited use to U.S. researchers for the following reasons: 1) excessive transverse reinforcement was provided (the calculated shear capacity exceeded the expected demand by a factor of more than 2.0), 2) strains in the transverse reinforcement and the calculated shear stiffness within the critical plastic hinge were not reported, 3) strains in the compression reinforcement were not reported, 4) specimens were not proportioned to represent conditions where reinforcement tensile strains control the deformation capacity, and 5) the reinforcement used in the specimens were not representative of the range of tensile-to-yield strength ratios of high-strength reinforcement available in the U.S. Therefore, published results do not address

important questions relating to shear strength, stiffness, compressive and tensile strain demands, degradation of shear resisting mechanisms, and effects of reinforcement tensile-to-yield strength ratio.

Other tests^[22,23,30,31,45] of reinforced concrete slender walls with steel bars having yield strengths greater than 60 ksi (420 MPa) have shown drift ratio capacities between 1 and 2%. Although results from these tests are informative, they are of limited use in evaluating the full range of variables necessary to characterize the effect of AHSS use because of the relatively low yield point (80 ksi or 550 MPa, instead of 100 ksi or 690 MPa) and use of boundary element transverse reinforcement amount and detailing not meeting the requirements of ACI 318^[6].

As a result of a paucity of test data on the behavior of AHSS reinforced shear walls, an industry led effort to develop design guidelines for use of AHSS in U.S. practice^[19,53] concluded that tests of slender walls with Grade 100 (690) and 120 (830) reinforcement subjected to displacement reversals in the nonlinear range are necessary to investigate the effects of mechanical properties of reinforcement, transverse and longitudinal reinforcement ratios, boundary element configurations, and axial and shear stress levels. This research will primarily address the effects of mechanical properties of AHSS on wall behavior.

3 EXPERIMENTAL PROGRAM

Results from tests of four large-scale T-shaped walls subjected to reversed cyclic loads are reported. The details of the test program are summarized in Table 1. The control specimen, T1, had Grade 60 (420) reinforcement with a nominal tensile-to-yield strength ratio of 1.35. Walls T2, T3, and T4 had Grade 100 (690) reinforcement with nominal tensile-to-yield strength ratios of 1.15, 1.25, and 1.35, respectively. The walls were 300-in. (7620-mm) tall, 10-in. (254-mm) thick, and had a 100-in. (2540-mm) long stem intersecting a 100-in. (2540-mm) long flange at one end. Figures 6 through 8 show the cross-section and reinforcement layout of the walls and Figures 9 through 12 show details of the confined boundary elements. Reinforcement data and wall section properties are given in Figure 13. A typical elevation view of the walls is shown in Figure 14. The walls were subjected to a loading protocol (Table 2 and Figure 15) based on FEMA 461^[34] with the lateral load applied at a nominal elevation of 300 in. (7620 mm) above the base block for a shear span-to-depth ratio of 3.0. Recorded test data (shear-drift data, strain gauge data, and coordinates of optical markers) are available for download at www.designsafe-ci.org, after publication of the dataset by Huq et al.^[40]

3.1 Specimen Design

The walls were designed so that flexural yielding controlled the strength, which was similar among the specimens. The target flexural strength was derived based on the calculated shear strength associated with the minimum transverse reinforcement ratio ($\rho_t = 0.25\%$) required by ACI 318-14^[6] for structural walls. The walls constructed with Grade 100 (690) reinforcement had a lower longitudinal reinforcement ratio ρ_ℓ than the wall with Grade 60 (420) reinforcement. All walls had nearly the same $\rho_\ell f_y$.

The control specimen T1 was designed to satisfy $0.9M_n \approx 0.6V_n h_w$, where M_n and V_n are the nominal flexural and shear strengths, and h_w is the nominal shear span or distance from the base of the wall to the point of lateral load application (at a nominal height of 300 in. or 7620 mm). The

strength reduction factors of 0.9 for flexure and 0.6 for shear follow the provisions in ACI 318-14^[6] for tension-controlled special structural walls.

The minimum transverse reinforcement was satisfied with two layers of No. 4 (13) bars spaced at 15 in. (380 mm), which resulted in $\rho_t = 0.27\%$ (above the minimum of 0.25%). The transverse reinforcement was anchored with 180-degree hooks because 90-degree hooks, which are more typical in practice, were harder to place within the confined boundary element at this scale. For the following nominal wall dimensions and material properties: $\ell_w = 100$ in. (2540 mm), $t_w = 10$ in. (254 mm), $f'_c = 8$ ksi (55 MPa), $f_y = 60$ ksi (420 MPa), the calculated shear strength of T1 is given by

$$V_n = V_c + V_s = 2\sqrt{f'_c(\text{psi})}\ell_w t_w + \rho_t f_y \ell_w t_w = 339 \text{ kips (1510 kN)} \quad \text{Eq. 1}$$

For walls reinforced with Grade 100 (690) reinforcement, ρ_t was not reduced, which resulted in a greater calculated shear strength. The flexural strength M_n associated with $V_n = 339$ kips (1510 kN) is given by

$$M_n = (0.6/0.9) V_n / h_w = 5650 \text{ ft-kips (7660 m-kN)} \quad \text{Eq. 2}$$

For the reinforcement data shown in Figure 13, the computed nominal flexural strength M_n of the walls is summarized in Table 3, showing a minimum flexural strength of 5610 ft-kips (7610 m-kN) for T1 and 5690 ft-kips (7710 m-kN) for T2, T3, and T4. The minimum flexural strength was controlled by the loading direction that induces compression in the flange, with values approximately 10% lower than those associated with the opposite loading direction. Assuming the width of the wall flange fully effective in compression, the calculated neutral axis depth was less than 3% of the wall depth at the nominal flexural strength, as shown in Table 3. For this condition, the small neutral axis depth resulted in large tensile strain demands on the wall stem reinforcement.

The shear strength was also checked for the maximum probable flexural strength (calculated assuming a maximum steel stress of $1.25 f_y$, $\phi = 1.0$, and stem in compression), resulting in a maximum probable flexural strength of 7630 ft-kips (10300 m-kN) for T1 and 7390 ft-kips (10000 m-kN) for T2, T3, and T4, which induce a maximum shear demand of 305 kips (1360 kN) or an average shear stress slightly below $3.5\sqrt{f'_c}$ (psi), ($0.29\sqrt{f'_c}$ (MPa)) calculated using the area of the stem (1000 in² or 645000 mm²). For this level of shear stress, the required ρ_t for T1 was slightly below the minimum of 0.25% prescribed in Chapter 18 of ACI 318-14^[6] for special structural walls.

All walls complied with ACI 318-14^[6] detailing requirements for special structural walls, with additional restrictions imposed on specimens with Grade 100 (690) bars. The requirement in ACI 318-14^[6] Section 18.7.5.3 that transverse reinforcement spacing not exceed $6d_b$ applies to confined boundary elements in special structural walls with Grade 60 (420) longitudinal bars. The spacing should be reduced to $5d_b$ and $4d_b$ for Grade 80 and 100 (550 and 690) longitudinal bars to maintain a similar buckling stress to yield stress ratio, as recommended in NIST^[53] and ATC 115^[19].

The Euler buckling equation shows that buckling stress is inversely proportional to the square of the unsupported bar length, which is typically expressed as a function of bar diameter d_b . As the grade of reinforcement increases, the unsupported length of the bar must decrease to maintain a similar buckling stress to yield stress ratio. The hoop spacing s_{100} required for Grade 100 (690) longitudinal bars to reach the same buckling-to-yield stress ratio (f_{cr}/f_y) as Grade 60 (420) bars, with $s_{60} = 6d_b$, is obtained by solving

$$\frac{f_{cr}}{f_y} = \frac{\pi^2 E_s}{f_y \left(k \frac{s}{d_b/4}\right)^2} = \frac{\pi^2 E_s}{100 \left(k \frac{s_{100}}{d_b/4}\right)^2} = \frac{\pi^2 E_s}{60 \left(k \frac{6d_b}{d_b/4}\right)^2} \quad \text{Eq. 3}$$

where E_s is the modulus of elasticity of reinforcement and k is the effective length factor. Solving Eq. 3 results in $s_{100} = 4.6d_b$. The value was rounded down to $4d_b$ to account for effects of construction

tolerances, as spacing tolerance has a proportionally greater impact on more tightly spaced hoops. The amount of No. 3 (10) hoops and crossties confining the boundary elements exceeded the requirements of Table 18.10.6.4(f) in ACI 318-14^[6] (for rectilinear hoops) by no more than 10%, except for the confined boundary element in the stem of T2, T3, and T4, where three Grade 100 (690) confining legs were used (instead of the two required) in the direction normal to t_w . This was done to ensure that the three No. 6 (19) longitudinal bars in the extreme layer of the confined boundary element in the stem were supported by either a crosstie or a corner of a hoop in all walls.

3.2 Materials

The specimens were cast using ready-mix concrete provided by a local supplier with a target concrete compressive strength of 8 ksi (55 MPa). The key dates for casting and testing the specimens are listed in Table 4. The concrete mixture proportions shown in Table 5 correspond to the actual concrete cast above the base block in the two wall segments (lift 1 and lift 2) bounded by the construction joints shown in Figure 14. The measured concrete compressive strengths and splitting tensile strengths, listed in Table 6, were obtained from tests of standard concrete cylinders following ASTM standards^[16,17].

The mechanical properties shown in mill certifications for the reinforcing bars used in T1 were compliant with ASTM A706^[14]. Mill certifications for reinforcing bars used in T2, T3, and T4 showed compliance with ASTM A615^[13]. Reinforcing bar mechanical properties (Table 7) were obtained from tensile tests in accordance with ASTM A370^[12]. Reported values correspond to average of two test results. Figures 16 and 17 show representative tensile test data for No. 6 (19) bars used as longitudinal reinforcement in the confined boundary elements and No. 4 (13) bars used as longitudinal and transverse reinforcement in the unconfined regions of the walls. The tensile-to-yield strength ratios of the No. 4 (13) and No. 6 (19) bars were different for each wall. Uniform elongation reported in Table 7 was determined in accordance with ASTM E8^[18]. ASTM E8^[18] includes

two methods for calculating the uniform elongation: 1) elongation at the peak stress, and 2) elongation at the mid-point of a “plateau” consisting of a horizontal line inscribed below the stress-strain relationship at 99.5% of peak stress. Both methods were used, and similar results were obtained. Data reported in Table 7 were based on the second method. All Grade 100 (690) No. 3 (10) bars, used as confining reinforcement (in T2, T3, and T4), were from the same heat of steel.

The No. 4 (13) bar in T2 had the lowest tensile-to-yield strength ratio ($f_t/f_y = 1.10$) and also the lowest uniform elongation ($\epsilon_{su} = 5.7\%$) of all of the bars used in the specimens. In tensile tests, these bars tended to fracture at the base of the lug as shown in Figure 18. The bars had similar deformation geometry as the bars that performed poorly in low cycle fatigue tests recently conducted at the University of Texas^[36]. Figure 19 shows a close-up view of the No. 4 (13) bar that was used in T2 and compares the lug base radius r with the lug height h , resulting in r/h approximately equal to 0.25. Previous studies^[38,42] have shown that r/h has a pronounced effect on the stress concentration factor K_t , especially for cases where $r/h \leq 1.25$. The recent study at the University of Texas^[36] also showed that the bars with low r/h exhibited below average performance in low cycle fatigue tests; coincidentally, the bars with low r/h also had the lowest f_t/f_y and ϵ_{su} when compared with other bars used in their test program.

Table 8 shows the chemical composition of the steel bars used as wall reinforcement. The reported values are based on mill certification documentation (values do not sum to unity because mill certifications do not include all constituent materials). The No. 4 (13) high-strength bars used in T2 had the lowest vanadium content (zero percent versus 0.245 and 0.133 percent for the No. 4 (13) bars used in T3 and T4, respectively) and the highest molybdenum content (0.051 percent versus 0.010 and 0.028 percent for the No. 4 (13) bars used in T3 and T4, respectively). Vanadium increases strength without a negative impact in weldability or notch toughness, whereas molybdenum increases strength but significantly decreases notch toughness. These differences in chemical

composition may have contributed to the fracture of No. 4 (13) bars early in the test of T2, as described in Section 4.1. Tests of additional walls are reported by Huq et al.^[39] that allow comparison between walls reinforced with steel bars differing in chemical composition but having low tensile-to-yield strength ratios ($f_t/f_y < 1.20$).

3.3 Specimen Construction

As indicated in Figure 14, each specimen was constructed in four phases with three construction joints (namely, the base block, Lift 1, Lift 2, and top block). Each construction phase included the assembly of reinforcing bar cages, preparation and erection of wooden formwork, and casting of the concrete. After casting, forms and cylinders were covered with wet burlap and plastic sheets until removal of the forms, which typically occurred three to four days after casting. After forms were removed, all specimens were kept in the laboratory until they were tested. Photos showing various stages of specimen construction are included in Figures 20 through 25.

The wall segments of T1 were constructed using Grade 60 (420) reinforcement, whereas T2, T3, and T4 were constructed using Grade 100 (690) reinforcement. The base block and top block of all specimens were built with nominally identical detailing using Grade 60 (420) reinforcement.

The longitudinal reinforcement of the walls was lap spliced near midheight right above the construction joint between Lift 1 and Lift 2, as shown in Figure 14. The splice lengths exceeded the development length for straight bars calculated following the design equation in ACI 408^[7].

To facilitate marking and visibility of the cracks, all walls were painted white with an oil-based formula between elevations 0 in. and 165 in. (4190 mm) above the base blocks.

3.4 Test Setup and Procedure

3.4.1 Description of Setup

For testing, the specimens were bolted to the laboratory strong floor with fourteen 1.7-in. (43-mm) diameter threaded bars passing through the base block (Figure 26). To distribute the hold-down forces, each of the threaded bars was connected to a steel spreader beam under the strong floor (Figure 27). The top of each wall was connected to two MTS 201.70 Hydraulic Actuators (Figure 26) acting in parallel and spaced 54 in. (1370 mm) apart but at equal distance from the wall stem. Each actuator had a stroke length of 40 in. (1020 mm) and a force capacity of 220 kips (980 kN) in both loading directions. Placing the actuators at the same elevation and on opposite sides of the wall stem allowed for control of twisting at the top of the wall during testing.

Steel fixtures were provided to brace the wall near midheight (at 13' above base block) as shown in Figure 26. Two separate bracing systems were used: 1) internal bracing to prevent instability of the stem or of the flange tips, and 2) external bracing of the stem to prevent global twisting of the wall. The diagonal braces in the internal bracing system were pinned at their ends to allow relative vertical displacements between brace points. The bearing connection between the external bracing and the specimen consisted of nylon pads attached to the end of the external bracing and a mirror-finished steel plate attached to each side of the wall stem.

3.4.2 Instrumentation

The location of the external instrumentation is shown in Figures 28 and 29. Lateral deflection of the top of the specimens, relative to the strong wall, was measured with three string potentiometers installed 10 in. (254 mm) below the plane of action of the actuators. Two of the potentiometers, with a 40-in. (1020-mm) stroke, were spaced 72 in. (1830 mm) apart to record lateral displacement (and twisting) of the specimen. The third potentiometer, with a 20-in. (508-mm) stroke, was centered on the wall stem as a redundant measurement of wall deflection. Two

potentiometers with a 4-in. (102-mm) stroke were mounted 19 in. (483 mm) above the strong floor and spaced 72 in. (1830 mm) apart to measure twisting and sliding of the base block relative to the laboratory floor.

To allow for calculation of wall elongation and flexural rotation, one string potentiometer, with a 20-in. (508-mm) stroke, was attached to the top of the base block near the tip of the wall stem and extended vertically to 100 in. (2540 mm) above the base block. A second potentiometer, with a 4-in. (102-mm) stroke, was connected to the tip of the wall stem at a height of 100 in. (2540 mm) above the base block and extended vertically to a height 10 in. (254 mm) below the plane of action of the actuators. This arrangement of potentiometers was repeated at the exterior face of the wall flange along the centerline of the wall stem (Figures 28 and 29). For T2 and T4, two additional potentiometers were placed in an “X” pattern between elevations of 100 in. (2540 mm) and 270 in. (6860 mm) above the base block to allow for calculation of the shear distortion in the top 200 in. (5080 mm) of the walls (Figure 28).

In addition to potentiometers, an infrared-based non-contact position measurement system was used to record the movement of 93 optical markers (the markers emit infrared light pulses that are detected by cameras, allowing their spatial coordinates to be triangulated at a selected frequency) with an accuracy of approximately 0.004 in. (0.1 mm). Throughout the lower 87 in. (2210 mm) of the wall, the markers were arranged in a 14-in. (356-mm) square grid (nominal dimensions) on one face of the wall stem (Figures 28 and 30) and 14-in. (356-mm) by 16-in. (406-mm) square grid (nominal dimensions) on half of the outside face of the wall flange (Figures 29 and 31). Additional markers were placed on top of the base block to measure movement of the base block (Figure 32).

Longitudinal and transverse reinforcement were instrumented with electrical resistance strain gauges as shown in Figures 33 through 36. Walls T1 and T3 had 28 gauges at the locations

shown in Figures 33 and 35. For T2 and T4, the number of gauges was increased to 35 as shown in Figures 34 and 36.

3.4.3 Loading Protocol

The sequence of displacements imposed on each specimen, shown in Table 2, was patterned after the protocol recommended in FEMA 461^[34]. The loading protocol for the test was displacement controlled, with the two actuators always imposing equal displacements. For each loading step, two cycles of displacements were applied to the top block at increasing amplitudes (Figure 15). The first half cycle of every step (positive drift ratio) induced compression in the stem.

The loading rate for drift ratios up to 0.75% was approximately 0.01 in./sec. (0.25 mm/sec). The rate was increased to 0.02 in./sec (0.51 mm/sec) for a drift ratio of 1%, and to 0.03 in./sec (0.76 mm/sec) for drift ratios greater than 1%. Early in the tests (first two steps in Table 2) displacements were increased until a target force was reached, to overcome imprecision of displacement measurements at small drift ratios. After the first two steps were completed, actuator displacements were increased until target displacements were reached. Prior to testing, several small cycles were imposed (with forces below the cracking force) to facilitate tightening of the threaded rods connecting the base block to the strong floor and the top block to the actuators.

All displacements and drift ratios reported in this study account for the translations and rotations of the base block. However, during the tests, tracking of displacements of the top of the wall neglected the base block rotation (due to uplift). For this reason, the target drift ratios (following the loading protocol) were generally greater than the actual reported drift ratios.

4 EXPERIMENTAL RESULTS AND ANALYSIS

4.1 Measured Shear versus Drift Ratio

The drift ratio, DR , is defined as the top displacement, corrected for movements of the base block (translations and rotations), divided by the height of the wall measured from the top of the base block to the level where the top displacement of the wall was measured, that is

$$DR = \frac{\delta_{top} - \delta_{base}}{h_y} - \theta_{base} \quad \text{Eq. 4}$$

where θ_{base} represents the rotation of the base block about an axis normal to the plane of the wall stem calculated using the positions of markers B1 and B8 (Figure 32); δ_{top} is the displacement measured at the level of the three potentiometers located 10 in. (254 mm) below the plane of action of the actuators; δ_{base} is the average reading of two potentiometers located 8 in. (203 mm) below the top of the base block (Figures 28 and 29) recording the horizontal translation of the base block in the direction of loading; and h_y is the height measured from the top of the base block to the level of the three potentiometers, 290 in. (7370 mm) for T1 and T3 and 287 in. (7290 mm) for T2 and T4. The term δ_{base} was not corrected for base rotation because the effect was negligible.

For drift ratios not exceeding 1%, δ_{top} was taken as the displacement measured with the potentiometer (centered on the wall stem) having a 20-in. (508-mm) stroke as it had better sensitivity to small displacements than the other two potentiometers at the top of the wall. For drift ratios between 1 and 3%, δ_{top} was taken as the average of the displacement readings from all three potentiometers at the top of the wall. Beyond a drift ratio of 3%, the average between the two potentiometers with 40-in. (1020-mm) stroke was used given that the displacements exceeded the range of the 20-in. (508-mm) stroke potentiometer.

The measured shear versus drift ratio for each of the walls is shown in Figures 37 through 40. The same figures are annotated in Figures 41 through 44 to indicate instances of bar fracture. All of the bars that fractured during the tests are identified in Figure 45.

The control specimen, T1, completed one cycle to 4% drift ratio (Step 9 of the loading protocol, Table 2) with less than a 10% drop in strength even though 2 of the 27 No. 6 (19) longitudinal bars in the confined stem fractured while loading to -4% drift ratio (stem in tension). For T1, when -4% drift ratio was reached, the load was briefly maintained for inspection of damage. The specimen was then loaded further in the negative direction (shown as a dotted line in Figures 37 and 41). Additional fracture of bars did not occur up to a drift ratio of -6.0% where the test was stopped due to limitations of the testing apparatus. Buckling of the longitudinal bars preceded bar fracture. Bars near the far edge of the confined stem were first observed to buckle during the second excursion to 3% drift ratio in the positive loading direction and fractured during the first excursion to 4% drift ratio in the negative loading direction.

The measured shear-drift response of T2 is shown in Figures 38 and 42. Wall T2 exhibited fracture of longitudinal bars in both the unconfined flange and stem during the first cycle to +2% drift ratio (Step 7 of the loading protocol, Table 2) that led to nearly 20% loss of strength. Two cycles at 2% drift ratio were completed, followed by an almost total loss of lateral load carrying capacity during the first cycle to +3% drift ratio (stem in compression) due to fracture of all longitudinal bars in one of the confined flange boundary elements. A total of 18 (identified in Figure 45) bars had fractured before the end of the test. Bar buckling was not observed in T2 throughout the test.

Wall T3 completed two cycles to 3% drift ratio (Step 8 of the loading protocol, Table 2) without any major reduction in lateral strength, as shown in Figures 39 and 43. During the first cycle to 4% drift ratio, T3 reached similar lateral force as in the previous cycles for the positive loading direction (stem in compression) but when loaded in the negative direction (stem in tension) several

longitudinal bars in the confined stem fractured. A total of seven No. 6 (19) bars fractured (identified in Figure 45) at a drift ratio of approximately -3% while loading the wall to a drift ratio of -4%. When the wall reached -4% drift ratio, it had lost more than 40% of its lateral strength for the negative loading direction. Similar to T1, buckling of the longitudinal bars in the confined stem of T3 preceded bar fracture. Bar buckling was first observed during the first excursion to +4% drift ratio, leading to bar fracture during the first excursion to -4% drift ratio. A difference between the behaviors of T3 and T1 is the effect of bar fracture on strength loss. Because T3 had fewer stem longitudinal bars than T1 (16 versus 27 No. 6 (19) bars), fracture of a single No. 6 (19) bar in T3 resulted in a larger loss of strength than in T1. This is evident when comparing the first cycle of loading to -4% drift ratio for the two specimens.

Wall T4 completed the first cycle to 4% drift ratio (Step 9 of the loading protocol, Table 2) with similar lateral force as in the previous cycles for each of the loading directions, as shown in Figures 40 and 44. During the first cycle to 4% drift ratio, T4 exhibited fracture of No. 4 (13) longitudinal bars in the unconfined flange when loading in the positive direction (stem in compression). During the second cycle to 4% drift ratio, the No. 6 (19) bars in the confined stem fractured when loading in the negative direction (stem in tension). Prior to bar fracture, buckling of the longitudinal bars at the unconfined flange occurred during the second excursion to -3% drift ratio while for the confined stem bar buckling occurred during the second excursion to +4% drift ratio. Buckling of bars in the confined stem resulted in a lateral strength loss of approximately 15%. Buckling and fracture of the No. 4 (13) bars in the unconfined flange had no observable effect on the lateral strength of the wall. Figure 45(d) identifies the bars that fractured in T4.

The maximum shears resisted by the walls were 303, 282, 275 and 293 kips (1350, 1250, 1220, and 1300 kN) for walls T1, T2, T3, and T4, respectively, as reported in Table 9. Given that the walls were designed to achieve nearly the same flexural strength (with ρf_y approximately constant),

the difference in lateral strength is mostly attributed to the combined effects of the tensile-to-yield strength ratio of the longitudinal reinforcement and the difference between the actual yield strength and the nominal yield strength. As shown in Table 7, the No. 6 (19) Grade 60 (420) bars in the confined boundary elements of T1 had a tensile-to-yield strength ratio of 1.34 and an actual yield strength of 70 ksi (483 MPa). For T2, T3, and T4, the No. 6 (19) Grade 100 (690) bars had tensile-to-yield strength ratios of 1.15, 1.23, and 1.36 with actual yield strengths of 108 ksi (745 MPa), 99 ksi (683 MPa), and 96 ksi (662 MPa), respectively. Walls T1, T3, and T4 reached the maximum shear force at 3% drift ratio while T2 reached the maximum shear force at +1.5% drift ratio because multiple No. 4 (13) longitudinal bars in the unconfined flange and stem fractured during the first excursion to +2% drift ratio.

The failure of T2 at a lower drift ratio compared with the other walls may be due to the following attributes of the No. 4 (13) bars in T2 (refer to Section 3.2): 1) The lowest tensile-to-yield strength ratio of the bars used in this study ($f_t/f_y = 1.10$); 2) the lowest uniform and fracture elongation of the bars used in this study ($\epsilon_{su} = 5.7\%$ and $\epsilon_{sf} = 10.0\%$); 3) the bar deformation pattern had a low lug base radius-to-height ratio ($r/h \leq 0.25$); 4) the lowest vanadium content (0%) and the highest molybdenum content (0.051%) of the high-strength bars used in this study; and 5) the location of strain gauges near the base of the wall could have created a weak spot at the point where the gauge was attached (0.5 in. or 13 mm above the top of the base block).

Figure 46 shows the wall drift ratio capacity (DR_{cap} from Table 9) versus the uniform elongation (ϵ_{su} from Table 7) of the longitudinal reinforcing bars for each wall. The data in Figure 46 suggest that for walls having longitudinal reinforcement with $\epsilon_{su} \geq 6\%$ and $f_t/f_y \geq 1.2$, drift capacity is likely to exceed 3%. Similarly, Figure 47 shows the wall drift capacity versus the fracture elongation ϵ_{sf} (from Table 7) of the longitudinal reinforcing bars for each wall. The figure indicates

that for walls where the longitudinal reinforcement has $\varepsilon_{sf} \geq 10\%$ and $f_t/f_y \geq 1.2$, drift capacity is likely to exceed 3%.

4.2 Progression of Damage

Photographs in Figures 48 through 59 show the condition of walls T1, T2, T3, and T4 at peak displacements during the second cycle to target drift ratios of 1, 2, and 3%. Photographs in Figures 60 through 63 correspond to peak displacements during the first cycle to a target drift ratio of 4%. Horizontal cracking associated with flexure was observed in the confined boundary elements at a vertical spacing of approximately 3 in. (76 mm), which coincided with the spacing of hoops. Inclined cracks were observed in the wall stem along the shear span of the wall. Cracks in the flange between the confined boundary elements and the intersection with the unconfined stem were inclined such that the cracks met the stem-to-flange intersection at a somewhat lower elevation than they met the confined boundary elements at the tips of the flange. These cracks in the unconfined flange were generally spaced at approximately 10 in. (254 mm), a much larger spacing than in the confined boundary elements. The first cracks were due to flexure and occurred at a drift ratio of approximately 0.2%. New cracks developed through drift ratios of 3%, after which the existing cracks continued to widen.

For all walls, concrete cover began to spall off the tip of the stem during the first cycle to a drift ratio of 1%. Buckling of the longitudinal reinforcement near the tip of the confined stem was first observed during the second cycle to a drift ratio of 3% for T1, first cycle to a drift ratio of 4% for T3, and second cycle to a drift ratio of 4% for T4. Bar buckling was not observed in T2. Table 10 identifies the drift cycle and bar location where bar buckling or bar fracture first occurred in each wall. Figures 64 through 83 show most of the events (bar buckling and bar fracture) identified in Table 10. Figures 84 through 87 show the condition of the wall stem (near the base of the wall) at the

peaks of the second cycle to 2% drift ratio for T1, T3, and T4. For T2, the second cycle to 1.5% drift ratio was chosen given that the wall experienced bar fracture during the cycle to 2% drift ratio.

The data from Table 10 indicate that bar fracture of the longitudinal bars of T1, T3, and T4 occurred after the bars had buckled in a previous cycle. However, none of the longitudinal bars that fractured in T2 were preceded by bar buckling (see Figure 45 for a map of fractured bars). The No. 4 (13) bars in the unconfined flange of T2 were the first to fracture, followed by the No. 4 (13) bars in the unconfined stem, eventually leading to fracture of all No. 6 (19) bars in one of the confined flanges. The first fracture occurred at the wide flexural crack at the base of the wall in the vicinity of the stem-flange intersection (shown in Figure 65 after bar fracture), which was reinforced with No. 4 (13) bars having the lowest tensile-to-yield strength ratio ($f_t/f_y = 1.10$) of the test program (Section 3.2 and Table 7). Bars did not fracture in the confined stem of T2.

The No. 4 (13) longitudinal bars in the unconfined stem and flange of T1, T2, and T3 were located outside the transverse reinforcement (Figures 6 and 7) with a clear cover of 1.4 in. (35 mm), as permitted in ACI 318-14^[6]. For T4, the No. 4 (13) longitudinal bars in the unconfined stem and flange were placed inside the transverse reinforcement (Figure 8) with a clear cover of 2.4 in. (60 mm). These No. 4 (13) bars in T4, with greater cover than the other walls, exhibited buckling during the second cycle to 3% drift ratio. In contrast, in walls T1 and T3, these bars buckled during the drift cycles to 2%. Buckling of these No. 4 (13) bars was not observed in T2 due to multiple bar fractures experienced during the drift cycle to 2%, which limited the force resisted by the wall. Although the added concrete cover to the No. 4 (13) longitudinal bars in T4 played a role in delaying buckling, the bars fractured in the cycle that followed bar buckling (as indicated in Table 10).

Wall T1 experienced damage in the top block near the confined flange boundary elements when loaded in the positive direction (flange in tension). The extent of damage was greater in the east flange than in the west flange as seen in Figure 88. Cracking of the top block was first observed

during the first excursion to 1.5% drift ratio (stem in compression). The cracks progressed around the confined flange boundary element reinforcement (i.e., 180-degree hooks of the No. 6 (19) longitudinal bars and the No. 3 (10) boundary element hoops) that extended into the top block according to the detailing shown in Figure 14. This type of damage was not observed in any of the other walls possibly due to a shorter embedment of the hooked No. 6 (19) bars into the top block of T1. The damage was limited to the intersection of the confined flange boundary elements with the top block, reducing the contributions of the flange at the top of the wall.

4.3 Measured Reinforcement Strains

Longitudinal and transverse reinforcement were instrumented with electrical resistance strain gauges at the locations shown in Figures 33 through 36. A total of 28 strain gauges were used in T1 and T3, and 34 strain gauges in T2 and T4. The use of six additional strain gauges in T2 and T4 was in response to the number of gauges that malfunctioned in T1 and T3, which were constructed and tested before T2 and T4. The measured strain data are shown in Figures 89 through 220. All strain gauge data are reported assuming zero strain in the reinforcement at the start of the tests.

4.3.1 Wall Stem Longitudinal Reinforcement

Figures 89 through 104 show the strains measured in the longitudinal reinforcement located in the confined stem below the base of the wall (i.e., inside the base block). The measured strains indicate that for T1 and T4, the longitudinal bars reached values slightly greater than the yield strain at depths of 18 in. (457 mm) into the base block after the wall reached a drift ratio of -2%. The strain gauge data in Figures 100 and 104, recorded at depths of 9 in. (229 mm) into the base block of T4, show strains of approximately 1.5% for a drift ratio of -3%.

Figures 105 through 144 show the strains measured by gauges on the longitudinal reinforcement in the confined stem at four different elevations between 0.5 in. (13 mm) and 100 in. (2540 mm) above the base block. Yielding of the reinforcement in the confined stem at the base of

the walls (0.5 in. or 13 mm above the base block) generally occurred while loading to a target drift ratio of -0.50% or -0.75%, as shown in Figures 105 through 120. Yielding of the longitudinal bars in the confined stem of T1 was also recorded by strain gauges located at 25 in. (635 mm) and 50 in. (1270 mm) above the base block at a drift ratio of approximately -0.5% (Figures 121 and 129). Reinforcement in the confined stem of T2 also showed yield strains at 25 in. (635 mm) above the base block at a drift ratio between -0.6 and -0.7% (Figures 122, 126, 130, and 134). For T3 and T4, yielding of the reinforcement in the confined stem at 25 in. (635 mm) above the base block occurred at a drift ratio between -0.6 and -0.8% (Figures 123, 124, 127, and 128); whereas at 50 in. (1270 mm) above the base block, yielding occurred at a drift ratio between -1% and -1.1% (Figures 131, 132, 135, and 136). Results from strain gauges located at 100 in. (2540 mm) above the base block in the confined stem show strains exceeding the yield strain but the drift ratio where yielding occurred is not apparent.

The largest strains recorded by gauges on the longitudinal bars in the confined stem at the base of the wall (0.5 in. or 13 mm above the base block) during the cycles to 2% drift ratio were approximately 3% for T1 (Figure 113), 7.5% for T2 (Figure 114), and 4% for T4 (Figure 112), with data not available for T3 because the gauges did not function properly. The strain gauge data in Figures 121 through 128 indicate that for all walls, the strain demands in the longitudinal bars in the confined stem at 25 in. (635 mm) above the base block were between 3 and 3.6% during the cycles to a target drift ratio of -2%. At the same level, strains in the confined stem of T4 (Figure 128) reached 5.7% during the cycles to a target drift ratio of 3%.

Strains measured in the instrumented longitudinal bars in the unconfined stem at the base of the wall (0.5 in. or 13 mm above the base block) are shown in Figures 145 through 148. The figures show that yielding occurred at a drift ratio slightly above 0.5% for T1 (Figure 145) and 0.7% for T4 (Figure 148). During the drift cycles to 1.5% (for both directions of loading), strain demands at the

base of the wall (0.5 in. or 13 mm above the base block) were approximately 2% in T1 and T4 (Figures 145 and 148). At 25 in. (635 mm) above the base block, Figures 150 and 152 indicate that yielding of reinforcement occurred at a drift ratio of approximately +0.75% for both T2 and T4. At 50 in. (1270 mm) above the base block, yielding of the reinforcement was observed at a drift ratio of approximately +1.5% for T4 (Figure 156). At the same level, yielding did not occur until approximately +3% drift ratio for T3 (Figure 155). At 100 in. (2540 mm) above the base block, strain gauge data in the unconfined stem did not clearly show the drift ratio where yielding occurred.

4.3.2 Wall Flange Longitudinal Reinforcement

Figures 161 through 184 show the strains recorded by gauges on the longitudinal bars in the confined flange between 0.5 in. (13 mm) and 100 in. (2540 mm) above the base block. The strain gauge data indicate that yielding of the reinforcement at the base of the wall (0.5 in. or 13 mm above the base block) first occurred at a drift ratio of approximately +0.75% for T2 (Figures 162 and 166) and T4 (Figure 168). Strain gauges at this elevation malfunctioned for T1 and T3. Figures 169 through 176 show that at 50 in. (1270 mm) above the base block, yielding of the bars in T1 occurred at a drift ratio near +0.7% (Figure 169), while for T2, T3, and T4, yielding occurred at drift ratios near +1.1% (Figures 170, 175, and 172, respectively). Yielding of the bars at 100 in. (2540 mm) above the base block occurred at drift ratios between 2 and 3%, as indicated in Figures 177 through 184. The data suggest that for walls reaching a drift ratio of +3%, reinforcement yielding occurred throughout the width of the flange and up to an elevation of not less than the wall length.

Figures 185 through 200 show the strain in the bars at the unconfined flange of the walls. For T1 and T2, yielding of the longitudinal reinforcement at the unconfined flange occurred during the cycles to a drift ratio of 0.5% (Figures 185 and 186). The strain demands at the base of the wall of T2 reached 5.6% when approaching a drift ratio of +1% (Figure 186), nearly six times the strain measured in T3 (Figure 187) and T4 (Figure 188) for the same drift ratio. These bars in T2 fractured

at a drift ratio near 1.5% during the first cycle to 2% drift ratio. Yielding of the bars in the unconfined flange in all four walls was recorded by gauges located between 25 in. (635 mm) and 100 in. (2540 mm) above the base block (Figures 189 through 200).

The strain gauge data recorded for the longitudinal reinforcement in the flange (Figures 161 through 200), show maximum strains of approximately 2.7% for T1 (Figure 185), 5.6% for T2 (Figure 186, except strains up to 9% in the confined flange are shown in Figure 162 after bar fracture in the unconfined flange), 4.1% for T3 (Figure 195), and 5.5% for T4 (Figure 196). The longitudinal reinforcement in the flange of T2 experienced bar fracture without prior bar buckling. Flange bars in T4 fractured after buckling in prior cycles. Flange bars did not fracture in T1 or T3 although some exhibited buckling.

4.3.3 Wall Transverse Reinforcement

Figures 201 through 212 show the recorded hoop strains in the confined stem. The data show that the hoops in all four walls did not exceed strains of 0.3% for drift cycles not exceeding 2%. The maximum measured strain in the instrumented hoops of T1 was nearly 0.6% (Figure 201) for a drift ratio of 3%, while for the hoops of T2, T3, and T4 (Figures 202, 203, and 204), the maximum strain was nearly 0.4% for the same drift ratio. It is important to note that all No. 3 (10) hoops in T2, T3, and T4 were made of the same Grade 100 (690) steel, as indicated in Table 7.

Figures 213 through 220 show the strains recorded by gauges on the horizontal bars in the unconfined stem. Horizontal bars located at 52.5 in. (1330 mm) above the base block exhibited a sharp strain increase at a drift ratio of approximately 0.5% in T1, T2, and T3. During cycles up to a target drift ratio of 2%, the recorded strains nearly reached 0.5% in T1 (Figure 217) and 0.4% in T2 and T3 (Figures 214 and 219). The maximum recorded strain at 3% drift ratio for T1 (Figure 217) was approximately 1% and remained less than 0.4% for T3 (Figure 219). This difference suggests a greater contribution (to overall drift) of shear deformations in T1 than the other walls (all walls had

the same transverse reinforcement ratio but different grade). Data for horizontal bars in T4 were not available because the gauges malfunctioned.

4.3.4 Comparisons

Figures 221 through 226 show the envelope of longitudinal reinforcement strains for the various regions of a wall (confined stem, confined flange, and unconfined flange) at the end of the cycles to target drift ratios of 1.5 and 2%. Figure 221 indicates that upon reaching a target drift ratio of 1.5%, the No. 6 (19) bars in the confined stem experienced significantly larger strains in T2 than in the other walls. The larger strains correlate with the lower tensile-to-yield strength ratio ($f_t/f_y = 1.15$) of the No. 6 (19) bars in T2 compared with the ratio for these bars in the other walls, as shown in Table 7. For all walls, the maximum strains in the confined stem at 100 in. (2540 mm) above the base block were very similar (between 0.004 and 0.005) up to a drift ratio of 1.5% (Figure 221), indicating vertical spread of yielding throughout ℓ_w from the base. As drift ratio increased to 2%, T2 had the largest increase in strain at the base of the wall (0.5 in. or 13 mm above the base block), as shown in Figure 222. However, at 25 in. (635 mm) and 50 in. (1270 mm) above the base block, the increase in strain associated with the increase in drift ratio (from 1.5% to 2%), was greater in T1, T3, and T4 than in T2. This indicates a concentration of strain in the longitudinal reinforcement of T2 near the base of the wall as the drift ratio increased.

Figure 223 shows the maximum strains recorded up to target drift ratios of 1.5% for the No. 6 (19) bars in the confined flange, where T2 exhibited larger strains than the other walls for the first 50 in. (1270 mm) above the base block. At 0.5 in. (13 mm) above the base block, the increase in drift ratio from 1.5% to 2% caused a larger strain increase in the bars at the confined flange of T2 than in the bars of the other walls. This is largely due to fracture of the adjacent No. 4 (13) bars in the unconfined flange while loading to 2% drift ratio. At an elevation of 50 in. (1270 mm) and above,

when increasing the drift ratio from 1.5% to 2%, the increase in strain for the bars of T2 was much smaller than for the bars of the other walls, as shown in Figure 224 when compared with Figure 223.

The maximum strains recorded in the No. 4 (13) bars of the unconfined flange are presented for target drift ratios up to 1.5 and 2% in Figures 225 and 226. The data associated with 1.5% drift ratio (Figure 225) suggest that T2 had slightly greater vertical spread of yielding than the other walls for bars in the first 100 in. (2540 mm) above the base block and in the vicinity of the flange-stem intersection. Limited data were available for T1 and T3 due to gauge malfunctions. The data for 2% drift ratio (Figure 226) suggest that T4 had larger strains than T1 and T3 in the unconfined flange throughout the first 100 in. (2540 mm) above the base block. Data for T2 were not available due to fracture of the bars in the unconfined stem and flange during the first excursion to a drift ratio of 2%.

4.4 Concrete Strain Profile

Data from the grid of optical markers shown in Figures 30 and 31 were used to calculate longitudinal (vertical) strains on the surface of the concrete. This surface strain, referred to as concrete strain, was calculated by dividing the change in vertical distance between two consecutive markers by the measured initial distance between the markers (nominally 14 in. or 356 mm). Reported concrete strains therefore represent an average, or smeared, strain on the wall surface. Reinforcing bar strains (Section 4.3) are therefore much greater at cracked sections than the reported concrete strain. Concrete strains were calculated for the peak drift ratio in the second loading cycle in both loading directions for target drift ratios of 1, 1.5, 2, and 3% (concrete strain data are not reported for wall T2 during the 3% drift cycle).

Concrete strains were calculated for both the stem and flange. Longitudinal strains calculated at each of the eight columns of markers on the stem (Figure 30) are shown in Figures 227 through 258 as elevation versus strain. The figures for the stem data show the vertical profile of concrete strains along the surface of the stem. Because each column had seven optical markers, concrete strain

was calculated for six layers distributed over the wall elevation from 3 to 87 in. (76 to 2210 mm) above the base block. The term layer is used to describe the space between two marker rows (e.g., Layer 1 is between marker Rows 1 and 2 as shown in Figures 30 and 31). In Figures 227 through 258, concrete strains are plotted at the midpoint of the respective layers. Flange concrete strains are shown in Figures 259 through 282, although they are presented differently than the stem concrete strains (Figures 227 through 258). The flange strain data are plotted per layer as concrete strain versus horizontal distance from the stem centerline to show the distribution of longitudinal strains along the flange width. Figures 283 through 288 show profiles of the envelope of the calculated concrete strains at peak drift ratio. The envelopes include the maximum and minimum concrete strains from data shown in Figures 227 through 282. The envelopes are shown as elevation versus concrete strain for the confined stem, confined flange, and unconfined flange at target drift ratios of 1.5 and 2%.

4.4.1 Wall Stem Concrete Strains

Concrete strains in the stem of T1, which had No. 6 (19) longitudinal bars with $f_t/f_y = 1.34$, are plotted in Figures 227 through 234. For the stem in tension, at a target drift ratio of -1%, maximum concrete strains in the confined stem (Columns 1 and 2) were between 0.003 in Layer 6 and 0.01 in Layer 1 (Figure 227). Concrete strain generally increased with drift ratio and the largest strain increases were evident near the wall base. The maximum concrete strains in the confined stem of T1 at target drift ratios of -1.5, -2, and -3% were 0.02, 0.025, and 0.037, all occurring in Column 1 located 1.5 in. (38 mm) from the wall edge (Figure 227). The pattern was different in the top-most layer of Columns 1 and 2 (Layer 6, with a centroid at 80 in. or 2030 mm), where concrete strain remained below 0.005 at drift ratios of -1, -1.5, and -2%. In the cycle to -3% drift ratio however, strains in Layer 6 increased significantly to values between 0.015 and 0.02 in Columns 1 and 2, approximately a four-fold increase over the strain at -2% drift ratio. This indicates that a change in behavior occurred during the cycle to -3% drift ratio and caused large strains to extend further from

the base of the wall. This change in behavior coincided with a large increase in transverse web reinforcement strains from 0.0047 to 0.01 (Figure 217) and a large increase in shear deformations within 87 in. (2210 mm) from the base of the wall (see Section 4.5.1). More pronounced inclined cracking during the cycle to -3% drift ratio may therefore have caused large longitudinal strains in the confined boundary element of the stem to extend further from the base. Upon reversal of the loading direction, from stem in tension to stem in compression (-3 to +3% drift ratio), concrete strain demands in the confined boundary element of the stem within the bottom two layers reduced and became negative (compressive) whereas concrete strains in Layer 3 and above did not (Figure 227). Strains in Layer 6 reduced from 0.020 in Figure 227(b) to 0.011 in Figure 227(a) but remained positive (elongation). Therefore, although large positive strains did extend throughout the first 87 in. (2210 mm) from the wall base, only the reinforcement near the wall base underwent large reversals of strain.

Concrete strains in T1 were greater in the confined stem (Columns 1 and 2) than in the unconfined stem (Columns 3 through 7). Strains were nevertheless large throughout much of the unconfined stem. At a drift ratio of 2% for the stem in tension, positive concrete strains between Columns 3 and 5 (Figures 229 through 231) were commonly between 0.01 and 0.025 in Layers 1 through 3. For both directions of loading, most of the unconfined stem showed positive concrete strains (elongation) with slightly greater strains generally for the negative loading direction (stem in tension). This is evident in Figure 230 showing Column 4 with maximum strains of 0.035 (stem in tension) and 0.03 (stem in compression) at peaks of the 3% drift cycle. This is consistent with this region of the wall remaining within the flexural tension zone for both loading directions.

Concrete strains in the stem of T2 (Figures 235 through 242), were more concentrated near the base of the wall than in T1 (Figures 227 and 228). This is evident in Figures 235 and 236, which show the concrete strain profile for the confined stem reinforced with No. 6 (19) longitudinal bars

having $f_t/f_y = 1.15$. For loading cycles to drift ratios of -1 and -1.5% (stem in tension), concrete strains did not exceed 0.006 in Layers 3 through 6 located between 31 and 87 in. (787 and 2210 mm) above the base block, much less than in wall T1 (where strains at these elevations were up to 0.02, as shown in Figure 227). Within the first two layers (up to 31 in. or 787 mm), concrete strains in the confined stem of T2 were approximately 0.016 at the peak of -1.5% drift ratio (Figure 235). In the cycle to -2% drift ratio, concrete strains near the base increased to approximately 0.023 in the first two layers of T2 (Figure 236) and up to 0.017 in Layer 3 (Figures 235 and 236), between 31 in. (787 mm) and 45 in. (1140 mm). In the unconfined stem (Columns 3 through 7) at the peak of 1.5 and 2% drift ratios, the maximum concrete strains in Column 3 within the first two layers of T2 (Figure 237) were larger than in T1 (Figure 229). For these drift ratios and both directions of loading, the concrete strains in the unconfined stem (Column 1) and flange (Column 8), Layer 3 and above, were generally smaller in T2 than in T1. Bar fracture in T2 during the +2% drift cycle caused a significant concentration of deformations at the base of the flange and a drop in the average concrete strain (in relation to the 1.5% drift cycle) above the base of the flange, as shown in Figures 241(a) and 242(a).

Average concrete strains in the stem of T3 are plotted in Figures 243 through 250. The confined stem of T3 had No. 6 (19) longitudinal bars with $f_t/f_y = 1.23$. At a drift ratio of -1% (stem in tension), average concrete strains in the confined stem (Columns 1 and 2) were between 0.003 in Layer 6 and 0.007 in Layer 1. As with T1, strain near the wall base increased with every increase in drift ratio. The maximum concrete strains in the confined stem (Figures 243 and 244) in cycles to drift ratios of -1.5, -2, and -3% were calculated to be 0.018, 0.024, and 0.041, all occurring within the first two layers (Figure 243). Similar to wall T1, in the top-most layer of Columns 1 and 2 (Layer 6, with a centroid at 80 in. or 2030 mm), concrete strains remained below 0.005 at drift ratios of -1, -1.5, and -2%. In the cycle to -3% drift ratio however, concrete strains in Layer 6 of the confined stem increased to 0.013 (Figure 243). The change in behavior noted for T1 was also noted for T3 with an increased contribution of shear deformations to the overall drift during the cycle to 3% drift ratio. As

with T1, the result was an increase in the spread of large concrete strains further from the base of the wall. In the unconfined stem (Columns 3 through 7), the maximum concrete strains in the cycles to drift ratios of +1.5, +2, and +3% were 0.014, 0.026, and 0.044, in Layers 1 through 3 (Figures 248 and 249). The largest concrete strain in the unconfined stem was 0.044 and occurred at a drift ratio of 3% in Layer 3 of Column 7, the column marker close to the stem-flange intersection. Upon reversal of load, Layer 3 of Column 7 had a concrete strain of approximately 0.001, 0.0025, and 0.004 in the cycles to drift ratios of +1.5, +2, and +3%, indicating that the unconfined concrete (and reinforcing bars) near the stem-to-flange intersection underwent very large strain reversals similar in magnitude to the region near the base (Layers 1 and 2) of the confined stem (Columns 1 and 2, Figures 243 and 244). It is therefore not surprising that reinforcement in the unconfined stem buckled (Table 10).

Concrete strains in the stem of T4 are shown in Figures 251 through 258. The longitudinal bars in the confined stem (Columns 1 and 2) of T4 consisted of No. 6 (19) bars with $f_t/f_y = 1.36$. The concrete strain profiles for the stem of T4 were similar to those of T1 and T3. At a drift ratio of -1% (stem in tension), maximum concrete strains occurred in Column 1 with values between 0.004 in Layer 6 and 0.007 in Layer 1 (Figure 251). With every increase in drift ratio, strains generally increased within 87 in. (2210 mm) from the base of the wall. The increase was greater near the wall base. The maximum concrete strain in the confined stem in the cycles to drift ratios of -1.5, -2, and -3% were approximately 0.014, 0.018, and 0.03, all occurring in Column 1 within Layers 1 and 2 (Figure 251). A difference between the concrete strain profiles of T4 and those of T1 and T3 is that concrete strains in Layer 6 of the confined stem was nearly 0.010 (Figure 251) beginning in the cycle to 2% drift ratio, earlier than for the other specimens. The reason for this difference is likely not attributable to f_t/f_y , as the No. 6 (19) bars in T1 and T4 had approximately the same f_t/f_y . The No. 6 (19) bars in T4 did however have a greater tangential modulus immediately after yielding (Figure 16). It is not clear whether this played a role. In the unconfined stem (Columns 3 through 7), the

maximum concrete strains at drift ratios of +1.5, +2, and +3% (stem in compression) were calculated to be 0.016, 0.023, and 0.035 within Layers 1 and 2 (Figures 254 through 257), controlled by data from Column 5 (Figure 255).

4.4.2 Wall Flange Concrete Strains

The profile of longitudinal (vertical) strains across the half-width of the flange and for six layers (Figure 31) above the base block are plotted in Figures 259 through 282 for the four walls. Average concrete strains were approximately constant throughout the width of the flange up to a drift ratio of 1.5% within 87 in. (2210 mm) from the base of the wall. In general, strains in Layers 1 and 2 of the flange exhibited the largest strains with maximum strains ranging between 0.006 and 0.011 for drift ratios of 1% and between 0.016 and 0.023 for drift ratios of 1.5%. Concrete strains in the flange of T1 are shown in Figures 259 through 264 with a maximum strain of 0.026 in Layers 2 and 3 (Figures 260 and 261) during the cycle to 3% drift ratio. Concrete strains remained approximately uniform over the width of the flange throughout other layers further from the wall base. The maximum concrete strains in the flange were 0.018, 0.019, and 0.026 at drift ratios of +1.5, +2, and +3%, approximately 10 to 30% smaller than the strains in the confined stem (0.02, 0.025, and 0.037 at drift ratios of -1.5, -2, and -3%) shown in Figure 227.

In T2, concrete strains were approximately uniform across the width of the flange, throughout the first 87 in. (2210 mm) from the base of the wall, for drift ratios up to +1.5% (Figures 265 through 270). At +2% drift ratio (stem in compression), concrete strains in the confined flange (Column 11 at 48.5 in. or 1230 mm from stem centerline) increased significantly in the first two layers relative to the concrete strains in the unconfined flange with a maximum strain of 0.045 (Figure 265) in the confined flange and 0.01 in the stem-flange intersection. The significant increase in strain was due to fracture of the longitudinal reinforcement at the base of the unconfined flange (below Row 1) during the +2% drift cycle that reduced force demands on the unconfined flange.

Concrete strains shown in Figures 271 through 276 were approximately uniform across the width of the flange in T3 throughout the first 87 in. (2210 mm) from the base of the wall for the duration of the test. This statement is based on consideration of trends in adjacent layers. For example, Figure 271 shows that in Layer 1, at a drift ratio of 3%, the maximum calculated concrete strain was 0.047 in the unconfined flange away from the stem centerline while the strain was 0.035 at the stem centerline. However, Figure 272 shows the opposite trend in Layer 2, where the maximum strain was 0.041 in the stem centerline and 0.024 in the unconfined flange away from the stem centerline. This is likely attributable to localized effects of cracking near markers and not indicative of differences in the global concrete strain profile across the flange width. The maximum concrete strains in the unconfined flange during the loading cycles to drift ratios of +1.5, +2, and +3% were 0.016, 0.027, and 0.047 (Figure 271). These peak strain demands were between 20 to 50% greater than those measured in the confined flange (0.013, 0.021, and 0.033 for loading cycles to drift ratios of +1.5, +2, and +3% in Figure 271).

The concrete strains in the flange of T4 were relatively uniform across the width of the flange and throughout the first 87 in. (2210 mm) from the base of the wall (Figures 277 through 282), even though it was sensitive to localized effects of cracking near individual markers (similar to T3). These localized cracking effects made concrete strains in the unconfined flange appear much larger than in the confined flange in Layer 2 (Figure 278) but smaller than in the confined flange in Layer 3 (Figure 279), with the maximum strains generally occurring in Layer 2. In the loading cycles to drift ratios of +1.5, +2, and +3%, the maximum strains were 0.023, 0.03, and 0.043, occurring in the unconfined flange. These were greater than the concrete strains in the confined stem (0.014, 0.018, and 0.03 in loading cycles to drift ratios of -1.5, -2, and -3%), where strains for drift ratios of -2 and -3% were not available for Row 1 Column 1 (Figure 251) due to concrete spalling.

4.4.3 Comparisons

Figures 283 through 288 show the envelope of concrete strains at target drift ratios of 1.5 and 2% for various regions of the wall (confined stem, confined flange, and unconfined flange). The profiles in these figures show the maximum and minimum concrete strains corresponding to peak drifts attained during the second loading cycle of Steps 6 and 7 (Table 2). Figures 283 and 284 show that at target drift ratios of 1.5 and 2%, concrete strains in Layer 2 of the confined stem in T2 were slightly greater than in the other walls, however, for the upper layers, strains in T2 were generally smaller than in the other walls. The smaller strains in the upper layers were likely attributable to the longitudinal reinforcement in the confined stem of T2 consisting of No. 6 (19) bars with $f_t/f_y = 1.15$, lower than f_t/f_y for the No. 6 (19) bars in the other walls (Table 6).

At a drift ratio of 1.5%, maximum positive strain (elongation) in the confined stem of T1 (Figure 283) was 0.020, slightly greater than the maximum strains of 0.017, 0.019, and 0.014 in the confined stem of T2, T3, and T4, respectively. At the same drift ratio, the maximum positive strain in the confined flange of T1 (Figure 285, stem in compression) was 0.018, also slightly greater than the maximum strains of 0.017, 0.013, and 0.016 in T2, T3, and T4, respectively. The maximum strains for T1 in the unconfined flange (Figure 287) was 0.014 at a drift ratio of 1.5%, smaller than the maximum strains of 0.019, 0.016, and 0.023 for T2, T3, and T4, respectively. The smaller strain in the unconfined flange of T1 is due, in part, to the No. 4 (13) longitudinal bars having tensile-to-yield strength ratio of 1.39 compared with 1.10, 1.21, and 1.20, in T2, T3, and T4, respectively. Similar trends were observed at a target drift ratio of 2% except for the unconfined flange of T2 due to bar fracture.

The envelope of concrete strain data suggests that the concrete strain in the confined stem was similar in magnitude to the strains in the confined and unconfined flange at the peak of loading cycles targeting 1.5 and 2% drift ratio.

Based on sectional analyses, the maximum tensile strain along the stem would be expected to be approximately 20-30% greater than the maximum tensile strain along the flange for a given curvature (tensile strain is theoretically proportional to $d_t - c$). The measured data indicate that the maximum tensile strains in the stem were approximately 10% greater than the maximum tensile strains along the flange (except T2, where large strains were recorded due to bar fractures along the flange). Compressive strains, which are theoretically proportional to c for a given curvature, were expected to be several times greater at the stem than the flange. This was not evident in the test data. The measured maximum compressive strains along the stem and along the flange were highly variable, and in some cases, showing elongation when under compression at the peak of a loading cycle. These observations suggest that for these walls, sectional analyses based on monotonic loading are of limited value and provide estimates of strain disconnected from actual wall behavior.

The concrete strain profiles also appear to be more indicative of the distribution of deformations than the profiles of reinforcement strains, which tended to show larger strains occurring in T2 than in the other walls at most gauge locations within 100 in. (2540 mm) of the base (Figures 221, 223, and 225) for both loading directions. This may be due to the effect of the reinforcement tensile-to-yield strength ratio on the concentration of bar strains near a crack after reinforcement yielding. For a given deformation demand, bars with low f_t/f_y tend to exhibit more strain at cracks than bars with high f_t/f_y .

4.5 Components of Drifts

4.5.1 Shear

Shear deformations were calculated throughout the six layers of the wall bounded by seven rows and eight columns of optical markers placed on the wall stem (Figure 30). The term layer is used to describe the horizontal strip of wall between rows of markers (Figure 289). Shear distortion

was calculated for each rectangular station of the marker grid and then averaged across each horizontal layer.

Shear distortion within a station of the marker grid was calculated from the recorded positions of the four corner markers that defined the station throughout the test. Distortion of a station, illustrated in Figure 290, resulted in changes to angles A , B , C , and D , which were calculated at time k using Eq. 5 through Eq. 8 (based on the law of cosines) from the calculated distances between station corners (Figure 290).

$$A_k = \cos^{-1} \left\{ \frac{h_t^2 + v_l^2 - d_2^2}{2 h_t v_l} \right\} \quad \text{Eq. 5}$$

$$B_k = \cos^{-1} \left\{ \frac{h_t^2 + v_r^2 - d_1^2}{2 h_t v_r} \right\} \quad \text{Eq. 6}$$

$$C_k = \cos^{-1} \left\{ \frac{h_b^2 + v_r^2 - d_2^2}{2 h_b v_r} \right\} \quad \text{Eq. 7}$$

$$D_k = \cos^{-1} \left\{ \frac{h_b^2 + v_l^2 - d_1^2}{2 h_b v_l} \right\} \quad \text{Eq. 8}$$

As shown in Eq. 9 through Eq. 12, the change in angles A_k , B_k , C_k , and D_k (relative to their initial values A_o , B_o , C_o , and D_o) due to deformation of the specimens is attributable to three distinct deformation components: flexural rotation θ , shear distortion γ , and expansion ψ (Figure 291).

$$A_k - A_o = -\theta/2 + \gamma' - \psi \quad \text{Eq. 9}$$

$$B_k - B_o = +\theta/2 - \gamma' - \psi \quad \text{Eq. 10}$$

$$C_k - C_o = +\theta/2 + \gamma' + \psi \quad \text{Eq. 11}$$

$$D_k - D_o = -\theta/2 - \gamma' + \psi \quad \text{Eq. 12}$$

Eq. 9 through Eq. 12 were combined to form Eq. 13, which defines the station shear distortion.

$$\gamma' = \frac{1}{4}[(A_k - A_o) - (B_k - B_o) + (C_k - C_o) - (D_k - D_o)] \quad \text{Eq. 13}$$

This approach assumes uniform curvature within the station, which is a reasonable assumption given that the layer dimension is small (14 in. or 356 mm, which is approximately $1/20 h_w$ and $1/7 \ell_w$).

The shear distortion of a layer was calculated with Eq. 14, which provides a weighted average of the shear distortions for the seven stations comprising one layer. In Eq. 14 subscript i indicates the layer number, subscript j indicates the station number, subscript k indicates the time increment, n_s is the number of stations, and ℓ is the width of the station. Although n_s was typically seven, stations associated with non-functioning markers were omitted from the weighted average. It was common for markers to stop functioning near the end of the test due to severe damage to the concrete surface. Eq. 14 has a negative sign so that positive shear distortion (Figures 289 and 291) coincides with positive drift ratios (stem in compression).

$$\gamma_{i,k} = - \frac{\sum_{j=1}^{n_s} \gamma'_{i,j,k} \ell_j}{\sum_{j=1}^{n_s} \ell_j} \quad \text{Eq. 14}$$

Figures 292 through 295 show the distribution of shear distortion in Layers 1 through 6 for T1, T2, T3, and T4. The shear distortion for a given layer is plotted at the elevation above the base block associated with the midheight of the layer. In each figure, shear distortions are plotted for drift ratios of 1, 1.5, 2, and 3%, where the given shear distortion represents the calculated value (based on Eq. 14) at the peak drift ratio in the second cycle to the target drift.

Figure 292 shows the calculated shear distortions along the wall height for T1. For positive drift ratios (stem in compression), shear distortions were found to be somewhat uniform throughout

the first six layers above the wall base. At drift ratios of 1% and 1.5%, the maximum shear distortions were approximately 0.0025 and 0.005 rad, respectively. For larger drift ratios, shear distortions were largest in Layer 3, with a midpoint located 38 in. (965 mm) above the base block. The shear distortions in this layer were approximately 0.01 and 0.017 rad at drift ratios of +2 and +3%. These calculated shear distortions were relatively large throughout the instrumented region, with the smallest shear distortion at +3% drift ratio being 0.012 rad in Layer 5 (0.013 rad in Layer 1). The distribution and magnitude of shear distortions were somewhat different when the wall was loaded to negative drift ratios (stem in tension). Under negative drift, T1 exhibited large overall shear distortions throughout the instrumented region with the largest distortions occurring near the base of the wall. At -1.5% drift ratio, shear distortions were largest in the first three layers above the base of the wall with a maximum of 0.007 rad. In the upper layers, shear distortion tapered down to 0.0025 rad in Layer 6. At -2 and -3% drift ratios, distortions in the first three layers of the wall were approximately 0.01 and 0.02 rad, with smaller shear distortions higher up the wall.

Shear distortions of T2 in Figure 293 were relatively small during the positive drift cycles (stem in compression), with shear distortion not exceeding 0.006 rad up to a drift ratio of +2%. This is because the shear force demands were smaller for this wall in the second cycle to +2% drift ratio than for other walls due to fracture of bars (during the first cycle to 2%, see Table 10) at the base of the flange. During cycles to negative drift ratios (stem in tension), there was a clear concentration of distortion within the bottom two layers (first 31 in. or 787 mm, of wall). Although at -1% drift ratio the shear distortion was nearly uniform over the height at approximately 0.002 rad, shear distortions increased to about 0.009 and 0.018 rad in Layer 1 for -1.5 and -2% drift ratios. In Layers 3 through 6, shear distortions were nearly uniform and did not exceed 0.005 rad.

Shear distortions for T3 are shown in Figure 294. During early cycles to positive drift ratios (stem in compression), shear distortions were somewhat uniform throughout the first six layers of

the wall. The maximum shear distortions were approximately 0.002 and 0.005 rad at +1 and +1.5% drift ratios, respectively. At +2% drift ratio, shear distortions were slightly greater in the first three layers of the wall, with a maximum of 0.008 rad calculated for Layer 3. At +3% drift ratio, the maximum shear distortions were large, with values of nearly 0.02 rad in Layers 2 and 3. Shear distortion gradually tapered to 0.005 rad in Layer 6. At a negative drift ratio (stem in tension) of -1%, the shear distortions were approximately uniform throughout the first six layers of the wall. The maximum shear distortions were 0.002, 0.005, and 0.009 rad at -1, -1.5 and -2% drift ratios. At -3% drift ratio, the maximum shear distortion was 0.028 rad in Layer 2 with the shear distortion decreasing to 0.013 in Layer 6.

Figure 295 shows the shear distortion along the wall height for T4. During the positive drift ratio (stem in compression), shear distortions were found to be approximately uniform throughout the first six layers of the wall for a drift ratio up to +3%. The maximum shear distortions were approximately 0.003, 0.005, 0.007, and 0.015 rad at +1, +1.5, +2, and +3% drift ratios. During cycles to negative drift ratio (stem in tension), the shear distortions were nearly uniform throughout the first six layers of the wall up to -2% drift ratio. The maximum shear distortions were 0.003, 0.006, and 0.011 rad at -1, -1.5, and -2% drift ratios. At -3% drift ratio, the maximum shear distortion of 0.022 occurred in Layers 5 and 6.

The shear distortions reported above are large, particularly for drift ratios greater than 2%. Experience has shown that shear distortions greater than approximately 0.01 rad in reinforced concrete members under displacement reversals often shortly precede large decreases in shear stiffness and subsequent decay in shear strength^[28]. Figures 292 through 295 suggest a steep decrease in shear stiffness, as shear distortion at 3% drift ratio was often (approximately) double that at 2% drift ratio despite a small increase in shear force (Figures 37 through 40). Shear stiffness

decay did not, however, cause noticeable shear strength decay in these tests, as deformation capacity was limited by longitudinal bar fracture.

4.5.2 Base Shearing

Base shearing was defined as the lateral movement of the wall base (in the direction of loading) relative to that of the base block. It was calculated by subtracting the average displacement of markers on the base block (B1 through B8 in Figure 32) from the average displacement of the markers in Row 1 (Columns 1 through 8 in Figure 30). This definition lumps together the effects of shear distortion and sliding near the wall base and neglects the effects of flexural rotation and expansion.

Figures 296 through 299 show the shear displacement due to base shearing versus drift ratio for T1 through T4. The figures show that when targeting a drift ratio of 3%, base shearing in all walls (except T2) accounted for a displacement not greater than 0.25 in. (6.4 mm). Maximum base shearing values for T1, T3, and T4, at a target drift ratio of 3%, were 0.24, 0.20, and 0.12 in. (6.1, 5.1, and 3.0 mm). For T2, the maximum shearing displacement of 0.34 in. (8.6 mm) was reached during the 2% drift cycle after fracture of the No. 4 (13) longitudinal bars.

4.5.3 Flexure

Flexural rotation was calculated throughout the test for each layer shown in Figure 30 as the difference between the rotation of the marker rows above and below the layer. For a given row of markers, rotation was calculated based on the vertical displacements of the two outermost markers in the row, using

$$\theta_i = \frac{(y_{R_{i+1}C_8} - y_{R_{i+1}C_1})}{\ell_{C_1C_8}} - \frac{(y_{R_iC_8} - y_{R_iC_1})}{\ell_{C_1C_8}} \quad \text{Eq. 15}$$

where θ_i is the flexural rotation of Layer i , y is the change in position of a marker along the longitudinal (vertical) wall axis relative to its initial elevation (indices refer to row and column number, see Figure 30), and $\ell_{C_1C_8}$ is the initial distance along the x-axis between two markers in a row. Typically, the outermost markers were those located in Columns 1 and 8 (Figure 30). In case one of the extreme column markers malfunctioned, markers from Column 2 were used instead of Column 1 and/or markers from Column 7 were used instead of Column 8.

Figures 300 through 303 show the distribution of flexural rotations between 3 and 87 in. (76 and 2210 mm) above the base block of T1, T2, T3, and T4. The flexural rotation calculated for each layer is plotted at the midheight of the layer. The plotted rotation values were calculated for the peak drift ratio in the second cycle to each target drift.

Figure 300 shows the distribution of flexural rotations for T1. During cycles to positive drift ratio (stem in compression), the maximum flexural rotation was calculated to be 0.0007, 0.0019, 0.003 and 0.0045 rad at drift ratios +1, +1.5, +2, and +3%, respectively. These peaks all occurred in Layer 1, near the base. At 3% drift ratio there was a second peak in Layer 4, with a flexural rotation of 0.0036 and flexural rotations less than zero in Layers 5 and 6. Although not certain, it is likely that these results are attributable to localized cracking that caused movement of some of the markers used in the calculation of flexural rotations. During the cycles to negative drift ratio (stem in tension), flexural rotations were largest in Layers 1 through 3, with peak values of 0.0013, 0.0028, 0.0034 and 0.0066 rad at drift ratios of -1, -1.5, -2, and -3%, respectively. These flexural rotation demands were greater than in the positive loading direction.

Flexural rotations for T2 are plotted in Figure 301. During cycles to positive drift ratio (stem in compression), at a drift ratio of +1%, flexural rotation was relatively uniform, with the maximum being approximately 0.0012 rad. At +1.5% drift ratio, the flexural rotation in the first two layers increased to peaks of 0.0023 and 0.0027 rad, significantly greater than in the upper layers. At +2%

drift ratio, flexural rotation in the lower layers decreased to nearly zero. This occurred because rotation was calculated using data from markers placed at the stem-flange intersection, where the longitudinal No. 4 (13) bars in the unconfined flange fractured while loading to +2% drift ratio. This fracture resulted in a drastic concentration of strain at the base of the wall and a reduction in positive strain demands along the stem-flange intersection. During cycles to negative drift ratio (stem in tension), flexural rotation remained uniform in Layers 3 through 6 up to -1.5% drift ratio. Flexural rotation was concentrated in the first two layers with maximum values of 0.002 and 0.0035 rad at -1.5 and -2% drift ratio, respectively.

The vertical distribution of flexural rotations is shown for T3 in Figure 302. While loading to positive drift ratio (stem in compression), flexural rotations were greatest in Layers 1 or 2, where maximum flexural rotations were calculated to be 0.001, 0.0022, 0.0035 and 0.0044 rad at drift ratios of +1, +1.5, +2, and +3%, respectively. During the cycles to negative drift ratio (stem in tension), flexural rotations were greater than those for positive drift ratio. Maximum rotation occurred near the base of the wall in Layer 1 and tapered down in upper layers. The maximum flexural rotations calculated were 0.0011, 0.0028, 0.0036 and 0.0058 at drift ratios of -1, -1.5, -2, and -3%, respectively.

Figure 303 shows the flexural rotations calculated for T4. During cycles to positive drift ratio (stem in compression), flexural rotation increased throughout Layers 1 through 6 with an increase in drift. The increase was higher closer to the base of the wall, similar to T1 and T3. The maximum flexural rotations, which occurred in Layer 2, were calculated to be 0.0017, 0.0033, 0.0041 and 0.0058 rad at drift ratios of +1, +1.5, +2, and +3%, respectively. During the cycles to negative drift ratio (stem in tension), flexural rotations were largest in Layer 1, with calculated maximum flexural rotations of 0.0009, 0.002, 0.0031 and 0.0059 at drift ratios of -1, -1.5, -2, and -3%, respectively.

4.5.4 Opening at the Base of the Wall

Rotations due to opening of a crack at the base of the wall, or base opening, is defined herein as the relative rotation, between the bottom row of markers on the wall (row 1, Figure 30) and those located on the top of the base block (Figure 32), that is

$$\theta_{bo} = \frac{(y_{R_1C_8} - y_{R_1C_1})}{\ell_{C_1C_8}} - \theta_{base} \quad \text{Eq. 16}$$

where θ_{bo} is the base opening rotation, y is the change in position of the marker identified by the subscript, along the vertical y axis, and θ_{base} is the rotation of the base block about an axis normal to the plane of the wall stem (as defined in section 4.1). This definition of base opening includes flexural rotations that occurred within the bottom-most 3 in. (76 mm) of the wall and rotation due to elongation of the bars within the base block.

Figures 304 through 307 show plots of base opening rotation versus drift ratio for the four specimens. For T1, base opening rotation was somewhat proportional to drift ratio up to 2% drift ratio, where the rotation was approximately 0.003 rad in the positive direction (stem in compression) and -0.002 rad in the negative direction (stem in tension). Beyond 2% drift ratio, the rotation did not further increase in the positive loading direction, with a base opening rotation of approximately 0.003 rad at 3% drift ratio. Peak force and deformation demands (measured by opening of the base of the flange) were nearly identical when the wall was loaded from +2 to +3% drift ratio. However, deformation demands did increase at the base of the stem, where base opening rotation changed from approximately -0.002 to -0.003 rad when the wall was loaded from -2% to -3% drift ratio (stem in tension).

Base opening rotation versus drift ratio for T2 is shown in Figure 305. Early in the test, the rotation was nearly proportional and symmetric, similar to T1, up to a maximum of 0.001 rad at 1%

drift ratio. In the second cycle to +1.5% drift ratio, there was a sudden increase in rotation from 0.002 to 0.0032 rad consistent with a sudden increase in tensile strain demands at the base of the flange. This increase led to base opening rotations at 1.5% drift ratio that were nearly 10% larger than in other walls, which is perhaps attributable to the low tensile-to-yield strength ratios of the longitudinal bars used in T2 (Table 7). In the first cycle to +2%, at a drift ratio of approximately +1.5%, there was a large increase in base opening rotation to more than 0.01 rad that coincided with fracture of several No. 4 (13) bars in the unconfined flange. Finally, in the first cycle to +3% drift ratio (stem in compression), base opening rotation rapidly increased to more than 0.03 rad due to fracture of multiple bars, including all No. 6 (19) bars in one of the confined flange boundary elements. A large increase in base opening with a small change in drift ratio is not representative of typical wall behavior, unless bar fracture occurs in the vicinity of the wall-base interface.

Figures 306 and 307 show the base opening rotation of T3 and T4 plotted versus drift ratio. In both specimens, at a drift ratio of 1%, maximum rotations were approximately 0.0015 rad. As drift ratio increased, the base opening rotation due to loading the specimen in the negative direction (stem in tension) increased more than that due to loading the specimen in positive direction (stem in compression). At +2% and -2% drift ratio the rotations were approximately 0.002 and 0.004 rad, respectively. At 3% drift ratio, base opening rotation at positive drift ratio (stem in compression) increased to nearly 0.0035 rad and at negative drift ratio (stem in tension) increased to 0.0055 rad.

Comparisons among specimens indicate that base opening rotations were somewhat smaller in T1 than in specimens with Grade 100 (690) reinforcement. At -3% drift ratio, T1 exhibited a base opening rotation of nearly -0.0035 whereas T3 and T4 exhibited rotations of approximately -0.0055. These differences may be attributable to increased elongation (due to strain penetration) of the high-strength bars within the base. Differences in base opening rotation among specimens were less clear in the positive loading direction (stem in compression), perhaps because the longitudinal

reinforcement in the unconfined flange was the same among the specimens and the total longitudinal reinforcement in the flange exceeded the reinforcement in the confined stem (inducing compression yielding of stem bars, closing of cracks, greater compressive strains, and greater neutral axis depth).

4.5.5 Comparisons

Based on the four deformation components (shear, base shearing, flexure, and base opening) described previously, the relative contributions of each to the total wall drift were calculated for the second cycle of loading to each target drift ratio from 0.5 to 3% (plots for T2 were limited to a drift ratio of 2% because of wall failure).

The total drift due to shear distortion within the region of the wall instrumented with optical markers (Figures 28 through 31) was calculated with Eq. 17. It is based on the sum over n_l layers of the product of average shear distortion γ_i for a given layer and the height h_i of the layer. Six layers ($n_l = 6$) were used, see Figure 30.

$$\Delta_v = \sum_{i=1}^{n_l} \gamma_i h_i \quad \text{Eq. 17}$$

The horizontal displacement of the wall relative to that of the base block, or displacement due to base shearing, was calculated with Eq. 18. The average horizontal displacement of Row 1 markers (Columns 1 through 8) (Figure 30) is referred to as $\Delta_{X_{R1}}$ and the average displacement of markers in the base block (markers B1 through B8) (Figure 32) is referred to as $\Delta_{X_{base}}$. Eq. 18 has a negative sign so that positive base shearing coincides with positive drift ratio (stem in compression).

$$\Delta_{bs} = -(\Delta_{X_{R1}} - \Delta_{X_{base}}) \quad \text{Eq. 18}$$

The total drift due to flexural rotation within the region of the wall instrumented with optical markers (Figures 28 through 31) was calculated with Eq. 19. It is based on the sum over n_l layers ($n_l = 6$) of the product of flexural rotation for a given layer θ_i and the distance $h_{y,i}$, from the potentiometers near the top of the wall to the centroid of that layer. This approach assumes curvature was uniformly distributed within each layer.

$$\Delta_f = \sum_{i=1}^{n_l} \theta_i h_{y,i} \quad \text{Eq. 19}$$

The total drift due to base opening was calculated with Eq. 20, using the product of the rotation due to opening of the base θ_{bo} and the height h_y from the base block to the potentiometers measuring drift (Figure 28). This approach lumps all flexural deformations (including those due to strain penetration) within the first 3 in. (76 mm) of the wall at the base of the wall, where a crack was observed to have formed along the cold joint (elevation +0'-0", Figure 14).

$$\Delta_{bo} = \theta_{bo} h_y \quad \text{Eq. 20}$$

Figures 308 through 311 show the calculated relative contributions to drift, as a percent of total drift, of each deformation component within the bottom 87 in. (2210 mm) of the wall, plotted versus drift ratio. The sum of the relative contributions do not add to 100% because contributions from the top 70% of the wall height is not accounted for. Except for T2 and the positive loading direction of T1, which will be discussed separately below, the specimens showed similar overall behavior in terms of the relative importance of the various components of drift. Flexural rotations were the largest deformation component, accounting for 50 to 70% of total drift for drift ratios between 1 and 3%. Shear distortion accounted for 5 to 20% of overall drift, with the overall

contribution increasing as drift ratio increased (at 1% drift ratio, shear accounted for approximately 5 to 10% of drift whereas the contribution was closer to 15 to 20% at 3% drift ratio). Because shear force demands did not differ much at drift ratios between 1 and 3%, this is consistent with a significant decrease in shear stiffness for drift ratios approaching 3%. Base shearing was not important in these tests, with contributions to overall drift generally less than 5%. The only somewhat notable difference among specimens T1, T3, and T4 in terms of components of drift was the importance of base opening, or rotation between Row 1 of markers and the base block. In the negative loading direction (stem in tension), for drift ratios greater than 1%, base opening accounted for approximately 10% of overall drift of T1 and 20% of overall drift of T3 and T4. This difference is likely attributable to the Grade 100 (690) longitudinal stem bars exhibiting greater slip over their development lengths within the base block than the Grade 60 bars in T1. The difference was less pronounced in the positive loading direction (stem in compression), with base opening accounting for approximately 10 to 15% of overall drift in T1, T3, and T4.

The exceptions to these trends were the results for T2 (both loading directions) and the positive loading direction for T1. For T2, the differences in behavior were due to fracture of flange reinforcement. Up to approximately 1.5% drift ratio, the trends were similar to those for T3 and T4. After some of the No. 4 (13) bars in the unconfined flange fractured, when loading to +2% drift ratio, the contribution of base opening to overall drift was nearly 75% in the positive loading direction (stem in compression), much greater than the typical 10 to 20% range of the other walls. Upon load reversal, a small but notable increase was observed in the contribution of base shearing, perhaps due to reduced stiffness at the wide crack at the base of the flange where bars had fractured. The causes of the somewhat different behavior observed for T1 in the positive loading direction are somewhat less clear. Beginning at approximately +1.5% drift ratio, flexural rotations contributed less to overall drift than in other specimens. In the negative loading direction, which governs the tensile strain

demands imposed on the wall stem, deformation demands in Layers 1 through 6 of T1 were similar to those of other specimens.

The percent contribution of each deformation component to overall drift is plotted again versus drift ratio, but in a cumulative manner, in Figures 312 through 315. As with data plotted in Figures 308 through 311, only deformations that occurred within the bottom-most 87 in. (2210 mm) of the wall were included because that is where the optical markers were located. Because deformations that occurred within the top-most 213 in. (5410 mm) of the wall were omitted, the sum of the considered drift components does not add to 100%.

The total share of overall drift accounted for by deformations within the bottom-most 87 in. (2210 mm) of the wall was smallest at drift ratios of 0.5 to 0.75% and largest at drift ratios of 3% because deformations increasingly concentrated near the wall base after reinforcement yielding. Between 1 and 3% drift ratio, the sum of calculated deformation components accounted for approximately 80 to 100% of overall wall drift except for the positive loading direction of T1.

In the top-most 200 in. (5080 mm) of the walls, deformations remained small throughout the tests. This is shown for T4 in Figures 316 and 317, which have the shear and flexural deformations within the top-most 200 in. (5080 mm) of the wall plotted versus drift ratio. Up to 2% drift ratio, shear and flexural deformations were small (less than 0.2 and 0.3% rad, respectively). Furthermore, flexural rotations appeared to plateau beginning around 1% drift ratio after yielding occurred near the wall base. In the top-most 200 in. (5080 mm) of T1, T2, and T3, shear and flexural deformation data were not available (the instrumentation malfunctioned).

4.6 Crack Widths

The potential for wider cracks at service loads are a concern with the use of smaller amounts of high-strength reinforcement as a replacement for Grade 60 (420) reinforcement. Though small

crack widths are a somewhat less important design aim for earthquake-resisting members, crack widths can be an approximate external measure of damage. Measurements of crack widths were made with crack comparators at four instances during the second cycle of each loading step: peak positive drift ratio, zero shear force, peak negative drift ratio, and again at zero shear force. These crack width data may be useful to those conducting post-earthquake reconnaissance. Measurements were taken at zero shear force to document the extent to which cracks close after unloading. Crack widths were not measured around the whole perimeter of the wall, as one side of the stem and half the flange were obstructed by instrumentation (Figures 28 and 29).

Figures 318 through 321 show the measured crack widths at peak drift plotted against drift ratio. Separate plots show the crack widths measured in the confined and unconfined regions of each specimen. Figure 318 shows that at peak positive drift ratio (stem in compression), walls T1, T2 and T4 had similar crack widths in the confined flange (up to approximately 0.13 in. or 3.3 mm, at 3% drift ratio). Wall T3 had significantly larger crack widths in the confined flange (up to approximately 0.3 in. or 7.6 mm, at 3% drift ratio). In the unconfined flange, crack widths at peak positive drift ratio were generally larger than in the confined flange, and all four specimens exhibited similar crack widths (as expected given that reinforcement ratios were the same in the unconfined regions of the walls). At zero shear force, following peak positive drift ratio, cracks tended to close somewhat in both the confined and unconfined regions of the flange (Figure 319). There was no clear difference between walls with Grade 60 (420) reinforcement and those with Grade 100 (690) in terms of the extent to which cracks closed after unloading. Crack widths in the unconfined flange at zero shear force, which tended to be larger than in the confined flange, were approximately 0.07, 0.13, and 0.20 in. (1.8, 3.3, and 5.1 mm) at target drift ratios of 1.5, 2, and 3%.

In the negative loading direction (stem in tension) walls with Grade 60 (420) and Grade 100 (690) reinforcement again exhibited similar crack widths and a similar degree of recovery after

unloading (Figures 320 and 321). In the confined stem, T3 had the largest crack widths (up to 0.25 in. or 6.4 mm) followed by T1, T4, and T2. In the unconfined stem, all walls exhibited similar crack widths (as expected given that reinforcement ratios were the same in the unconfined regions of the walls). At zero shear force, after reaching peak negative drift, measured crack widths were again smaller than at peak drift and showed no clear difference in behavior between walls with Grade 60 (420) and Grade 100 (690) reinforcement. After reaching target drift ratios of 2%, T1 had a maximum measured crack width in the confined and unconfined stem of 0.13 in. (3.3 mm) at zero shear force (Figure 321), while T3 and T4 had maximum measured values of 0.19 in. (4.8 mm) and 0.13 in. (3.3 mm), respectively.

To evaluate the extent to which cracks close after loading, a crack width ratio was calculated as crack width at zero shear force (w_{zero}) divided by crack width at the preceding peak displacement (w_{peak}). Crack width ratio is plotted in Figure 322 for the confined and unconfined flange for loading in the positive direction and in Figure 323 for the confined and unconfined stem for loading in the negative direction. Based on Figures 322 and 323, for drift ratio cycles at or below 1%, the measured crack widths at zero shear force were about 1/3 of those measured at peak drifts. For drift ratio cycles greater than 1%, the measured crack widths at zero shear force were about 2/3 of those measured at peak drifts. There is no consistent difference in crack width ratio between walls with Grade 60 (420) and Grade 100 (690) reinforcement. In general, for drift ratios greater than 1% in the positive loading direction, walls with Grade 100 (690) reinforcement (except T2) had slightly lower crack width ratios than T1 but no trend was identified in the negative loading direction.

4.7 Wall Elongation

Elongation of each layer of the wall within 87 in. (2210 mm) of the base is plotted in Figures 324 through 327 for all four walls, at target drift ratios of 0.75, 1, 1.5, 2, and 3% (except 3% drift ratio was not included for T2). Elongation was calculated as the change in vertical distance between

markers of consecutive rows at the instance of zero shear force after completing the second cycle to each target drift ratio. Elongation of a layer was then defined as the average elongation calculated for markers in Columns 1 through 8 for that layer (Figure 30). To facilitate comparisons, if a marker was not working in one of the specimens, that marker was omitted from calculations of elongation for all other specimens. Note that the elongation plotted at 1.5 in. (38 mm) above the base of the wall occurred over a 3-in. (76-mm) thick layer (without an assigned layer number) whereas all other elongation data occurred over 14-in. (356-mm) thick layers (Layers 1 through 6, refer to Figure 30).

The figures show that at 1% drift ratio wall elongation per layer was less than approximately 0.05 in. (1.3 mm) in all specimens, indicating that damage and residual deformations were minimal in all specimens. After two cycles to 1.5% drift ratio, the largest elongation per layer observed in each specimen was between 0.09 and 0.12 in. (2.3 and 3.0 mm), with the maximum elongations all occurring within 31 in. (787 mm) of the base. Although the maximum values were similar among specimens at a drift ratio of 1.5%, there were differences: T1, T3, and T4 exhibited elongations per layer between 0.03 and 0.09 in. (0.76 and 2.3 mm) in Layers 3 and 4, at elevations between 31 and 59 in. (787 and 1500 mm), whereas T2 exhibited elongations per layer that were less than 0.03 in. (0.76 mm) for Layers 3 and above. These observations support that plasticity and the associated residual deformations were more concentrated near the base in T2 than in other specimens.

At 2% drift ratio, modest differences were observed between T1, T3, and T4 (excluding T2 because bars fractured when loading to 2% drift ratio). The distributions of residual elongation were similar in T1 and T4, which had similar tensile-to-yield strength ratio for the longitudinal reinforcement ($f_t/f_y=1.34$ and 1.36 for No. 6 (19) bars). After loading to 3% drift ratio, elongations ranged from 0.16 to 0.28 in. (4.1 to 7.1 mm) in T1 and 0.14 to 0.26 in. (3.6 to 6.6 mm) in T4. This contrasts with T3, which exhibited residual elongations ranging from 0.08 to 0.47 in. (2.0 to 12 mm). Wall T3 therefore exhibited more concentrated residual elongation, a measure of damage, than T1 or

T4. This may be attributable to the low tensile-to-yield strength ratios of the longitudinal reinforcement in T3, with $f_t/f_y = 1.23$ for No. 6 (19) bars and 1.21 for No. 4 (13) bars.

4.8 Stiffness

Stiffness is defined as the force required to cause a unit displacement. In this section, stiffness refers to the lateral force required at the top of the wall to move the top a unit distance with respect to the base of the wall. The level for displacement measurement was located 10 in. (254 mm) below the level at which the load was applied, shown in Figure 28 as the plane of action for actuators. For each of the tested walls, stiffness was determined using data from the measured shear versus drift ratio (Figures 37 through 40). Two stiffness measures are presented, the effective initial stiffness K_e and the unloading stiffness K_u . Stiffness K_e represents the secant stiffness to the notional yield point (Δ_y, F_y) generally used in the definition of an idealized force-displacement curve (Figure 328). The unloading stiffness K_u represents the secant stiffness from the maximum displacement of a loading cycle to the point of zero shear force (Figure 328). Both K_e and K_u have been identified as key parameters for numerical models that support the seismic analysis and design of reinforced concrete members [57,76].

4.8.1 Effective Initial Stiffness

The envelope of the measured force-displacement response for each of the four walls is shown in Figures 329 through 332. For each of these figures, the bottom horizontal axis refers to the drift ratio and the top horizontal axis to the displacement measured at the top of the wall (both corrected for movement of the base block), while the vertical axis refers to the shear force applied at the top of the wall. Figure 28 shows the point of application for the lateral load (300 in. or 7620 mm above the base block for T1 and T3, 297 in. or 7540 mm for T2 and T4) and the point of measurement for the lateral displacement (290 in. or 7370 mm for T1 and T3, 287 in. or 7290 mm for T2 and T4).

The coordinates of each data point defining the envelope in Figures 329 through 332 are presented in Table 11. The envelope was determined by identifying the drift ratio (for each loading direction) associated with the peak shear attained for each step of the loading protocol (Table 2).

To allow for a direct comparison of the wall envelopes, data from Figures 329 through 332 are combined in Figure 333. The figure shows that values of V_{max} for each loading direction exceeded the shear (V_{Mn}^+ and V_{Mn}^-) associated with the development of the nominal flexural strength calculated using specified material properties (as reported in Table 3). In the negative loading direction, T2 reached the lowest lateral strength (237 kips or 1050 kN) and in the positive direction, T3 reached the lowest lateral strength (275 kips or 1220 kN), as reported in Table 9. The envelope of T1 exceeds that of other walls mainly due to the higher measured-to-nominal yield strength of its flexural reinforcement, with the No. 6 (19) and No. 4 (13) Grade 60 (420) bars exhibiting actual yield strengths of 70 and 76 ksi (483 and 524 MPa), see Table 7.

The envelope of the measured force-displacement curve was used to determine the effective initial stiffness K_e based on the secant to 80% of the maximum force resisted by the walls in each loading direction. The selection of 80% of the maximum shear force to determine the notional yield point (Δ_y, F_y) is justified based on data shown in Figure 333, where the 80% threshold consistently identified the onset of a significant reduction in stiffness (as measured by the slope of the shear-drift curve). The value of the shear force associated with 80% of the maximum ($V_{0.8}^+$ and $V_{0.8}^-$) and the corresponding secant stiffness (K_e^+ and K_e^-) are shown at the bottom of Table 11. The average value of K_e obtained for T1 was 163 kips/in. (28.5 kN/mm), approximately 40% greater than the average of 115 kips/in. (20.1 kN/mm) obtained for T2, T3, and T4. The values of K_e (which are based on shear-drift measurements) include the effects flexural deformations, shear distortion, and strain penetration. Values of K_e in Table 11 are shown in Figure 334 normalized by the flexural stiffness of a cantilever wall subjected to a single lateral force applied at a distance h_w from support, based on gross section

properties, $K_{f,I_g} = 3 E_c I_g / h_w^3$. The figure shows values of $K_e / K_{f,I_g}$ varying from approximately 1/6 for T1 to approximately 1/9 (on average) for T2, T3, and T4. Figure 334 indicates, K_e for walls with high-strength reinforcement was approximately 70% of K_e for the wall with conventional reinforcement.

The ratio of calculated cracked moment of inertia I_{cr} (calculated based on the measured material properties) to gross moment of inertia I_g for each wall is shown in Figure 335. This ratio clearly only accounts for flexure. On average, I_{cr} / I_g had values of 0.24 for T1 and 0.15 for T2, T3, and T4. Similar to $K_e / K_{f,I_g}$, I_{cr} for walls with high-strength reinforcement was approximately 70% of I_{cr} for the wall with conventional reinforcement.

Stiffness was also calculated accounting for deformations due to flexure, shear, and strain penetration and assuming cracked section properties throughout the height of the wall, as shown in Table 12 (with notations and definitions in APPENDIX A: NOTATION). The ratios of measured-to-calculated stiffness at the bottom of Table 12 ranged between 0.91 and 0.98, with a mean of 0.95 indicating that the calculated stiffness is generally greater than the measured stiffness, consistent with observations by others^[35,74].

Most variables listed in Table 12 are commonly used by practicing engineers, except for ϕ_K and λ . Parameter ϕ_K is a stiffness reduction factor to account for shear cracking and increases the contribution of shear deformations to the overall displacement of the wall. A general expression for ϕ_K is presented in Reference 52 and is proportional to the amount of transverse reinforcement. For low transverse reinforcement ratios, values of ϕ_K may range between 1/20 and 1/10.

Parameter λ is used to define the effective embedment length of the primary flexural reinforcement into the foundation to develop f_y assuming a uniform bond stress. This effective length, calculated as $2\lambda d_b$, is used to estimate rotation at the wall base attributed to strain penetration. The bar is thus assumed to be subjected to an average strain of $\varepsilon_y / 2$ throughout $2\lambda d_b$. Using the design equation for development length in ACI 408^[7], the embedment length corresponding to $\phi = 1$, confined concrete, and actual f_y and f_{cm} , results in $16d_b$, $31d_b$, $27d_b$, and $26d_b$ for T1, T2,

T3, and T4, respectively. On the basis of these calculated values, λ was set to 8, 15, 14, and 13 for T1, T2, T3, and T4 (Table 12). Values of λ as high as 25 have been recommended^[74,75].

4.8.2 Unloading Stiffness

The unloading stiffness, K_u , is defined as the secant stiffness from the maximum drift of a loading cycle to the point of zero shear force (Figure 328). Table 13 contains the measured shear versus drift data used for calculating K_u . The data correspond to the peak drift (and the associated shear force) measured during the second cycles of the loading steps (Table 2) with target drift ratios of 0.75% or greater. Values of K_u in Table 13 are presented in Figure 336 as a function of the target drift ratio, while in Figure 337, K_u is normalized by the flexural stiffness based on gross section properties, $K_{f,lg}$. The data in Figures 336 and 337 suggest a reduction of K_u by a factor of approximately 0.6 for an increase in drift ratio from 1 to 3%.

For reinforced concrete members, K_u is generally defined as a function of the effective initial stiffness K_e ^[57] using

$$K_u = K_e \left(\frac{\Delta_y}{\Delta_{max}} \right)^\alpha \quad \text{Eq. 21}$$

where Δ_y is the notional yield displacement (refer to Section 4.8.1), Δ_{max} is the previously attained maximum displacement in a direction of loading, and α is the stiffness reducing exponent. Separate values of K_u , K_e , Δ_y , and Δ_{max} are assigned to each direction of loading.

The effect of parameter α on several aspects of the calculated seismic response of numerical models is significant, including on response amplitude, response waveform, residual displacement, and hysteresis shape. Parameter α controls the amount of stiffness retained during unloading. For a

perfectly elastoplastic system, $\alpha = 0$. For reinforced concrete, α normally ranges between 0 and 0.5^[57,67].

For each of the tested walls, the value of α was determined for different drift ratios based on Eq. 21 with data from Table 11 for K_e and Δ_y , and from Table 13 for K_u and Δ_{max} . The values of Δ_y are derived from data in Table 11 assuming that the force $V_{0.8}$ defines the notional yield force V_y . The resulting values of α are shown in Figure 338 as a function of Δ_{max}/Δ_y for both directions of loading. For values of Δ_{max}/Δ_y between 2 and 4, the values of α ranged between 0.17 and 0.34 for T1 and between 0.20 and 0.43 for walls reinforced with Grade 100 (690) steel bars.

4.9 Hysteresis

4.9.1 Takeda Model

The measured response of the walls is compared with a force-deformation relationship based on a simplified version of the Takeda hysteresis model^[57, 76]. The model, described in Figure 328, is defined by four parameters: the effective initial stiffness, K_e ; the yield force, F_y ; the post-yield stiffness K_{py} ; and the stiffness reducing exponent, α .

The simplified Takeda model uses a bilinear primary curve with an initial slope K_e and a post-yield slope K_{py} , where a single value of K_e (for each wall) is adopted for both loading directions using the average of the two values of $K_{wall,meas}$ reported in Table 12. The force F_y is obtained from Table 11 using the values associated with $V_{0.8} = 0.8 V_{max}$. The post-yield stiffness K_{py} is defined as a fraction (between 0 and 0.1) of the initial effective stiffness K_e . Values of $K_{py} = 0.05 K_e$ are in reasonable agreement with the measured shear-drift response of walls T1 through T4.

The stiffness reducing exponent α were examined in Section 4.8.2. The data in Figure 338 show that values of α for T1 were slightly lower than those for T2, T3, and T4. Thus, adopting a value of $\alpha = 0.3$ for T1 would imply values of α between 0.3 and 0.4 for the other walls. Figures 339

through 342 compare the measured response with the Takeda model. The figures show reasonable agreement between the breakpoints of the model and the measured response, indicating that the values assigned to the four hysteresis parameters (K_e , F_y , K_{py} , and α) are satisfactory.

The coordinates of the line segments representing the Takeda model were derived following the hysteresis rules defined by Takeda et al.^[76] The initial line segments of the model connect the origin to the yield points, of coordinates $(F_y/K_e, F_y)$ followed by post-yield line segments of slope K_{py} connecting the points representing the peak drift (reported in Table 13) attained during second cycles of each step of the loading protocol (Figure 15). At each peak drift, the model unloads and reloads in the opposite direction following the loading protocol. The unloading line segment is controlled by parameter α , as indicated in Figure 328, while the reloading line segment is controlled by the previously attained maximum displacement. The close agreement between the measured zero-shear displacements and those corresponding to the Takeda model supports the selected values for the model parameters. The last segments of the Takeda model for T2 (Figure 340) deviate considerably from the measured response due to bar fractures at a drift ratio of +1.5% en route to a drift ratio of +2%.

4.9.2 Energy Dissipation

The shear-drift relationships measured during the second cycle to 1, 1.5, 2, and 3% drift ratios are shown in Figures 343 through 346. The data in the figures were used to calculate the hysteretic energy dissipation index^[57] for each of the tested walls using

$$E_h = \left(\frac{W}{\pi \Delta_m V_m} \right) \quad \text{Eq. 22}$$

where W is the amount of hysteretic energy dissipated per half cycle for each loading direction resisting a force V_m at the peak displacement Δ_m , as illustrated in Figure 347. The value of the index

represents the equivalent viscous damping factor of a linear-elastic system capable of dissipating energy W in one cycle under steady-state oscillation^[57]. In reference 57, E_h was defined with a denominator of $2\pi\Delta_m V_m$ to account for W being calculated for a full loading cycle. Figure 348 shows the values of E_h^+ and E_h^- for the positive (stem in compression) and negative (stem in tension) loading directions. For drift ratios of 1, 1.5, 2, and 3%, values of E_h^+ for T1 were 0.11, 0.19, 0.20, and 0.22, respectively, while for T2, T3, and T4 the average E_h^+ for drift ratios of 1, 1.5, 2, and 3% were 0.08, 0.13, 0.17, and 0.21, respectively. For drift ratios of 1, 1.5, 2, and 3%, values of E_h^- for T1 were 0.09, 0.17, 0.18, and 0.19, respectively, while for T2, T3, and T4 the average E_h^- for drift ratios of 1, 1.5, 2, and 3% were 0.07, 0.12, 0.15, and 0.18, respectively.

The above data indicate that for drift ratios between 1 and 2%, the hysteretic energy dissipation index E_h for walls with high-strength reinforcement (T2, T3, and T4) was on average approximately 80% of E_h for the wall with conventional reinforcement (T1). Similarly, data presented in Section 4.8 showed that the value of K_e for walls with high-strength reinforcement was approximately 70% of K_e for the wall with conventional reinforcement. Additional studies are needed to investigate the combined effects of reduced K_e and E_h on the nonlinear seismic response of wall systems with Grade 100 (690) reinforcement.

4.9.3 Modeling Parameters

Basic modeling parameters to define the generalized force-deformation relationship for structural walls are given in ASCE 41 (2017)^[11] for calculating nonlinear seismic response. Table 14 shows the main parameters defining the expected envelope of the hysteretic response following Figure 10-1(a) from ASCE 41 (2017). The envelope is defined by points A through E, where point B represents the effective yield point, point C the strength or peak force, point D the post-peak strength, and point E the loss of strength. The coordinates of these points are given in Table 14 for structural

walls controlled by flexure and subjected to low axial and shear stresses (see footnotes in Table 14) from combined gravity and seismic loading.

Figure 349 compares the measured hysteretic response with the envelopes defined in accordance with Table 14. The plotted data show that the proposed value for effective flexural stiffness (with coefficients of 1/5 for T1 and 1/7 for T2, T3, and T4) and effective shear stiffness (with coefficient of 1/10) are more realistic than those based on ASCE 41 (2017). The proposed coefficients differ from those in Section 4.8.1, where the coefficient only applied to flexural rigidity with the intent of representing the combined effects of deformations due to flexure, shear, and strain penetration with a single coefficient. The line AB in Figure 349 is based on the combined use of the flexural stiffness coefficient (1/5 for Grade 60 and 1/7 for Grade 100) and the shear stiffness coefficient (1/10 for all grades), as shown in Table 14. In ASCE 41 (2017) the flexural stiffness coefficient includes the effects of strain penetration.

The data in Figure 349 also show that for all cases, the measured response intersects the proposed post-yield line between points B and C, while the post-yield line based on ASCE 41 (2017) represents unattainable values. The proposed value of $1.1M_n$ instead of M_{pr} (refer to footnote g in Table 14) provides a reasonable estimate. Regarding the deformation capacity, based on exceeding the horizontal segment defined by points D and E, all walls (except T2) exceeded DE in two consecutive cycles.

Based on the above observations, the modeling parameters in ASCE 41 (2017) for structural walls (subjected to low axial and shear stresses) need to be modified, particularly for values of initial stiffness (coordinates of point B) and strength (coordinates of point C).

5 CALCULATION OF FORCE-DEFORMATION RELATIONSHIPS

5.1 Material Models

5.1.1 Stress-strain Relationships for Concrete in Compression

Idealized stress-strain curves for compressed concrete (unconfined and confined) are shown in Figure 350. The relationships are modified versions of the model proposed by Park et al.^[58] A plateau was used to associate a larger strain with the peak concrete stress following the models proposed by others^[52, 71]. Figure 351 shows the stress-strain curves for confined and unconfined concrete adopted for moment-curvature analyses of T1, T2, T3, and T4. The curves are based on the model in Figure 350 with the parameter values shown in Table 15.

For unconfined concrete, the peak stress f_c'' was taken from the average of the concrete compressive strengths of lifts 1 and 2 (reported in Table 6). The strain ϵ_0 corresponding to the peak stress was defined based on the experimental curves shown by Darwin et al.^[29] for f_c'' from 3,000 psi to 12,000 psi (21 to 83 MPa), where ϵ_0 is nearly a linear function of f_c'' . In Figure 350, the descending slope of the stress-strain curve for unconfined concrete under compression is controlled by the parameter Z , where Z_{uc} and Z_{cc} refer to unconfined concrete and confined concrete. The values of Z in Table 15 were derived considering the experimental data presented by Mander et al.^[49, 50]. The behavior in tension is assumed to be linear up to a tensile strength of $7.5\sqrt{f_c''}$ (psi) ($0.62\sqrt{f_c''}$ (MPa)) with zero post-cracking strength.

Parameter K_{cc} in Figure 350 and Table 15 was based on the modified Kent and Park stress-strain model^[58] using

$$K_{cc} = 1 + \frac{\rho_s f_{yh}}{f_c''} \quad \text{Eq. 23}$$

The peak stress of confined concrete f_{cc}'' was calculated using

$$f_{cc}'' = K_{cc} f_c'' \quad \text{Eq. 24}$$

where ρ_s is the ratio of volume of rectangular steel hoops to volume of concrete core measured to the outside of the peripheral hoop; f_{yh} is the measured yield strength of steel hoops corresponding to No. 3 (10) bars in Table 7.

5.1.2 Stress-Strain Relationships for Reinforcing Steel

Assumed stress-strain relationships for reinforcing steel were based on the actual stress-strain curves (Figure 16) obtained from tests of longitudinal bars. Due to limitations of the moment-curvature program, all longitudinal bars were modeled based on the characteristics of the No. 6 (19) bars.

For each wall, moment-curvature analyses were conducted using two steel models: an elastoplastic model and a strain-hardening model, both representing the No. 6 (19) longitudinal bars. Idealizations of these models are shown in Figure 352. The key parameters defining the shape of the curves are listed in Table 16 with parameter values adjusted to provide a stress-strain curve in close agreement with the measured stress-strain data (Figure 16). Figure 353 shows a comparison between measured (Figure 16) and parametric (Table 16) stress-strain relationships.

5.2 Moment-Curvature Relationships

5.2.1 Assumptions

The computer program QBIAx, developed by Dragovich^[32] for computing biaxial moment-curvature relationships of reinforced concrete sections, was used to calculate monotonic moment-curvature responses. The program operates by discretizing the cross section into a dense array of

subsections with a specified area and centroidal coordinates. Each subsection represents unconfined concrete, confined concrete, or reinforcing steel with their corresponding constitutive relationships. For a target curvature, the program uses an iterative process to determine the neutral axis based on axial force equilibrium. Calculated moment-curvature relationships for walls T1, T2, T3, and T4 are shown in Figures 354 through 358. Concrete and steel properties considered for the analysis are listed in Tables 15 and 16. Axial load was assigned based on the values reported in Table 3. Each wall was analyzed for two loading directions: stem in compression and stem in tension. The wall sections were reinforced according to data shown in Figure 13, and the axial compressive loads were assumed to act at the geometric centroid. The confined concrete in the boundary elements was assumed to extend to the outside of the transverse reinforcement, which had a concrete clear cover of 0.75 in. (19 mm).

Key points identified in Figures 354 through 358 are associated with six events: (1) first yield (where yield strain is reached at extreme tension reinforcement); (2) yield at $0.8\ell_w$ (where yield strain is reached at a distance $0.8\ell_w$ from the extreme compression fiber); (3) flexural strength M_n (where the maximum stress in reinforcing steel is limited to its yield strength and the maximum strain in the compressed concrete is limited to 0.003); (4) compressive strain of 0.01 is reached in the confined concrete; (5) compressive strain of 0.015 is reached in the confined concrete; and (6) uniform elongation ε_{su} is reached at the extreme tension reinforcement.

5.2.2 Moment-Curvature Relationships for Walls with Grade 60 (420) Reinforcement

Moment-curvature data for T1 are shown in Figure 354. As expected, the plotted data show that the computed value of M_n (in accordance with Chapter 22 of ACI 318-14^[6]) is below the maximum moment calculated for each direction of analysis. In the positive loading direction (stem in compression), the maximum curvature was controlled by the maximum usable strain ε_{su} of the No.

4 (13) bars in the unconfined flange. In the negative loading direction (stem in tension), the maximum curvature was limited by ϵ_{su} of the No. 6 (19) bars in the wall stem.

5.2.3 Moment-Curvature Relationships for Walls with Grade 100 (690) Reinforcement

Moment-curvature relationships for T2, T3, and T4 are shown in Figures 355 through 357. For all walls reinforced with Grade 100 (690) reinforcement, regardless of the tensile-to-yield strength ratio (f_t/f_y), the sequence of key events in the plotted data for a given direction was similar. The plotted data show that the computed value of M_n is consistently below the maximum calculated moment for each direction of analysis and regardless of f_t/f_y . These results support the use of M_n based on ACI 318-14^[6] for design of walls with Grade 100 (690) reinforcement.

In the positive loading direction (stem in compression), the maximum curvature was controlled by the maximum usable strain ϵ_{su} of the No. 4 (13) bars in the unconfined flange. In all three walls, the No. 4 (13) bars had a lower maximum usable strain than the No. 6 (19) bars. In the negative loading direction (stem in tension), the maximum curvature was limited by the ϵ_{su} of the No. 6 (19) bars in the wall stem.

5.2.4 Comparisons

For all walls, the computed value of M_n was consistently below the maximum moment calculated for different steel types and loading directions. In the positive loading direction (stem in compression), the curvature associated with bar fracture in the unconfined flange for T1 was more than twice that of walls with Grade 100 (690) reinforcement (T2, T3, and T4). This may be attributed to No. 4 (13) bars in T1 having nearly twice the uniform elongation of the No. 4 (13) bars in the Grade 100 (690) walls. In the negative loading direction (stem in tension), the curvature associated with bar fracture in the confined stem for T1 was approximately 50% more than that of all Grade 100 (690) walls.

To facilitate comparison, Figure 358 overlays moment-curvature plots for all walls. Wall T1 shows greater moment capacity than the other walls mainly due to the actual-to-nominal yield strength ratio of the flexural reinforcement. All walls were proportioned to have nearly identical ρf_y with f_y based on nominal yield strength of 60 ksi (414 MPa) for T1 and 100 ksi (690 MPa) for T2, T3, and T4, see Table 7 for actual yield strengths. Figure 358 also suggests that the slope of the moment-curvature diagram, from the origin to the apparent yield point, is greater for T1 than for the other walls.

Figure 359 shows the maximum measured moment ($V_{max}h_w$) during testing normalized to the maximum calculated moment \bar{M} from moment-curvature analysis. The figure shows that the maximum measured moment did not exceed the maximum calculated moment. The ratios are between 0.9 and 1.0 for the positive loading direction (stem in compression) and between 0.8 and 0.9 for the negative loading direction (stem in tension). The lower ratio in the negative loading direction is most likely due to having each loading cycle start with the positive loading direction (stem in compression). Plastic deformations of the flange reinforcement in tension during positive loading were not fully recovered during negative loading, which affected the contribution of the flange concrete in compression.

The maximum measured moment ($V_{max}h_w$) during testing is normalized to the nominal flexural strength M_n in Figure 360. The maximum measured moment during the test is consistently greater than the calculated nominal strength for all walls, except for T2 in the negative loading direction (stem in tension). This is due to the failure of the wall in the other direction (stem in compression) before reaching the full capacity in the negative loading direction (stem in tension).

Figure 361 shows the curvatures calculated at relevant events for all walls in both loading directions. In the positive loading direction the sequence of relevant events was similar for all specimens (yield point, nominal flexural strength M_n , confined core at strains of 0.01 and 0.015, and

reinforcement at uniform elongation ε_{su}). However, in the negative loading direction (stem in tension), the sequence of relevant events for T1 (yield point, nominal flexural strength M_n , and reinforcement at uniform elongation ε_{su}) was different than that of T2, T3, and T4, where curvature for M_n exceeded the curvature for ε_{su} . It is important to note that the curvature corresponding to M_n is based on an elastoplastic model for the reinforcing steel. Using a more realistic strain-hardening model (see Figures 355 through 357) shows that the curvature associated with $M = M_n$ are appreciably smaller than those obtained with an elastoplastic model.

5.3 Deformation Capacity

5.3.1 Assumptions

A general simplified model was used to evaluate the deformation capacity of the walls. The model was based on the plastic hinge model illustrated in Figure 362, where flexural deformations consider elastic and plastic curvatures. The model relies on the calculated monotonic flexural response (from moment-curvature analysis) of wall cross sections.

For the cantilever wall represented in Figure 362, the plastic hinge model is used to determine the lateral displacement at a distance h_w from the support. Figure 362 (b) shows the curvature distribution assuming a triangular moment diagram, with maximum moments at the support, and linear-elastic behavior up to yielding of the tension reinforcement. The drift $\Delta_{f,y}$ associated with the yield curvature ϕ_y is obtained using

$$\Delta_{f,y} = \phi_y h_w^2 / 3 \quad \text{Eq. 25}$$

The yield curvature is taken from the moment-curvature diagram assuming the reinforcement yield strain is reached at a distance $0.8\ell_w$ from the extreme compression fiber.

Loading the member beyond flexural yielding is assumed to induce plastic curvature over the plastic hinge length ℓ_p . Based on Figure 362 (c), the drift $\Delta_{f,p}$ corresponding to the plastic curvature is defined by

$$\Delta_{f,p} = (\phi_u - \phi_y) \ell_p \left(h_w - \frac{\ell_p}{2} \right) \quad \text{Eq. 26}$$

where ϕ_u is the maximum curvature reached at the support. A variety of different expressions have been proposed for ℓ_p , primarily as a function of ℓ_w and the shear span ratio ℓ_w/h_w . The simple expression $\ell_p = 0.5\ell_w$ or $0.3\ell_w$ is adopted here, where ℓ_w is the length of wall section in the direction of the shear force. A value of $0.5\ell_w$ is commonly used when considering only deformations due to flexure, while $0.3\ell_w$ is more appropriate when adding the effects of shear and strain penetration. The use of $0.3\ell_w$ corresponds to a linear distribution of curvature from ϕ_y to ϕ_u over a length of approximately $0.2h_w$, which provides a plastic rotation of $0.5(\phi_u - \phi_y)0.6\ell_w$ for $h_w/\ell_w = 3$.

Based on the displacements associated with the elastic and plastic curvatures, the total deformation due to flexure Δ_f is obtained using

$$\Delta_f = \Delta_{f,y} + \Delta_{f,p} \quad \text{Eq. 27}$$

To account for the displacement due to shear distortion Δ_v along the shear span, Eq. 28 was used. It allows for different effective shear stiffnesses for the elastic and plastic regions of the wall.

$$\Delta_v = \frac{V_u}{A_{cv} G_c} \left(\frac{\ell_p}{\phi_{K,bot}} + \frac{h_w - \ell_p}{\phi_{K,top}} \right) \quad \text{Eq. 28}$$

where V_u is the shear force corresponding to the moment associated with the limiting curvature ϕ_u . The average shear distortion in the bottom 50 in. (127 mm) of each wall (Figures 292 through 295) was used to estimate $\phi_{K,bot}$. Figure 363 shows that the effective $\phi_{K,bot}$ varied with increases in drift ratio and differed in the positive and negative loading directions. Based on the proposed relationship between $\phi_{K,bot}$ and drift ratio shown in Figure 364, $\phi_{K,bot}$ was taken as 1/100 for all walls. This value of $\phi_{K,bot}$ was used in estimations of deformation capacity because the calculated deformation capacities were close to 3%. For $\phi_{K,top}$ a value of 1/10 was used for all four walls, consistent with the recommended value in Table 12 for determining the effective stiffness of the walls.

To account for the displacement due to effects of strain penetration, the derivation in APPENDIX B provides

$$\Delta_{sp} = \alpha_{sp} \lambda d_b \phi_y h_w \quad \text{Eq. 29}$$

where ϕ_y is the yield curvature, d_b is the diameter of the primary longitudinal reinforcement, and λ is the number of bar diameters over which reinforcement strain is assumed to occur uniformly to develop f_y . Considering all three sources of deformation: flexure (f), shear (v), and strain penetration (sp), the deformation capacity Δ_{cap} is determined using

$$\Delta_{cap} = \Delta_f + \Delta_v + \Delta_{sp} \quad \text{Eq. 30}$$

where Δ_f , Δ_v , and Δ_{sp} are based on Eqs. 27, 28, and 29, respectively.

5.3.2 Deformation Capacity of T-Shaped Walls

The deformation capacity of T1, T3, and T4 was controlled by bar fracture in the confined stem due to loading in the negative direction (stem in tension). Except for T2, bar fracture was preceded by bar buckling (see Section 4.2). Given that the moment-curvature analysis is limited to monotonic loading and does not account for bar buckling, the moment-curvature data were used with special limitations for estimating the deformation capacity of walls subjected to cyclic loading. Considering that the deformation capacity of walls T1, T3, and T4 was controlled by the negative loading direction (stem in tension) due to bar fracture (following bar buckling), the deformation capacity was determined by limiting the compressive strain in the confined core of the stem for the positive loading direction.

Deformation capacity of the walls was calculated using two methods. The first method was based only on deformations due to flexure (Δ_f). For this method, the concrete compressive strain in the confined core ($\varepsilon_{c,core}$) was limited to 0.015 [79]. The curvature ϕ_u associated with a strain of 0.015 in the confined stem was used to calculate the deformation capacity of the wall based on Eq. 27. The deformation capacity (based on flexure only) was calculated using a plastic hinge length of $\ell_p = 0.5 \ell_w$. The key parameters used in this method are listed in Table 18.

The second method calculates the deformation capacity using contributions from flexure, shear, and strain penetration. Considering the additional contributions of deformations due to shear and strain penetration, the contribution of flexural deformations was limited to the use of a plastic hinge length of $\ell_p = 0.3 \ell_w$. The key parameters used in this method are listed in Table 19.

5.3.3 Comparisons

The calculated deformation capacities for each wall are compared to the measured deformation capacity in Figure 365. The data show that the calculated deformation capacities were conservative for T1, T3, and T4. In general, the calculated deformation capacity based on flexure only was approximately 10% greater than the deformation capacity based on combined flexure, shear, and strain penetration, indicating that the use of $\ell_p = 0.5 \ell_w$ instead of $0.3 \ell_w$ compensates for neglecting deformations due to shear and strain penetration. However, the two methods failed to provide a conservative estimate for the deformation capacity of T2. The relatively low measured deformation capacity of T2 is related to the low tensile-to-yield strength ratio ($f_t/f_y = 1.1$) of the No. 4 (13) longitudinal bars. A plausible explanation is that the low value of f_t/f_y reduced the plastic hinge length ℓ_p for T2. Figure 366 shows the deformation capacity of T2 based on a reduced plastic hinge length. The figure shows that a value of ℓ_p between $0.1 \ell_w$ and $0.3 \ell_w$ is required for a conservative estimate of the deformation capacity of T2.

5.4 Strain-Drift Relationships

5.4.1 Assumptions

The plastic hinge model was used to calculate the maximum strains associated with a target displacement to compare with the maximum measured strains. The measured strain data were taken from reinforcement strain gauge data and concrete strain data reported in Chapter 4. The data associated with target drift ratios of 1.5 and 2% were selected given that most of the gauges stopped working for target drift ratios greater than 2%.

To calculate strain for a specific target drift ratio Δ_{target} , it is necessary to determine the associated curvature ϕ' from

$$\Delta_{target} = \phi_y h_w^2/3 + (\phi' - \phi_y) \ell_p \left(h_w - \frac{\ell_p}{2} \right) + \frac{V}{A_{cv} G_c} \left(\frac{\ell_p}{\phi_{K,bot}} + \frac{h_w - \ell_p}{\phi_{K,top}} \right) + \alpha_{sp} \lambda d_b \phi_y h_w \quad \text{Eq. 31}$$

where deformations due to flexure, shear, and strain penetration are accounted for, and $\ell_p = 0.3 \ell_w$.

The value of α_{sp} in Eq. 31 is estimated based on data in Figure B.3 using

$$\alpha_{sp} = 2DR \quad \text{Eq. 32}$$

where DR is the drift ratio (in percent) limited to values between 1 and 2%, for which α_{sp} varies between 2 and 4.

Alternatively, the curvature ϕ' may be derived from

$$\Delta_{target} = \phi_y h_w^2/3 + (\phi' - \phi_y) \ell_p \left(h_w - \frac{\ell_p}{2} \right) \quad \text{Eq. 33}$$

where only deformations due to flexure are accounted for, and $\ell_p = 0.5 \ell_w$.

From Eq. 31 or Eq. 33, the strain corresponding to the specific target drift ratio Δ_{target} is determined with the combined use of ϕ' and the depth of the neutral axis (corresponding to ϕ').

5.4.2 Strain-Drift Relationships of T-shaped Walls

Calculated strains for T1, T3, and T4 when subjected to drift ratios between 1 and 2% (in both loading directions) are shown in Figures 367 through 369. Figure 367 shows the comparison of maximum calculated reinforcement tensile strains with maximum measured strains (based on strain

gauge data). The figure shows data for three walls and four drift ratios, for a total of 12 cases. In 10 out of 12 cases, the measured strains were greater than the calculated strains. The data in Figure 367 clearly indicate that the plastic hinge model is inappropriate for estimating strains in the longitudinal reinforcement. Maximum reinforcement strains were generally underestimated, with average measured-to-calculated maximum tensile strains approaching 1.3. The result is not surprising given the numerous limitations of the model, including an inability to capture reinforcement strain concentrations at cracks and member elongation under repeated inelastic cyclic loading.

Figure 368 shows a comparison of maximum calculated concrete tensile strains with maximum measured concrete surface strains (based on optical markers). The calculated maximum tensile strains of concrete were generally greater than the measured strain, suggesting that the plastic hinge model is appropriate for estimating the strains on the concrete surface. Similarly, Figure 369 shows the comparison of maximum calculated concrete compressive strains with maximum measured concrete surface strains. The plotted data show that the calculated concrete compressive strains were significantly lower than the strains measured in the stem (for positive drift ratios) but much closer to the strains measured in the flange (for negative drift ratios).

The observations noted above regarding Figures 367 through 369 are also supported with the average of measured-to-calculated strain ratios reported in Figures 370 through 372.

6 CONCLUDING REMARKS

Results were reported from tests of four large-scale T-shaped reinforced concrete shear walls (T1, T2, T3, and T4) subjected to reversed cyclic displacements. All specimens had the same nominal concrete compressive strength and wall dimensions, and nearly the same nominal flexural strength. The walls were designed so that flexural yielding controlled their lateral strength and induced an average shear stress not exceeding $3.5\sqrt{f'_c}$, psi ($0.29\sqrt{f'_c}$, MPa).

The walls were not subjected to externally applied axial loads other than the weight of the testing apparatus and self-weight. Wall T1 was constructed with conventional Grade 60 (420) reinforcement and T2, T3, and T4 were constructed with high-strength Grade 100 (690) reinforcement. Wall T1 had flexural reinforcement with tensile-to-yield strength ratios (f_t/f_y) of 1.34 and 1.39 for the No. 6 (19) and No. 4 (13) bars, respectively. Walls with Grade 100 (690) reinforcement had f_t/f_y of 1.15 and 1.10 for T2, 1.23 and 1.21 for T3, and 1.36 and 1.20 for T4. All No. 6 (19) bars were placed in boundary elements confined by No. 3 (10) transverse reinforcement at 3-in. (76-mm) spacing of the same grade as the flexural reinforcement.

The main findings and observations from these tests are summarized as follows:

- 1) Based on limited experimental results, it is recommended that Grade 100 (690) reinforcement used in earthquake-resistant design satisfy a tensile-to-yield strength ratio (f_t/f_y) ≥ 1.2 , uniform elongation (ϵ_{su}) $\geq 6\%$, and fracture elongation (ϵ_{sf}) $\geq 10\%$.
- 2) Walls designed for a target flexural strength using Grade 60 (420) or Grade 100 (690) reinforcement with similar f_t/f_y for the primary flexural reinforcement had similar strength and deformation capacity. This is evidenced by T1 and T4, which had a minimum drift ratio capacity of 3.7 and 3.9%, respectively.

- 3) The drift ratio associated with longitudinal bar fracture was not strongly correlated with either the uniform or fracture elongation of the reinforcement (Table 20). The No. 6 (19) longitudinal bars in the confined boundary elements of T1, T3, and T4 fractured during a cycle to 4% drift ratio after buckling in prior loading cycles. The drift ratio capacity of T2 was limited by fracture of No. 4 (13) bars in the unconfined flange (without prior buckling) during a cycle to 2% drift ratio that eventually led to fracture of No. 6 (19) bars in the confined flange during a cycle to 3% drift ratio. Several factors were identified as possibly causing the early fracture of the No. 4 (13) bars in T2, these include: low f_t/f_y (1.10), low ϵ_{su} (5.7%), and low lug base radius-to-height ratio (≤ 0.25).
- 4) Bar buckling occurred despite having the confining reinforcement spaced at four times the longitudinal bar diameter (i.e., 3-in. or 76-mm spacing). Bar buckling was first observed in the confined stem during a cycle to 3% drift ratio in T1 and during a cycle to 4% drift ratio in T3 and T4. Minor spalling was first observed in all four walls at the base of the confined stem during the cycles to 1% drift ratio.
- 5) Buckling of longitudinal bars in regions not confined by closely spaced transverse reinforcement was delayed in the wall with additional concrete cover (T4). In the unconfined stem and flange of the walls, buckling of No. 4 (13) longitudinal bars was first observed during a cycle to 2% drift ratio in T1 and T3, which had the longitudinal bars (with clear cover of 1-3/8 in. or 35 mm) placed outside the transverse reinforcement, and during a cycle to 3% drift ratio in T4, which had the transverse reinforcement placed outside the longitudinal bars (with clear cover of 2-3/8 in. or 60 mm). Buckling of the No. 4 (13) longitudinal bars had no observable effect on wall strength or deformation capacity.
- 6) For slender T-shaped walls with low axial loads, consideration of flexural cracking alone is not sufficient to estimate the effective initial stiffness K_e (the value of K_e was determined using the secant to the measured force-displacement curve at 80% of the maximum force). Comparisons of

the measured stiffness (K_e) with the calculated stiffness (based on gross section flexural properties) resulted in measured-to-calculated stiffness ratios of approximately 0.16 for T1 and 0.11 for T2, T3, and T4. The ratio of the moment of inertia based on cracked section properties to the moment of inertia based on gross section properties was approximately 0.24 for T1 and 0.15 for T2, T3, and T4.

- 7) The effective initial stiffness, K_e , for T1 was approximately 40% greater than the average K_e for T2, T3, and T4, although the area of longitudinal reinforcement in T1 was 67% greater than in T2, T3, and T4. Furthermore, during loading cycles to drift ratios of 1, 1.5, and 2%, the hysteretic energy dissipation index E_h for walls with high-strength reinforcement was on average 75% of E_h for the wall with Grade 60 (420) reinforcement (T1). Additional studies are needed to investigate the combined effects of reduced K_e and E_h on the nonlinear dynamic response of wall systems with Grade 100 (690) reinforcement.
- 8) The distribution of deformations within one member depth, ℓ_w , from the base of the wall was similar in T1, T3, and T4. Surface strain measurements in T2 indicated that deformations concentrated closer to the base of the wall (within approximately $0.5\ell_w$) than in the other walls. T2 had reinforcement with the lowest f_t/f_y , 1.15 for No. 6 (19) bars and 1.10 for No. 4 (13) bars.
- 9) Recorded reinforcement tensile strains from strain gauges resulted in a poor measure of the distribution of deformations in a wall. In T2, recorded reinforcement strains were generally larger than in other walls throughout a distance ℓ_w from the base of the wall. This was unlike measured surface strains, which showed deformations concentrating near the base of T2.
- 10) Clear differences in crack widths were not observed between walls with Grade 60 (420) and Grade 100 (690) reinforcement. Before yielding of the longitudinal reinforcement, the crack width ratio (crack width at zero lateral force to crack width at previous peak drift) was approximately 1/3. After yielding, the crack width ratio increased to approximately 2/3.

- 11) Wall deformation was primarily due to flexure. For all walls, regardless of reinforcement grade, measured deformations within a distance ℓ_w from the base of the wall indicated that shear deformations contributed approximately 5 to 10% of the total drift at a drift ratio of 1% and approximately 15 to 20% at a drift ratio of 3%.
- 12) Large reductions in shear stiffness occurred as drift ratio increased, even though shear stresses were low throughout the test ($\leq 3.5\sqrt{f'_c}$, psi or $0.29\sqrt{f'_c}$, MPa). At 1% drift ratio, the shear stiffness within a distance $0.5\ell_w$ from the wall base was approximately 1/10 of the uncracked shear stiffness, whereas at 3% drift ratio, the shear stiffness was less than 1/100 of the uncracked shear stiffness.
- 13) The deformation capacity of T1, T3, and T4 was conservatively estimated using a plastic hinge model with a limiting strain of 0.015 in the confined concrete core and a plastic hinge length of $0.3\ell_w$ when considering the effects of flexure, shear, and strain penetration. When considering the effects of flexure only, a plastic hinge length of $0.5\ell_w$ was appropriate.
- 14) Calculated maximum concrete strains for drift ratios between 1 and 2% were generally conservative based on the plastic hinge model using a plastic hinge length of $0.3\ell_w$ when considering the effects of flexure, shear, and strain penetration. When considering the effects of flexure only, a plastic hinge length of $0.5\ell_w$ was appropriate. However, predictions of reinforcement strains were highly variable. Maximum reinforcement strains were generally underestimated with average of measured-to calculated maximum tensile strains approaching 1.3.

7 REFERENCES

1. ACI ITG-6 (2010). "Design Guide for the Use of ASTM A1035/A1035M Grade 100 (690) Steel Bars for Structural Concrete (ACI ITG-6R-10)". American Concrete Institute, Farmington Hills, Michigan.
2. ACI 318 (1983). "Building Code Requirements for Reinforced Concrete (ACI 318-83)". American Concrete Institute, Detroit, Michigan.
3. ACI 318 (1999). "Building Code Requirements for Structural Concrete (ACI 318-99) and Commentary". American Concrete Institute, Farmington Hills, Michigan.
4. ACI 318 (2008). "Building Code Requirements for Structural Concrete (ACI 318-08) and Commentary". American Concrete Institute, Farmington Hills, Michigan.
5. ACI 318 (2011). "Building Code Requirements for Structural Concrete (ACI 318-11) and Commentary". American Concrete Institute, Farmington Hills, Michigan.
6. ACI 318 (2014). "Building Code Requirements for Structural Concrete (ACI 318-14) and Commentary". American Concrete Institute, Farmington Hills, Michigan.
7. ACI 408 (2003). "Bond and Development of Straight Reinforcing Bars in Tension (ACI 408R-03)". American Concrete Institute, Farmington Hills, Michigan.
8. Ali, A. and Wight, J. K. (1991). RC Structural Walls with Staggered Door Openings. ASCE Journal of Structural Engineering, 117(5), 1514-1531.
9. Aoyama, H. ed. (2001). Design of Modern Highrise Reinforced Concrete Structures. Imperial College Press, London, United Kingdom.
10. ASCE 7 (2017). "Minimum Design Loads for Buildings and Other Structures (ASCE/SEI 7-16)". American Society of Civil Engineers, Reston, Virginia.
11. ASCE 41 (2017). "Seismic Evaluation and Retrofit of Existing Buildings (ASCE/SEI 41-17)". American Society of Civil Engineers, Reston, Virginia.
12. ASTM A370 (2017). "Standard Test Methods and Definitions for Mechanical Testing of Steel Products (ASTM A370-17)". ASTM International, West Conshohocken, Pennsylvania.
13. ASTM A615 (2016). "Standard Specification for Deformed and Plain Carbon-Steel Bars for Concrete Reinforcement (ASTM A615/A615M-16)". ASTM International, West Conshohocken, Pennsylvania.
14. ASTM A706 (2016). "Standard Specification for Deformed and Plain Low-Alloy Steel Bars for Concrete Reinforcement (ASTM A706/A706M-16)". ASTM International, West Conshohocken, Pennsylvania.
15. ASTM A1035 (2016). "Standard Specification for Deformed and Plain Low-Carbon, Chromium, Steel Bars for Concrete Reinforcement (ASTM A1035/A1035M-16b)". ASTM International, West Conshohocken, Pennsylvania.
16. ASTM C39 (2017). "Standard Test Method for Compressive Strength of Cylindrical Concrete Specimens (ASTM C39/C39M-17a)". ASTM International, West Conshohocken, PA.
17. ASTM C496 (2011). "Standard Test Method for Splitting Tensile Strength of Cylindrical Concrete Specimens (ASTM C496/C496M-11)". ASTM International, West Conshohocken, Pennsylvania.
18. ASTM E8 (2016). "Standard Test Methods for Tension Testing of Metallic Materials (ASTM E8/E8M-16a)". ASTM International, West Conshohocken, Pennsylvania.

19. ATC 115 (2014). "Roadmap for the Use of High-Strength Reinforcement in Reinforced Concrete Design". Applied Technology Council, Redwood City, California.
20. Bertero, V. V., Popov, E. P., and Wang, T. Y. (1974). "Hysteretic Behavior of Reinforced Concrete Flexural Members with Special Web Reinforcement". Report No. EERC 74-9, Earthquake-Engineering Research Center, University of California, Berkeley.
21. Bertero, V. V. (1980). Seismic Behavior of R/C Wall Structural Systems. Proceedings, 7th World Conference on Earthquake Engineering, Istanbul, Turkey.
22. Behrouzi, A., Welt, T., Lehman, D., Lowes, L., LaFave, J., and Kuchma, D. (2017). Experimental and Numerical Investigation of Flexural Concrete Wall Design Details. Proceedings, ASCE/SEI Structures Congress, Denver, Colorado.
23. Beyer, K., Dazio, A., and Priestley, M. J. N. (2011). Shear Deformations of Slender Reinforced Concrete Walls under Seismic Loading. *ACI Structural Journal*, 108(2), 167-177.
24. Brown, R. H. and Jirsa, J. O. (1974). Shear Transfer of Reinforced Concrete Beams under Reversed Loading. *ACI Special Publication 42, Shear in Reinforced Concrete*, Detroit, Michigan, 347-357.
25. Burgueno, R., Liu, X., and Hines, E. M. (2014). Web Crushing Capacity of High-Strength Concrete Structural Walls: Experimental Study. *ACI Structural Journal*, 111(1), 37-48.
26. Cardenas, A. E., Hanson, J. M., Corley, W. G., and Hognestad, E. (1973). Design Provisions for Shear Walls. *ACI Journal Proceedings*, 70(3), 221-230.
27. Cheng, M. Y., Hung, S. C., Lequesne, R. D., and Lepage, A. (2016). Earthquake-Resistant Squat Walls Reinforced with High-Strength Steel. *ACI Structural Journal*, 113(5), 1065-1076.
28. Chompreda, P. and Parra-Montesinos, G. J. (2005). "Deformation Capacity and Shear Strength of Fiber Reinforced Cement Composite Flexural Members Subjected to Displacement Reversals". Report No. UMCEE 05-03, Department of Civil and Environmental Engineering, University of Michigan, Ann Arbor, Michigan.
29. Darwin, D., Dolan, C. W., and Nilson, A. H. (2016). *Design of Concrete Structures*, 15th Edition, McGraw-Hill Education, New York.
30. Dazio, A., Buzzini, D., and Trub, M. (2008). Nonlinear Cyclic Behaviour of Hybrid Fibre Concrete Structural Walls. *Engineering Structures*, 30(11), 3141-3150.
31. Dhakal, R. P. and Fenwick, R. C. (2008). Detailing of Plastic Hinges in Seismic Design of Concrete Structures. *ACI Structural Journal*, 105(6), 740-749.
32. Dragovich, J. J. (1996). "An Experimental Study of Torsional Response of Reinforced Concrete Structures to Earthquake Excitation", Ph.D. Thesis, University of Illinois, Urbana.
33. Eom, T. S., Park, H. G., Kim, J. Y., and Lee, H. S. (2013). Web Crushing and Deformation Capacity of Low-Rise Walls Subjected to Cyclic Loading. *ACI Structural Journal*, 110(4), 575-584.
34. FEMA (2007). "Interim Testing Protocols for Determining the Seismic Performance Characteristics of Structural and Nonstructural Components (FEMA 461)". Applied Technology Council, Redwood City, California.
35. Fenwick, R. and Bull, D. (2000). What is the Stiffness of Reinforced Concrete Walls? *SESOC Journal*, 13(2), 23-32.

36. Ghannoum, W. M. and Slavin, C. M. (2015). "Defining Structurally Acceptable Properties of High-Strength Steel Bars through Material and Column Testing – Part I: Material Testing Report", Research Grant Agreement #05-14, Charles Pankow Foundation, Vancouver, Washington.
37. Green, N. B. (1968). Factors in the Aseismic Design of Reinforced Concrete Shear Walls without Openings. *ACI Journal Proceedings*, 65(8), 629-633.
38. Hanson, J. M., Burton, K. T., and Hognestad, E. (1968). Fatigue Tests of Reinforcing Bars-Effect of Deformation Pattern. *Journal of the PCA Research and Development Laboratories*, 10(3), 2-13.
39. Huq, M. S., Burgos, A. E., Lequesne, R. D., and Lepage, A. (2018). High-Strength Steel Bars in T-Shaped Concrete Walls. *Proceedings, 11th U.S. National Conference on Earthquake Engineering*, Los Angeles, California.
40. Huq, M. S., Lequesne, R., and Lepage, A., (2017). "Earthquake-Resistant T-Shaped Concrete Walls with High-Strength Steel Bars", *Designsafe-CI, Dataset*, DOI 10.17603/DS2738Q.
41. ICC (2015). "International Building Code (IBC 2015)". International Code Council, Washington, DC.
42. Jhamb, I. C. and MacGregor, J. G. (1974). Stress Concentrations Caused by Reinforcing Bar Deformations, *ACI Special Publication 41, Fatigue of Concrete – Abeles Symposium*, Detroit, Michigan, 169-182.
43. Kabeyasawa, T. and Hiraishi, H. (1998). Tests and Analyses of High-Strength Reinforced Concrete Shear Walls in Japan. In C. W. French and M. E. Kreger (Eds.), *ACI Special Publication 176, High-Strength Concrete in Seismic Regions*, Farmington Hills, Michigan, 281-310.
44. Kimura, H. and Ishikawa, Y. (2008). Seismic Performance of High-Strength Reinforced Concrete Slender Walls Subjected to High Axial Loading. *8th International Symposium on Utilization of High-Strength and High-Performance Concrete*, Tokyo, Japan, Oct. 27-29, S1-4-4, 945-950.
45. Lowes, L. N., Lehman, D. E., Birely, A. C., Kuchma, D. A., Marley, K. P., and Hart, C. R. (2012). Earthquake Response of Slender Planar Concrete Walls with Modern Detailing. *Engineering Structures*, 43, 31-47.
46. Lepage, A., Tavallali, H., Pujol, S., and Rautenberg, J. (2008). Towards Earthquake-Resistant Concrete Structures with Ultrahigh-Strength Steel Reinforcement. *14th World Conference on Earthquake Engineering*, Beijing, China.
47. Lepage, A., Yasso, S., and Darwin, D. (2018). Recommended Provisions and Commentary on Development Length for High-Strength Reinforcement in Tension. *FIB Bulletin: Advances on Bond in Concrete*, International Federation for Structural Concrete. (In Press).
48. Mander, J. B., Panthaki, F. D., and Kasalanati, A. (1994). Low-Cycle Fatigue Behavior of Reinforcing Steel. *ASCE Journal of Materials in Civil Engineering*, 6(4), 453-468.
49. Mander, J. B., Priestley, M. J. N., and Park, R. (1988). Theoretical Stress-Strain Model for Confined Concrete. *ASCE Journal of Structural Engineering*, 114(8), 1804-1826.
50. Mander, J. B., Priestley, M. J. N., and Park, R. (1988). Observed Stress-Strain Behavior of Confined Concrete. *ASCE Journal of Structural Engineering*, 114(8), 1827-1849.
51. Moehle, J. and Deierlein, G. G. (2004). A Framework Methodology for Performance-Based Earthquake Engineering. *Proceedings, 13th World Conference on Earthquake Engineering*, Vancouver, Canada.

52. Moehle, J. (2014). *Seismic Design of Reinforced Concrete Buildings*. McGraw Hill Education.
53. NIST (2014). "Use of High-Strength Reinforcement in Earthquake-Resistant Concrete Structures (NIST GCR 14-917-30)". National Institute of Standards and Technology, Gaithersburg, Maryland.
54. Oesterle, R. G., Fiorato, A. E., Aristizabal-Ochoa, J. D., and Corley, W. G. (1980). Hysteretic Response of Reinforced Concrete Structural Walls. ACI Special Publication 63, Reinforced Concrete Structures Subjected to Wind and Earthquake Forces, Detroit, Michigan, 243-273.
55. Oesterle, R. G., Fiorato, A. E., Aristizabal-Ochoa, J. D., and Corley, W. G. (1980). "Reinforcement Details for Earthquake-Resistant Structural Walls". *Concrete International*, 2(12), 55-66.
56. Oesterle, R. G. (1986). "Inelastic Analysis for In-Plane Strength of Reinforced Concrete Shear Walls". PhD Dissertation, Northwestern University, Evanston, Illinois.
57. Otani, S. (1981). Hysteresis Models of Reinforced Concrete for Earthquake Response Analysis. *The University of Tokyo Journal of Faculty of Engineering*. 36(2), 407-441.
58. Park, R., Priestley, M. J. N, and Gill, W. D. (1982). Ductility of Square-Confined Concrete Columns. *ASCE Journal of the Structural Division*, 108(4), 929-950.
59. Paulay, T. (1969). Reinforced Concrete Shear Walls. *New Zealand Engineering*, 24(10), 315-321.
60. Paulay, T. (1972). Some Aspects of Shear Wall Design. *Bulletin of New Zealand Society for Earthquake Engineering*, 5(3), 89-105.
61. Paulay, T. (1975). Design Aspects of Shear Walls for Seismic Areas. *Canadian Journal of Civil Engineering*, 2(3), 321-344.
62. Paulay, T. and Williams, R. L. (1980). The Analysis and Design of and the Evaluation of Design Actions for Reinforced Concrete Ductile Shear Wall Structures. *Bulletin of New Zealand National Society for Earthquake Engineering*, 13(2), 108-143.
63. Paulay, T. (1986). A Critique of the Special Provisions for Seismic Design of the Building Code Requirements for Reinforced Concrete (ACI 318-83). *ACI Journal Proceedings*, 83(2), 274-283.
64. Paulay, T. (1986). The Design of Ductile Reinforced Concrete Structural Walls for Earthquake Resistance. *Earthquake Spectra*, 2(4), 783-823.
65. Post, N. (2007). "High-Strength Rebar Called Revolutionary". *Engineering News Record, McGraw-Hill Construction*, August 27/September 3, 10-12.
66. Price, K. R., Fields, D., and Lowes, L. N. (2014). "The Impact of High-Strength Reinforcing Steel on Current Design Practice". Research Grant Agreement #01-13, Charles Pankow Foundation, Vancouver, Washington.
67. Rothe, D. H. and Sozen, M. A. (1983). "A SDOF Model to Study Nonlinear Dynamic Response of Large- and Small-Scale R/C Test Structures". *Civil Engineering Studies, Structural Research Series No. 512*, University of Illinois, Urbana.
68. Salse, E. A. B. and Fintel, M. (1973). Strength, Stiffness and Ductility Properties of Slender Shear Walls. *Proceedings, 5th World Conference on Earthquake Engineering*, Rome, Italy.
69. Scribner, C. F. and Wight, J. K. (1980). Strength Decay in R/C Beams under Load Reversals. *ASCE Journal of Structural Engineering*, 106(ST4), 861-876.
70. Sezen, H. and Moehle, J.P. (2003). Bond-Slip Behavior of Reinforced Concrete Members. *Proceedings, fib Symposium on Concrete Structures in Seismic Regions*, Athens, Greece.

71. Sheikh, S. A. and Uzumeri, S. M. (1982). Analytical Model for Concrete Confinement in Tied Columns. *ASCE Journal of the Structural Division*, 108(12), 2703-2722.
72. Shiu, K. N., Daniel, J. I., Aristizabal-Ochoa, Fiorato, A. E., and Corley, W. G. (1981). "Earthquake Resistant Structural Walls – Tests of Walls With and Without Openings". Report to National Science Foundation, Construction Technology Laboratories, Skokie, Illinois.
73. Sozen, M. A. (1989). Earthquake Response of Buildings with Robust Walls. Proceedings, 5th Chilean Conference on Earthquake Engineering, Santiago, Chile.
74. Sozen, M. A. and Moehle, J. P. (1993). Stiffness of Reinforced Concrete Walls Resisting In-Plane Shear (EPRI TR-102731 Tier 1). Electric Power Research Institute.
75. Sozen, M. A. (2004). Seismic Behavior of Reinforced Concrete Buildings. In Y. Bozorgnia and V. V. Bertero (Eds.), *Earthquake Engineering: From Engineering Seismology to Performance-Based Engineering* (Chapter 13). CRC Press.
76. Takeda, T., Sozen, M. A., and Nielsen, M. N. (1970). Reinforced Concrete Response to Simulated Earthquakes. *ASCE Journal of the Structural Division*, 96(ST12), 2557-2573.
77. Thomas, A., Davis, B., Dadi, G. B., and Goodrum, P. M. (2013). Case Study on the Effect of 690 MPa (100 ksi) Steel Reinforcement on Concrete Productivity in Buildings. *ASCE Journal of Construction Engineering and Management*, 139(11), 040130251-9.
78. Thomsen IV, J. H. and Wallace, J. W. (1995). "Displacement-Based Design of Reinforced Concrete Structural Walls: An Experimental Investigation of Walls with Rectangular and T-Shaped Cross-Sections". Report No. CU/CEE-95-06, Clarkson University.
79. UBC (1997). "Uniform Building Code". International Conference of Building Officials, Whittier, California.
80. Vallenias, J. M., Bertero, V. V., and Popov, E. P. (1979). "Hysteretic Behavior of Reinforced Concrete Structural Walls". Report No. UCB/EERC-79/20, University of California, Berkeley, California.
81. Wallace, J. W. and Moehle, J. P. (1992). Ductility and Detailing Requirements of Bearing Wall Buildings. *ASCE Journal of Structural Engineering*, 118(6), 1625-1644.
82. Wallace, J. W. (1994). New Methodology for Seismic Design of RC Shear Walls. *ASCE Journal of Structural Engineering*, 120(3), 863-884.
83. Wallace, J. W. (1995). Seismic Design of RC Structural Walls. Part I: New Code Format. *ASCE Journal of Structural Engineering*, 121(1), 75-87.
84. Wallace, J. W. and Thomsen IV, J. H. (1995). Seismic Design of RC Structural Walls. Part II: Applications. *ASCE Journal of Structural Engineering*, 121(1), 88-101.
85. Wallace, J. W. and Orakcal, K. (2002). ACI 318-99 Provisions for Seismic Design of Structural Walls. *ACI Structural Journal*, 99(4), 499-508.
86. Wight, J. K. and Sozen, M. A. (1975). Strength Decay of RC Columns under Shear Reversals. *ASCE Journal of Structural Engineering*, 101(ST5), 1053-1065.
87. Wight, J. K., Wood, S. L., Moehle, J. P., and Wallace, J. W. (1996). On Design Requirements for Reinforced Concrete Structural Walls. In J. K. Wight and M. E. Kreger (Eds.) *ACI Special Publication 162, Mete A. Sozen Symposium – A Tribute from his Students*, Farmington Hills, Michigan, 431-456.
88. Wood, S. L. (1989). Minimum Tensile Reinforcement Requirements in Walls. *ACI Structural Journal*, 86(5), 582-591.

89. Wood, S. L. (1991). Performance of Reinforced Concrete Buildings during the 1985 Chile Earthquake: Implications for the Design of Structural Walls. *Earthquake Spectra*, 7(4), 607-638.
90. Zuidema, B., Denner, S., Engl, B., and Sperle, J. (2001). New High Strength Steels Applied to the Body Structure of ULSAB-AVC. SAE Technical Paper 2001-01-3042.

TABLES

Table 1 – Summary of test program (1 ksi = 6.89 MPa)

all	Yield Strength f_y^a ksi	Tensile-to-Yield Strength Ratio f_t/f_y^b	Concrete Compressive Strength $f_c'^b$ ksi
T1 ^c	60	1.35	8
T2 ^d	100	1.15	8
T3 ^c	100	1.25	8
T4 ^d	100	1.35	8

^aNominal yield strength for longitudinal and transverse reinforcement.

^bTarget values, see Table 6 (concrete) and Table 7 (reinforcing steel) for measured properties.

^cTested in fall of 2015.

^dTested in summer of 2016.

Table 2 – Loading protocol

Step ^a	Drift Ratio
	DR ^b %
1 ^c	0.2
2 ^c	0.3
3 ^d	0.5
4 ^d	0.75
5 ^d	1
6 ^d	1.5
7 ^d	2
8 ^d	3
9 ^d	4

^a Two cycles of loading in each step, following recommendations in FEMA 461^[34], see Figure 15.

^b Drift (lateral displacement) divided by height (from base of wall to point of drift measurement).

^c Displacement-controlled to a target force (based on stiffness estimates).

^d Displacement-controlled to a target displacement.

Table 3 – Data associated with computed nominal flexural strength (1 in. = 25.4 mm, 1 ft = 305 mm, 1 kip = 4.45 kN)

Wall	f'_c	f_y^a	P^b	$M_n^+^c$	c^+^d	$V_{Mn}^+^e$	$M_n^-^c$	c^-^d	$V_{Mn}^-^e$
	ksi	ksi	kips	ft-kips	in.	kips	ft-kips	in.	kips
T1	8	60	61	6340	17.48	254	5610	2.52	224
T2, T3, T4	8	100	61	6160	17.93	246	5690	2.55	228

^aNominal yield strength of reinforcement.

^bTotal axial load at base of wall due to self-weight (44.9 kips (200 kN)), top block (9.0 kips (40.1 kN)), internal bracing (0.2 kips (0.9 kN)), and tributary weight of loading apparatus (6.8 kips (30.3 kN)).

^cNominal flexural strength, M_n^+ for stem in compression and M_n^- for stem in tension. Based on general principles of reinforced concrete in ACI 318, where concrete strain is limited to 0.003, concrete stress is defined by the equivalent rectangular stress block, and reinforcing steel stress is limited to the yield strength f_y . For reinforcement area and location, see Figure 13.

^dNeutral axis depth measured from extreme compression fiber, c^+ and c^- correspond to M_n^+ and M_n^- , see footnote c.

^eShear associated with M_n based on a nominal shear span of 300 in. (7620 mm).

Table 4 – Key dates for specimen casting and testing

Location	Specimen											
	T1			T2			T3			T4		
	Cast day	Test day	Age days	Cast day	Test day	Age days	Cast day	Test day	Age days	Cast day	Test day	Age days
Base Block	3/18/2015		223	12/18/2015		173	4/2/2015		188	1/28/2016		147
Wall Lift 1	5/28/2015	10/27/2015	152	2/11/2016	6/8/2016	118	6/12/2015	10/7/2015	117	2/24/2016	6/23/2016	120
Wall Lift 2	7/16/2015		103	4/5/2016		64	6/30/2015		99	3/18/2016		97
Top Block	8/14/2015		74	4/21/2016		48	8/7/2015		61	5/3/2016		51

Table 5 – Batched proportions for concrete mixture (1 gal = 3.79 liters, 1 oz = 0.278 N, 1 lb = 4.45 N, 1 in. = 25.4 mm)

Proportions (per cubic yard)	Unit	Specimen							
		T1		T2		T3		T4	
		Lift 1	Lift 2	Lift 1	Lift 2	Lift 1	Lift 2	Lift 1	Lift 2
Water	gal	35	37	34	35	36	35	34	34
Cementitious Material (CM):									
Cement	lb	656	664	663	645	644	658	647	645
Fly Ash	lb	150	150	149	150	156	149	149	150
Fine Aggregate	lb	1751	1714	1714	1725	1731	1767	1737	1718
Coarse Aggregate ^a	lb	1180	1180	1180	1179	1189	1180	1183	1183
Admixtures:									
Retarder	oz	24	24	32	24	24	24	24	24
Rheology Modifier	oz	48	48	48	48	48	48	48	48
Water Reducer ^b	oz	36	54	56	56	54	54	56	56
Water/CM		0.36	0.38	0.35	0.36	0.37	0.36	0.36	0.36
Initial Slump ^c	in.	7.5	8.5	7.25	9.0	7.5	7.5	7.5	9.0

^a Maximum aggregate size of ½ in. (13 mm).

^b Concrete arrived at laboratory with tabulated amounts of admixtures. Supplemental water-reducing admixture was added in the laboratory to achieve a minimum 20-in. (508-mm) spread before casting.

^c Slump measured when concrete arrived at laboratory.

Table 6 – Measured concrete strength at test day (1 ksi = 6.89 MPa)

Location	Specimen							
	T1		T2		T3		T4	
	f_{cm}^a ksi	f_{ct}^b ksi	f_{cm}^a ksi	f_{ct}^b ksi	f_{cm}^a ksi	f_{ct}^b ksi	f_{cm}^a ksi	f_{ct}^b ksi
Base Block	8.0 ^c	–	6.9 ^c	0.42 ^c	7.6 ^c	–	7.4 ^c	0.52 ^d
Wall Lift 1	7.2 ^d	0.55 ^d	7.9 ^c	0.48 ^c	7.3 ^d	0.52 ^d	8.6 ^c	0.52 ^d
Wall Lift 2	7.4 ^d	0.46 ^d	7.7 ^c	0.48 ^c	7.2 ^c	0.54 ^d	7.2 ^c	0.54 ^d
Lift Average	7.3	0.51	7.8	0.48	7.3	0.53	7.9	0.53
Top Block	6.8 ^d	0.50 ^d	6.4 ^c	0.46 ^c	5.4 ^c	0.39 ^d	6.6 ^c	0.44 ^d

^a Compressive strength of concrete following ASTM C39^[16]. Tests of cylinders conducted within one week of test day (Table 4).

^b Splitting tensile strength of concrete following ASTM C496^[17]. Tests of cylinders conducted within one week of test day (Table 4).

^c Cylinder size of 4 by 8 in. (100 by 200 mm), reported value is average of three cylinders, sampled from each of two trucks that delivered the concrete for the base block.

^d Cylinder size of 6 by 12 in. (150 by 300 mm), reported value is average of two cylinders.

Table 7 – Reinforcing steel properties (1 in. = 25.4 mm, 1 ksi = 6.89 MPa)

Wall	Bar Designation No.	Nominal Bar Diameter in.	Yield Strength f_y ksi	Tensile Strength f_t ksi	f_t/f_y	Uniform Elongation ϵ_{su} ^a	Fracture Elongation ϵ_{sf} ^b
T1	6 (19)	0.750	70 ^c	94 ^c	1.34	12.2% ^c	15.0% ^d
	4 (13)	0.500	76 ^c	106 ^c	1.39	11.0% ^c	14.0% ^d
	3 (10)	0.375	60 ^d	91 ^d	1.52	–	16.5% ^d
T2	6 (19)	0.750	108 ^c	124 ^c	1.15	8.9% ^c	13.0% ^d
	4 (13)	0.500	108 ^c	119 ^c	1.10	5.7% ^c	10.0% ^d
	3 (10)	0.375	109 ^d	134 ^d	1.23	–	11.3% ^d
T3	6 (19)	0.750	99 ^c	122 ^c	1.23	9.4% ^c	12.5% ^d
	4 (13)	0.500	101 ^c	122 ^c	1.21	6.6% ^c	12.5% ^d
	3 (10)	0.375	109 ^d	134 ^d	1.23	–	11.3% ^d
T4	6 (19)	0.750	96 ^c	131 ^c	1.36	8.6% ^c	12.5% ^d
	4 (13)	0.500	107 ^c	128 ^c	1.20	6.5% ^c	10.9% ^d
	3 (10)	0.375	109 ^d	134 ^d	1.23	–	11.3% ^d

^aCorresponds to strain at peak stress following ASTM E8^[18].

^bBased on 8-in. (203-mm) gauge length following ASTM A370^[12].

^cMeasured from laboratory tests following ASTM A370^[12] using the 0.2%-offset method. Reported values correspond to average of two test results.

^dReported on manufacturer mill certification.

Table 8 – Chemical composition of reinforcing bars

Element ^a	Wall											
	T1			T2			T3			T4		
	No. 3 (10)	No. 4 (13)	No. 6 (19)	No. 3 (10)	No. 4 (13)	No. 6 (19)	No. 3 (10)	No. 4 (13)	No. 6 (19)	No. 3 (10)	No. 4 (13)	No. 6 (19)
Carbon, <i>C</i>	0.220	0.280	0.260	0.270	0.230	0.340	0.270	0.290	0.290	0.270	0.420	0.420
Manganese, <i>Mn</i>	1.080	1.150	1.190	1.250	0.820	0.980	1.250	1.190	1.190	1.250	1.320	1.320
Phosphorus, <i>P</i>	0.008	0.010	0.014	0.013	0.009	0.013	0.013	0.010	0.010	0.013	0.013	0.013
Sulfur, <i>S</i>	0.039	0.029	0.029	0.027	0.029	0.025	0.027	0.022	0.022	0.027	0.043	0.043
Silicon, <i>Si</i>	0.200	0.180	0.220	0.210	0.190	0.300	0.210	0.220	0.220	0.210	0.220	0.220
Copper, <i>Cu</i>	0.300	0.310	0.370	0.250	0.490	0.330	0.250	0.190	0.190	0.250	0.290	0.290
Chromium, <i>Cr</i>	0.140	0.100	0.130	0.140	0.130	0.110	0.140	0.110	0.110	0.140	0.120	0.120
Nickel, <i>Ni</i>	0.100	0.110	0.110	0.110	0.170	0.100	0.110	0.070	0.070	0.110	0.100	0.100
Molybdenum, <i>Mo</i>	0.030	0.019	0.022	0.020	0.051	0.023	0.020	0.010	0.010	0.020	0.028	0.028
Vanadium, <i>V</i>	0.023	0.000	0.001	0.194	0.000	0.100	0.194	0.245	0.245	0.194	0.133	0.133
Niobium, <i>Nb</i>	0.000	0.000	0.000	0.001	0.000	0.000	0.001	0.024	0.024	0.001	0.002	0.002
Tin, <i>Sn</i>	0.012	0.011	0.012	0.000	0.013	0.011	0.000	0.000	0.000	0.000	0.000	0.020
Aluminum, <i>Al</i>	0.000	0.001	0.001	0.000	0.002	0.001	0.000	0.000	0.000	0.000	0.000	0.000
Nitrogen, <i>N</i>	0.0000	0.0156	0.0101	0.0000	0.0021	0.0200	0.0000	0.0000	0.0000	0.0000	0.0000	0.0000

^a Elements and values (in weight percentages) as reported on manufacturer mill certification. Values do not sum to unity because mill certifications do not include all constituent materials.

Table 9 – Maximum measured shear force and drift ratio (1 kip = 4.45 kN, 1 psi = 0.00689 MPa)

Wall	V_{max}^a		v_{max}^b		DR_{max}^c		DR_{cap}^d
	kips		$\sqrt{f_{cm}} \text{ (psi)}$		%		%
	–	+	–	+	–	+	
T1	-282	303	3.3	3.5	-6.00 ^e	3.73	3.7
T2	-237	282	2.7	3.2	-1.80	2.05	1.8
T3	-242	275	2.8	3.2	-2.95	3.95	3.0
T4	-253	293	2.8	3.3	-3.87	4.05	3.9

^a Maximum measured shear force per loading direction during the loading protocol (Table 2).

^b Shear stress calculated using $V_{max}/(\ell_w t_w)$ expressed as a fraction of $\sqrt{f_{cm}} \text{ (psi)}$, where $t_w = 10$ in. (254 mm), $\ell_w = 100$ in. (2540 mm), and f_{cm} is taken from Table 6 (lift average).

^c Maximum drift ratio attained in a loading direction (based on the loading protocol, Table 2) while maintaining a shear force not less than 80% of V_{max} .

^d Drift ratio capacity obtained from the minimum DR_{max} .

^e After reaching the target drift ratio of 4% in each loading direction, T1 was subjected to a final push up to the limitations of the testing apparatus, which was a displacement of nearly 20 in. (508 mm) at the horizontal plane of action of the actuators.

Table 10 – Drift cycle and bar location where bar buckling or bar fracture first occurred

Wall	Bar Location ^a		Drift Cycle ^b											
			2%				3%				4%			
			i+	i-	ii+	ii-	i+	i-	ii+	ii-	i+	i-	ii+	ii-
T1	Flange	Unconfined	B											
		Confined												
	Stem	Unconfined									B			
		Confined									F			
T2	Flange	Unconfined	F				F							
		Confined												
	Stem	Unconfined	F											
		Confined												
T3	Flange	Unconfined									B			
		Confined												
	Stem	Unconfined									B			
		Confined									B F			
T4	Flange	Unconfined									B			
		Confined									F			
	Stem	Unconfined												
		Confined									B F			

^a Confined regions refer to boundary elements with closely spaced transverse reinforcement. Unconfined flange includes the intersection of flange and stem (See Figures 33 through 36).

^b Notation:

i+ : first cycle, stem in compression; i- : first cycle, stem in tension;

ii+ : second cycle, stem in compression; ii- : second cycle, stem in tension;

B: buckling of longitudinal reinforcement; F: fracture of longitudinal reinforcement.

Table 11 – Secant stiffness from measured shear-drift envelope (1 in. = 25.4 mm, 1 kip = 4.45 kN)

T1				T2				T3				T4			
Drift Ratio	Shear		Secant Stiffness	Drift Ratio	Shear		Secant Stiffness	Drift Ratio	Shear		Secant Stiffness	Drift Ratio	Shear		Secant Stiffness
DR^a	V	V/V_{max}^b	K^c	DR^a	V	V/V_{max}^b	K^c	DR^a	V	V/V_{max}^b	K^c	DR^a	V	V/V_{max}^b	K^c
%	kip		kip/in.	%	kip		kip/in.	%	kip		kip/in.	%	kip		kip/in.
												-4.26	-159	0.63	13
-5.98	-262	0.93	15					-3.99	-123	0.51	11	-4.17	-176	0.70	15
-3.92	-262	0.93	23					-3.24	-165	0.68	18	-3.73	-251	0.99	23
-2.79	-282	1.00	35					-2.90	-242	1.00	29	-2.73	-253	1.00	32
-1.72	-266	0.94	53	-1.76	-236	0.99	47	-1.88	-231	0.95	42	-1.77	-238	0.94	47
-1.18	-258	0.91	76	-1.21	-237	1.00	69	-1.35	-221	0.91	57	-1.24	-229	0.91	64
-0.74	-253	0.90	118	-0.73	-221	0.93	105	-0.81	-220	0.91	94	-0.75	-218	0.86	101
-0.52	-236	0.84	157	-0.53	-178	0.75	117	-0.57	-193	0.79	116	-0.52	-192	0.76	128
-0.32	-175	0.62	188	-0.32	-134	0.56	146	-0.35	-148	0.61	146	-0.31	-147	0.58	163
0.00	0	0	-	0.00	0	0	-	0.00	0	0	-	0.00	0	0	-
0.48	232	0.77	168	0.45	189	0.67	148	0.37	163	0.59	151	0.43	192	0.65	154
0.65	277	0.91	147	0.69	223	0.79	114	0.58	204	0.74	120	0.68	233	0.80	120
1.19	298	0.98	86	0.94	264	0.94	99	0.80	240	0.87	103	0.93	261	0.89	97
1.70	289	0.95	59	1.45	282	1.00	68	1.26	267	0.97	73	1.40	277	0.95	69
2.76	303	1.00	38	1.50 ^d	252	0.89	59	1.73	261	0.95	52	1.96	279	0.95	50
3.50	302	1.00	30	1.78	224	0.80	44	2.83	275	1.00	33	2.99	293	1.00	34
				2.04	217	0.77	37	3.90	273	0.99	24	4.02	283	0.96	24
				2.79	210	0.74	26								
$V_{0.8}^- =$	-225	$K_e^- =$	162	$V_{0.8}^- =$	-190	$K_e^- =$	114	$V_{0.8}^- =$	-194	$K_e^- =$	115	$V_{0.8}^- =$	-202	$K_e^- =$	117
$V_{0.8}^+ =$	243	$K_e^+ =$	163	$V_{0.8}^+ =$	226	$K_e^+ =$	113	$V_{0.8}^+ =$	220	$K_e^+ =$	113	$V_{0.8}^+ =$	235	$K_e^+ =$	119

^a Identifies drift ratio DR associated with peak force for each step (two cycles per step) of the loading protocol starting from Step 2 (Table 2). DR is the measured drift divided by height h_y , where $h_y = 290$ in. (7370 mm) for T1 and T3 and 287 in. (7290 mm) for T2 and T4.

^b V_{max} is the maximum measured shear force per loading direction.

^c K is calculated using $V/(DR h_y)$ see footnote a. The value of K_e at the base of this table corresponds to the secant stiffness at $V = V_{0.8} = 0.8V_{max}$, based on linear interpolation.

^d Drift associated with peak force (No. 4 (13) bars at stem-flange intersection fractured) during the first cycle to 2% drift.

Table 12 – Wall data for cracked stiffness calculation (1 in. = 25.4 mm, 1 kip = 4.45 kN)

Term ^a	Unit	T1		T2		T3		T4	
		V ⁻	V ⁺	V ⁻	V ⁺	V ⁻	V ⁺	V ⁻	V ⁺
h_w	in.	300	300	297	297	300	300	297	297
h_y	in.	290	290	287	287	290	290	287	287
ℓ_w	in.	100	100	100	100	100	100	100	100
t_w	in.	10	10	10	10	10	10	10	10
f_{cm} ^b	ksi	7.3	7.3	7.8	7.8	7.3	7.3	7.9	7.9
f_y ^c	ksi	70	70	108	108	99	99	96	96
E_c ^d	ksi	4,870	4,870	5,030	5,030	4,870	4,870	5,070	5,070
G_c ^e	ksi	2,030	2,030	2,100	2,100	2,030	2,030	2,110	2,110
E_s	ksi	29,000	29,000	29,000	29,000	29,000	29,000	29,000	29,000
$X_{cg,cr}$	in.	10.2	28.9	8.1	23.7	8.2	23.9	8.0	23.6
I_{cr}	in. ⁴	446,000	421,000	270,000	262,000	278,000	269,000	268,000	260,000
ϕ_K		1/10	1/10	1/10	1/10	1/10	1/10	1/10	1/10
d_b	in.	0.75	0.75	0.75	0.75	0.75	0.75	0.75	0.75
λ ^f		8	8	15	15	13	13	13	13
K_f ^g = $\frac{6E_c I_{cr}}{h_y^2(3h_w - h_y)}$	kip/in.	254	240	164	159	158	153	164	159
K_v ^h = $\frac{G_c \ell_w t_w \phi_K}{h_y}$	kip/in.	700	700	732	732	700	700	735	735
K_{sp} ⁱ = $\frac{E_c I_{cr}}{h_w h_y (\lambda d_b)}$	kip/in.	4160	3930	1420	1370	1600	1540	1630	1590
$K_{wall,calc}$ ^j	kip/in.	178	171	122	119	119	116	124	121
$K_{wall,meas}$ ^k	kip/in.	162	163	114	113	115	113	117	119
$\frac{K_{wall,meas}}{K_{wall,calc}}$		0.91	0.95	0.93	0.95	0.97	0.97	0.94	0.98

^a For notation and definitions see APPENDIX A: NOTATION.

^b Measured average compressive strength of concrete (average of lift 1 and 2, from Table 6).

^c Measured yield strength of reinforcement (No. 6 (19) bar, from Table 7).

^d Modulus of elasticity of concrete, $57\sqrt{1000 f_{cm}}$, ksi.

^e Shear modulus of concrete: $E_c/2.4$.

^f From $2\lambda = \ell_d/d_b$ where ℓ_d is based on Eq. (4-11a) in ACI 408^[7] using $\phi=1$, $\omega=1$, and $(c\omega + K_{tr})/d_b = 4$:

$$\ell_d/d_b = \left(\frac{1000 f_y}{f_c^{1/4}} - 2400 \right) / 305, \text{ where } f_c' = 1000 f_{cm}, f_{cm} \text{ for base block in Table 6.}$$

^g From flexural deflection Δ_f at elevation h_y for a cantilever beam with flexural rigidity $E_c I_{cr}$ and subjected to point load V at h_w :

$$\Delta_f = V h_y^2 (3h_w - h_y) / (6E_c I_{cr}).$$

^h From shear deflection Δ_v at elevation h_y for a cantilever beam with shear rigidity $G_c \ell_w t_w \phi_K$ and subjected to point load V at h_w (see Reference 52 for typical values of ϕ_K):

$$\Delta_v = V h_y / (G_c \ell_w t_w \phi_K).$$

ⁱ From deflection due to strain penetration Δ_{sp} at elevation h_y assuming an additional curvature of $V h_w / (E_c I_{cr})$ over a distance λd_b lumped at the base of the wall:

$$\Delta_{sp} = V h_w h_y \lambda d_b / (E_c I_{cr}).$$

^j Calculated stiffness of wall: $K_{wall,calc} = 1 / (1/K_f + 1/K_{sp} + 1/K_v)$.

^k Based on K_e , secant stiffness from measured shear-drift envelope, see Table 11, footnote c.

Table 13 – Unloading stiffness derived from measured shear versus drift ratio (1 in. = 25.4 mm, 1 kip = 4.45 kN)

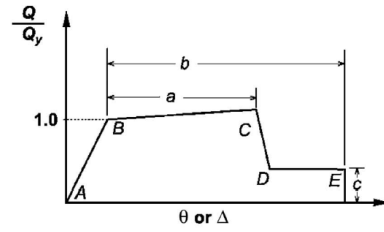
Target Drift Ratio <i>DR</i> ^a %		T1			T2			T3			T4		
		Actual Drift	Shear	Unloading Stiffness	Actual Drift	Shear	Unloading Stiffness	Actual Drift	Shear	Unloading Stiffness	Actual Drift	Shear	Unloading Stiffness
		Δ^a in.	V_{peak}^a kips	K_u^b kips/in.	Δ^a in.	V_{peak}^a Kips	K_u^b kips/in.	Δ^a in.	V_{peak}^a kips	K_u^b kips/in.	Δ^a in.	V_{peak}^a kips	K_u^b kips/in.
-3	Δ_{peak}	-8.20	-274	81				-8.48	-239	64	-7.98	-246	62
	Δ_0	-4.83	0					-4.77	0		-4.03	0	
-2	Δ_{peak}	-5.13	-263	107				-5.51	-227	72	-5.07	-232	75
	Δ_0	-2.66	0					-2.36	0		-1.97	0	
-1.5	Δ_{peak}	-3.63	-256	134	-3.61	-224	87	-3.93	-220	87	-3.61	-222	90
	Δ_0	-1.72	0		-1.05	0		-1.41	0		-1.15	0	
-1	Δ_{peak}	-2.25	-248	149	-2.14	-216	122	-2.39	-215	113	-2.13	-212	123
	Δ_0	-0.59	0		-0.36	0		-0.48	0		-0.40	0	
-0.75	Δ_{peak}	-1.54	-230	174	-1.52	-171	133	-1.68	-189	118	-1.47	-187	158
	Δ_0	-0.22	0		-0.24	0		-0.08	0		-0.28	0	
0.75	Δ_{peak}	1.39	225	230	1.97	219	133	1.71	198	159	2.00	232	141
	Δ_0	0.41	0		0.32	0		0.47	0		0.36	0	
1	Δ_{peak}	1.99	266	174	2.68	256	115	2.25	233	142	2.74	251	112
	Δ_0	0.46	0		0.45	0		0.61	0		0.49	0	
1.5	Δ_{peak}	3.55	278	141	4.16	252	98	3.74	245	97	4.24	261	89
	Δ_0	1.57	0		1.59	0		1.22	0		1.31	0	
2	Δ_{peak}	5.02	278	108				5.24	250	82	5.74	263	75
	Δ_0	2.45	0					2.21	0		2.24	0	
3	Δ_{peak}	8.17	292	90				8.32	263	69	8.70	276	63
	Δ_0	4.92	0					4.54	0		4.35	0	

^a For a given target drift ratio *DR*, shear V_{peak} corresponds to peak drift Δ_{peak} during second cycle to *DR*. Drift Δ_0 corresponds to zero shear (unloading from Δ_{peak}) and is measured during second cycle to *DR*.

^b K_u is calculated using $V_{peak}/(\Delta_{peak} - \Delta_0)$.

Table 14 – Modeling parameters for nonlinear seismic analysis

Parameters ^a	ASCE 41(2017)	Proposed
a	0.015	0.015
b	0.020	0.020
c	0.75	0.75
I_{eff}/I_g ^c	0.35	1/5 (Grade 60) ^b 1/7 (Grade 100) ^b
$A_{cv,eff}/A_{cv}$ ^c	1.0	1/10
Q_B ^d	M_n ^e	$0.9M_n$ ^e
Q_C ^f	M_{pr} ^g	$1.1M_n$ ^e



From ASCE 41 (2017) Figure 10-1 (a)

^a Refer to Figure 10-1 (a) in this table. Parameter values correspond to cases where axial force

$$P \leq 0.10f_{cm}A_g \text{ and shear force } V \leq 4\sqrt{f_{cm}(\text{psi})}A_{cv}.$$

^b Grade of flexural reinforcement.

^c Effective section property expressed as a fraction of gross section property.

^d Force at yielding point B.

^e M_n based on expected (or measured) material properties.

^f Force at capping point C.

^g According to ASCE 41 (2017)^[11], M_{pr} shall be based on $1.25f_y$, where f_y is based on expected (measured) value.

Table 15 – Stress-strain parameters for concrete (1 ksi = 6.89 MPa)

Parameter	Unit	Wall			
		T1	T2	T3	T4
Unconfined concrete					
f_c'' ^a	ksi	7.3	7.8	7.3	7.9
ϵ_0 ^b		0.0025	0.0025	0.0025	0.0025
Z_{uc} ^c		117	120	110	120
f_r ^d	ksi	0.64	0.66	0.64	0.67
E_c ^e	ksi	4870	5030	4870	5070
Confined concrete					
K_{cc} ^f		1.20	1.29	1.31	1.29
$K_{cc}\epsilon_0$		0.0030	0.0032	0.0033	0.0032
f_{cc}'' ^g	ksi	8.8	10.1	9.6	10.2
ϵ_{cc} ^h		0.0050	0.0061	0.0064	0.0061
Z_{cc} ⁱ		21	14	13	14
f_r ^d	ksi	0.64	0.66	0.64	0.67
E_c ^e	ksi	4870	5030	4870	5070

^a Peak stress for unconfined concrete, based on f_{cm} (see Table 12).

^b Strain corresponding to peak stress for unconfined concrete.

^c Parameter defining the slope of the linear post-peak branch for unconfined concrete.

^d Modulus of rupture of concrete, $(7.5\sqrt{1000 f_c''})/1000$, ksi.

^e Modulus of elasticity of concrete, $E_c = 57\sqrt{1000 f_c''}$, ksi.

^f Ratio of confined to unconfined concrete compressive strength.

^g Peak stress for confined concrete, $f_{cc}'' = K_{cc}f_c''$.

^h Strain corresponding to peak stress for confined concrete.

ⁱ Parameter defining the slope of the linear post-peak branch for confined concrete.

Table 16 – Stress-strain parameters for reinforcing steel bars (1 ksi = 6.89 MPa)

Parameter ^a	Unit	Wall			
		T1	T2	T3	T4
f_{yp} ^b	ksi	70	108	99	92
E_s	ksi	29000	29000	29000	29000
f_t ^c	ksi	94	124	122	131
ϵ_{sh} ^d		1.1%	1.7%	1.2%	0.3%
E_{sh} ^d	ksi	630	670	790	1380
ϵ_{su} ^c		12.2%	8.9%	9.4%	8.6%
ϵ_{st} ^e		16.4%	10.9%	10.6%	10.4%
f_{st} ^c	ksi	93	123	122	130

^a For notation and definitions, see APPENDIX A: NOTATION.

^b Reinforcement stress defining proportional limit, $f_{yp} = f_y$ only for reinforcement with a yield plateau intersected by the line defined by the 0.2%-offset method.

^c Refer to data for No. 6 (19) bars in Table 7.

^d Required variable to define the strain-hardening model, see Figures 352 and 353. Values were derived from the measured stress-strain relationships in Figure 16.

^e Based on data from Figure 16.

Table 17 – Moment-curvature data (1 in. = 25.4 mm, 1 ft = 305 mm, 1 kip = 4.45 kN)

Wall	Loading Direction		Event ^a							
			First Yield	Yield at $0.8\ell_w$	M_n	\bar{M}	$\varepsilon_{c,Core} = 0.01$	$\varepsilon_{c,Core} = 0.015$	$\varepsilon_{t,No.4} = \varepsilon_{su}$	$\varepsilon_{t,No.6} = \varepsilon_{su}$
T1	+	M, ft-kips	5860	6710	7300	8060	8030	7760	7740	7770
	+	ϕ , $10^{-4}/in.$	0.348	0.462	1.69	4.15	4.79	6.32	20.6	23.0
	-	M, ft-kips	4830	5710	6590	8540	-	-	-	8530
	-	ϕ , $10^{-4}/in.$	0.276	0.342	11.4	14.3	-	-	-	12.7
T2	+	M, ft-kips	5500	6150	6640	7110	7010	6650	6460	6270
	+	ϕ , $10^{-4}/in.$	0.498	0.654	1.81	4.18	5.23	6.74	7.78	13.0
	-	M, ft-kips	4630	5370	6130	6950	-	-	-	6930
	-	ϕ , $10^{-4}/in.$	0.414	0.516	13.2	11.0	-	-	-	9.28
T3	+	M, ft-kips	5010	5640	6130	6790	6730	6400	6180	6130
	+	ϕ , $10^{-4}/in.$	0.462	0.600	1.82	4.24	5.16	6.62	9.30	13.9
	-	M, ft-kips	4150	4890	5630	6810	-	-	-	6790
	-	ϕ , $10^{-4}/in.$	0.378	0.474	13.4	11.0	-	-	-	9.79
T4	+	M, ft-kips	5170	5530	6070	7240	7190	6840	6610	6560
	+	ϕ , $10^{-4}/in.$	0.444	0.576	1.96	4.49	5.14	6.56	9.22	12.6
	-	M, ft-kips	4310	4890	5470	7270	-	-	-	7250
	-	ϕ , $10^{-4}/in.$	0.366	0.462	14.9	9.90	-	-	-	8.93

^aFor notation and definitions see APPENDIX A: NOTATION.

Table 18 – Calculated deformation capacity due to flexure only (for a maximum compressive strain of 0.015 in the confined stem) (1 in. = 25.4 mm)

Term ^a	Unit	Wall			
		T1	T2	T3	T4
h_w	in.	300	300	300	300
ℓ_w	in.	100	100	100	100
t_w	in.	10	10	10	10
ℓ_p ^b	in.	50	50	50	50
ϕ_y ^c	10 ⁻³ /in.	0.046	0.065	0.060	0.058
ϕ_u ^d	10 ⁻³ /in.	0.63	0.67	0.66	0.66
$\Delta_{f,y}$ ^e	in.	1.38	1.95	1.80	1.74
$\Delta_{f,p}$ ^f	in.	8.03	8.32	8.25	8.28
Δ_f ^g	in.	9.41	10.27	10.05	10.02
$DR_{f,calc}$ ^h	%	3.1	3.4	3.4	3.3

^a For notation and definitions see APPENDIX A: NOTATION.

^b Plastic hinge length, assumed equal to $0.5\ell_w$.

^c Yield curvature corresponding to the yield strain (in tension) at a distance $0.8\ell_w$ from the extreme compression fiber (stem in compression).

^d Ultimate curvature corresponding to a maximum concrete strain of 0.015 in confined concrete (stem in compression).

^e Based on Eq. 25.

^f Based on Eq. 26.

^g Based on Eq. 27.

^h Calculated drift ratio capacity based only on flexural deformations, $DR_{f,calc} = \Delta_f/h_w$.

Table 19 – Calculated deformation capacity due to flexure, shear, and strain penetration (for a maximum compressive strain of 0.015 in the confined stem) (1 in. = 25.4 mm, 1 kip = 4.45 kN)

Term ^a	Unit	Wall			
		T1	T2	T3	T4
h_w	in.	300	300	300	300
ℓ_w	in.	100	100	100	100
t_w	in.	10	10	10	10
ℓ_p ^b	in.	30	30	30	30
ϕ_y ^c	10 ⁻³ /in.	0.046	0.065	0.060	0.058
ϕ_u ^d	10 ⁻³ /in.	0.63	0.67	0.66	0.66
c ^e	in.	24.5	23.0	23.4	23.6
$\Delta_{f,y}$ ^f	in.	1.38	1.95	1.80	1.74
$\Delta_{f,p}$ ^g	in.	4.99	5.17	5.13	5.15
V_u ^h	kip	322	284	272	290
A_{cv}	in. ²	1000	1000	1000	1000
G_c	ksi	2030	2100	2030	2110
$\phi_{K,bot}$ ⁱ		1/100	1/100	1/100	1/100
$\phi_{K,top}$ ^j		1/10	1/10	1/10	1/10
α_{sp} ^k		6.2	4.8	5.0	5.1
λ		8	15	13	13
d_b	in.	0.75	0.75	0.75	0.75
Δ_f ^l	in.	6.37	7.12	6.93	6.89
Δ_v ^m	in.	0.91	0.77	0.76	0.78
Δ_{sp} ⁿ	in.	0.51	1.05	0.88	0.87
$DR_{t,calc}$ ^o	%	2.6	3.0	2.9	2.8

^a For notation and definitions see APPENDIX A: NOTATION.

^b Plastic hinge length, assumed equal to $0.3\ell_w$ if accounting for effects of flexure, shear, and strain penetration.

^c Yield curvature corresponding to the yield strain (in tension) at a distance $0.8\ell_w$ from the extreme compression fiber (stem in compression).

^d Ultimate curvature corresponding to a maximum concrete strain of 0.015 in the confined concrete (stem in compression), see Table 17.

^e Distance from extreme compression fiber to neutral axis associated with ϕ_u .

^f Based on Eq. 25.

^g Based on Eq. 26.

^h Based on $V_u = \bar{M}^+ / h_w$, see Table 17.

ⁱ Ratio of effective shear stiffness to uncracked stiffness throughout the assumed plastic hinge length, ℓ_p .

^j Ratio of effective shear stiffness to uncracked stiffness outside the assumed plastic hinge region, $h_w - \ell_p$.

^k Based on Eq. B.11 using $\beta_\ell = 1/3$, $\varepsilon_y = f_y / E_s$ (based on Table 12), $\varepsilon_s = \phi_u(d_t - c)$ with ϕ_u and c following footnotes d and e, and $d_t = 98.5$ in.

^l Based on Eq. 27.

^m Based on Eq. 28.

ⁿ Based on Eq. 29.

^o Calculated drift ratio capacity due to effects of flexure, shear, and strain penetration:

$$DR_{t,calc} = (\Delta_f + \Delta_v + \Delta_{sp}) / h_w.$$

Table 20 – Maximum drift cycle completed without bar fracture and comparison with bar elongation properties

Wall	Drift Ratio ^a (%)		Uniform Elongation ^b		Fracture Elongation ^c	
	(without Bar Fracture)		ϵ_{su} (%)		ϵ_{sf} (%)	
	No. 6 (19)	No. 4 (13)	No. 6 (19)	No. 4 (13)	No. 6 (19)	No. 4 (13)
T1	3 ⁱⁱ	– ^d	12.2	11.0	15.0	14.0
T2	2 ⁱⁱ	1.5 ⁱⁱ	8.9	5.7	13.0	10.0
T3	3 ⁱⁱ	– ^d	9.4	6.6	12.5	12.5
T4	4 ⁱ	3 ⁱⁱ	8.6	6.5	12.5	10.9

^a Refers to the target drift ratio of the last cycle that was completed without bar fracture (i first cycle and ii second cycle).

^b Corresponds to strain at peak stress following ASTM E8^[17]. Data from Table 7.

^c Based on 8-in. (203-mm) gauge length following ASTM A370^[12]. Data from Table 7.

^d Bar fracture was not observed.

FIGURES



(a) Base of a medium-rise wall building



(b) Base of a tall core-wall building

Figure 1 – Base of walls with Grade 60 (420) reinforcement in Western United States (Lepage, A., ca. 2006)

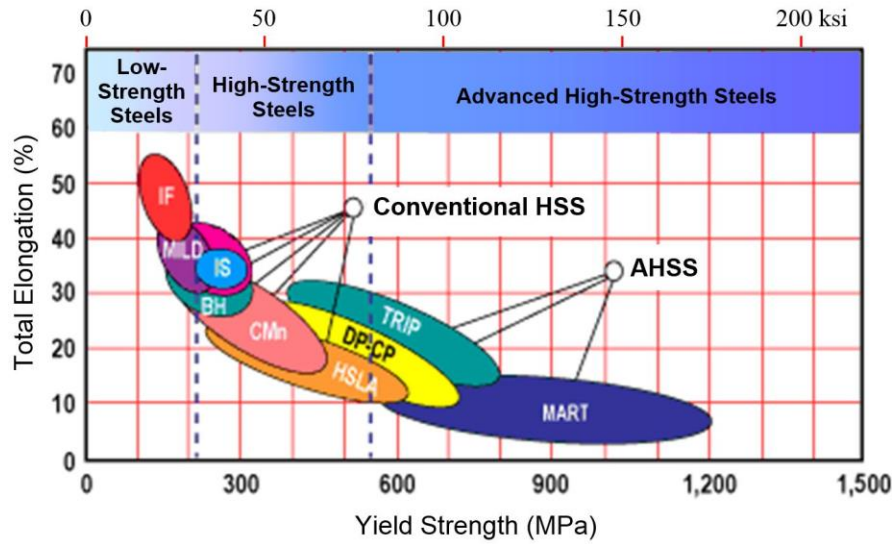


Figure 2 – Elongation and strength for conventional and advanced high-strength steels, adapted from Zuidema et al.^[90]

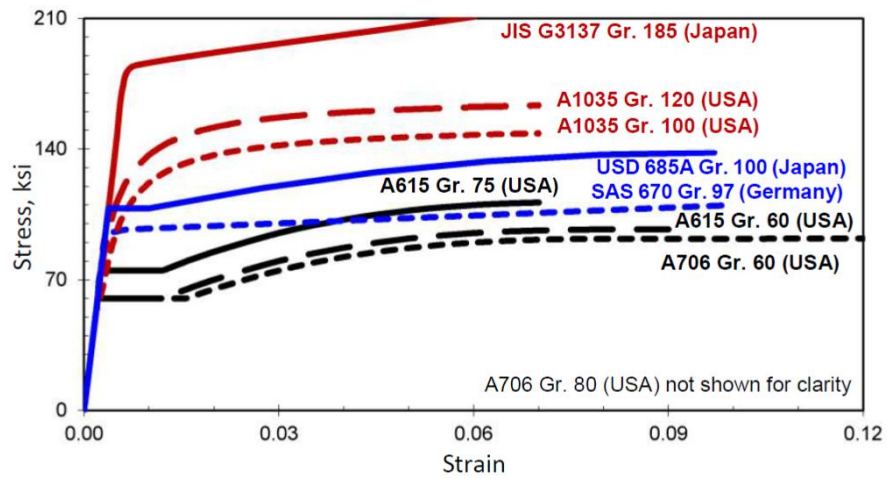


Figure 3 – Stress-strain curves representative of conventional steel and advanced high-strength steel reinforcement, adapted from Lepage et al.^[46] (1 ksi = 6.89 MPa)

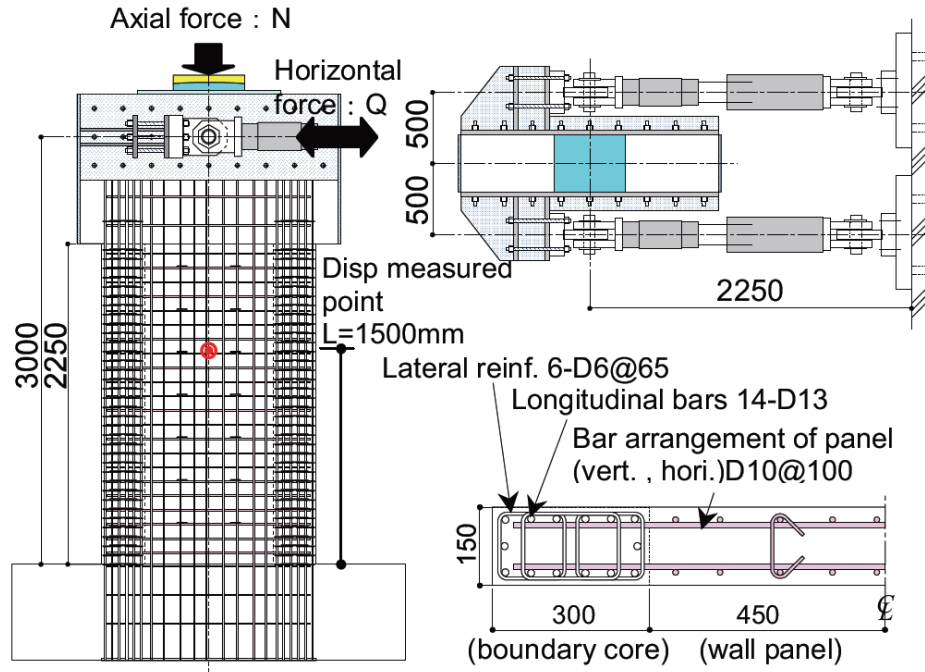


Figure 4 - Test setup and specimen details used by Kimura and Ishikawa^[44]

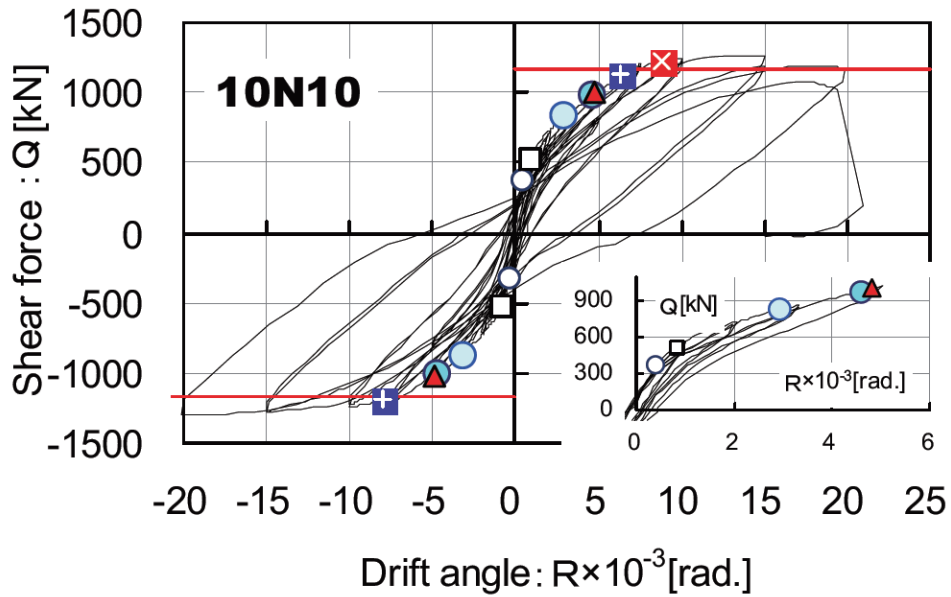
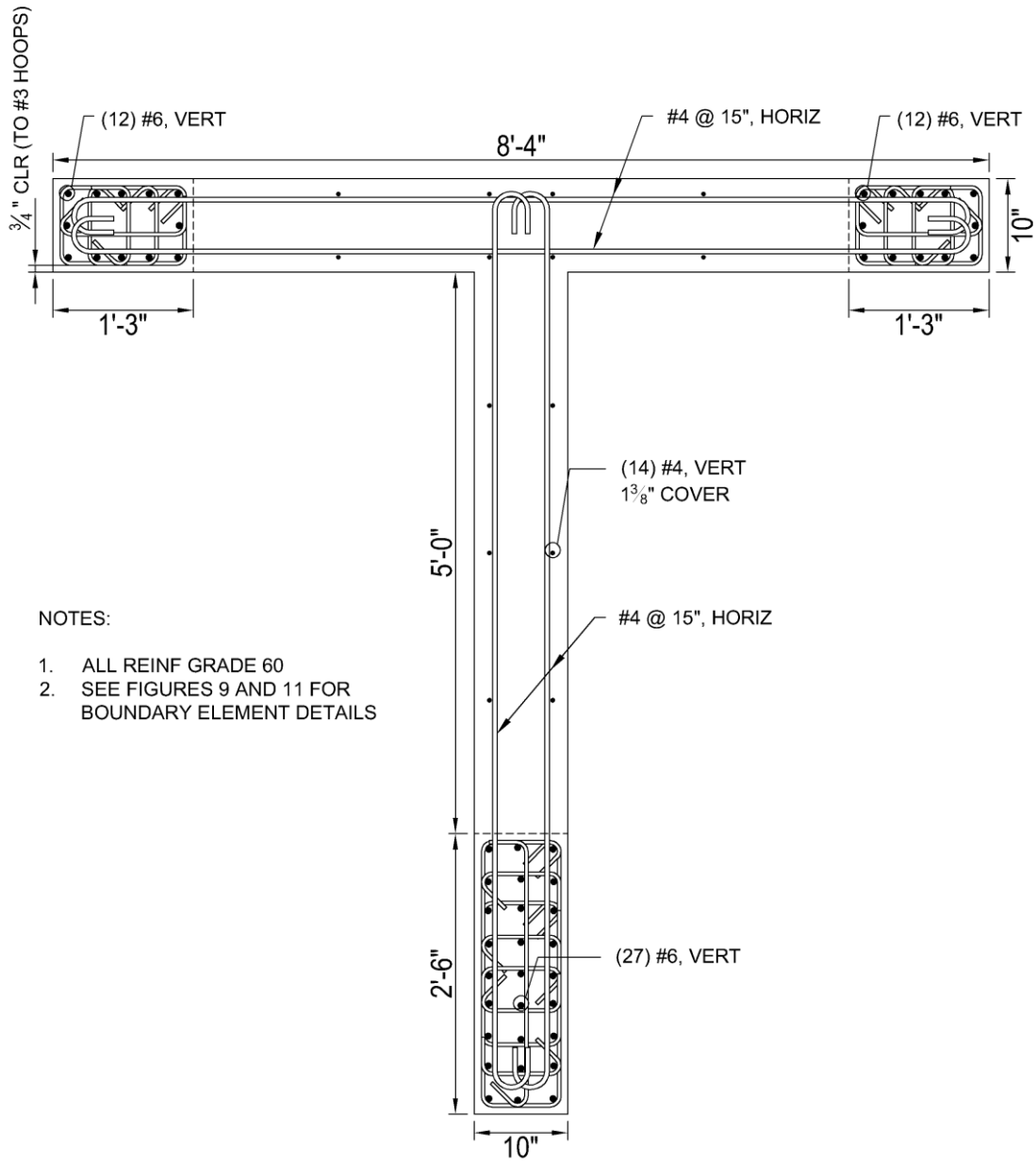


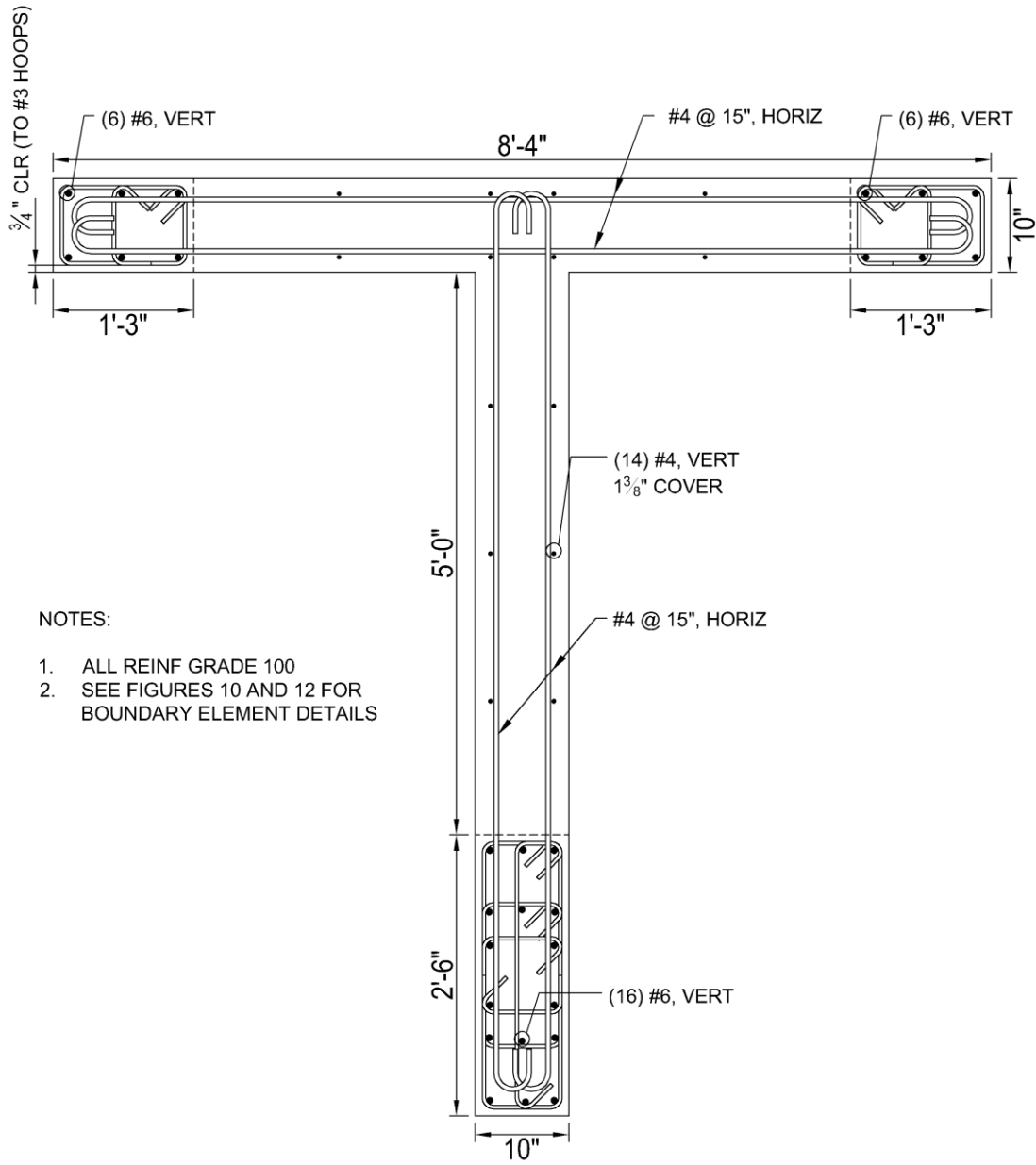
Figure 5 - Shear force versus drift ratio response reported by Kimura and Ishikawa^[44] for specimen with axial load of $0.10A_g f'_c$, where $f'_c = 15 \text{ ksi (105 MPa)}$ and $f_y = 100 \text{ ksi (690)}$



NOTES:

1. ALL REINF GRADE 60
2. SEE FIGURES 9 AND 11 FOR BOUNDARY ELEMENT DETAILS

Figure 6 – Reinforcement layout for T1 (1 in. = 25.4 mm)



NOTES:

1. ALL REINF GRADE 100
2. SEE FIGURES 10 AND 12 FOR BOUNDARY ELEMENT DETAILS

Figure 7 – Reinforcement layout for T2 and T3 (1 in. = 25.4 mm)

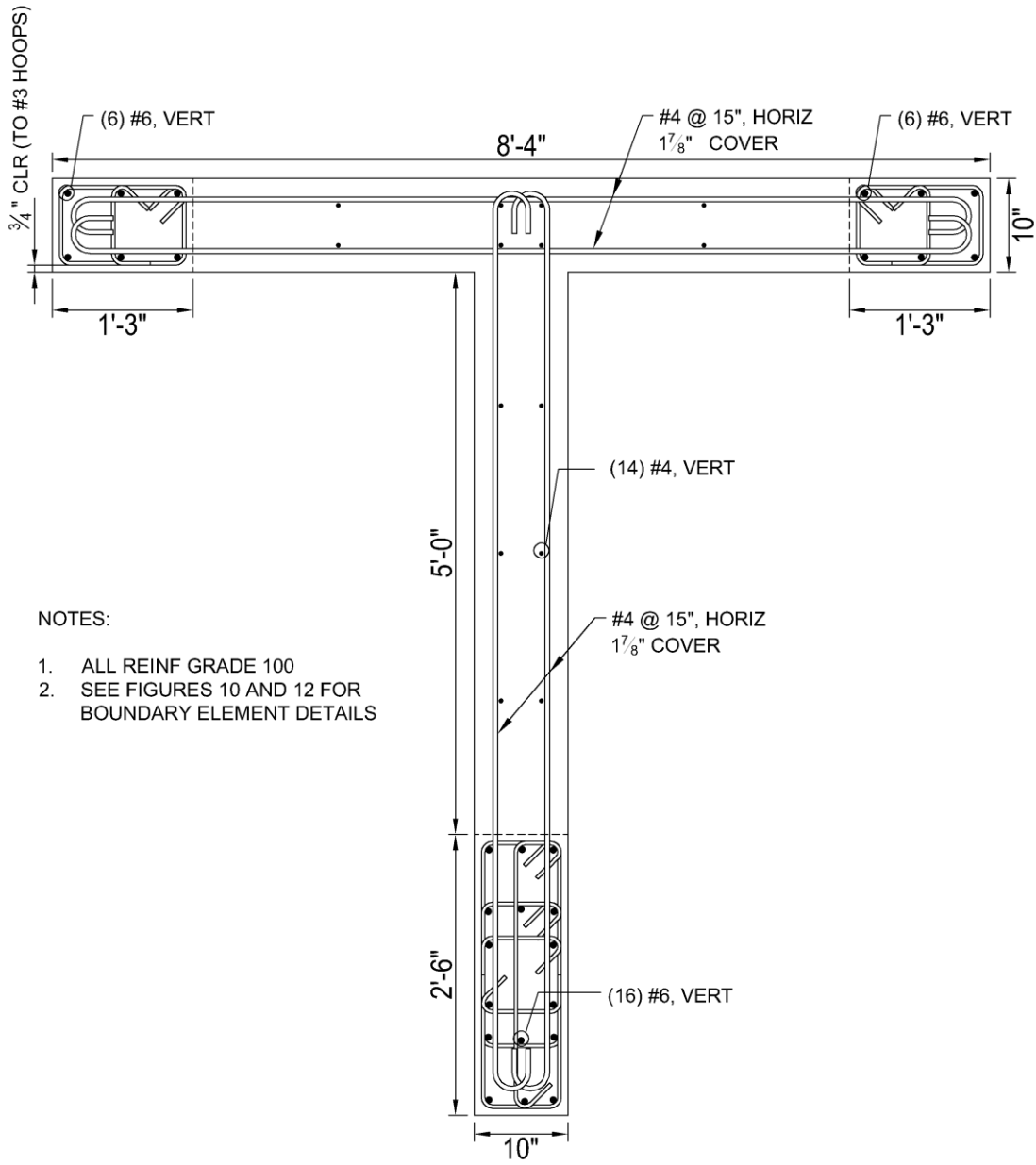


Figure 8 – Reinforcement layout for T4 (1 in. = 25.4 mm)

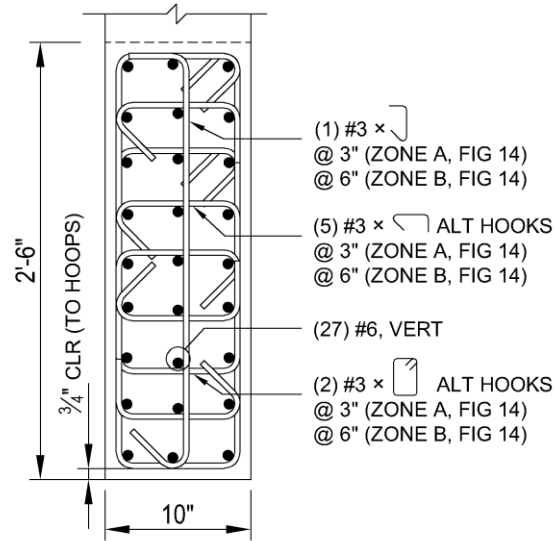


Figure 9 – Confined boundary element in stem of T1 (1 in. = 25.4 mm)

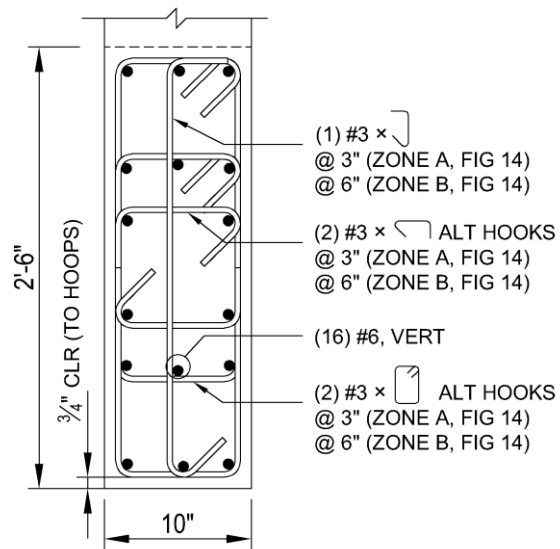


Figure 10 – Confined boundary element in stem of T2, T3, and T4 (1 in. = 25.4 mm)

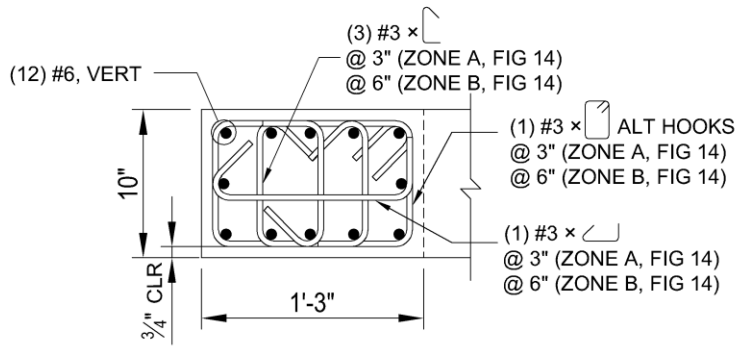


Figure 11 – Confined boundary element in flange of T1 (1 in. = 25.4 mm)

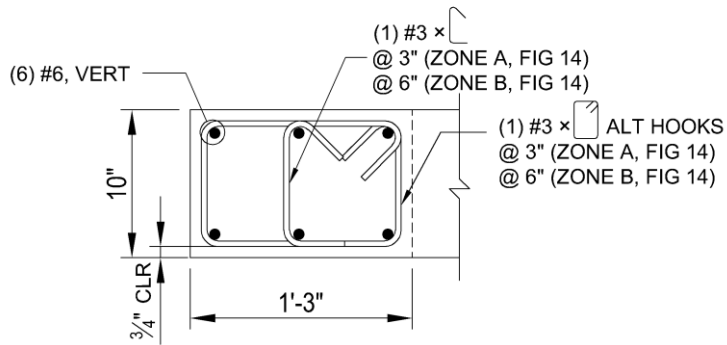


Figure 12 – Confined boundary element in flange of T2, T3, and T4 (1 in. = 25.4 mm)

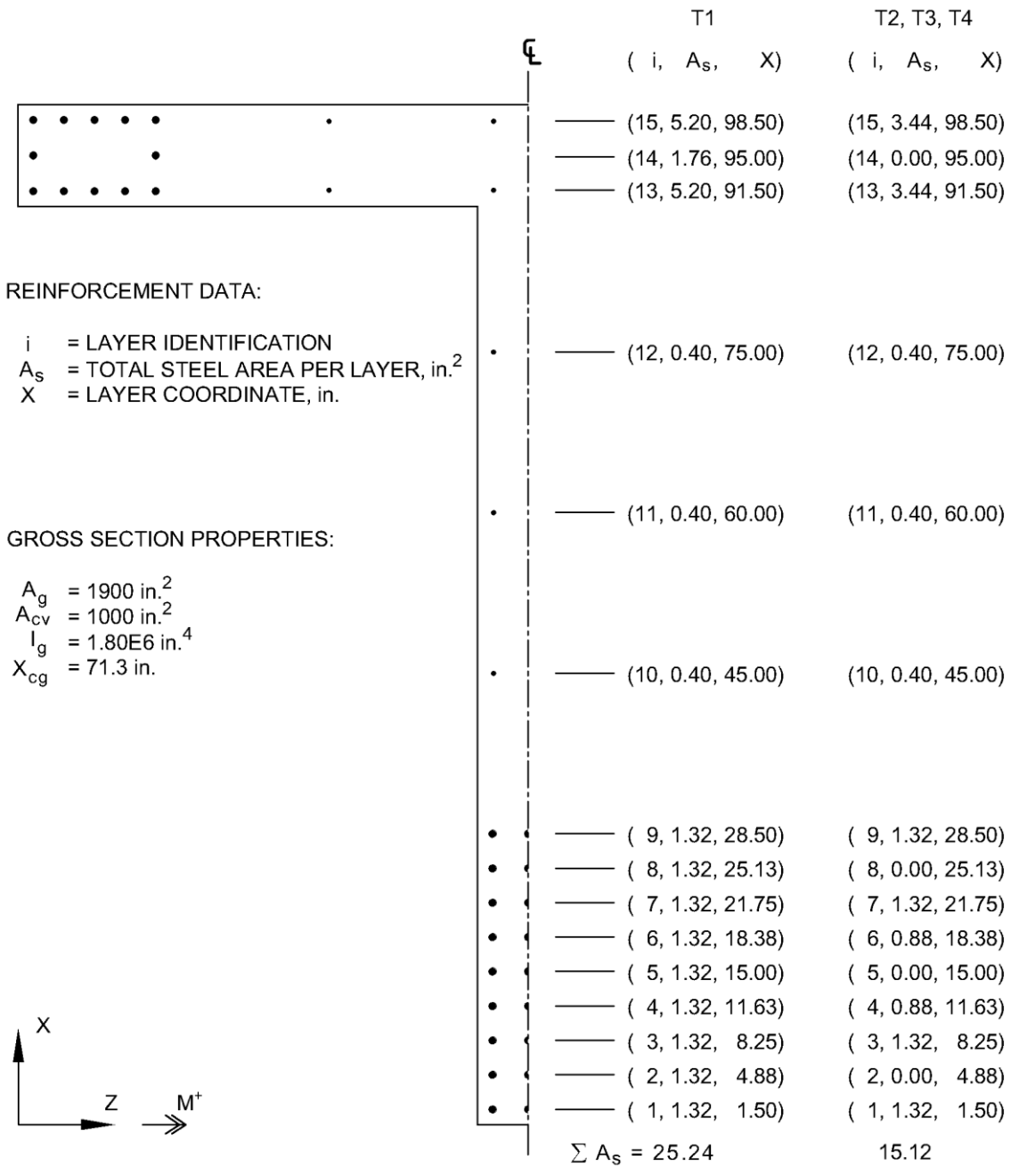


Figure 13 – Reinforcement data and wall section properties (1 in. = 25.4 mm)

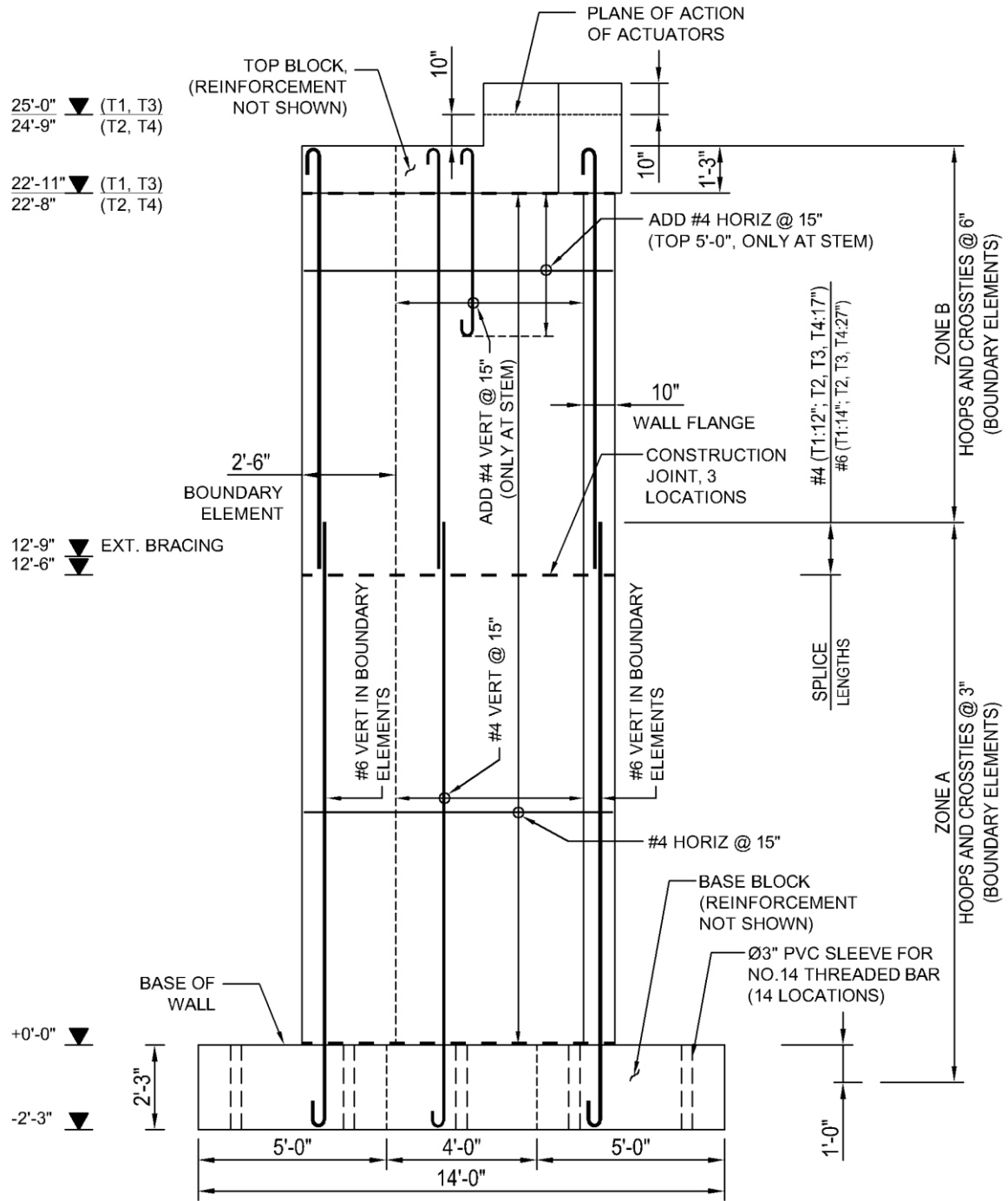


Figure 14 - Typical wall elevation (1 in. = 25.4 mm)

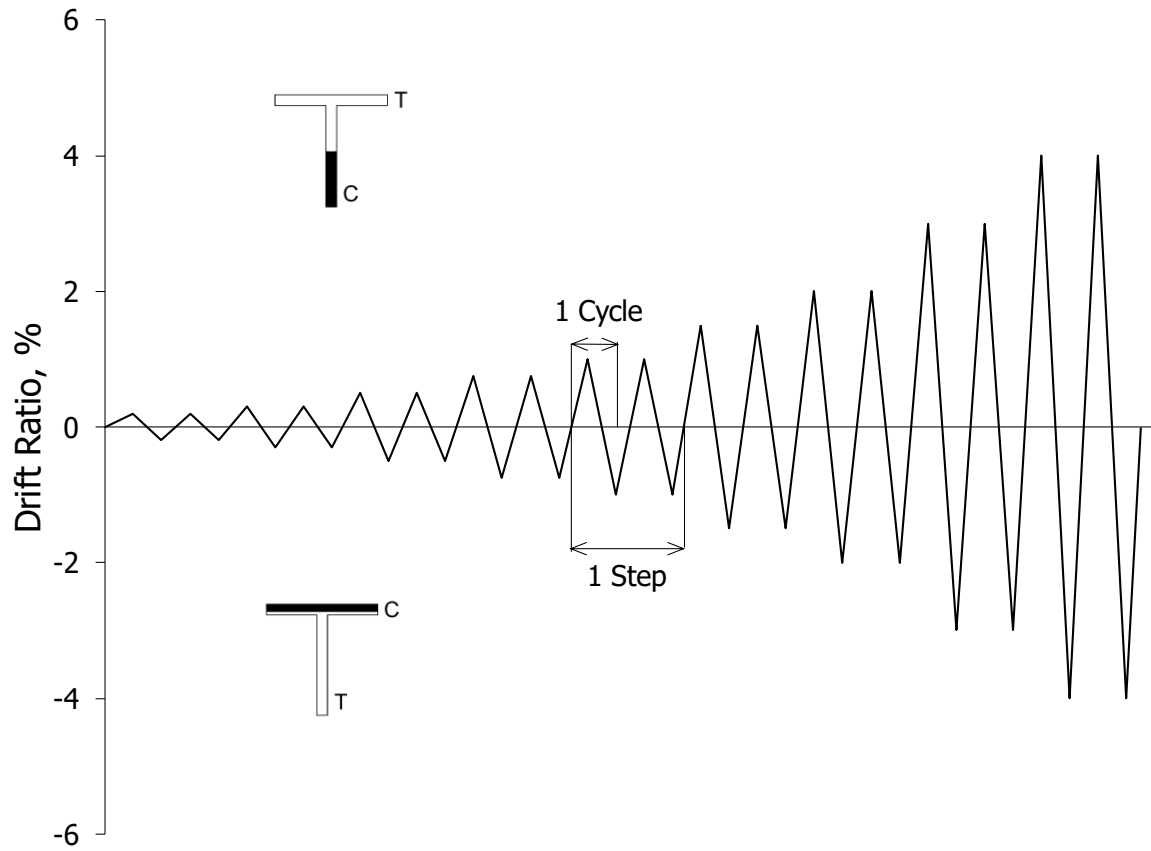


Figure 15 – Illustration of loading protocol described in Table 2

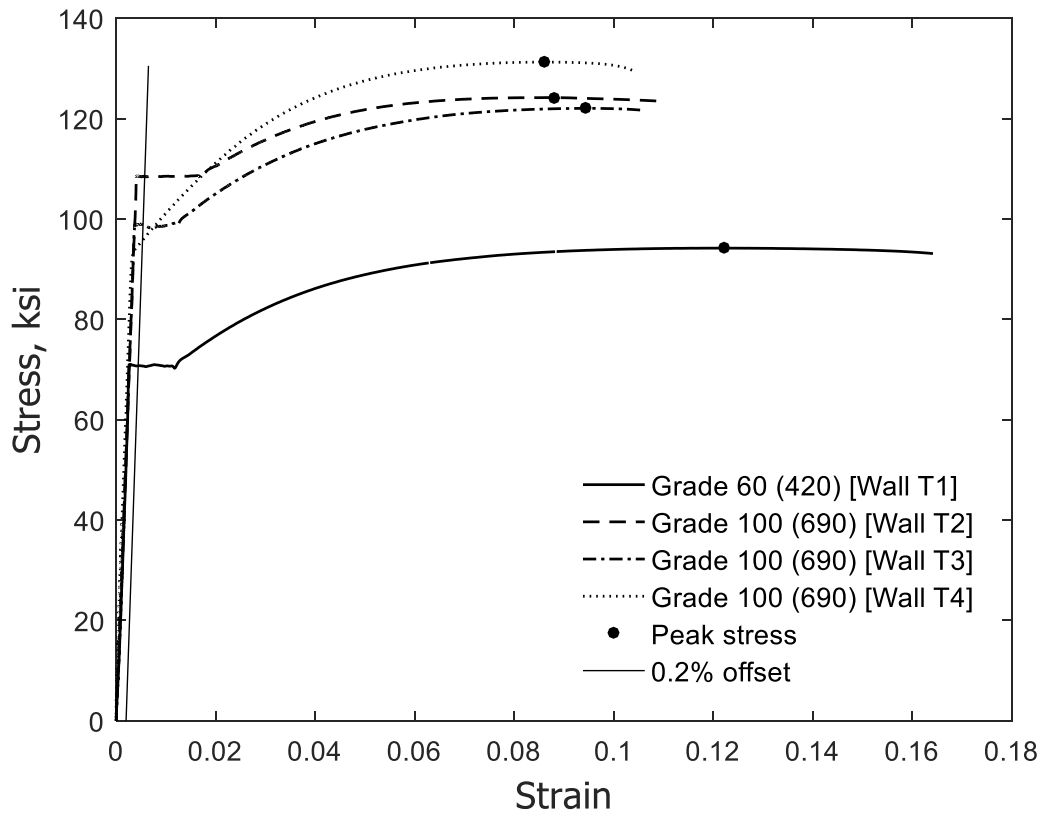


Figure 16 – Measured stress versus strain for No. 6 (19) bars (1 ksi = 6.89 MPa)

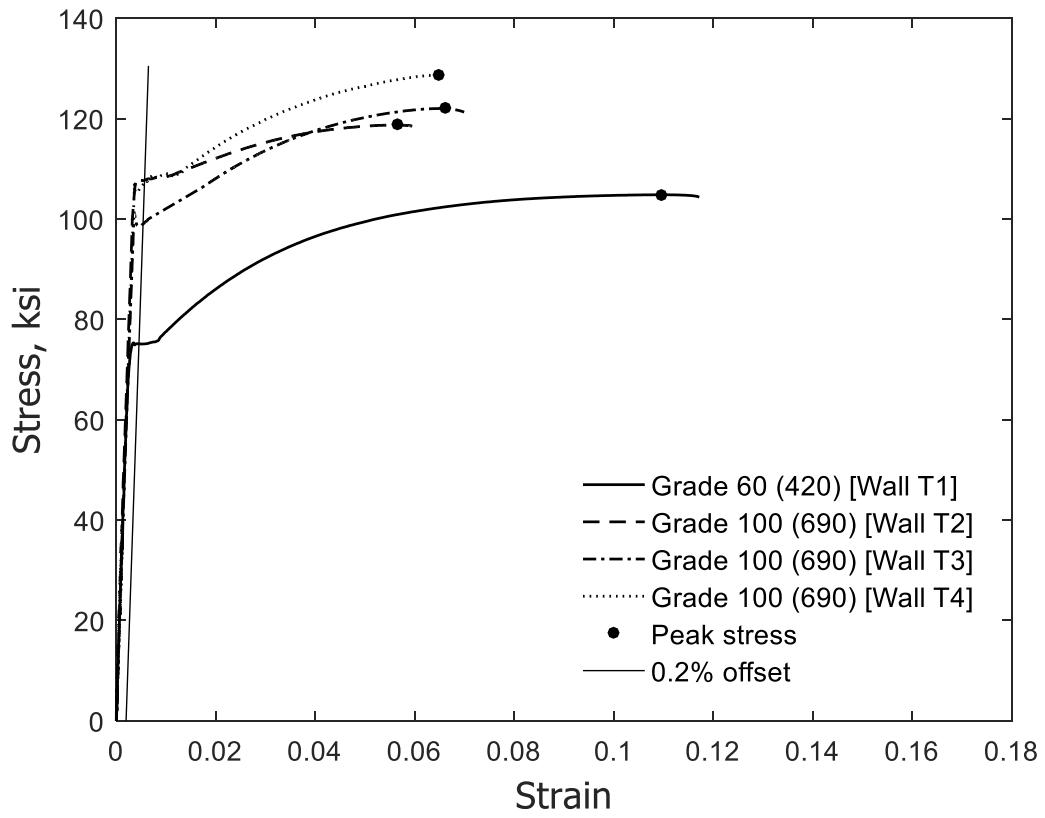


Figure 17 – Measured stress versus strain for No. 4 (13) bars (1 ksi = 6.89 MPa)

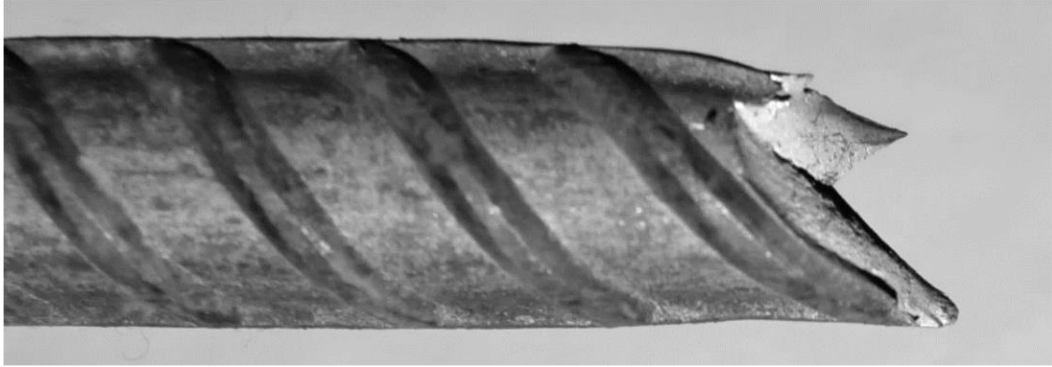


Figure 18 – Fractured No. 4 (13) bar from T2 after tensile test

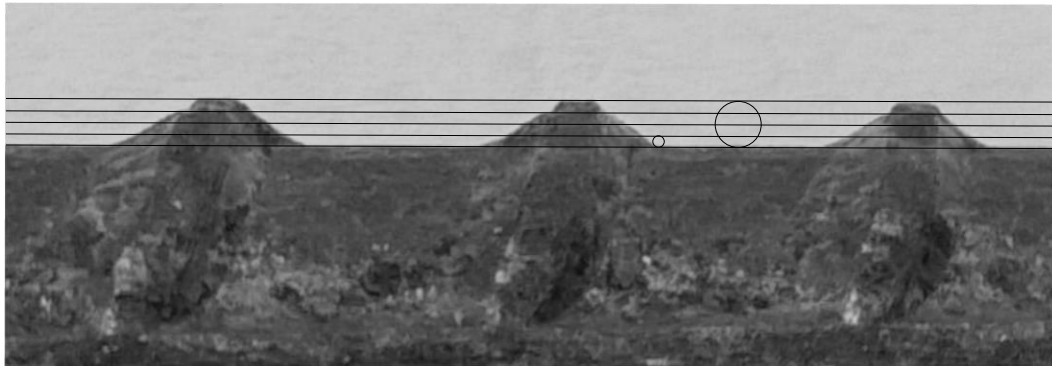


Figure 19 – Bar deformation details for No. 4 (13) bar in T2



Figure 20 – Casting of base block for T1



Figure 21 – Preparing concrete cylinders and in-situ tests during casting

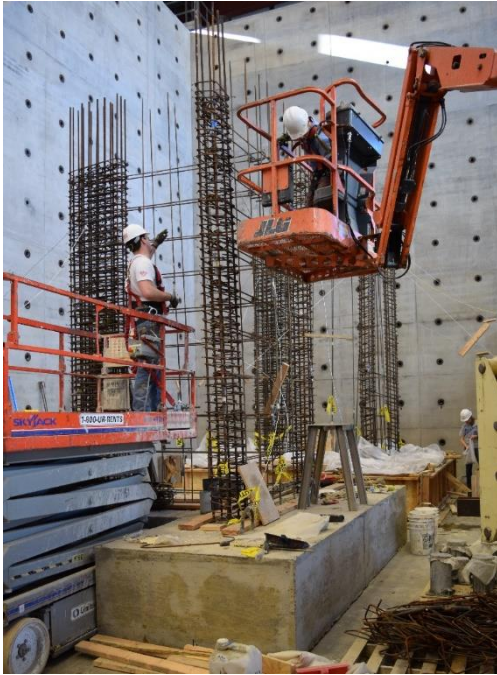


Figure 22 – Lift 1 reinforcement assembly (T2)



Figure 23 – Lift 1 formwork assembly (T1)



Figure 24 – Lift 2 casting (T3)

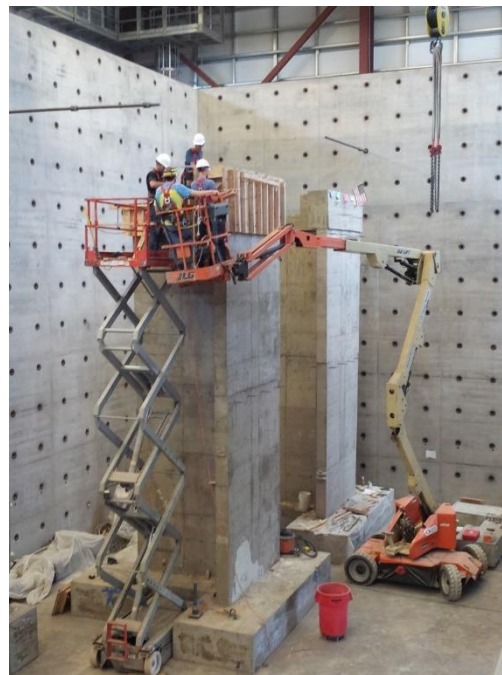


Figure 25 – Top block formwork assembly (T1)

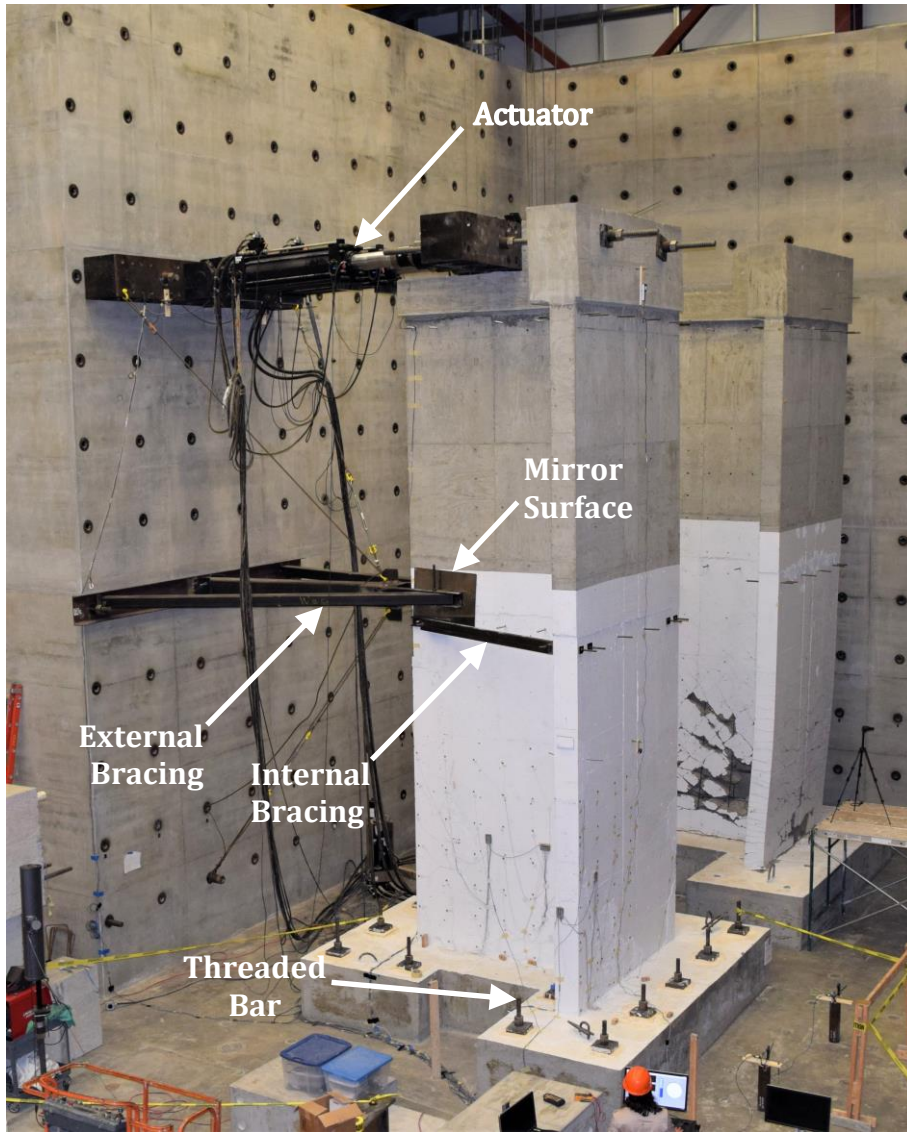


Figure 26 – Test setup

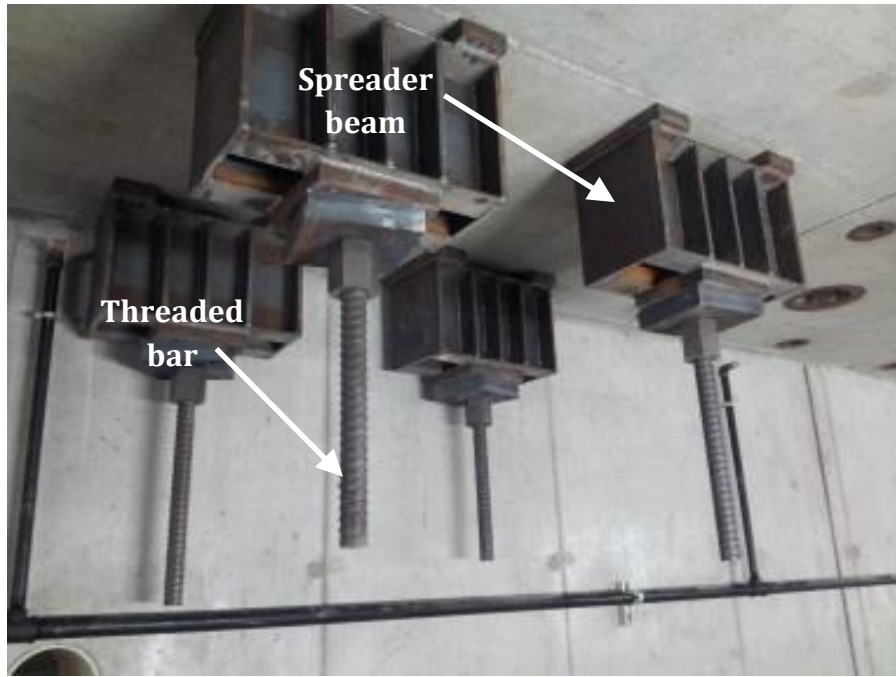


Figure 27 – Steel spreader beams below laboratory strong floor for base block hold-downs

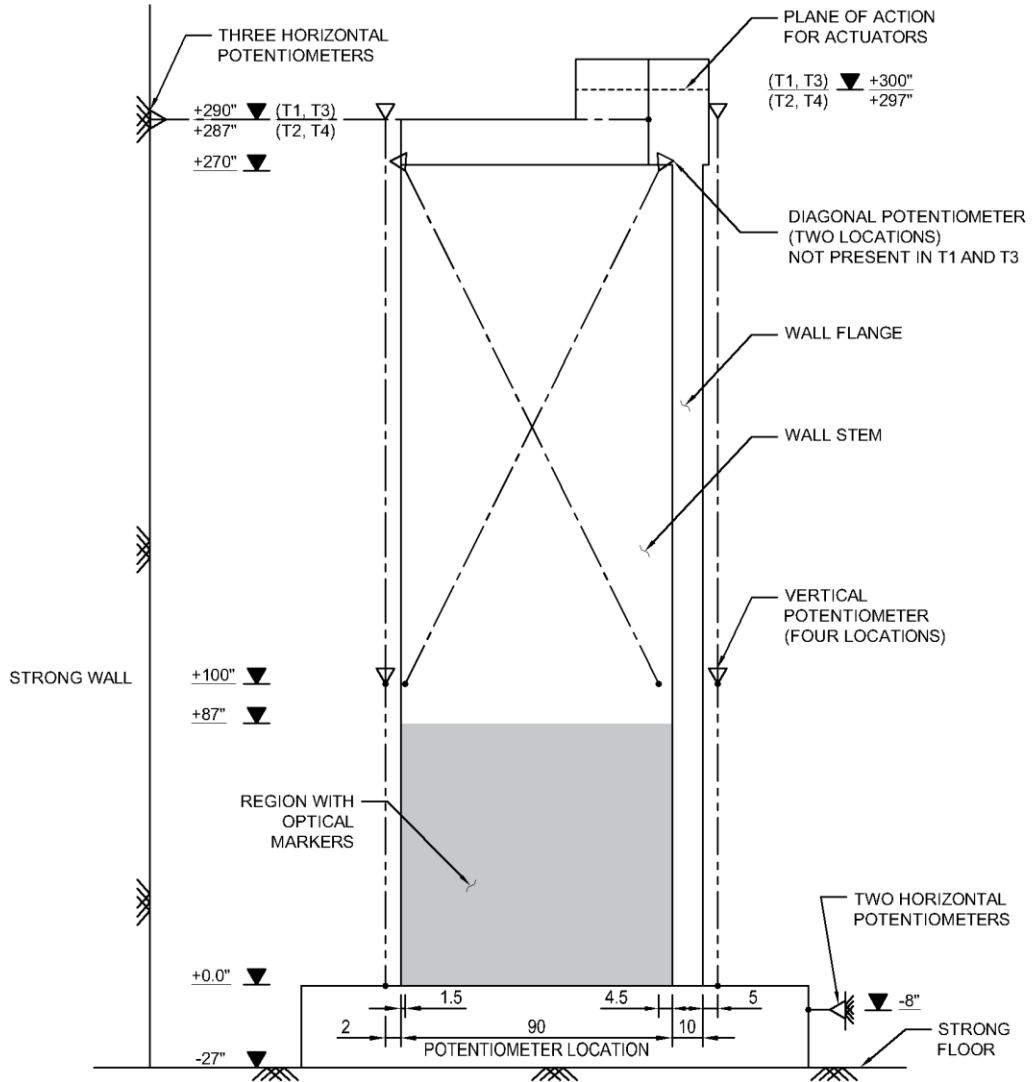


Figure 28 – Wall instrumentation (elevation view of wall stem) (1 in. = 25.4 mm)

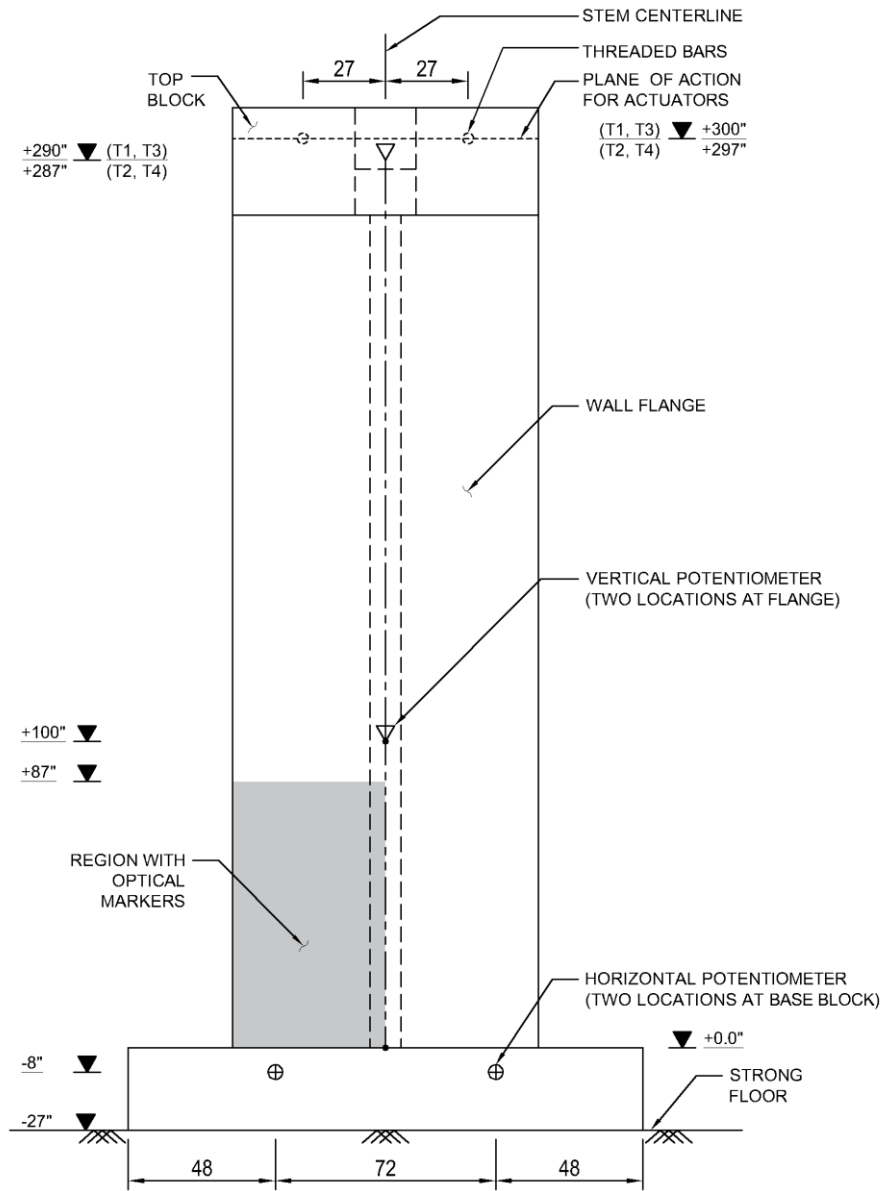


Figure 29 – Wall instrumentation (elevation view of wall flange) (1 in. = 25.4 mm)

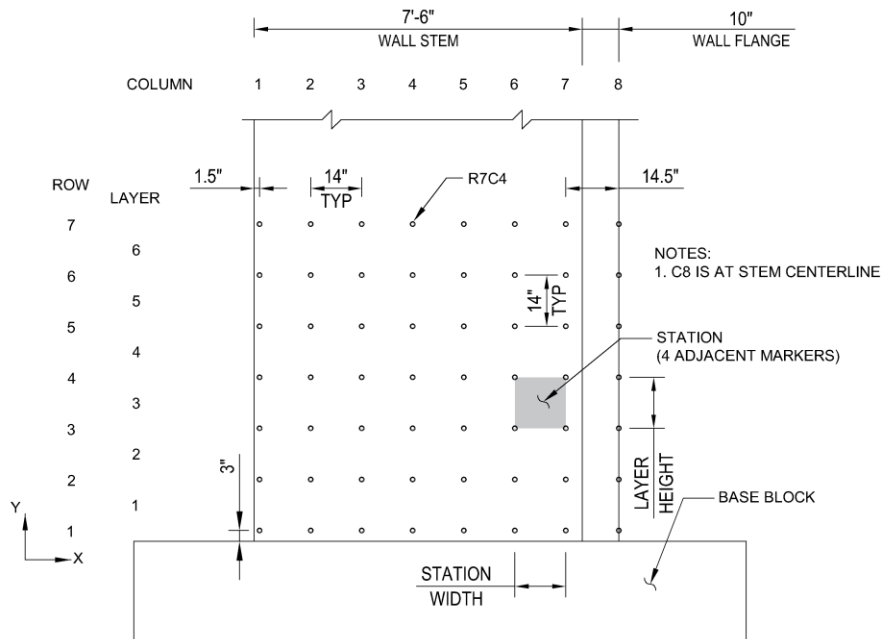


Figure 30 – Locations of optical markers on wall stem (1 in. = 25.4 mm)

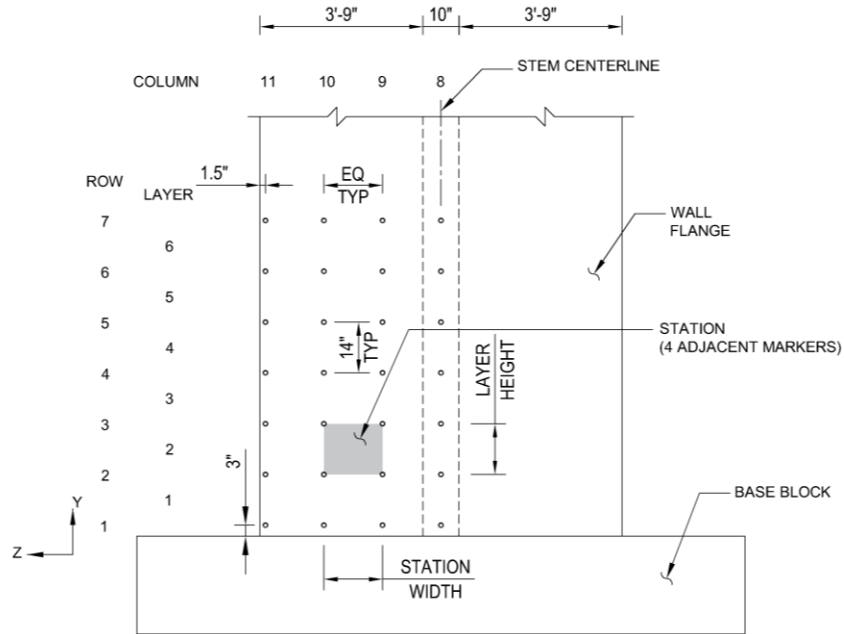


Figure 31 – Locations of optical markers on wall flange (1 in. = 25.4 mm)

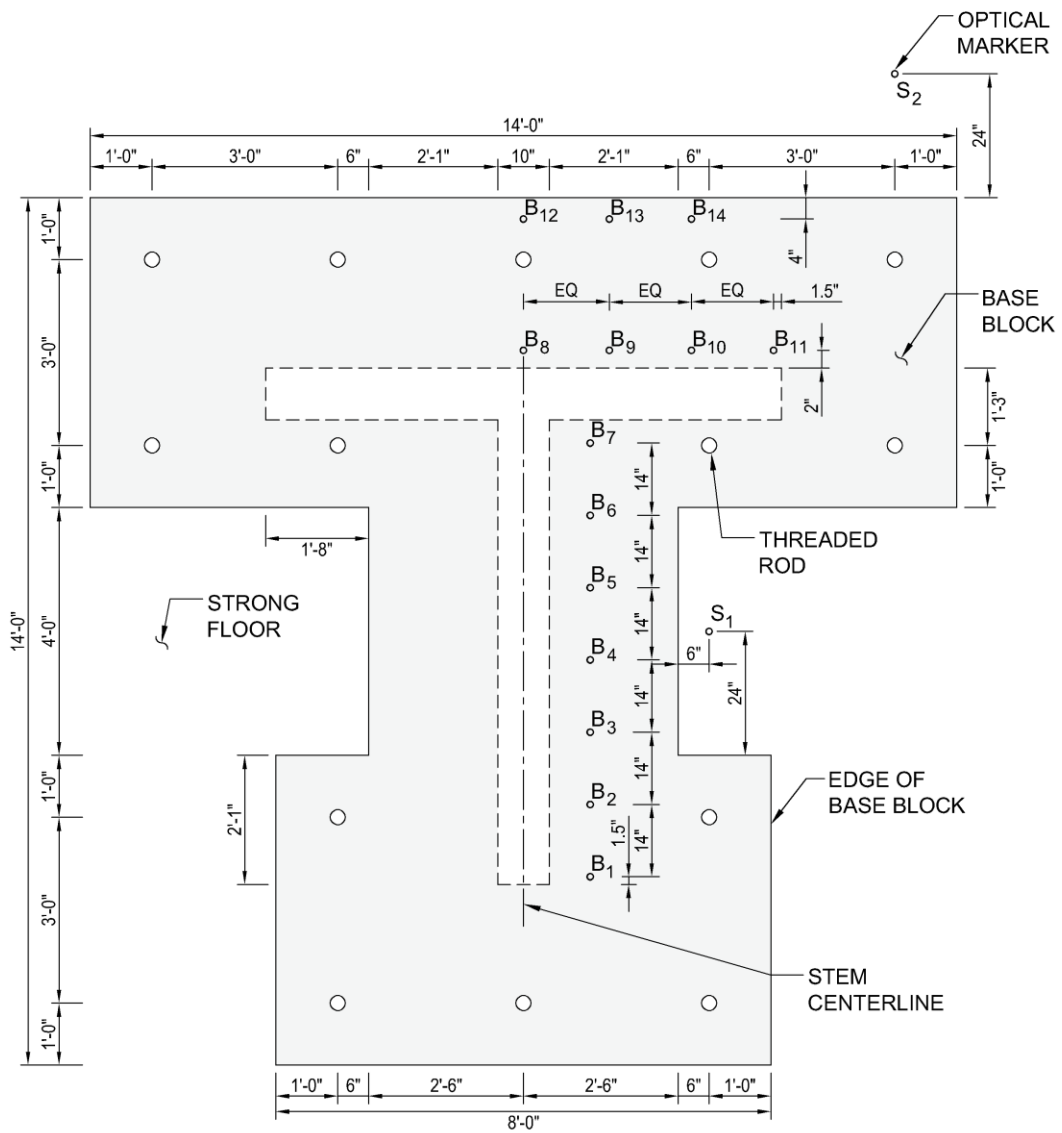


Figure 32 – Plan view of base block indicating locations of optical markers (1 in. = 25.4 mm)

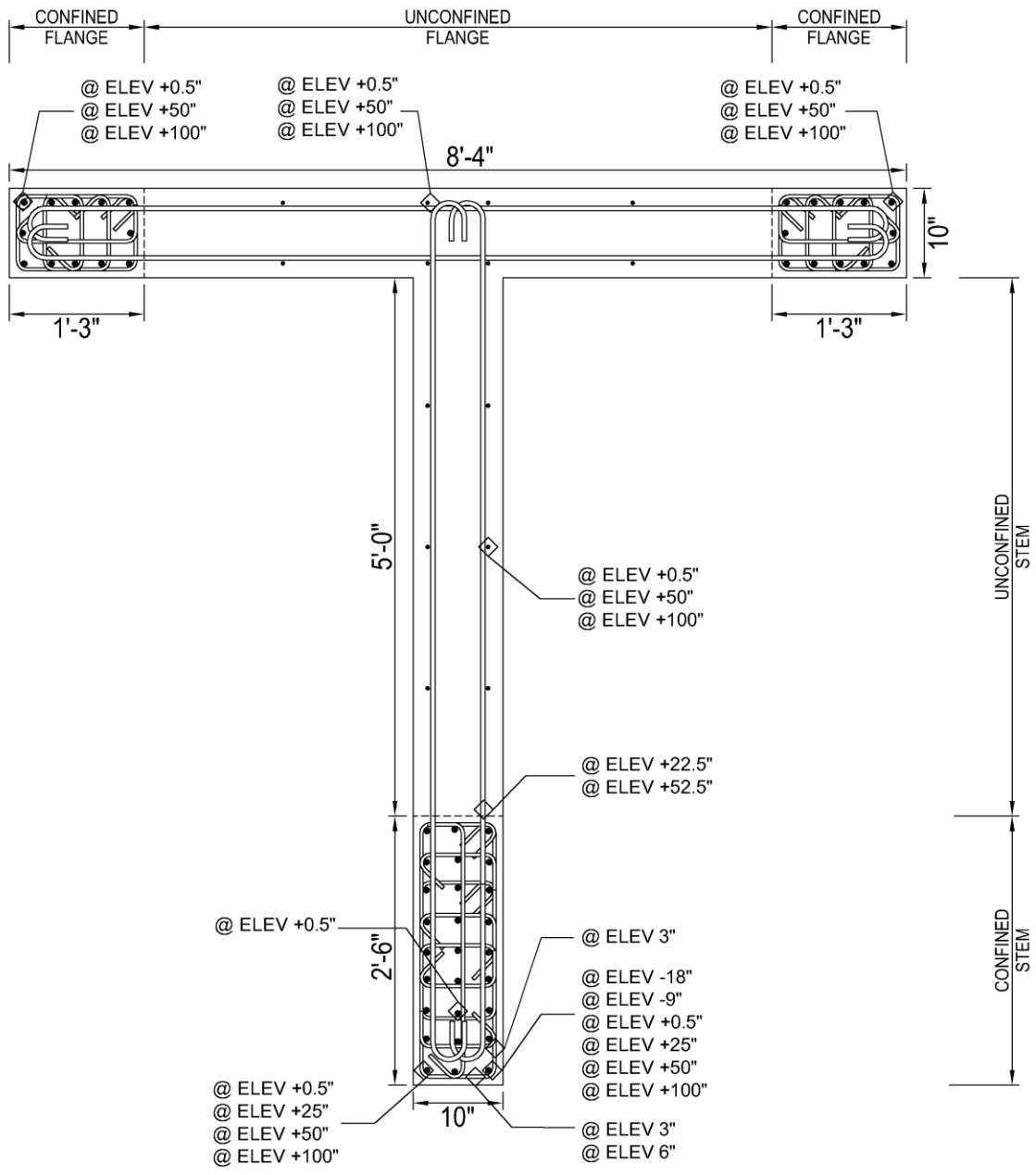


Figure 33 – Wall T1 strain gauge locations (1 in. = 25.4 mm)

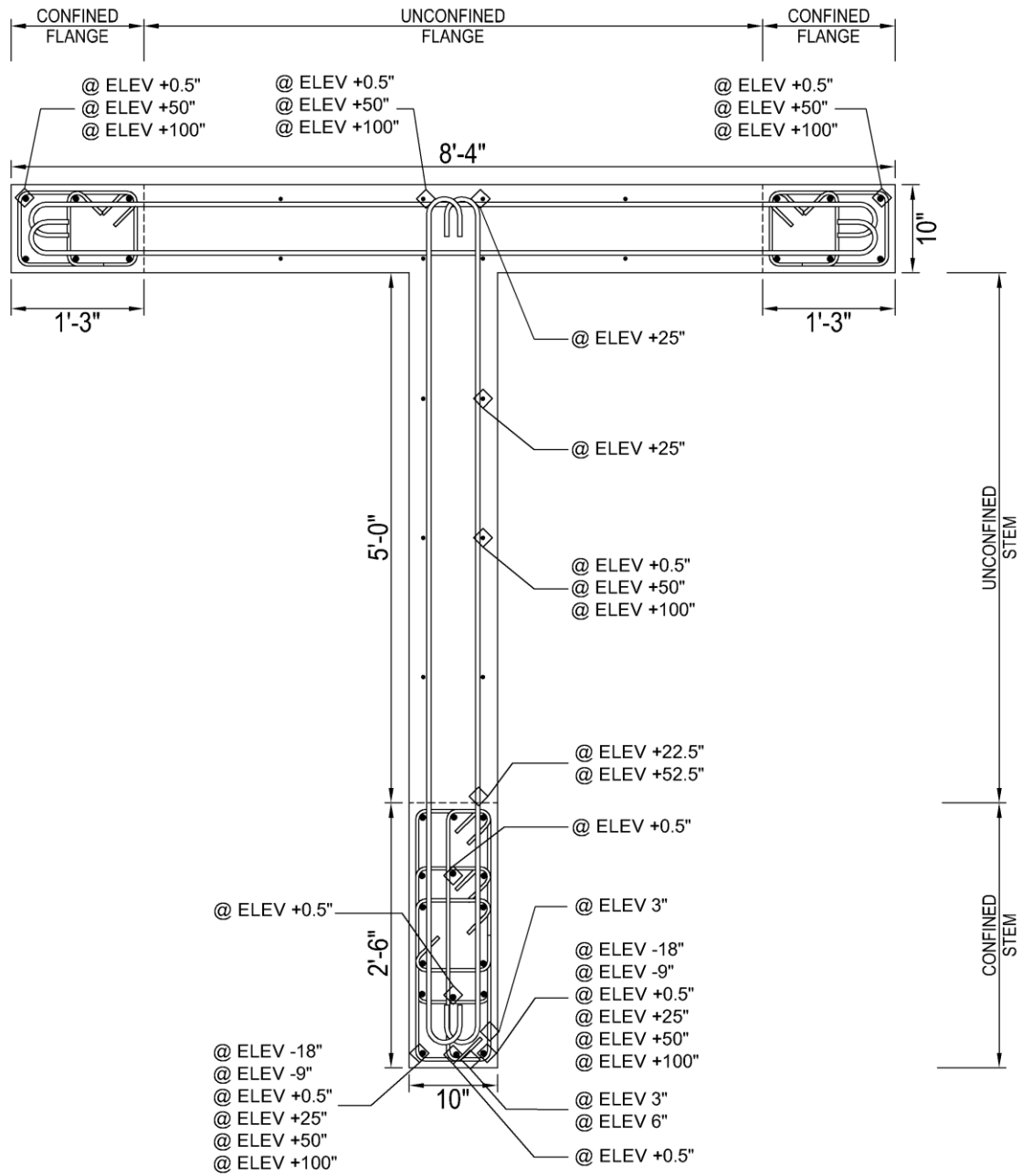


Figure 34 – Wall T2 strain gauge locations (1 in. = 25.4 mm)

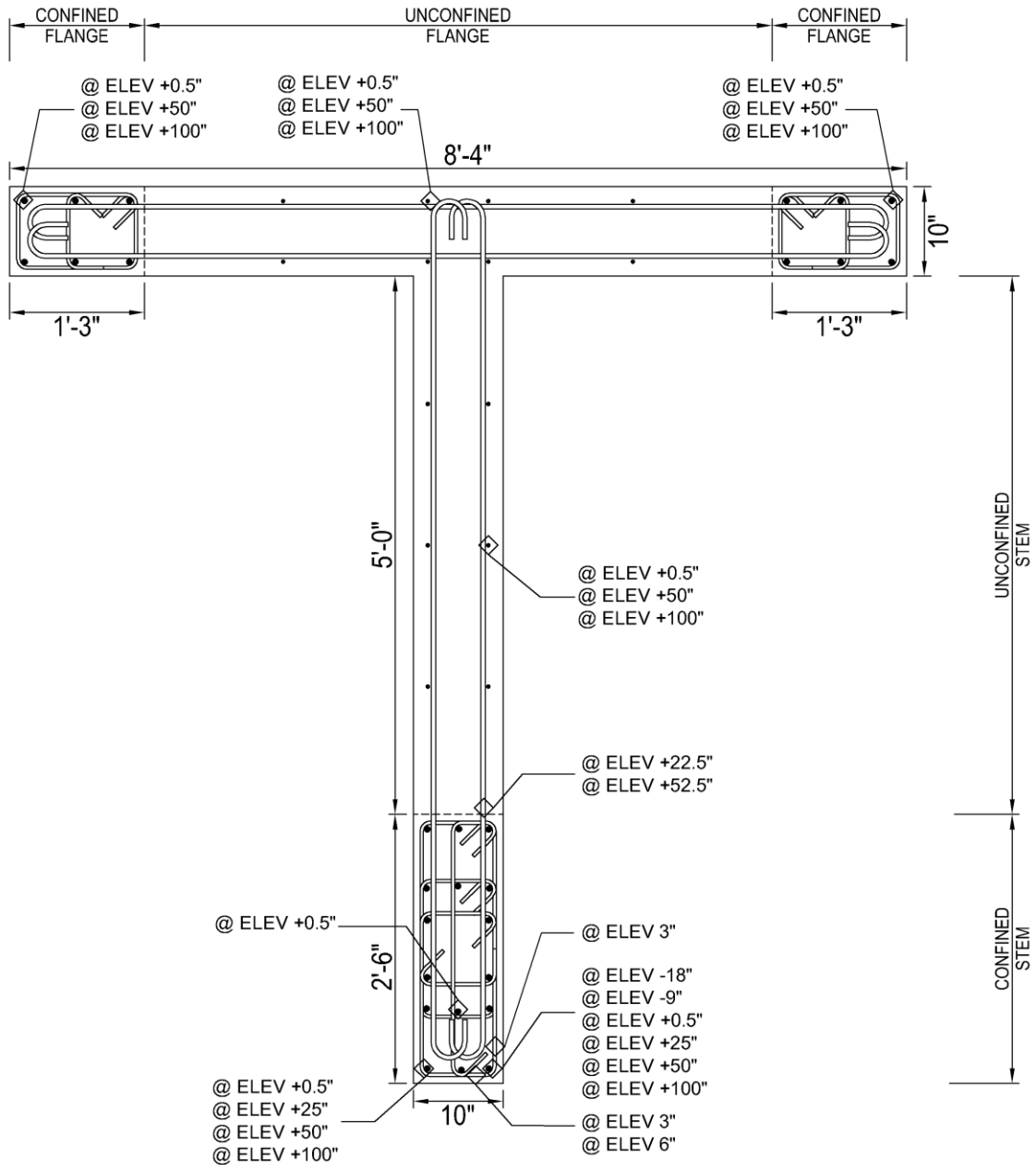


Figure 35 – Wall T3 strain gauge locations (1 in. = 25.4 mm)

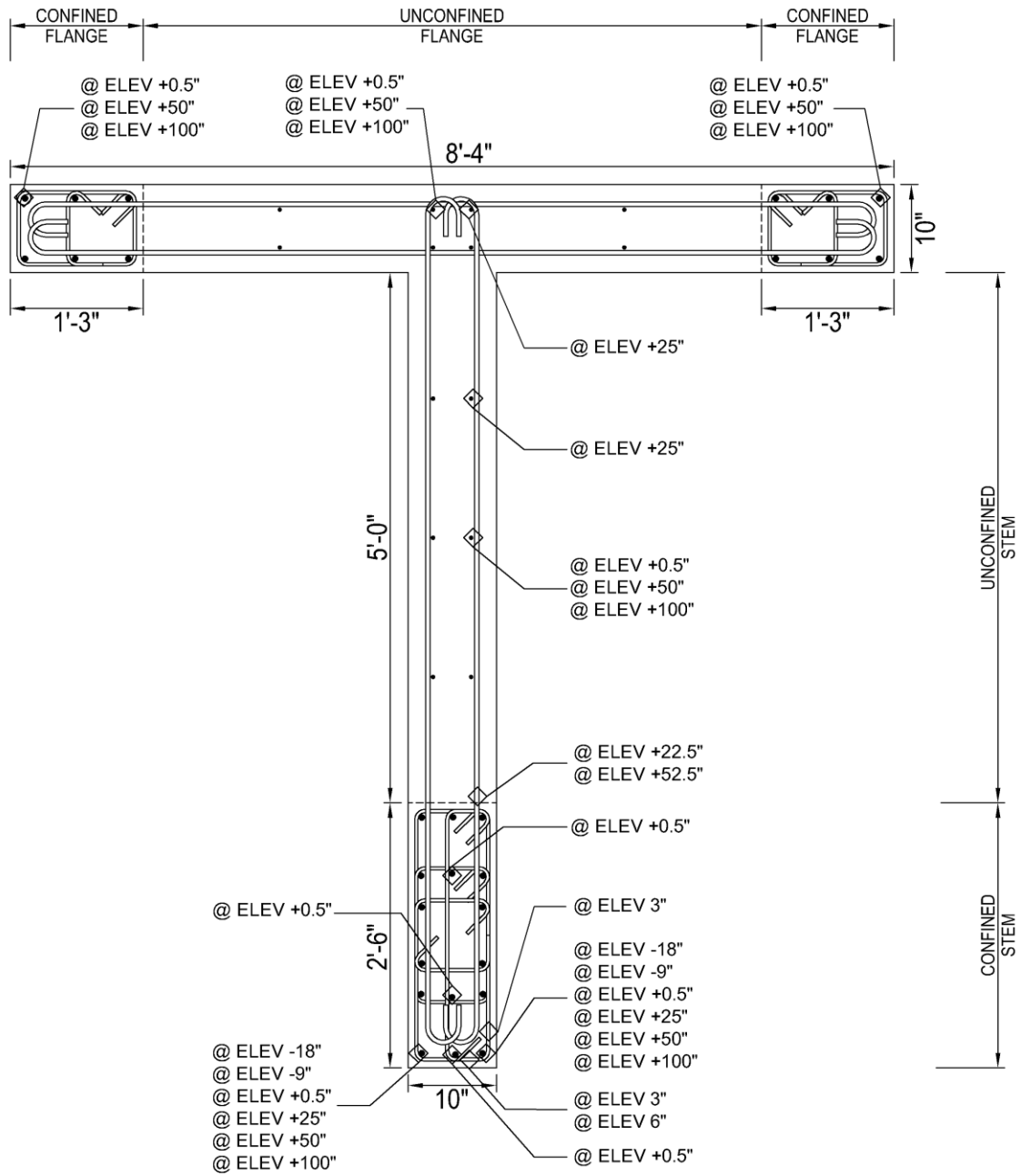


Figure 36 – Wall T4 strain gauge locations (1 in. = 25.4 mm)

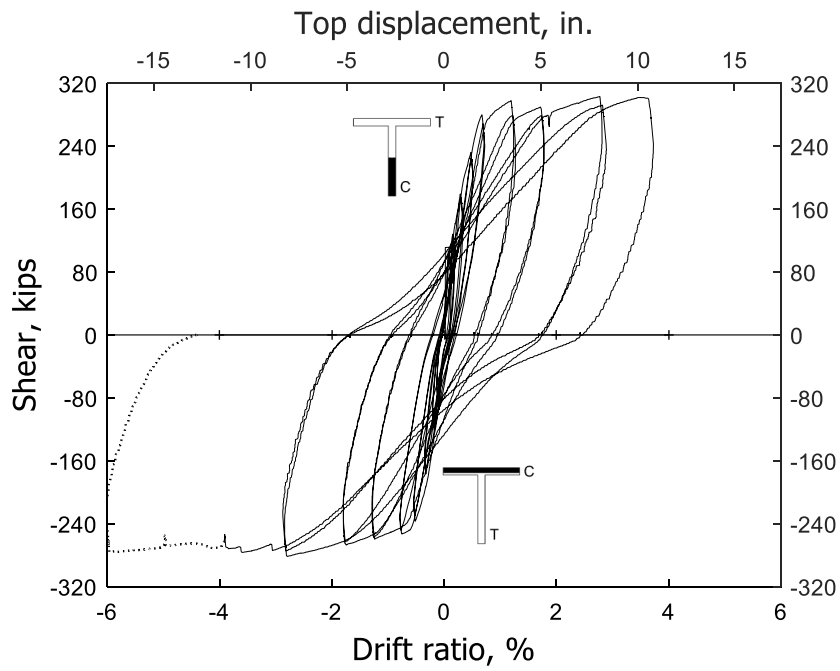


Figure 37 – Shear versus drift ratio for T1 (1 in. = 25.4 mm, 1 kip = 4.45 kN)

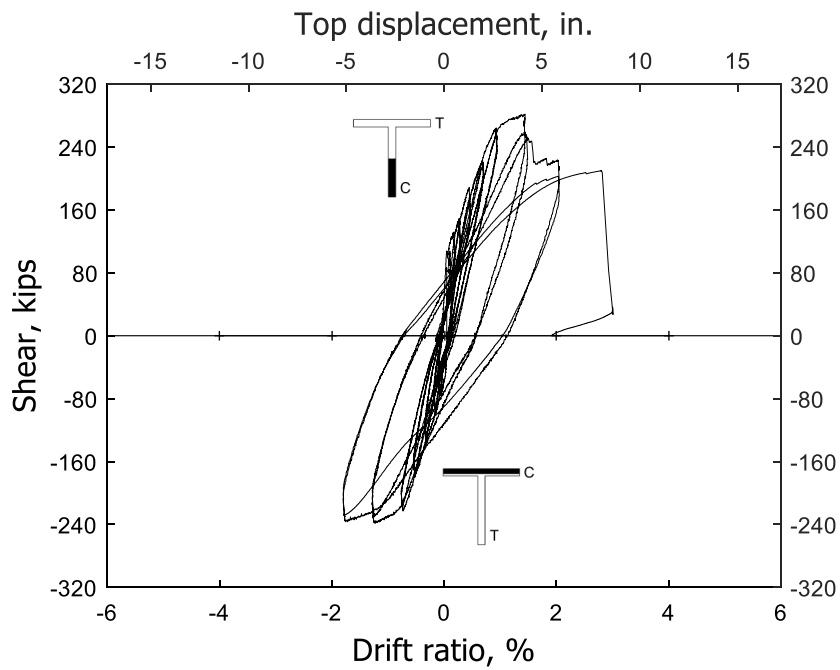


Figure 38 – Shear versus drift ratio for T2 (1 in. = 25.4 mm, 1 kip = 4.45 kN)

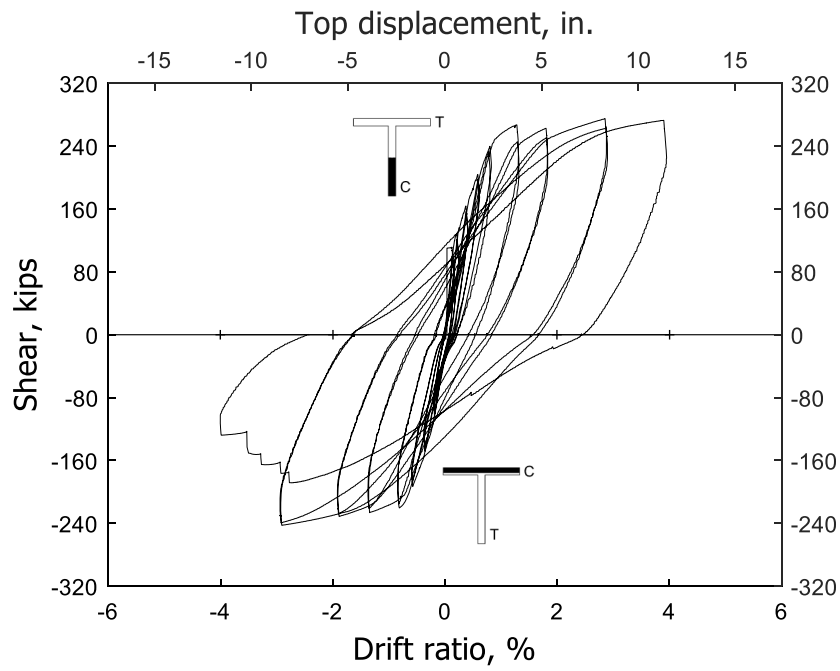


Figure 39 – Shear versus drift ratio for T3 (1 in. = 25.4 mm, 1 kip = 4.45 kN)

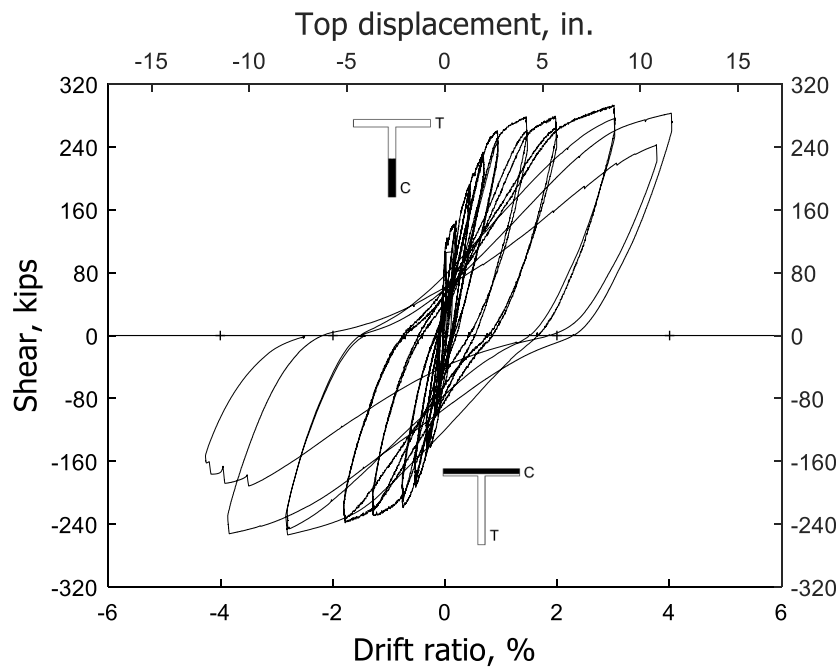


Figure 40 – Shear versus drift ratio for T4 (1 in. = 25.4 mm, 1 kip = 4.45 kN)

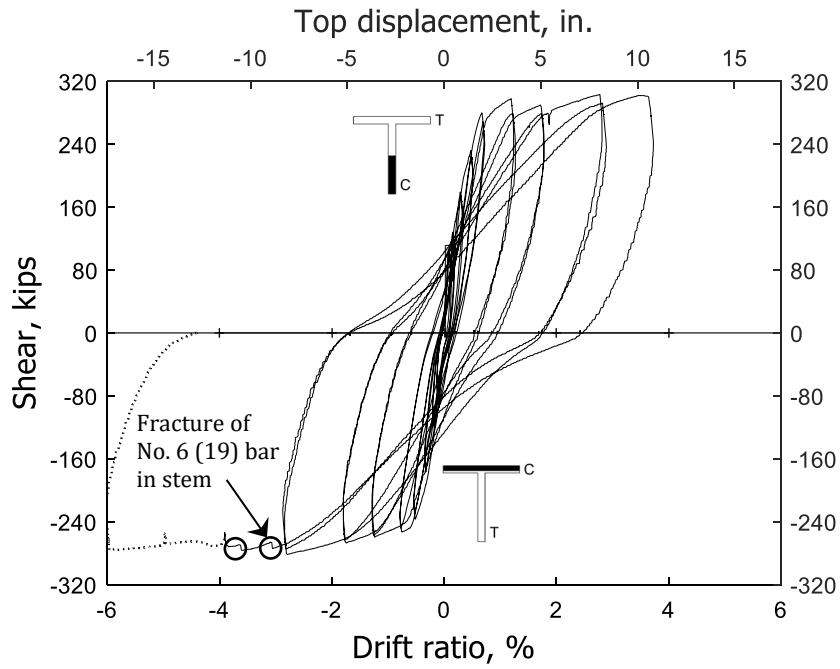


Figure 41 – Shear versus drift ratio for T1 indicating fracture of longitudinal bars
 (1 in. = 25.4 mm, 1 kip = 4.45 kN)

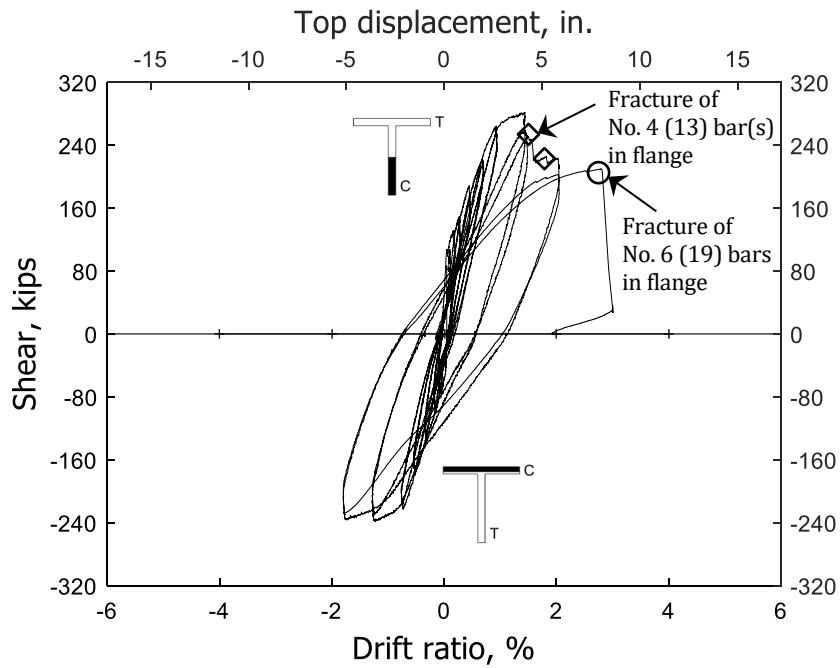


Figure 42 – Shear versus drift ratio for T2 indicating fracture of longitudinal bars
 (1 in. = 25.4 mm, 1 kip = 4.45 kN)

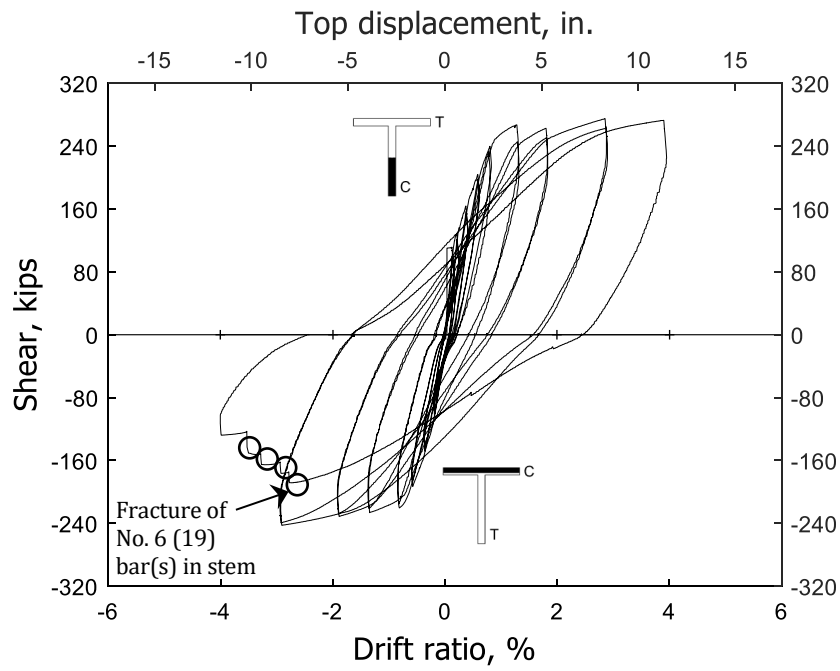


Figure 43 – Shear versus drift ratio for T3 indicating fracture of longitudinal bars
(1 in. = 25.4 mm, 1 kip = 4.45 kN)

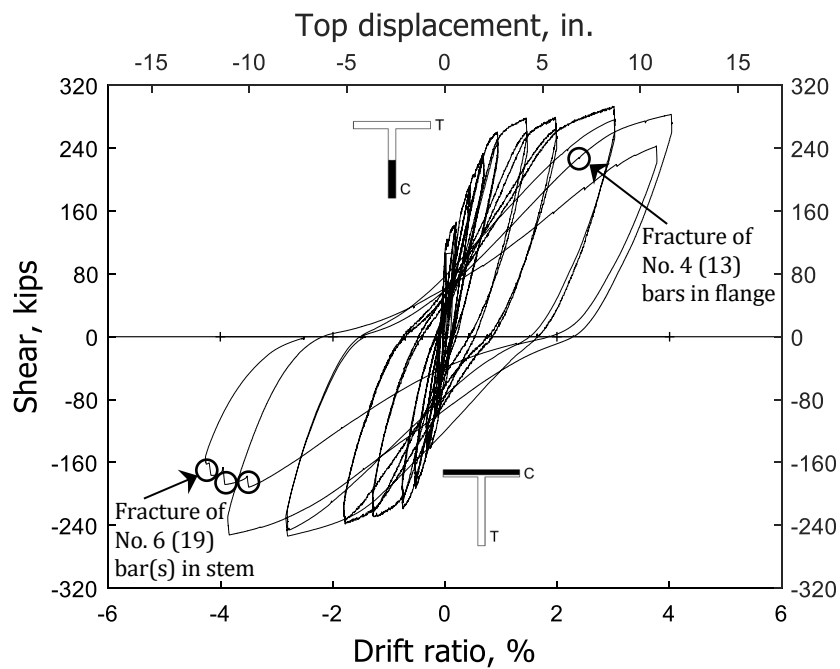
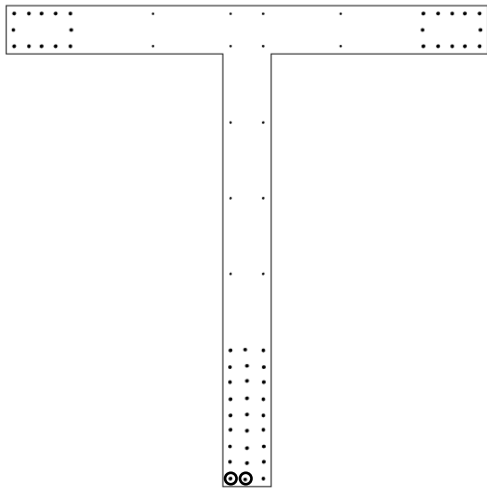
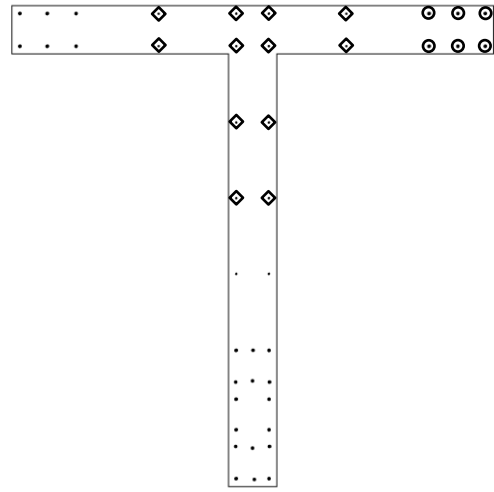


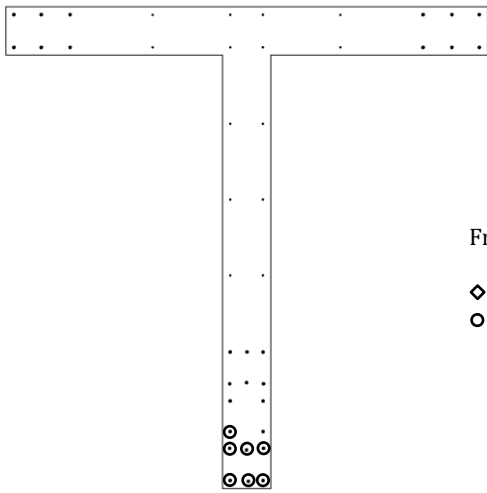
Figure 44 – Shear versus drift ratio for T4 indicating fracture of longitudinal bars
(1 in. = 25.4 mm, 1 kip = 4.45 kN)



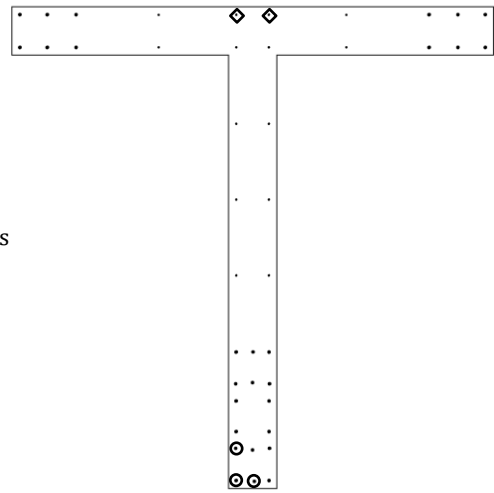
(a) Wall T1



(b) Wall T2



(c) Wall T3



(d) Wall T4

Fractured Bars

- ◇ No. 4 (13)
- No. 6 (19)

Figure 45 – Map of fractured bars

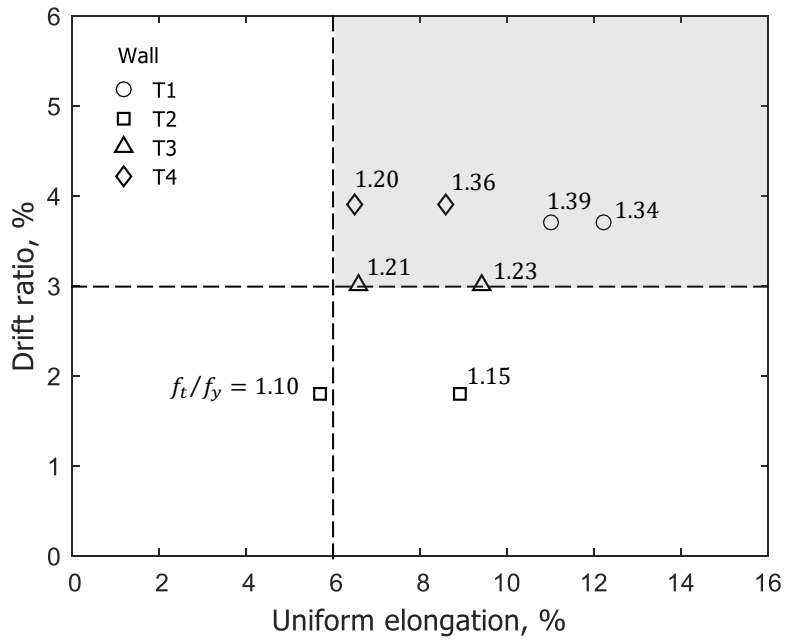


Figure 46 – Wall drift ratio capacity versus uniform elongation of longitudinal reinforcing bars, based on data from Table 7

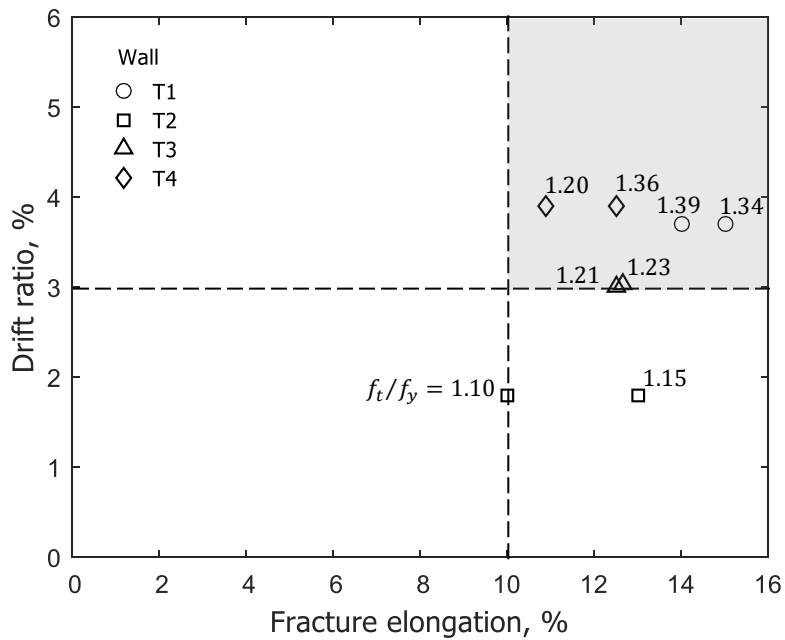


Figure 47 – Wall drift ratio capacity versus fracture elongation of longitudinal reinforcing bars, based on data from Table 7



(a) Stem in compression



(b) Stem in tension

Figure 48 – Wall T1 at 1% drift ratio



(a) Stem in compression



(b) Stem in tension

Figure 49 – Wall T2 at 1% drift ratio



(a) Stem in compression



(b) Stem in tension

Figure 50 – Wall T3 at 1% drift ratio



(a) Stem in compression



(b) Stem in tension

Figure 51 – Wall T4 at 1% drift ratio



(a) Stem in compression



(b) Stem in tension

Figure 52 – Wall T1 at 2% drift ratio



(a) Stem in compression



(b) Stem in tension

Figure 53 – Wall T2 at 2% drift ratio

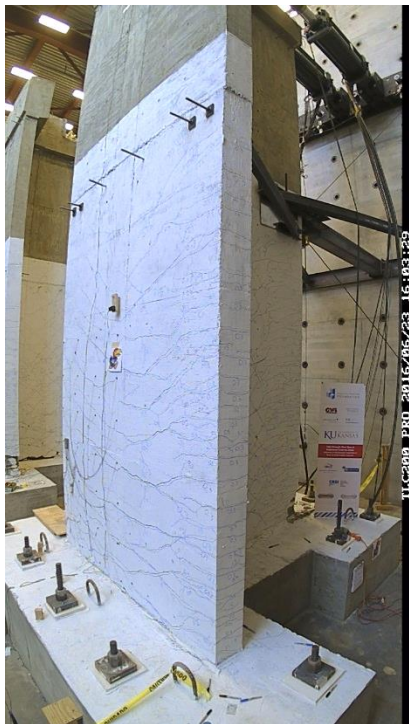


(a) Stem in compression



(b) Stem in tension

Figure 54 – Wall T3 at 2% drift ratio



(a) Stem in compression



(b) Stem in tension

Figure 55 – Wall T4 at 2% drift ratio

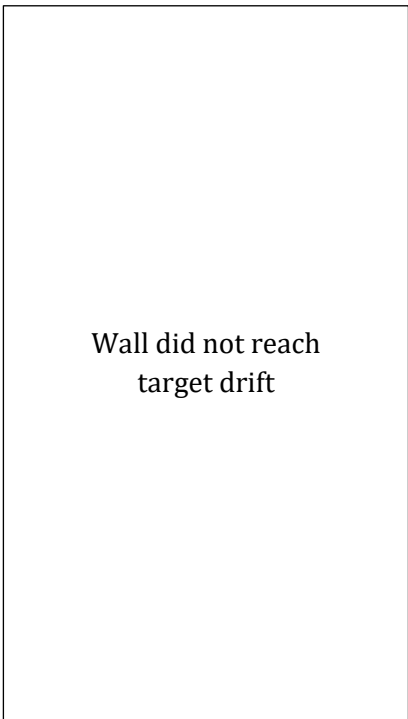


(a) Stem in compression

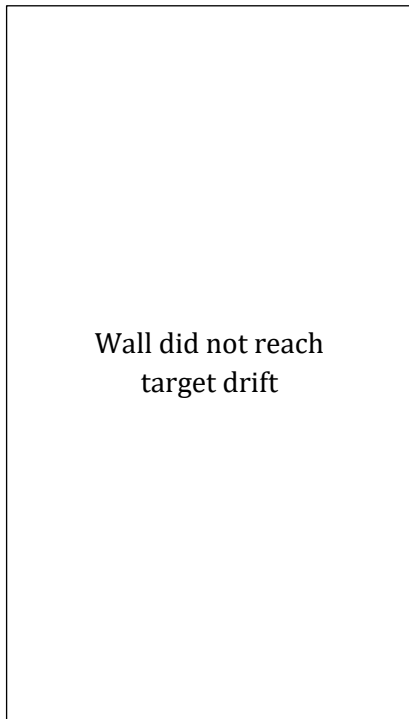


(b) Stem in tension

Figure 56 – Wall T1 at 3% drift ratio



(a) Stem in compression



(b) Stem in tension

Figure 57 – Wall T2 at 3% drift ratio



(a) Stem in compression

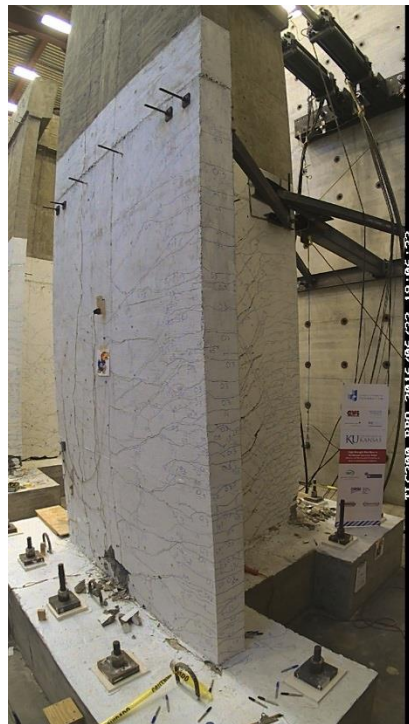


(b) Stem in tension

Figure 58 – Wall T3 at 3% drift ratio



(a) Stem in compression



(b) Stem in tension

Figure 59 – Wall T4 at 3% drift ratio

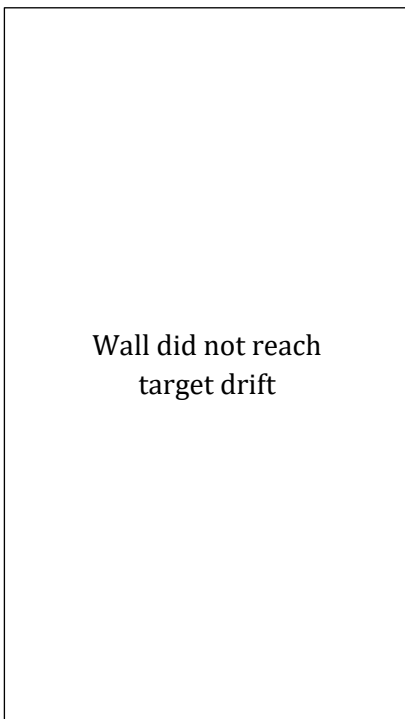


(a) Stem in compression

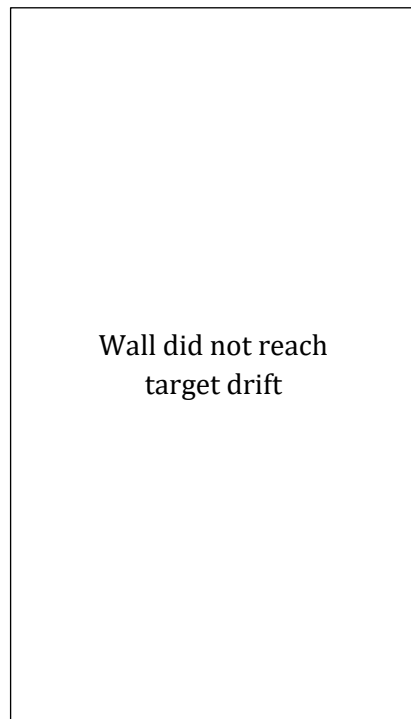


(b) Stem in tension

Figure 60 – Wall T1 at 4% drift ratio



(a) Stem in compression



(b) Stem in tension

Figure 61 – Wall T2 at 4% drift ratio



(a) Stem in compression



(b) Stem in tension

Figure 62 – Wall T3 at 4% drift ratio



(a) Stem in compression



(b) Stem in tension

Figure 63 – Wall T4 at 4% drift ratio

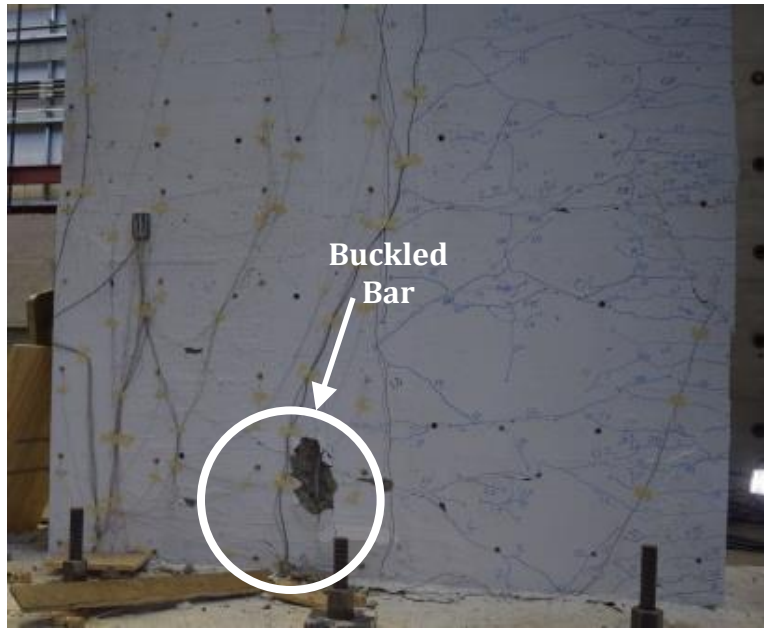


Figure 64 – Wall T1 with bar buckling in unconfined flange during first cycle to 2% drift ratio (stem in tension)

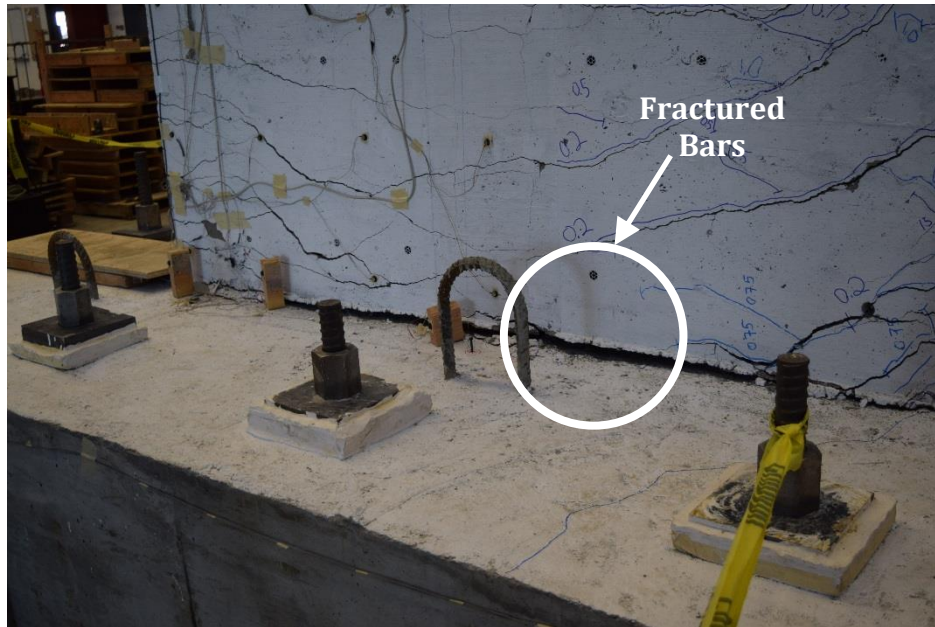


Figure 65 – Wall T2 with bar fracture in unconfined flange at base during first cycle to 2% drift ratio (stem in compression)

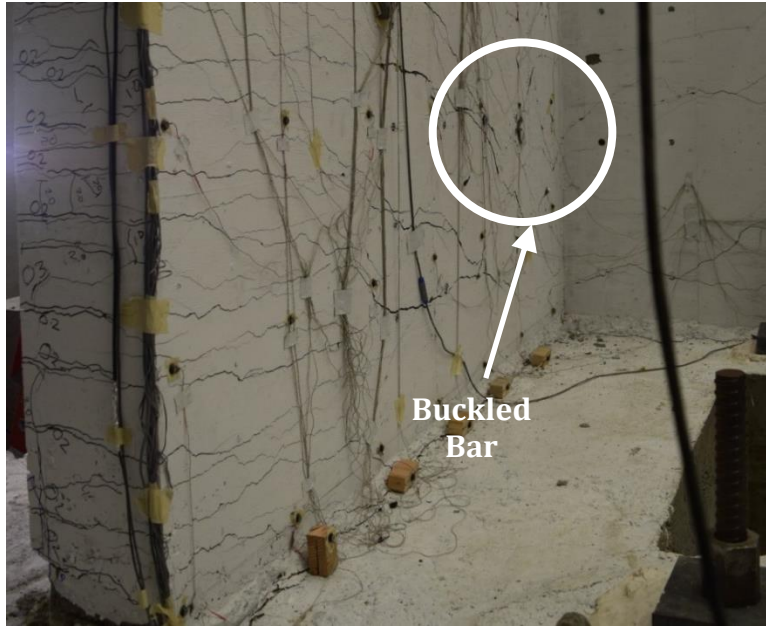


Figure 66 – Wall T3 with bar buckling in unconfined stem during second cycle to 2% drift ratio (stem in tension)



Figure 67 – Wall T4 without bar buckling or fracture in unconfined flange during second cycle to 2% drift ratio (stem in compression)

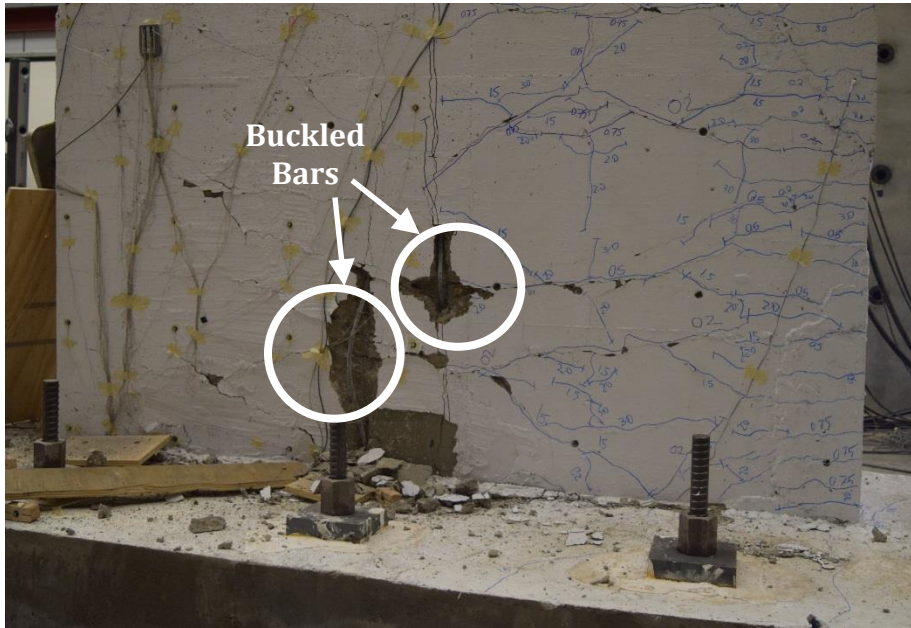


Figure 68 – Wall T1 with additional bar buckling in unconfined flange during second cycle to 3% drift ratio (stem in tension)

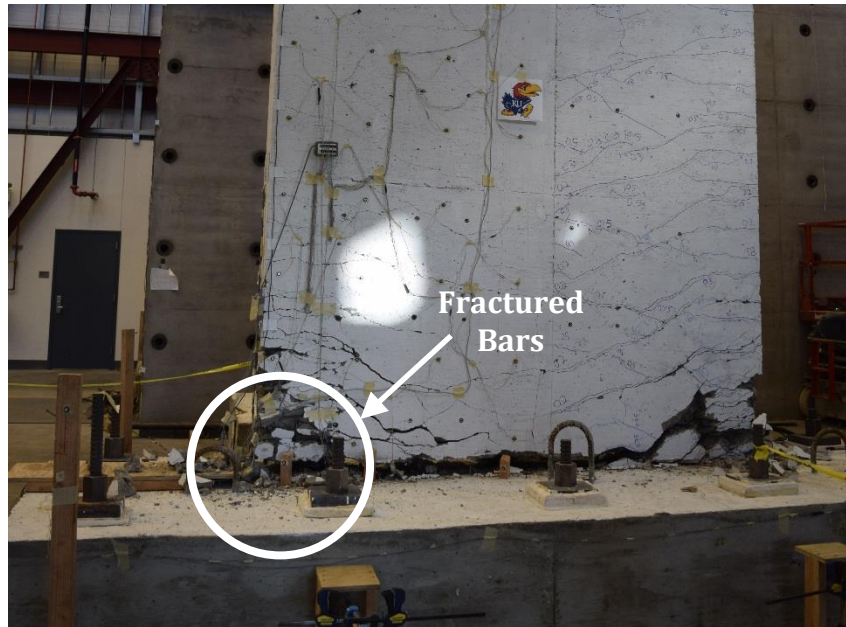


Figure 69 – Wall T2 with bar fracture in confined flange at base during first cycle to 3% drift ratio (stem in compression)

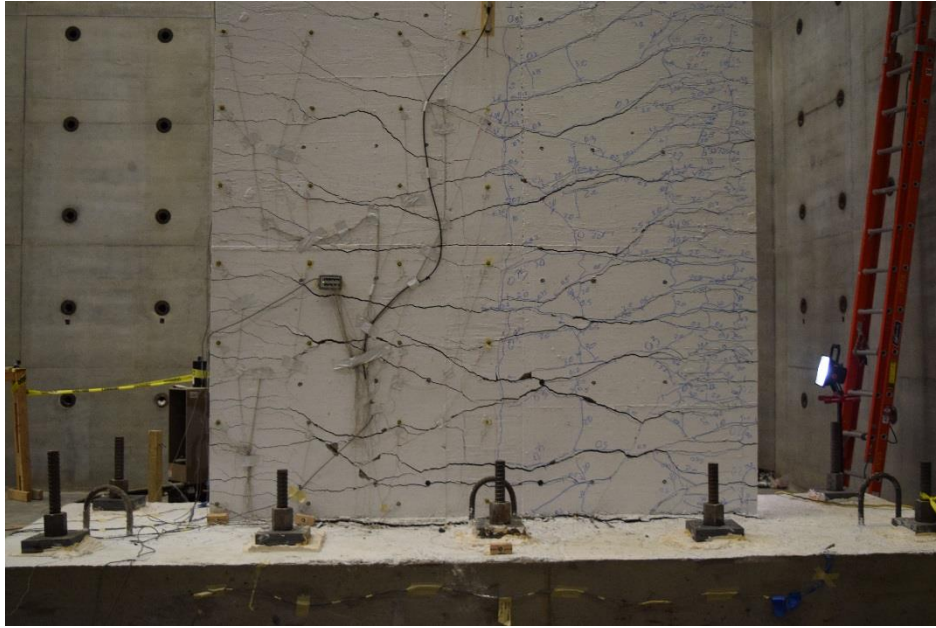


Figure 70 – Wall T3 without bar buckling or fracture in unconfined flange during second cycle to 3% drift ratio (stem in compression)



Figure 71 – Wall T4 with bar buckling in unconfined flange during second cycle to 3% drift ratio (stem in tension)

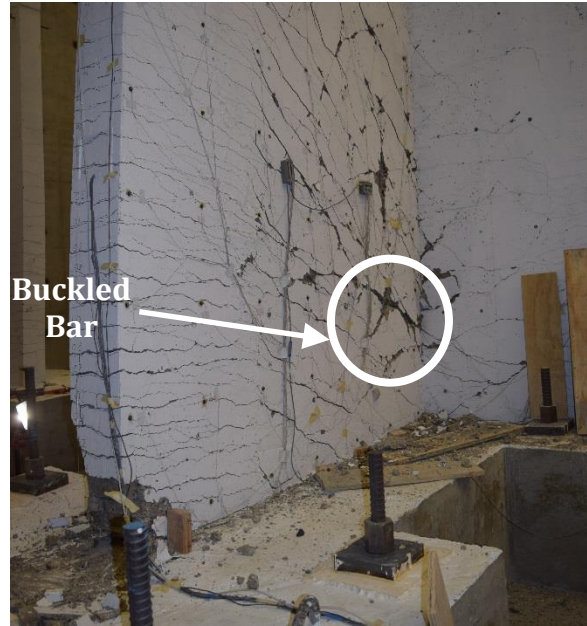
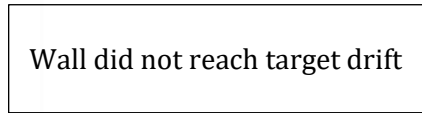


Figure 72 – Wall T1 with bar buckling in unconfined stem during first cycle to 4% drift ratio (stem in tension)



Figure 73 – Wall T1 with bar fracture in confined stem during first cycle to 4% drift ratio (stem in tension)



Wall did not reach target drift

Figure 74 – Wall T2 at 4% drift ratio



Wall did not reach target drift

Figure 75 – Wall T2 at 4% drift ratio

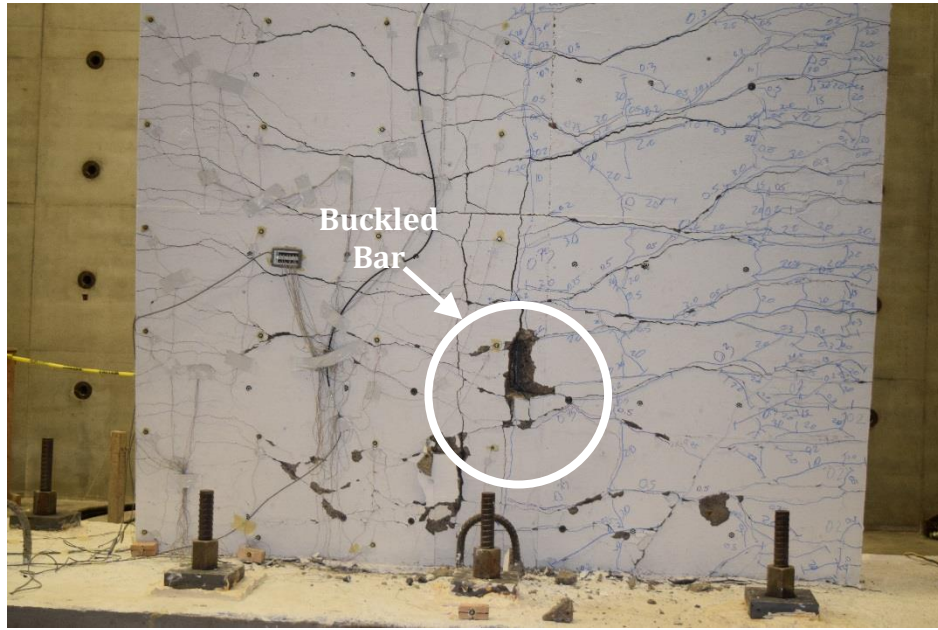


Figure 76 – Wall T3 with bar buckling in unconfined flange during first cycle to 4% drift ratio (stem in tension)

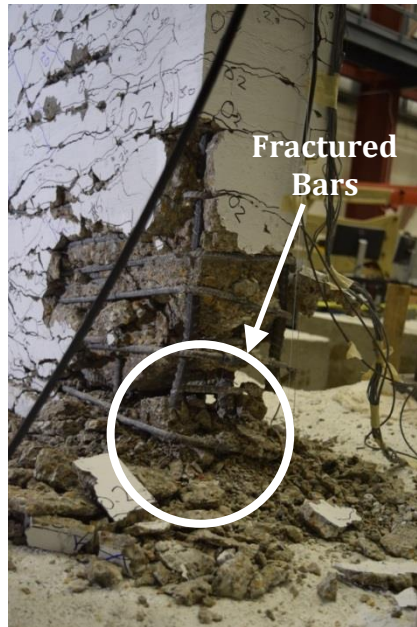


Figure 77 – Wall T3 with bar fracture in confined stem during first cycle to 4% drift ratio (stem in tension)

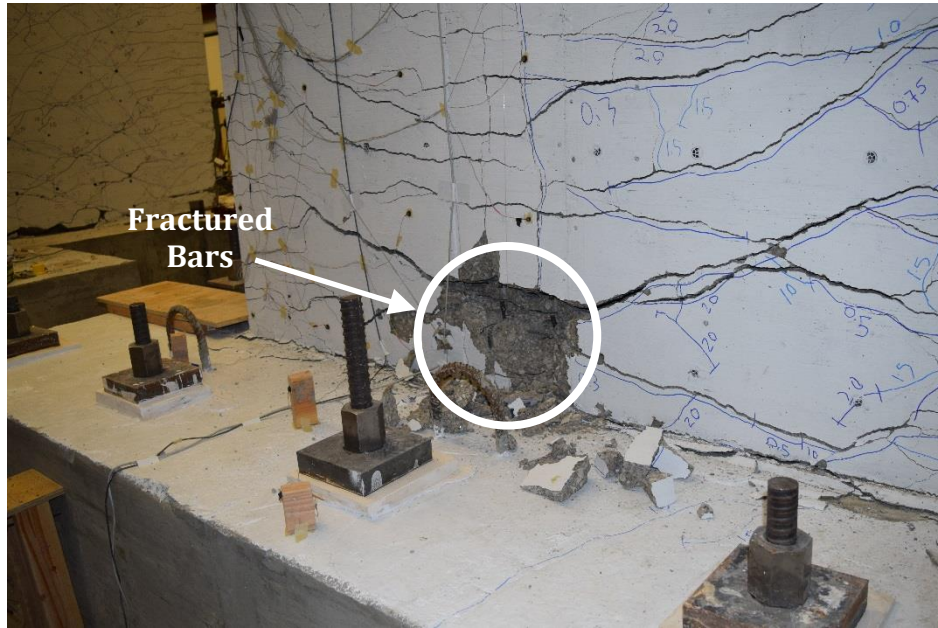
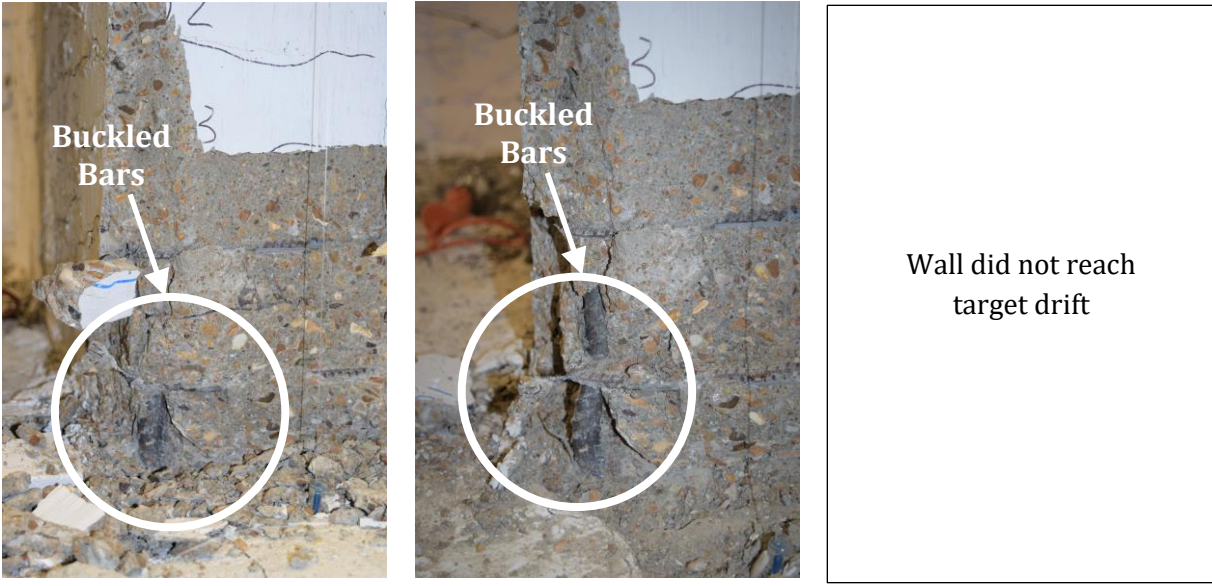


Figure 78 – Wall T4 with bar fracture in unconfined flange during first cycle to 4% drift ratio (stem in compression)

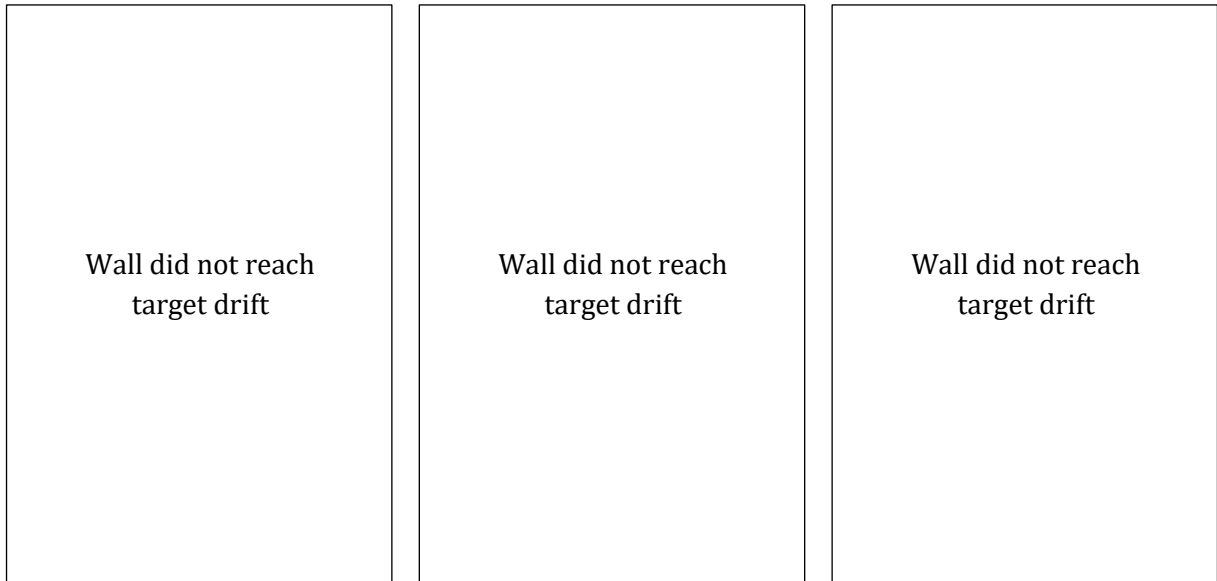


Figure 79 – Wall T4 with bar fracture in confined stem during second cycle to 4% drift ratio (stem in tension)



(a) Second cycle to 3% drift (b) First cycle to 4% drift (c) Second cycle to 4% drift

Figure 80 – Condition of confined stem in compression leading to bar buckling before bar fracture in T1



(a) Second cycle to 3% drift (b) First cycle to 4% drift (c) Second cycle to 4% drift

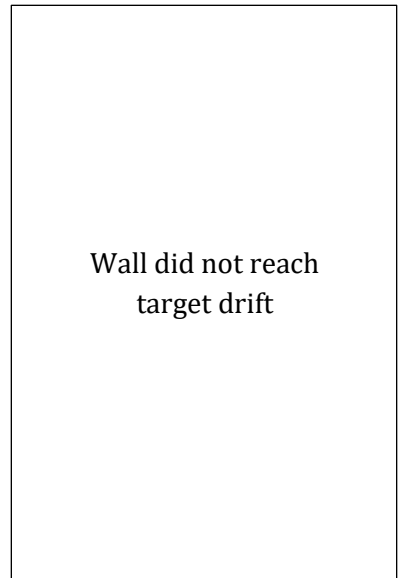
Figure 81 – Condition of confined stem in T2



(a) Second cycle to 3% drift



(b) First cycle to 4% drift

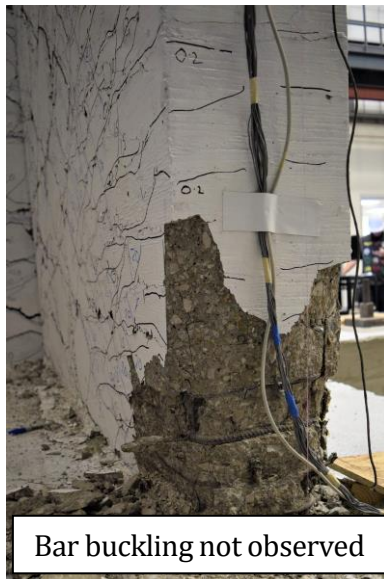


(c) Second cycle to 4% drift

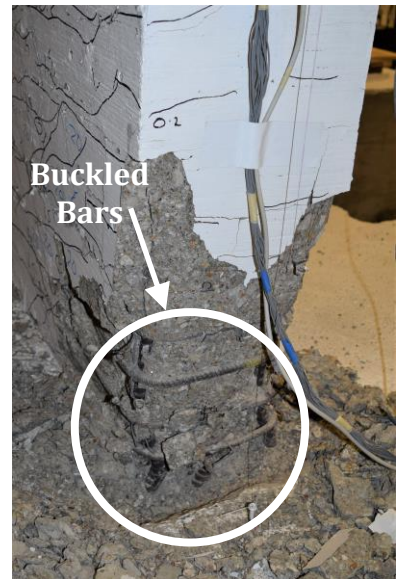
Figure 82 – Condition of confined stem in compression leading to bar buckling before bar fracture in T3



(a) Second cycle to 3% drift

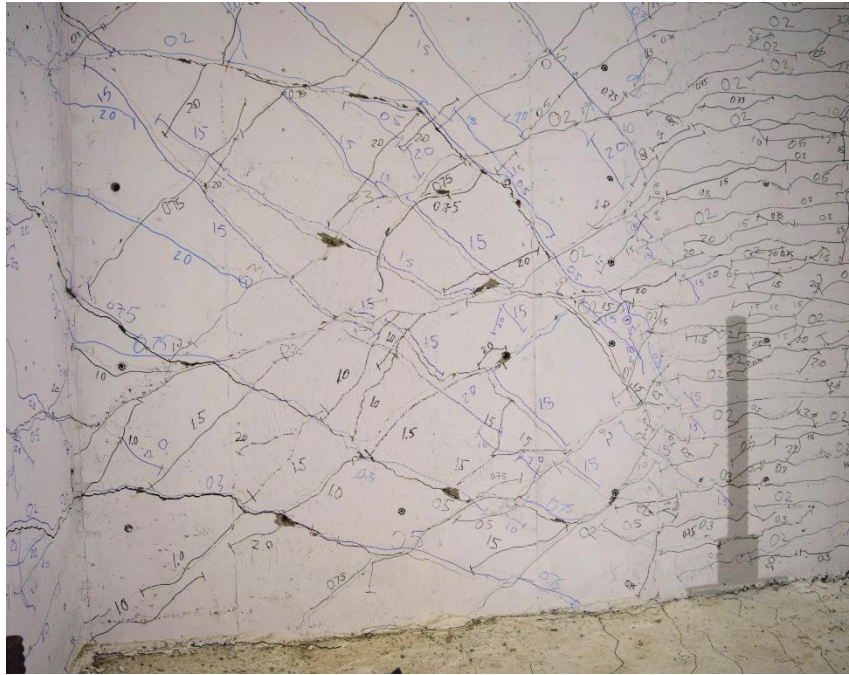


(b) First cycle to 4% drift

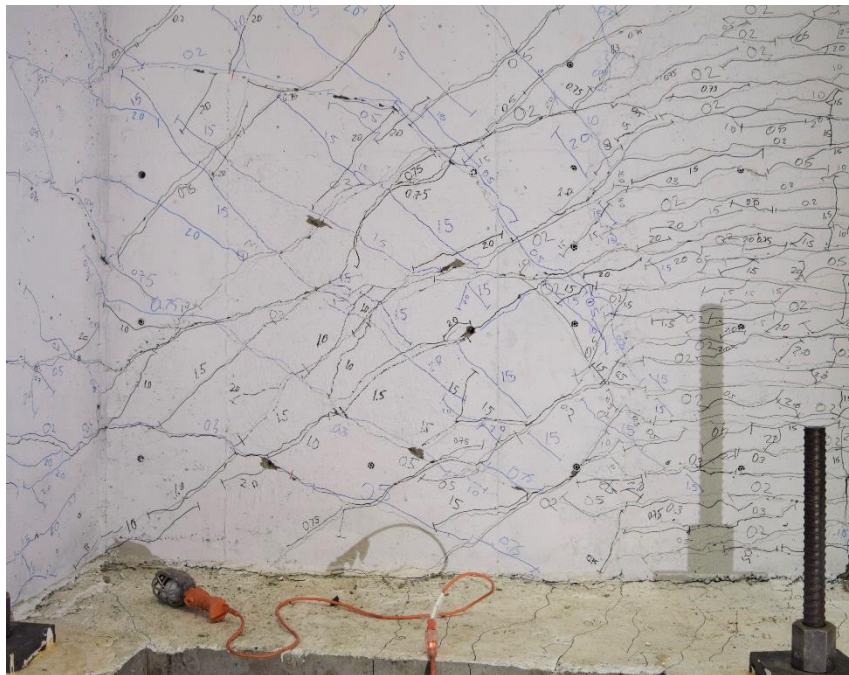


(c) Second cycle to 4% drift

Figure 83 – Condition of confined stem in compression leading to bar buckling before bar fracture in T4



(a) Stem in compression

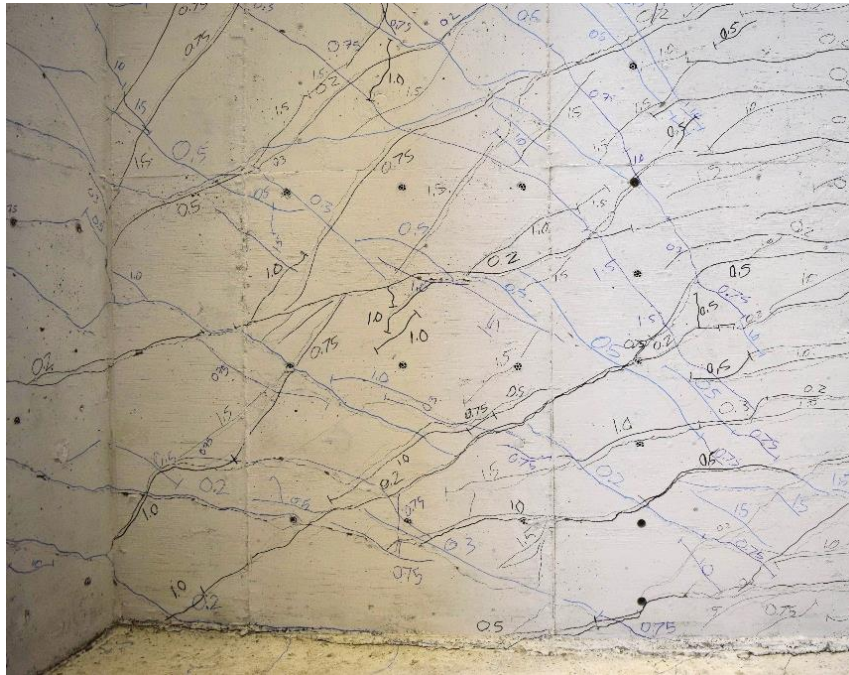


(b) Stem in tension

Figure 84 – Condition of stem in T1 at peak of second cycle to 2% drift ratio



(a) Stem in compression

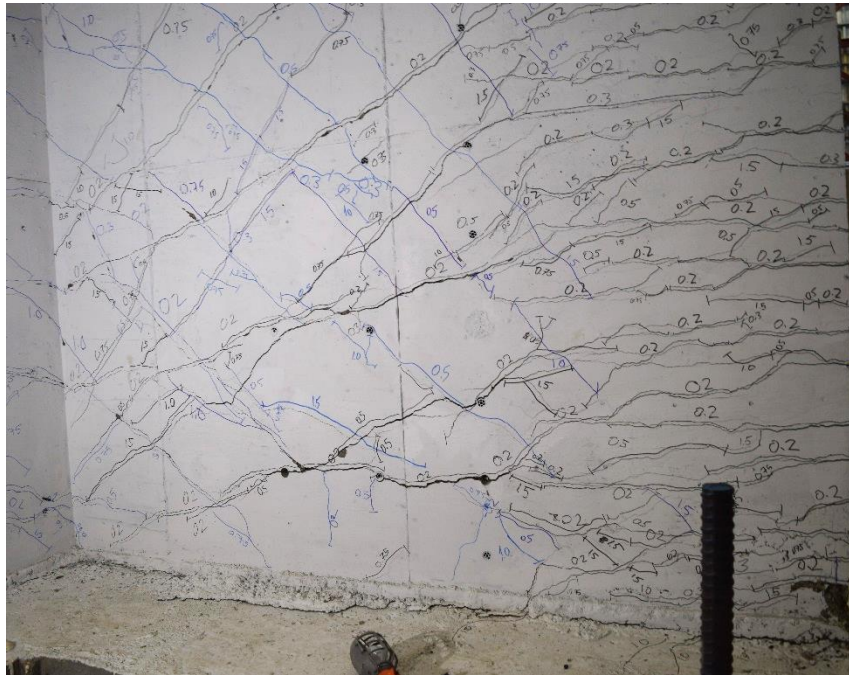


(b) Stem in tension

Figure 85 – Condition of stem in T2 at peak of second cycle to 1.5% drift ratio



(a) Stem in compression



(b) Stem in tension

Figure 86 – Condition of stem in T3 at peak of second cycle to 2% drift ratio

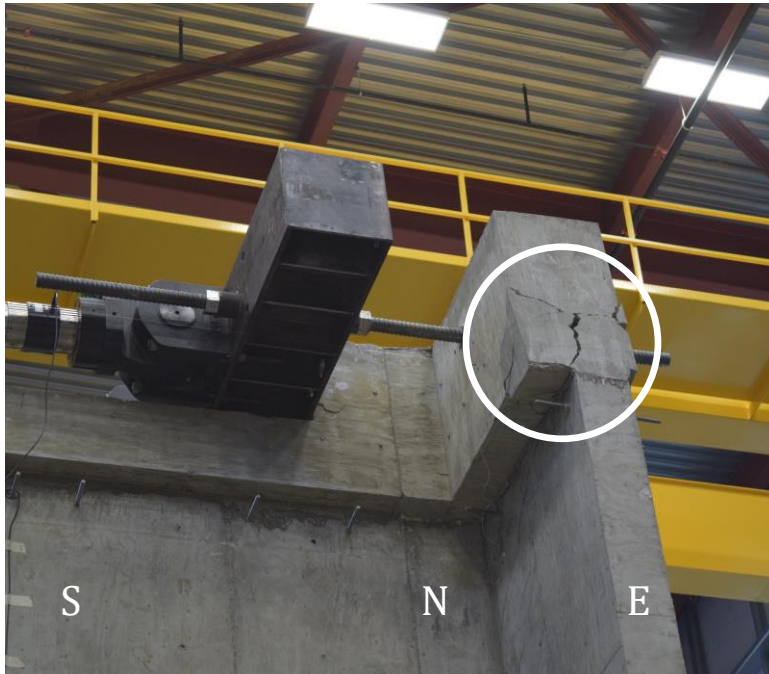


(a) Stem in compression

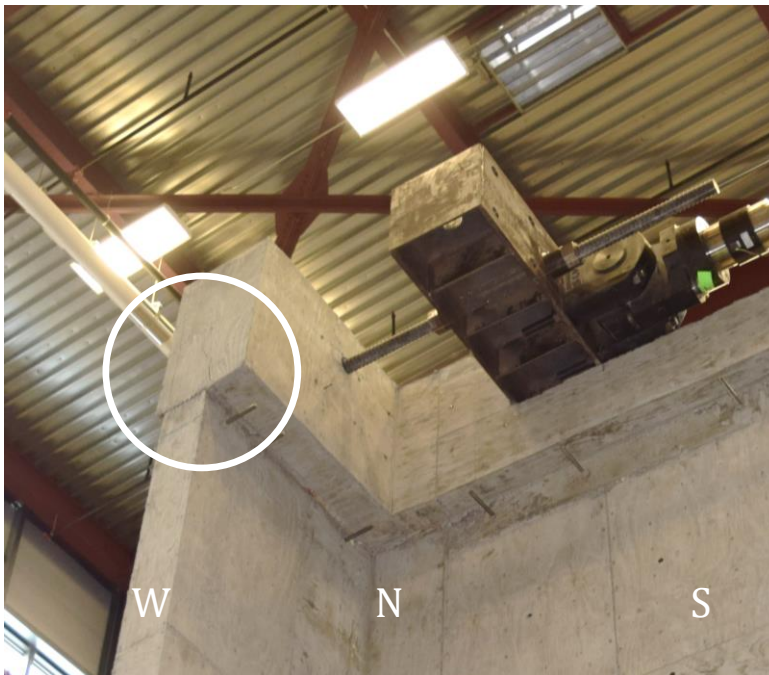


(b) Stem in tension

Figure 87 – Condition of stem in T4 at peak of second cycle to 2% drift ratio



(a) East side



(b) West side

Figure 88 - Top block damage in T1 at 2% drift

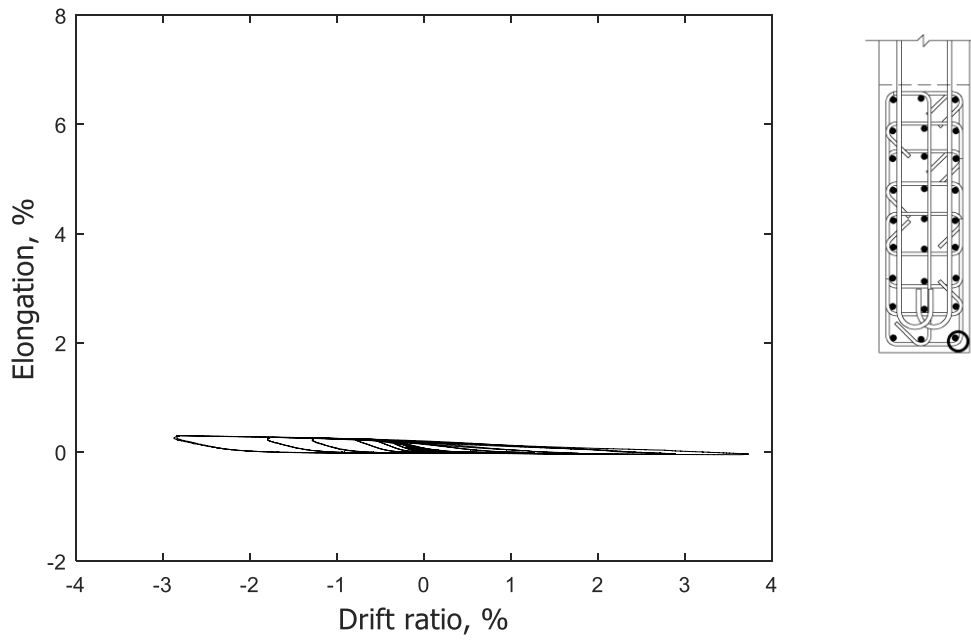


Figure 89 – Measured strain in longitudinal bar at confined stem 18 in. (457 mm) below base of T1

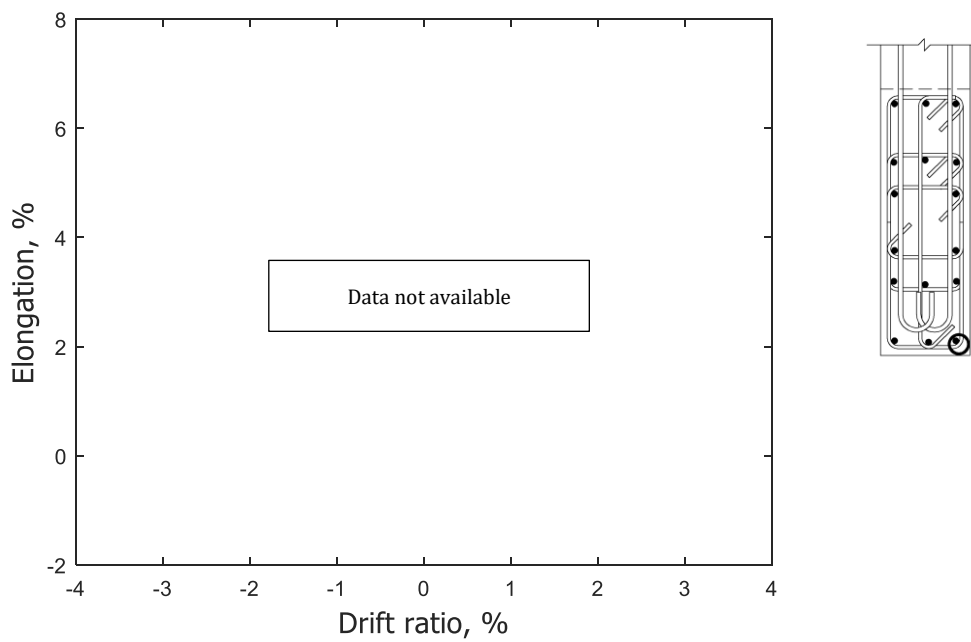


Figure 90 – Measured strain in longitudinal bar at confined stem 18 in. (457 mm) below base of T2

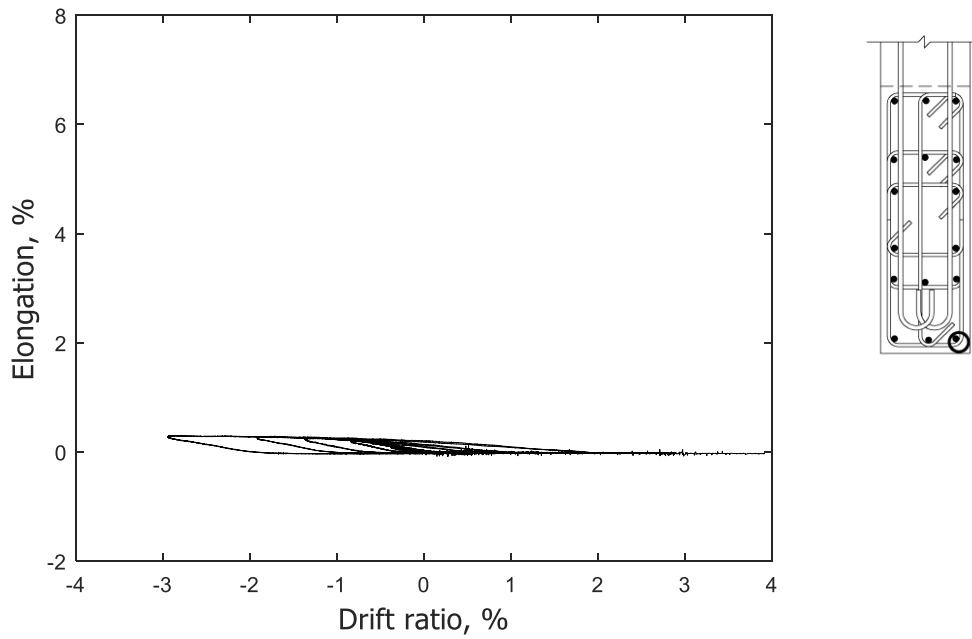


Figure 91 – Measured strain in longitudinal bar at confined stem 18 in. (457 mm) below base of T3

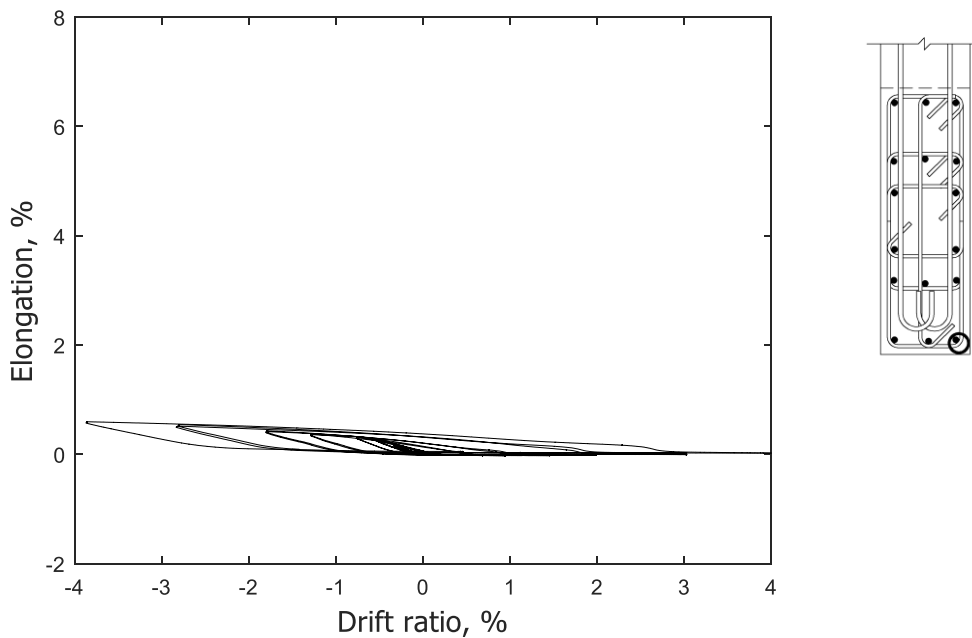


Figure 92 – Measured strain in longitudinal bar at confined stem 18 in. (457 mm) below base of T4

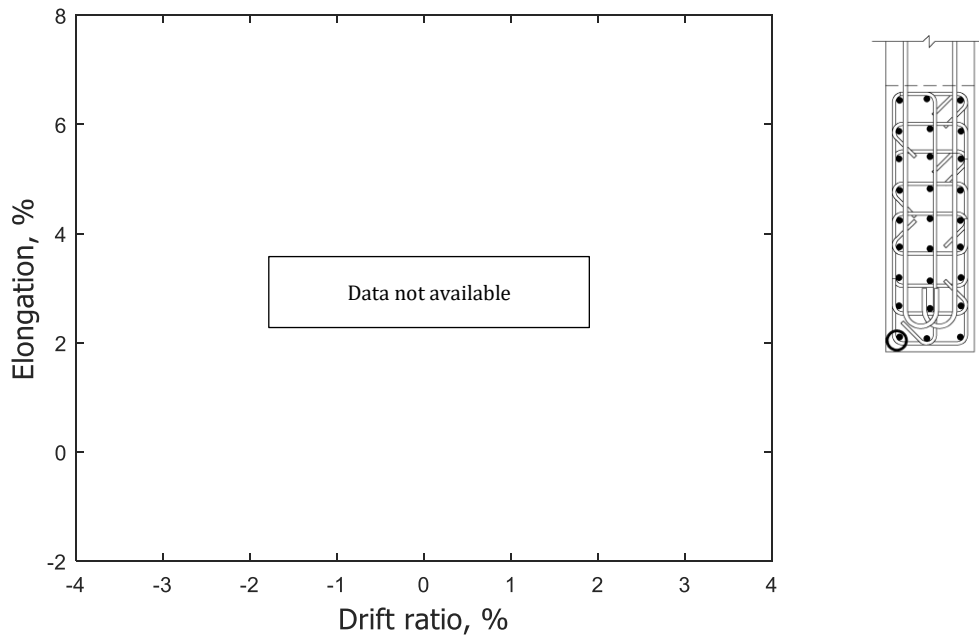


Figure 93 – Measured strain in longitudinal bar at confined stem 18 in. (457 mm) below base of T1

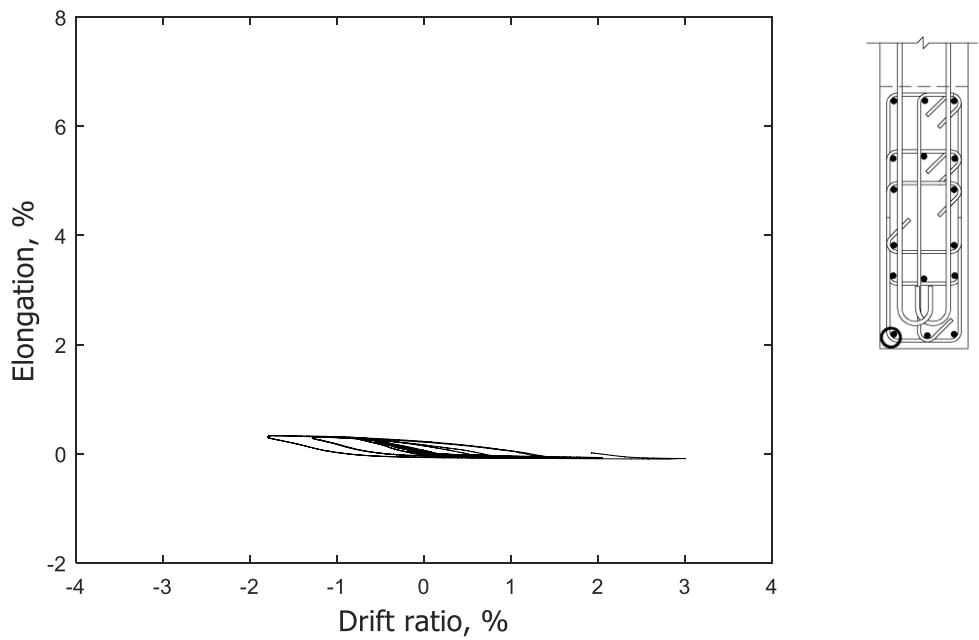


Figure 94 – Measured strain in longitudinal bar at confined stem 18 in. (457 mm) below base of T2

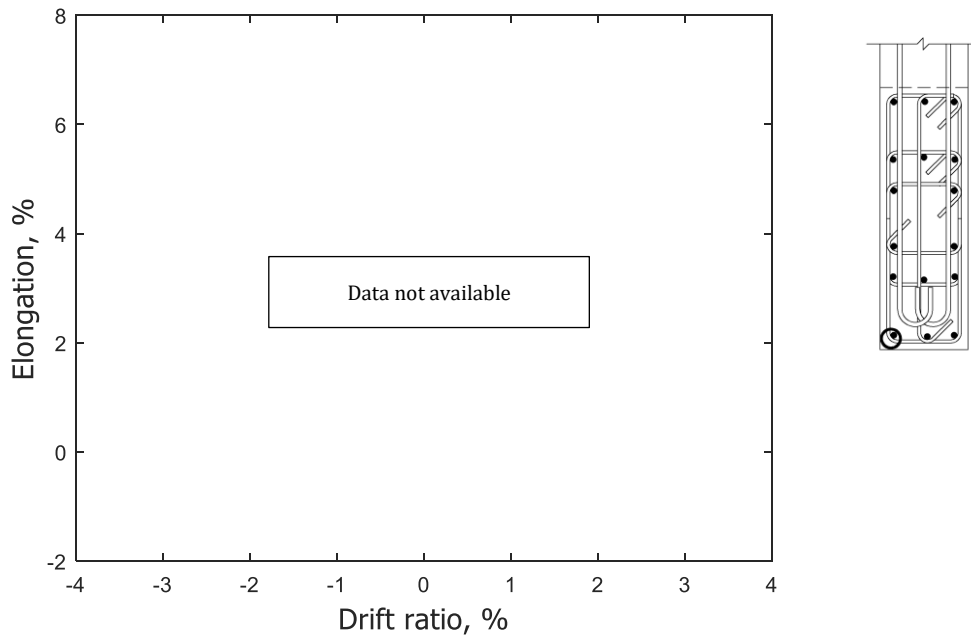


Figure 95 – Measured strain in longitudinal bar at confined stem 18 in. (457 mm) below base of T3

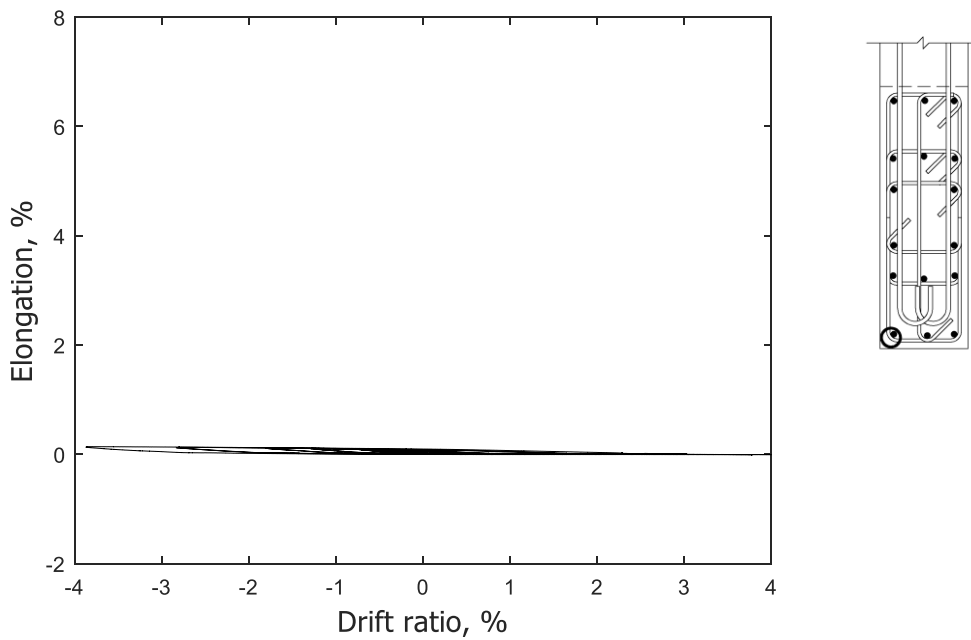


Figure 96 – Measured strain in longitudinal bar at confined stem 18 in. (457 mm) below base of T4

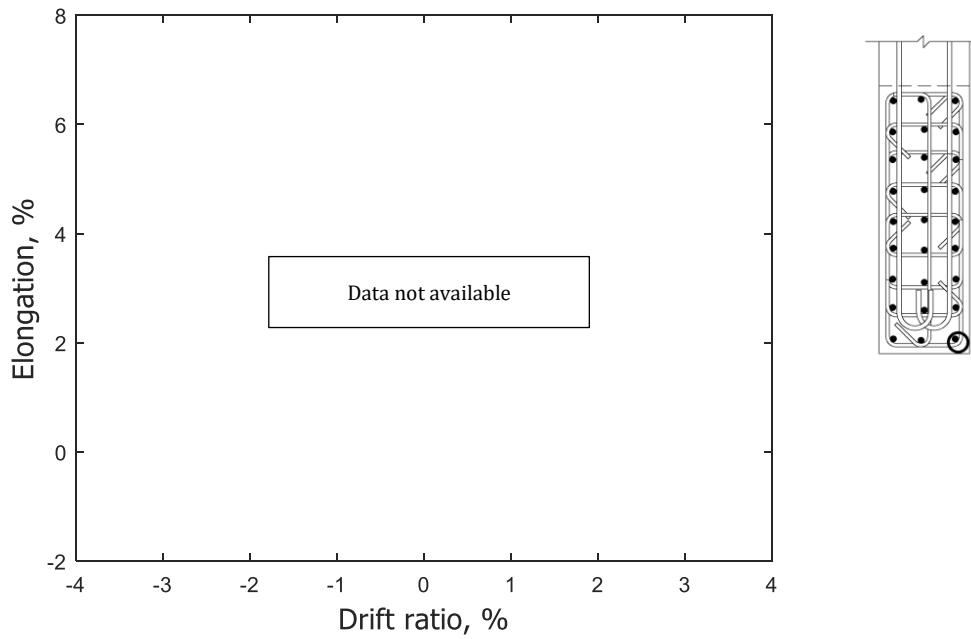


Figure 97 – Measured strain in longitudinal bar at confined stem 9 in. (229 mm) below base of T1

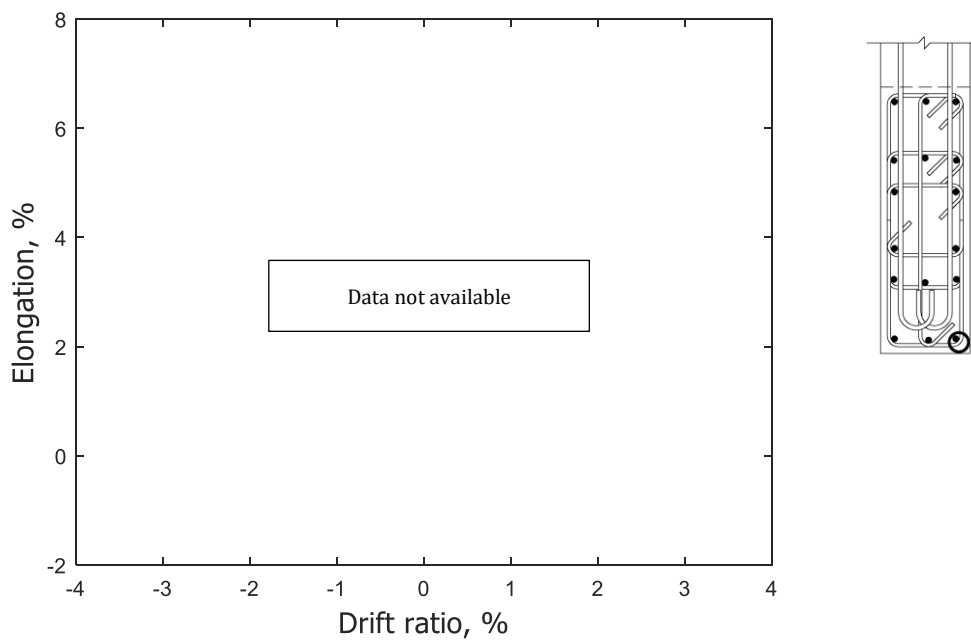


Figure 98 – Measured strain in longitudinal bar at confined stem 9 in. (229 mm) below base of T2

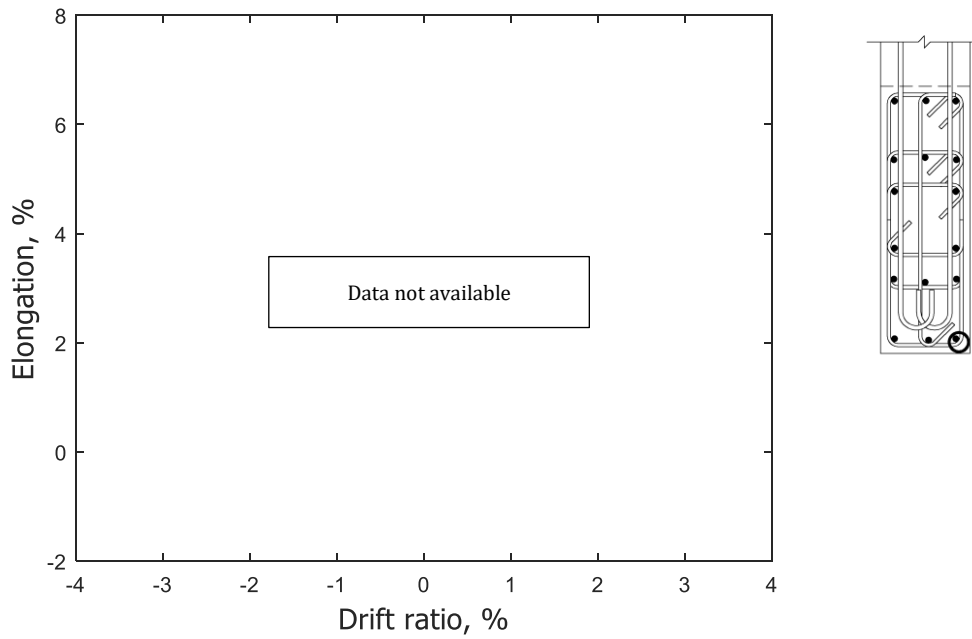


Figure 99 – Measured strain in longitudinal bar at confined stem 9 in. (229 mm) below base of T3

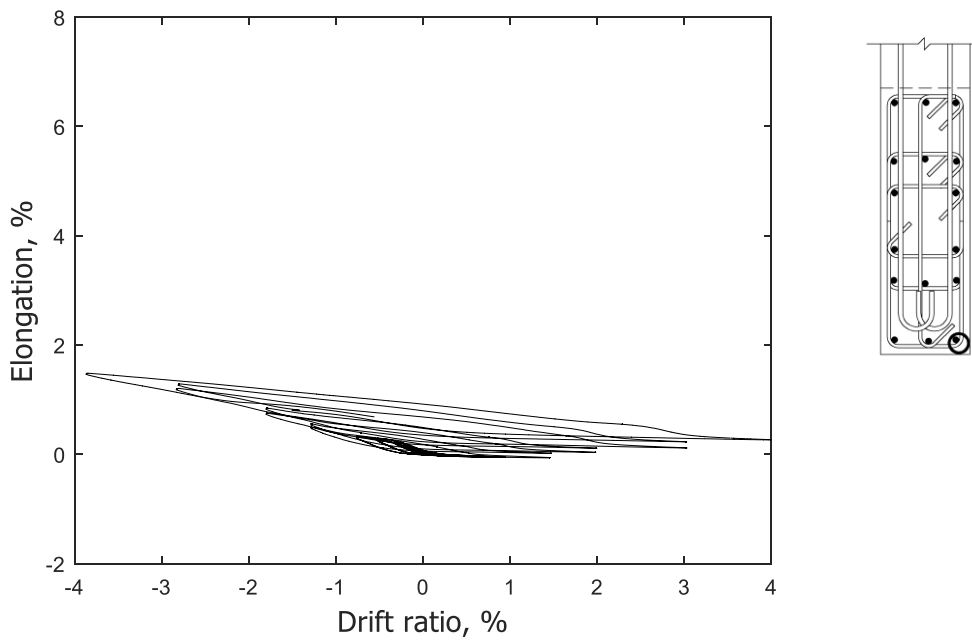


Figure 100 – Measured strain in longitudinal bar at confined stem 9 in. (229 mm) below base of T4

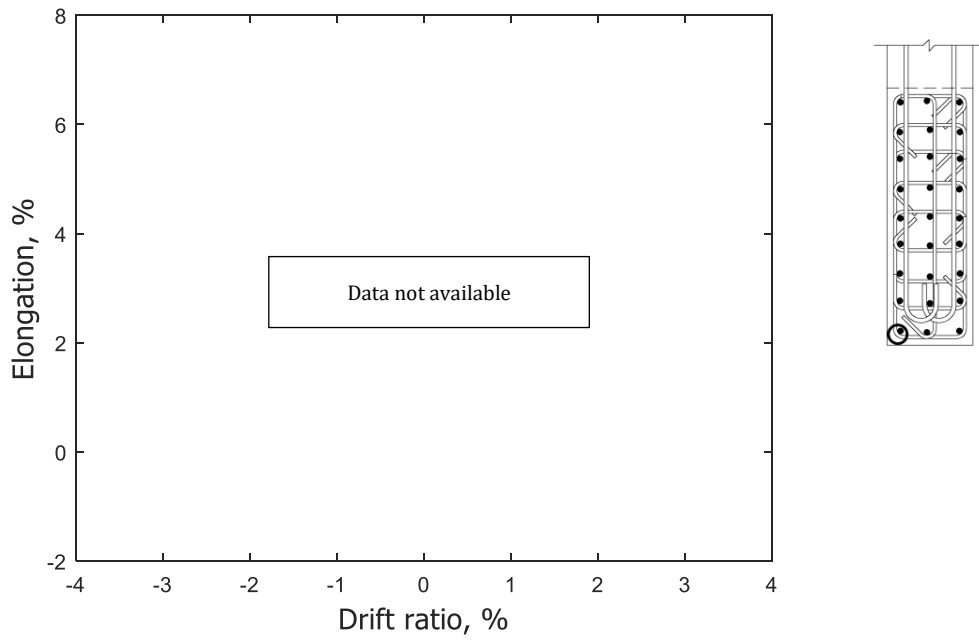


Figure 101 – Measured strain in longitudinal bar at confined stem 9 in. (229 mm) below base of T1

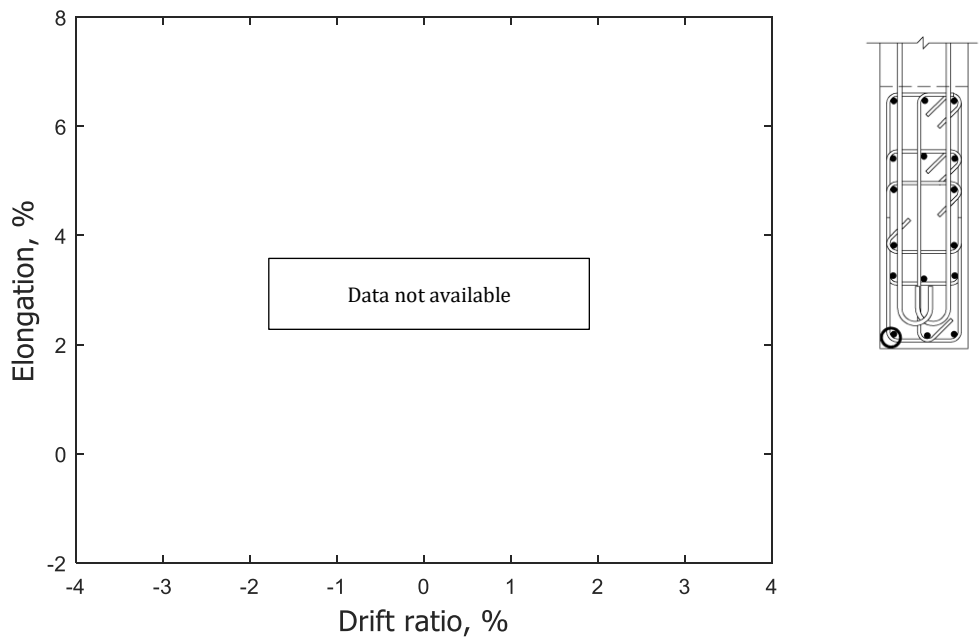


Figure 102 – Measured strain in longitudinal bar at confined stem 9 in. (229 mm) below base of T2

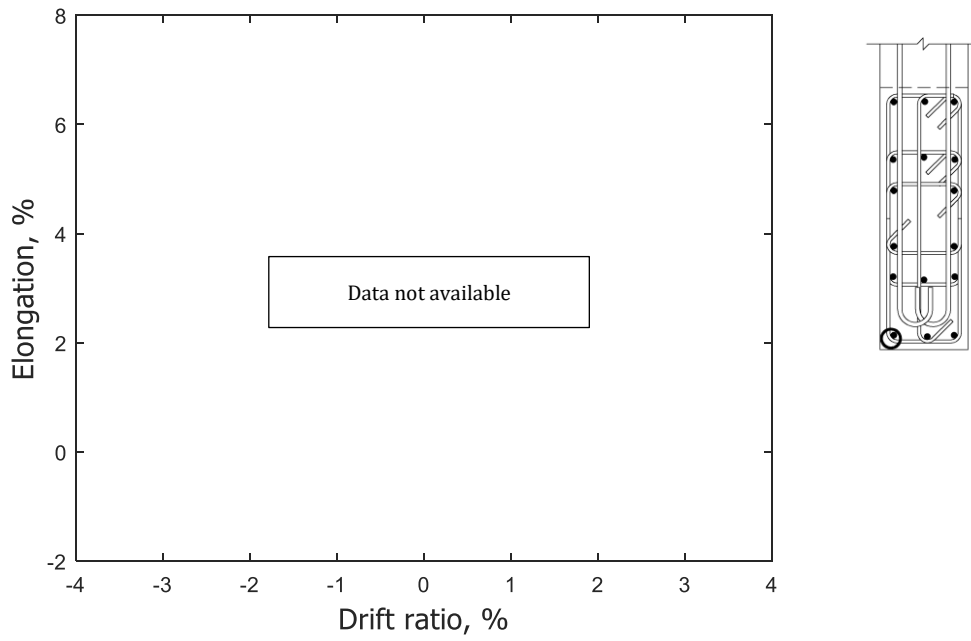


Figure 103 – Measured strain in longitudinal bar at confined stem 9 in. (229 mm) below base of T3

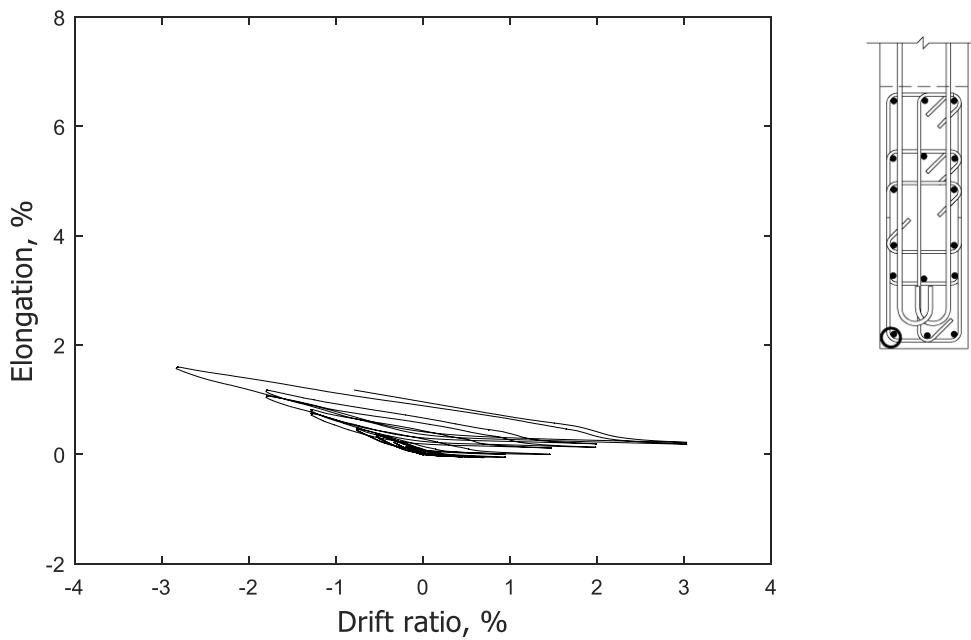


Figure 104 – Measured strain in longitudinal bar at confined stem 9 in. (229 mm) below base of T4

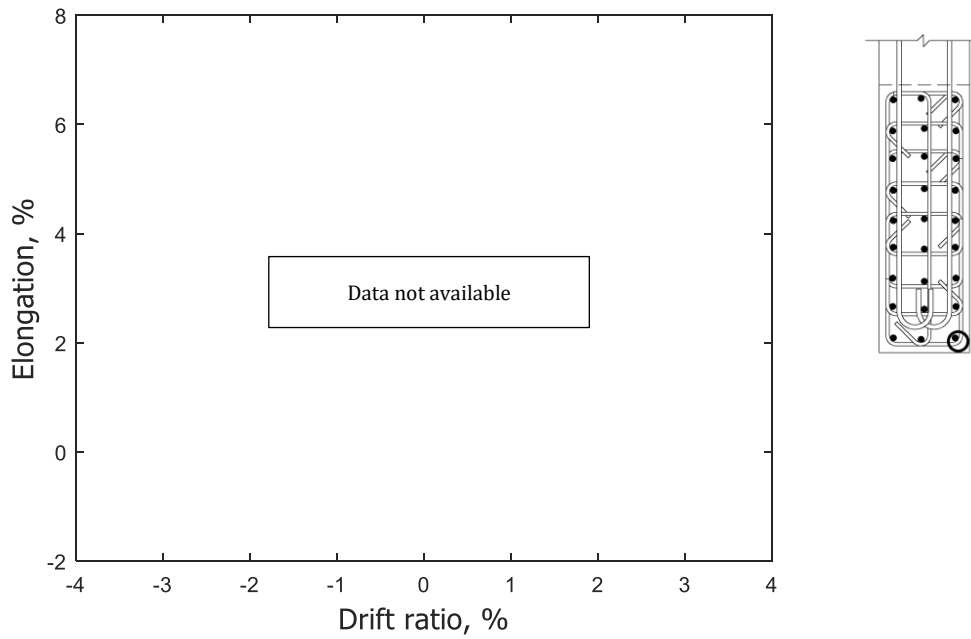


Figure 105 – Measured strain in longitudinal bar at confined stem 0.5 in. (13 mm) above base of T1

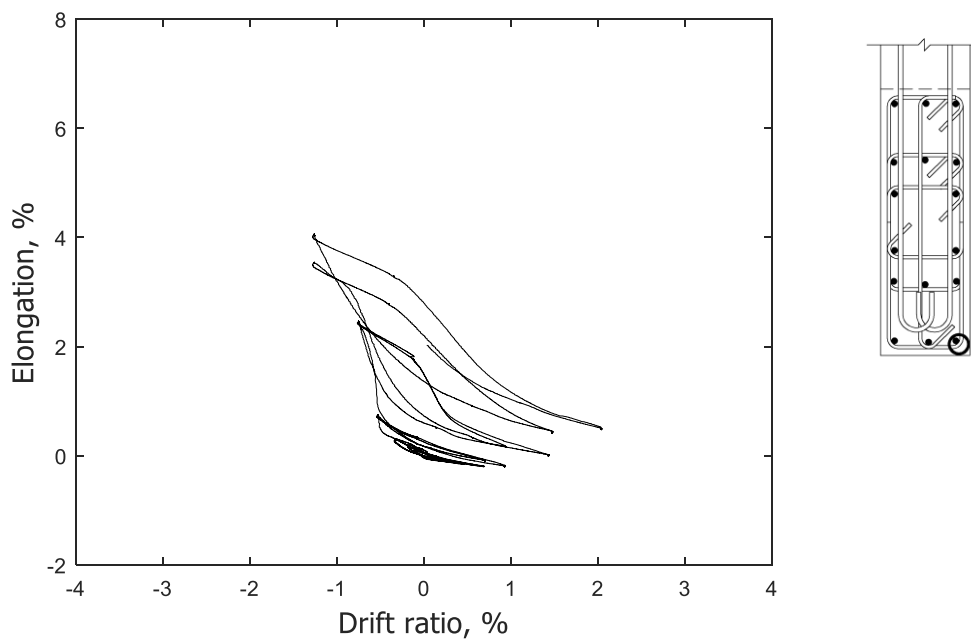


Figure 106 – Measured strain in longitudinal bar at confined stem 0.5 in. (13 mm) above base of T2

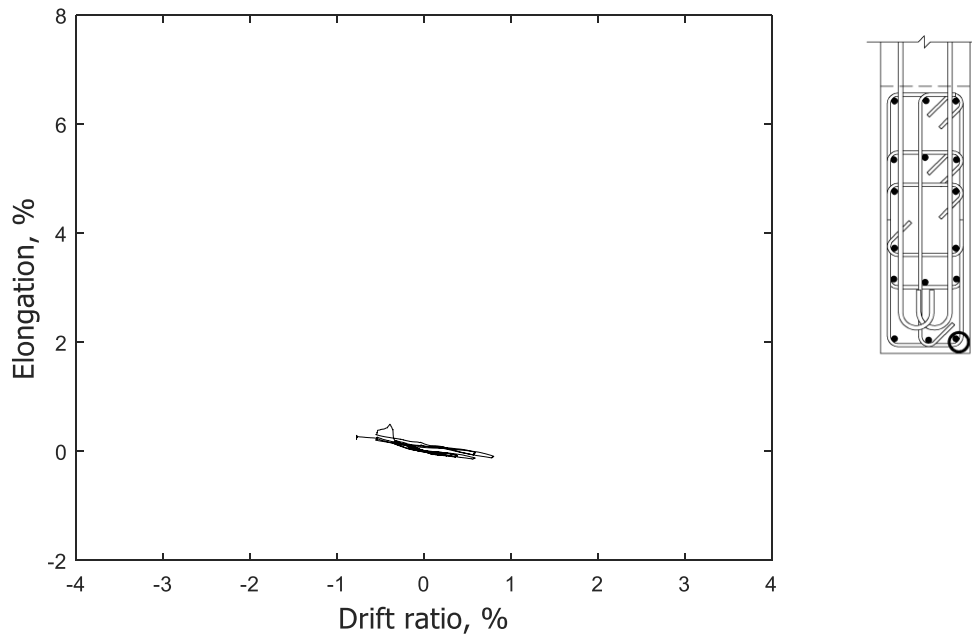


Figure 107 – Measured strain in longitudinal bar at confined stem 0.5 in. (13 mm) above base of T3

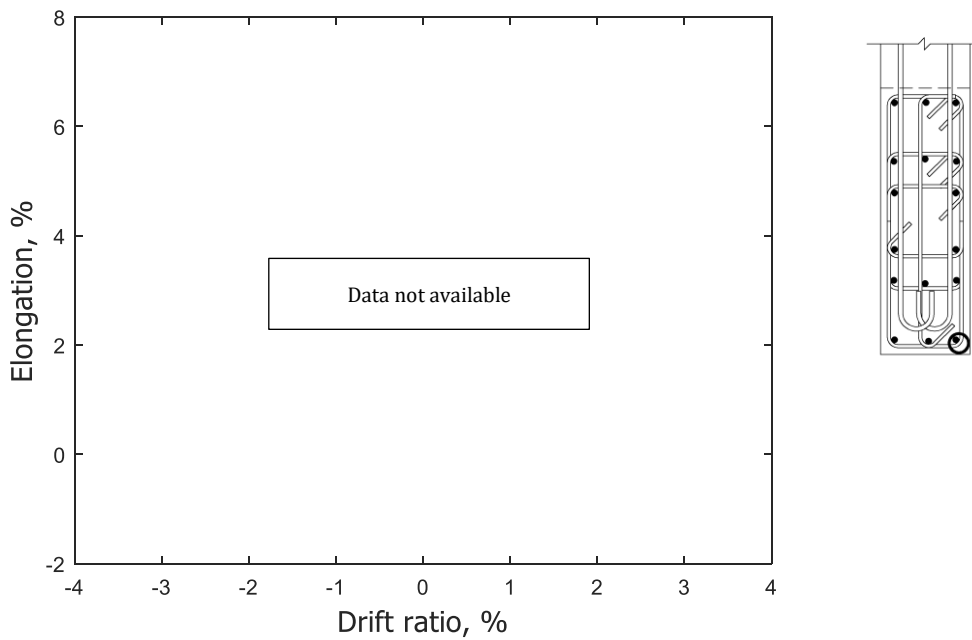


Figure 108 – Measured strain in longitudinal bar at confined stem 0.5 in. (13 mm) above base of T4

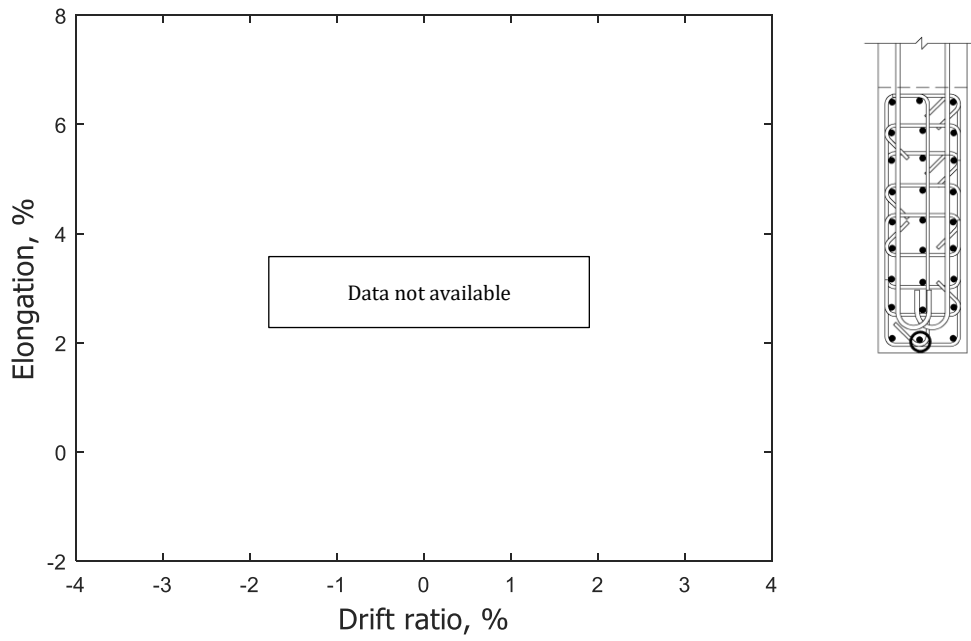


Figure 109 – Measured strain in longitudinal bar at confined stem 0.5 in. (13 mm) above base of T1

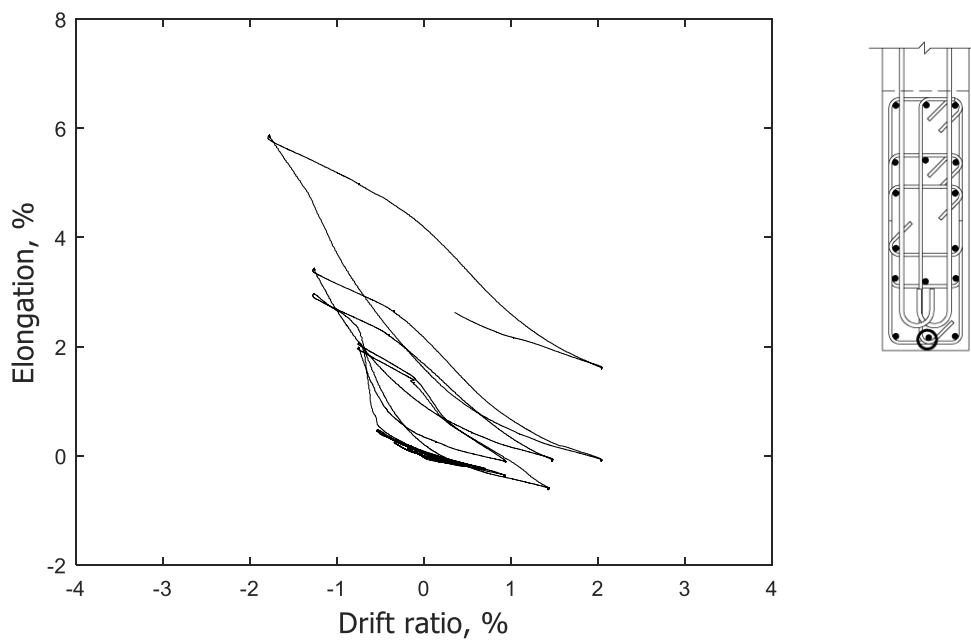


Figure 110 – Measured strain in longitudinal bar at confined stem 0.5 in. (13 mm) above base of T2

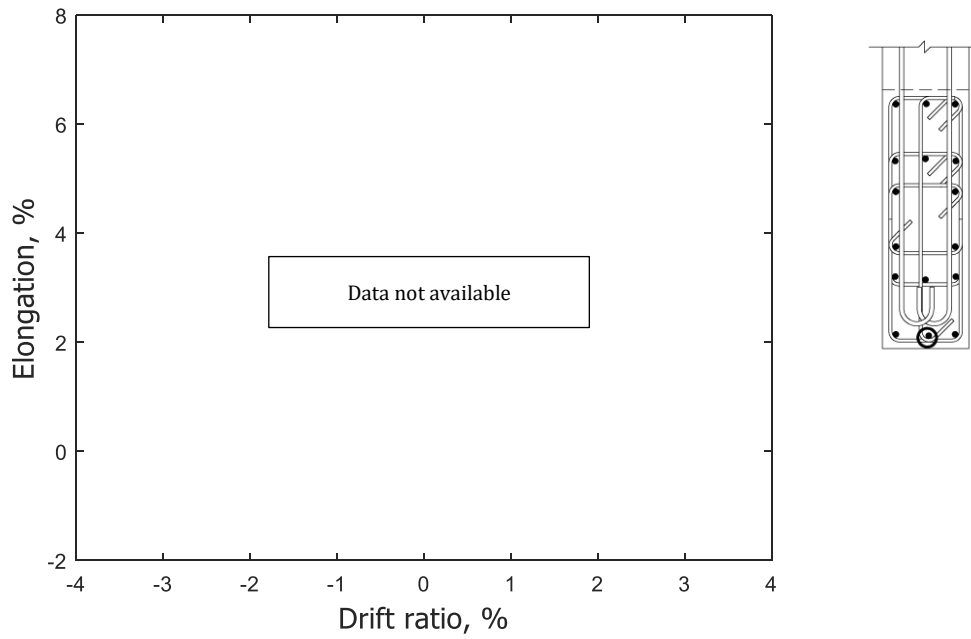


Figure 111 – Measured strain in longitudinal bar at confined stem 0.5 in. (13 mm) above base of T3

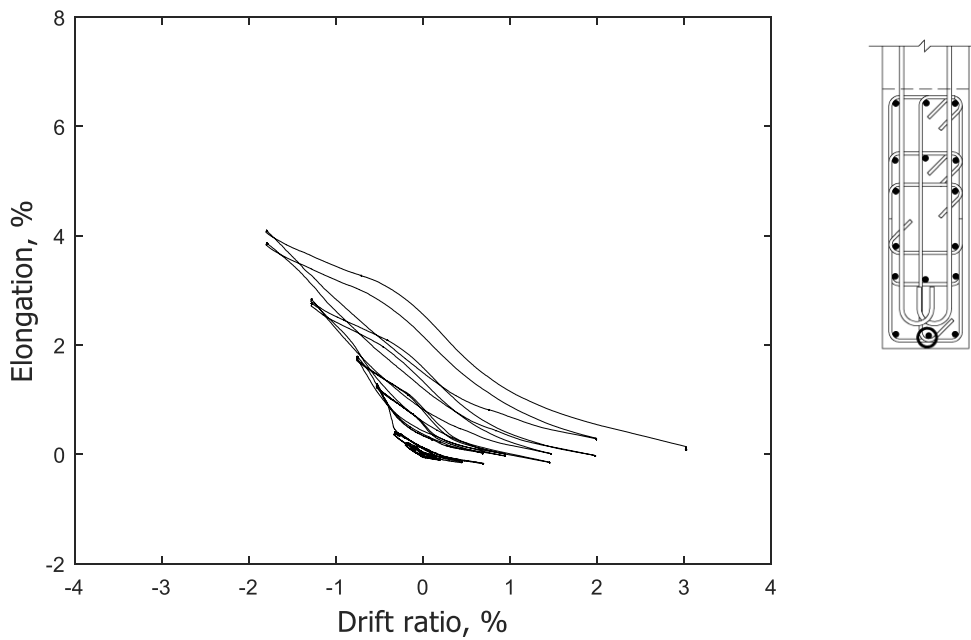


Figure 112 – Measured strain in longitudinal bar at confined stem 0.5 in. (13 mm) above base of T4

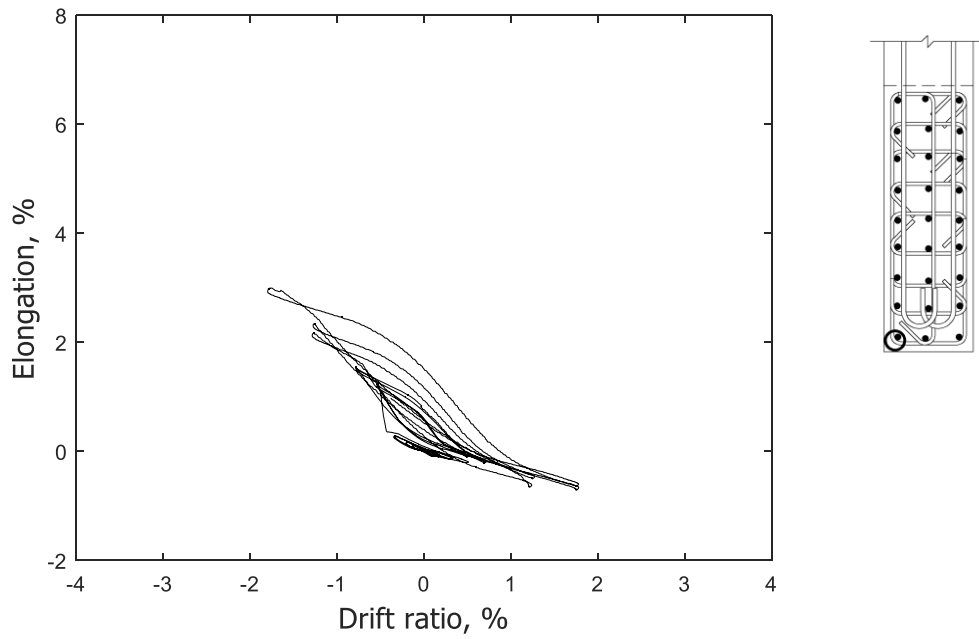


Figure 113 – Measured strain in longitudinal bar at confined stem 0.5 in. (13 mm) above base of T1

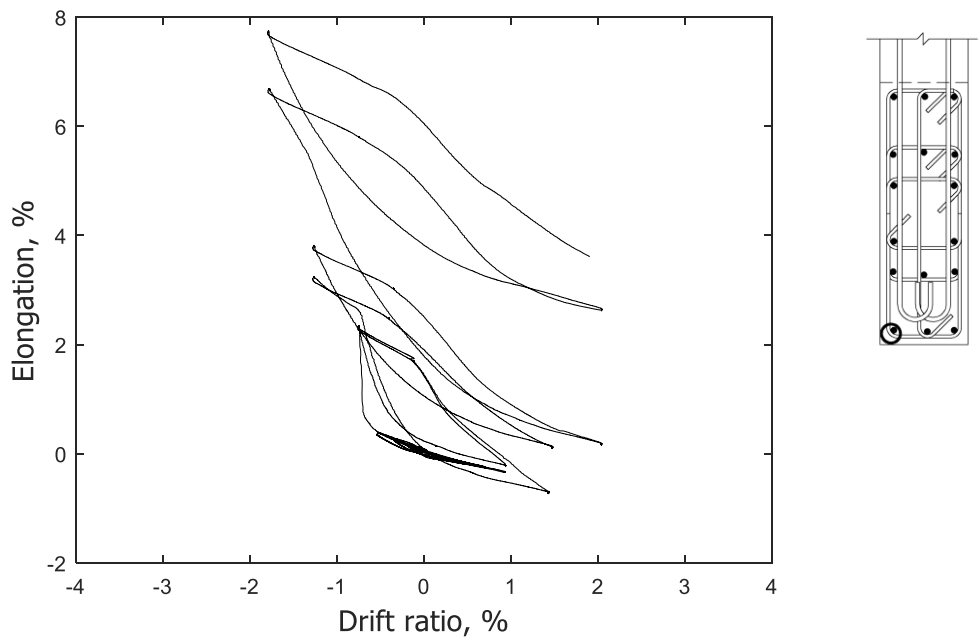


Figure 114 – Measured strain in longitudinal bar at confined stem 0.5 in. (13 mm) above base of T2

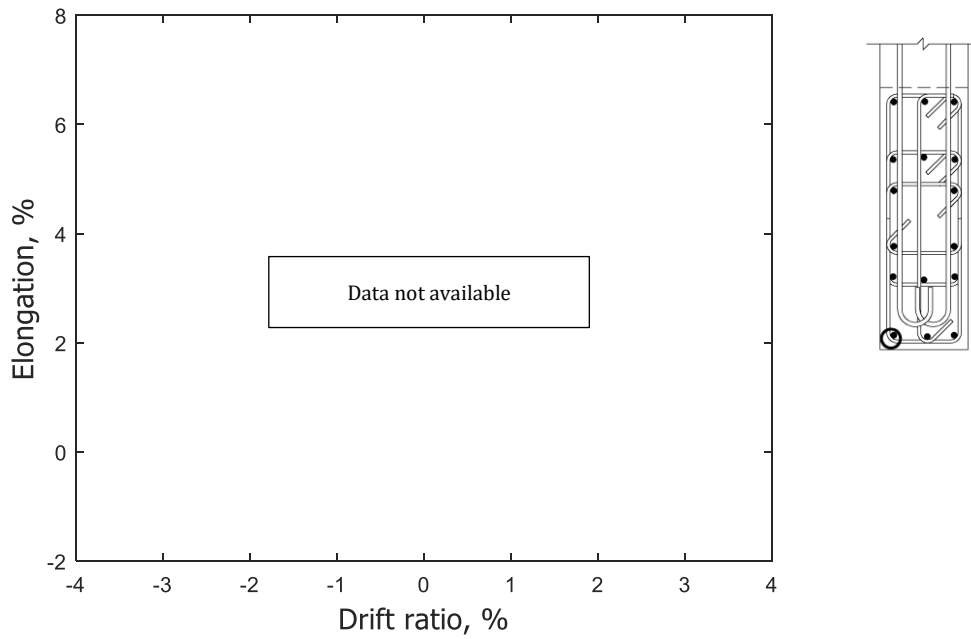


Figure 115 – Measured strain in longitudinal bar at confined stem 0.5 in. (13 mm) above base of T3

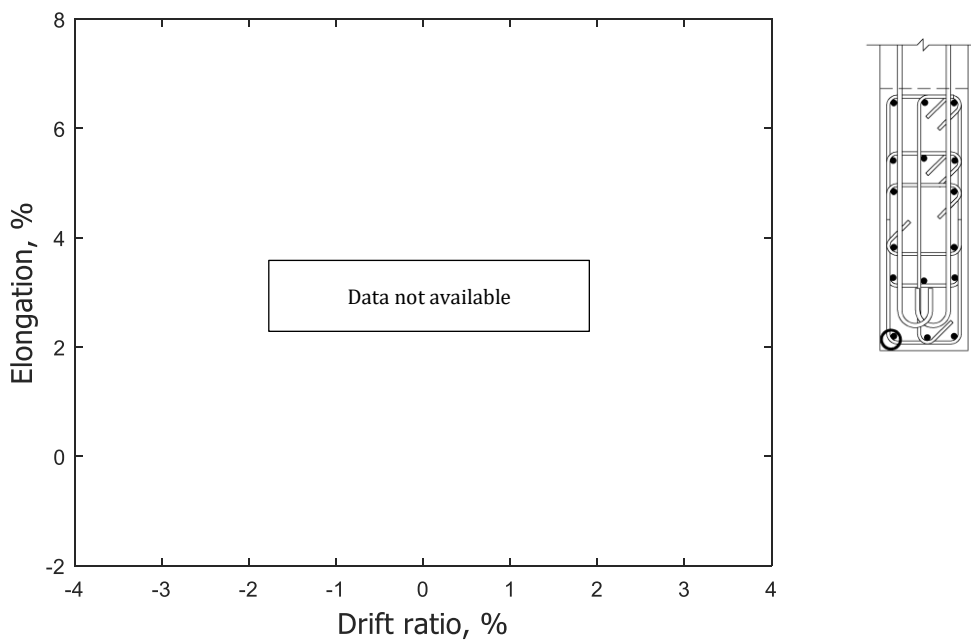


Figure 116 – Measured strain in longitudinal bar at confined stem 0.5 in. (13 mm) above base of T4

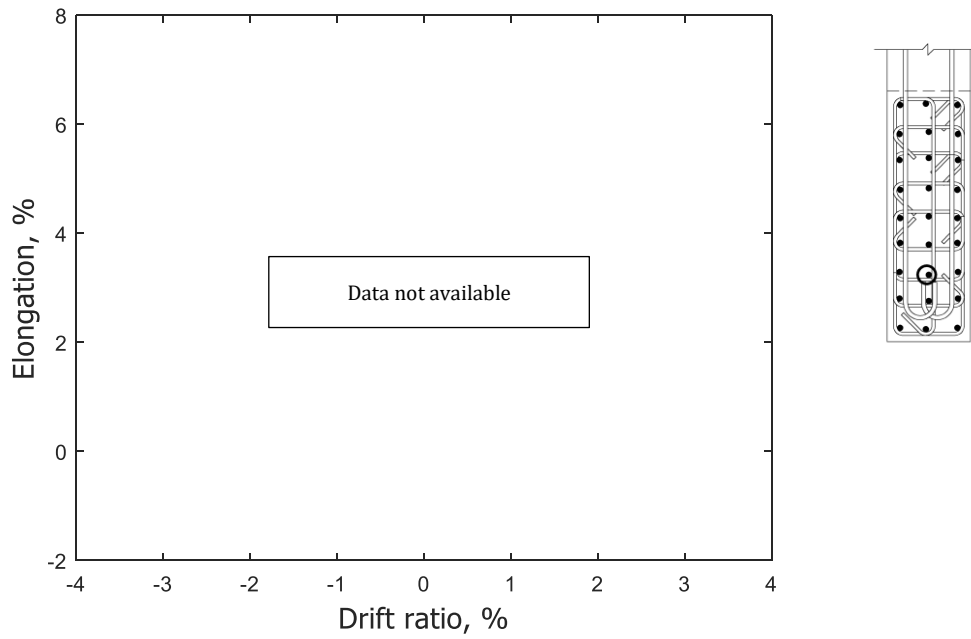


Figure 117 – Measured strain in longitudinal bar at confined stem 0.5 in. (13 mm) above base of T1

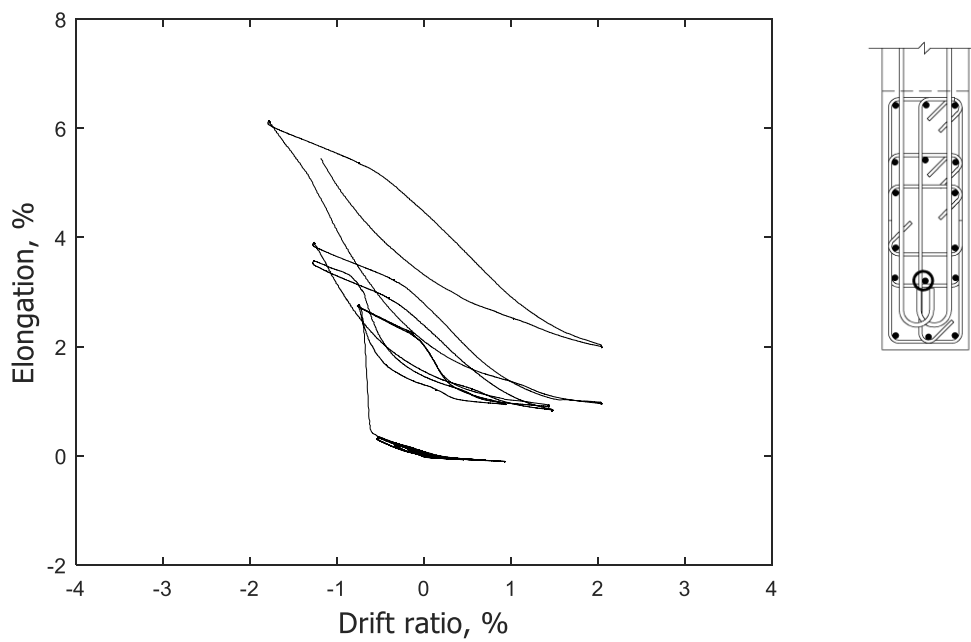


Figure 118 – Measured strain in longitudinal bar at confined stem 0.5 in. (13 mm) above base of T2

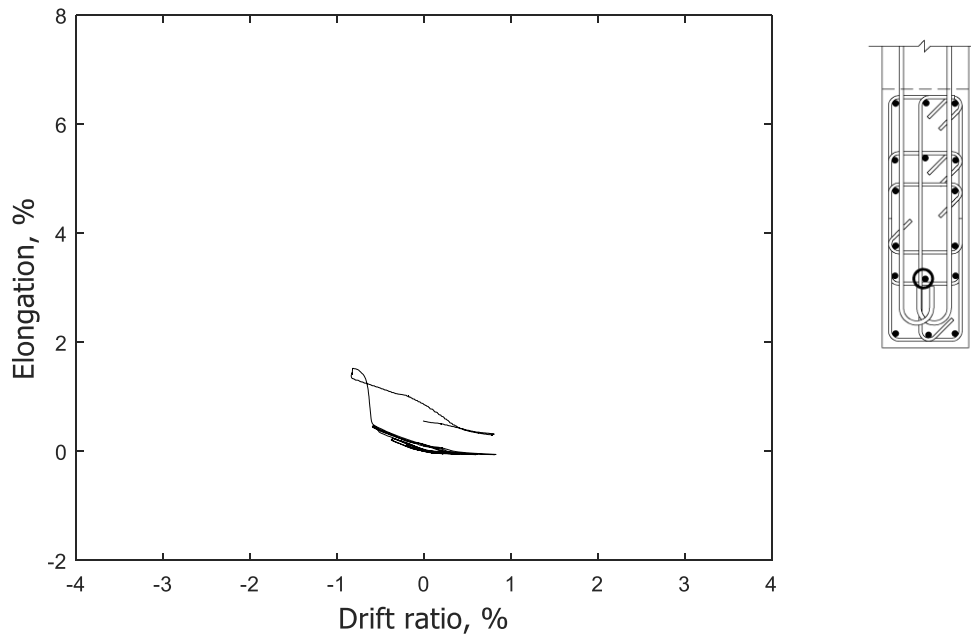


Figure 119 – Measured strain in longitudinal bar at confined stem 0.5 in. (13 mm) above base of T3

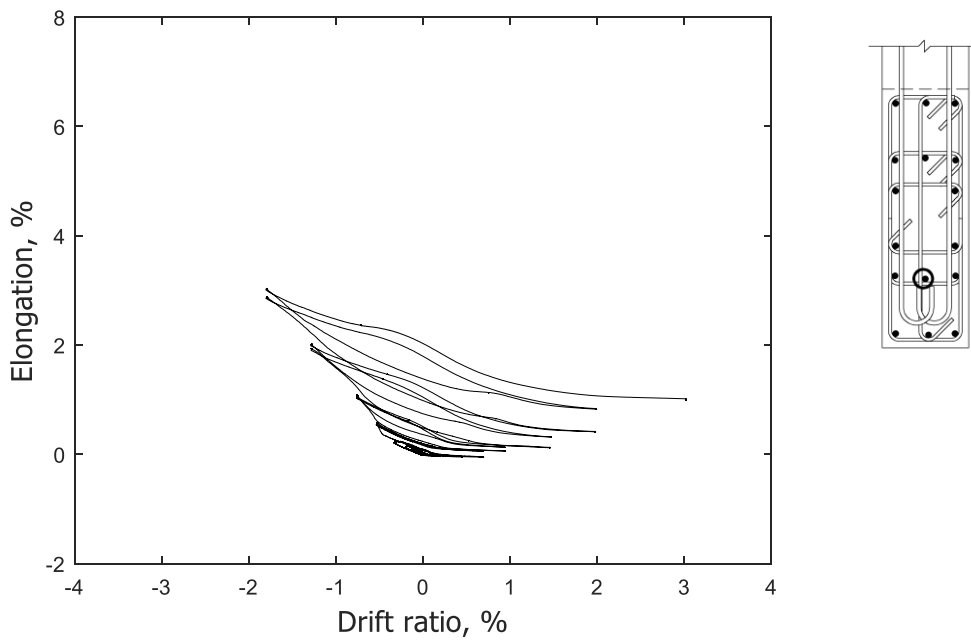


Figure 120 – Measured strain in longitudinal bar at confined stem 0.5 in. (13 mm) above base of T4

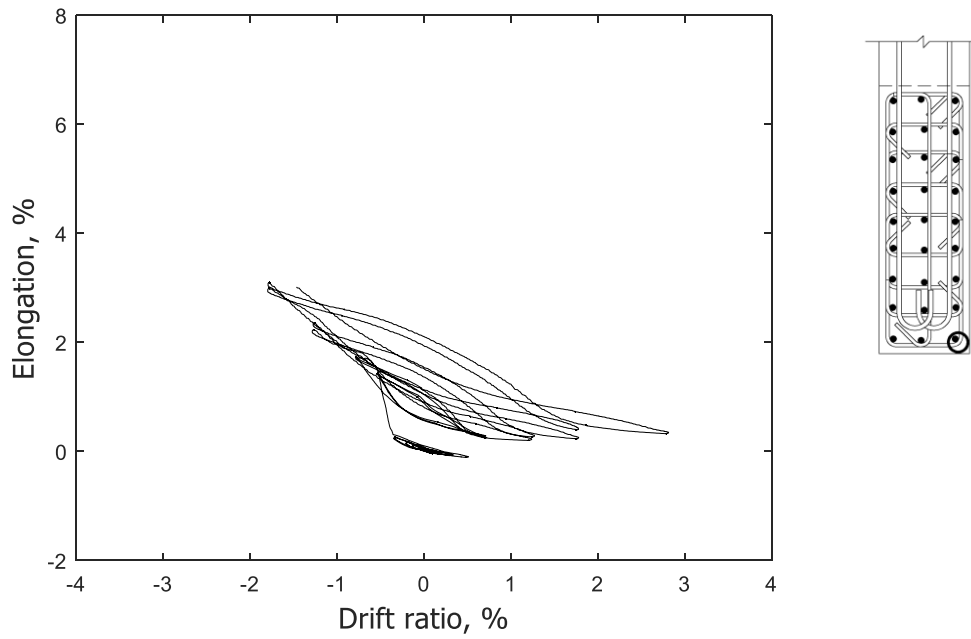


Figure 121 – Measured strain in longitudinal bar at confined stem 25 in. (635 mm) above base of T1

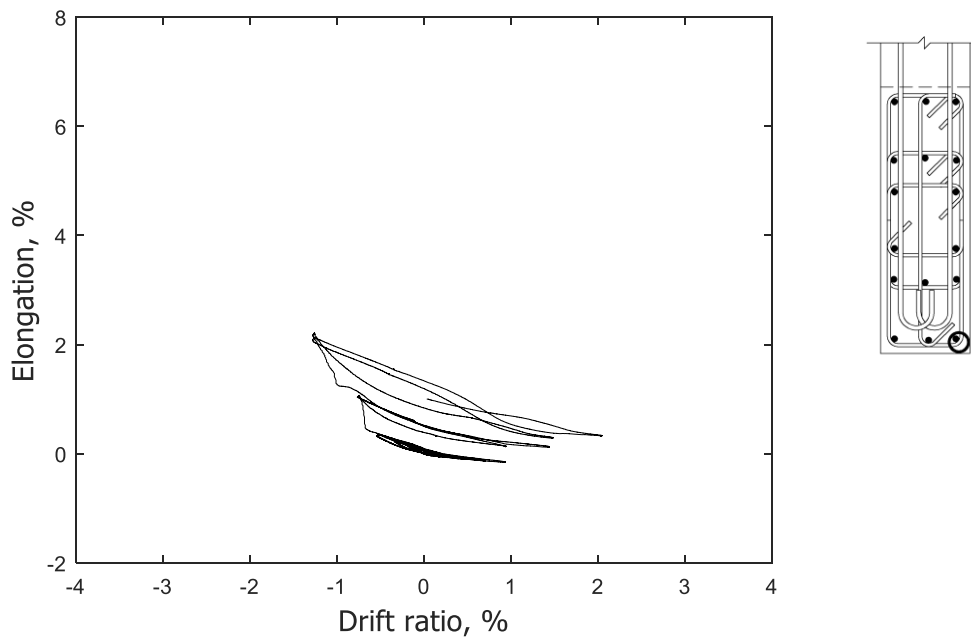


Figure 122 – Measured strain in longitudinal bar at confined stem 25 in. (635 mm) above base of T2

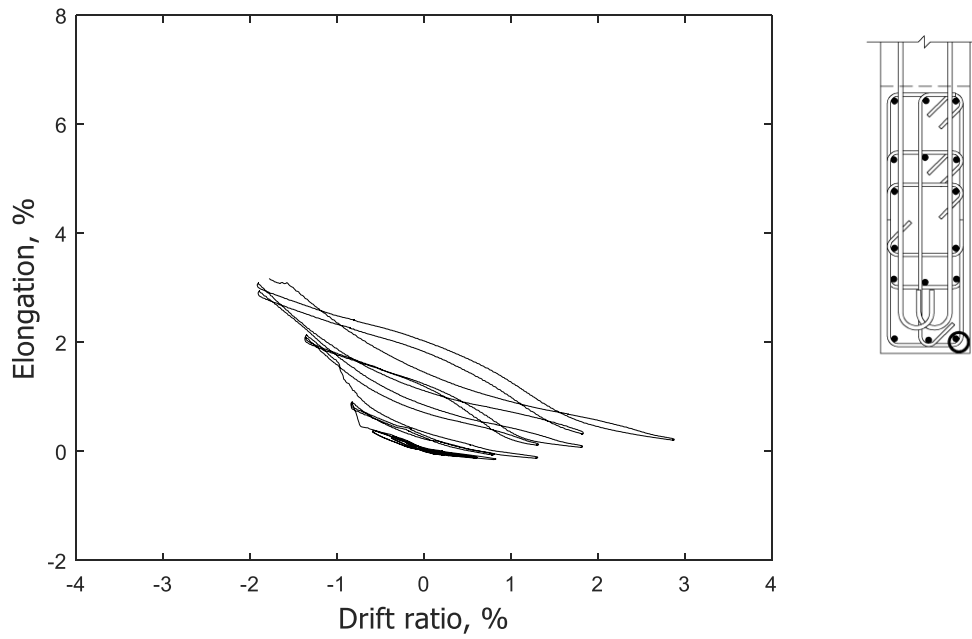


Figure 123 – Measured strain in longitudinal bar at confined stem 25 in. (635 mm) above base of T3

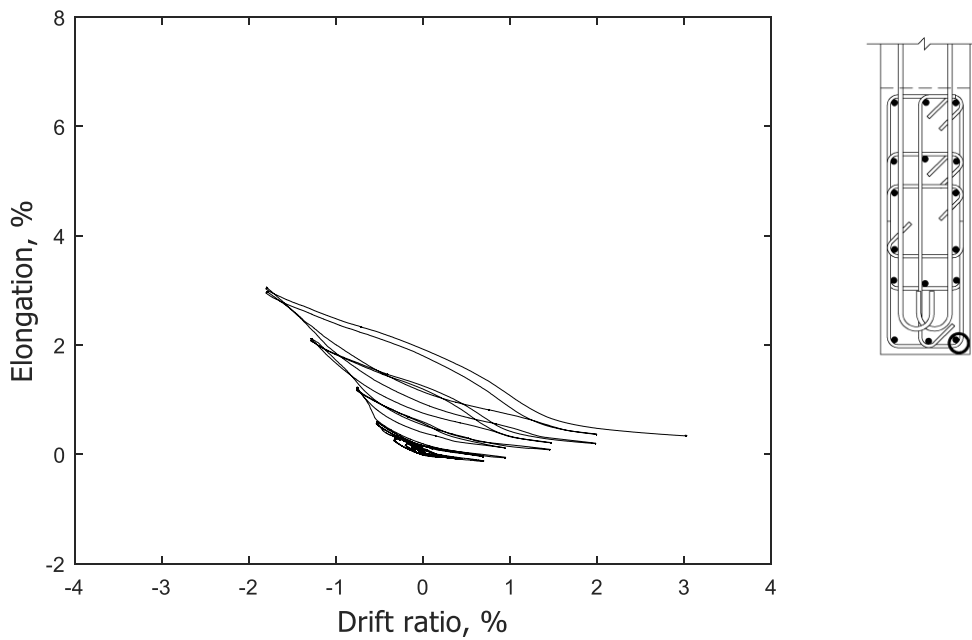


Figure 124 – Measured strain in longitudinal bar at confined stem 25 in. (635 mm) above base of T4

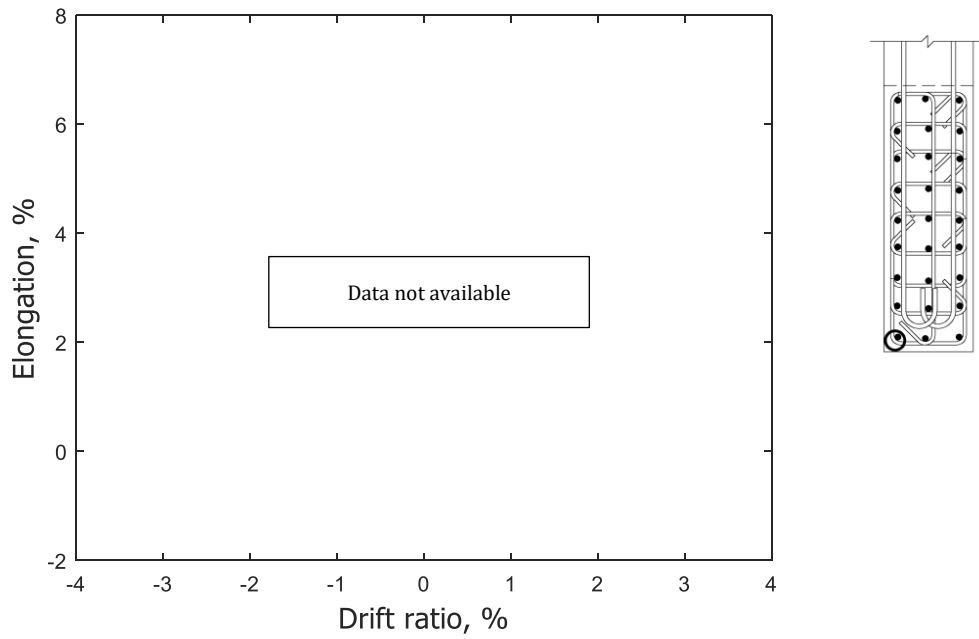


Figure 125 – Measured strain in longitudinal bar at confined stem 25 in. (635 mm) above base of T1

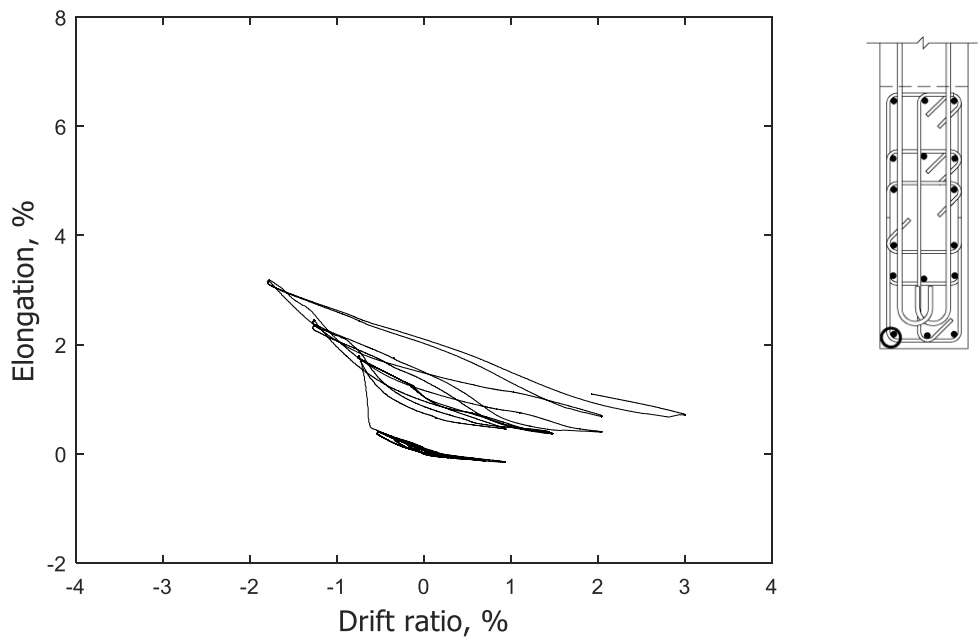


Figure 126 – Measured strain in longitudinal bar at confined stem 25 in. (635 mm) above base of T2

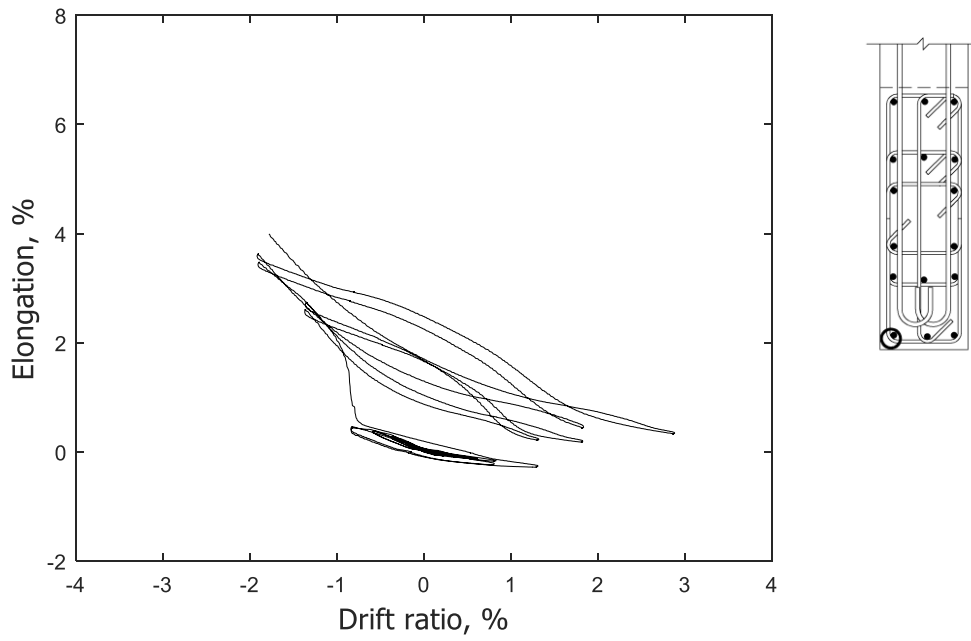


Figure 127 – Measured strain in longitudinal bar at confined stem 25 in. (635 mm) above base of T3

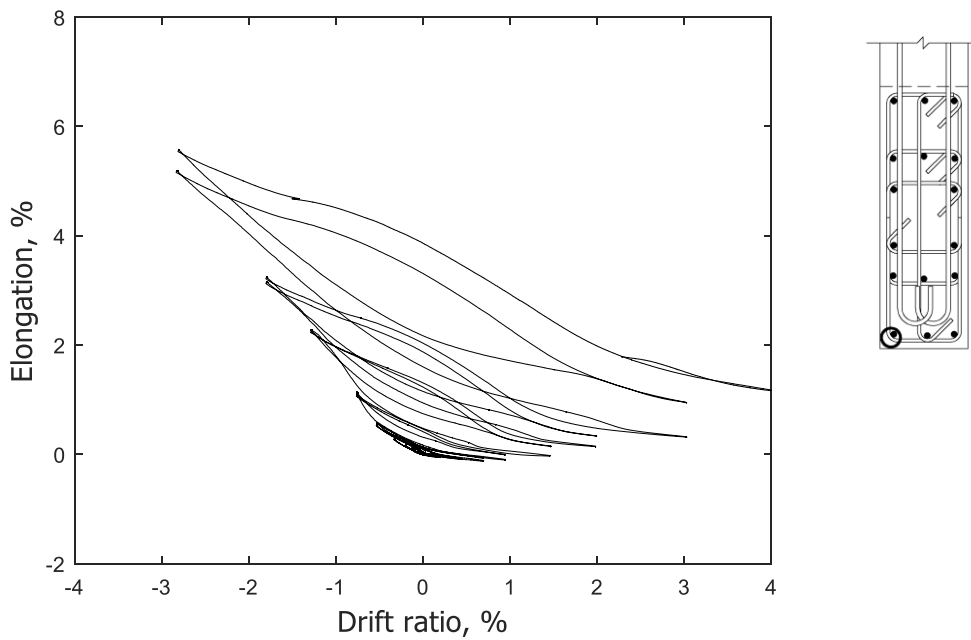


Figure 128 – Measured strain in longitudinal bar at confined stem 25 in. (635 mm) above base of T4

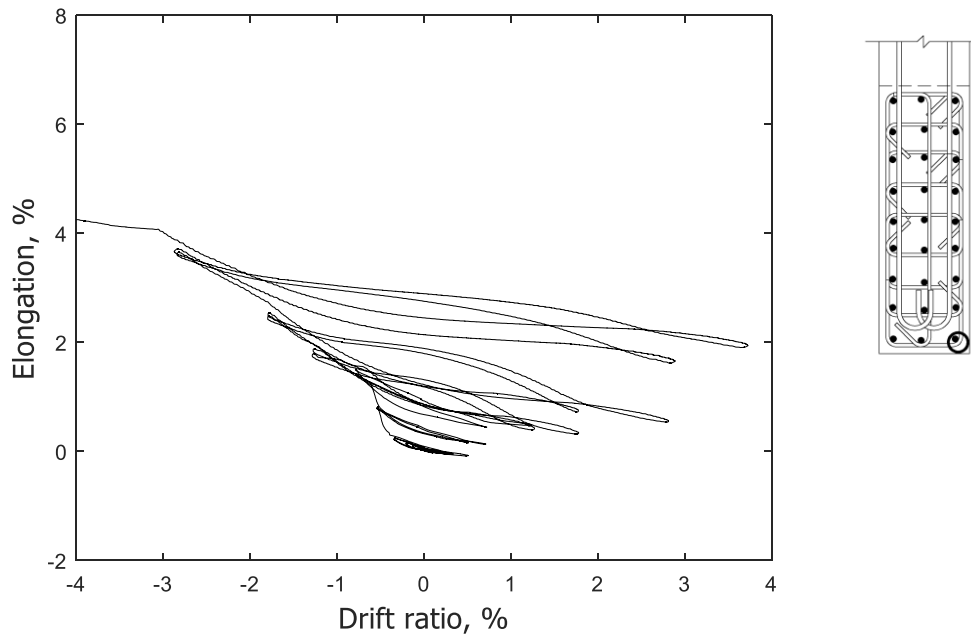


Figure 129 – Measured strain in longitudinal bar at confined stem 50 in. (1270 mm) above base of T1

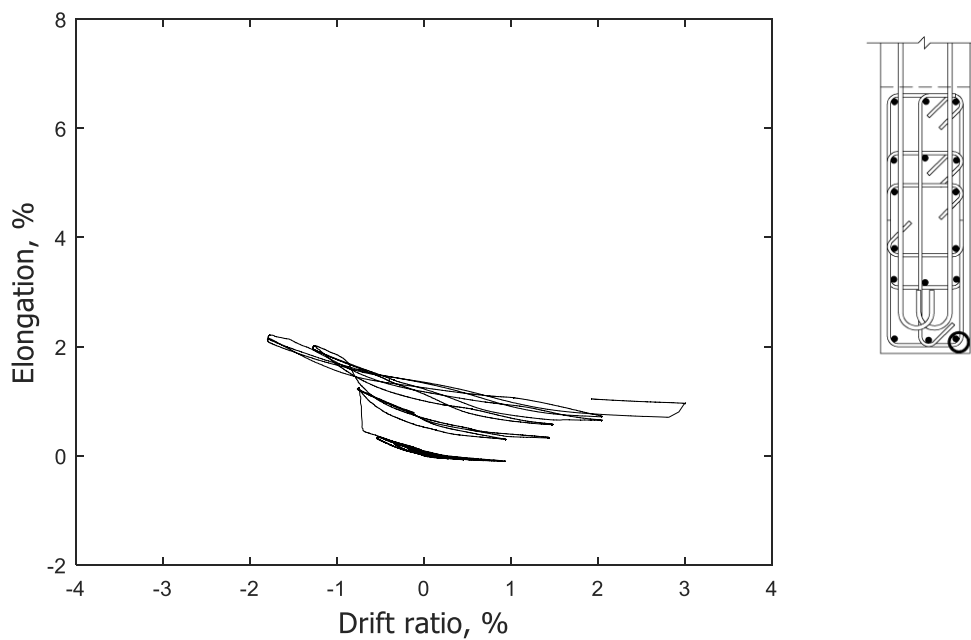


Figure 130 – Measured strain in longitudinal bar at confined stem 50 in. (1270 mm) above base of T2

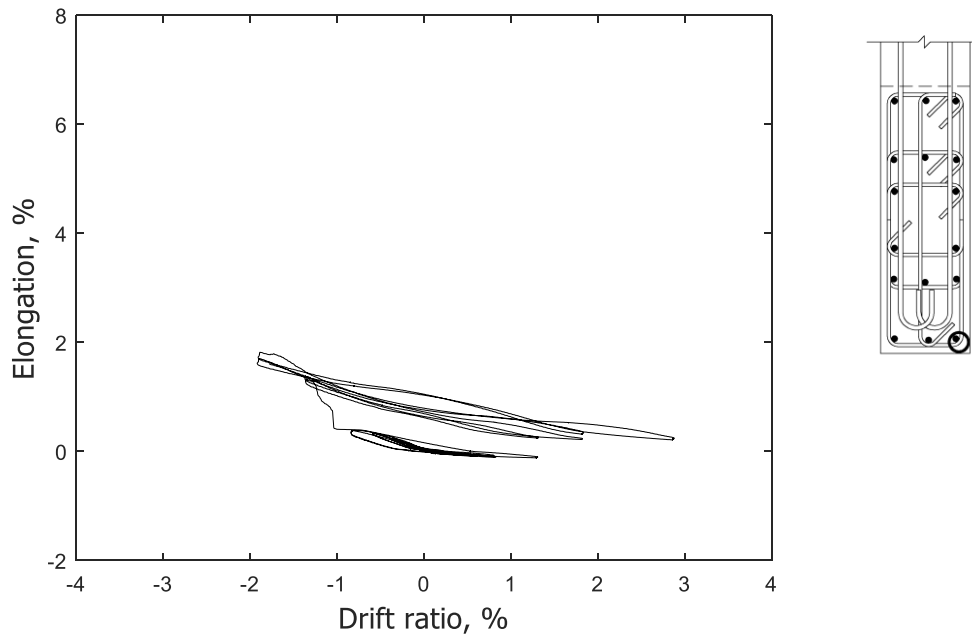


Figure 131 – Measured strain in longitudinal bar at confined stem 50 in. (1270 mm) above base of T3

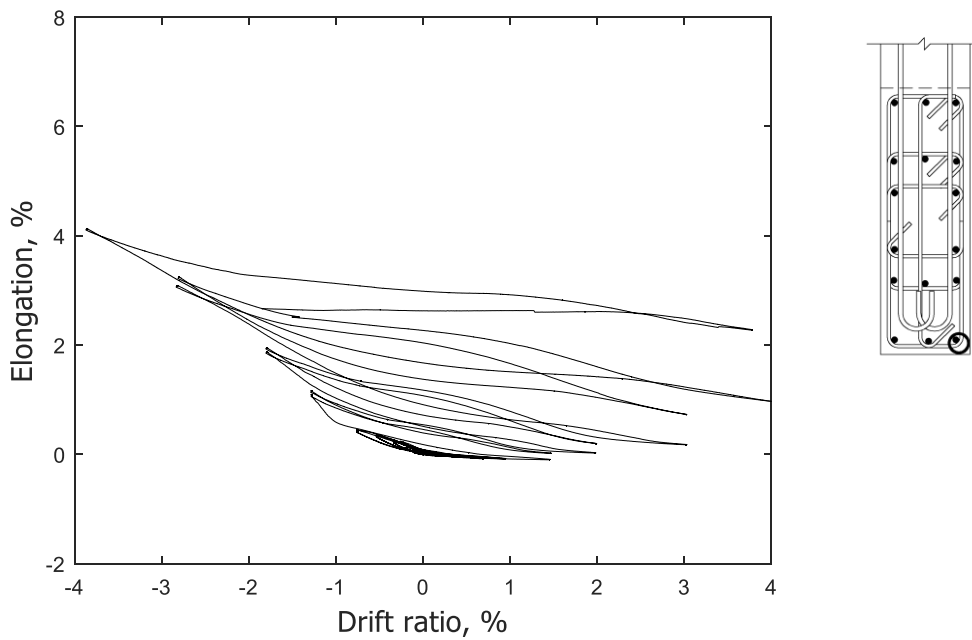


Figure 132 – Measured strain in longitudinal bar at confined stem 50 in. (1270 mm) above base of T4

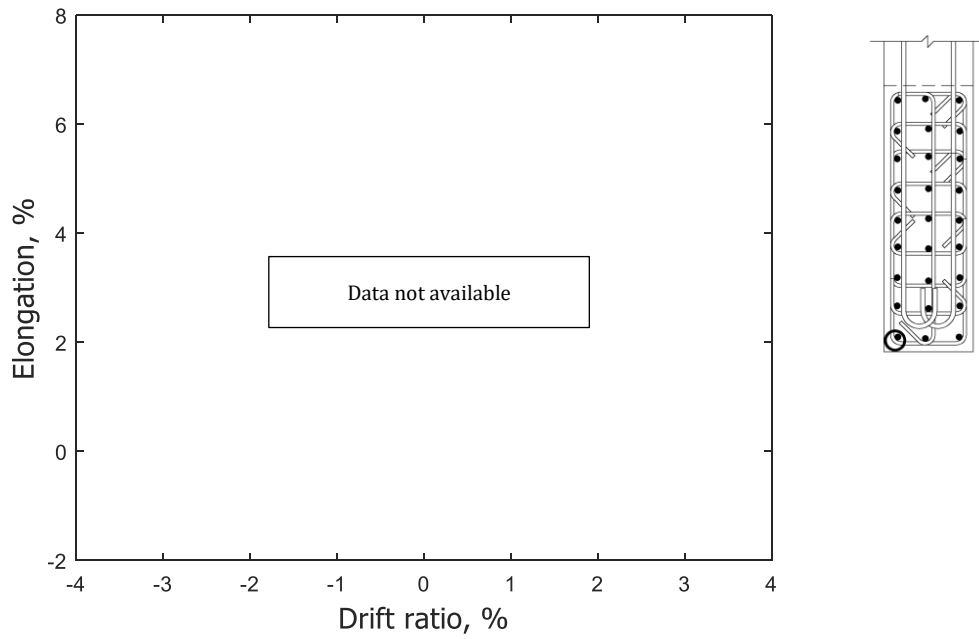


Figure 133 – Measured strain in longitudinal bar at confined stem 50 in. (1270 mm) above base of T1

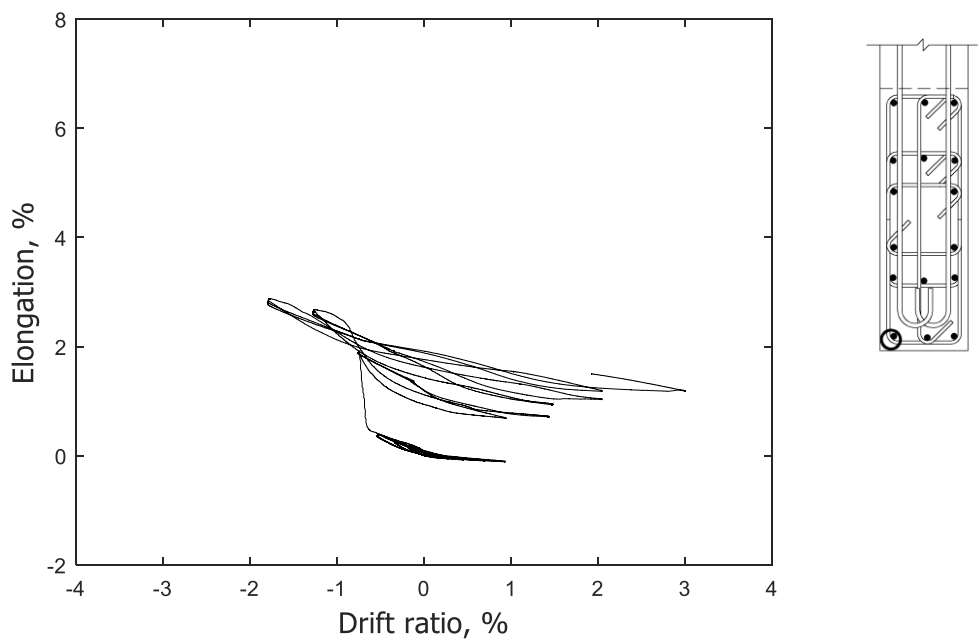


Figure 134 – Measured strain in longitudinal bar at confined stem 50 in. (1270 mm) above base of T2

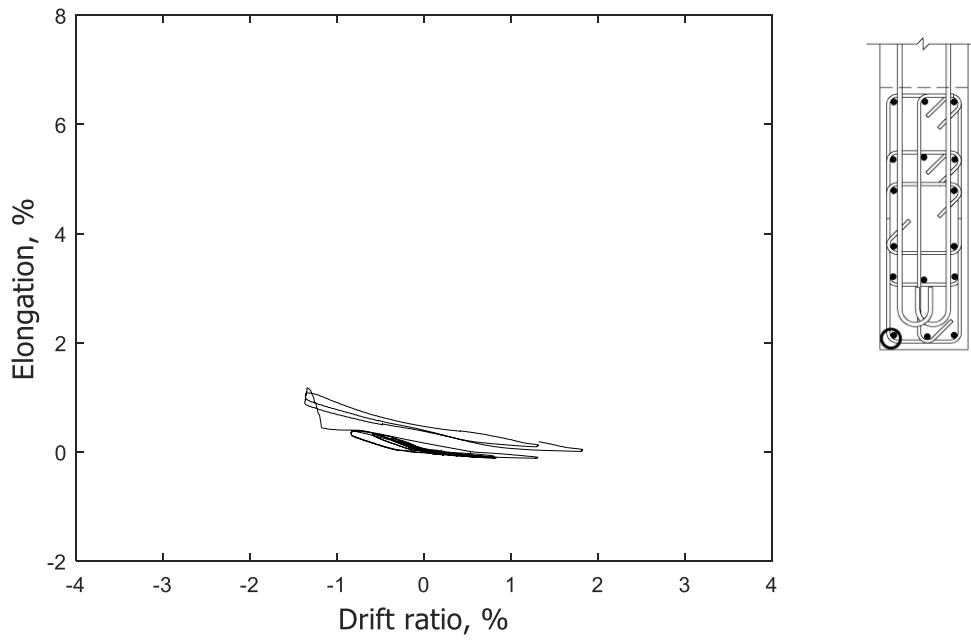


Figure 135 – Measured strain in longitudinal bar at confined stem 50 in. (1270 mm) above base of T3

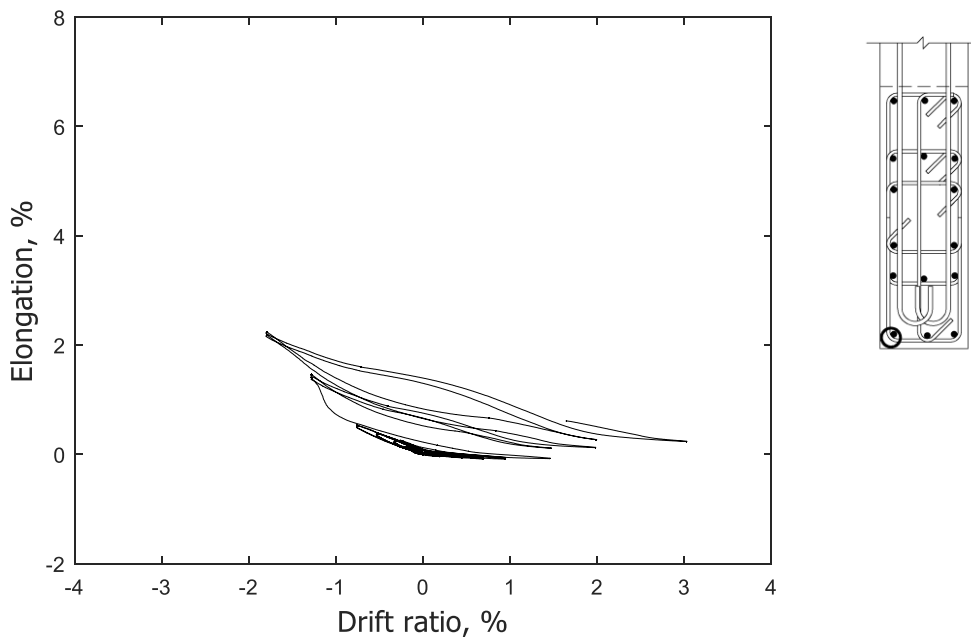


Figure 136 – Measured strain in longitudinal bar at confined stem 50 in. (1270 mm) above base of T4

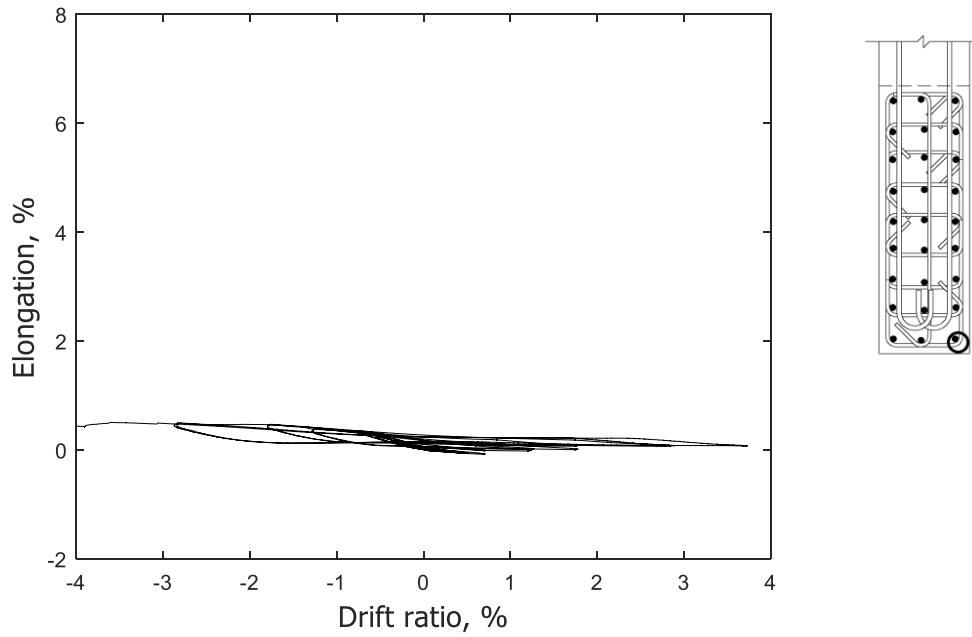


Figure 137 – Measured strain in longitudinal bar at confined stem 100 in. (2540 mm) above base of T1

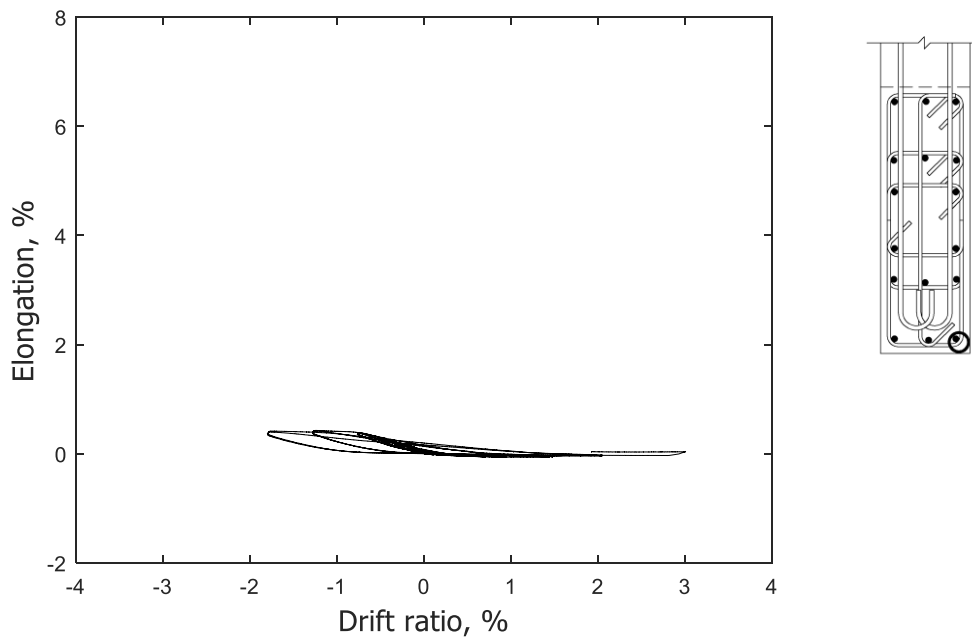


Figure 138 – Measured strain in longitudinal bar at confined stem 100 in. (2540 mm) above base of T2

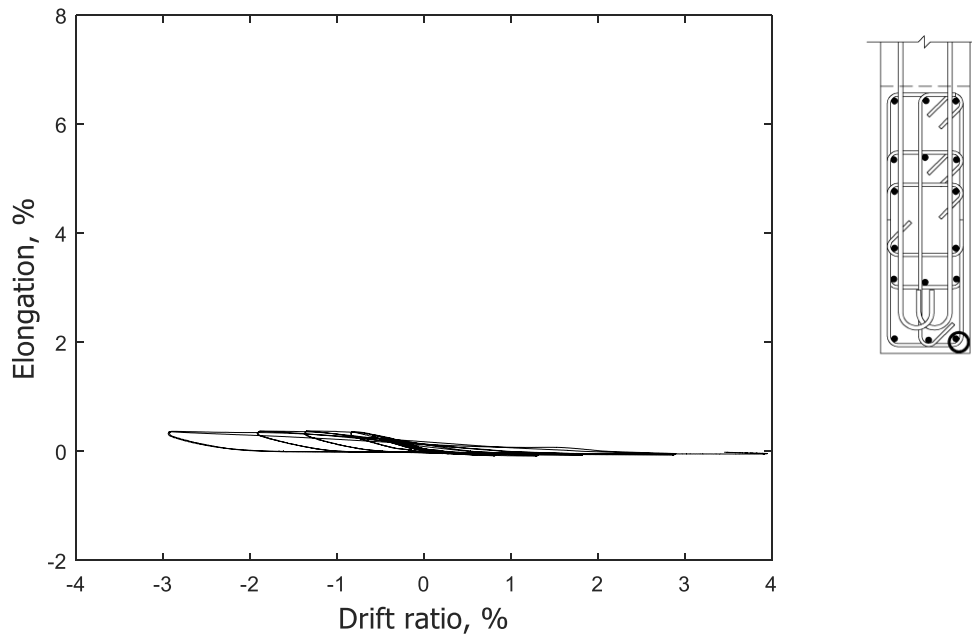


Figure 139 – Measured strain in longitudinal bar at confined stem 100 in. (2540 mm) above base of T3

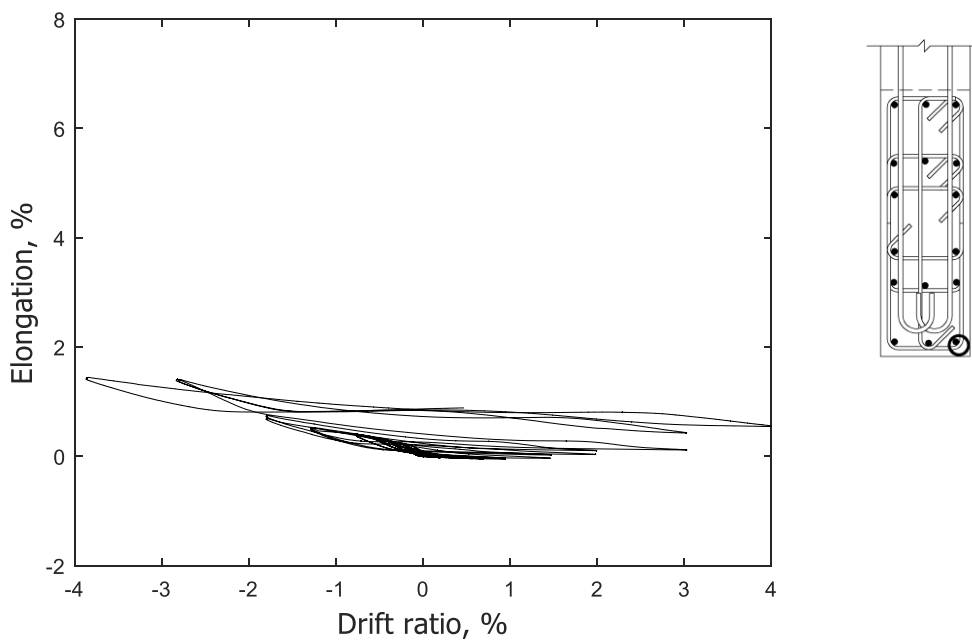


Figure 140 – Measured strain in longitudinal bar at confined stem 100 in. (2540 mm) above base of T4

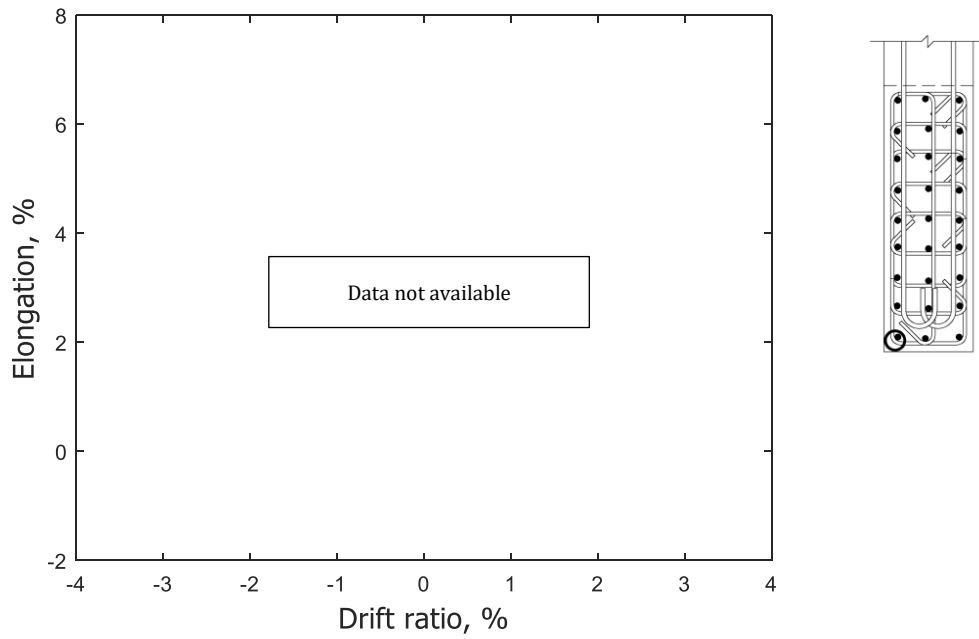


Figure 141 – Measured strain in longitudinal bar at confined stem 100 in. (2540 mm) above base of T1

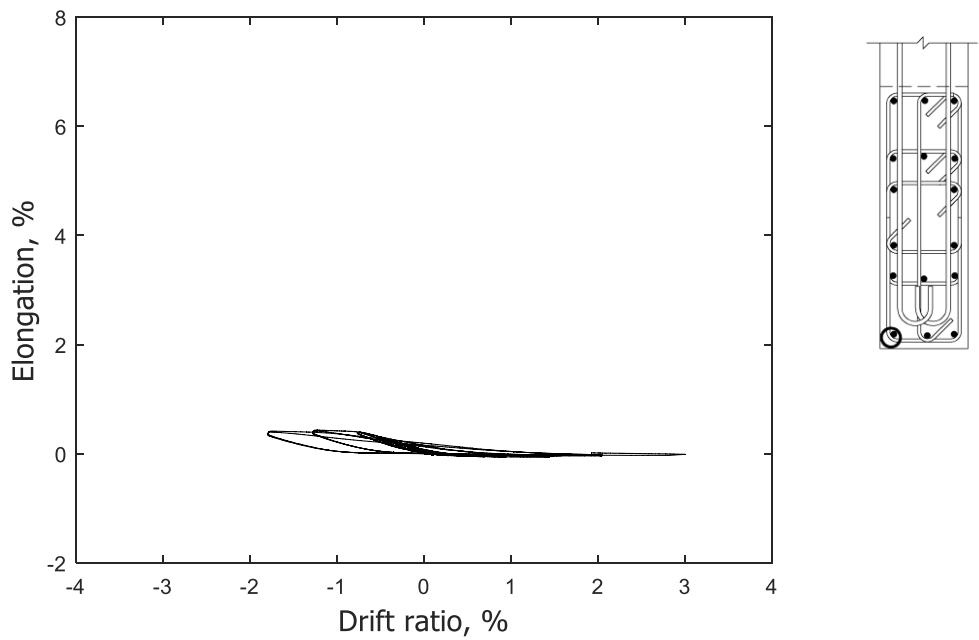


Figure 142 – Measured strain in longitudinal bar at confined stem 100 in. (2540 mm) above base of T2

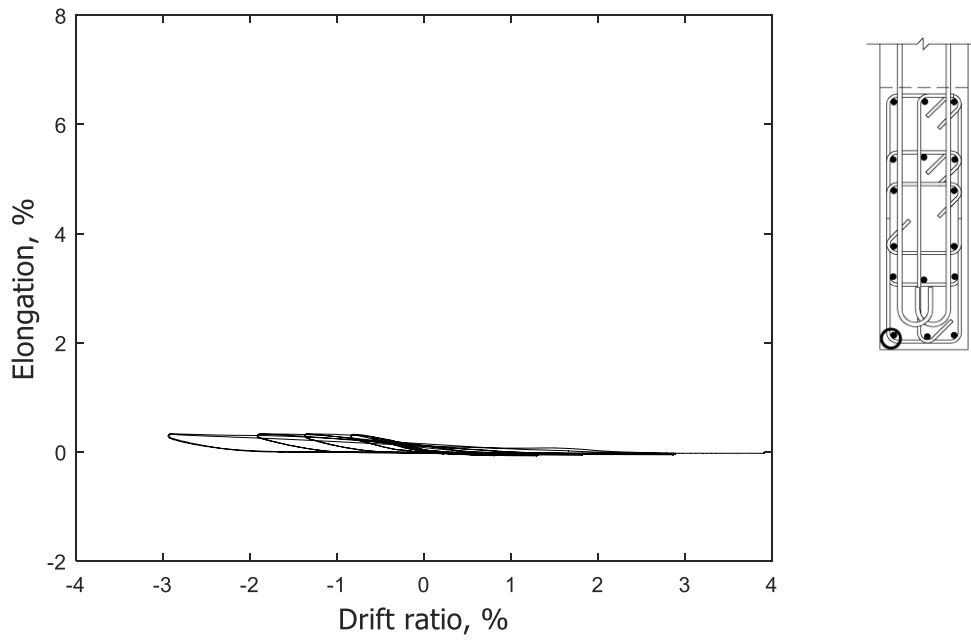


Figure 143 – Measured strain in longitudinal bar at confined stem 100 in. (2540 mm) above base of T3

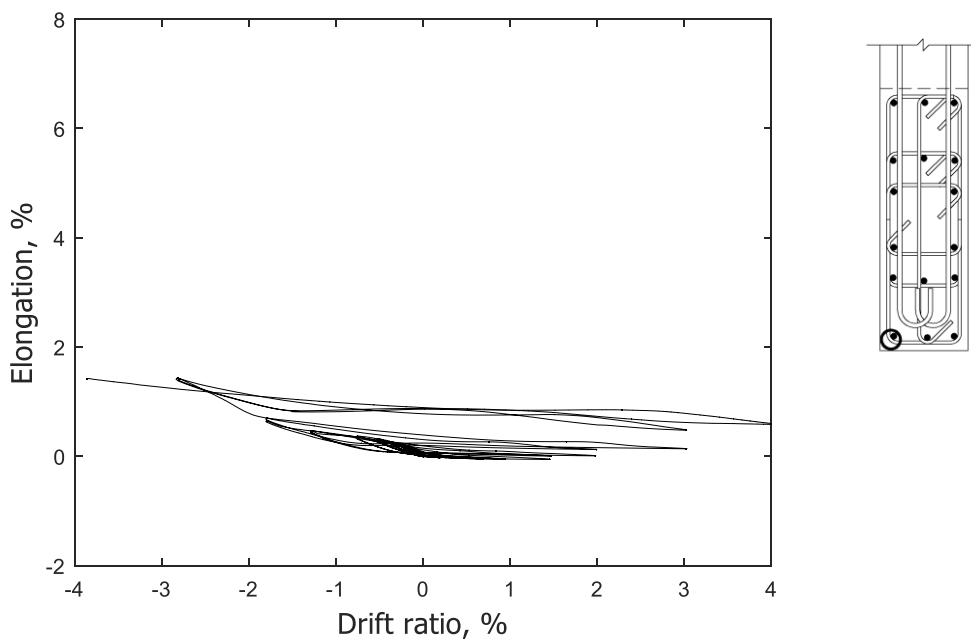


Figure 144 – Measured strain in longitudinal bar at confined stem 100 in. (2540 mm) above base of T4

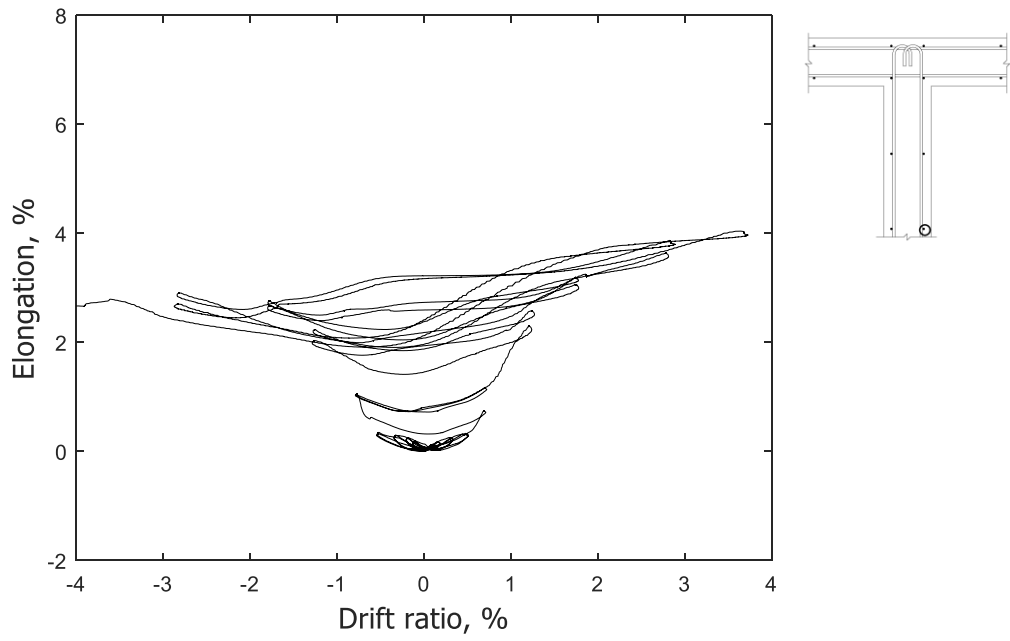


Figure 145 – Measured strain in longitudinal bar at unconfined stem 0.5 in. (13 mm) above base of T1

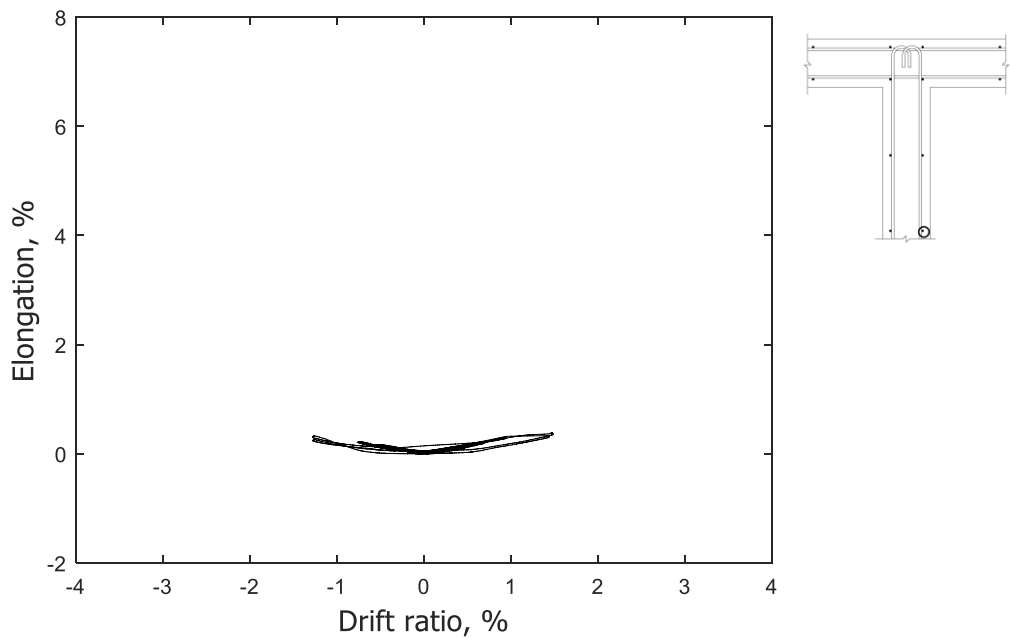


Figure 146 – Measured strain in longitudinal bar at unconfined stem 0.5 in. (13 mm) above base of T2

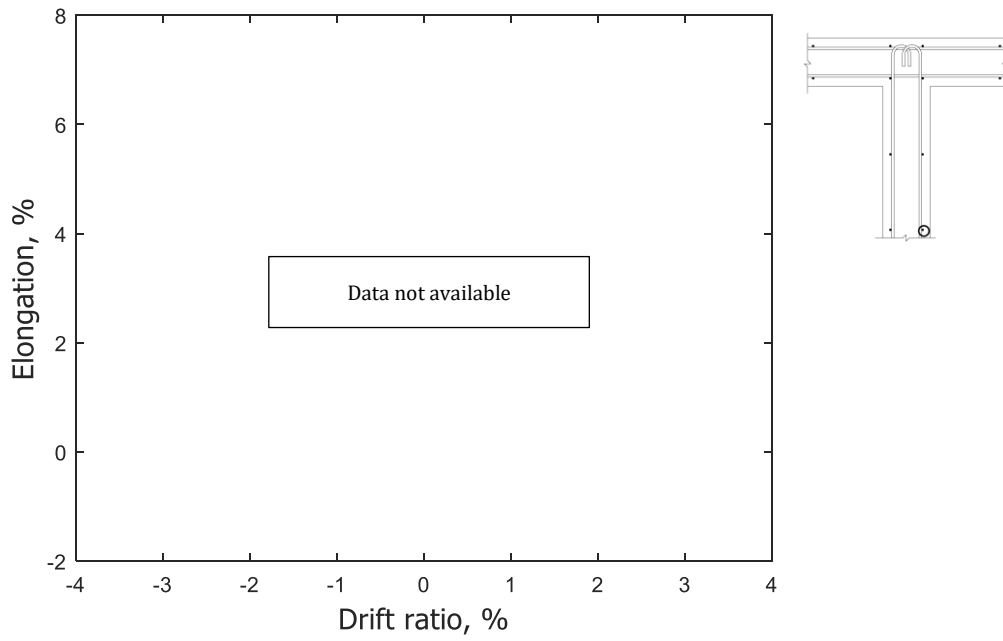


Figure 147 – Measured strain in longitudinal bar at unconfined stem 0.5 in. (13 mm) above base of T3

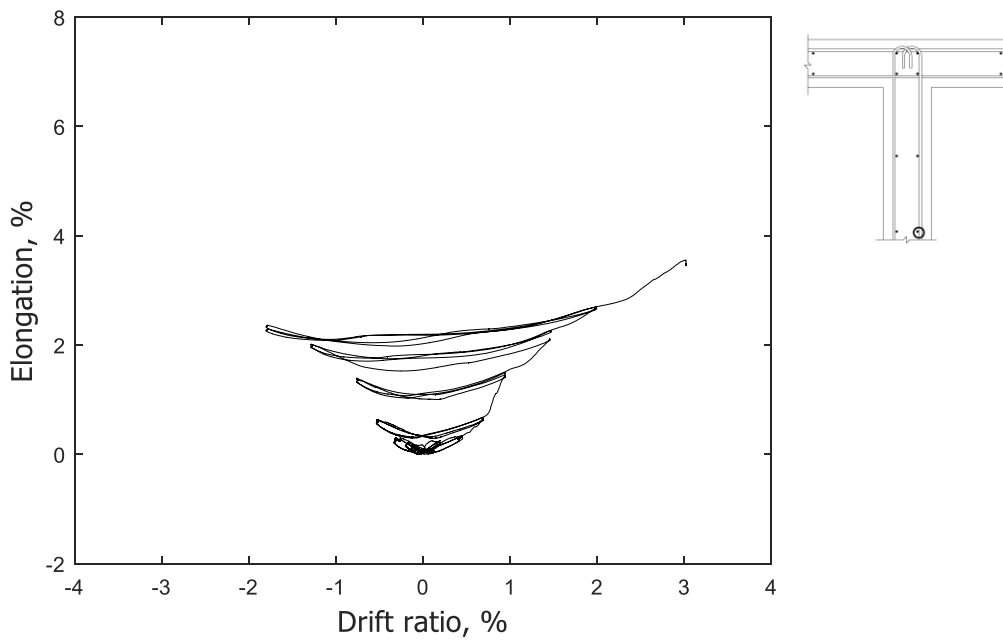


Figure 148 – Measured strain in longitudinal bar at unconfined stem 0.5 in. (13 mm) above base of T4

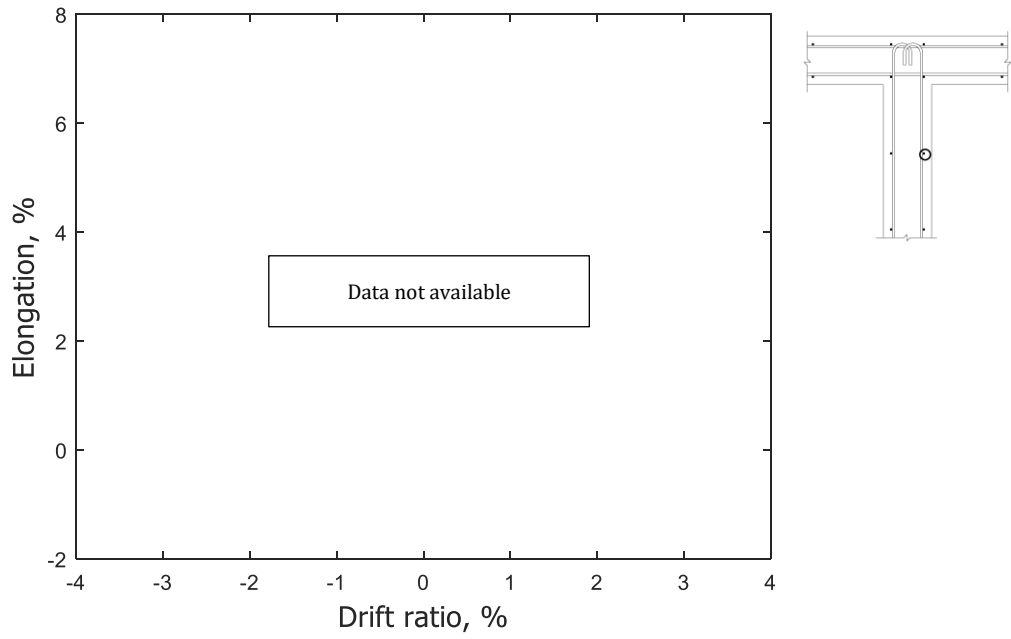


Figure 149 – Measured strain in longitudinal bar at unconfined stem 25 in. (635 mm) above base of T1

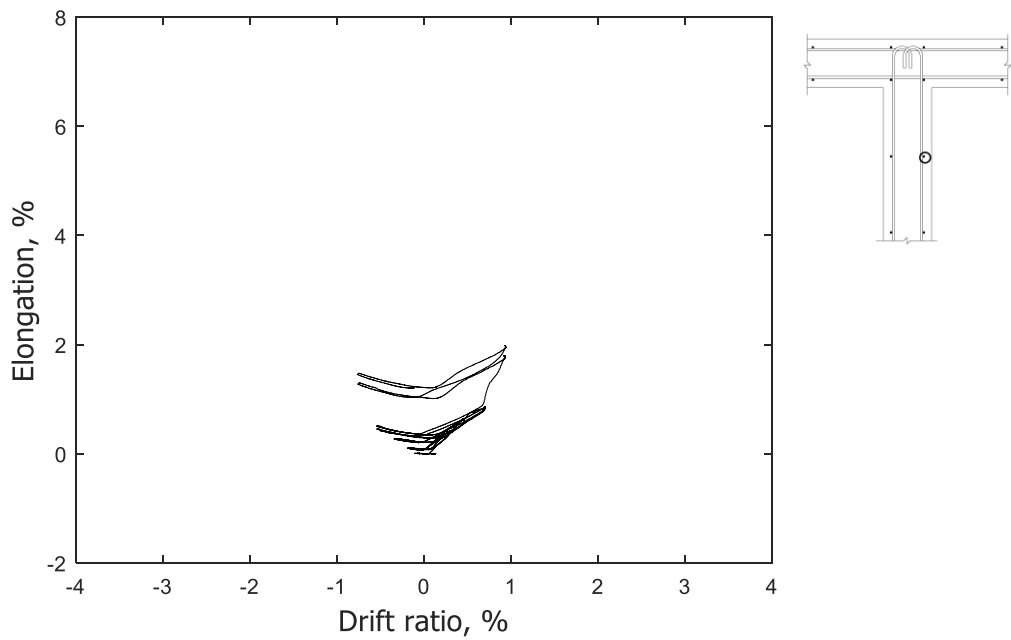


Figure 150 – Measured strain in longitudinal bar at unconfined stem 25 in. (635 mm) above base of T2

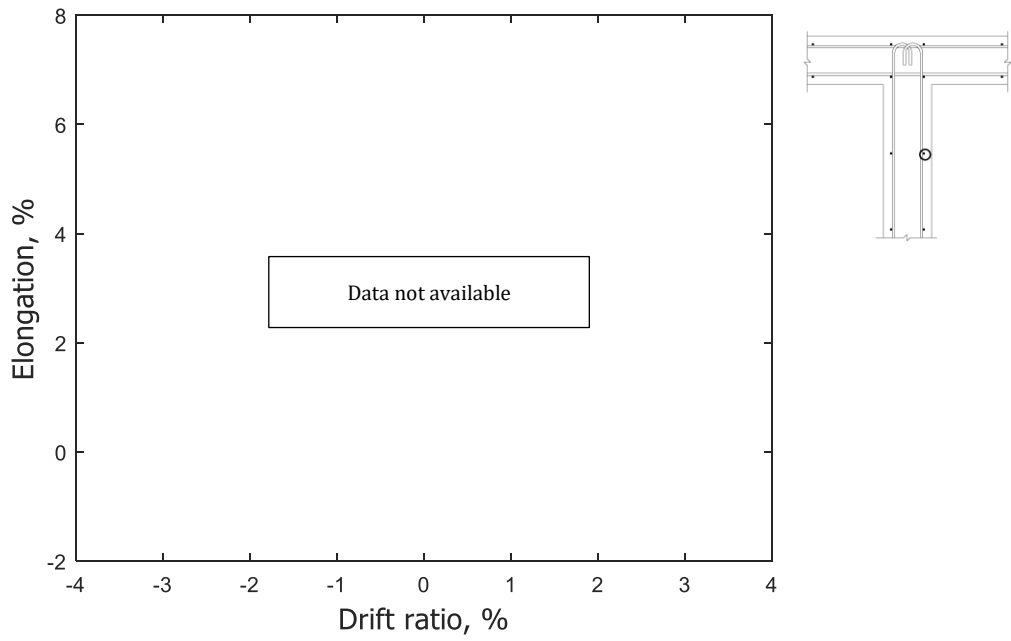


Figure 151 – Measured strain in longitudinal bar at unconfined stem 25 in. (635 mm) above base of T3

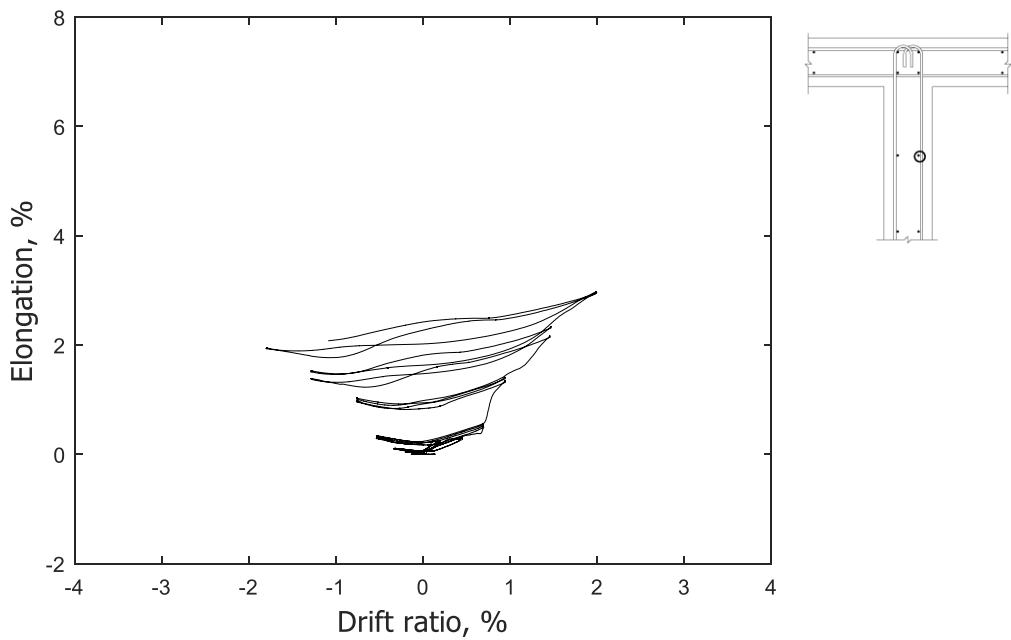


Figure 152 – Measured strain in longitudinal bar at unconfined stem 25 in. (635 mm) above base of T4

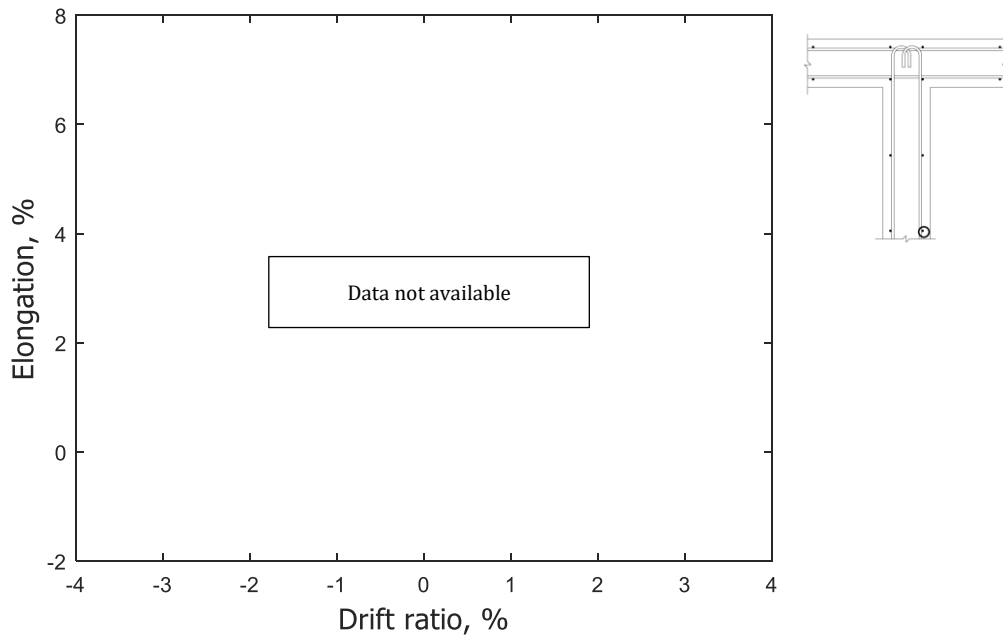


Figure 153 – Measured strain in longitudinal bar at unconfined stem 50 in. (1270 mm) above base of T1

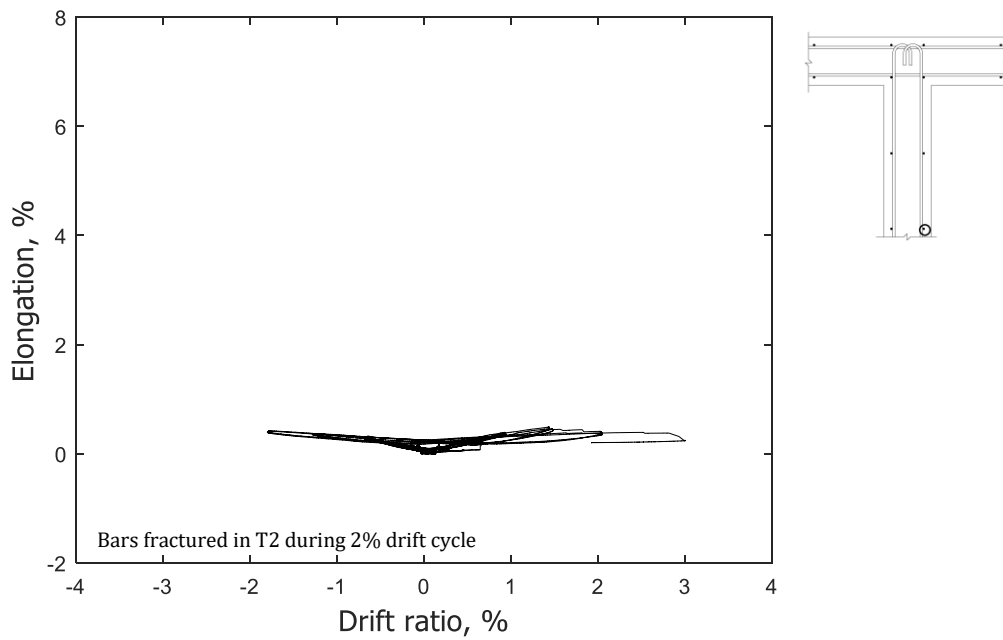


Figure 154 – Measured strain in longitudinal bar at unconfined stem 50 in. (1270 mm) above base of T2

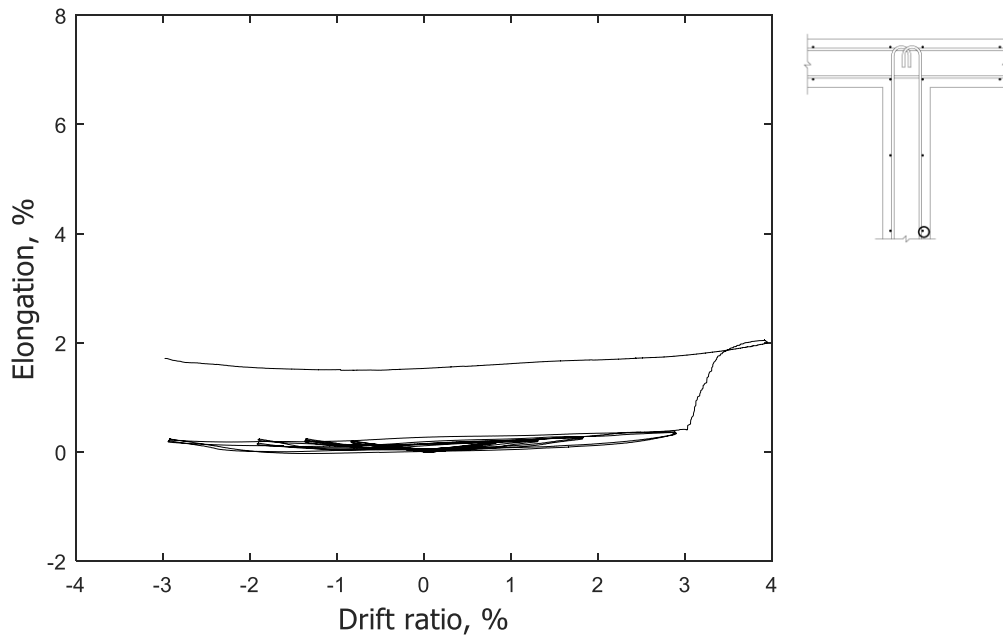


Figure 155 – Measured strain in longitudinal bar at unconfined stem 50 in. (1270 mm) above base of T3

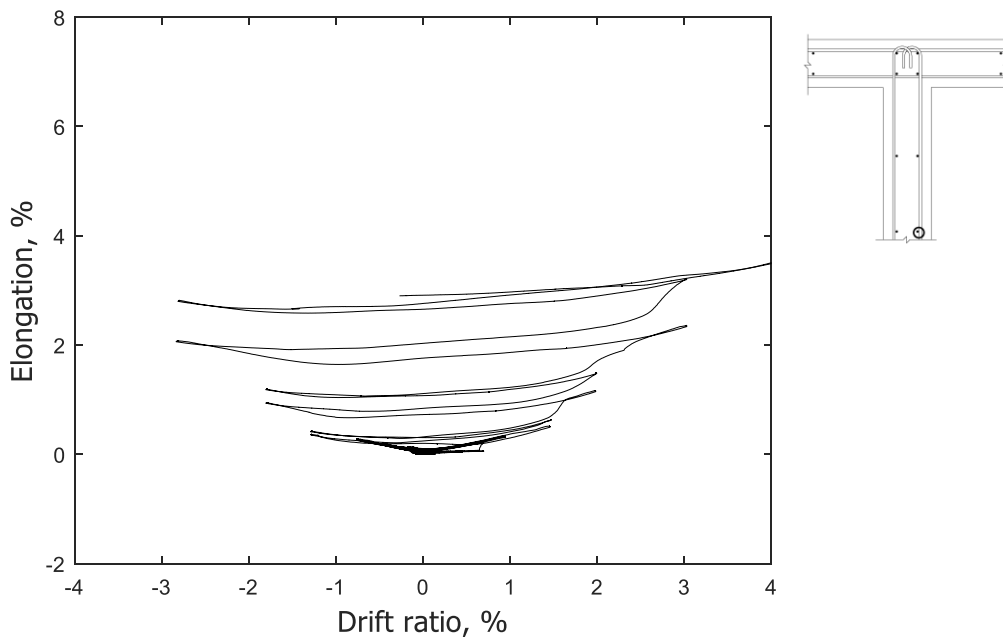


Figure 156 – Measured strain in longitudinal bar at unconfined stem 50 in. (1270 mm) above base of T4

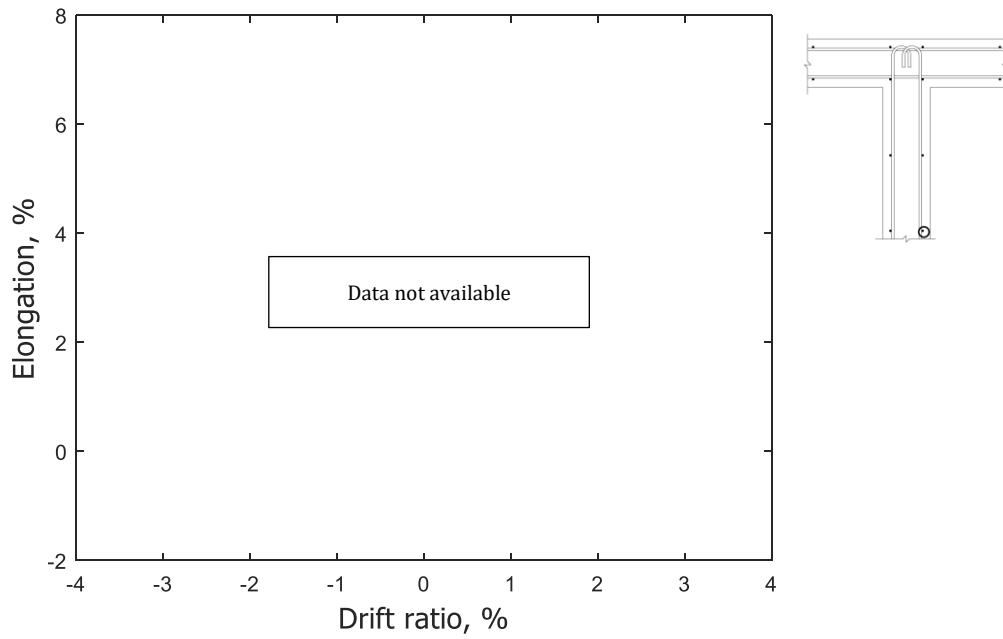


Figure 157 – Measured strain in longitudinal bar at unconfined stem 100 in. (2540 mm) above base of T1

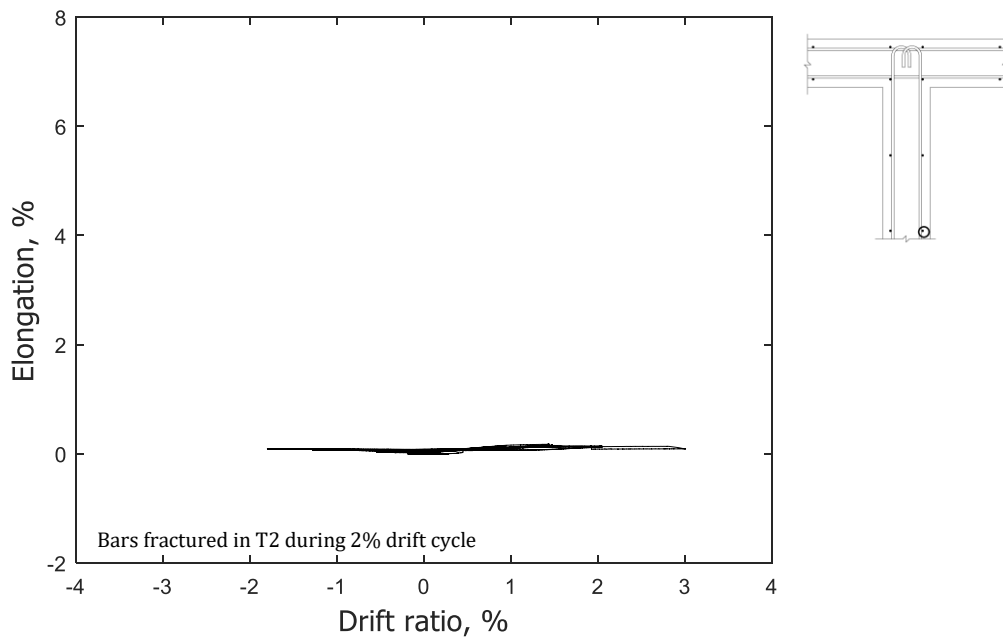


Figure 158 – Measured strain in longitudinal bar at unconfined stem 100 in. (2540 mm) above base of T2

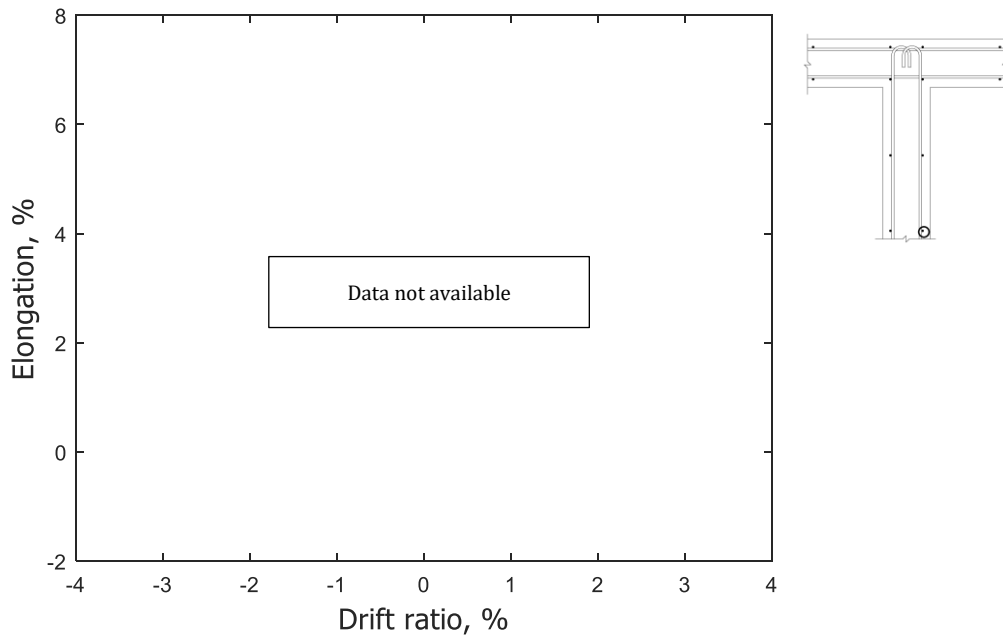


Figure 159 – Measured strain in longitudinal bar at unconfined stem 100 in. (2540 mm) above base of T3

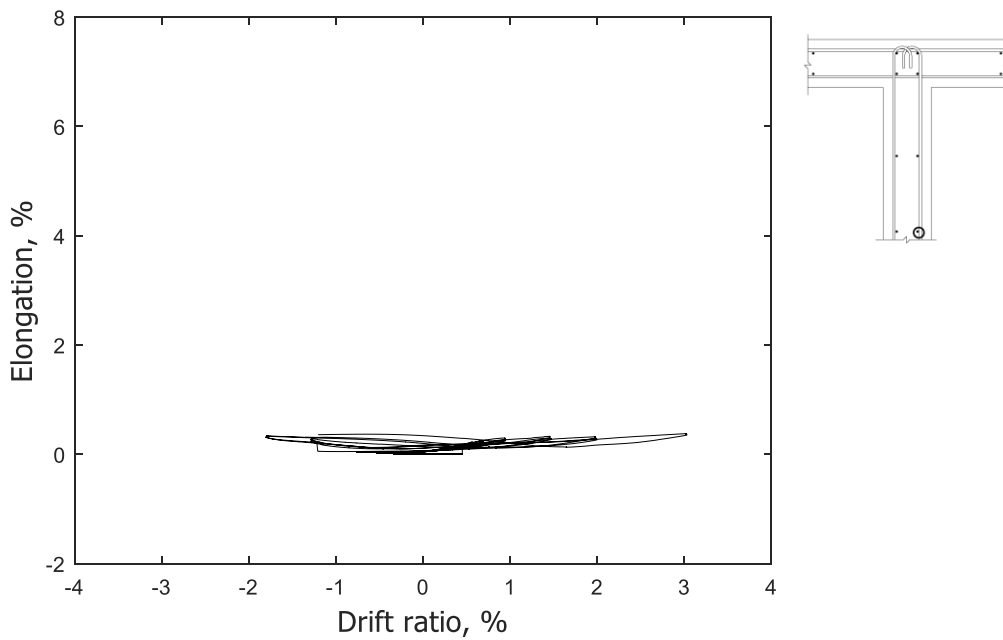


Figure 160 – Measured strain in longitudinal bar at unconfined stem 100 in. (2540 mm) above base of T4

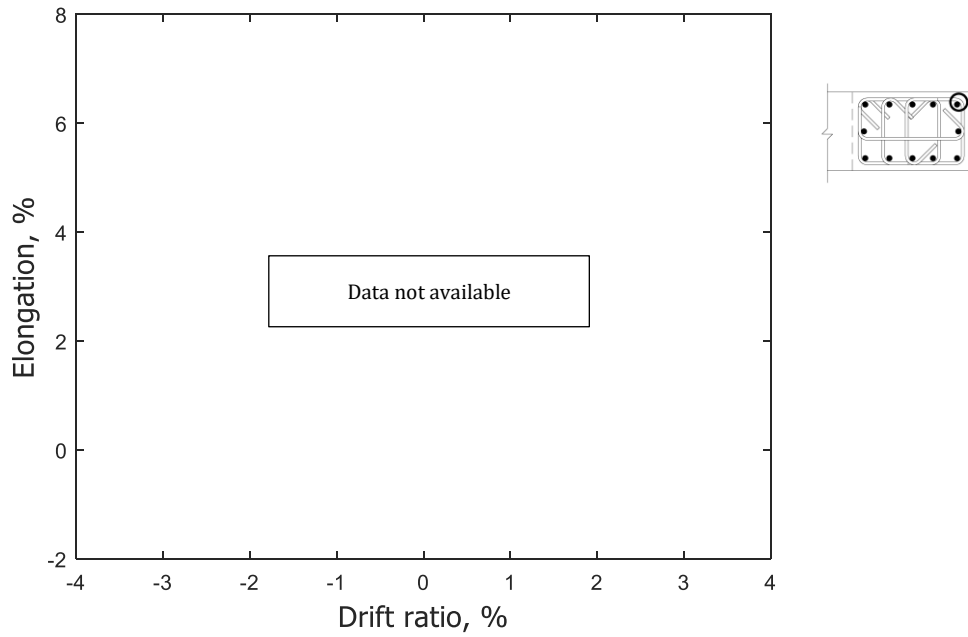


Figure 161 – Measured strain in longitudinal bar at confined flange 0.5 in. (13 mm) above base of T1

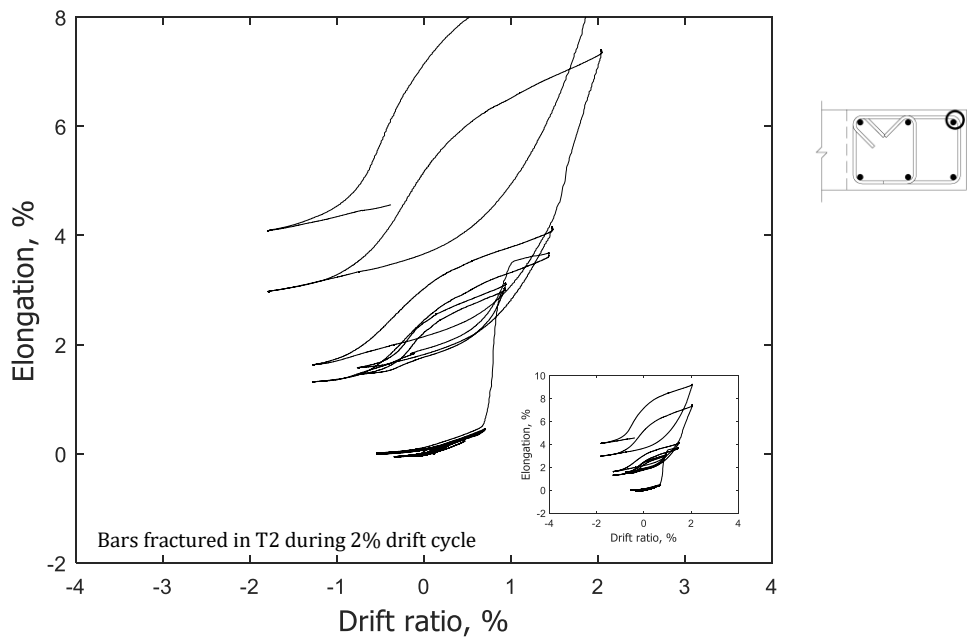


Figure 162 – Measured strain in longitudinal bar at confined flange 0.5 in. (13 mm) above base of T2

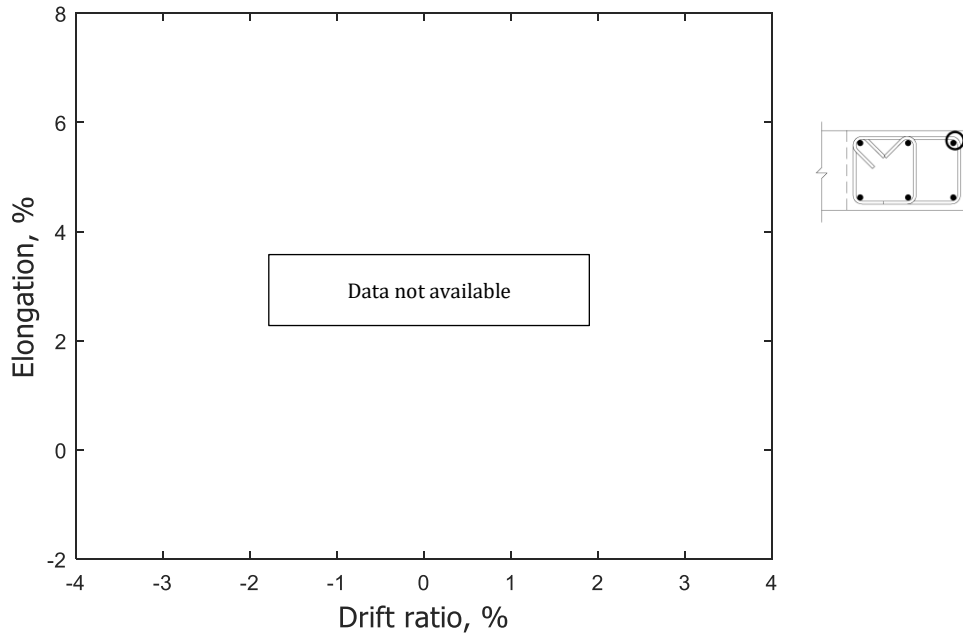


Figure 163 – Measured strain in longitudinal bar at confined flange 0.5 in. (13 mm) above base of T3

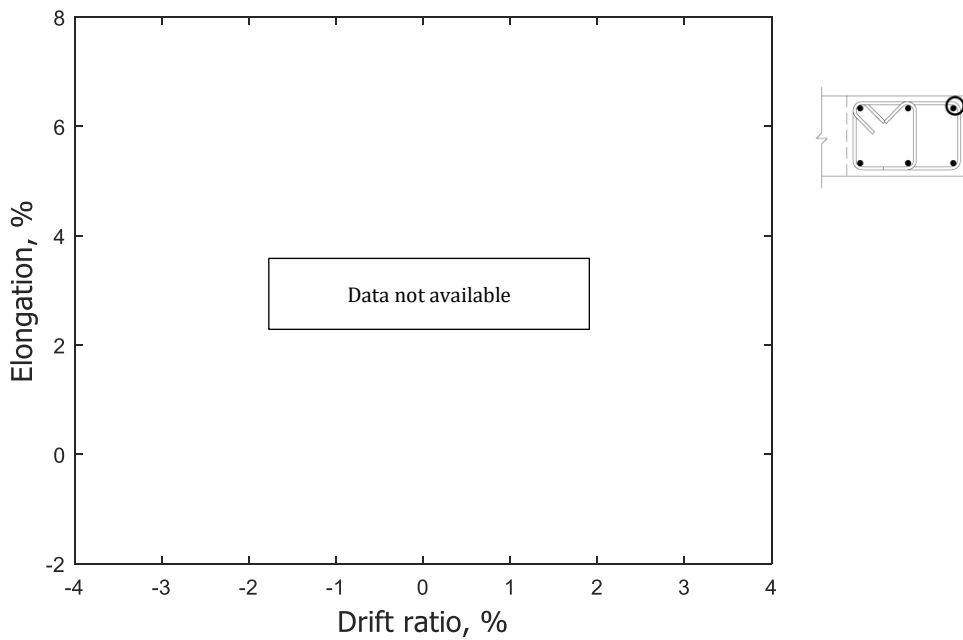


Figure 164 – Measured strain in longitudinal bar at confined flange 0.5 in. (13 mm) above base of T4

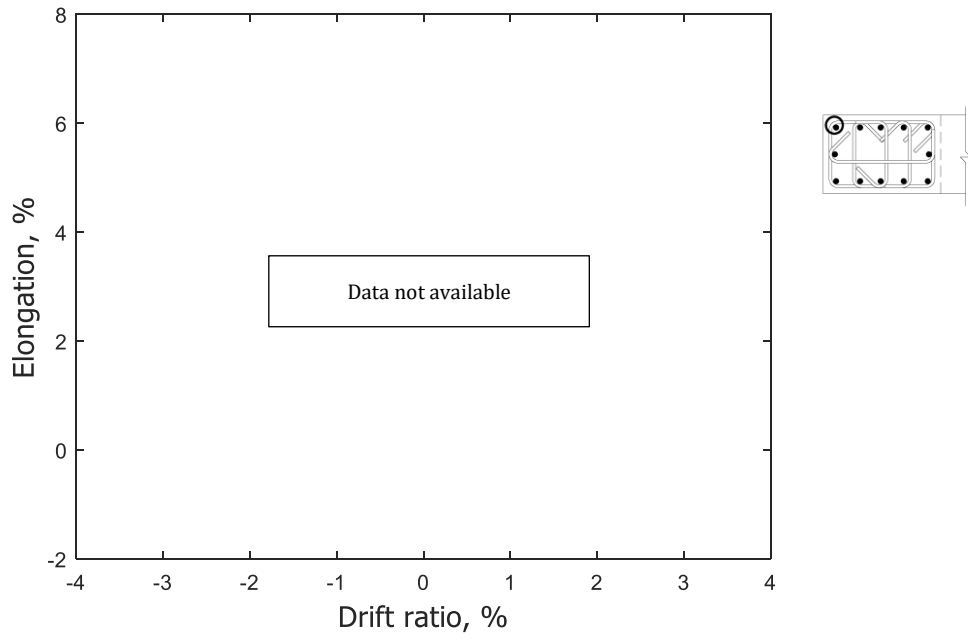


Figure 165 – Measured strain in longitudinal bar at confined flange 0.5 in. (13 mm) above base of T1

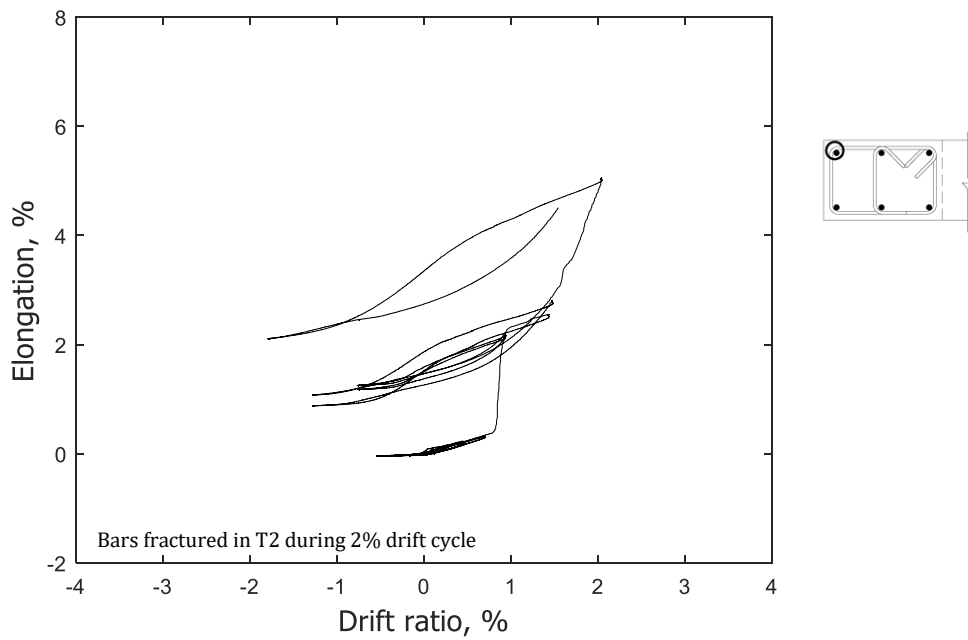


Figure 166 – Measured strain in longitudinal bar at confined flange 0.5 in. (13 mm) above base of T2

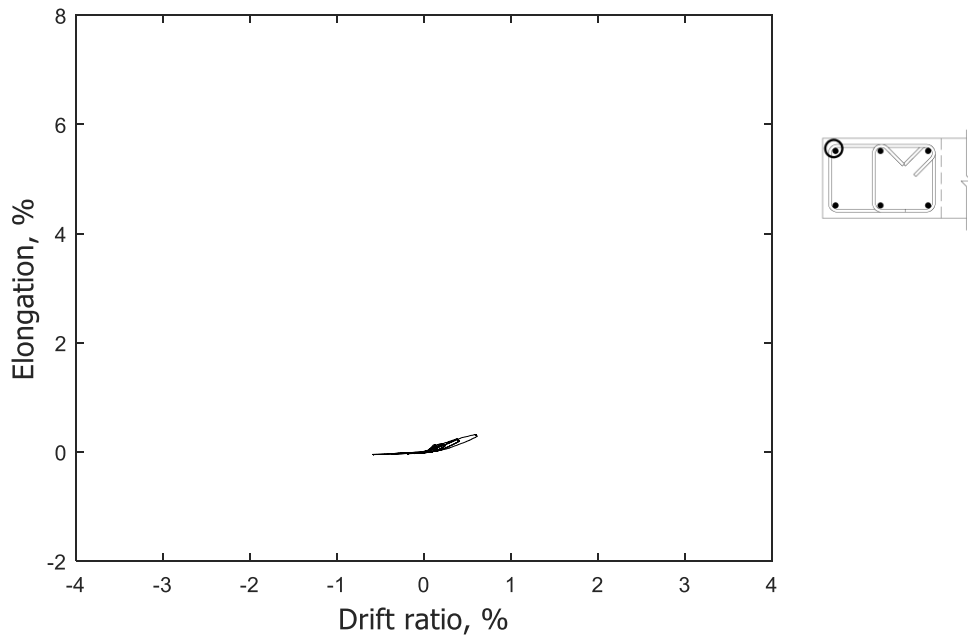


Figure 167 – Measured strain in longitudinal bar at confined flange 0.5 in. (13 mm) above base of T3

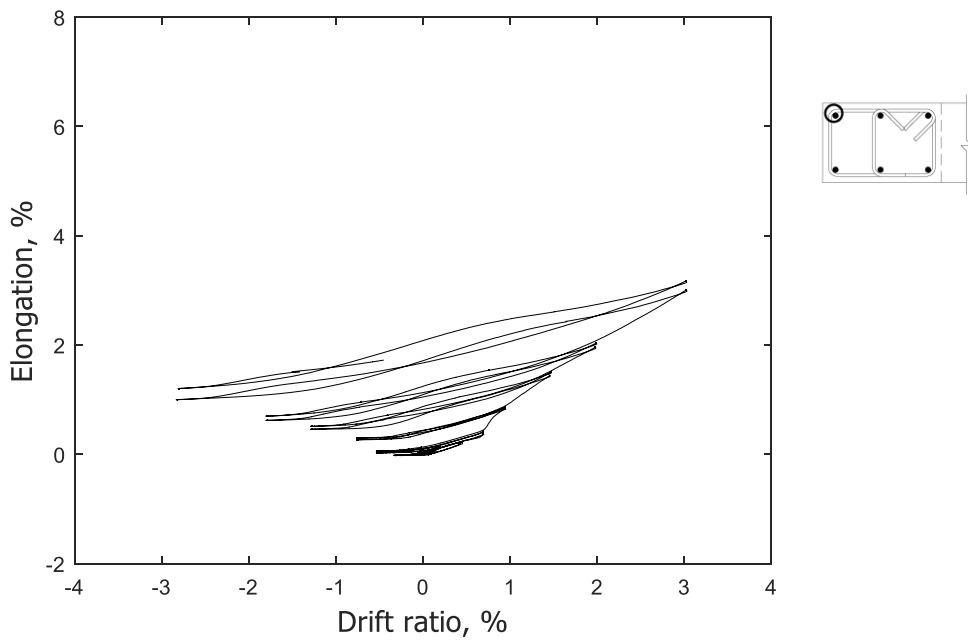


Figure 168 – Measured strain in longitudinal bar at confined flange 0.5 in. (13 mm) above base of T4

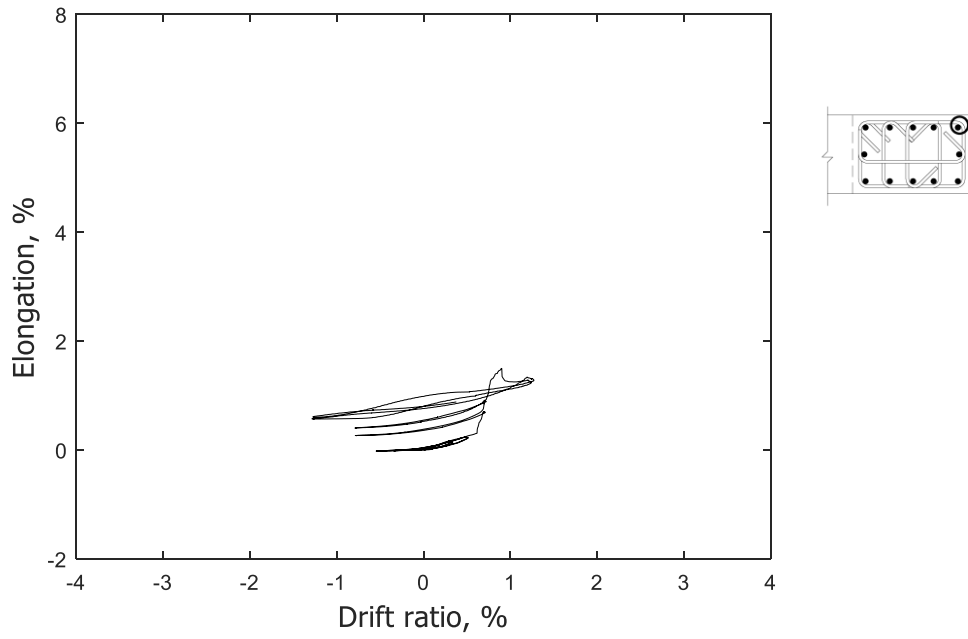


Figure 169 – Measured strain in longitudinal bar at confined flange 50 in. (1270 mm) above base of T1

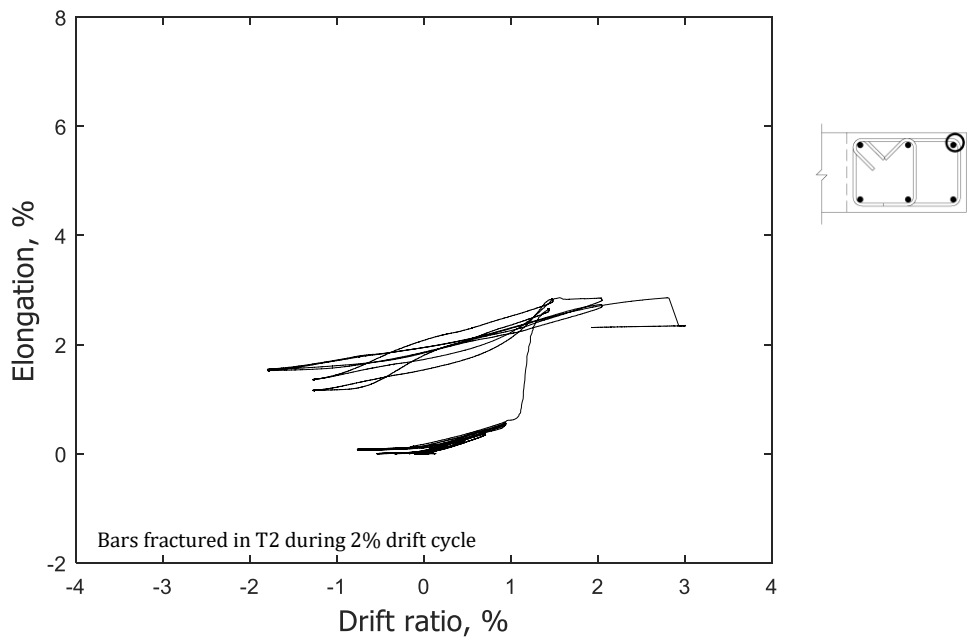


Figure 170 – Measured strain in longitudinal bar at confined flange 50 in. (1270 mm) above base of T2

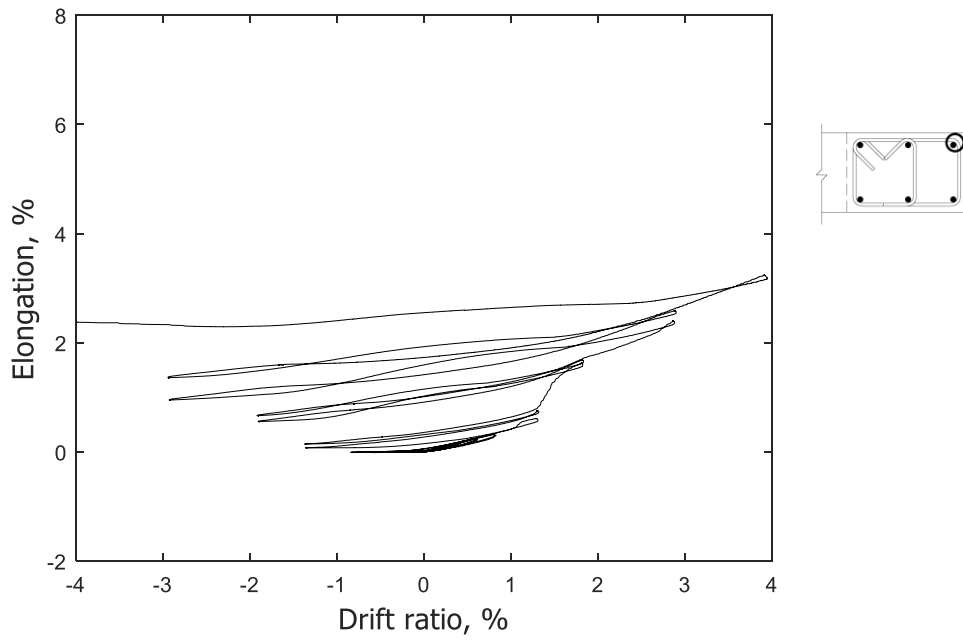


Figure 171 – Measured strain in longitudinal bar at confined flange 50 in. (1270 mm) above base of T3

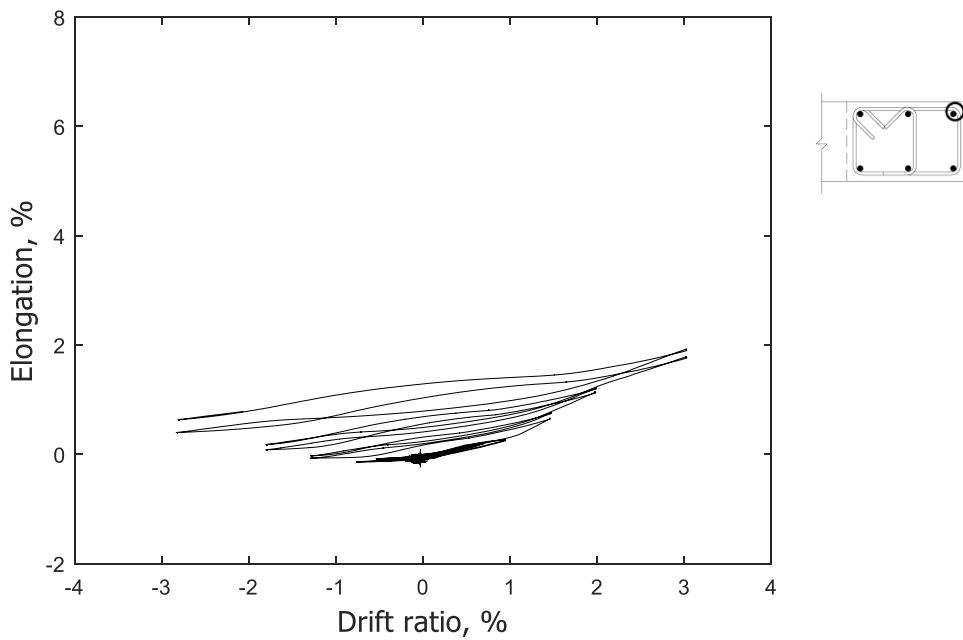


Figure 172 – Measured strain in longitudinal bar at confined flange 50 in. (1270 mm) above base of T4

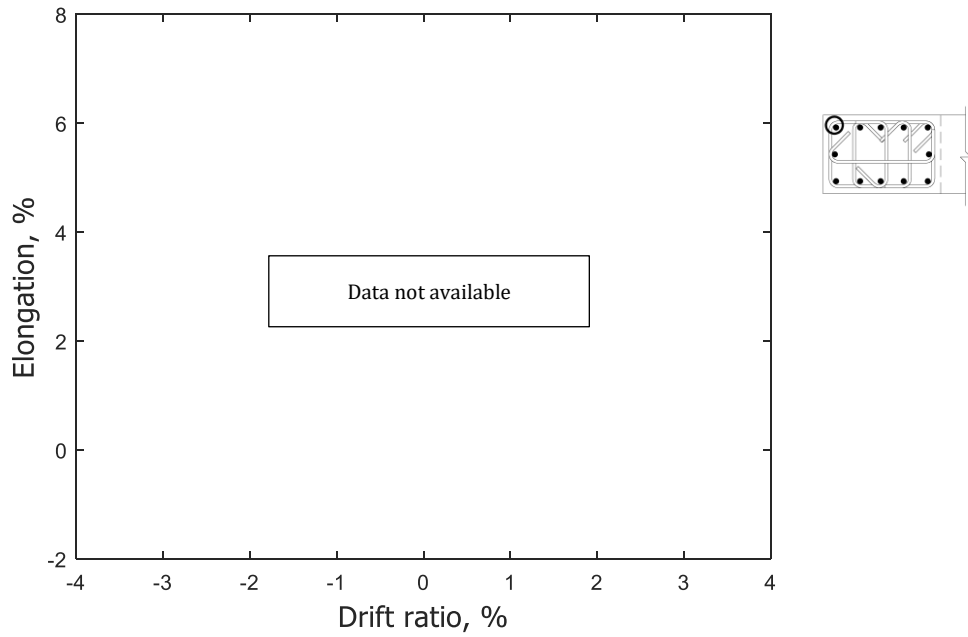


Figure 173 – Measured strain in longitudinal bar at confined flange 50 in. (1270 mm) above base of T1

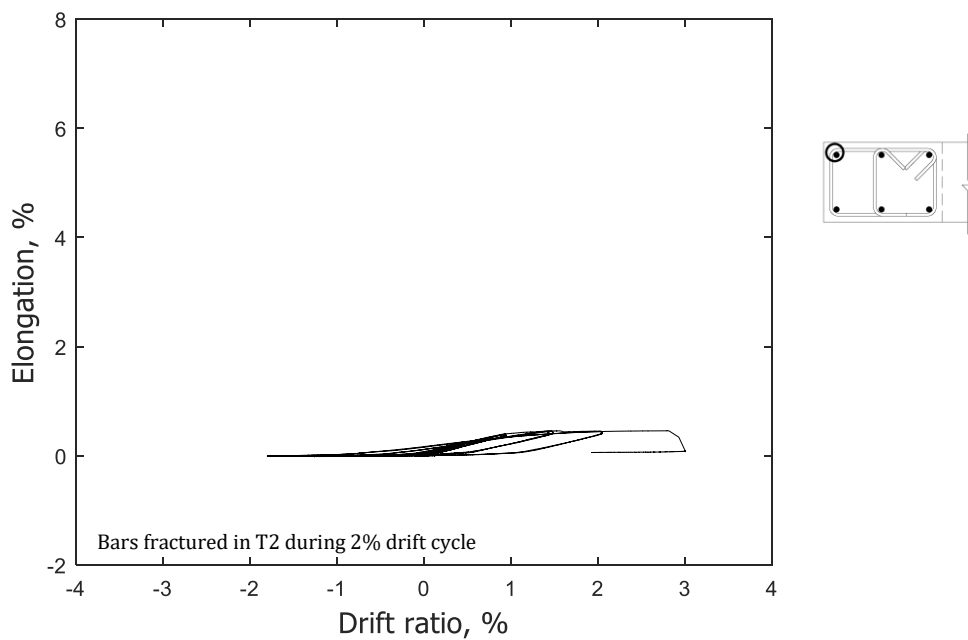


Figure 174 – Measured strain in longitudinal bar at confined flange 50 in. (1270 mm) above base of T2

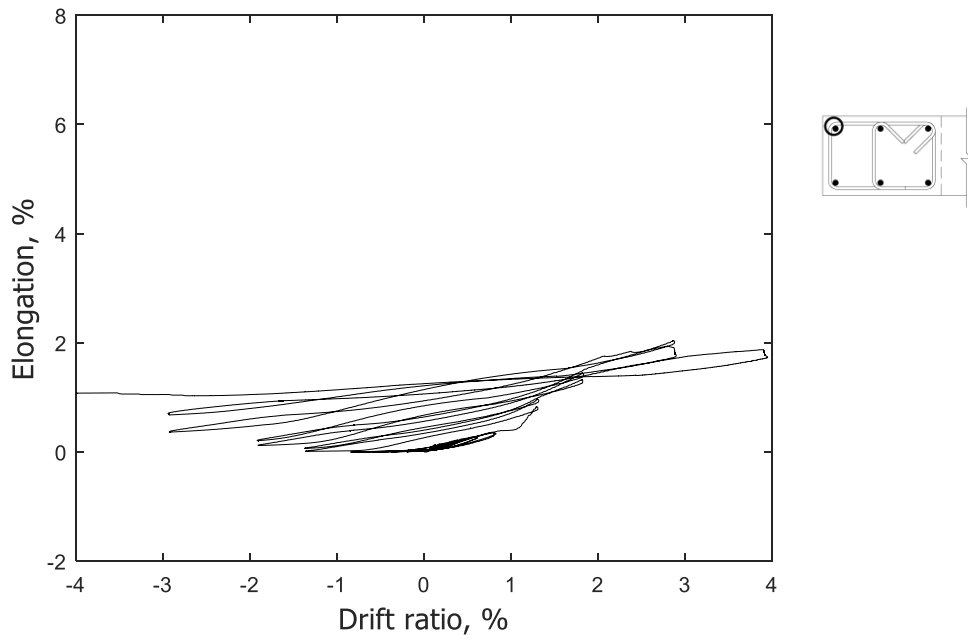


Figure 175 – Measured strain in longitudinal bar at confined flange 50 in. (1270 mm) above base of T3

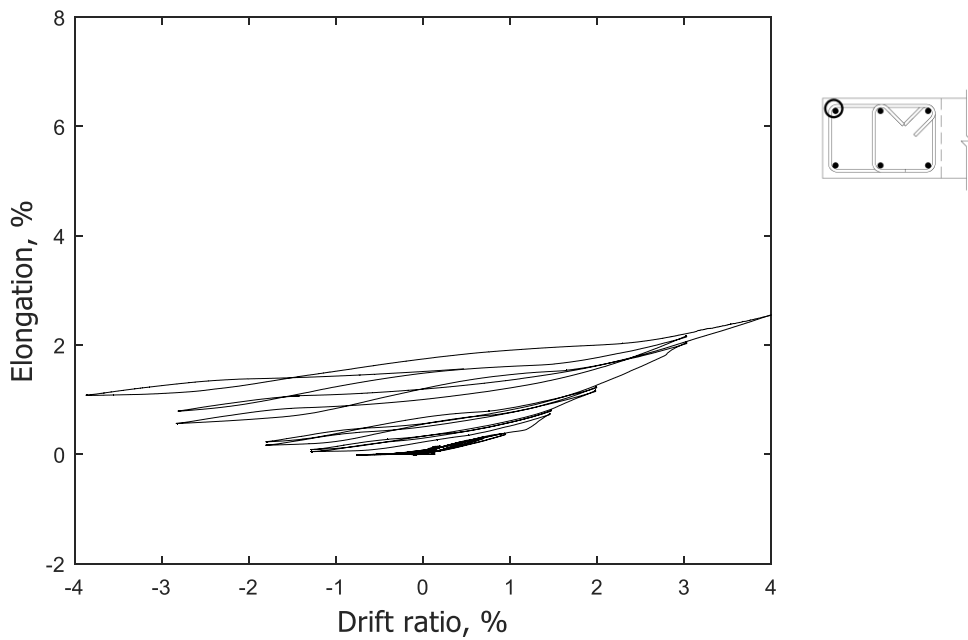


Figure 176 – Measured strain in longitudinal bar at confined flange 50 in. (1270 mm) above base of T4

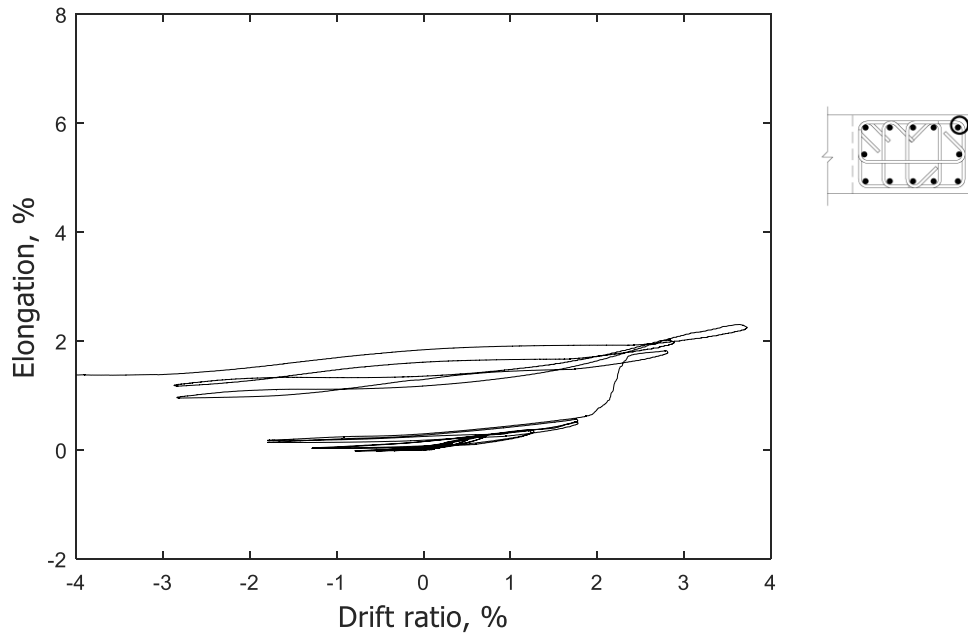


Figure 177 – Measured strain in longitudinal bar at confined flange 100 in. (2540 mm) above base of T1

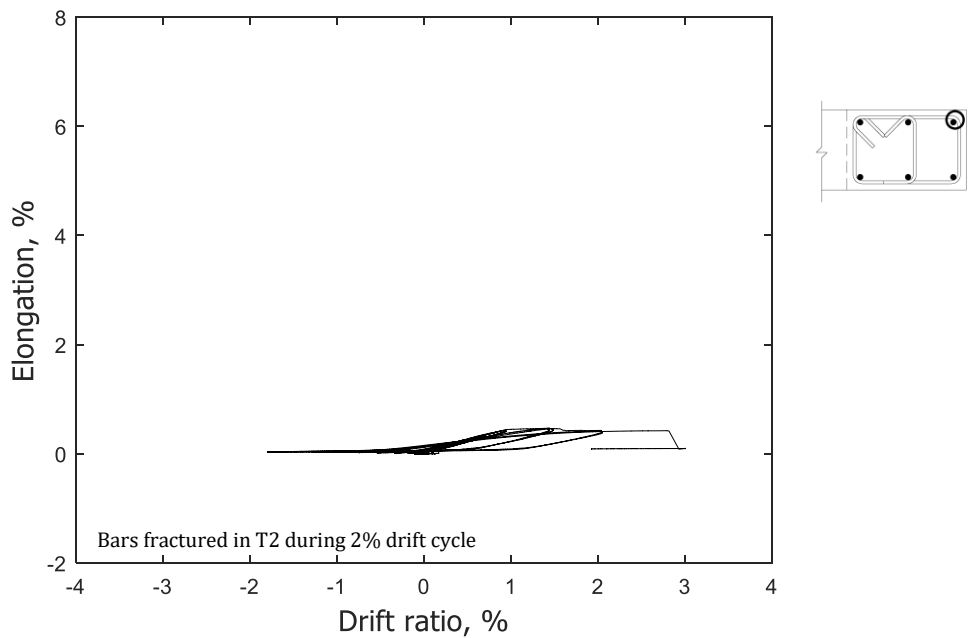


Figure 178 – Measured strain in longitudinal bar at confined flange 100 in. (2540 mm) above base of T2

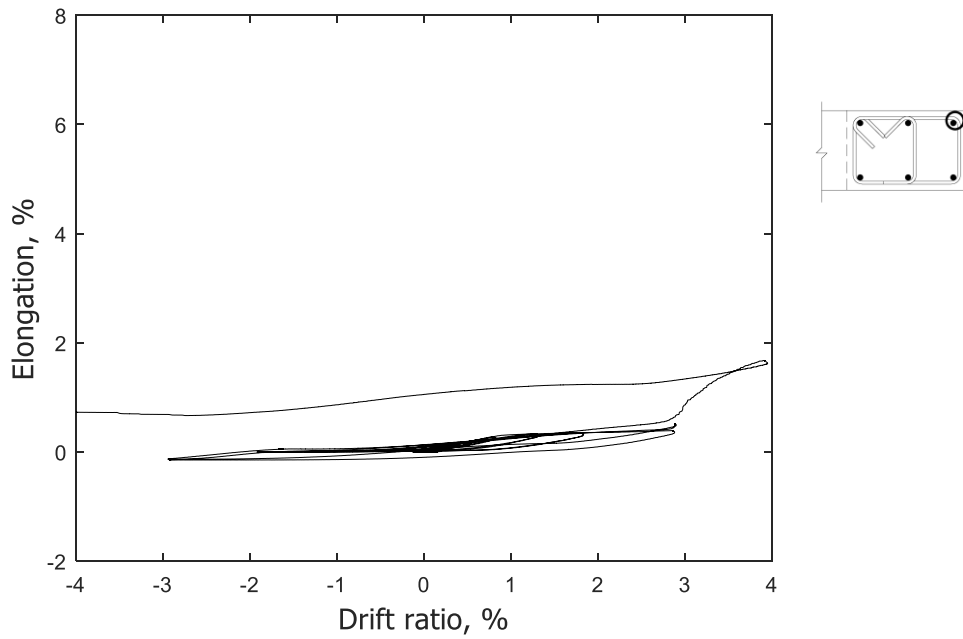


Figure 179 – Measured strain in longitudinal bar at confined flange 100 in. (2540 mm) above base of T3

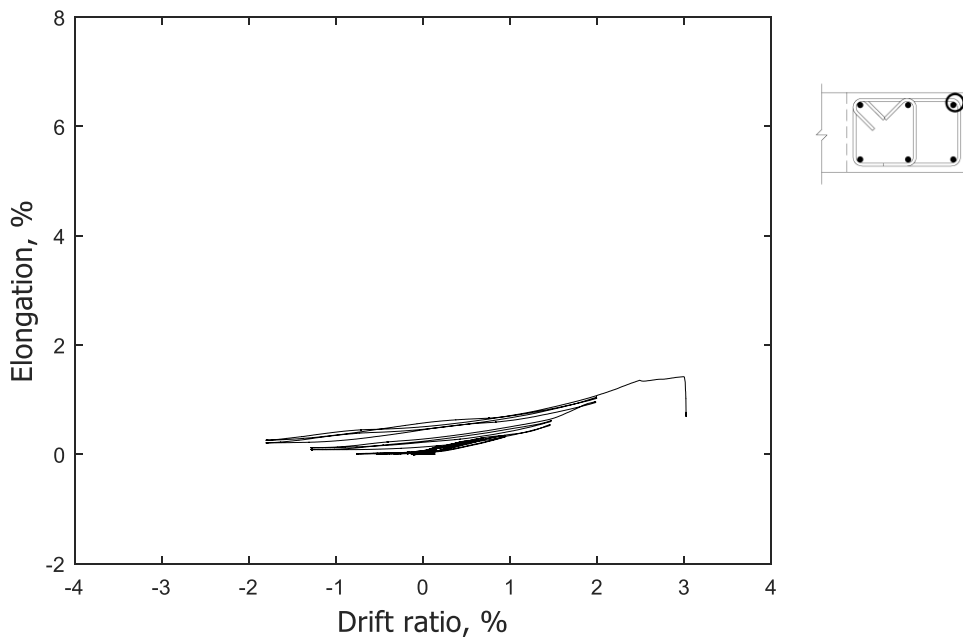


Figure 180 – Measured strain in longitudinal bar at confined flange 100 in. (2540 mm) above base of T4

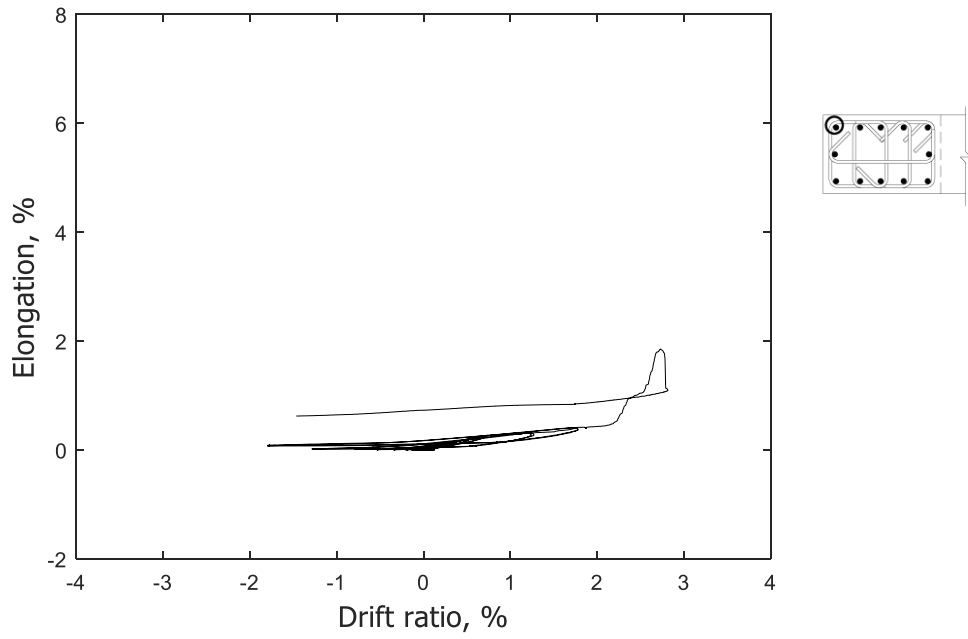


Figure 181 – Measured strain in longitudinal bar at confined flange 100 in. (2540 mm) above base of T1

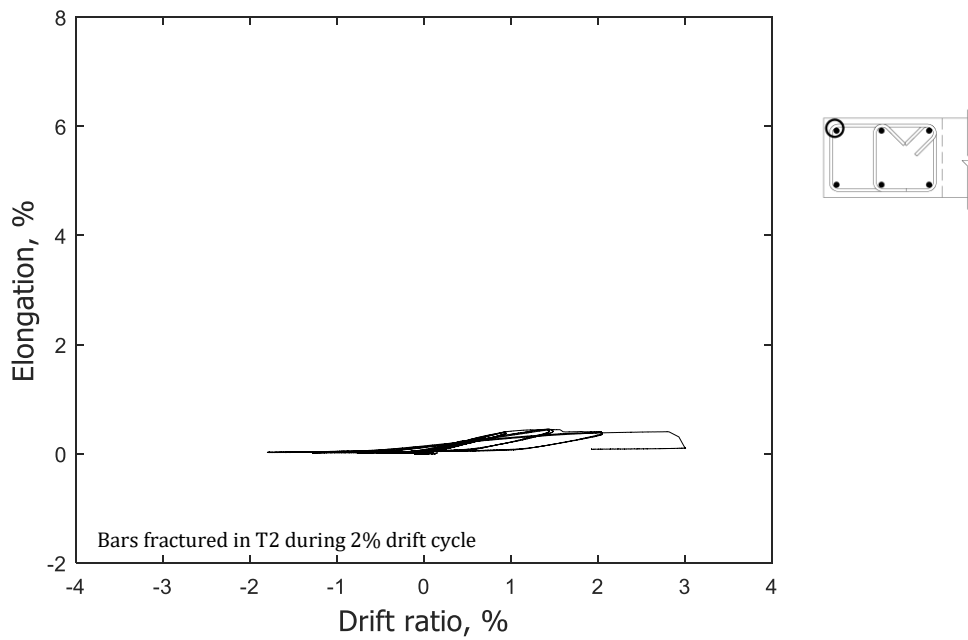


Figure 182 – Measured strain in longitudinal bar at confined flange 100 in. (2540 mm) above base of T2

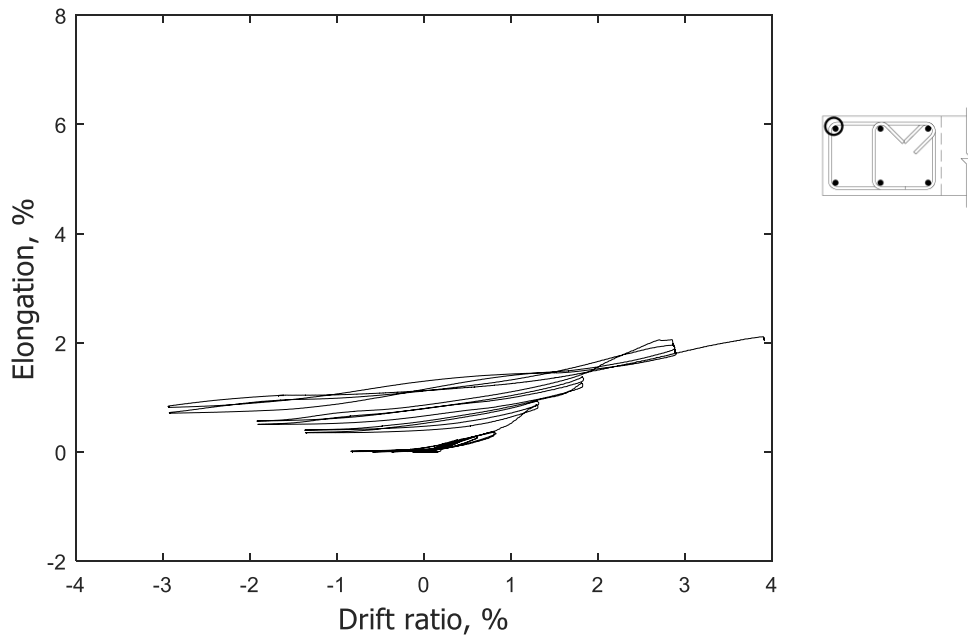


Figure 183 – Measured strain in longitudinal bar at confined flange 100 in. (2540 mm) above base of T3

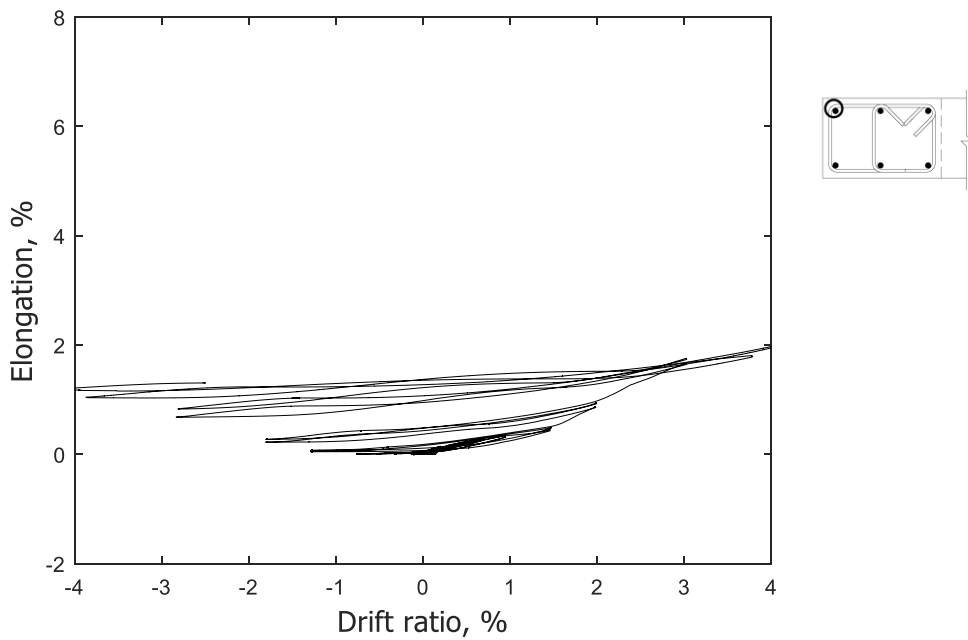


Figure 184 – Measured strain in longitudinal bar at confined flange 100 in. (2540 mm) above base of T4

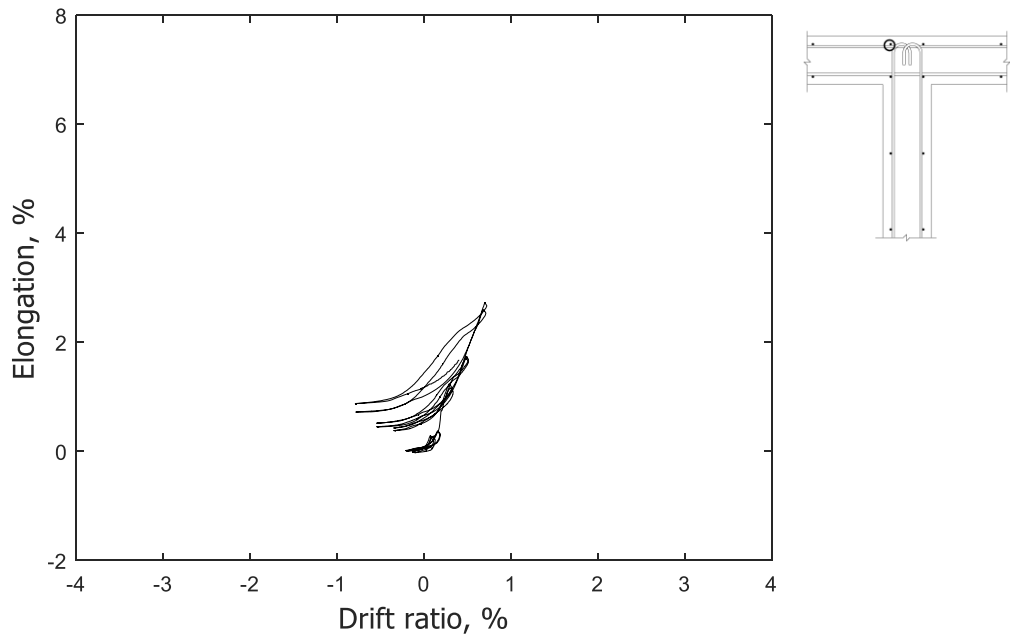


Figure 185 – Measured strain in longitudinal bar at unconfined flange 0.5 in. (13 mm) above base of T1

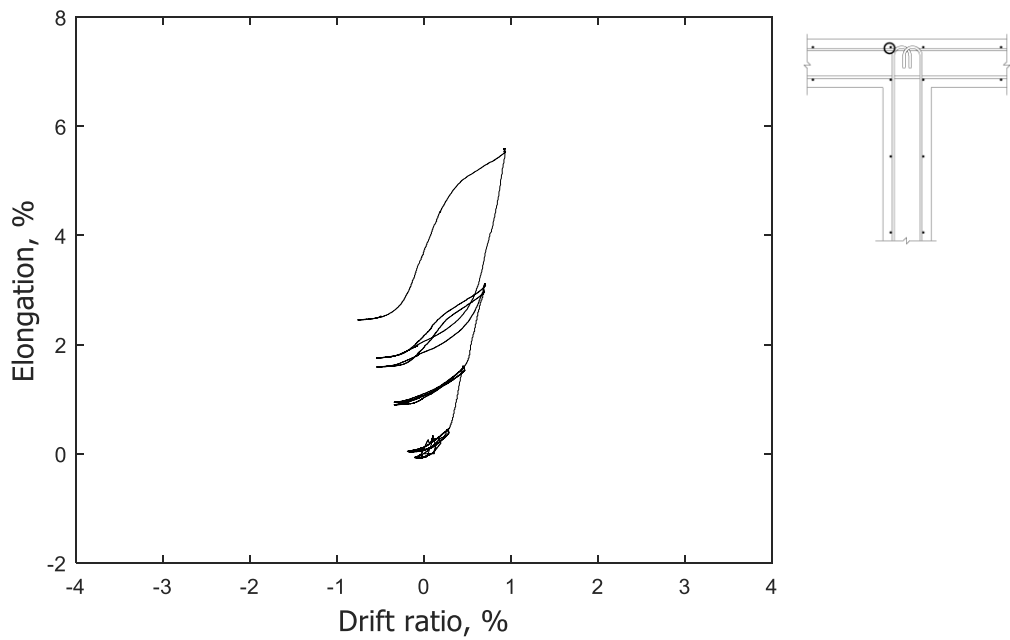


Figure 186 – Measured strain in longitudinal bar at unconfined flange 0.5 in. (13 mm) above base of T2

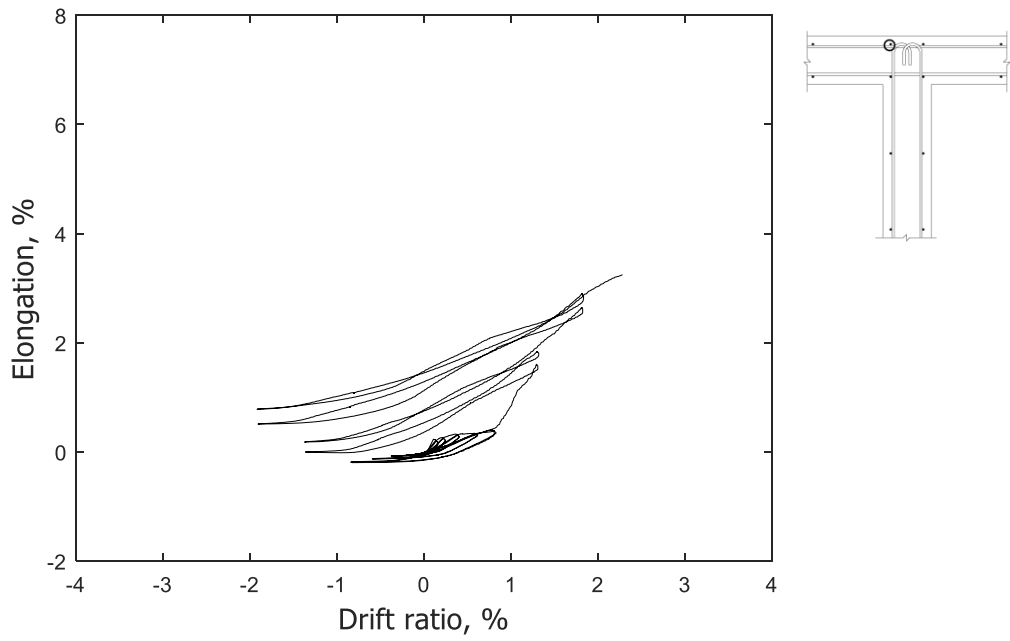


Figure 187 – Measured strain in longitudinal bar at unconfined flange 0.5 in. (13 mm) above base of T3

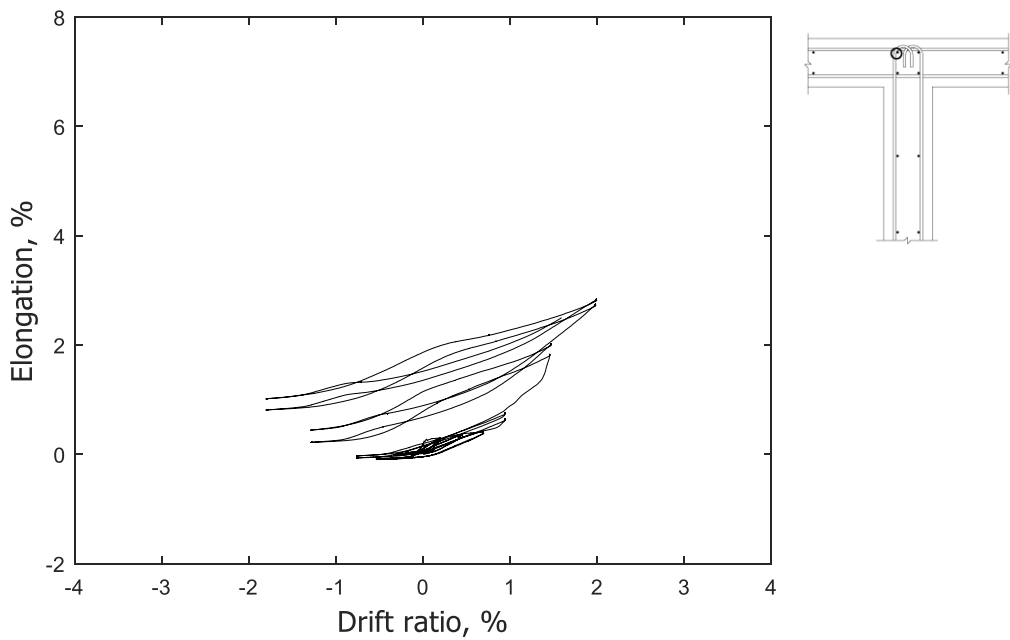


Figure 188 – Measured strain in longitudinal bar at unconfined flange 0.5 in. (13 mm) above base of T4

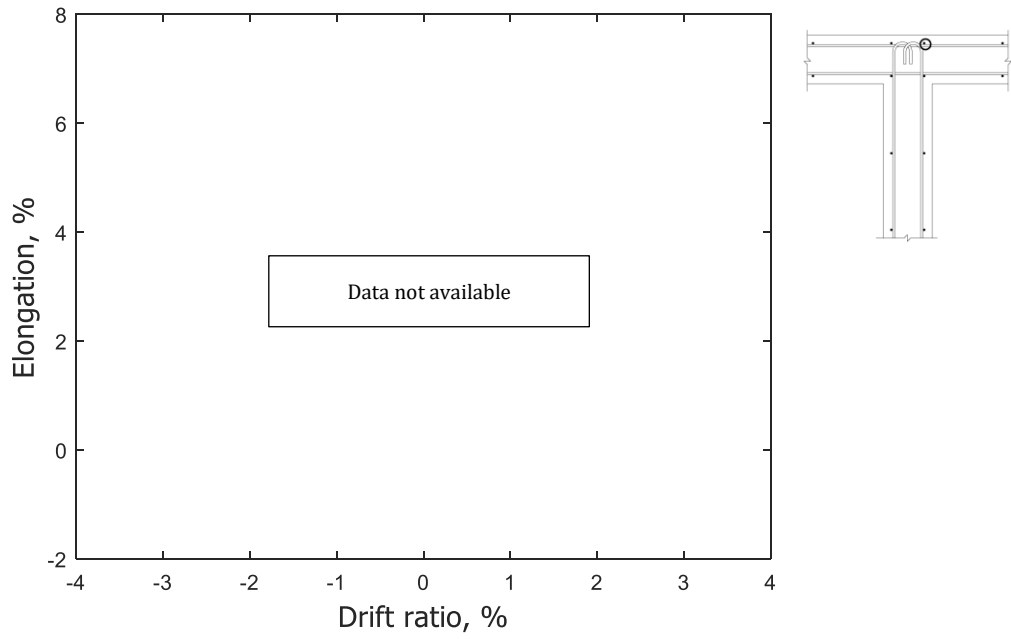


Figure 189 – Measured strain in longitudinal bar at unconfined flange 25 in. (635 mm) above base of T1

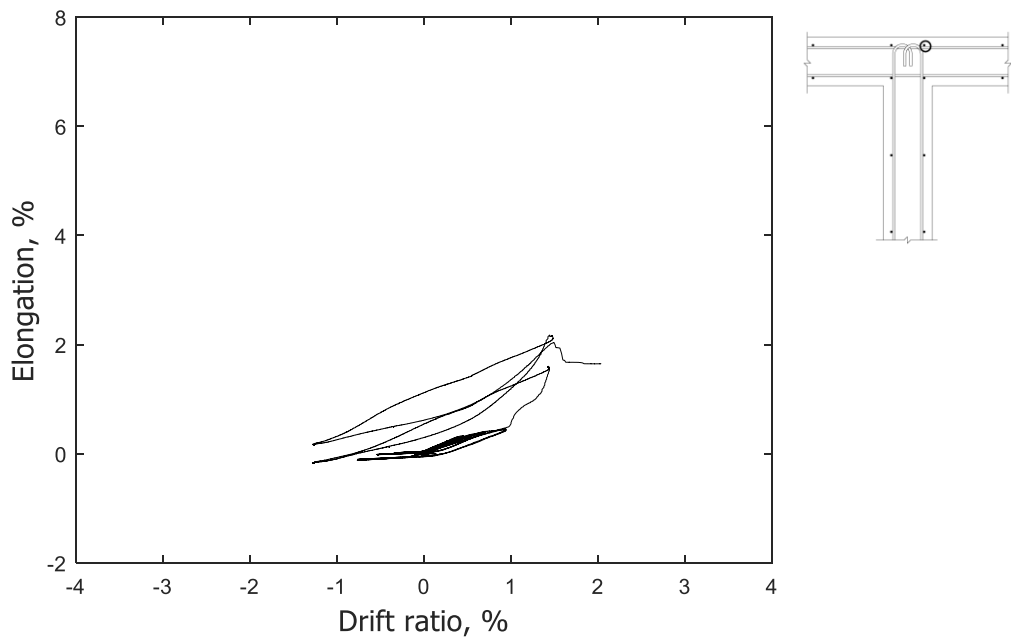


Figure 190 – Measured strain in longitudinal bar at unconfined flange 25 in. (635 mm) above base of T2

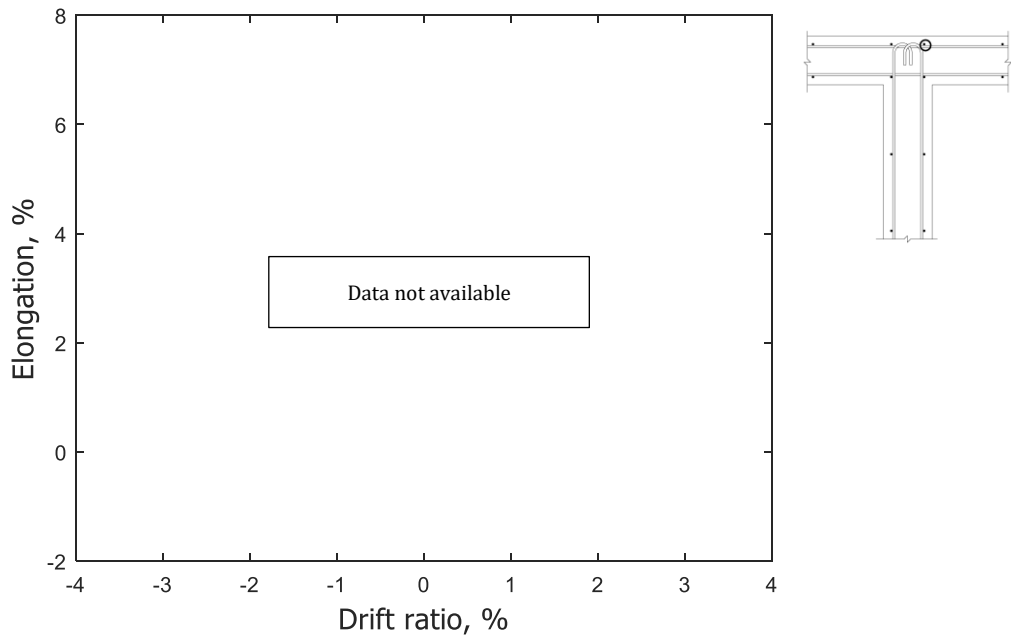


Figure 191 – Measured strain in longitudinal bar at unconfined flange 25 in. (635 mm) above base of T3

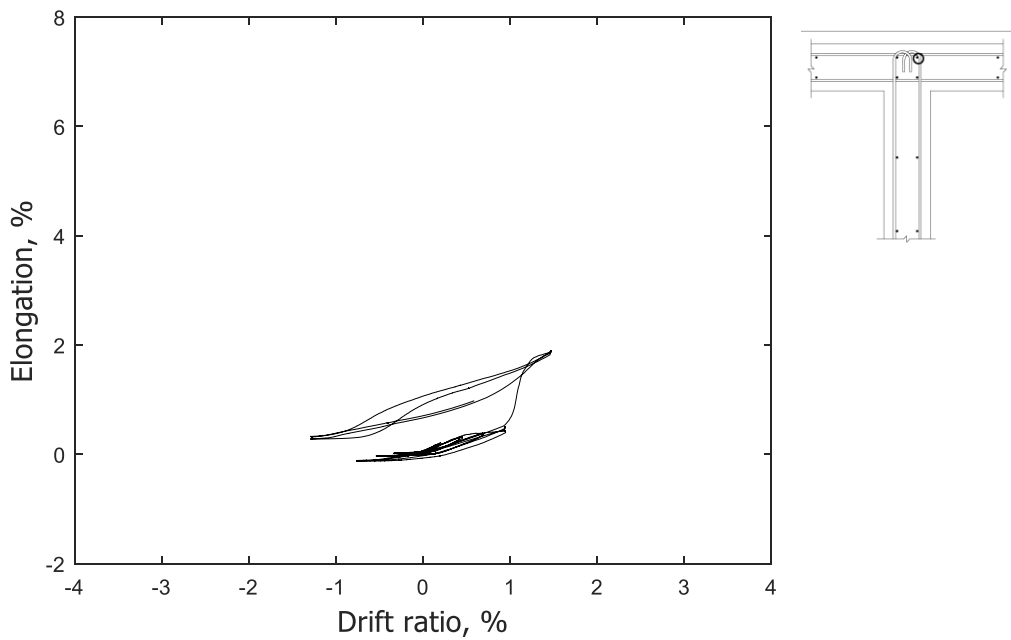


Figure 192 – Measured strain in longitudinal bar at unconfined flange 25 in. (635 mm) above base of T4

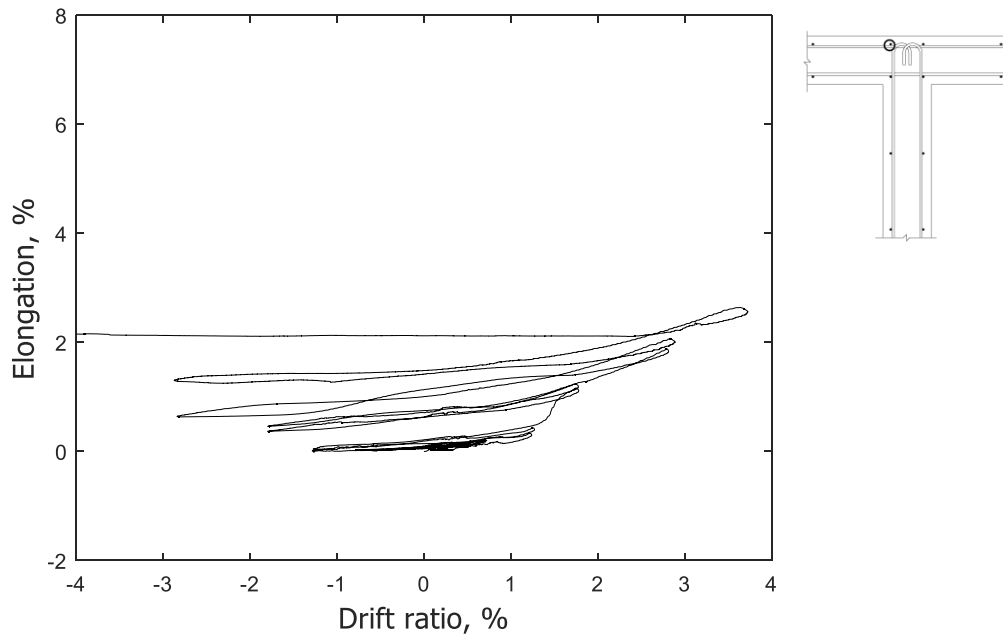


Figure 193 – Measured strain in longitudinal bar at unconfined flange 50 in. (1270 mm) above base of T1

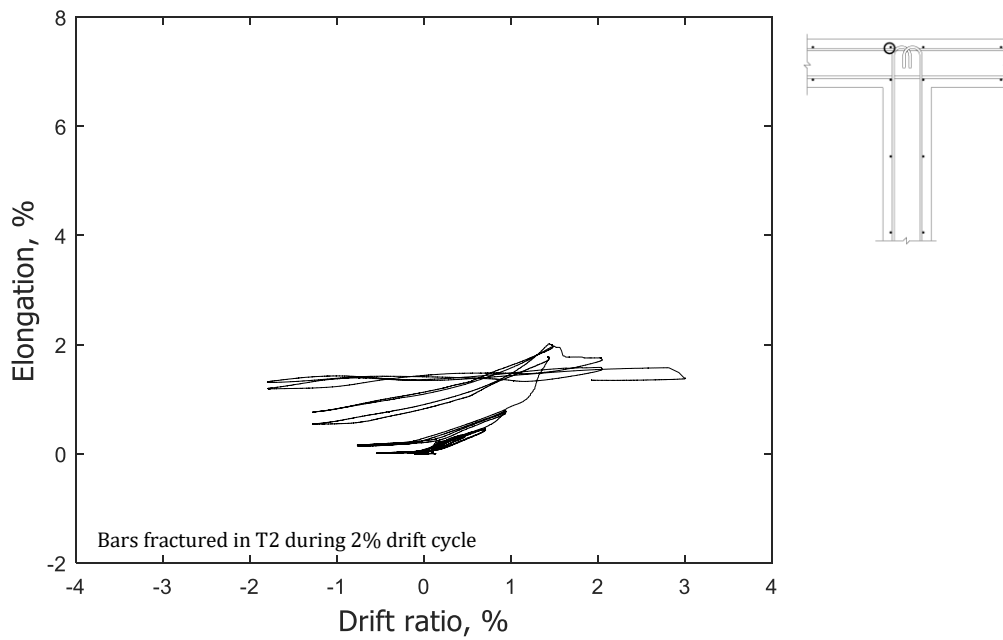


Figure 194 – Measured strain in longitudinal bar at unconfined flange 50 in. (1270 mm) above base of T2

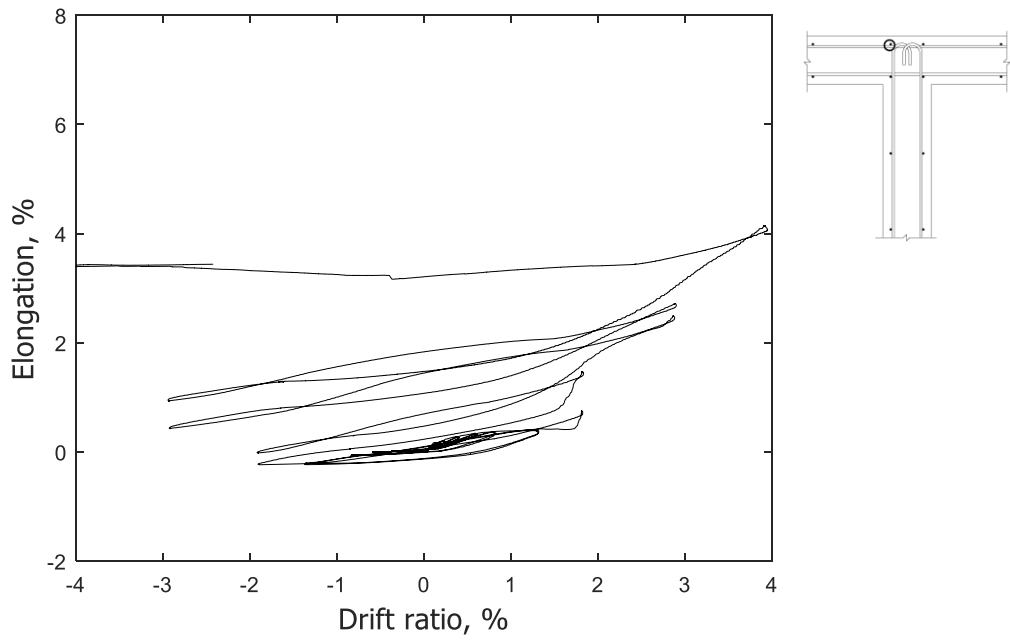


Figure 195 – Measured strain in longitudinal bar at unconfined flange 50 in. (1270 mm) above base of T3

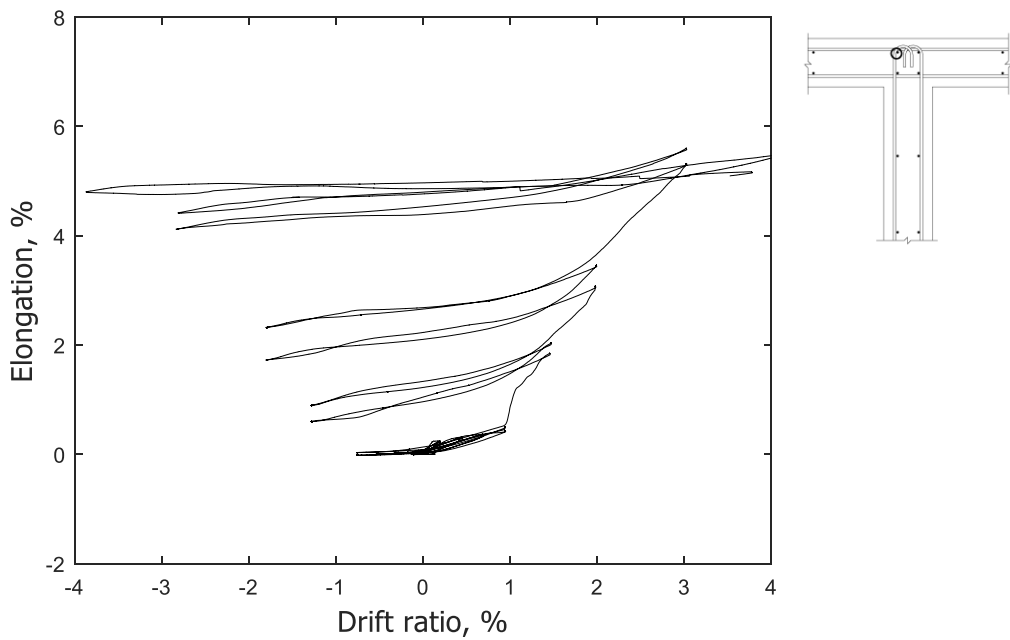


Figure 196 – Measured strain in longitudinal bar at unconfined flange 50 in. (1270 mm) above base of T4

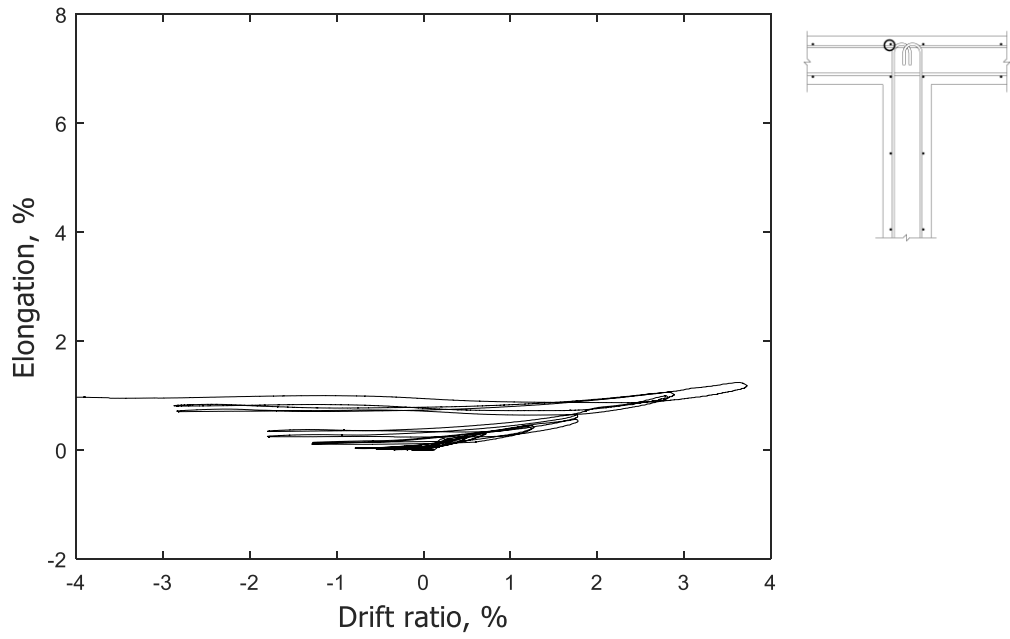


Figure 197 – Measured strain in longitudinal bar at unconfined flange 100 in. (2540 mm) above base of T1

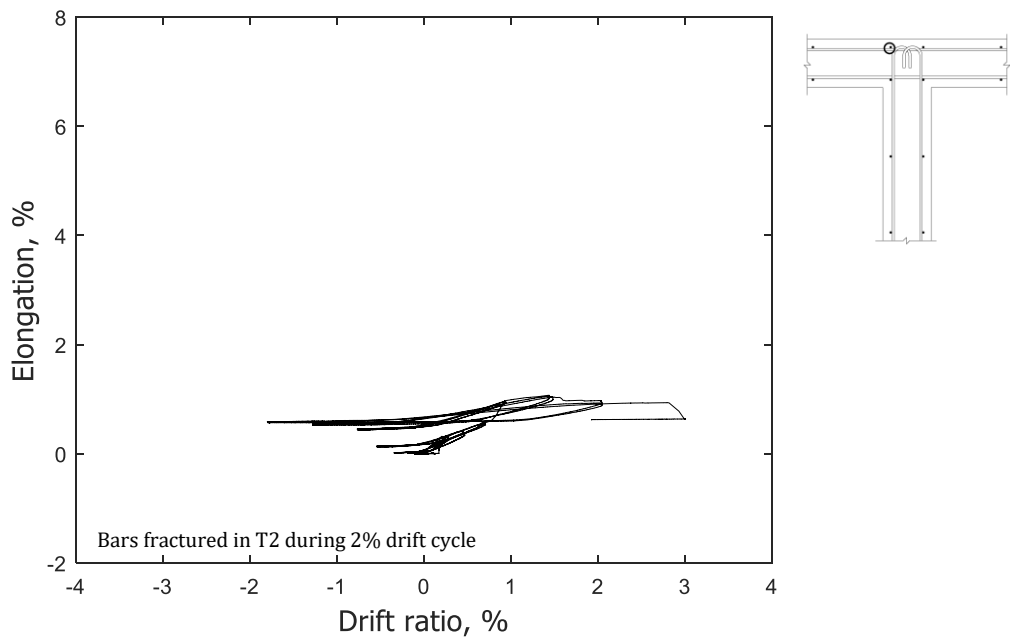


Figure 198 – Measured strain in longitudinal bar at unconfined flange 100 in. (2540 mm) above base of T2

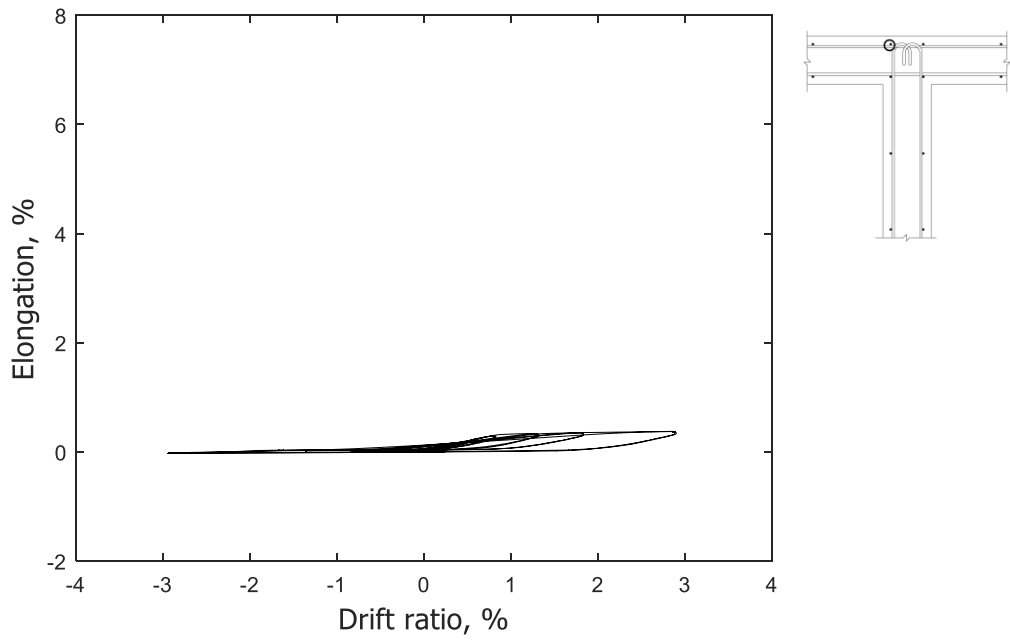


Figure 199 – Measured strain in longitudinal bar at unconfined flange 100 in. (2540 mm) above base of T3

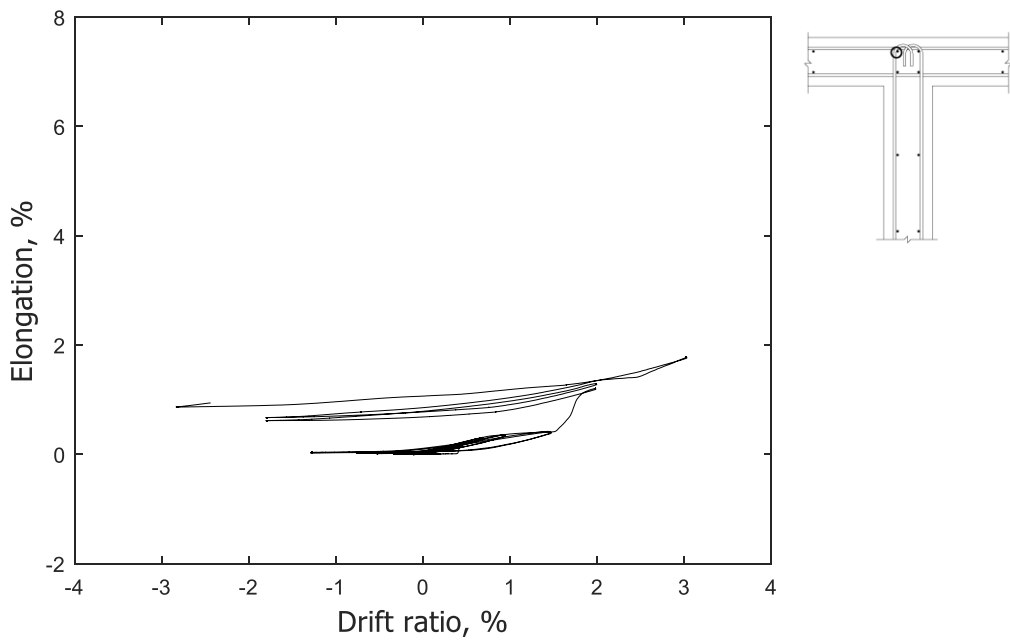


Figure 200 – Measured strain in longitudinal bar at unconfined flange 100 in. (2540 mm) above base of T4

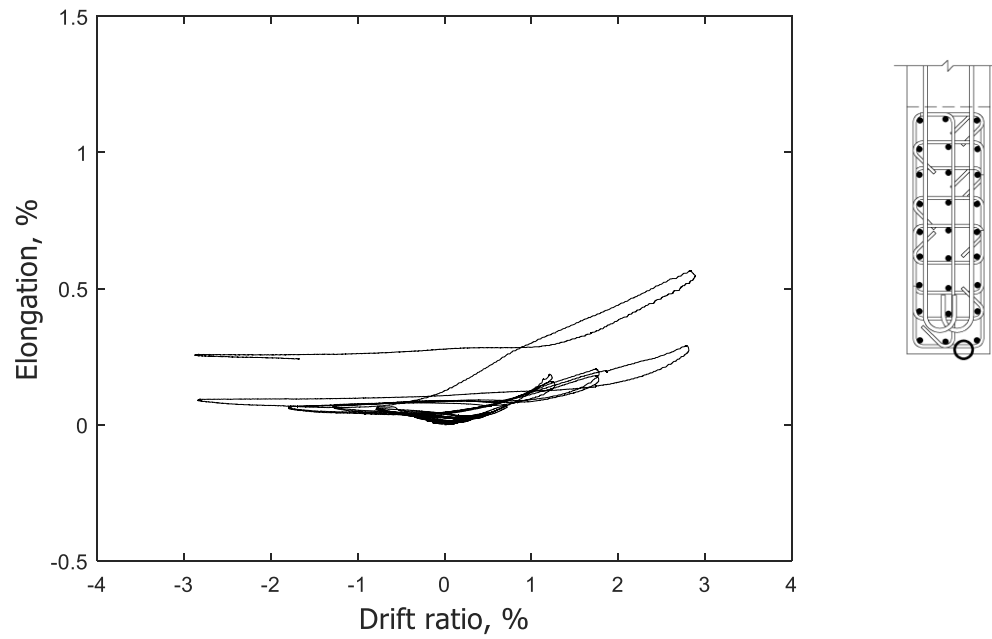


Figure 201 – Measured strain in hoop at confined stem 3 in. (76 mm) above base of T1

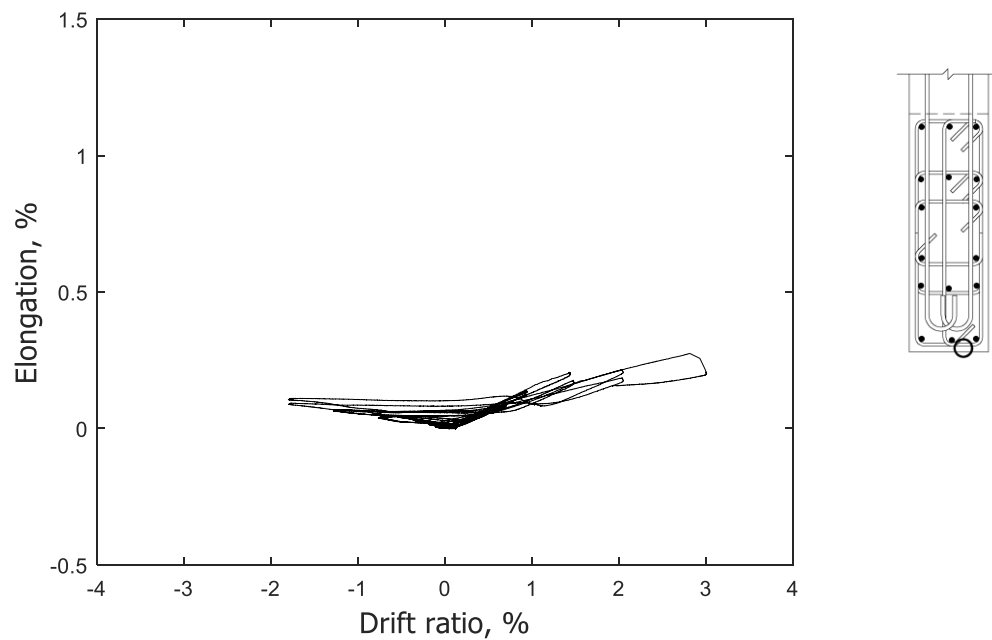


Figure 202 – Measured strain in hoop at confined stem 3 in. (76 mm) above base of T2

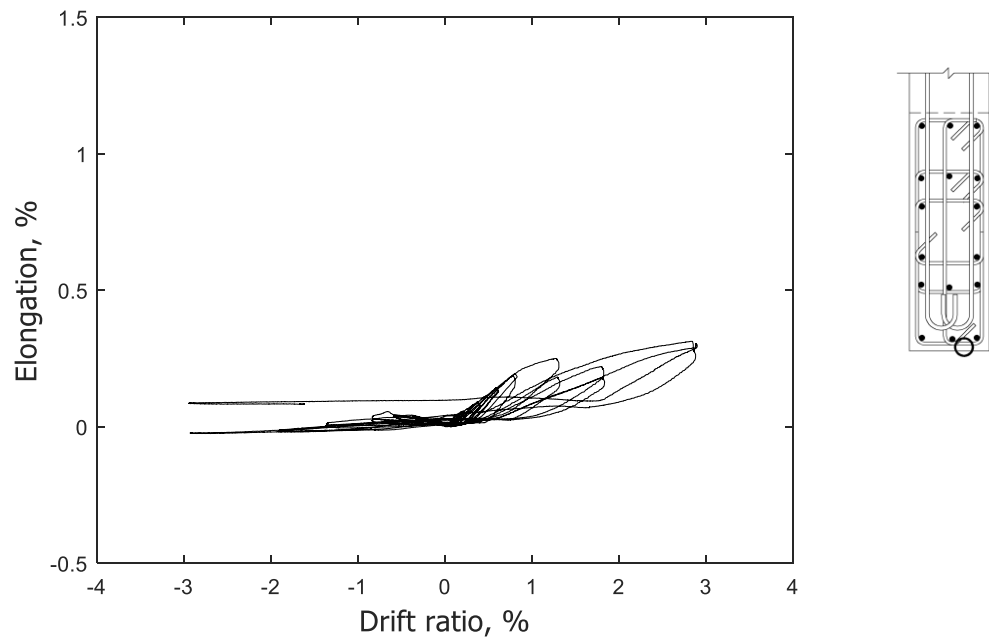


Figure 203 – Measured strain in hoop at confined stem 3 in. (76 mm) above base of T3

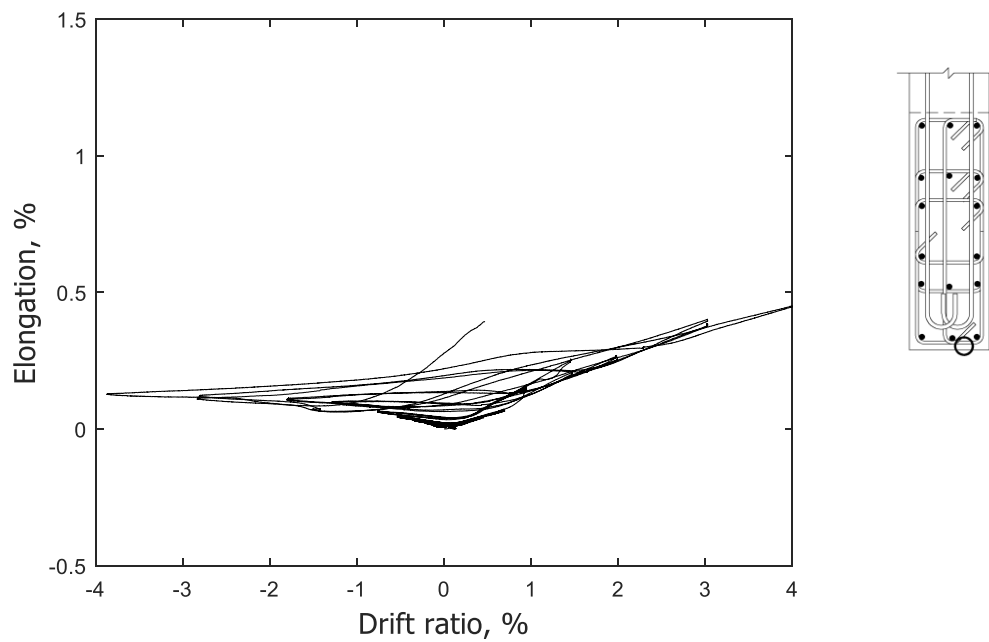


Figure 204 – Measured strain in hoop at confined stem 3 in. (76 mm) above base of T4

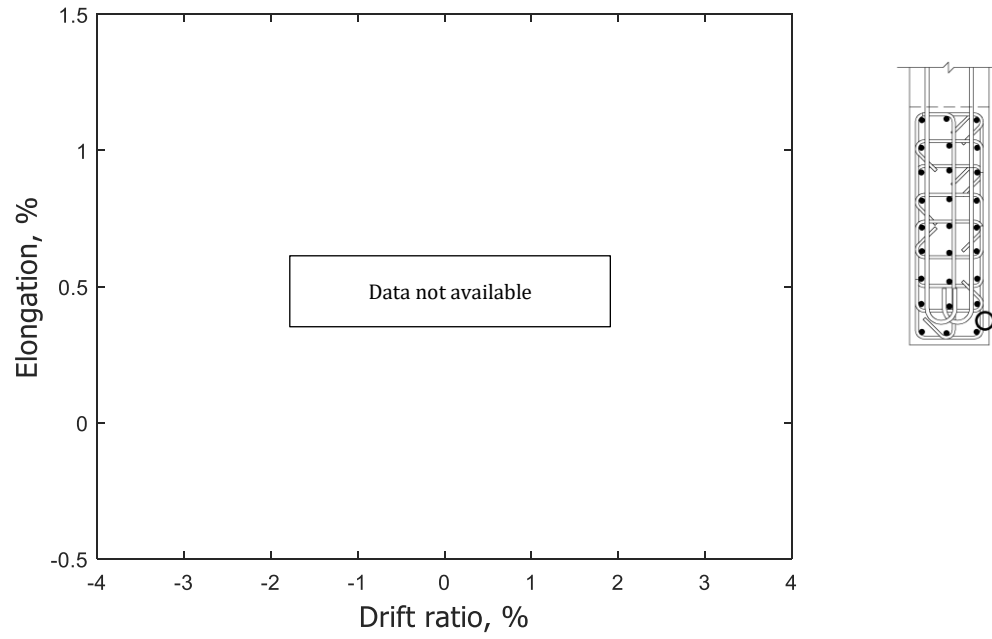


Figure 205 – Measured strain in hoop at confined stem 3 in. (76 mm) above base of T1

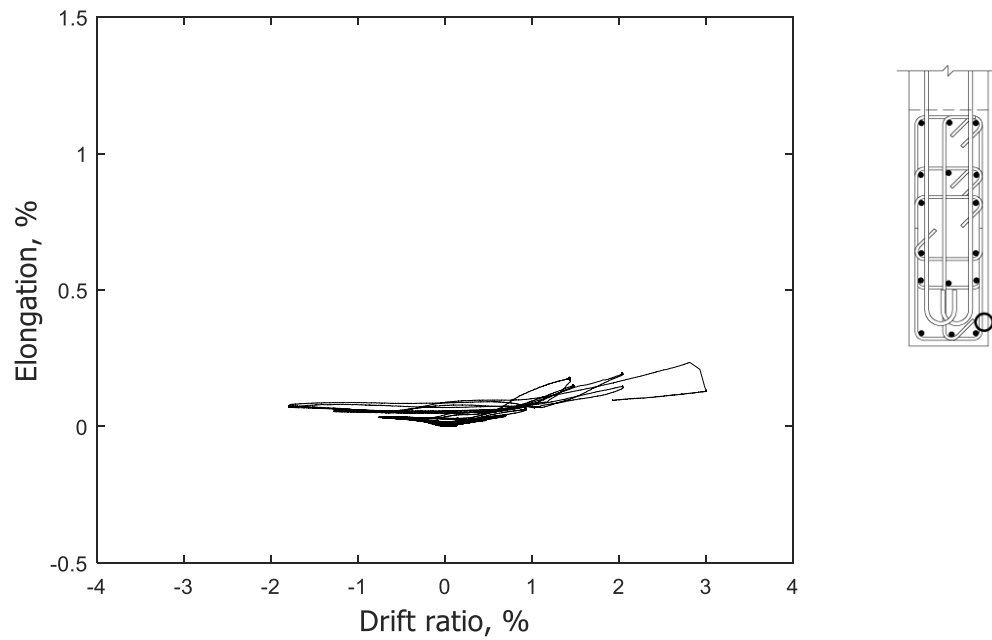


Figure 206 – Measured strain in hoop at confined stem 3 in. (76 mm) above base of T2

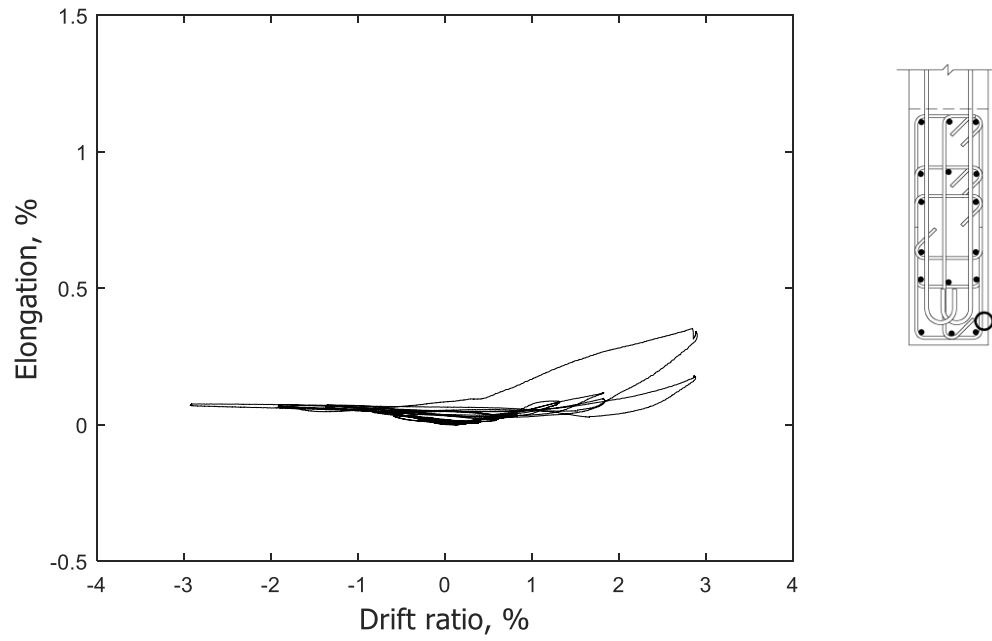


Figure 207 – Measured strain in hoop at confined stem 3 in. (76 mm) above base of T3

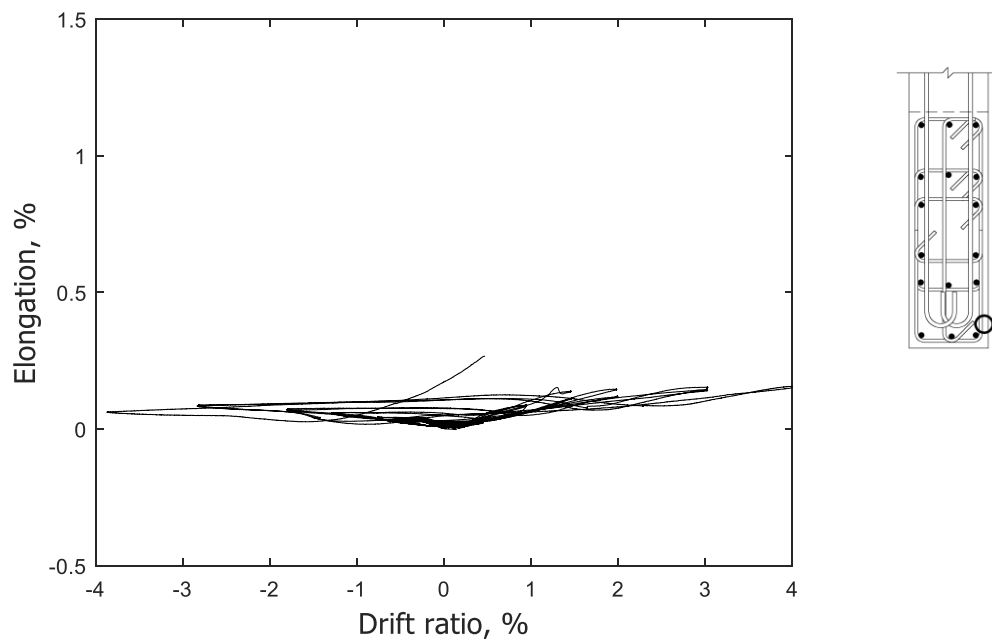


Figure 208 – Measured strain in hoop at confined stem 3 in. (76 mm) above base of T4

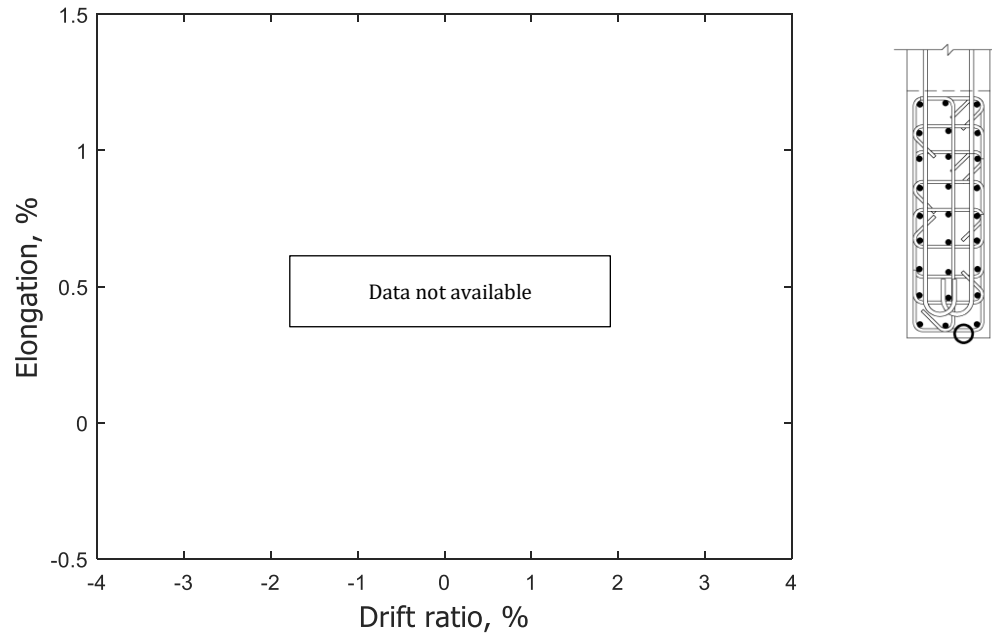


Figure 209 – Measured strain in hoop at confined stem 6 in. (152 mm) above base of T1

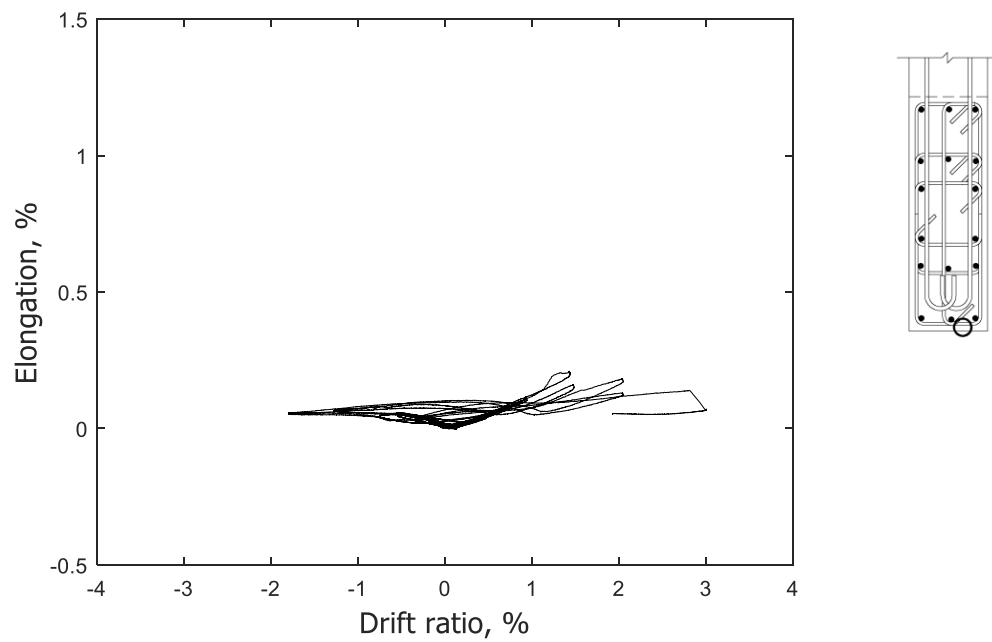


Figure 210 – Measured strain in hoop at confined stem 6 in. (152 mm) above base of T2

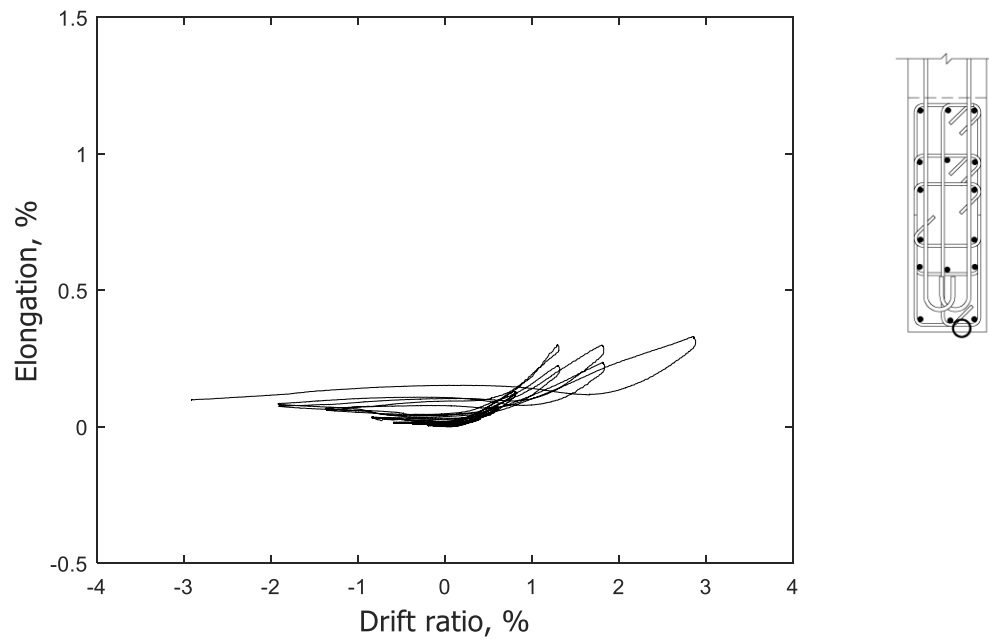


Figure 211 – Measured strain in hoop at confined stem 6 in. (152 mm) above base of T3

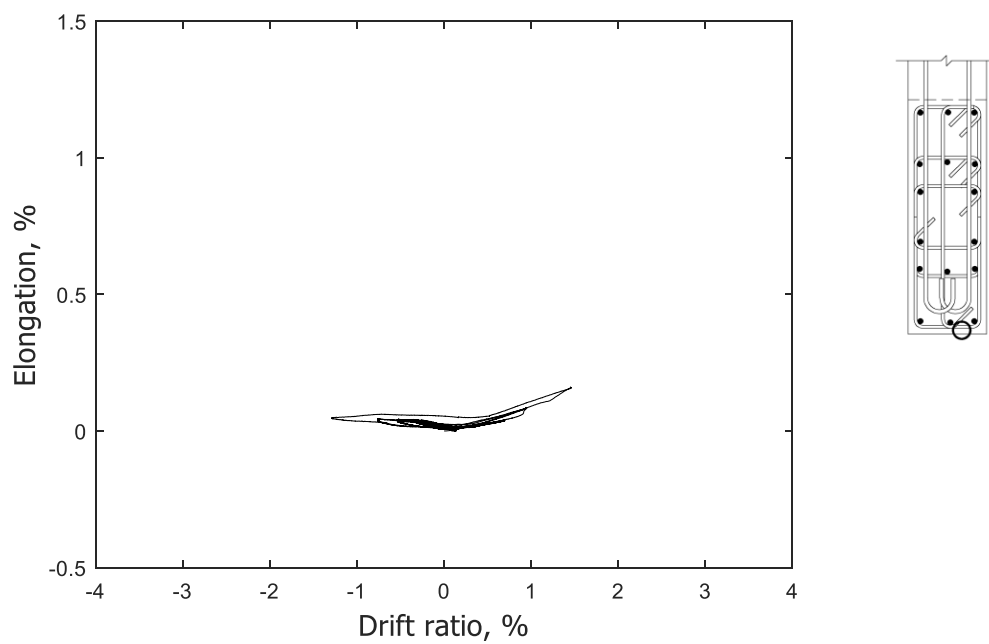


Figure 212 – Measured strain in hoop at confined stem 6 in. (152 mm) above base of T4

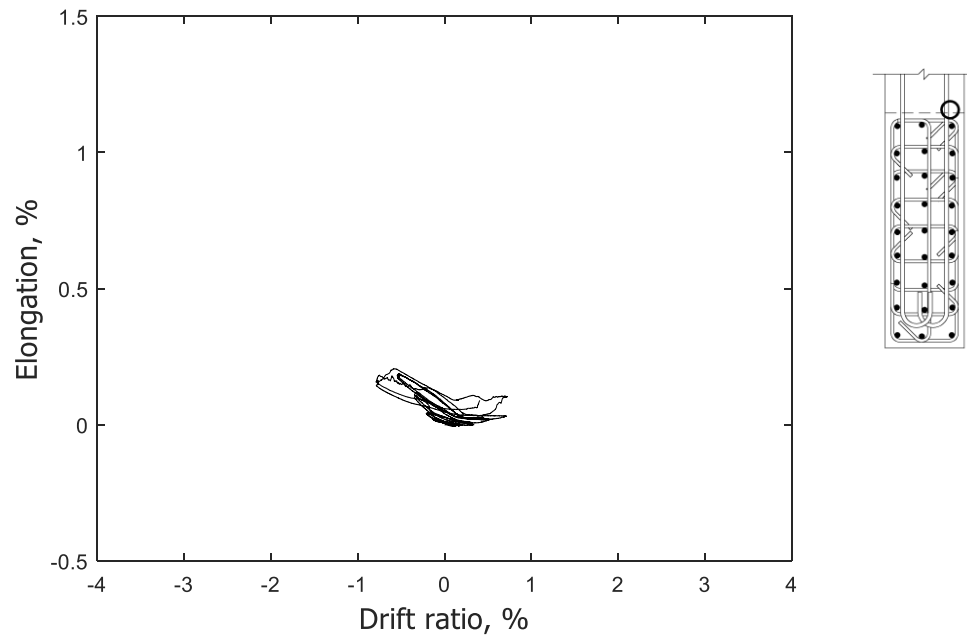


Figure 213 – Measured strain in horizontal bar at unconfined stem 22.5 in. (572 mm) above base of T1

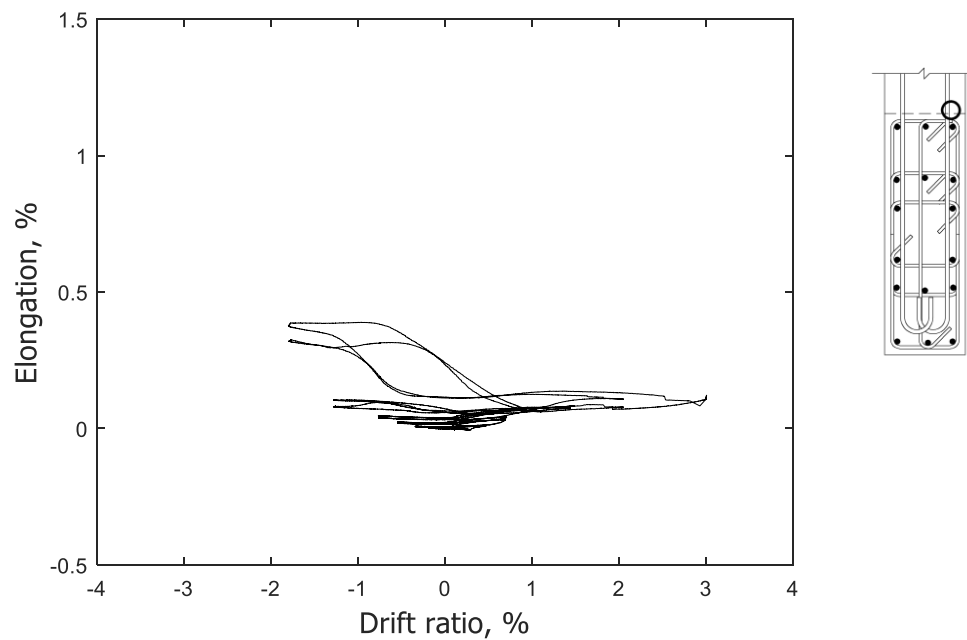


Figure 214 – Measured strain in horizontal bar at unconfined stem 22.5 in. (572 mm) above base of T2

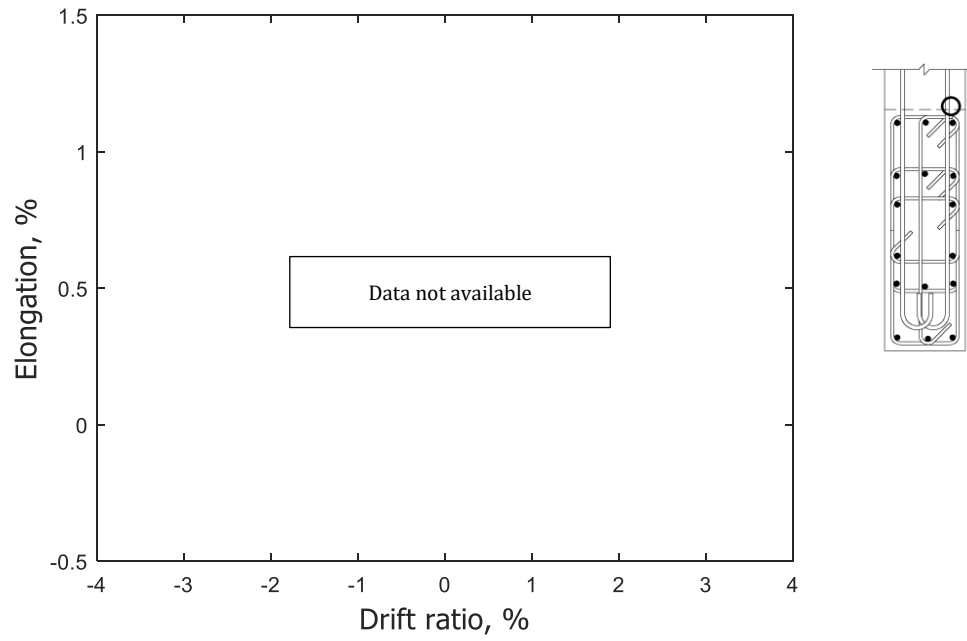


Figure 215 – Measured strain in horizontal bar at unconfined stem 22.5 in. (572 mm) above base of T3

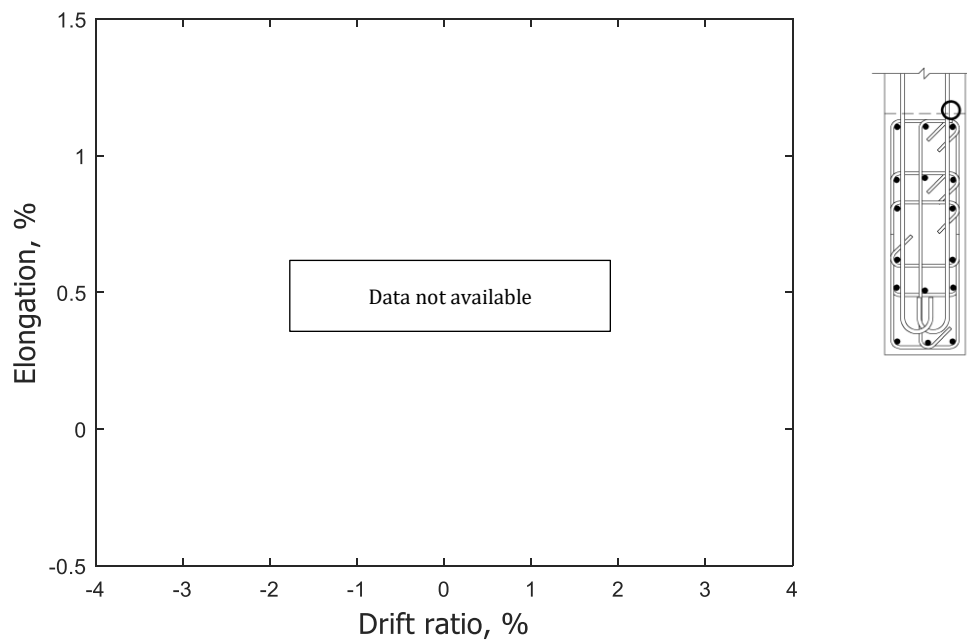


Figure 216 – Measured strain in horizontal bar at unconfined stem 22.5 in. (572 mm) above base of T4

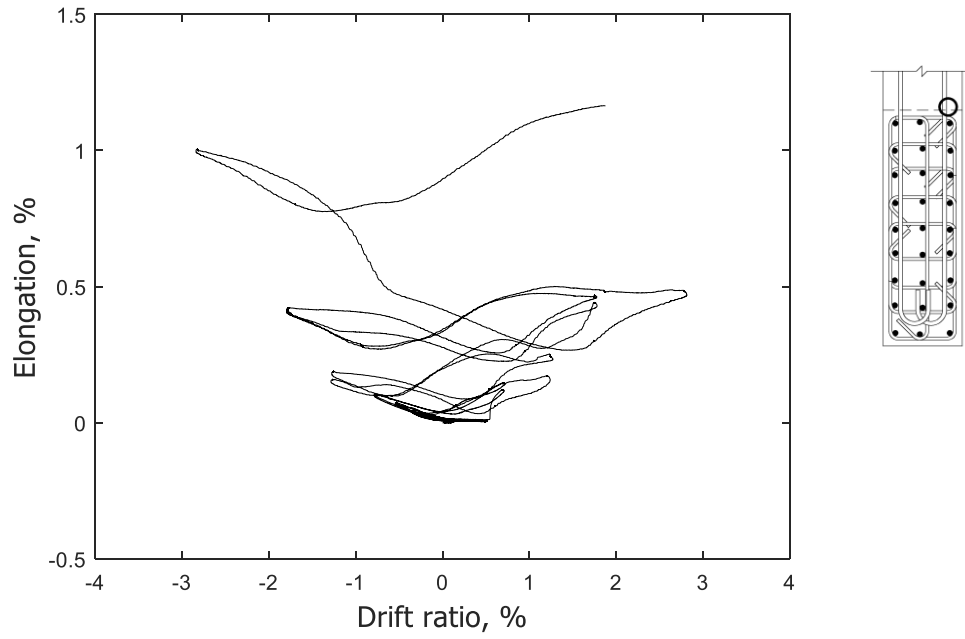


Figure 217 – Measured strain in horizontal bar at unconfined stem 52.5 in. (1330 mm) above base of T1

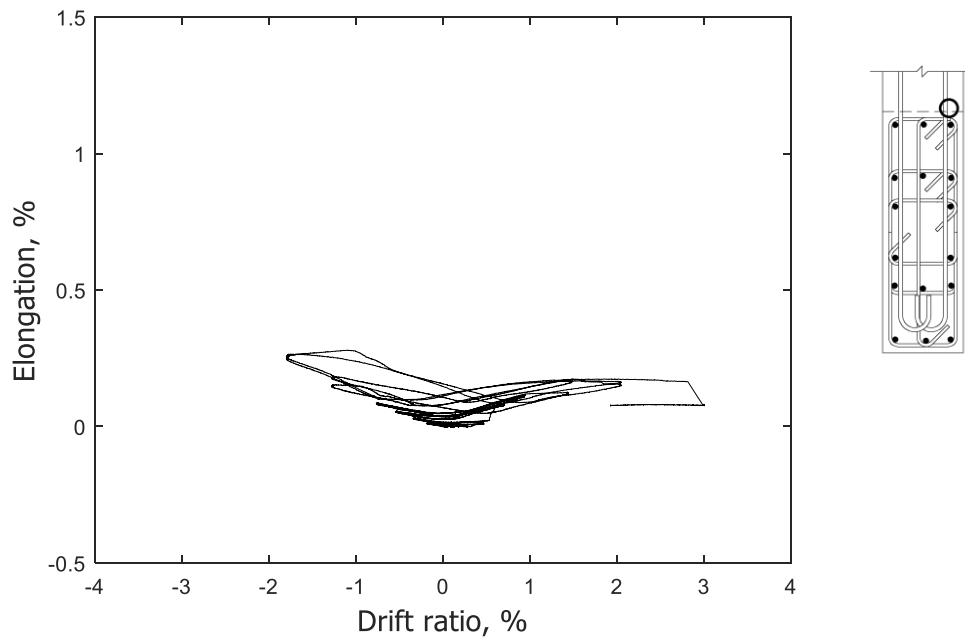


Figure 218 – Measured strain in horizontal bar at unconfined stem 52.5 in. (1330 mm) above base of T2

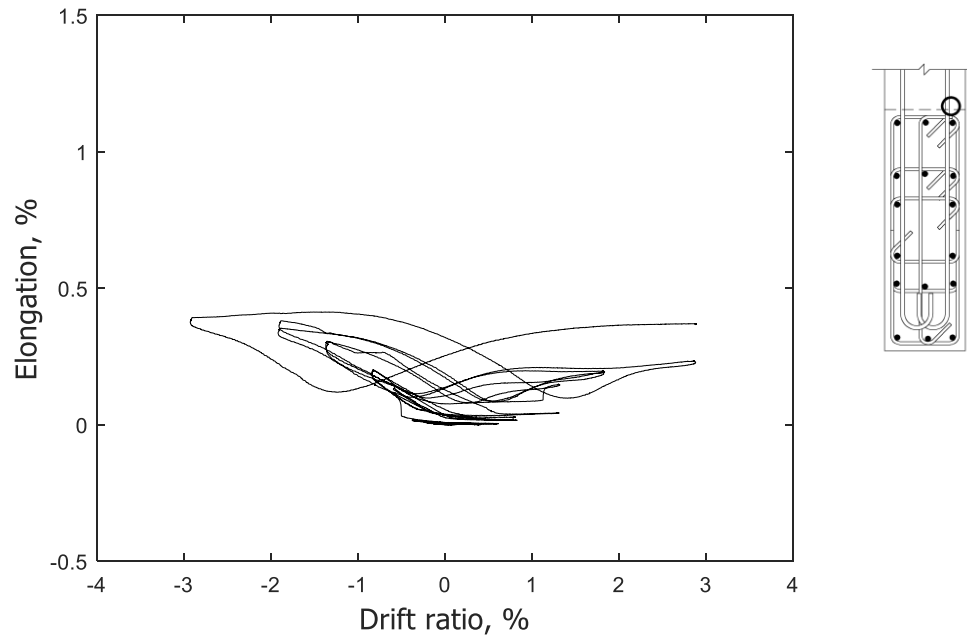


Figure 219 – Measured strain in horizontal bar at unconfined stem 52.5 in. (1330 mm) above base of T3

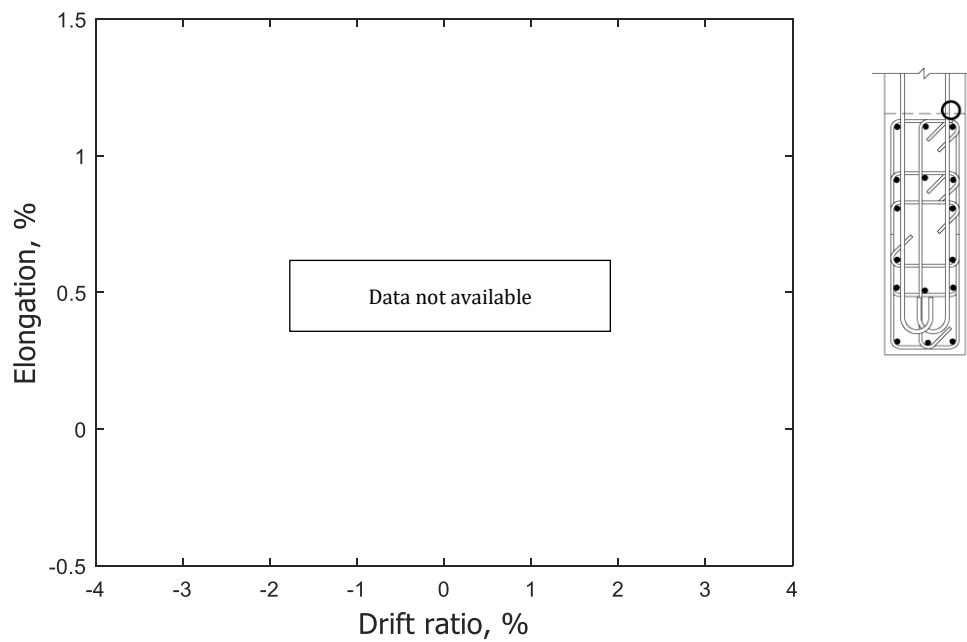
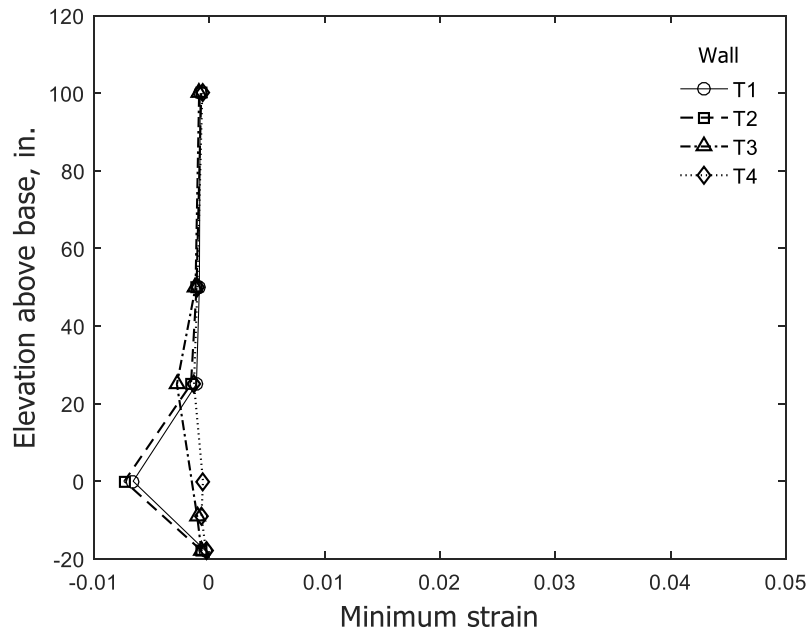
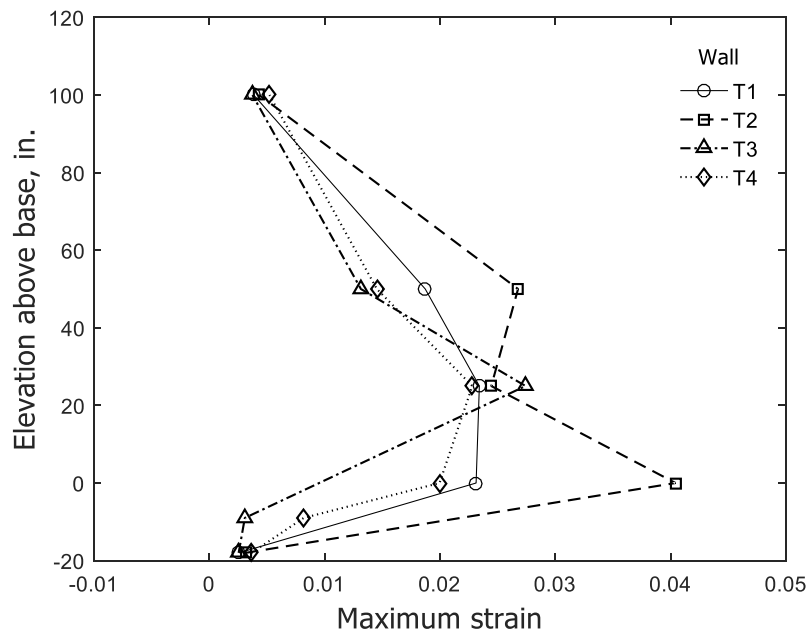


Figure 220 – Measured strain in horizontal bar at unconfined stem 52.5 in. (1330 mm) above base of T4

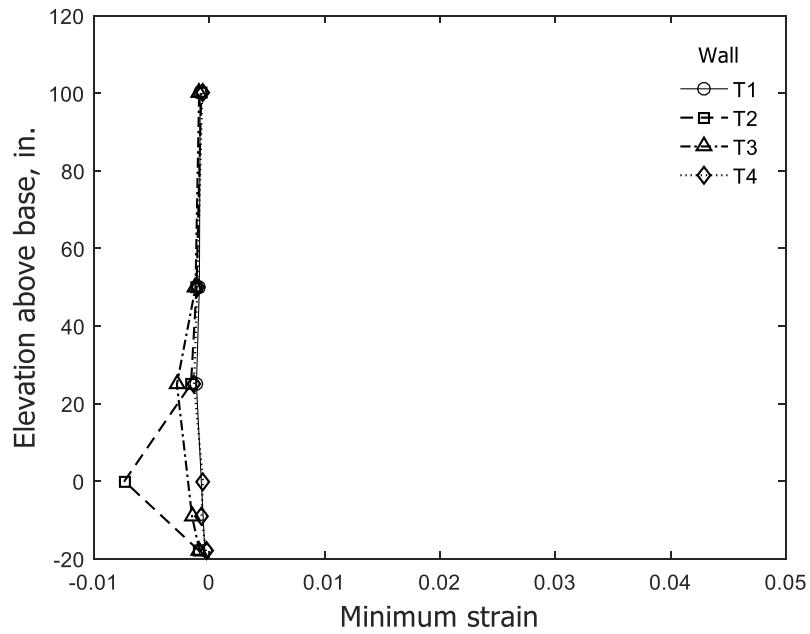


(a) Stem in compression

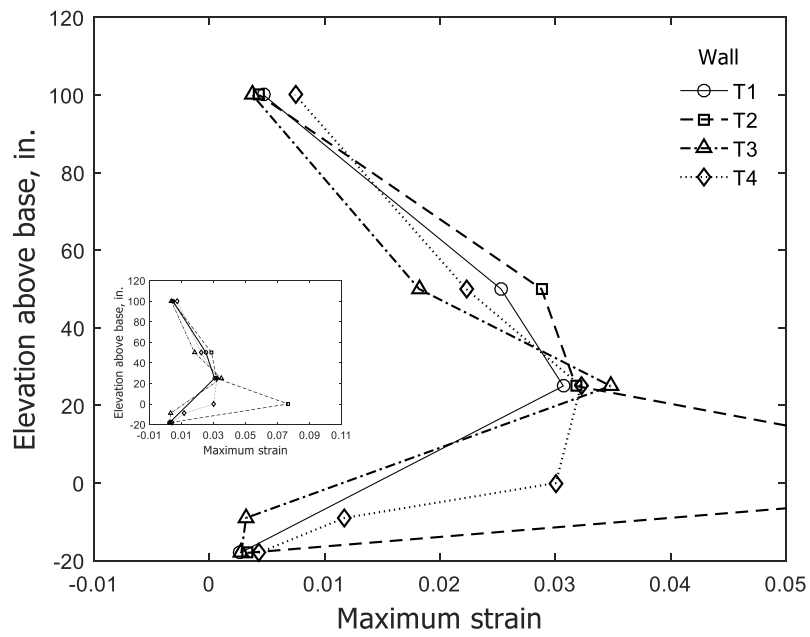


(b) Stem in tension

Figure 221 – Envelope of measured strain in longitudinal bars at confined stem for 1.5% drift ratio (1 in. = 25.4 mm)

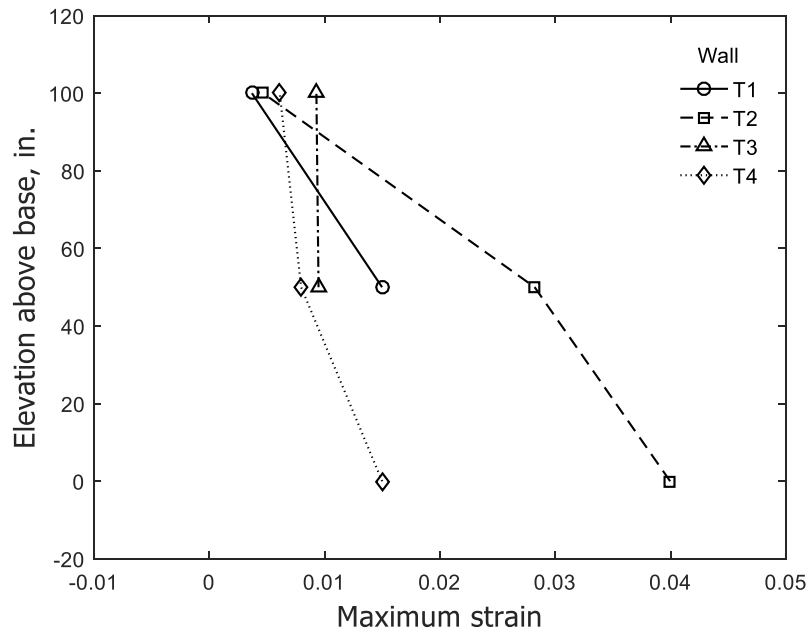


(a) Stem in compression

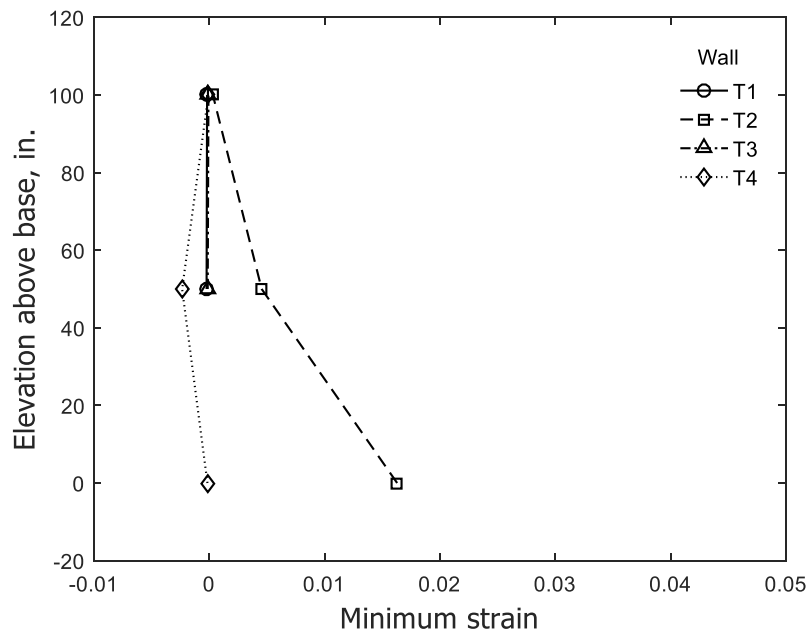


(b) Stem in tension

Figure 222 – Envelope of measured strain in longitudinal bars at confined stem for 2% drift ratio (1 in. = 25.4 mm)

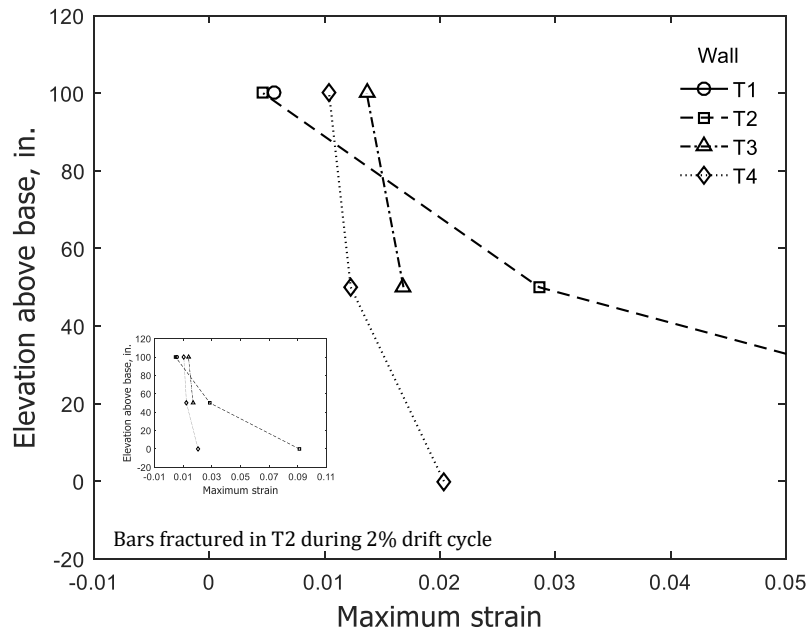


(a) Stem in compression

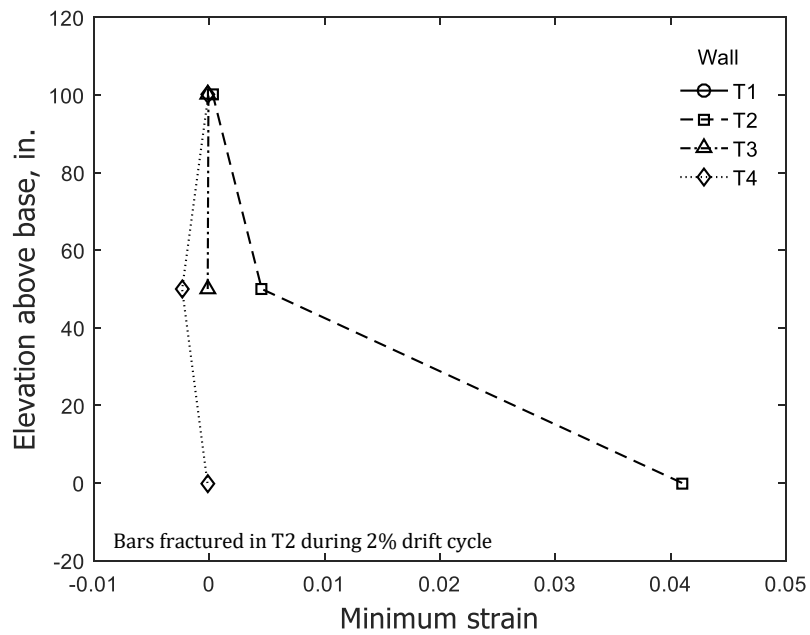


(b) Stem in tension

Figure 223 – Envelope of measured strain in longitudinal bars at confined flange for 1.5% drift ratio (1 in. = 25.4 mm)

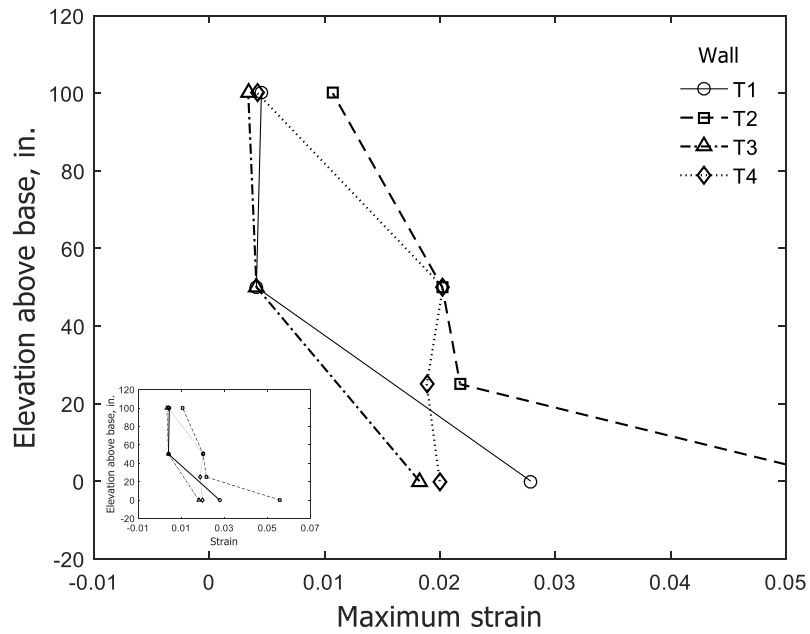


(a) Stem in compression

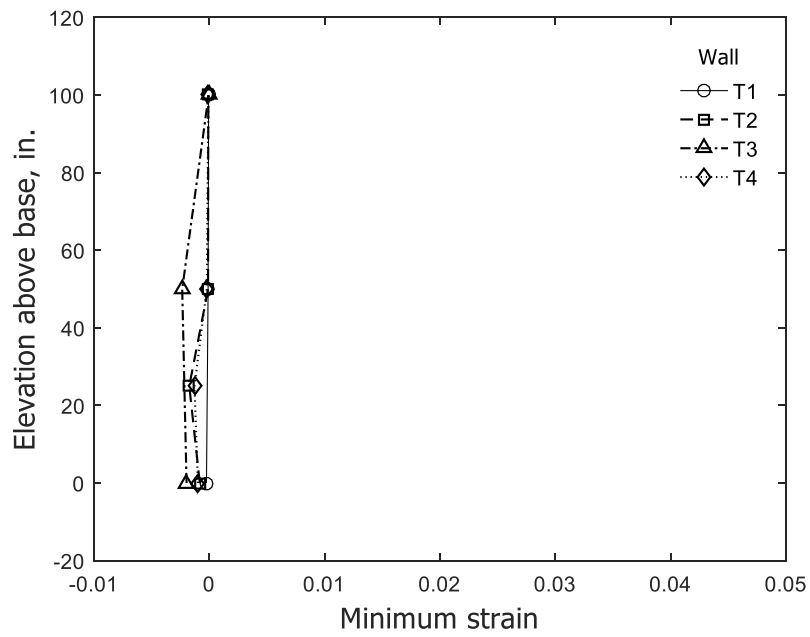


(b) Stem in tension

Figure 224 – Envelope of measured strain in longitudinal bars at confined flange for 2% drift ratio (1 in. = 25.4 mm)

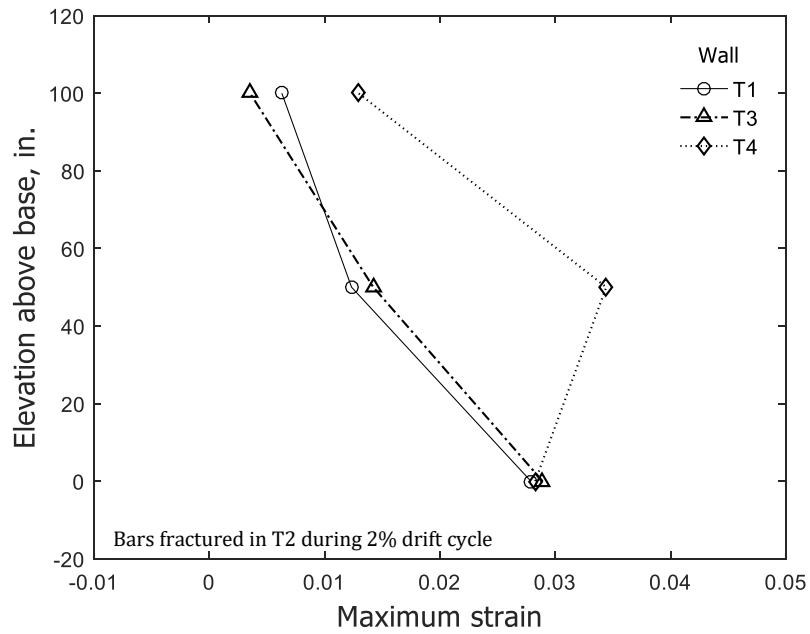


(a) Stem in compression

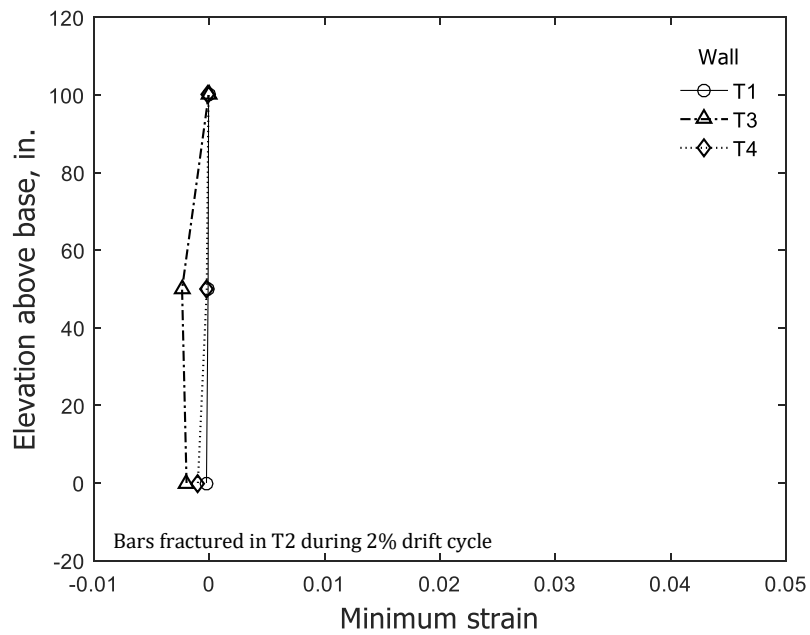


(b) Stem in tension

Figure 225 – Envelope of measured strain in longitudinal bars at unconfined flange for 1.5% drift ratio (1 in. = 25.4 mm)

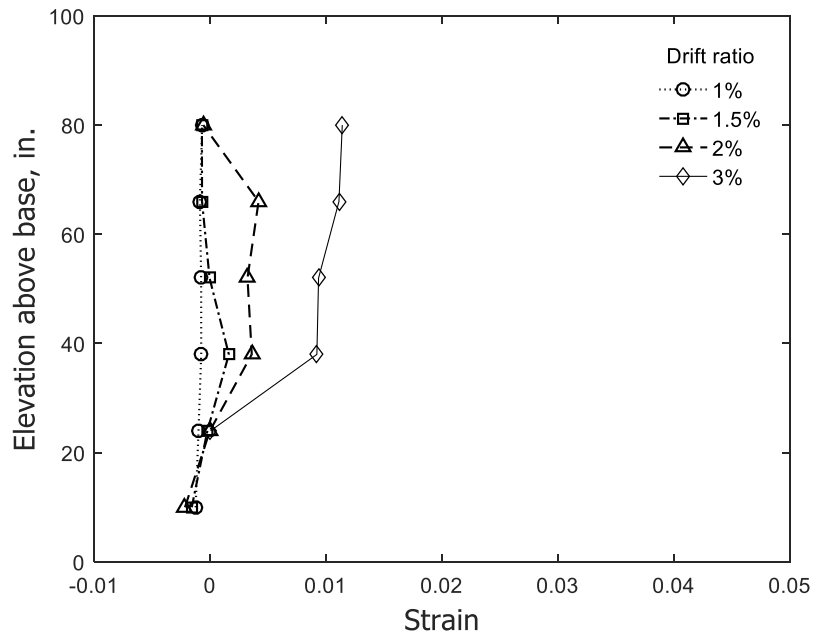


(a) Stem in compression

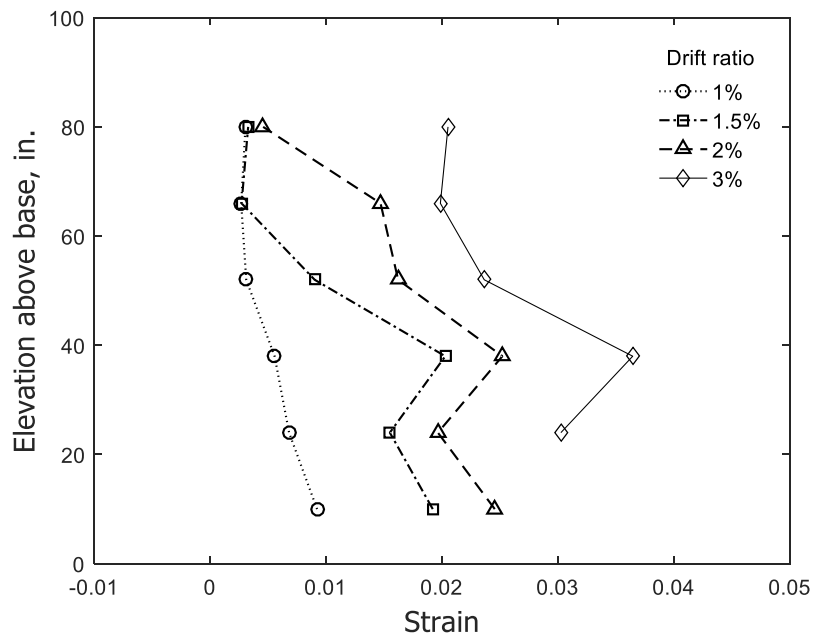


(b) Stem in tension

Figure 226 – Envelope of measured strain in longitudinal bars at unconfined flange for 2% drift ratio (1 in. = 25.4 mm)

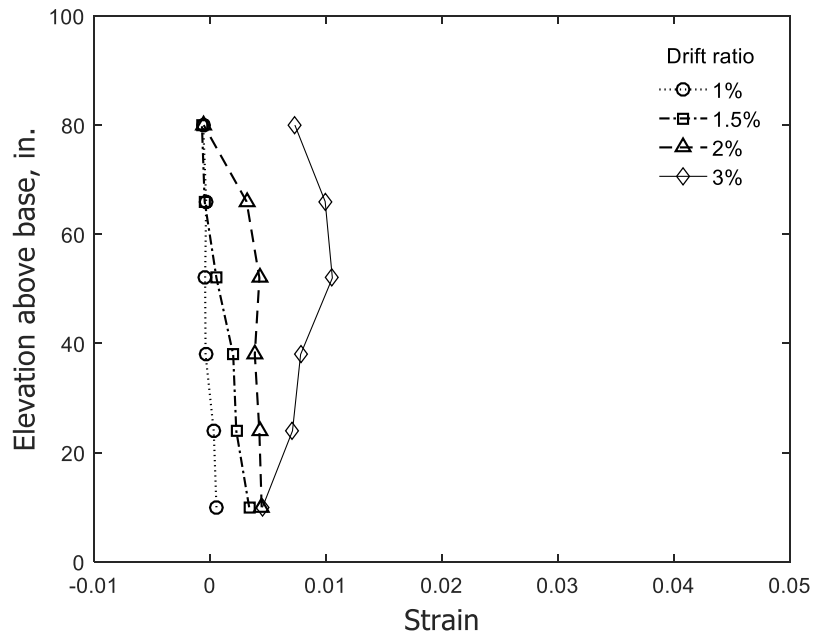


(a) Stem in compression

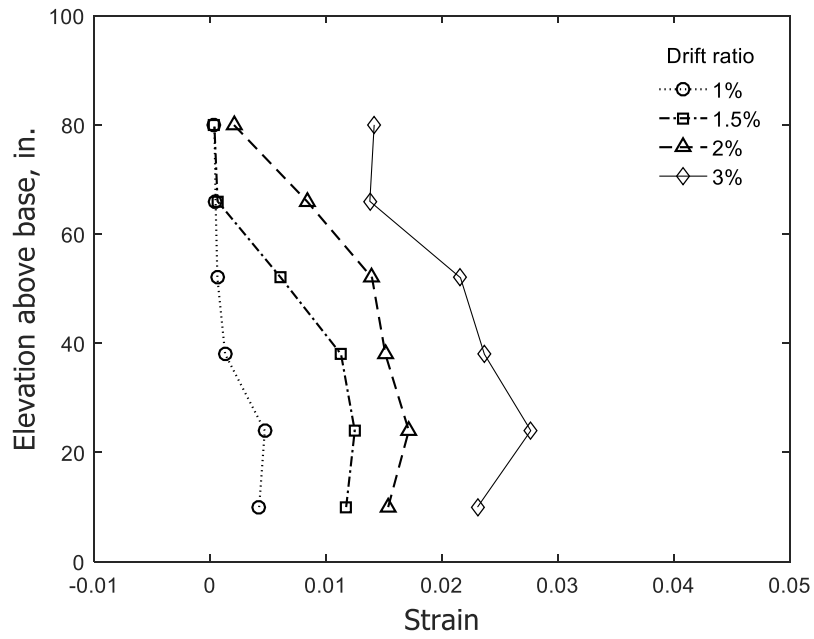


(b) Stem in tension

Figure 227 – Calculated concrete strain along Column 1 for stem of T1 (1 in. = 25.4 mm)

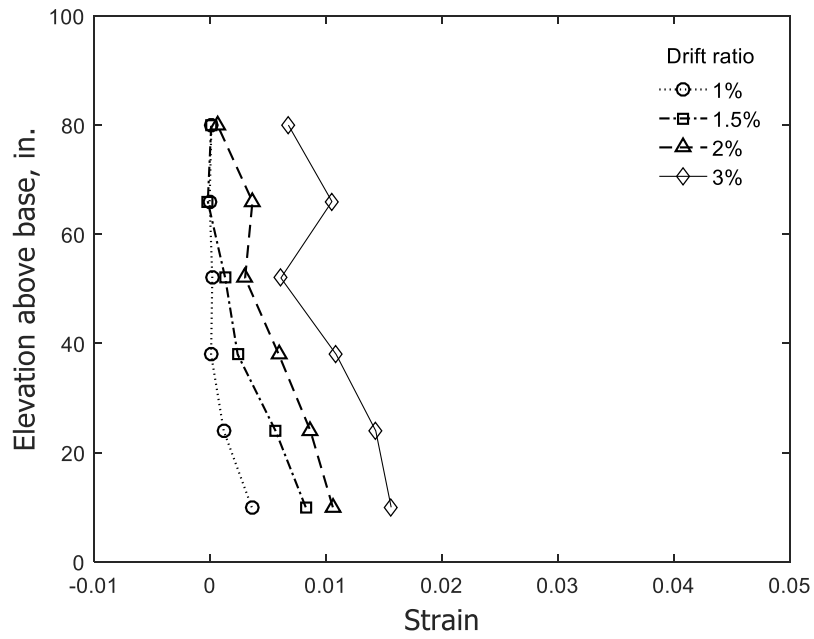


(a) Stem in compression

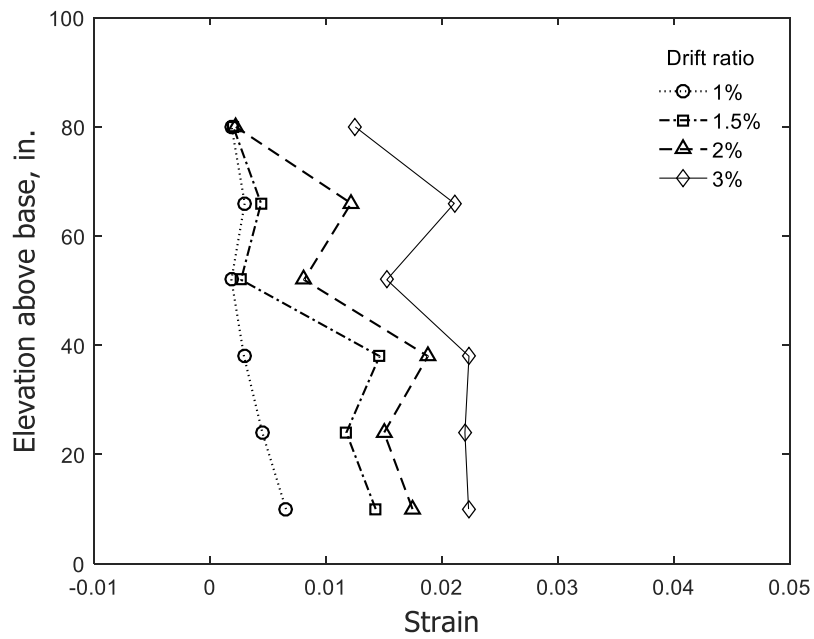


(b) Stem in tension

Figure 228 – Calculated concrete strain along Column 2 for stem of T1 (1 in. = 25.4 mm)

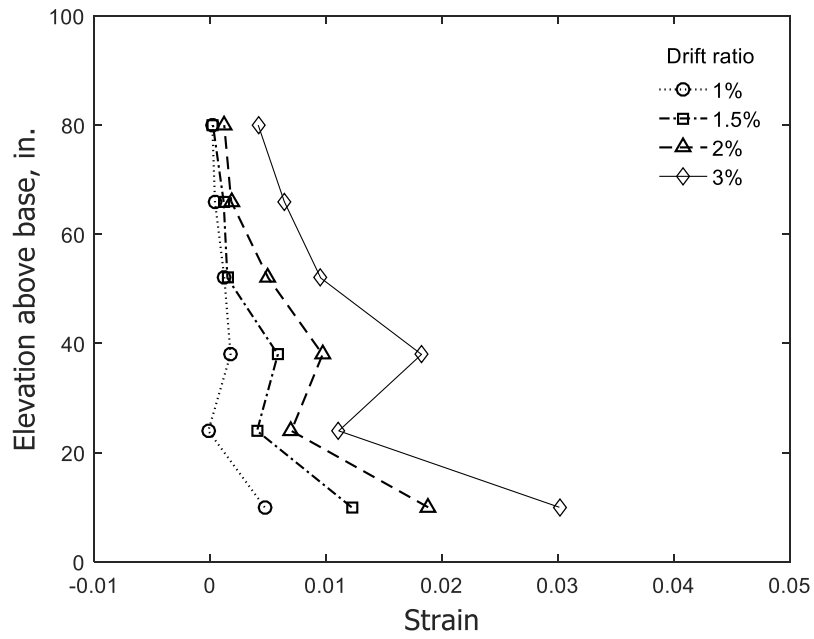


(a) Stem in compression

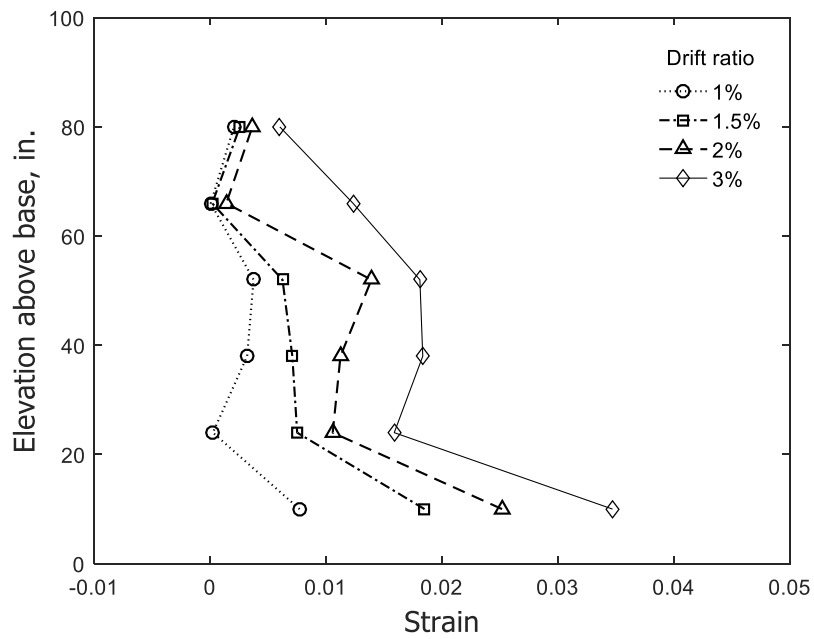


(b) Stem in tension

Figure 229 – Calculated concrete strain along Column 3 for stem of T1 (1 in. = 25.4 mm)

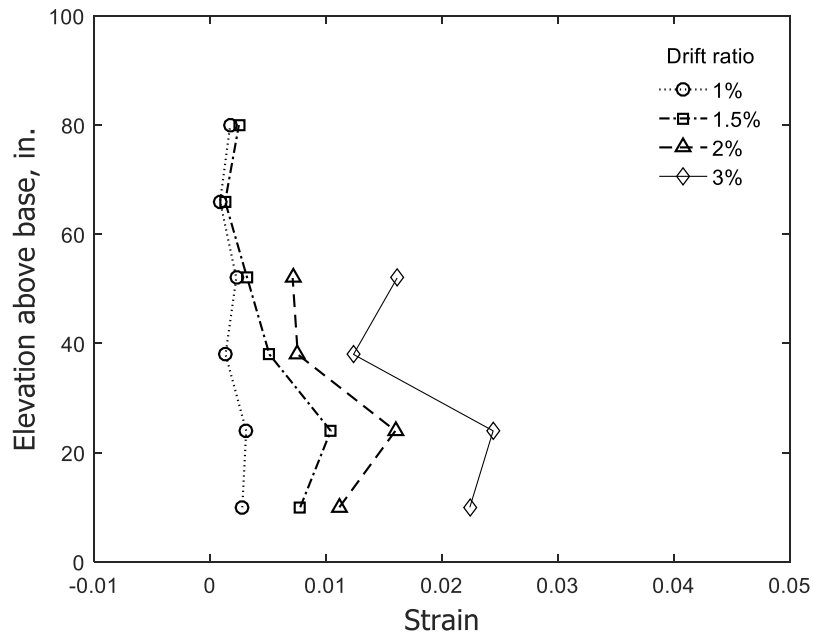


(a) Stem in compression

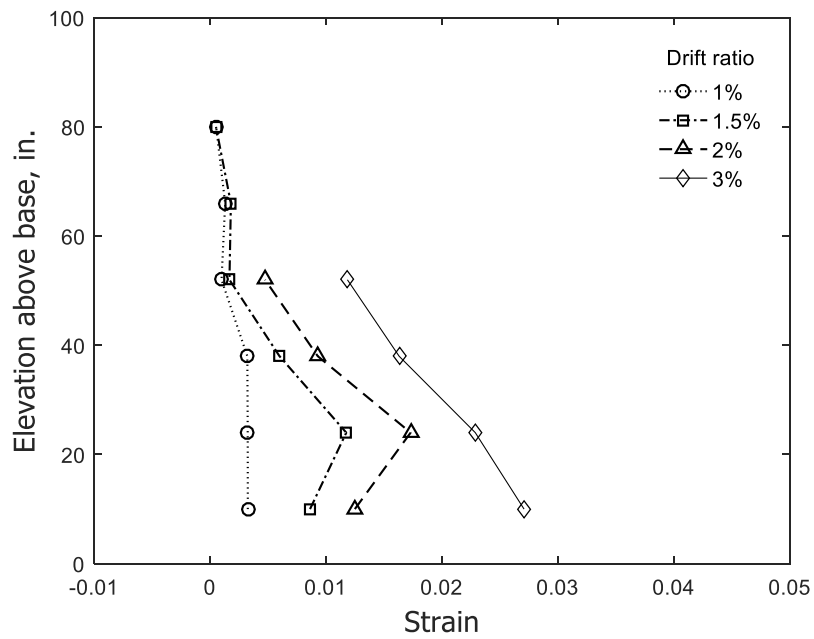


(b) Stem in tension

Figure 230 – Calculated concrete strain along Column 4 for stem of T1 (1 in. = 25.4 mm)

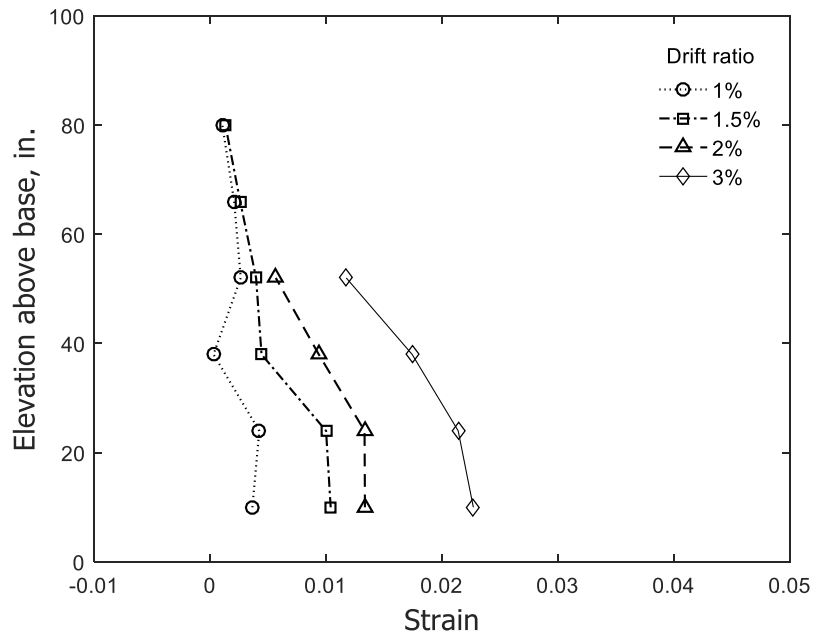


(a) Stem in compression

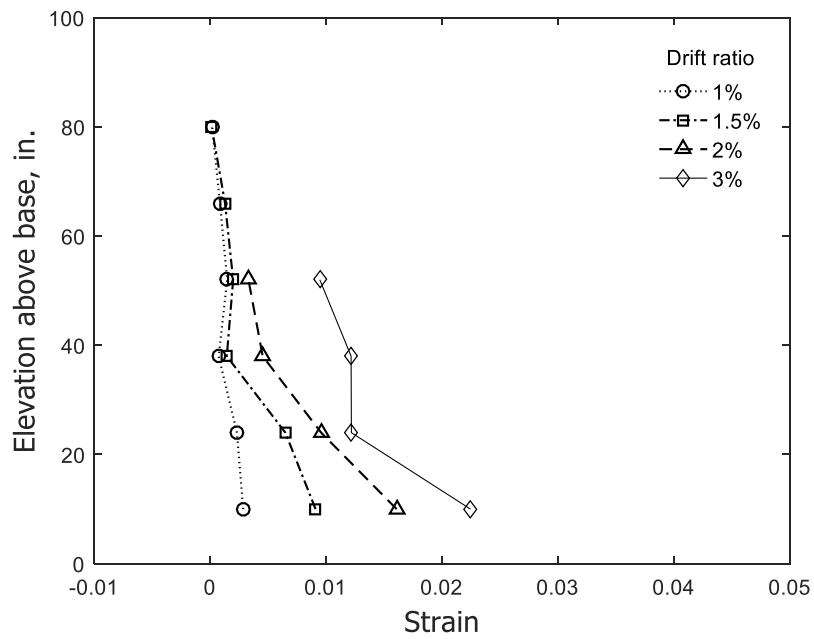


(b) Stem in tension

Figure 231 – Calculated concrete strain along Column 5 for stem of T1 (1 in. = 25.4 mm)

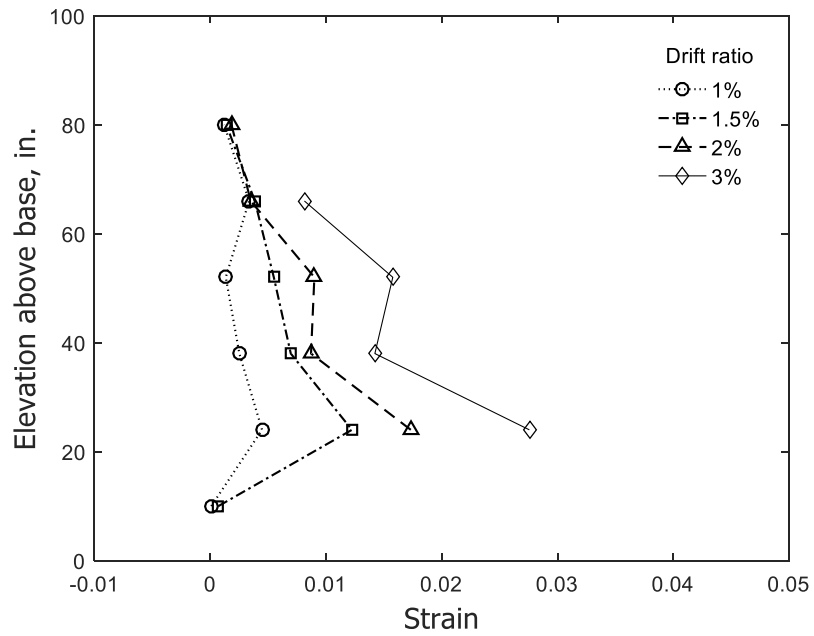


(a) Stem in compression

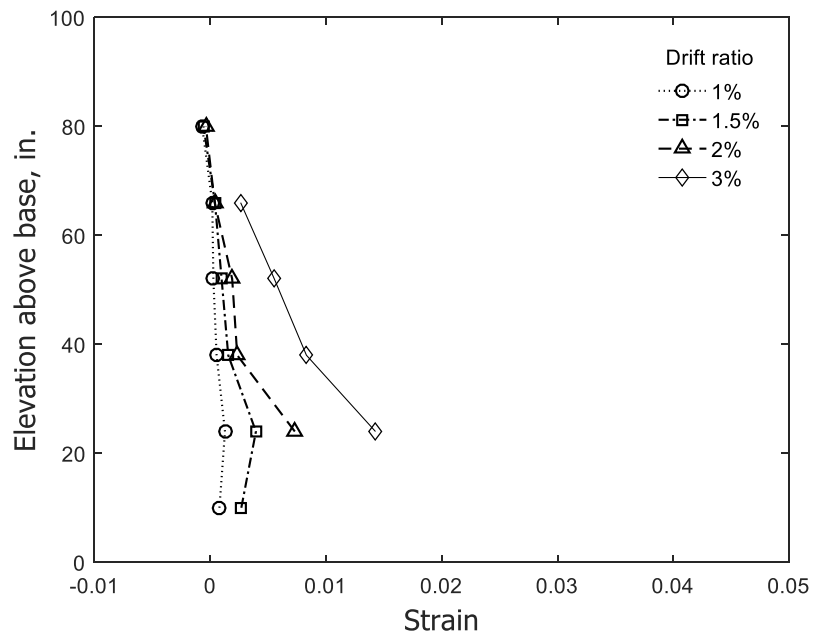


(b) Stem in tension

Figure 232 – Calculated concrete strain along Column 6 for stem of T1 (1 in. = 25.4 mm)

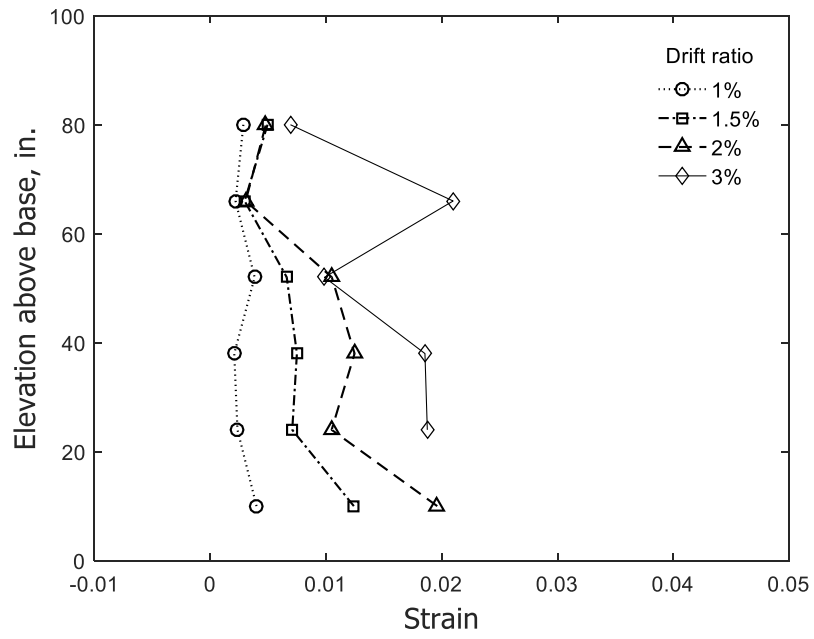


(a) Stem in compression

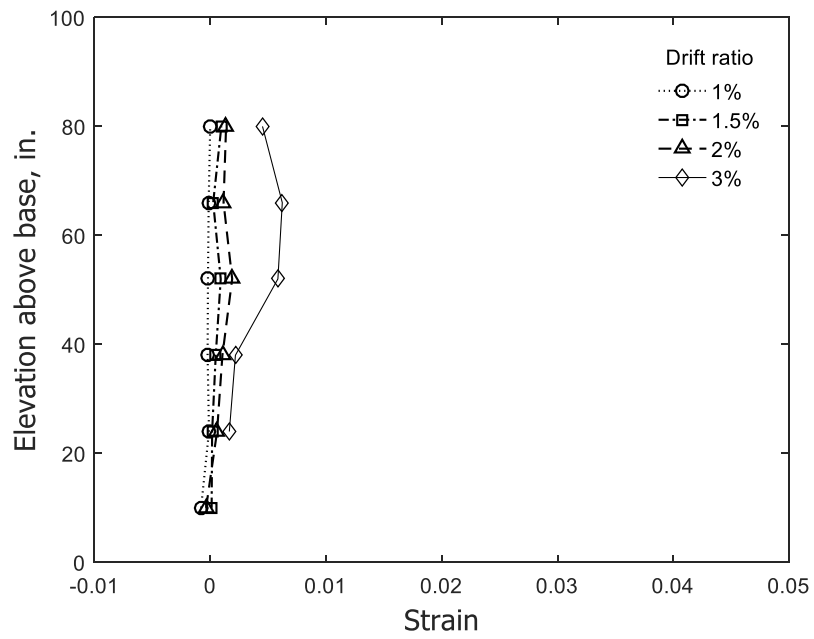


(b) Stem in tension

Figure 233 – Calculated concrete strain along Column 7 for stem of T1 (1 in. = 25.4 mm)

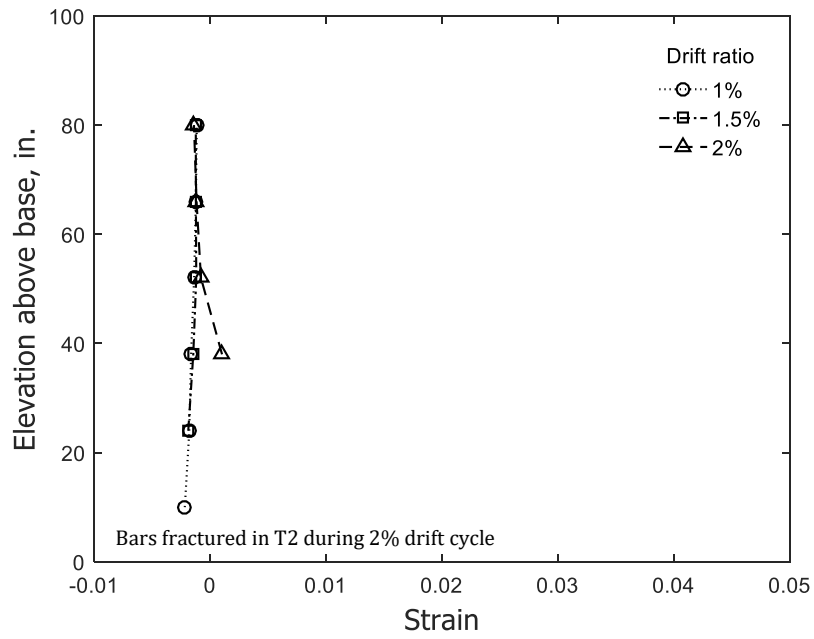


(a) Stem in compression

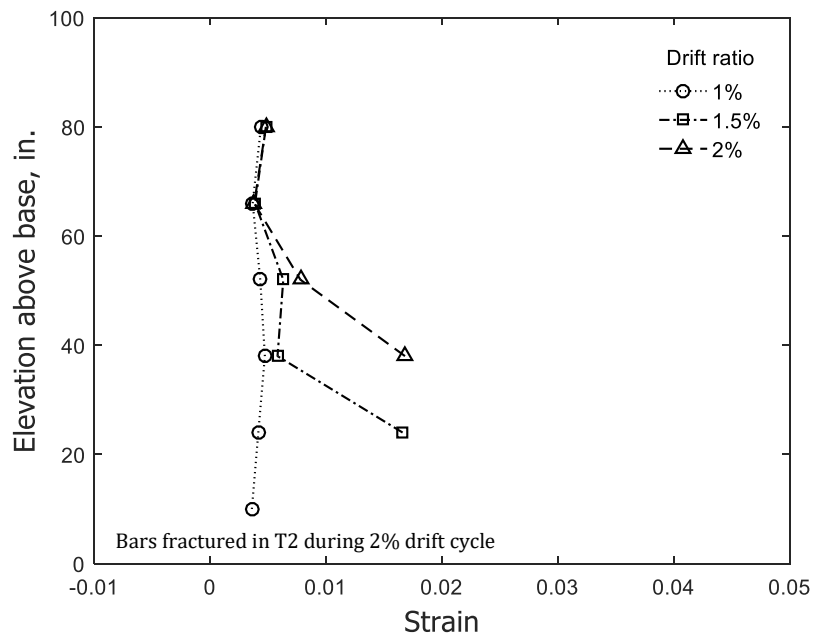


(b) Stem in tension

Figure 234 – Calculated concrete strain along Column 8 for stem of T1 (1 in. = 25.4 mm)

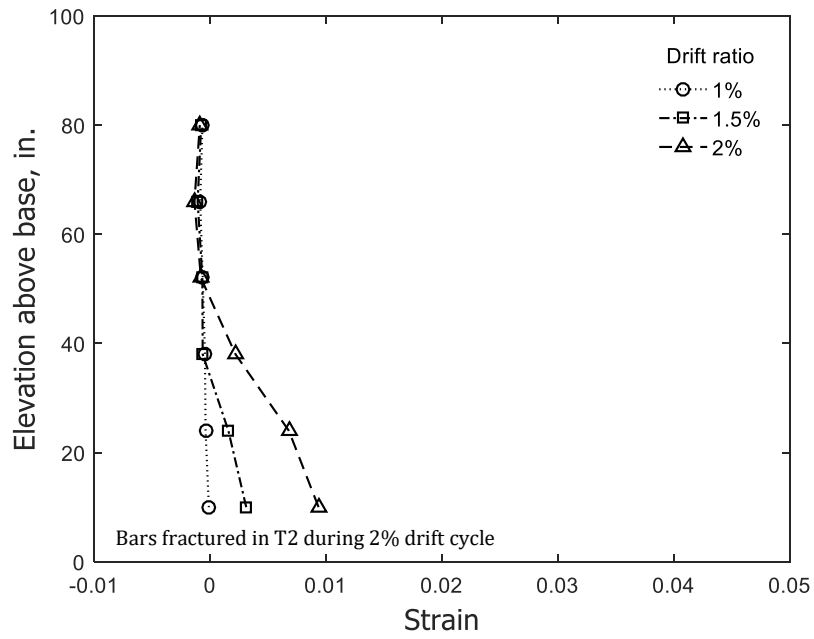


(a) Stem in compression

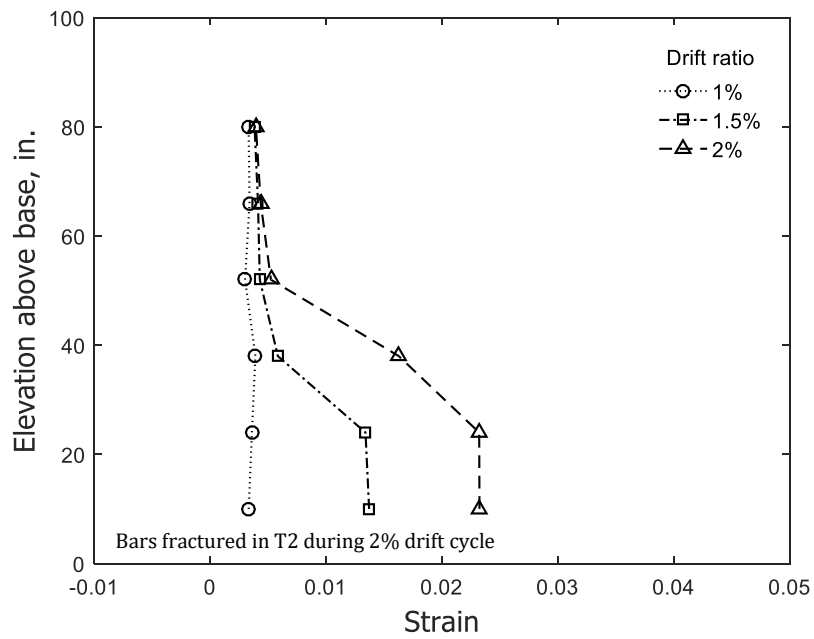


(b) Stem in tension

Figure 235 – Calculated concrete strain along Column 1 for stem of T2 (1 in. = 25.4 mm)

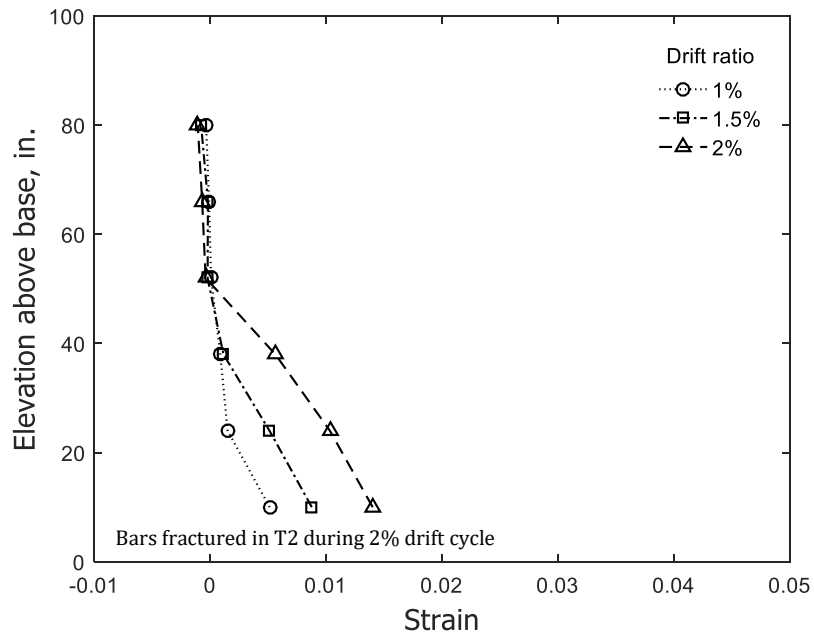


(a) Stem in compression

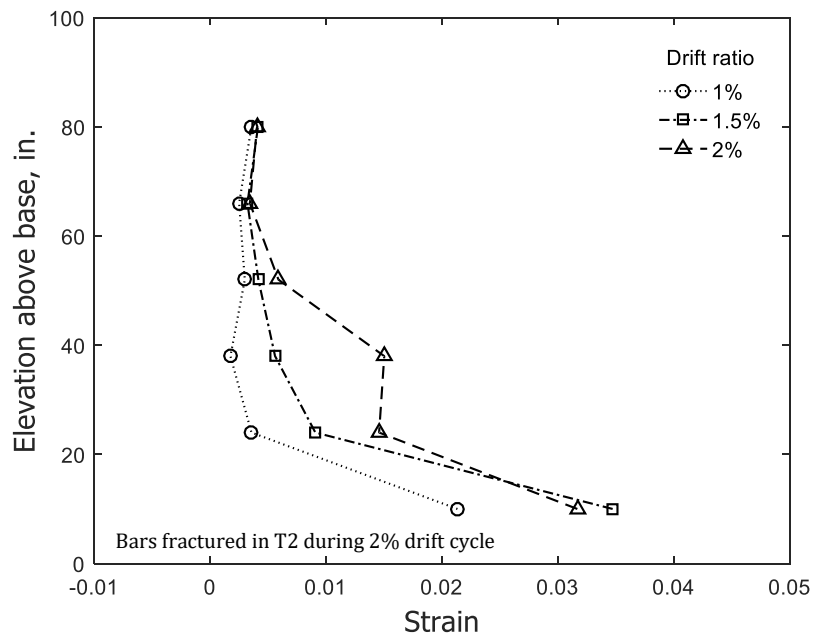


(b) Stem in tension

Figure 236 – Calculated concrete strain along Column 2 for stem of T2 (1 in. = 25.4 mm)

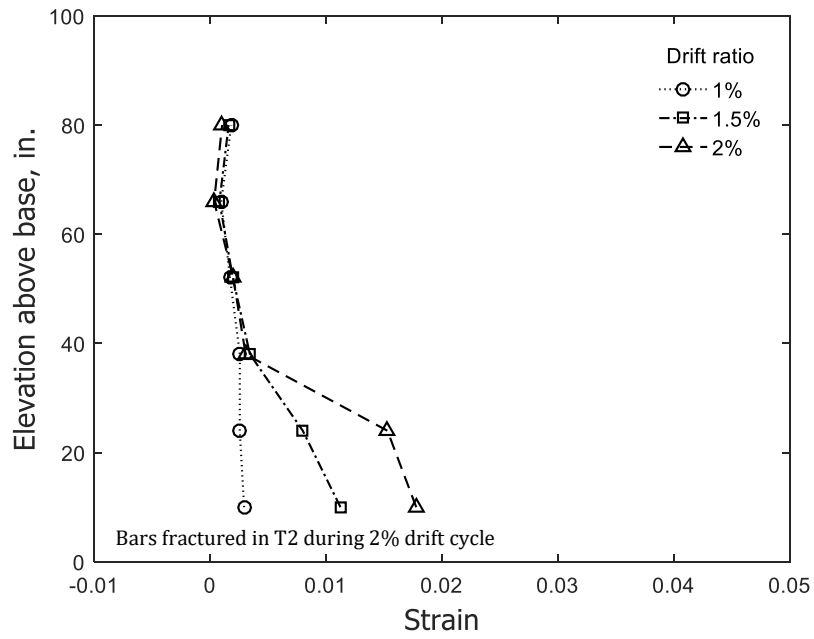


(a) Stem in compression

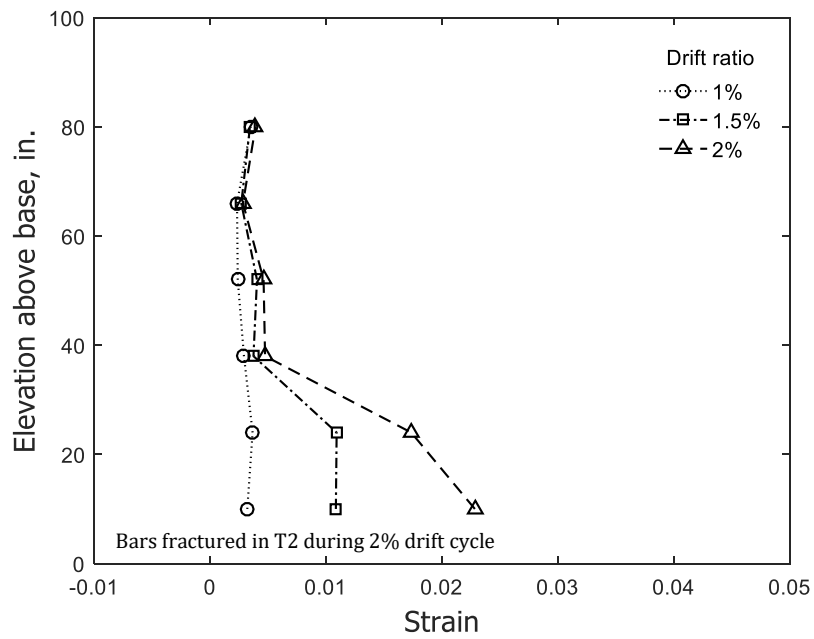


(b) Stem in tension

Figure 237 – Calculated concrete strain along Column 3 for stem of T2 (1 in. = 25.4 mm)

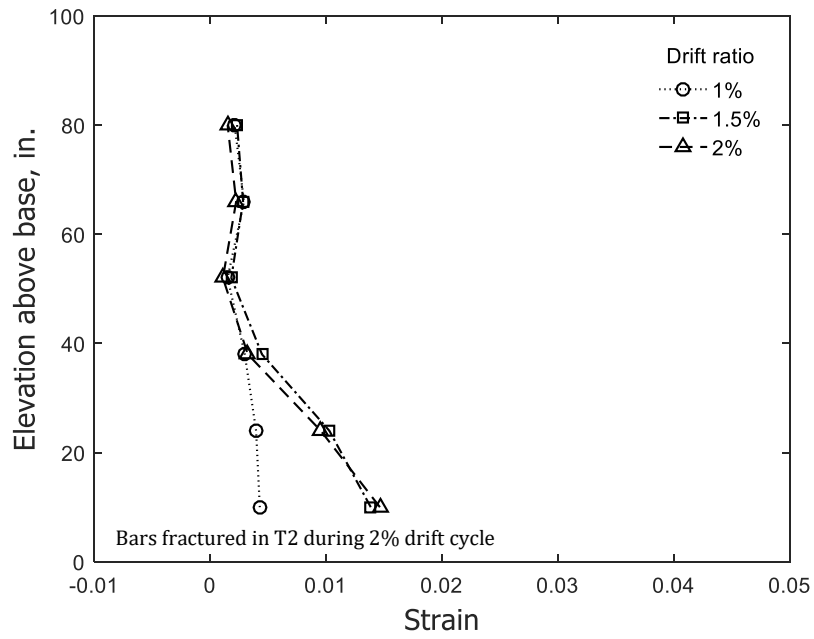


(a) Stem in compression

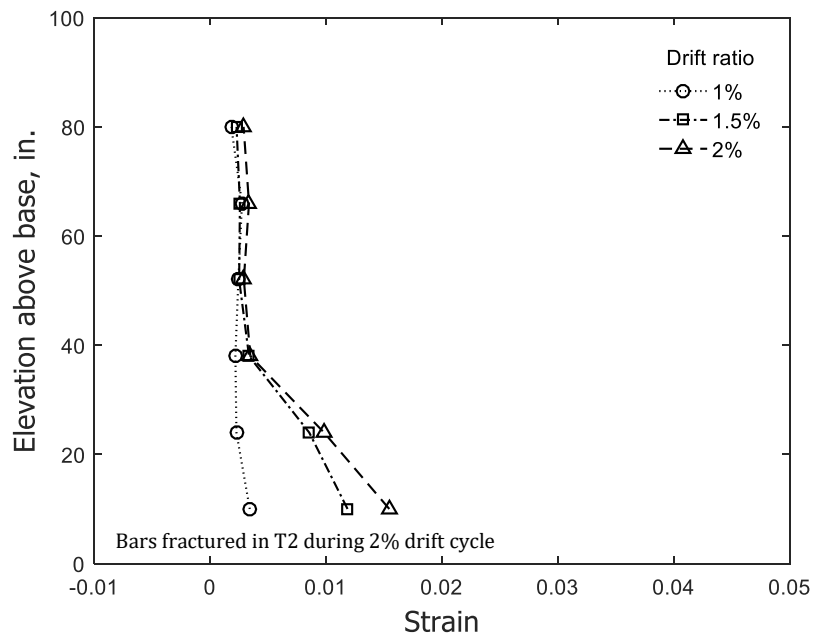


(b) Stem in tension

Figure 238 – Calculated concrete strain along Column 4 for stem of T2 (1 in. = 25.4 mm)

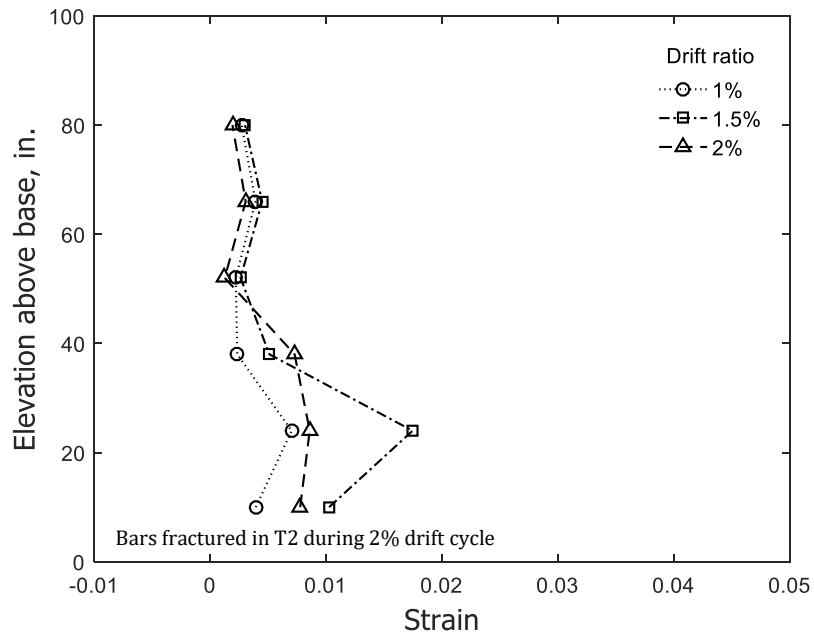


(a) Stem in compression

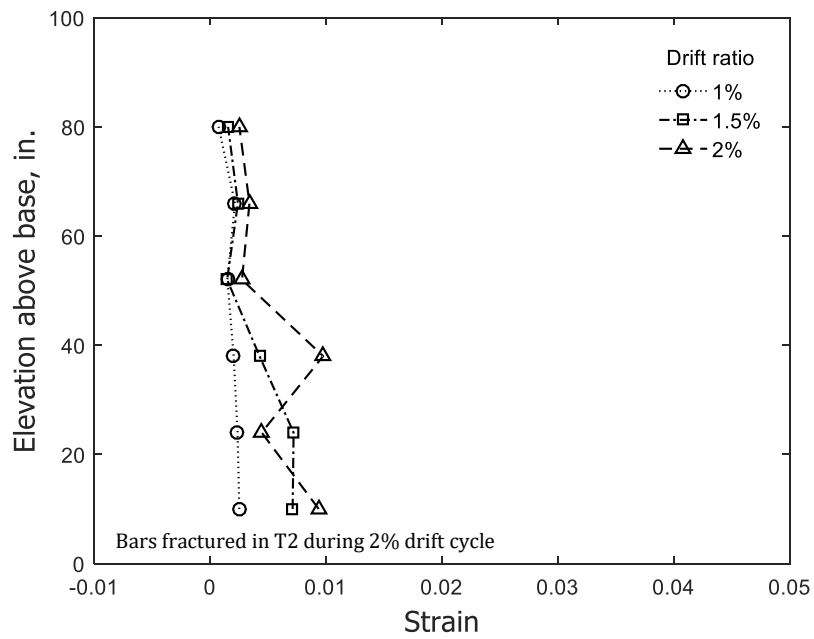


(b) Stem in tension

Figure 239 – Calculated concrete strain along Column 5 for stem of T2 (1 in. = 25.4 mm)

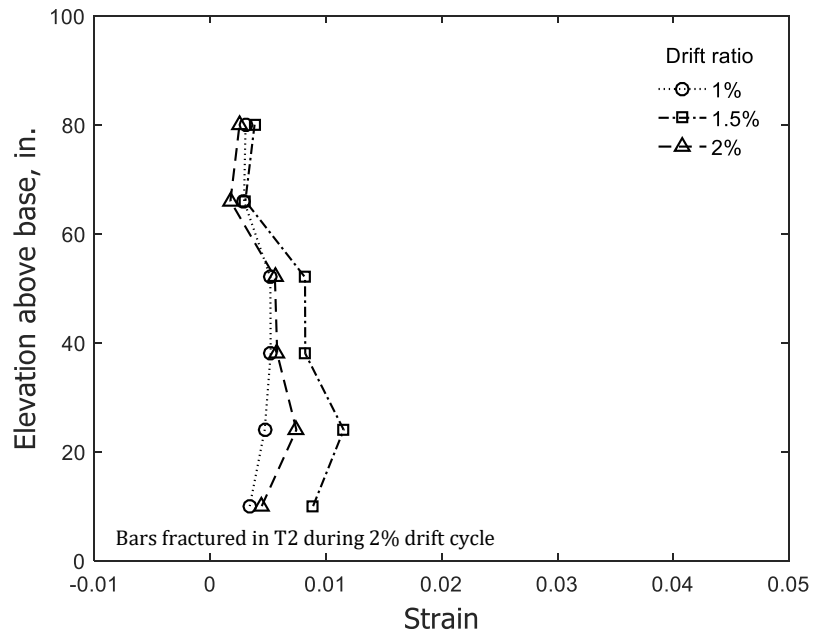


(a) Stem in compression

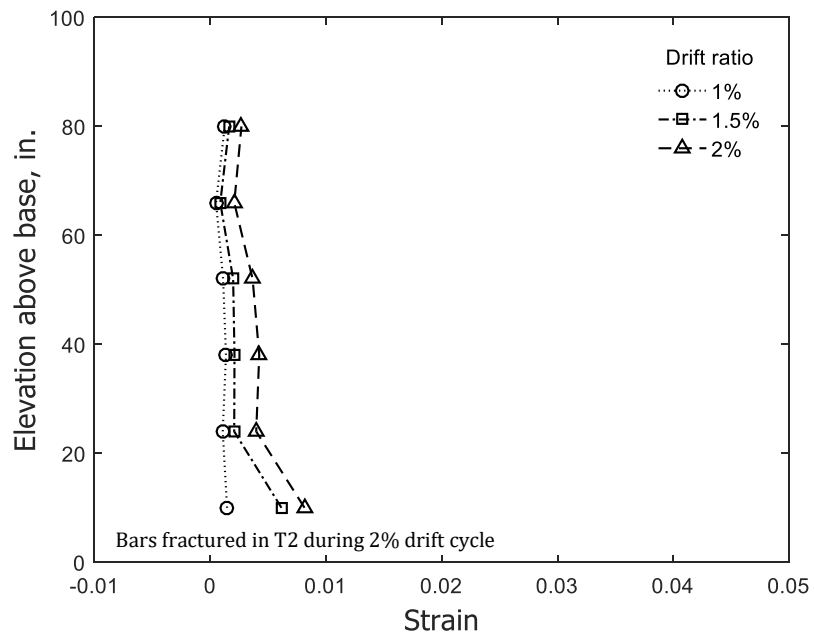


(b) Stem in tension

Figure 240 – Calculated concrete strain along Column 6 for stem of T2 (1 in. = 25.4 mm)

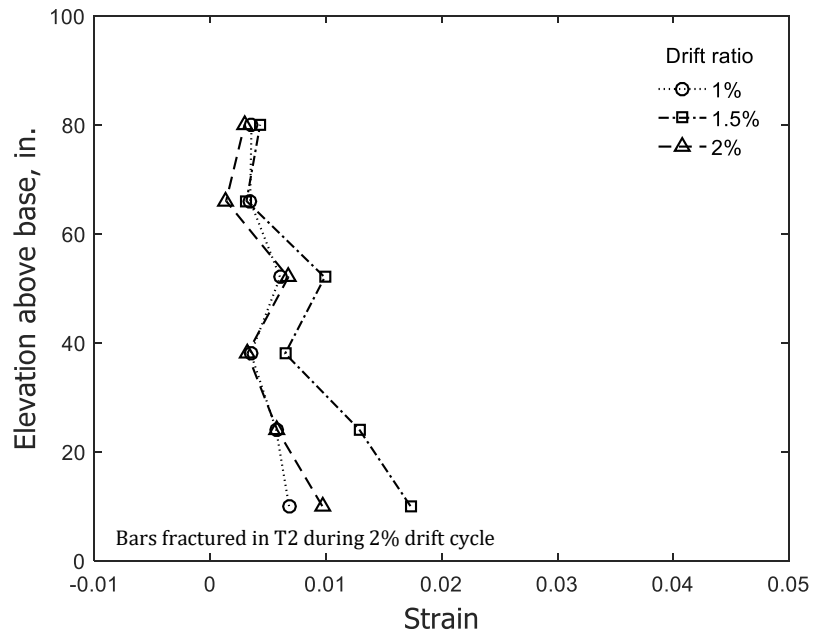


(c) Stem in compression

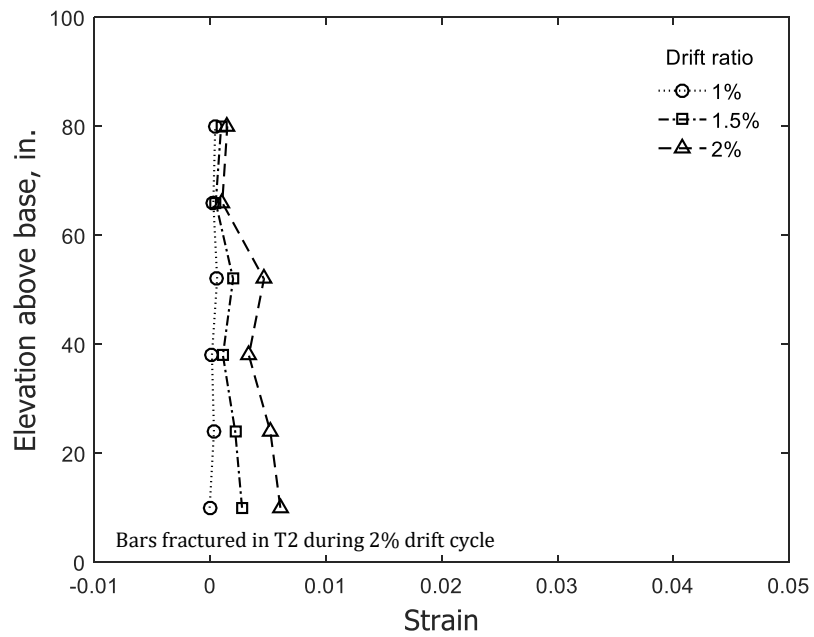


(d) Stem in tension

Figure 241 – Calculated concrete strain along Column 7 for stem of T2 (1 in. = 25.4 mm)

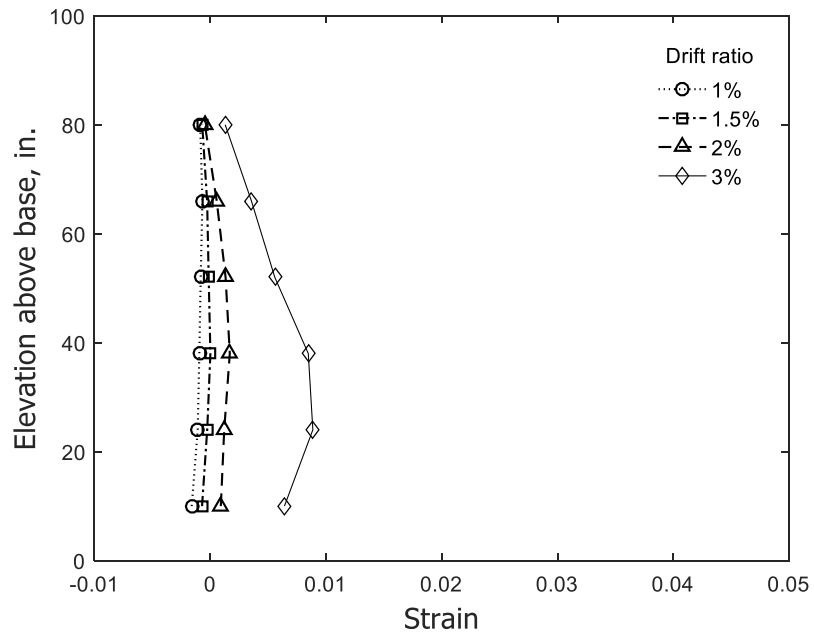


(a) Stem in compression

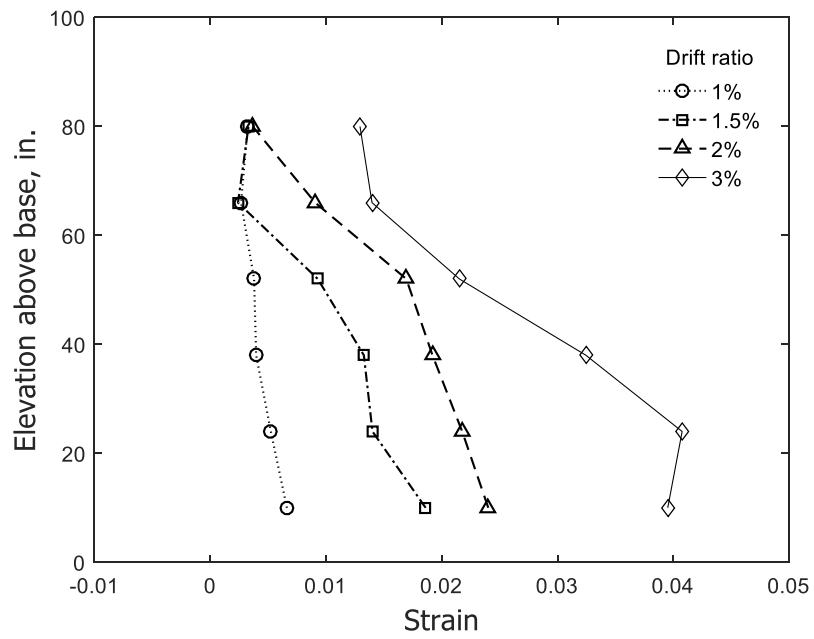


(b) Stem in tension

Figure 242 – Calculated concrete strain along Column 8 for stem of T2 (1 in. = 25.4 mm)

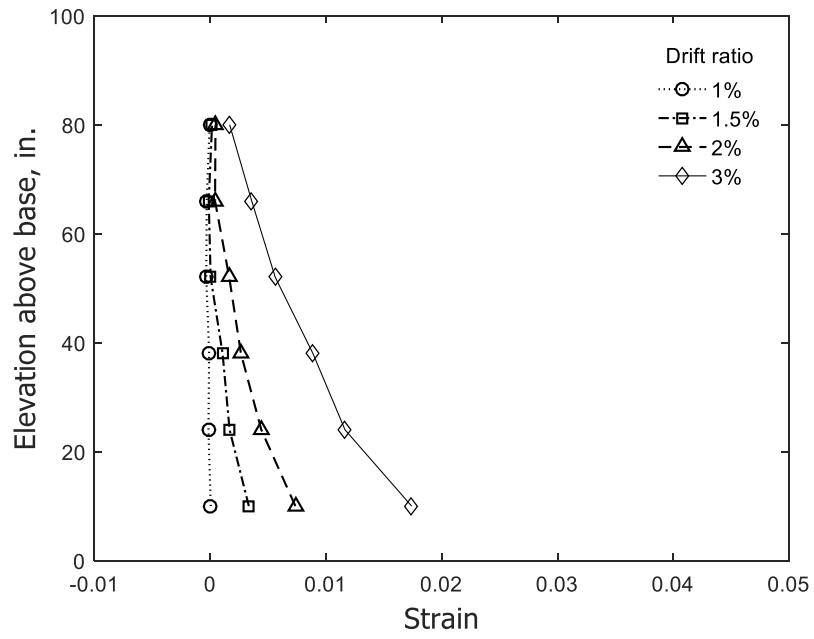


(a) Stem in compression

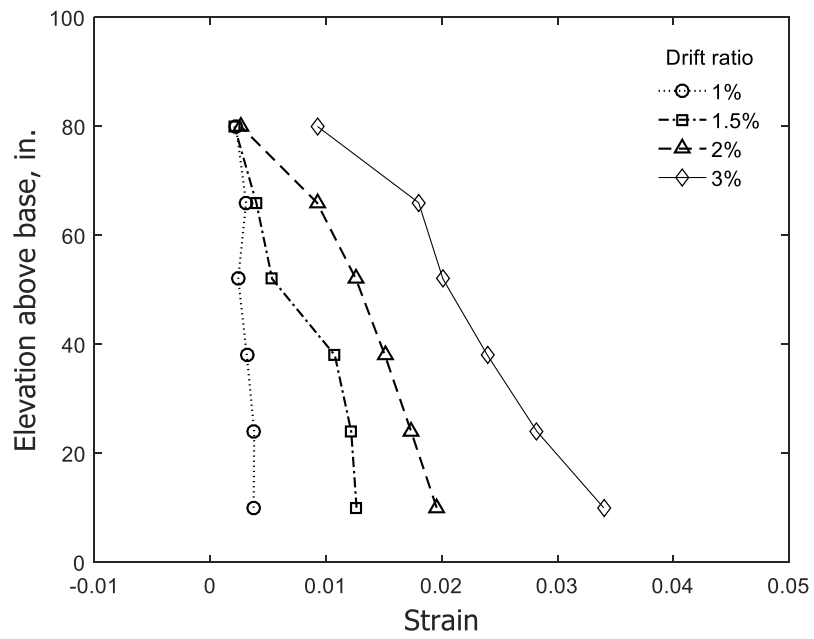


(b) Stem in tension

Figure 243 – Calculated concrete strain along Column 1 for stem of T3 (1 in. = 25.4 mm)

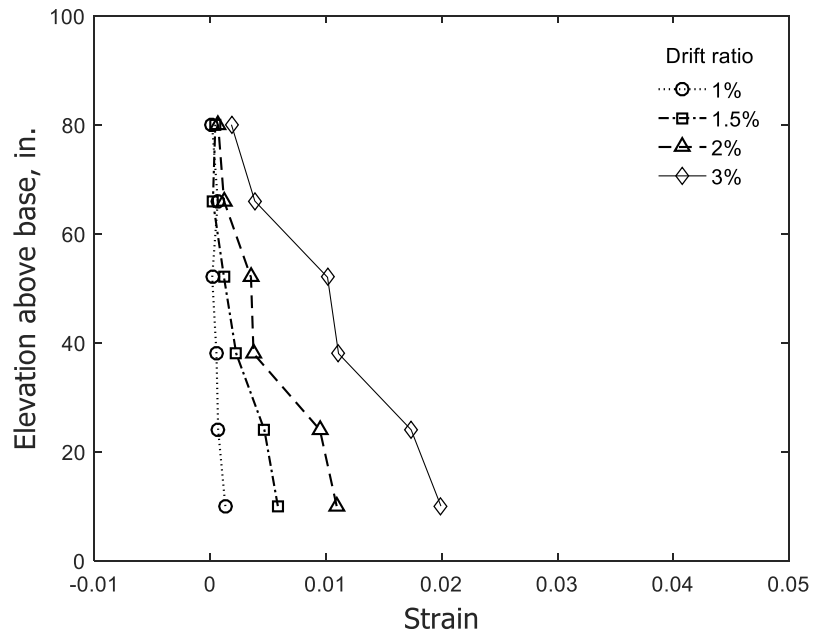


(a) Stem in compression

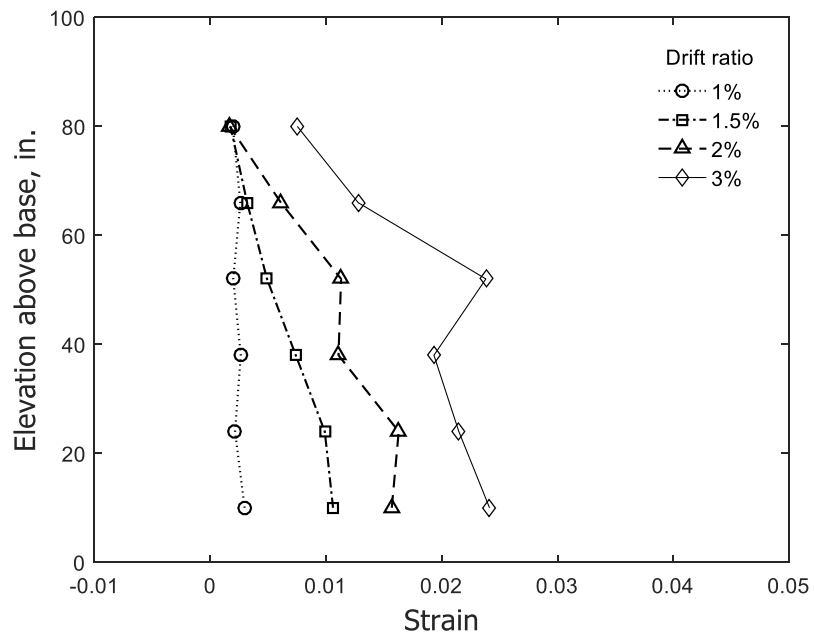


(b) Stem in tension

Figure 244 – Calculated concrete strain along Column 2 for stem of T3 (1 in. = 25.4 mm)

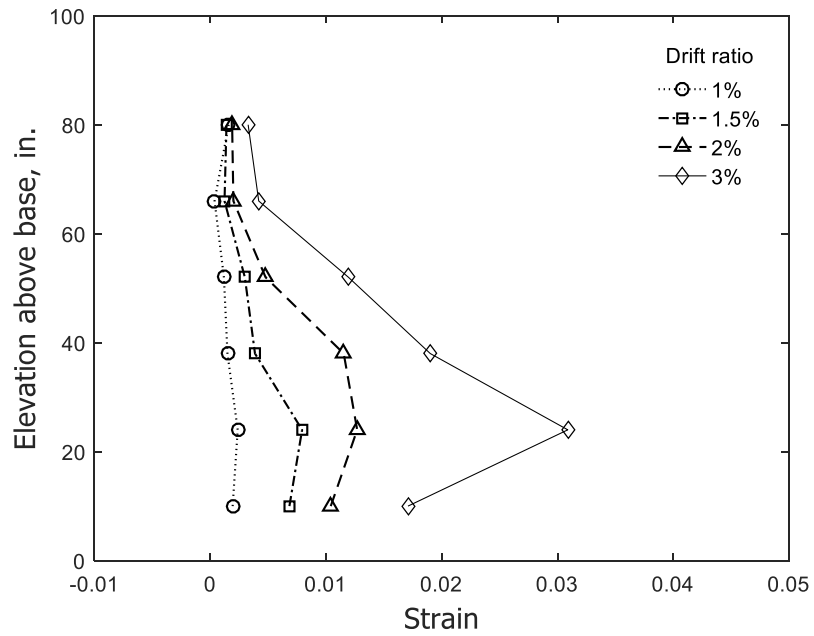


(a) Stem in compression

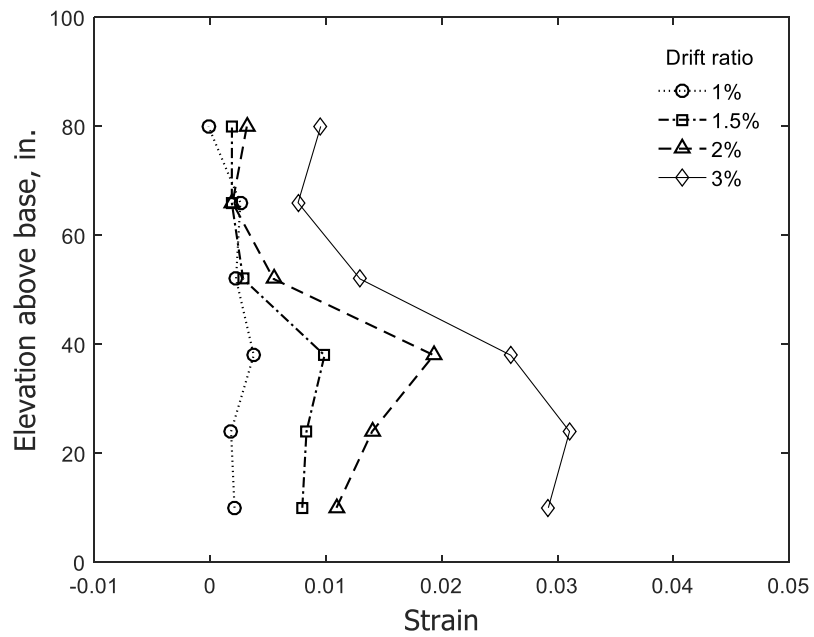


(b) Stem in tension

Figure 245 – Calculated concrete strain along Column 3 for stem of T3 (1 in. = 25.4 mm)

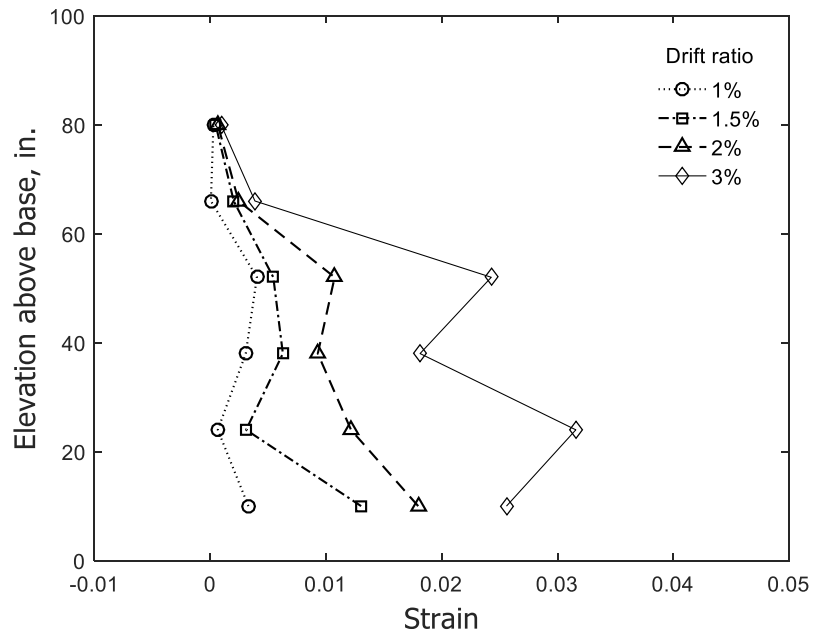


(a) Stem in compression

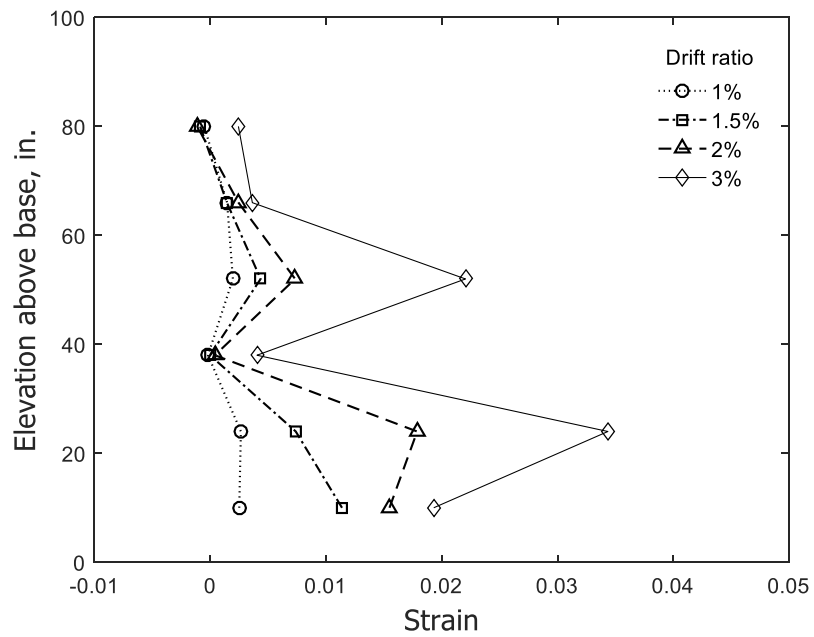


(b) Stem in tension

Figure 246 – Calculated concrete strain along Column 4 for stem of T3 (1 in. = 25.4 mm)

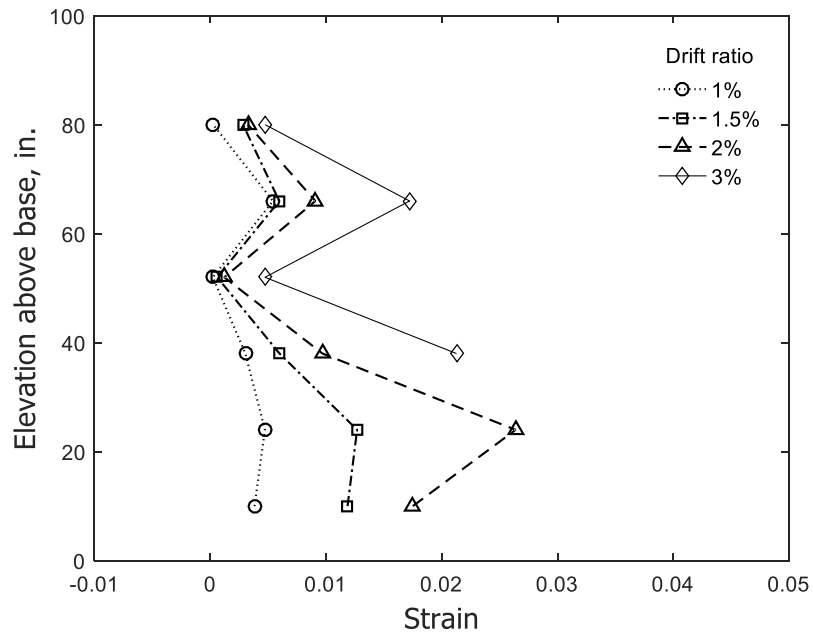


(a) Stem in compression

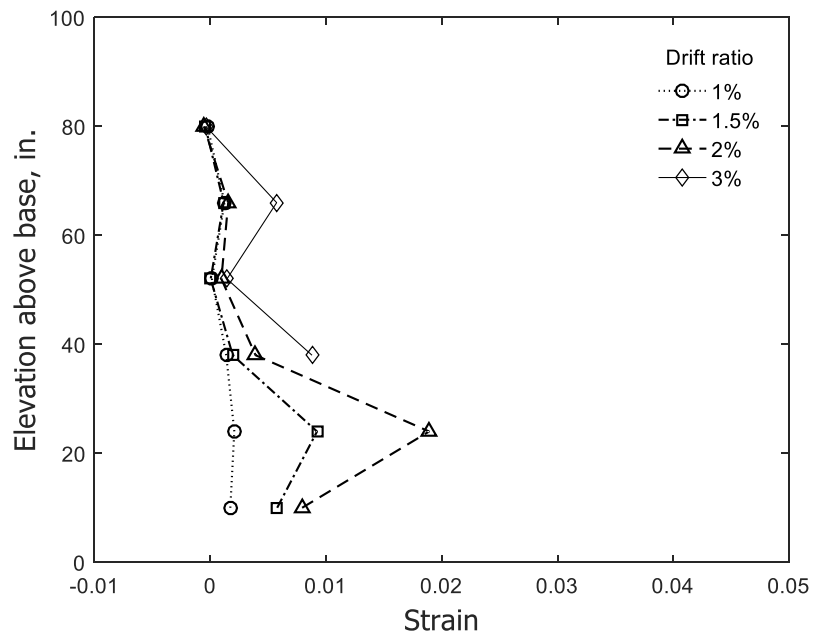


(b) Stem in tension

Figure 247 – Calculated concrete strain along Column 5 for stem of T3 (1 in. = 25.4 mm)

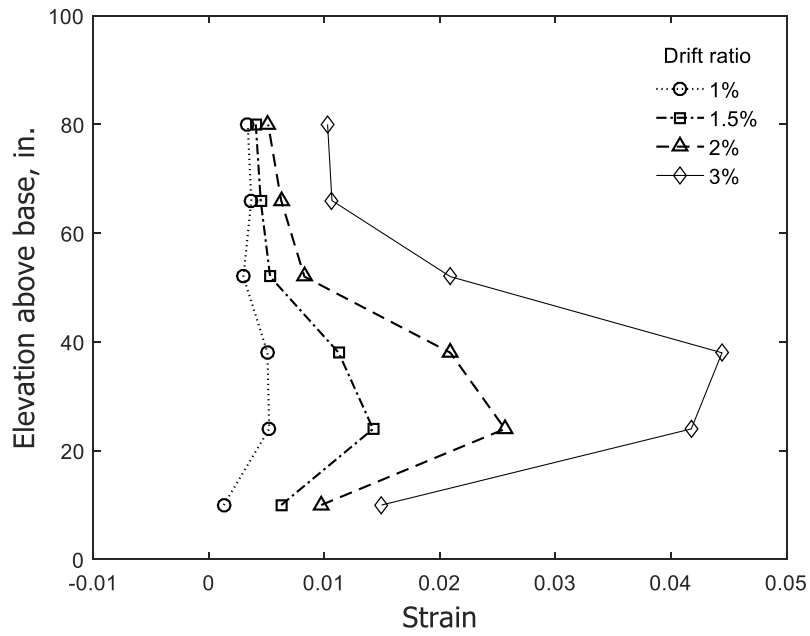


(a) Stem in compression

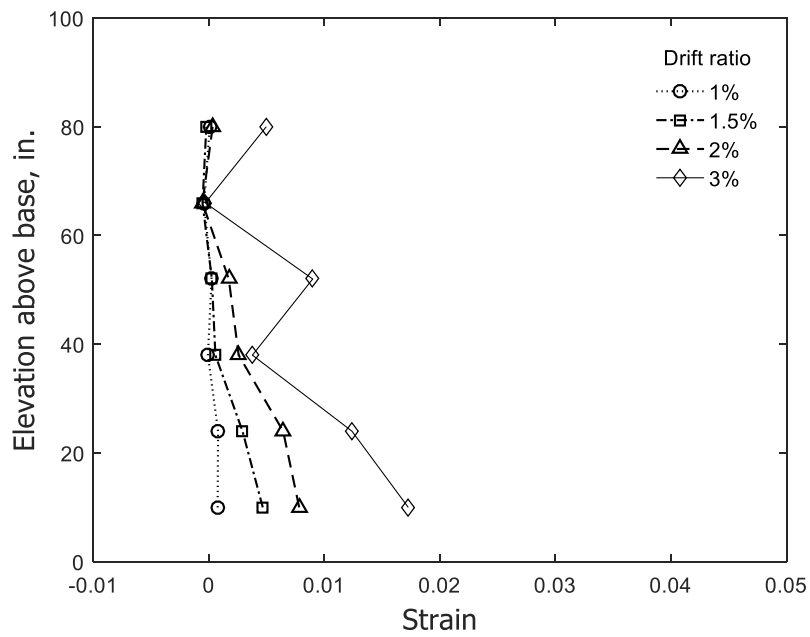


(b) Stem in tension

Figure 248 – Calculated concrete strain along Column 6 for stem of T3 (1 in. = 25.4 mm)

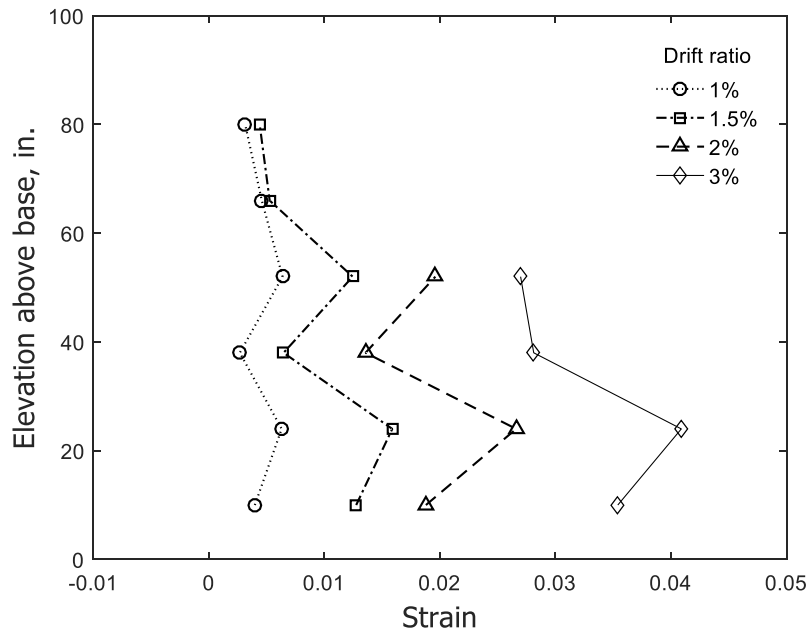


(a) Stem in compression

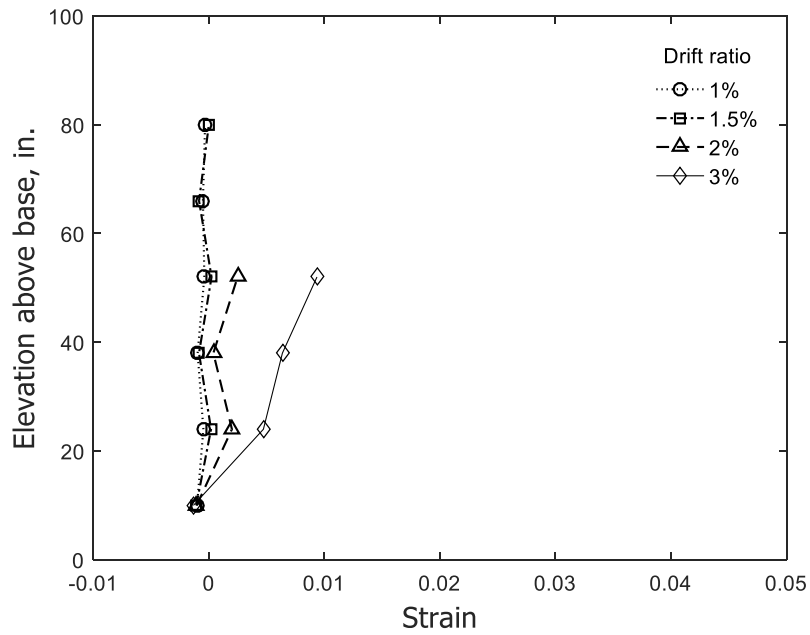


(b) Stem in tension

Figure 249 – Calculated concrete strain along Column 7 for stem of T3 (1 in. = 25.4 mm)

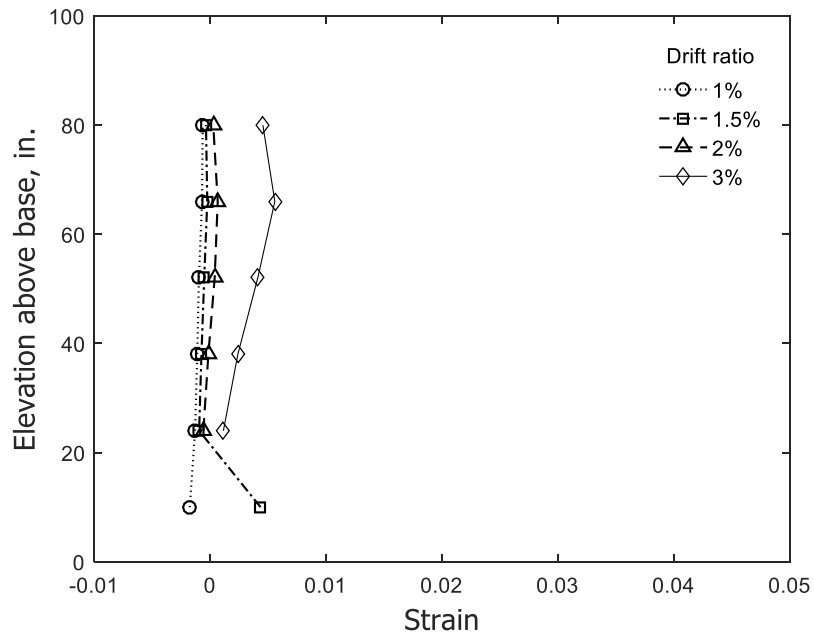


(a) Stem in compression

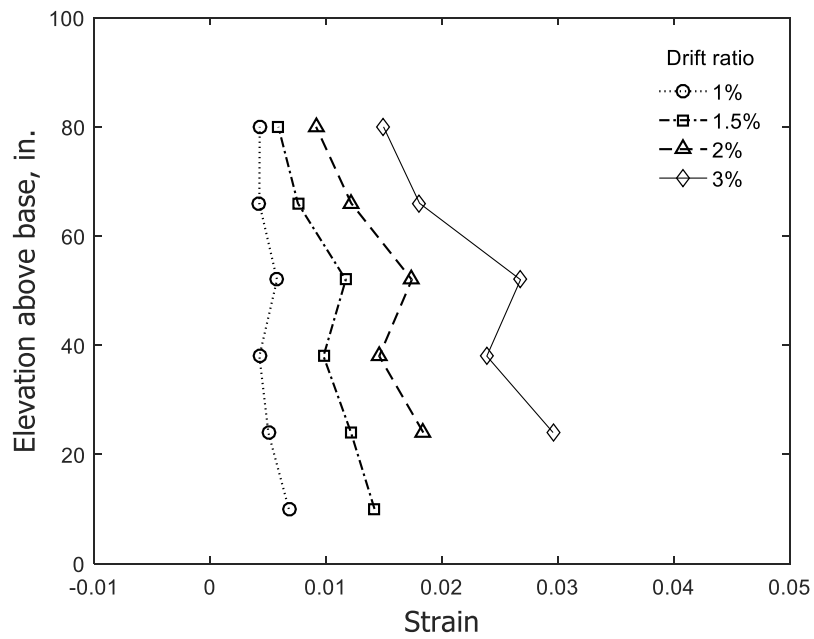


(b) Stem in tension

Figure 250 – Calculated concrete strain along Column 8 for stem of T3 (1 in. = 25.4 mm)

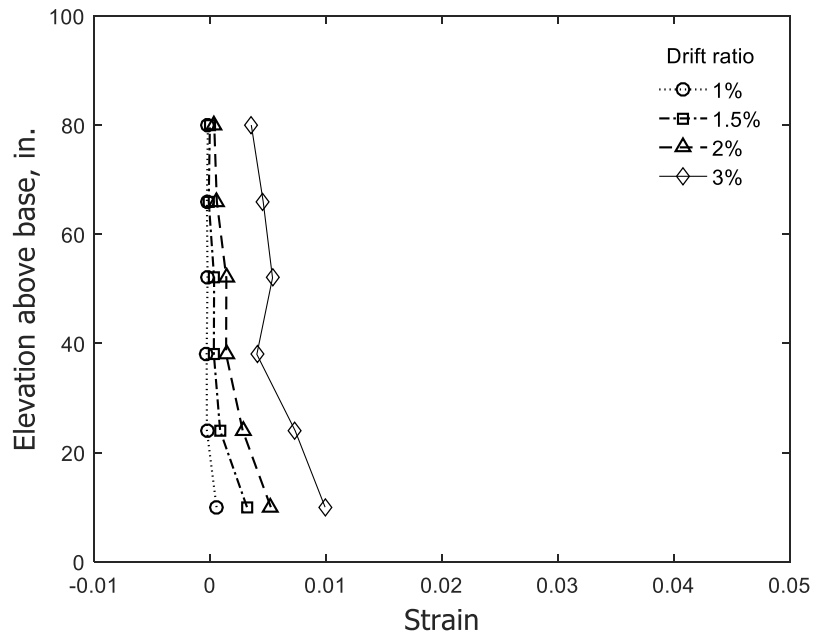


(a) Stem in compression

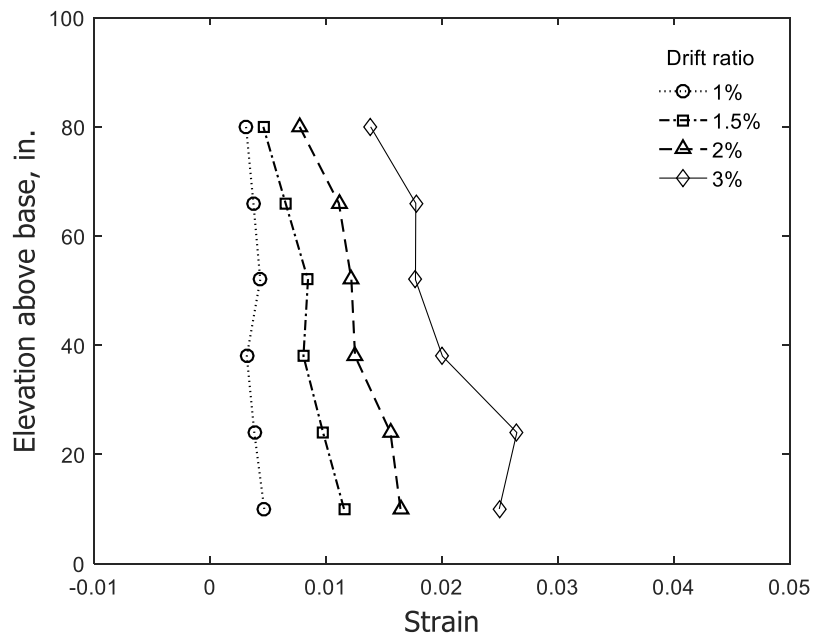


(b) Stem in tension

Figure 251 – Calculated concrete strain along Column 1 for stem of T4 (1 in. = 25.4 mm)

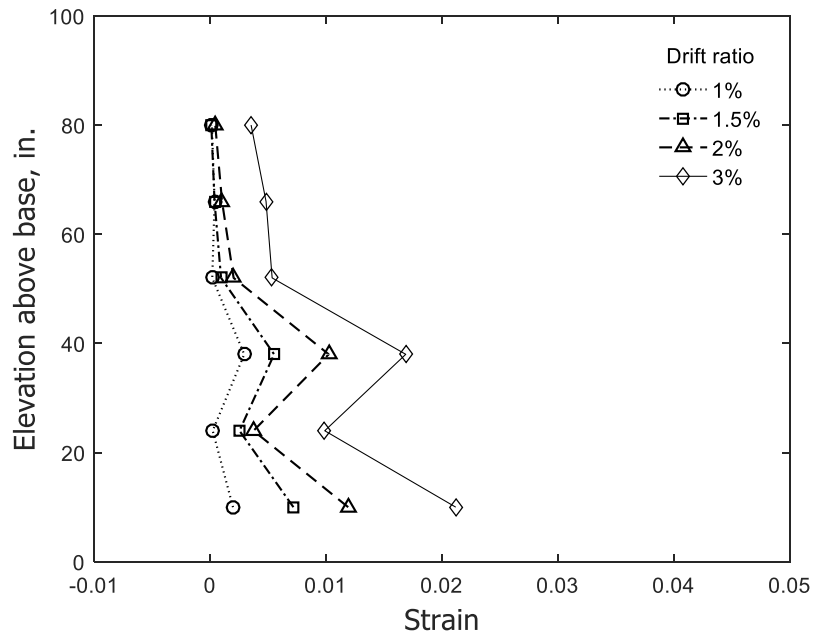


(a) Stem in compression

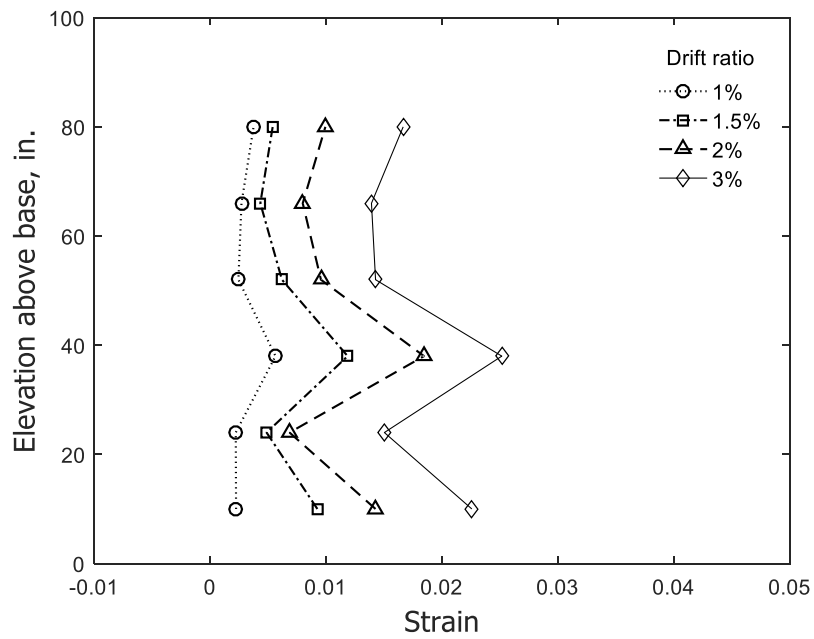


(b) Stem in tension

Figure 252 – Calculated concrete strain along Column 2 for stem of T4 (1 in. = 25.4 mm)

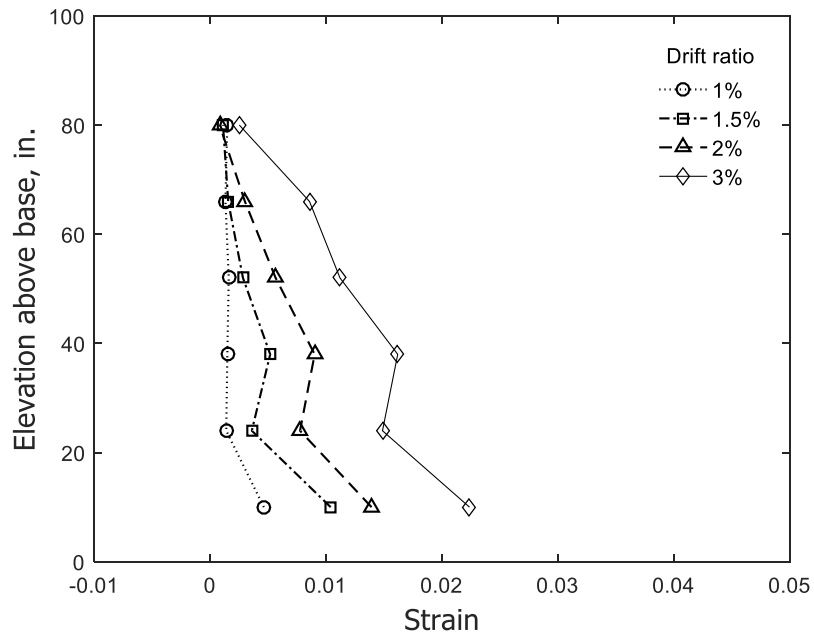


(a) Stem in compression

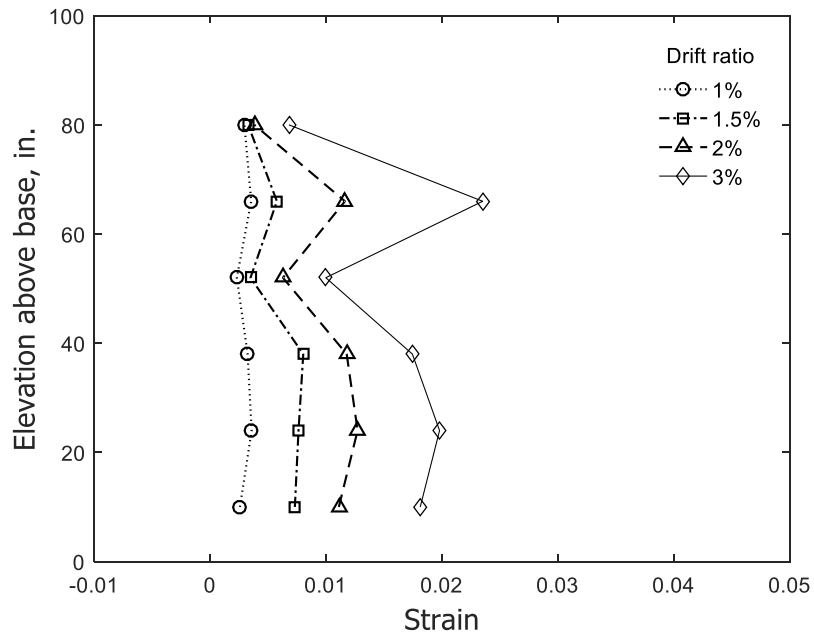


(b) Stem in tension

Figure 253 – Calculated concrete strain along Column 3 for stem of T4 (1 in. = 25.4 mm)

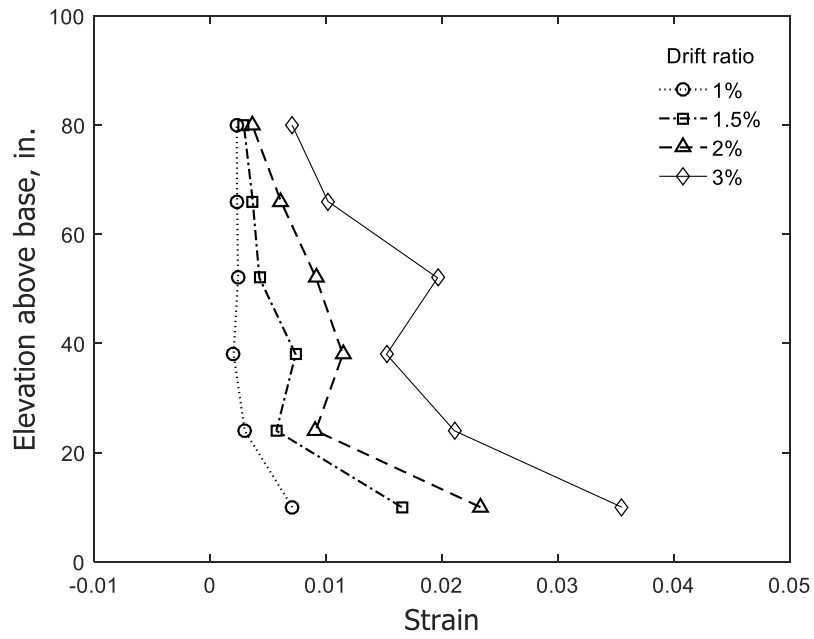


(a) Stem in compression

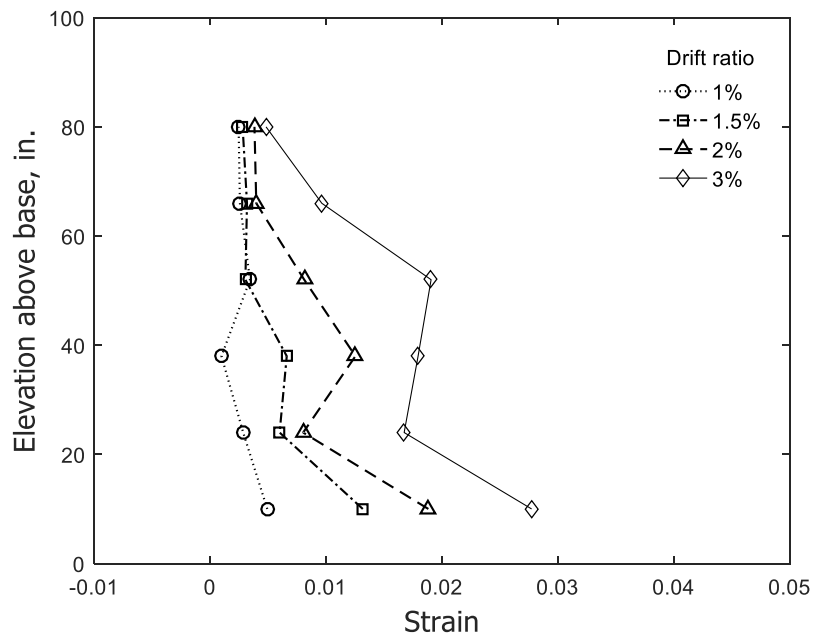


(b) Stem in tension

Figure 254 – Calculated concrete strain along Column 4 for stem of T4 (1 in. = 25.4 mm)

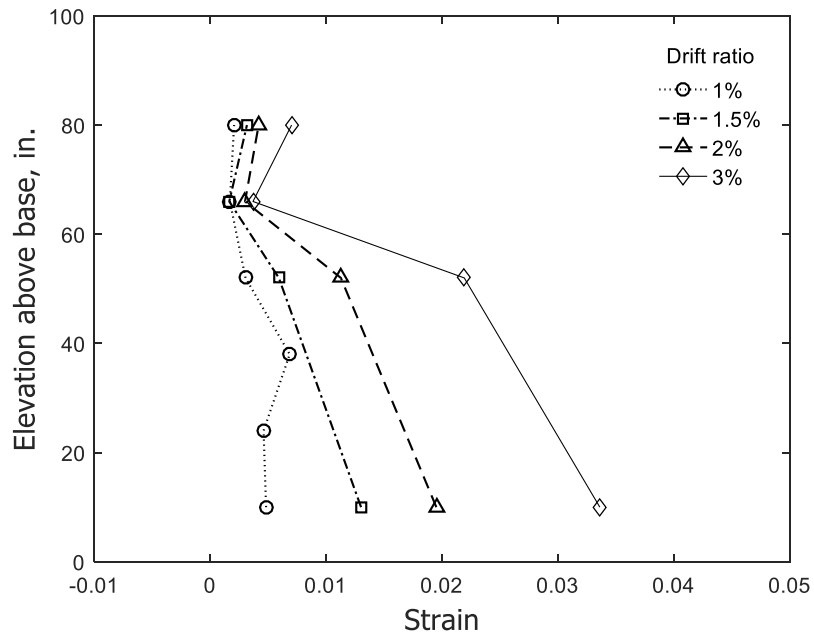


(a) Stem in compression

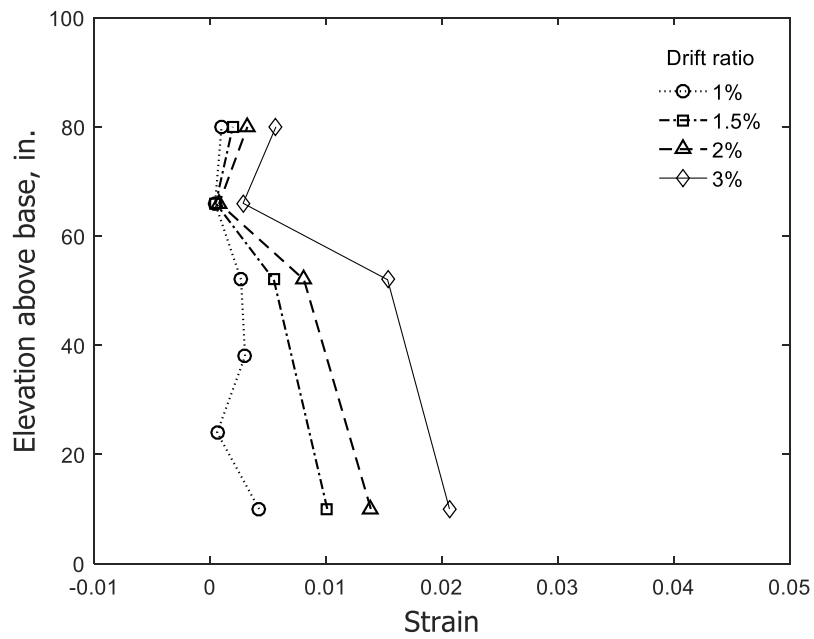


(b) Stem in tension

Figure 255 – Calculated concrete strain along Column 5 for stem of T4 (1 in. = 25.4 mm)

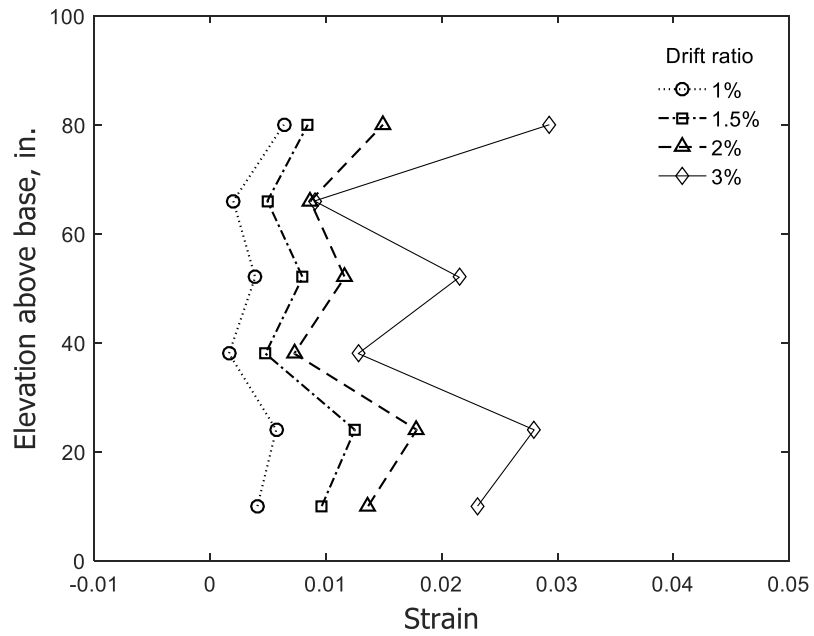


(a) Stem in compression

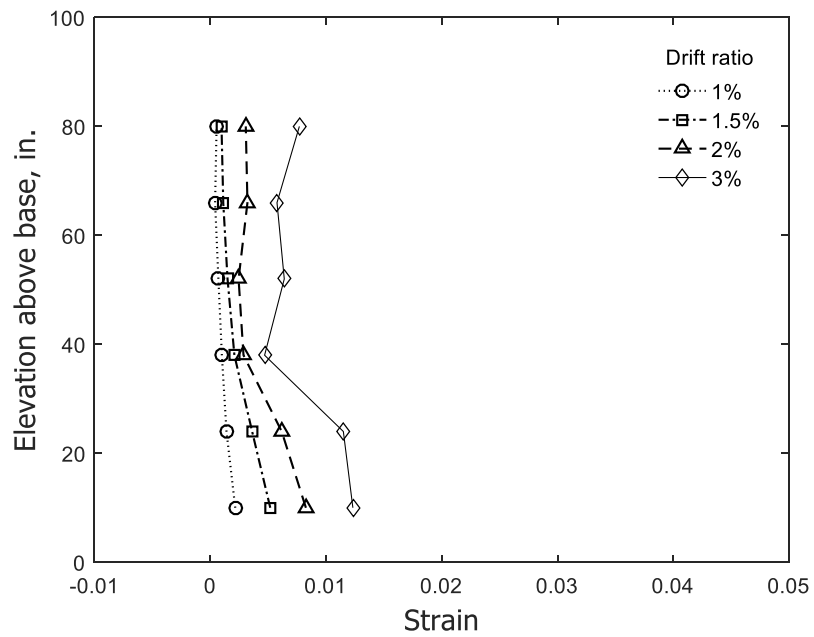


(b) Stem in tension

Figure 256 – Calculated concrete strain along Column 6 for stem of T4 (1 in. = 25.4 mm)

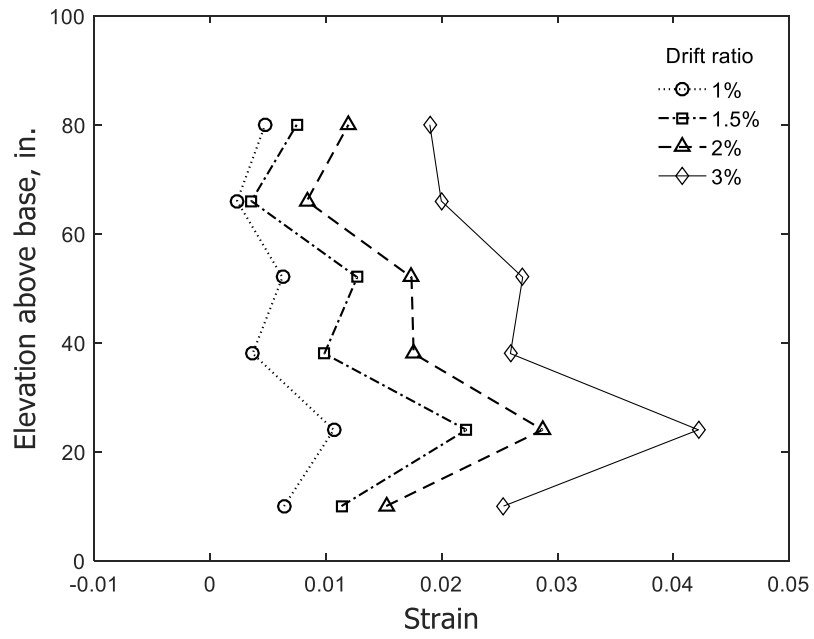


(a) Stem in compression

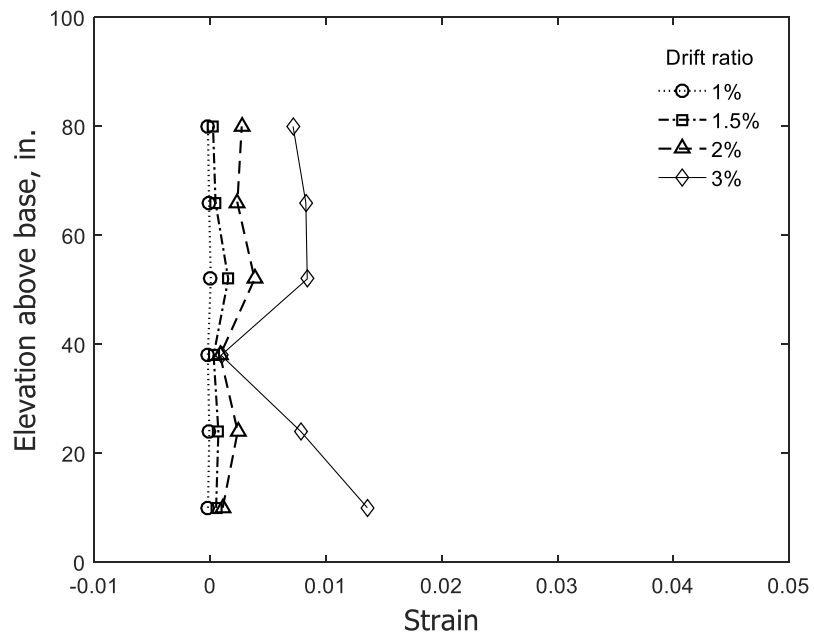


(b) Stem in tension

Figure 257 – Calculated concrete strain along Column 7 for stem of T4 (1 in. = 25.4 mm)

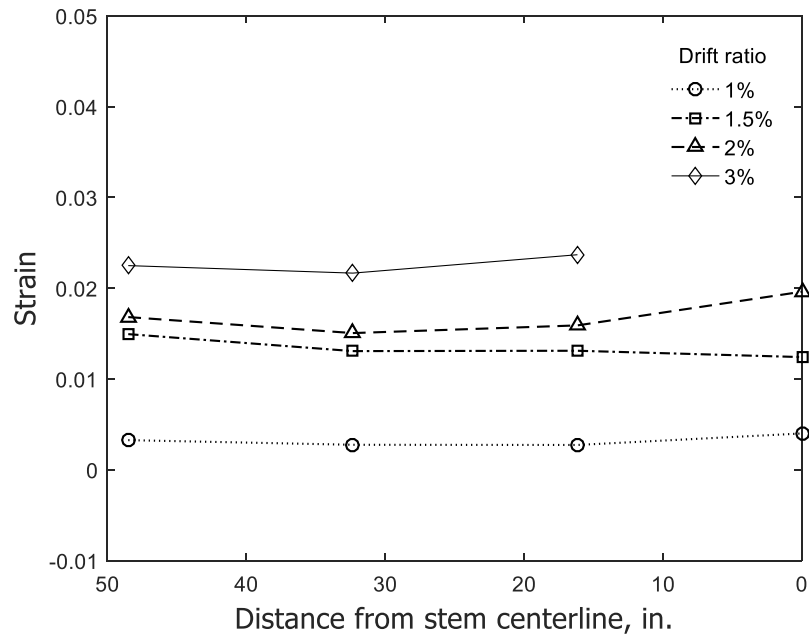


(a) Stem in compression

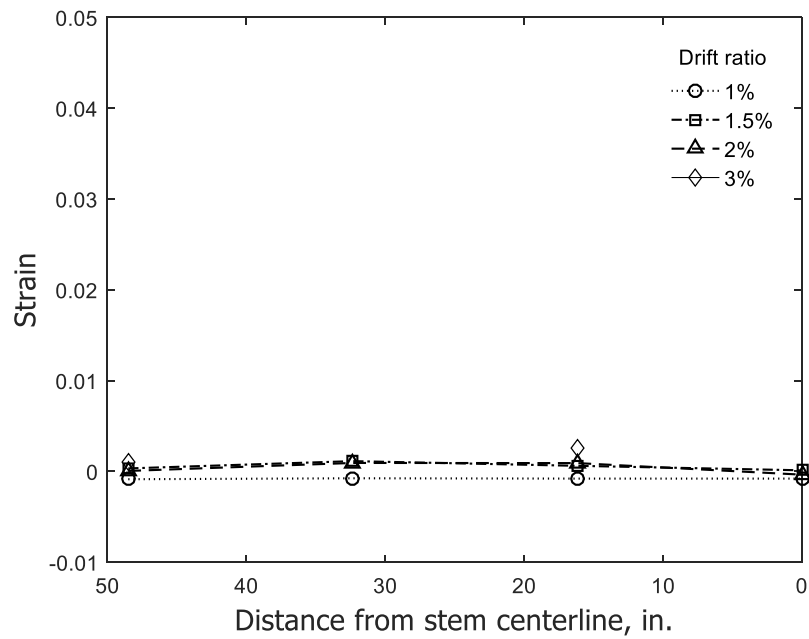


(b) Stem in tension

Figure 258 – Calculated concrete strain along Column 8 for stem of T4 (1 in. = 25.4 mm)

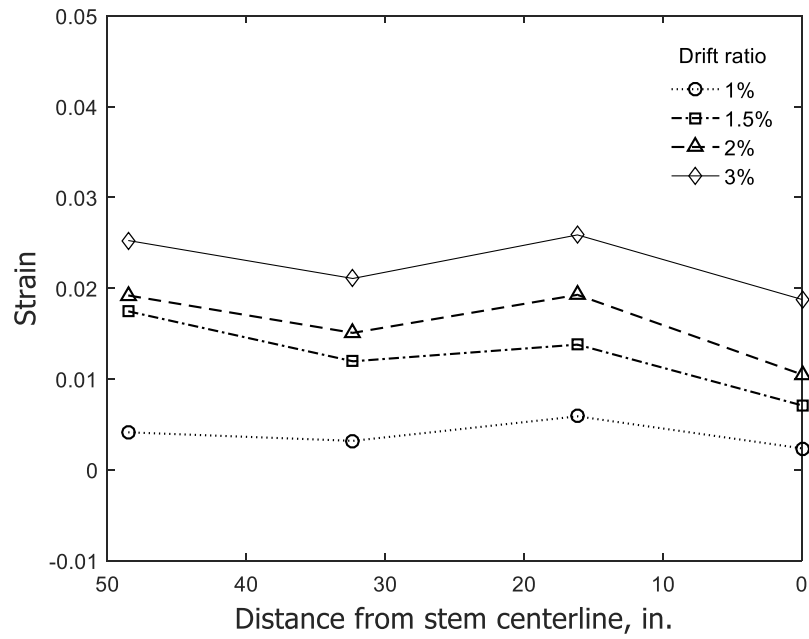


(a) Stem in compression

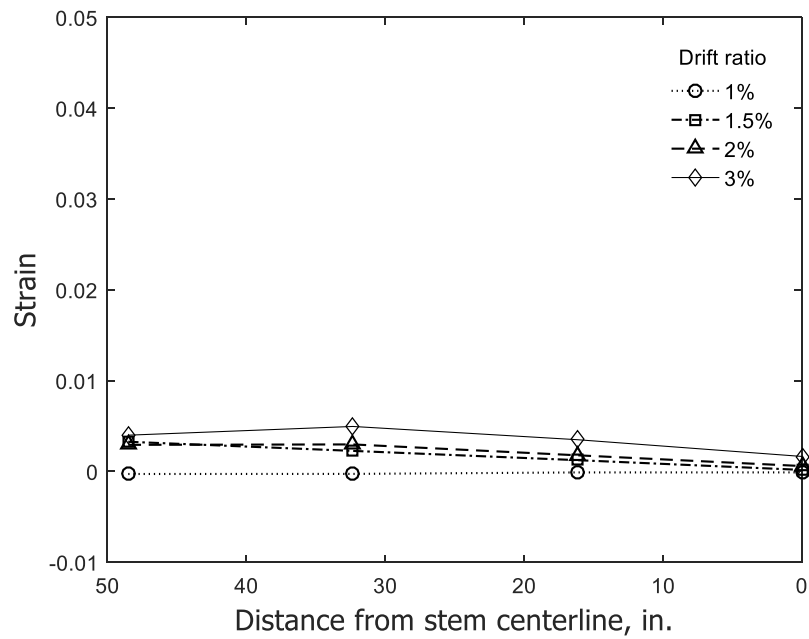


(b) Stem in tension

Figure 259 – Calculated concrete strain in Layer 1 for flange of T1 (1 in. = 25.4 mm)

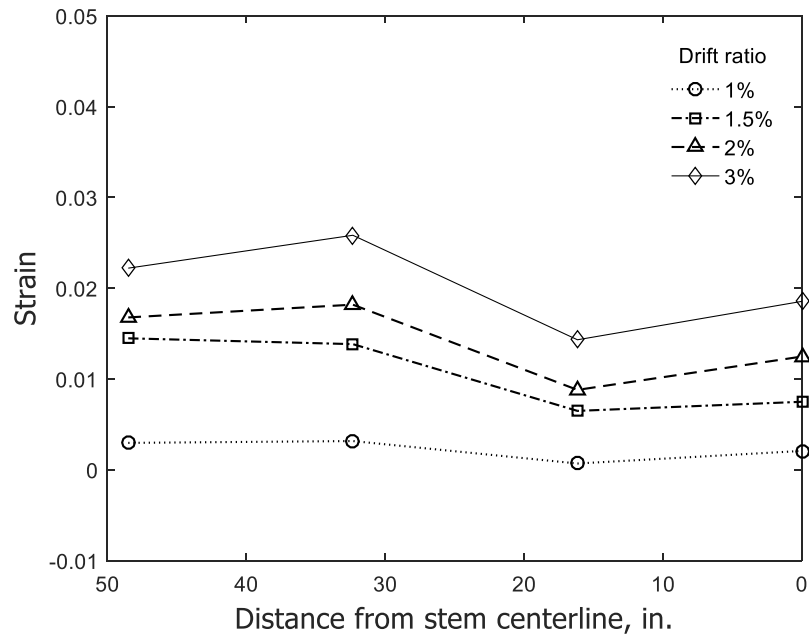


(a) Stem in compression

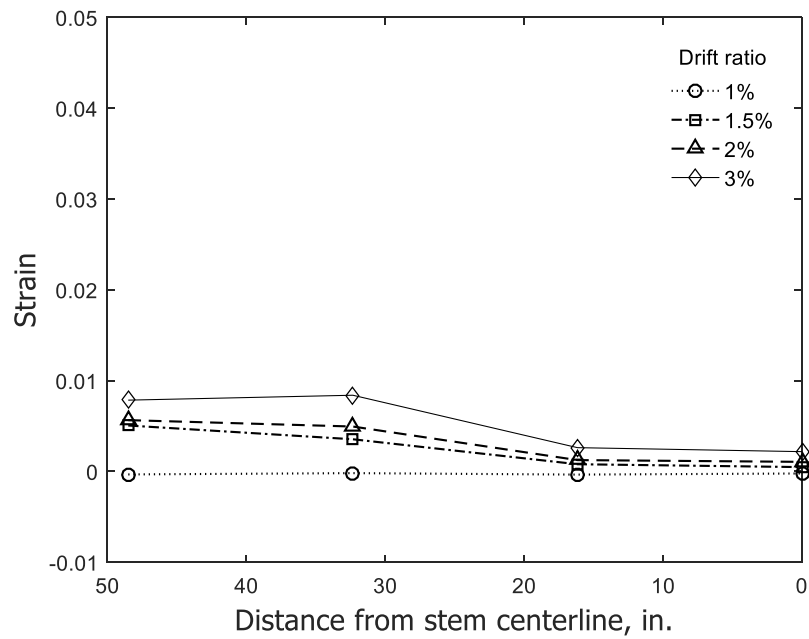


(b) Stem in tension

Figure 260 – Calculated concrete strain in Layer 2 for flange of T1 (1 in. = 25.4 mm)

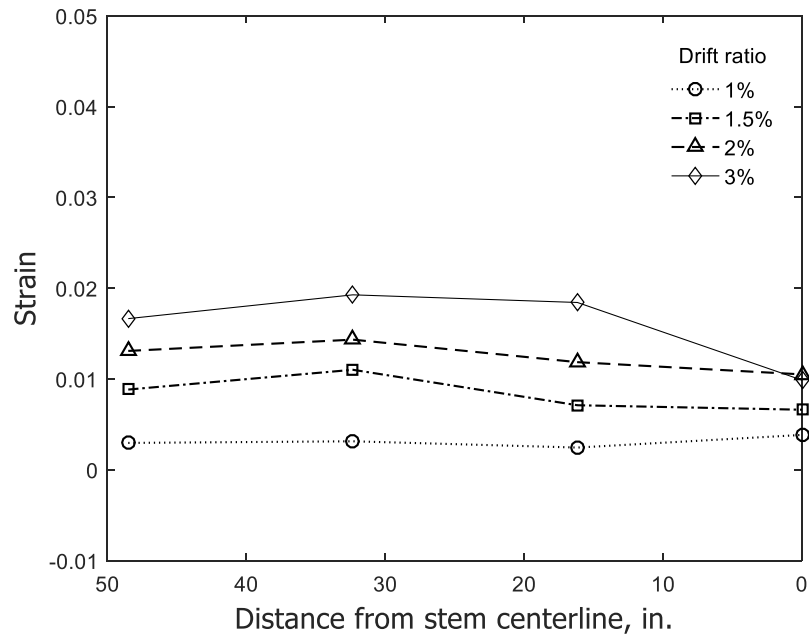


(a) Stem in compression

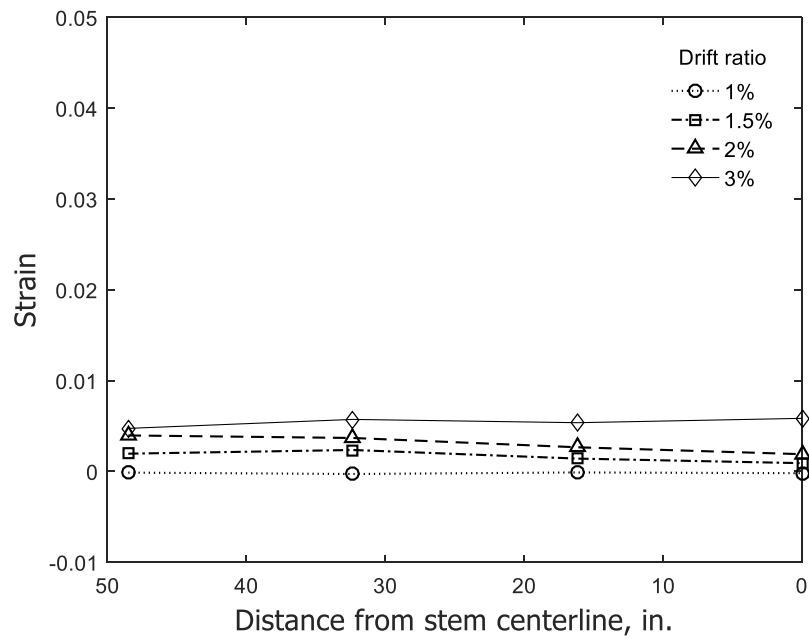


(b) Stem in tension

Figure 261 – Calculated concrete strain in Layer 3 for flange of T1 (1 in. = 25.4 mm)

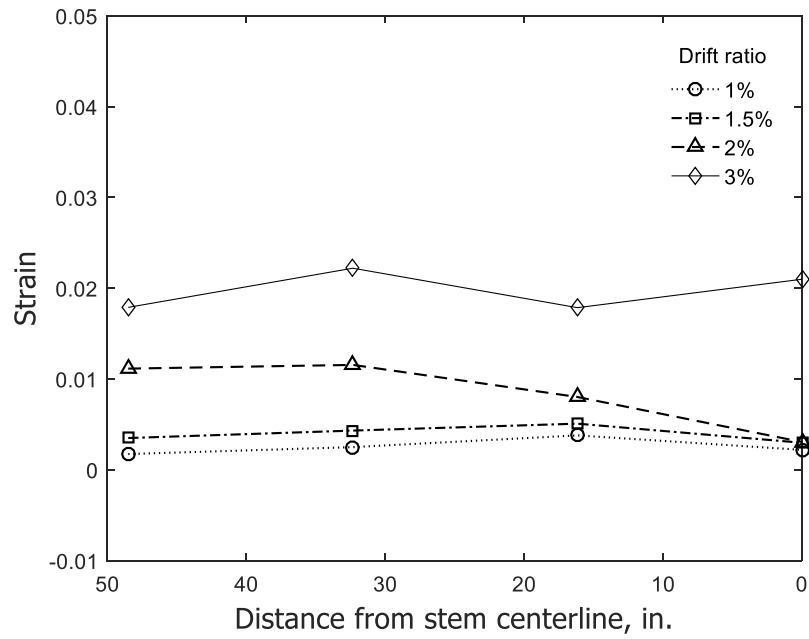


(a) Stem in compression

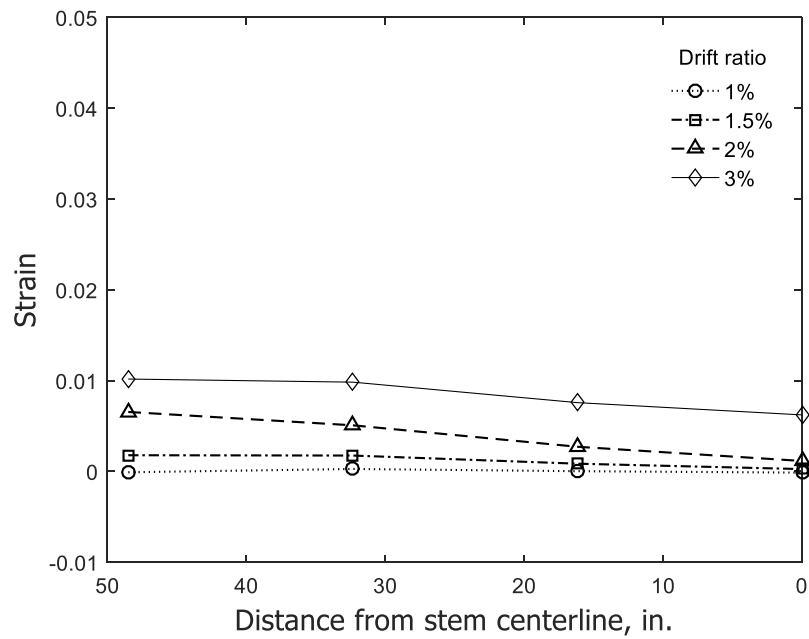


(b) Stem in tension

Figure 262 - Calculated concrete strain in Layer 4 for flange of T1 (1 in. = 25.4 mm)

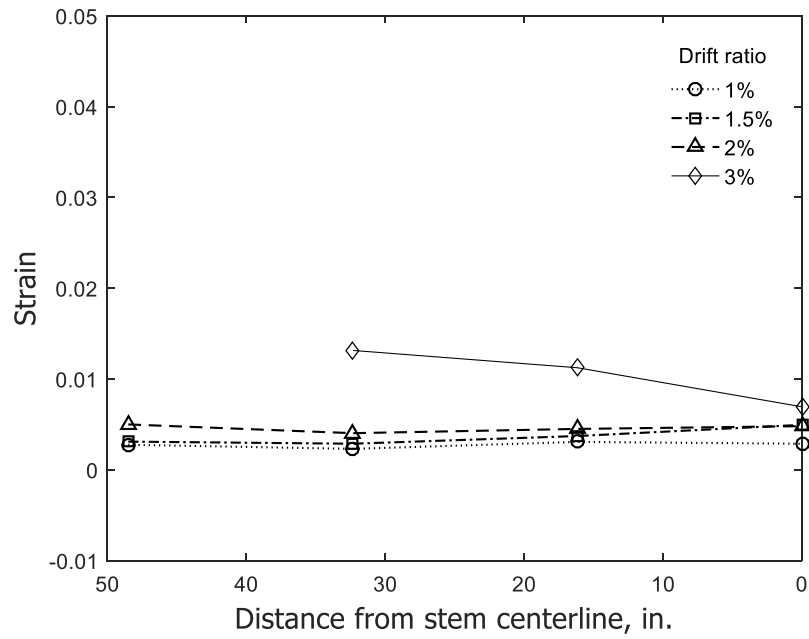


(a) Stem in compression

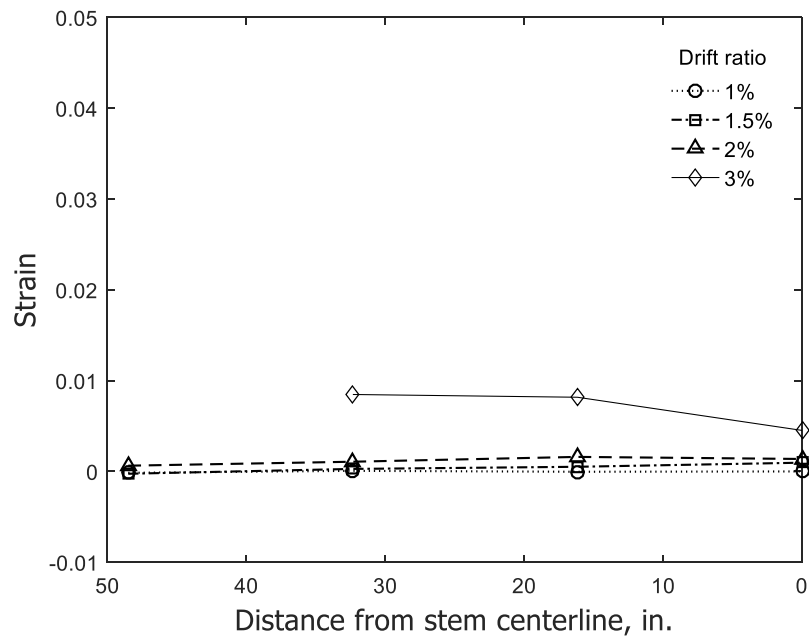


(b) Stem in tension

Figure 263 - Calculated concrete strain in Layer 5 for flange of T1 (1 in. = 25.4 mm)

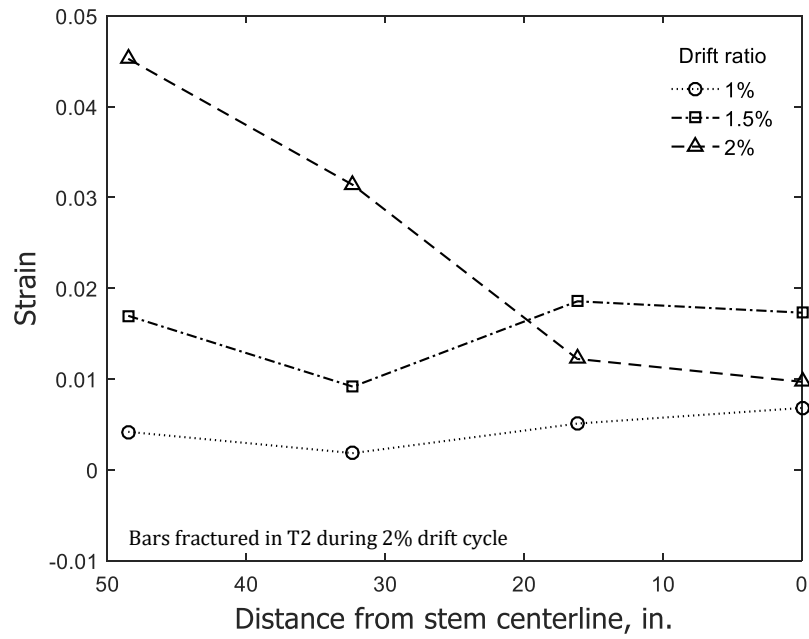


(a) Stem in compression

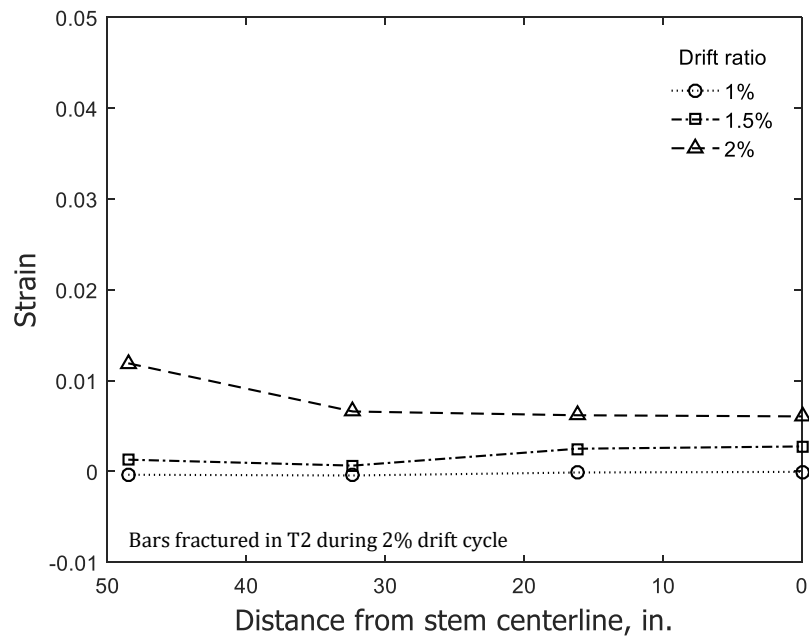


(b) Stem in tension

Figure 264 – Calculated concrete strain in Layer 6 for flange of T1 (1 in. = 25.4 mm)

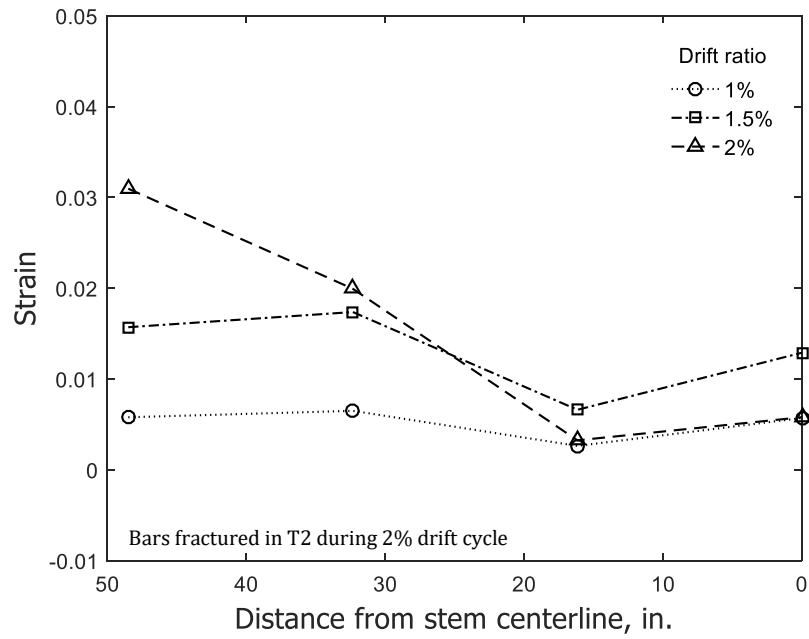


(a) Stem in compression

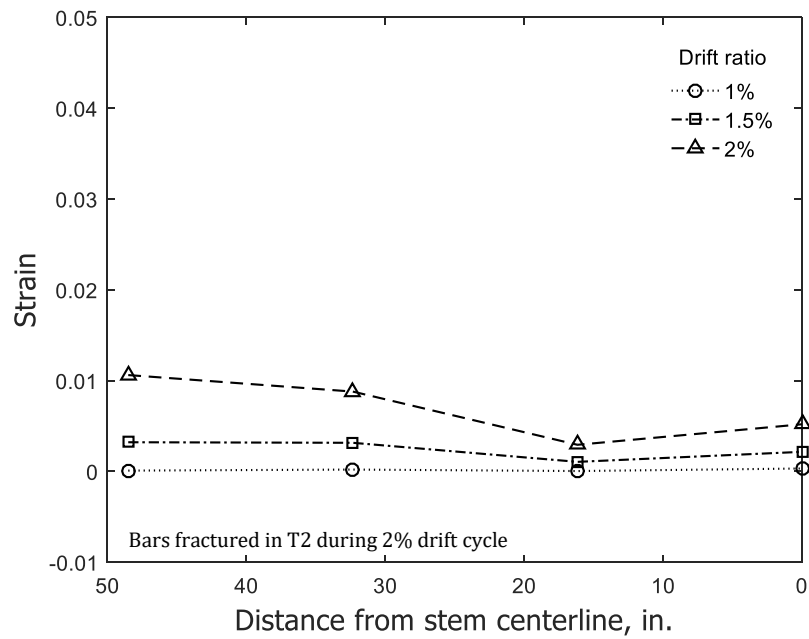


(b) Stem in tension

Figure 265 – Calculated concrete strain in Layer 1 for flange of T2 (1 in. = 25.4 mm)

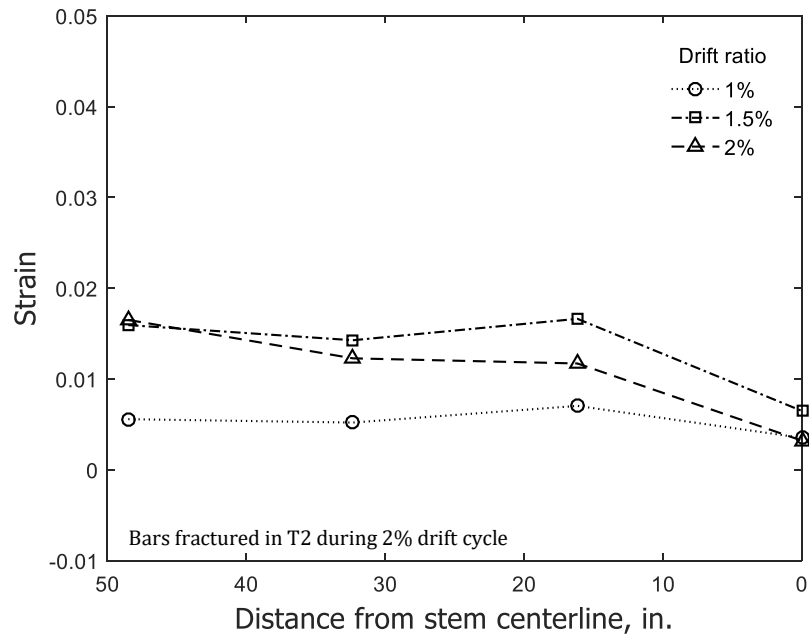


(a) Stem in compression

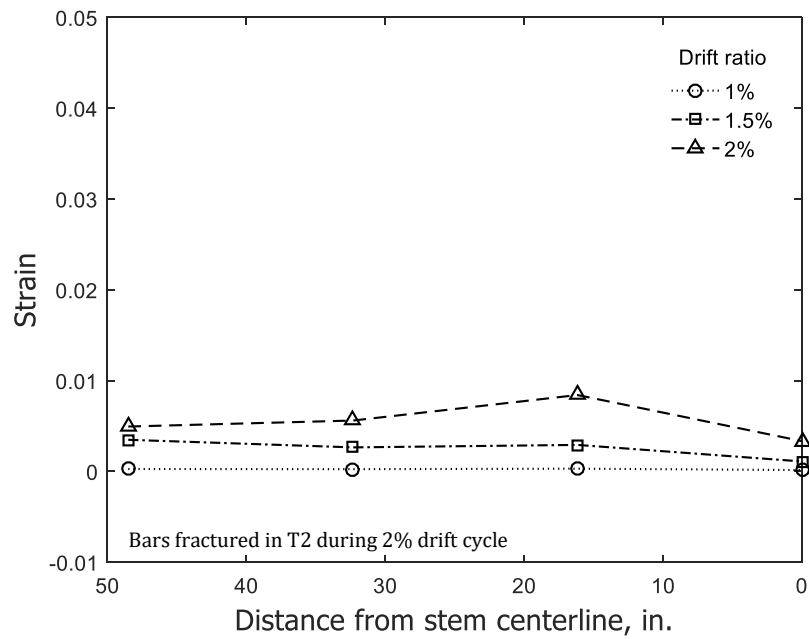


(b) Stem in tension

Figure 266 – Calculated concrete strain in Layer 2 for flange of T2 (1 in. = 25.4 mm)

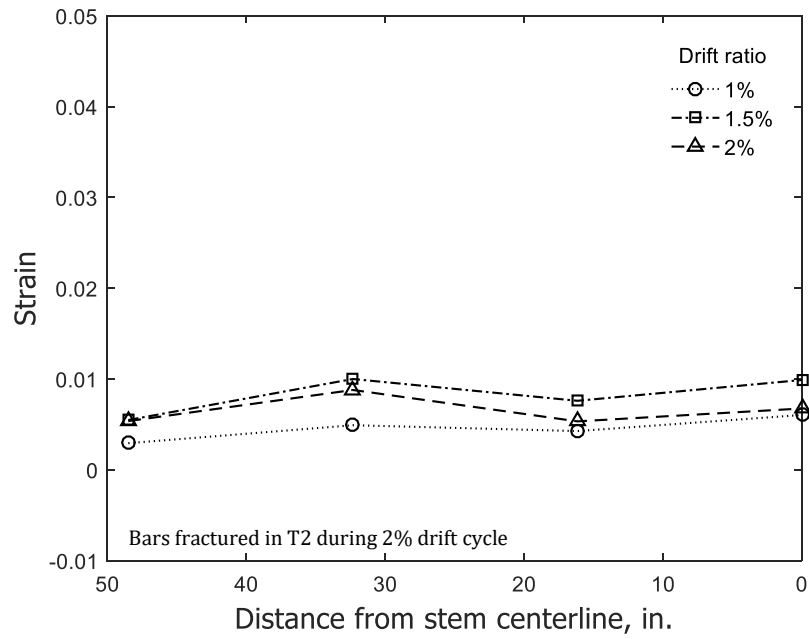


(a) Stem in compression

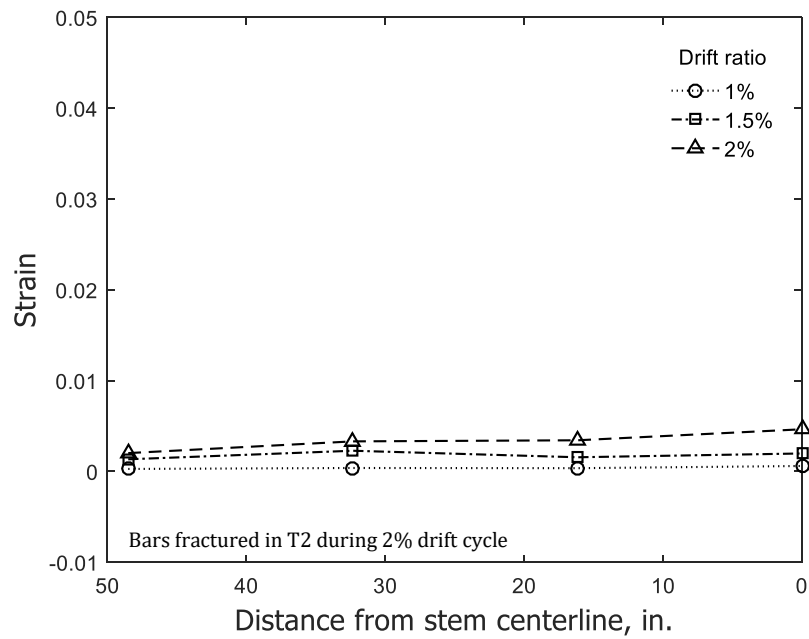


(b) Stem in tension

Figure 267 – Calculated concrete strain in Layer 3 for flange of T2 (1 in. = 25.4 mm)

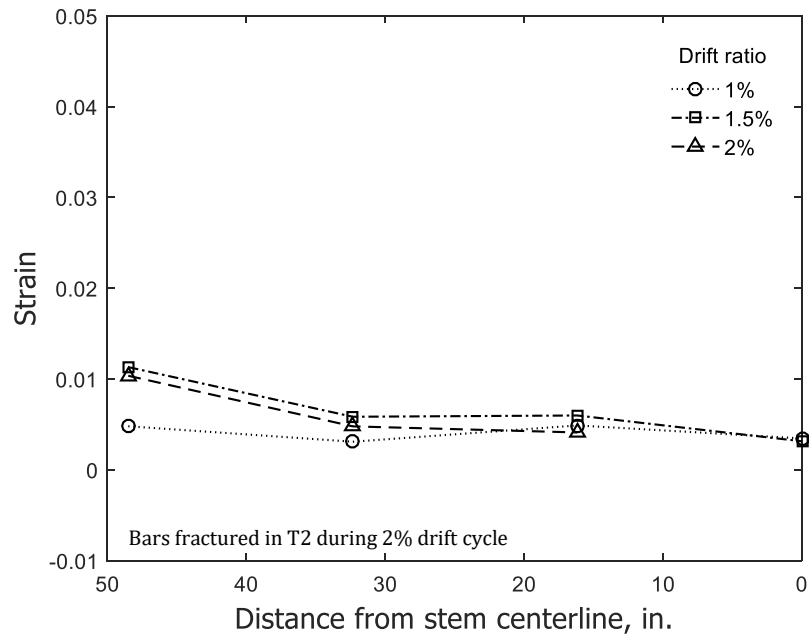


(a) Stem in compression

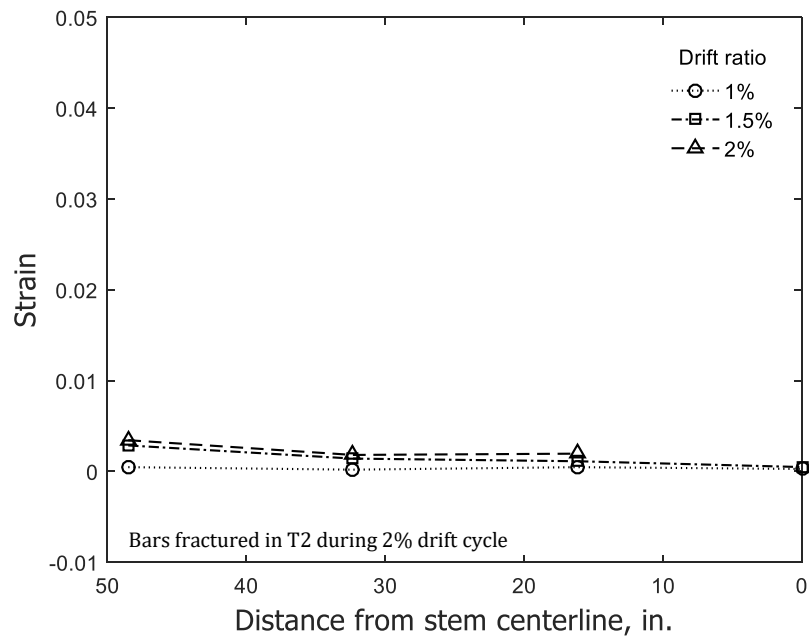


(b) Stem in tension

Figure 268 – Calculated concrete strain in Layer 4 for flange of T2 (1 in. = 25.4 mm)

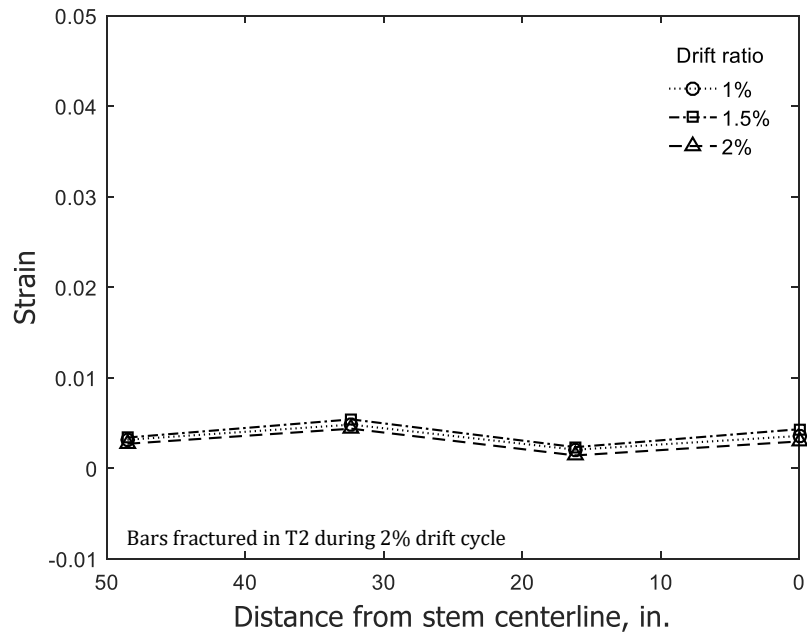


(a) Stem in compression

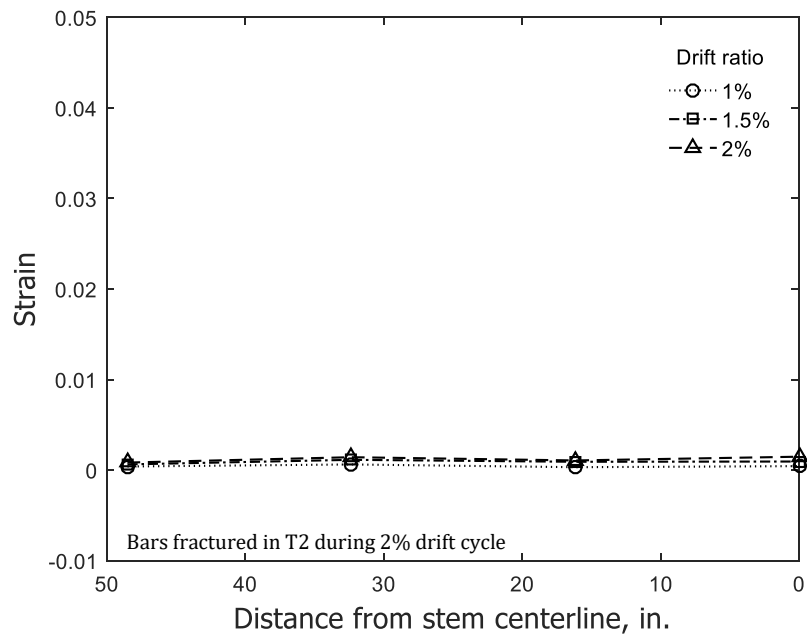


(b) Stem in tension

Figure 269 – Calculated concrete strain in Layer 5 for flange of T2 (1 in. = 25.4 mm)

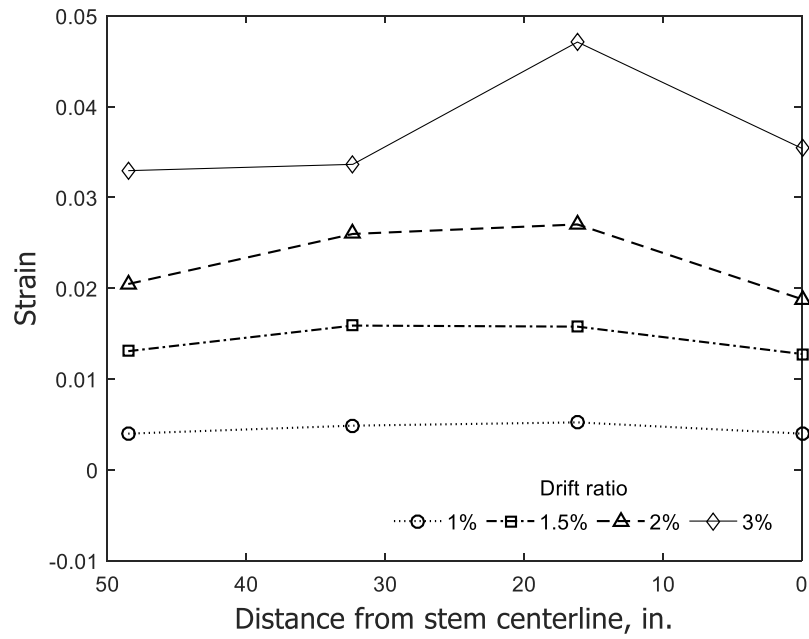


(a) Stem in compression

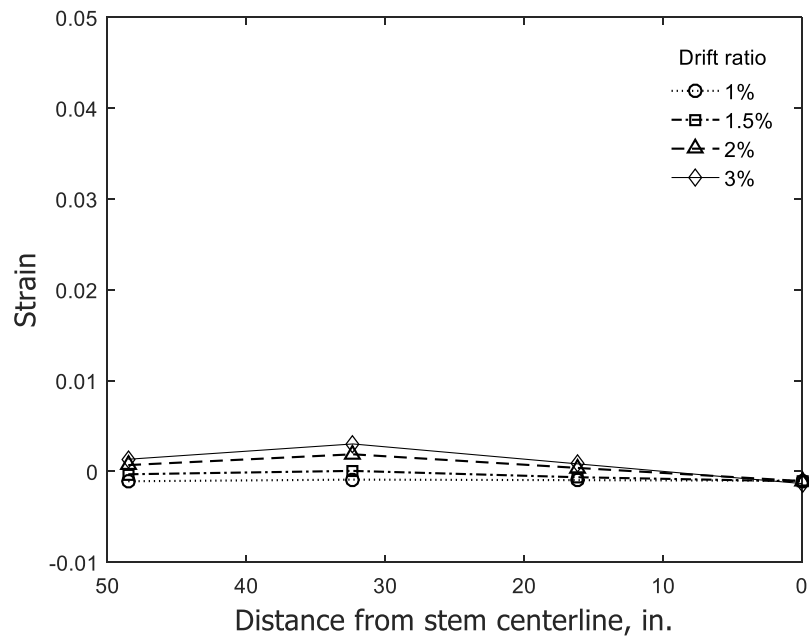


(b) Stem in tension

Figure 270 – Calculated concrete strain in Layer 6 for flange of T2 (1 in. = 25.4 mm)

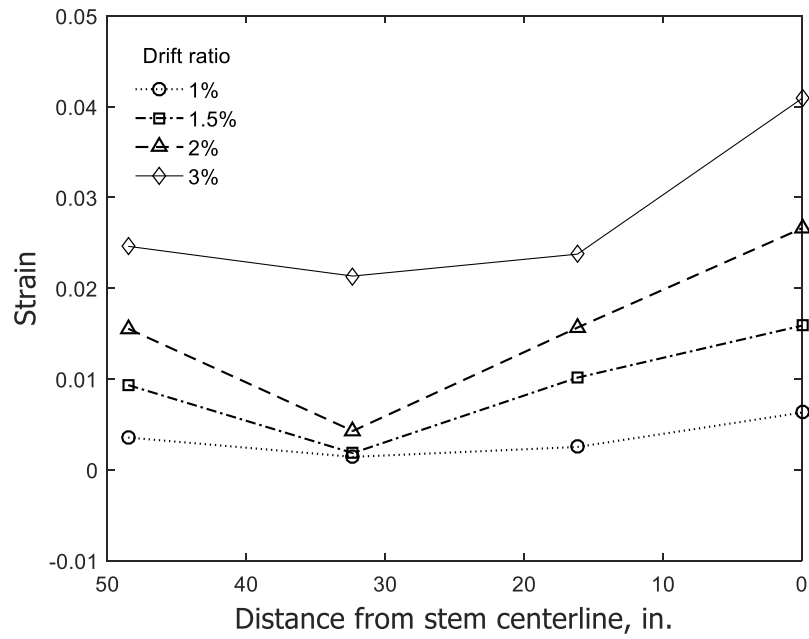


(a) Stem in compression

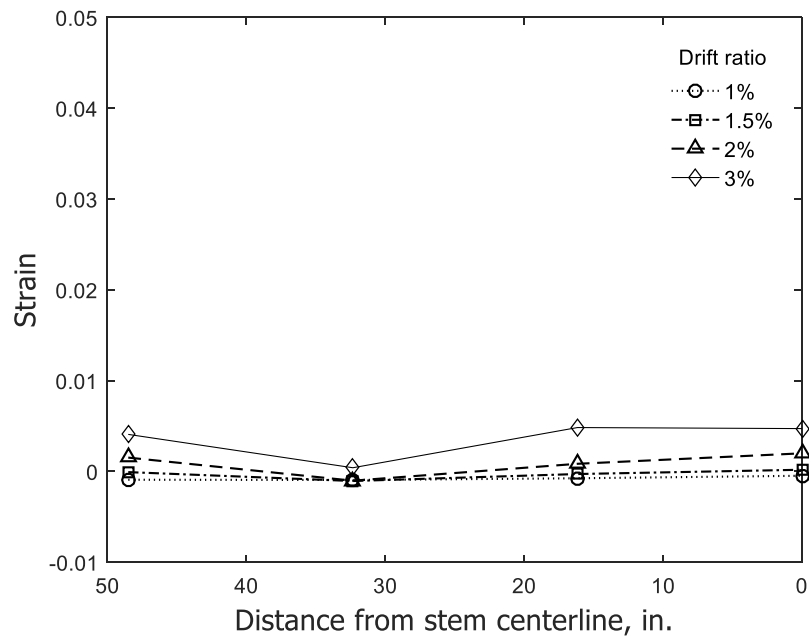


(b) Stem in tension

Figure 271 - Calculated concrete strain in Layer 1 for flange of T3 (1 in. = 25.4 mm)

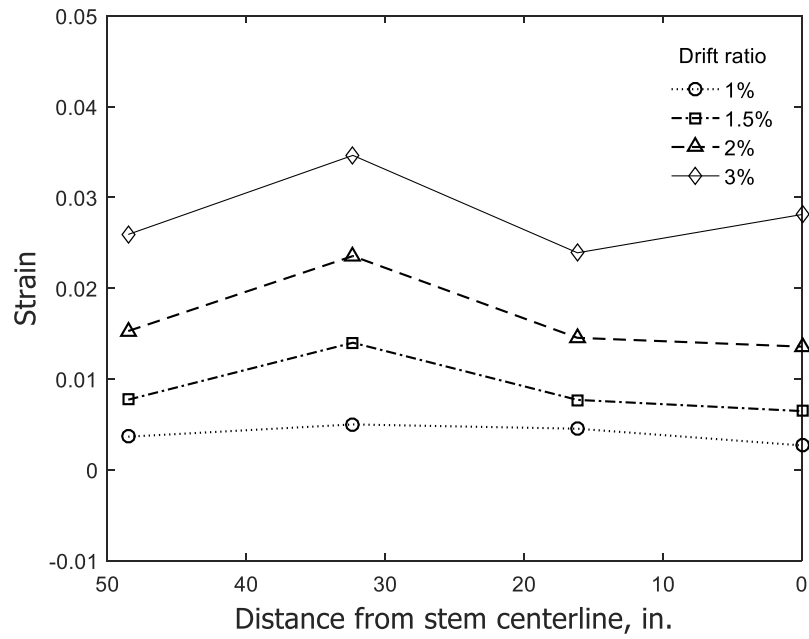


(a) Stem in compression

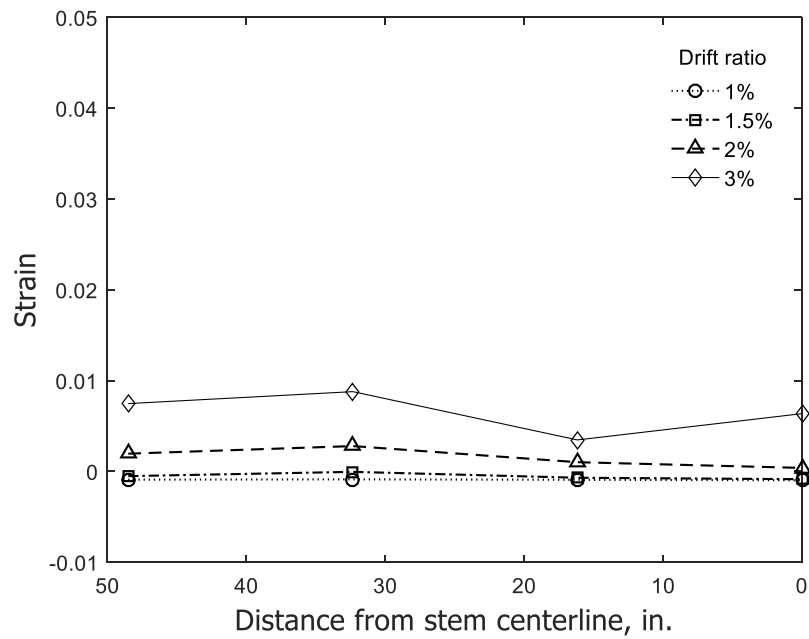


(b) Stem in tension

Figure 272 – Calculated concrete strain in Layer 2 for flange of T3 (1 in. = 25.4 mm)

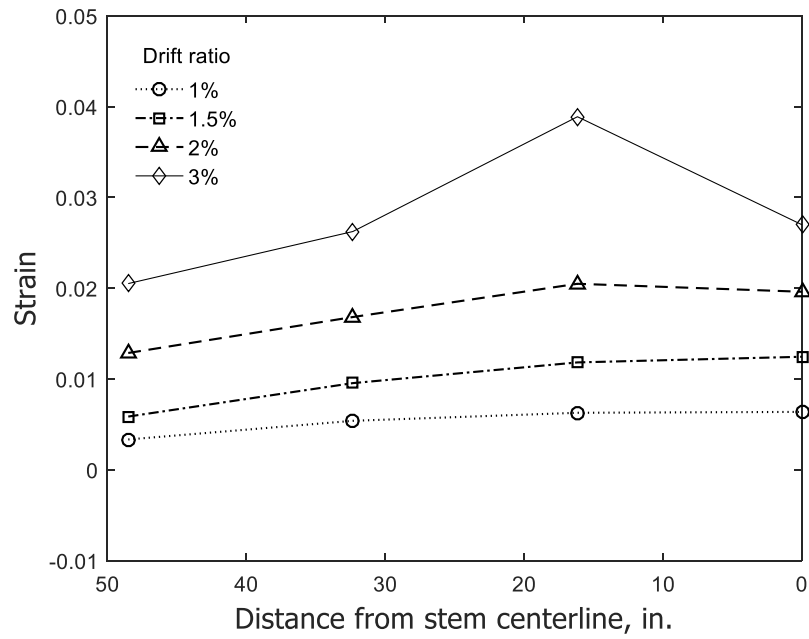


(a) Stem in compression

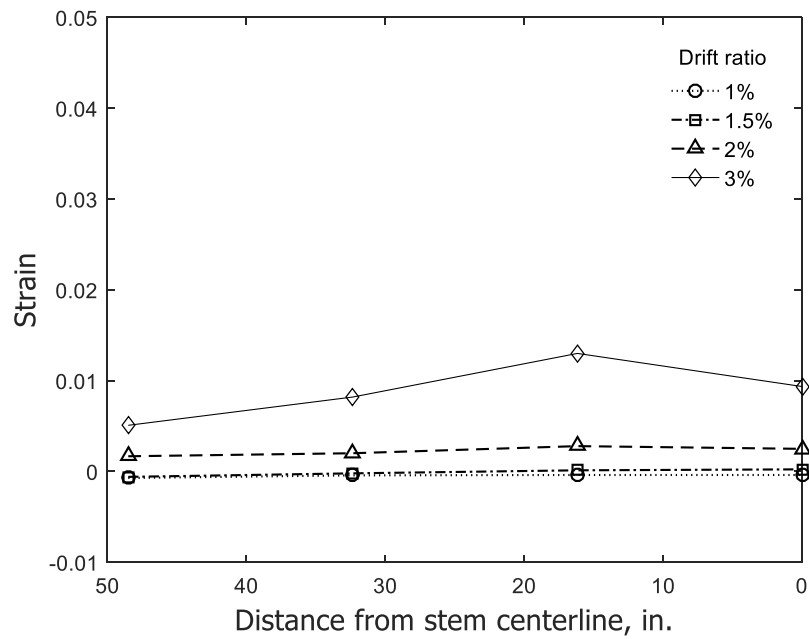


(b) Stem in tension

Figure 273 – Calculated concrete strain in Layer 3 for flange of T3 (1 in. = 25.4 mm)

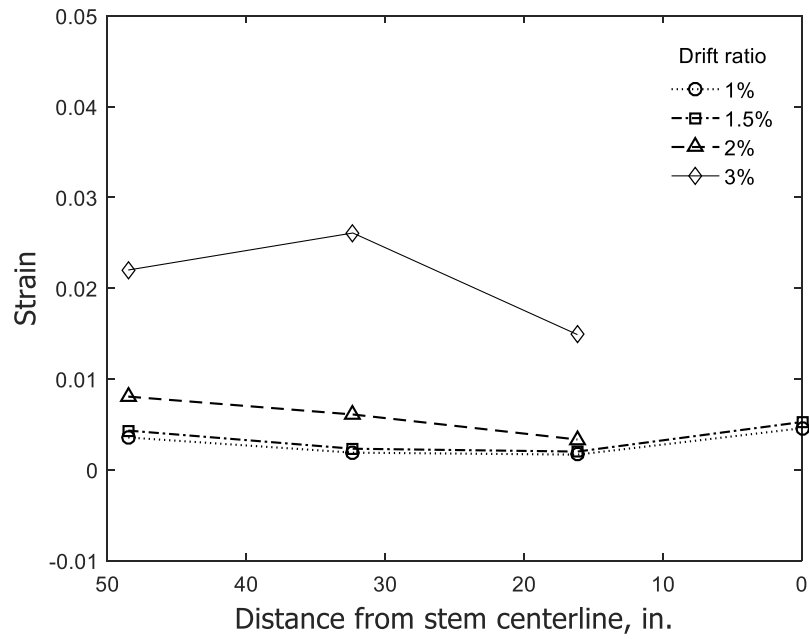


(a) Stem in compression

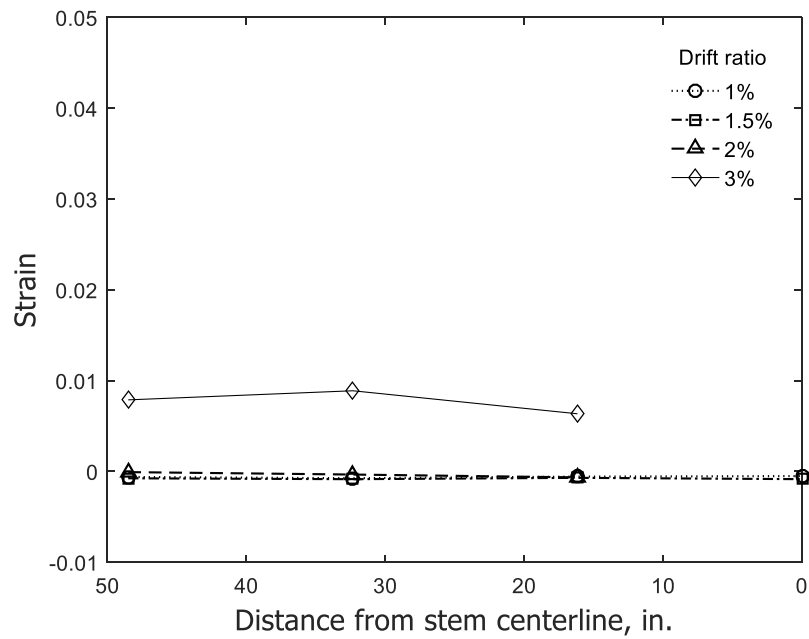


(b) Stem in tension

Figure 274 – Calculated concrete strain in Layer 4 for flange of T3 (1 in. = 25.4 mm)

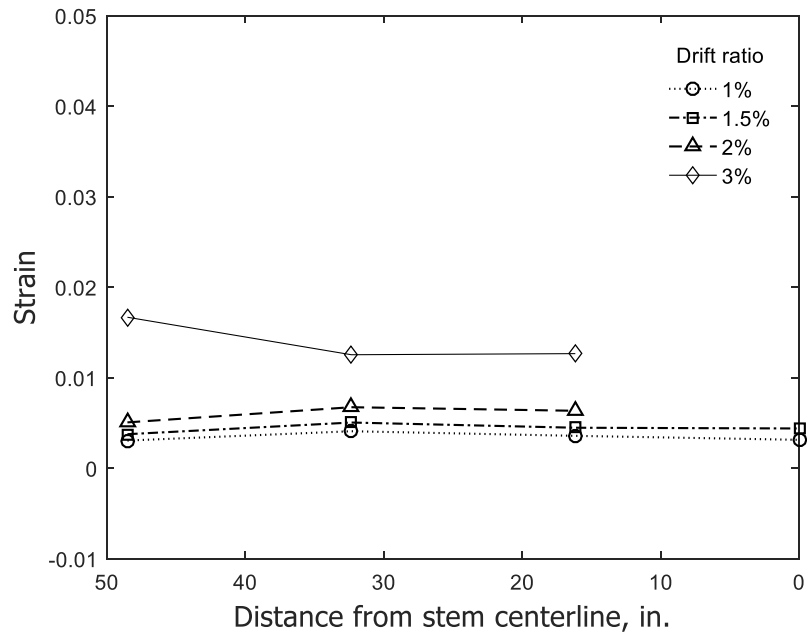


(a) Stem in compression

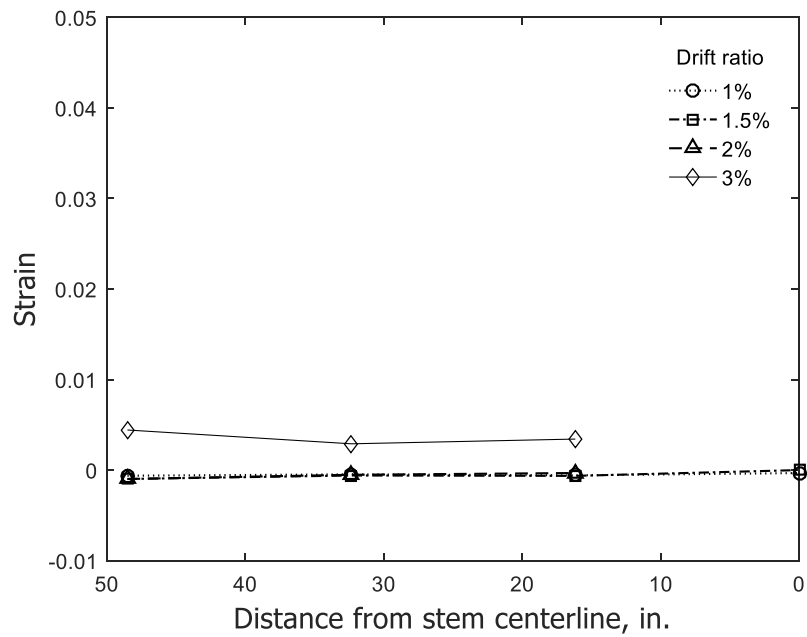


(b) Stem in tension

Figure 275 – Calculated concrete strain in Layer 5 for flange of T3 (1 in. = 25.4 mm)

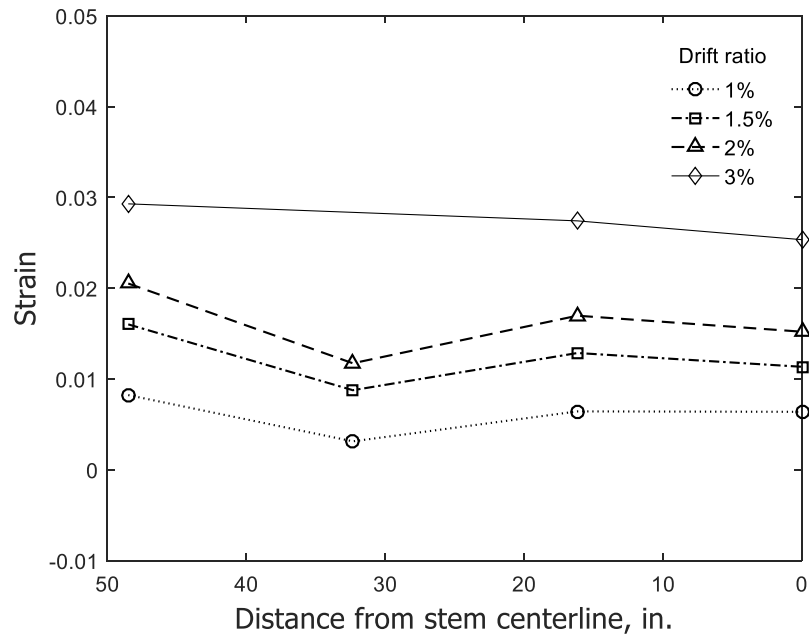


(a) Stem in compression

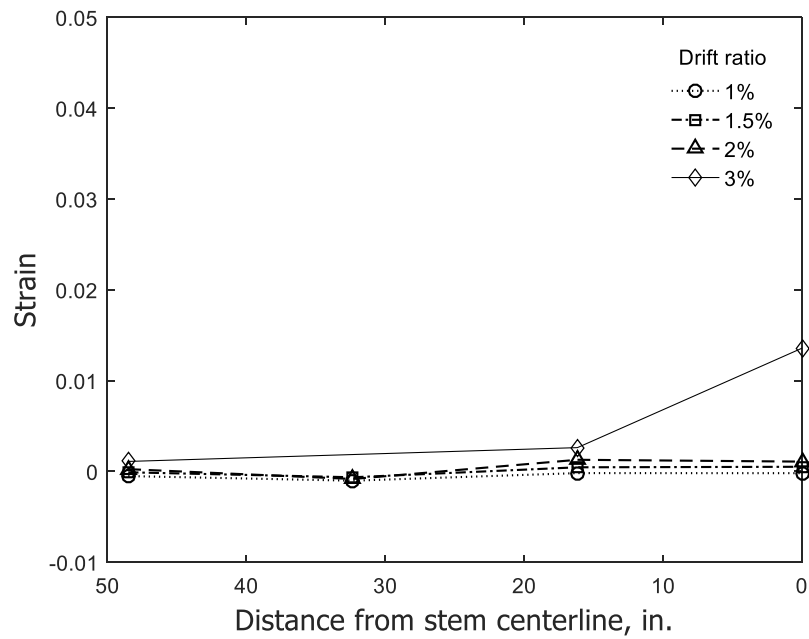


(b) Stem in tension

Figure 276 – Calculated concrete strain in Layer 6 for flange of T3 (1 in. = 25.4 mm)

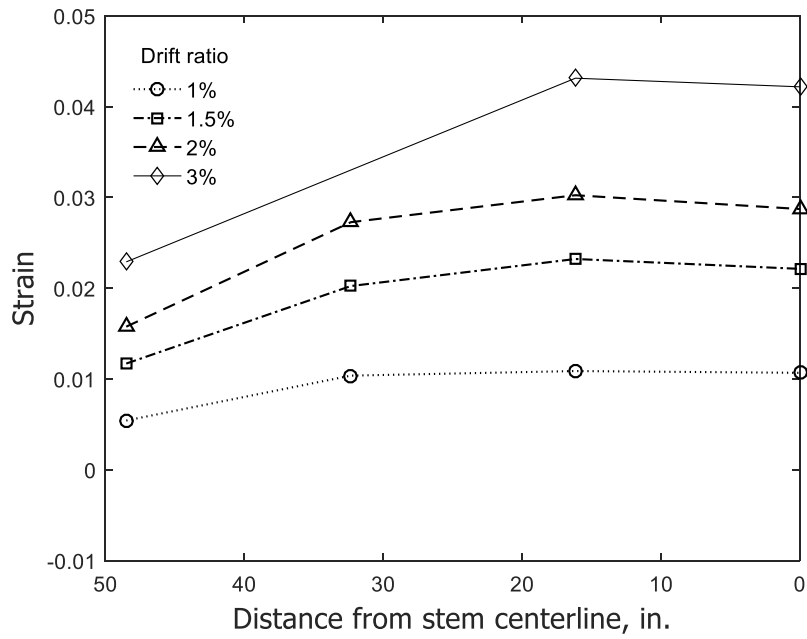


(a) Stem in compression

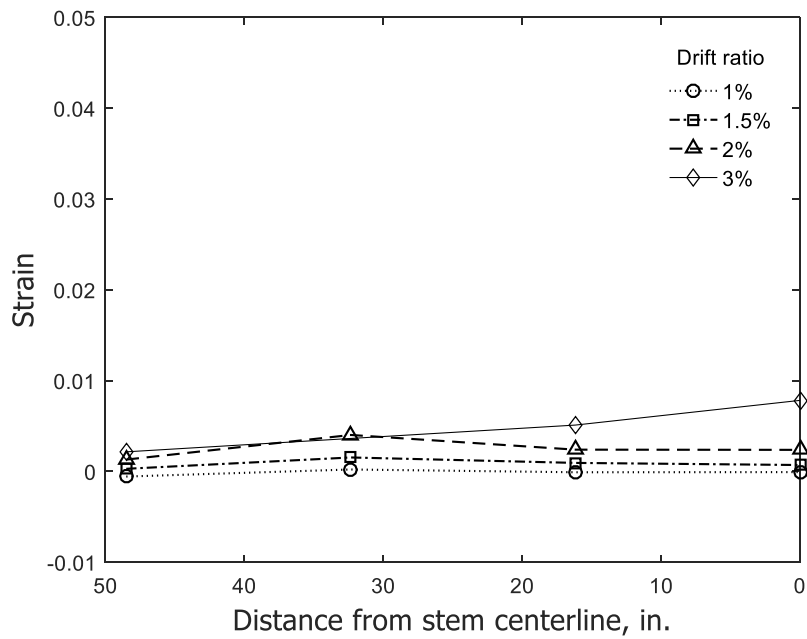


(b) Stem in tension

Figure 277 – Calculated concrete strain in Layer 1 for flange of T4 (1 in. = 25.4 mm)

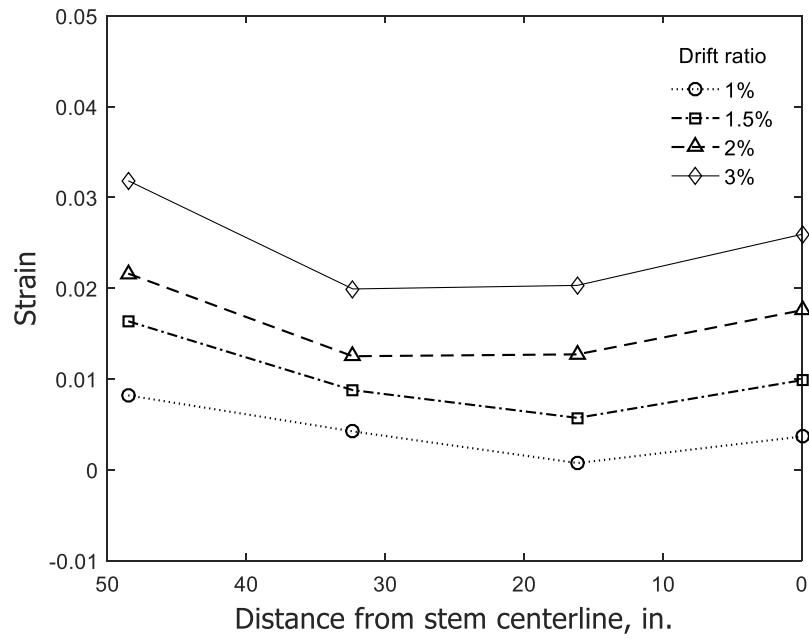


(a) Stem in compression

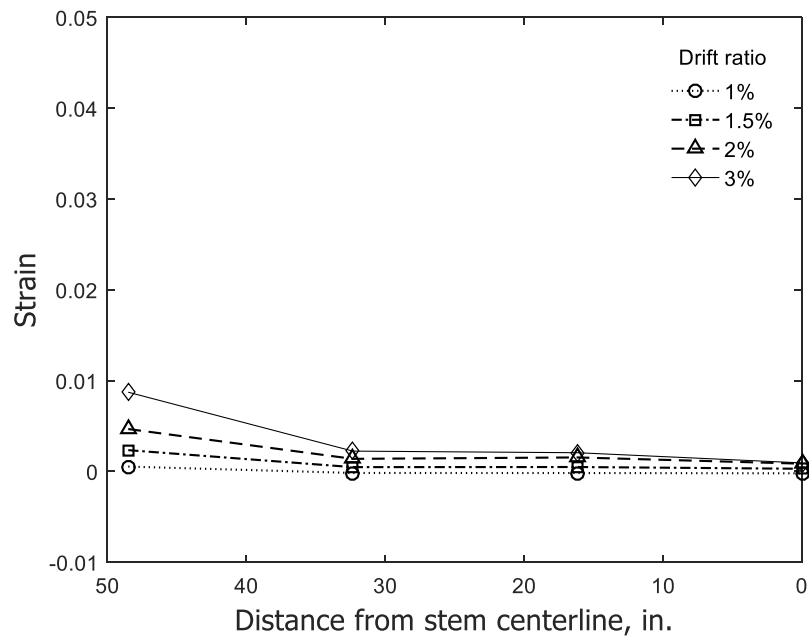


(b) Stem in tension

Figure 278 – Calculated concrete strain in Layer 2 for flange of T4 (1 in. = 25.4 mm)

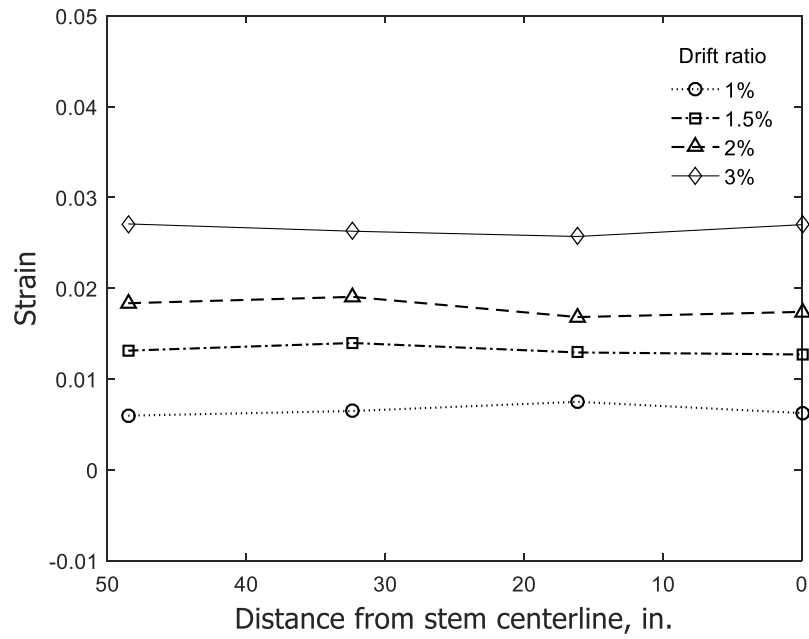


(a) Stem in compression

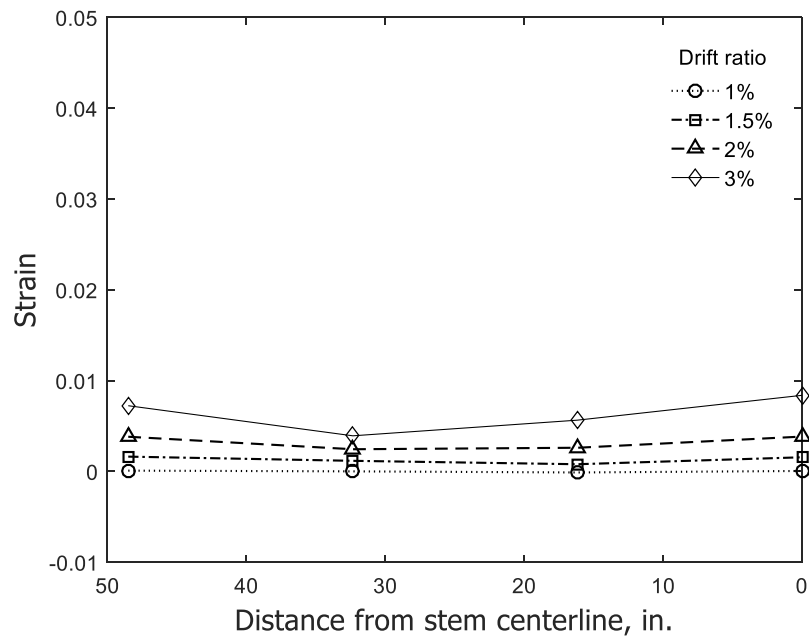


(b) Stem in tension

Figure 279 – Calculated concrete strain in Layer 3 for flange of T4 (1 in. = 25.4 mm)

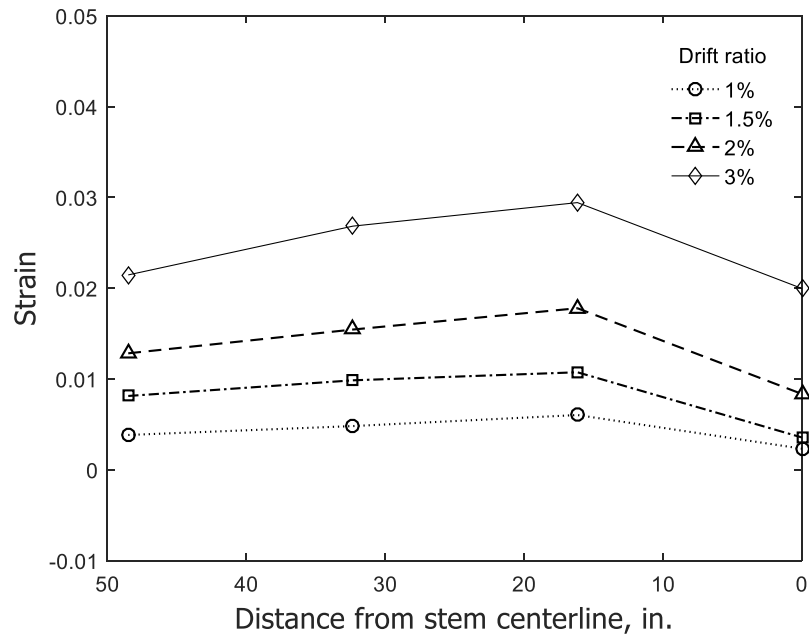


(a) Stem in compression

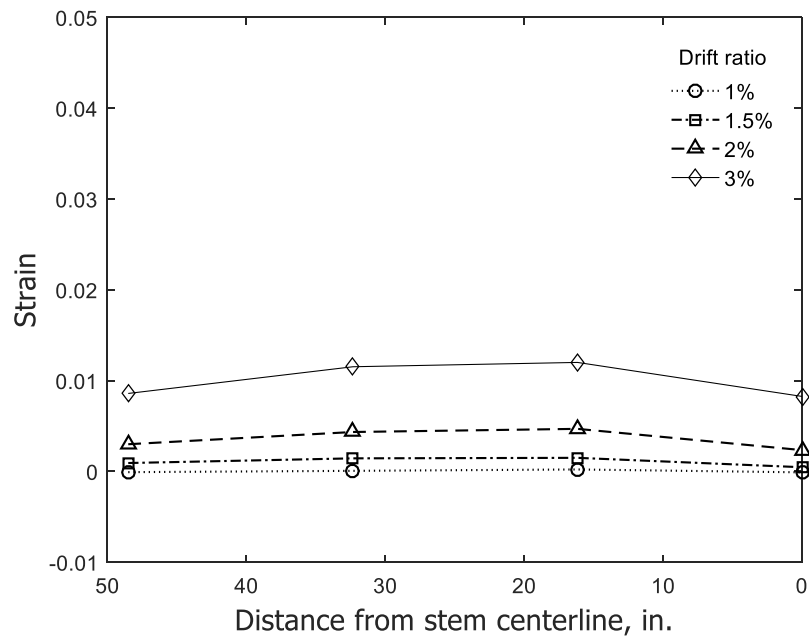


(b) Stem in tension

Figure 280 – Calculated concrete strain in Layer 4 for flange of T4 (1 in. = 25.4 mm)

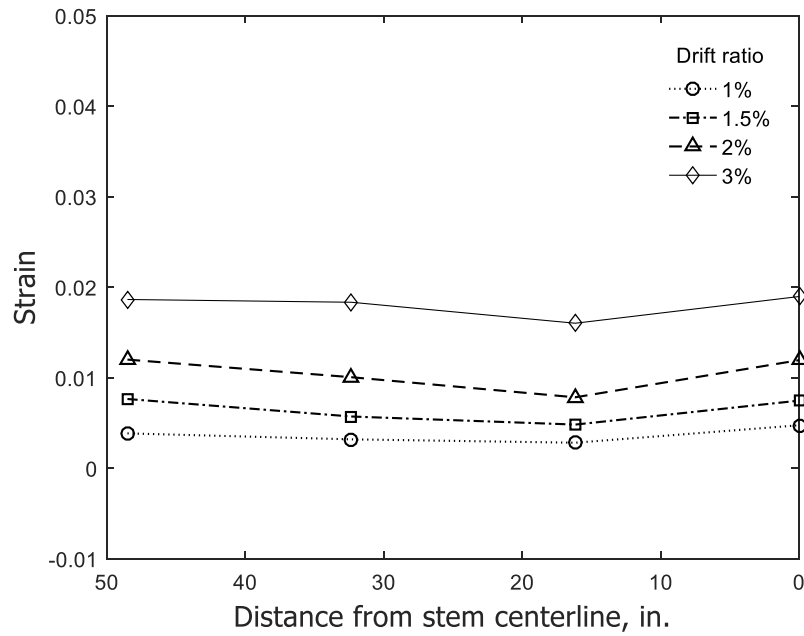


(a) Stem in compression

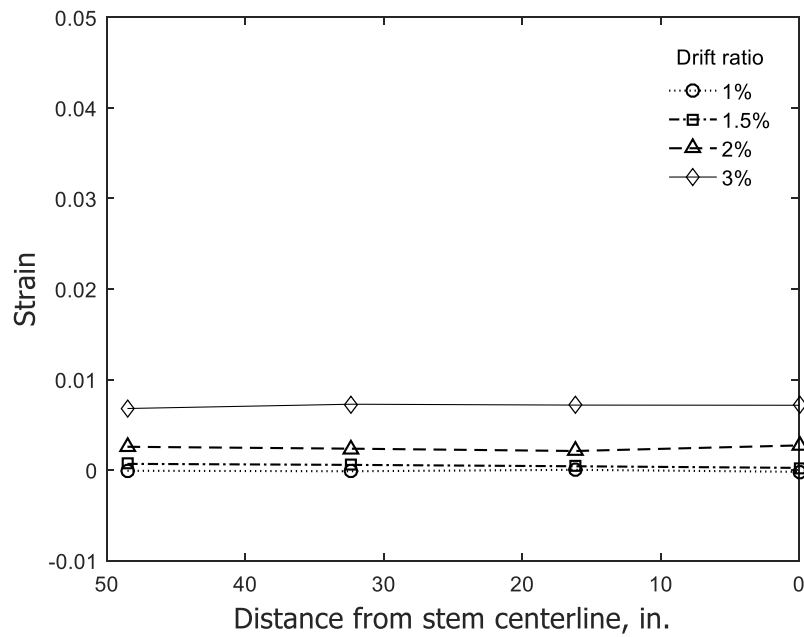


(b) Stem in tension

Figure 281 - Calculated concrete strain in Layer 5 for flange of T4 (1 in. = 25.4 mm)

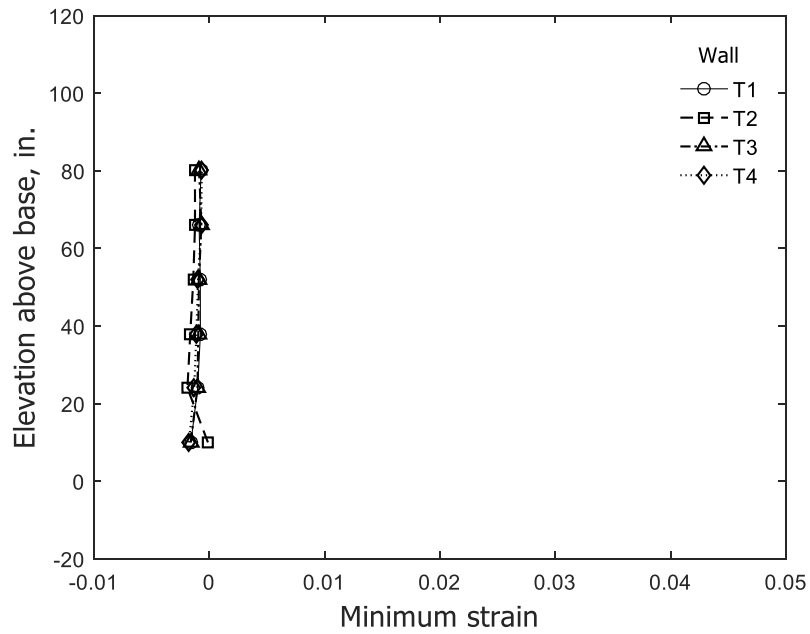


(a) Stem in compression

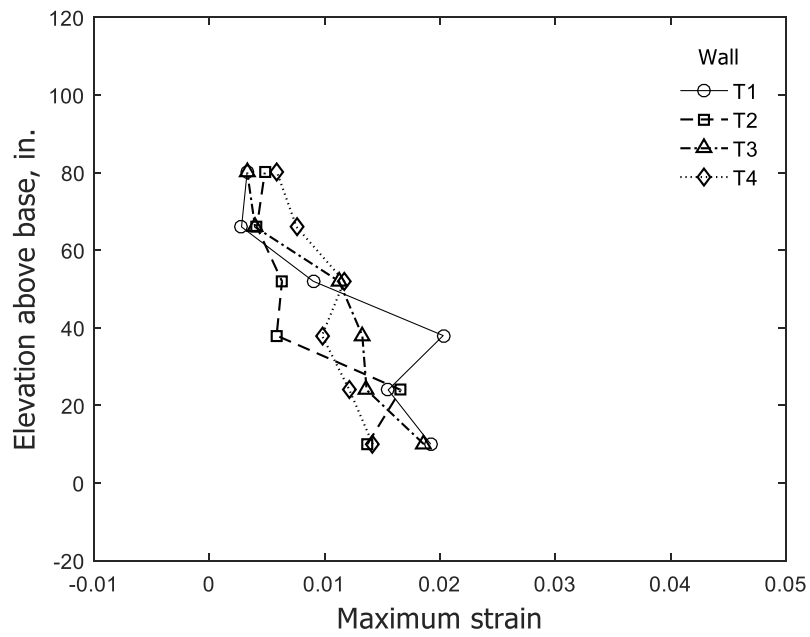


(b) Stem in tension

Figure 282 – Calculated concrete strain in Layer 6 for flange of T4 (1 in. = 25.4 mm)

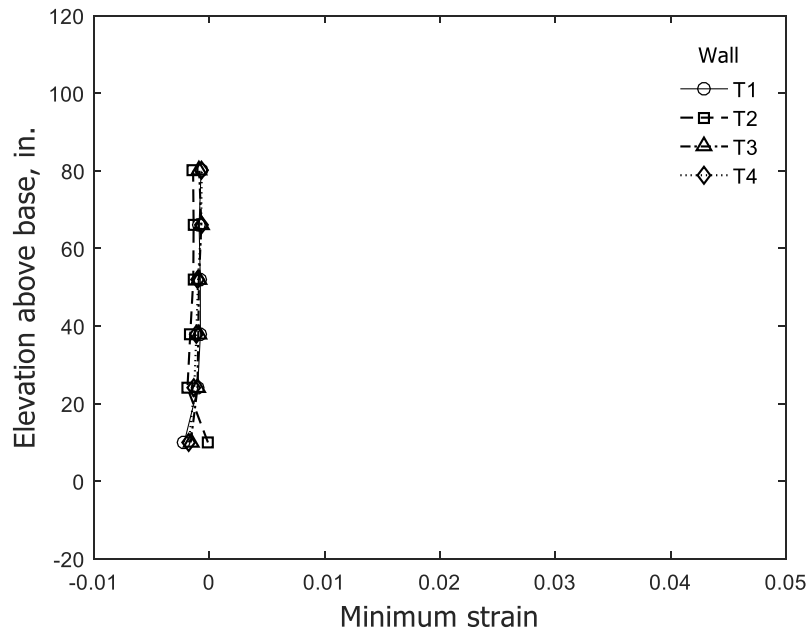


(a) Stem in compression

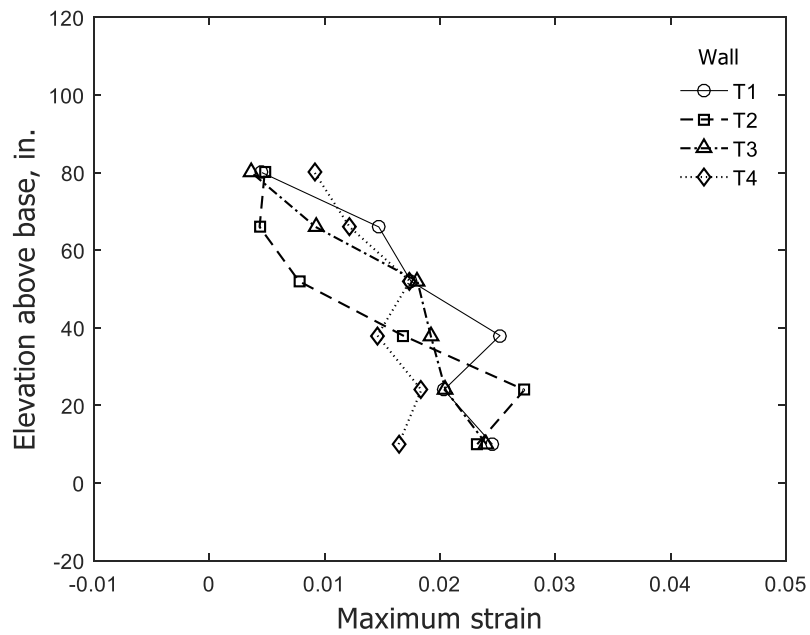


(b) Stem in tension

Figure 283 – Envelope of concrete strain for confined stem at 1.5% drift ratio (data from optical markers along Columns 1 and 2) (1 in. = 25.4 mm)

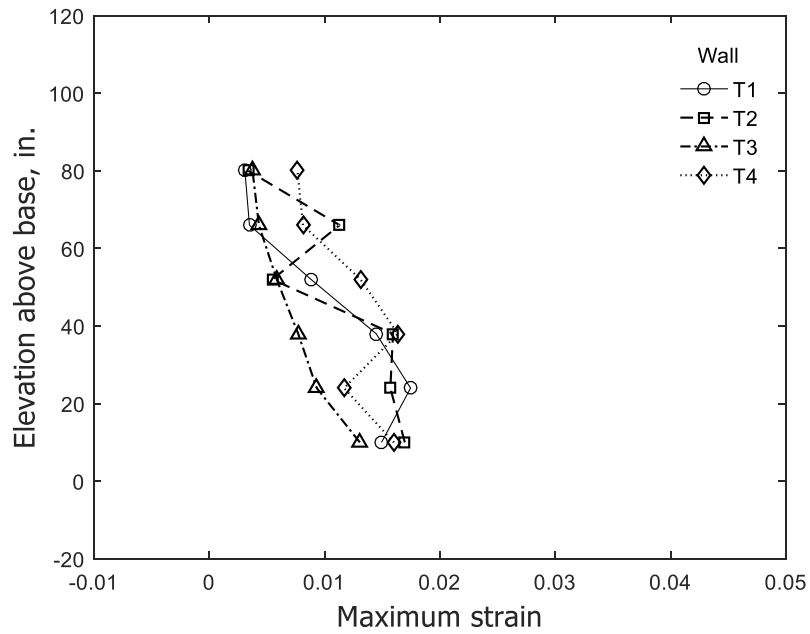


(a) Stem in compression

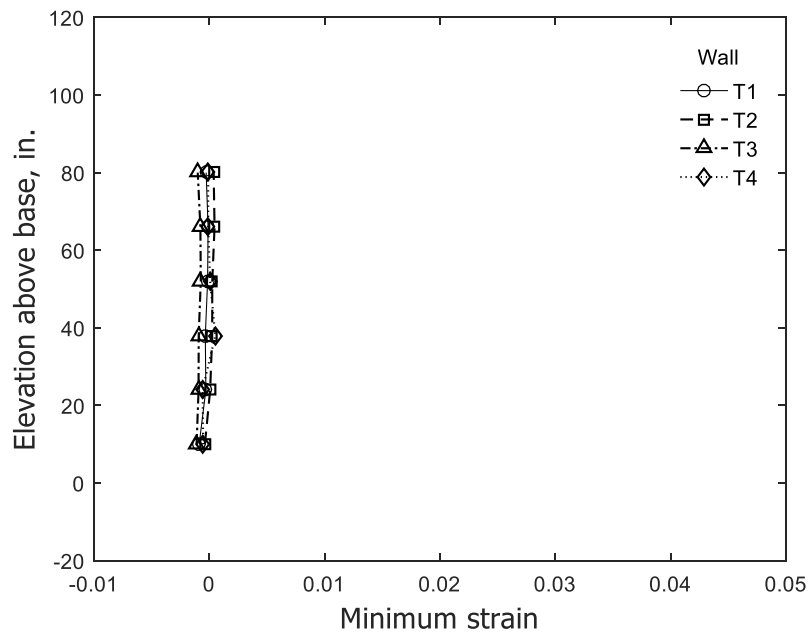


(b) Stem in tension

Figure 284 – Envelope of concrete strain for confined stem at 2% drift ratio (data from optical markers along Columns 1 and 2) (1 in. = 25.4 mm)

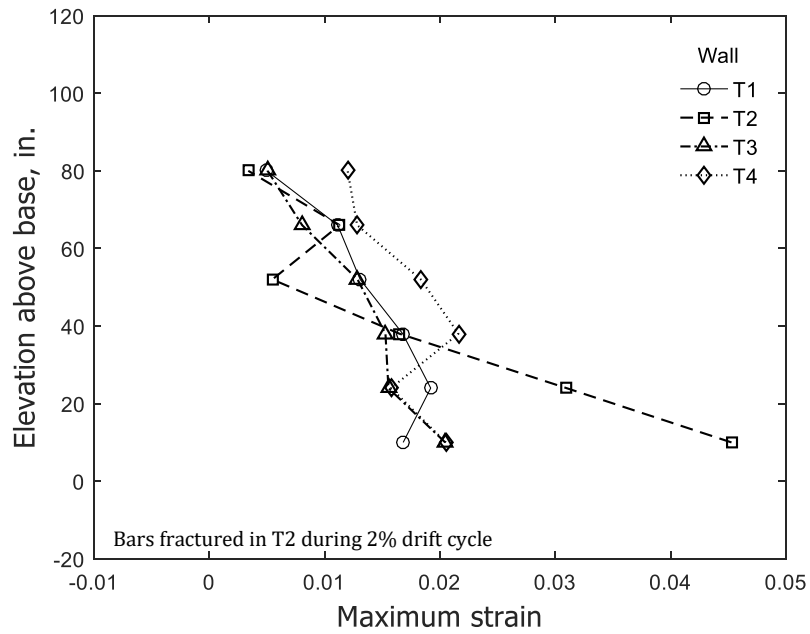


(a) Stem in compression

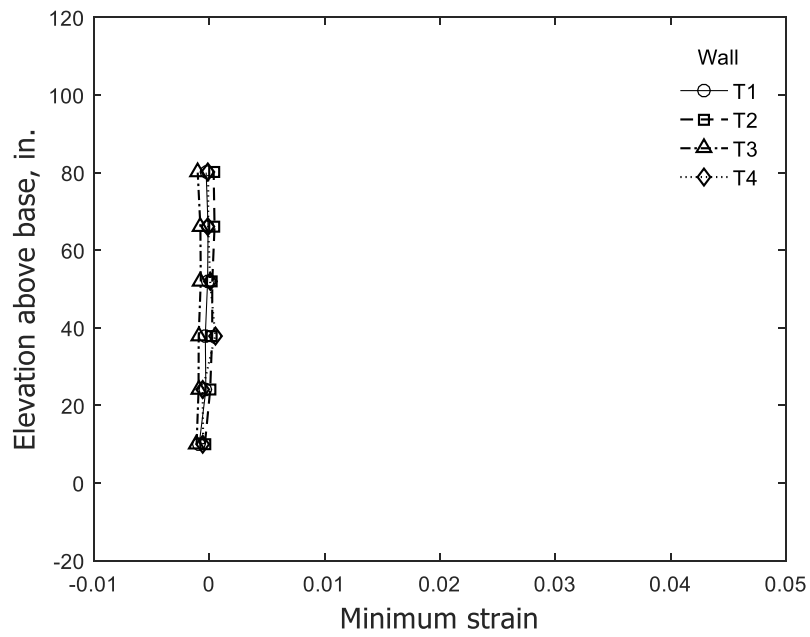


(b) Stem in tension

Figure 285 – Envelope of concrete strain for confined flange at 1.5% drift ratio (data from optical markers along Column 11) (1 in. = 25.4 mm)

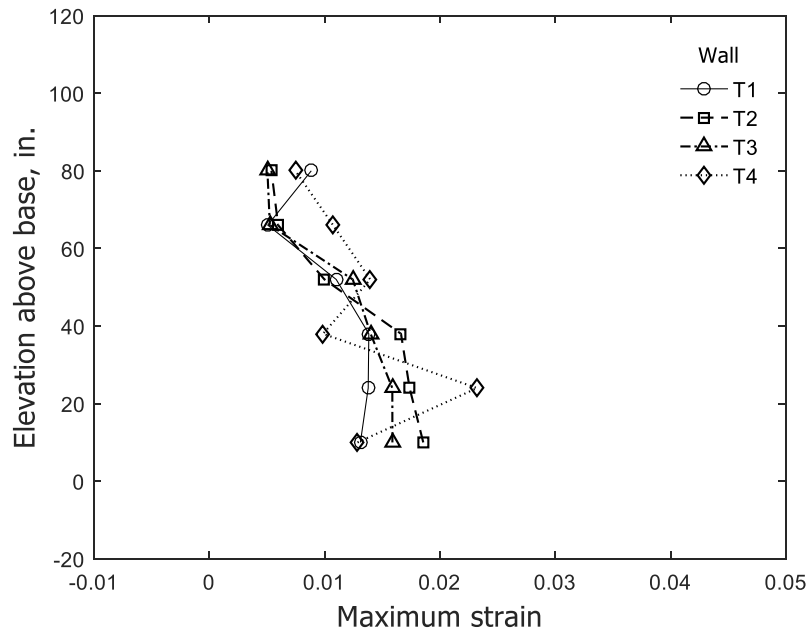


(a) Stem in compression

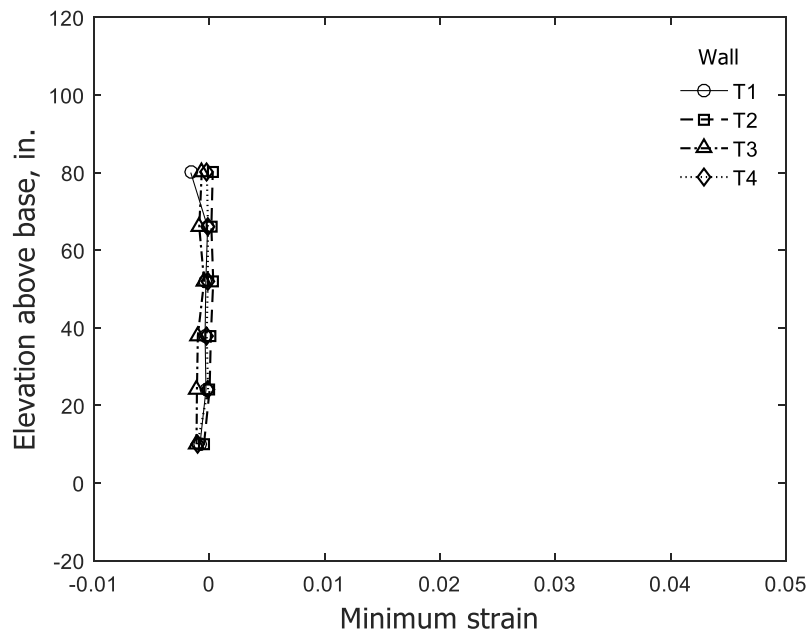


(b) Stem in tension

Figure 286 – Envelope of concrete strain for confined flange at 2% drift ratio (data from optical markers along Column 11) (1 in. = 25.4 mm)

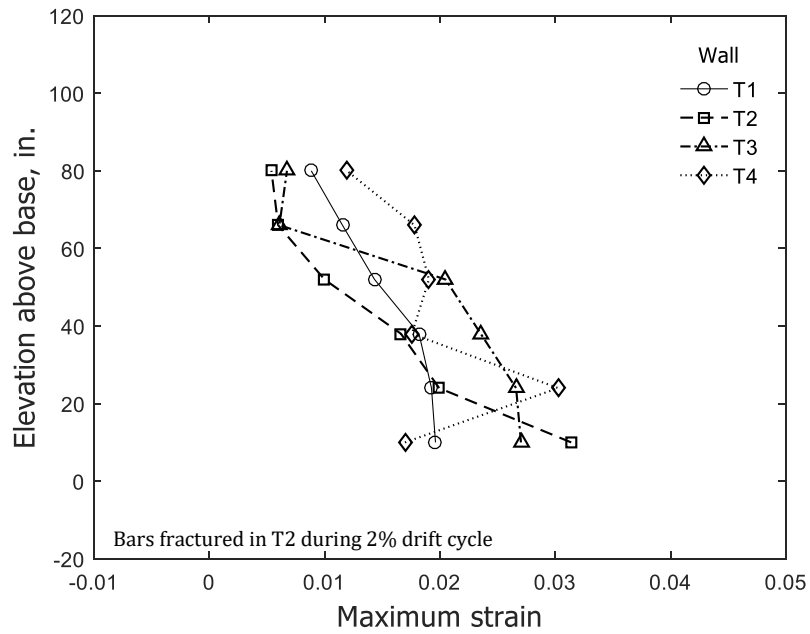


(a) Stem in compression

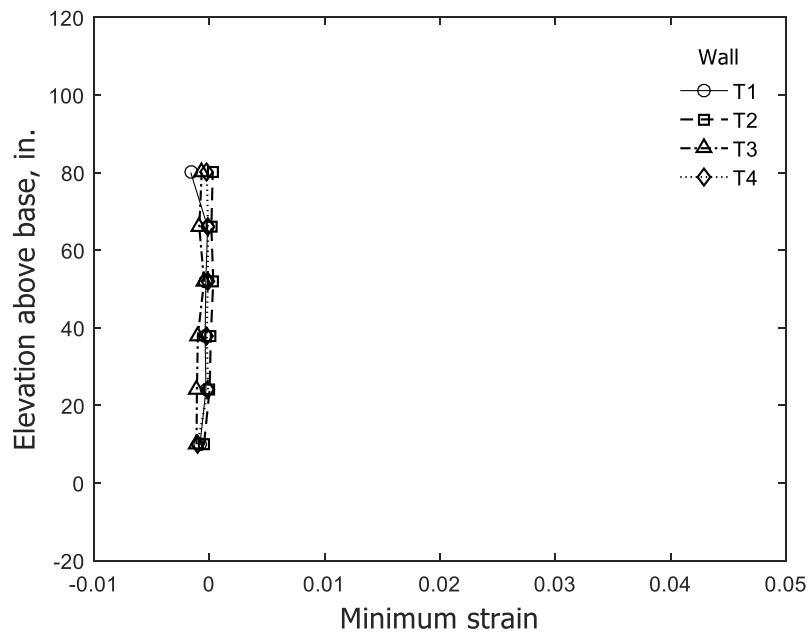


(b) Stem in tension

Figure 287 – Envelope of concrete strain for unconfined flange at 1.5% drift ratio (data from optical markers along Columns 8, 9, and 10) (1 in. = 25.4 mm)



(a) Stem in compression



(b) Stem in tension

Figure 288 – Envelope of concrete strain for unconfined flange at 2% drift ratio (data from optical markers along Columns 8, 9, and 10) (1 in. = 25.4 mm)

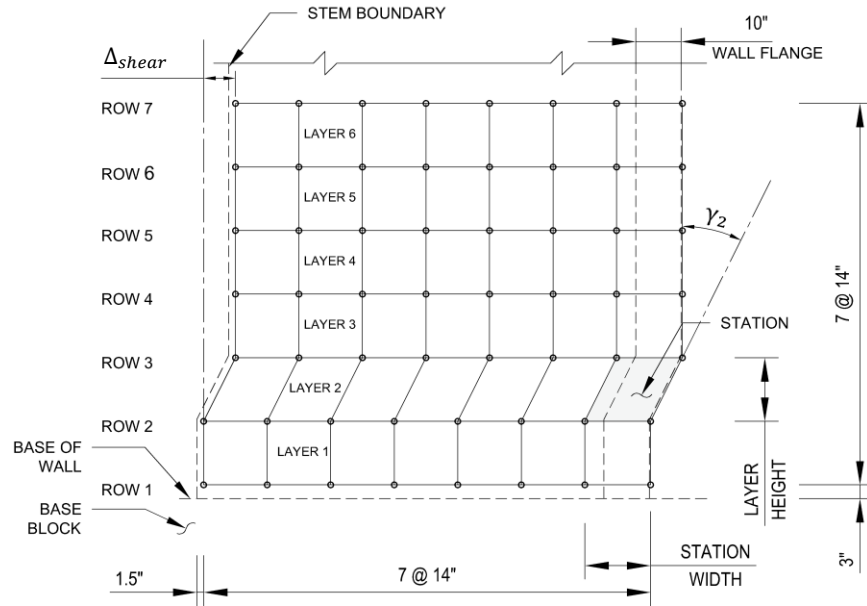


Figure 289 – Displacement Δ_{shear} due to shear distortion of Layer 2 (1 in. = 25.4 mm)

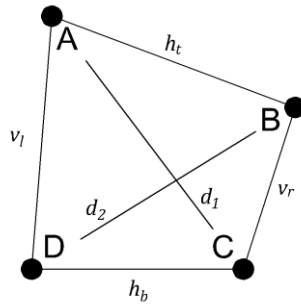


Figure 290 – General deformed shape of a station

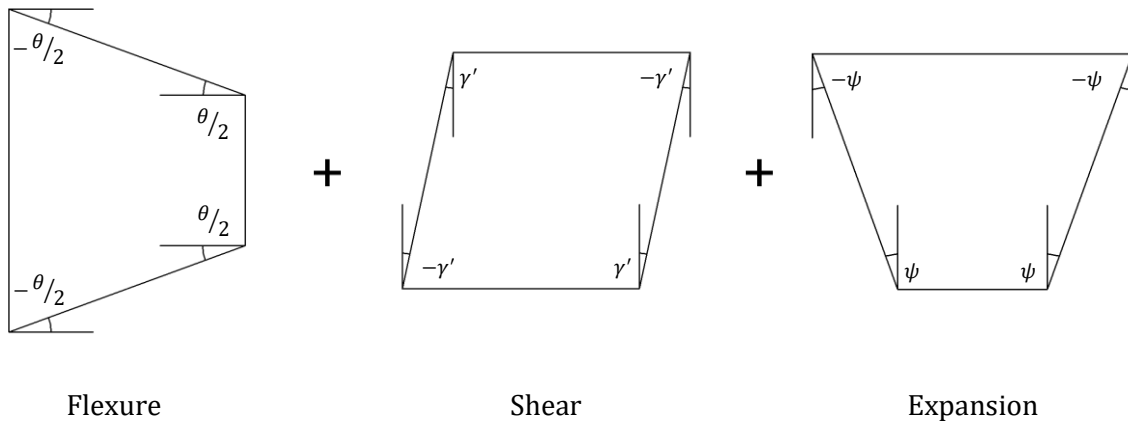
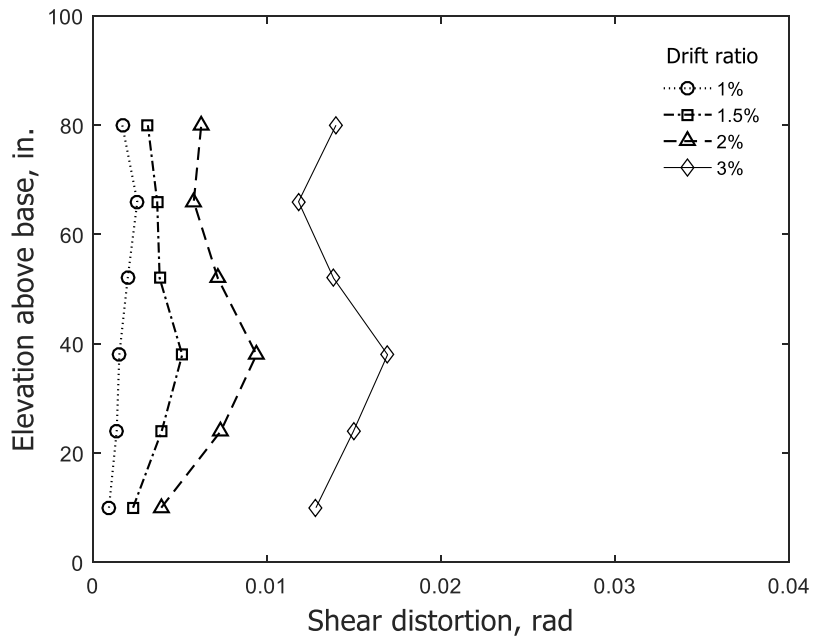
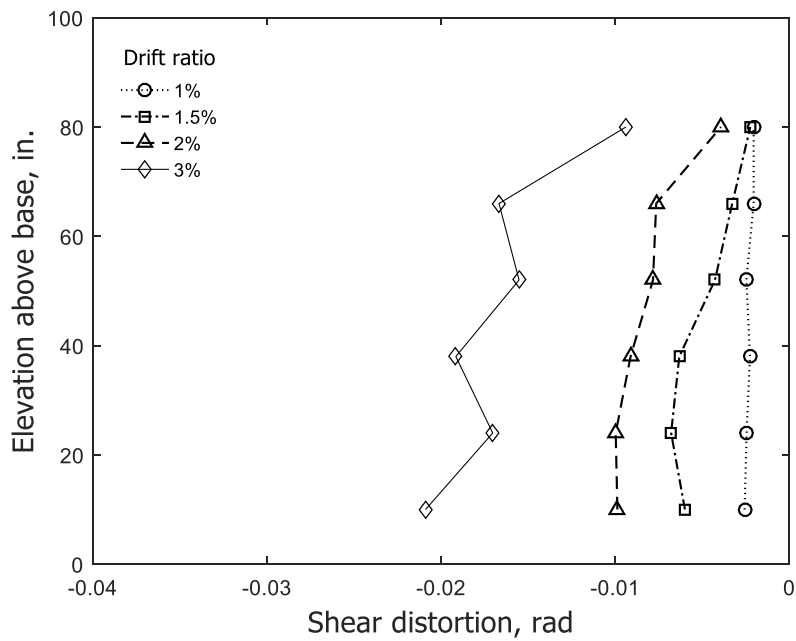


Figure 291 – Components of angular change for a station

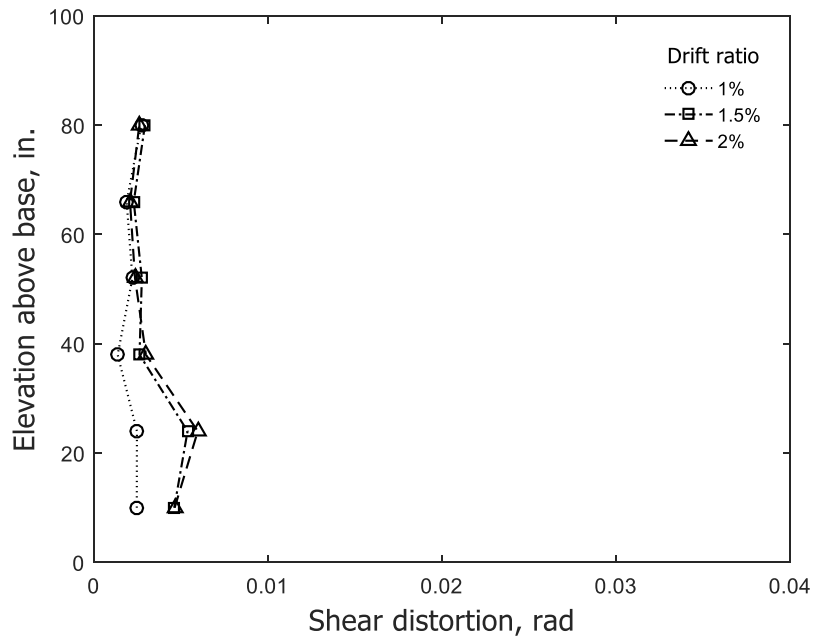


(a) Stem in compression

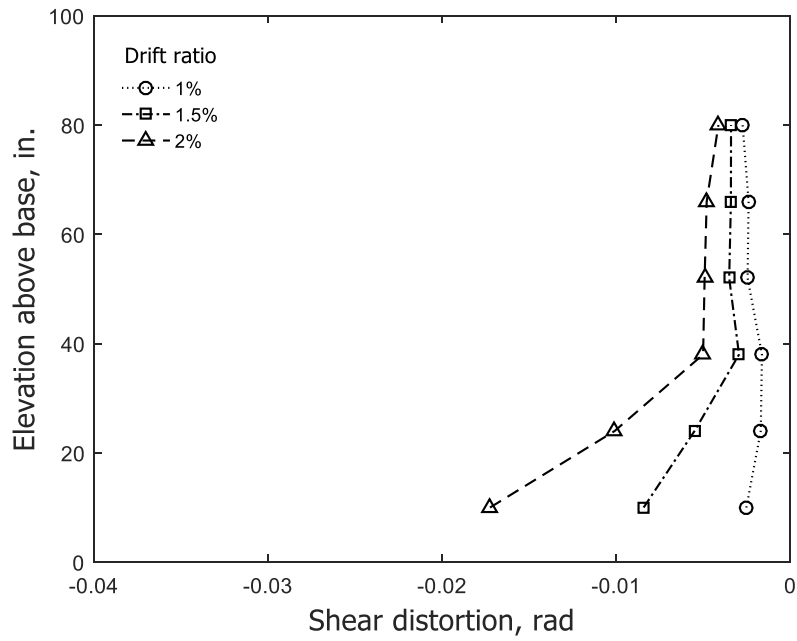


(b) Stem in tension

Figure 292 – Calculated shear distortion for T1 (data from optical markers, Columns 1 through 8) (1 in. = 25.4 mm)

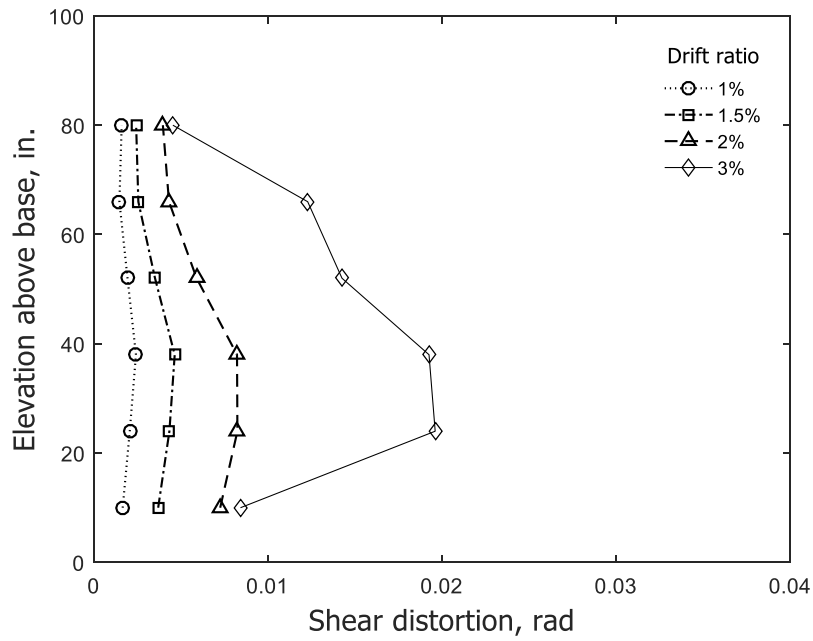


(a) Stem in compression

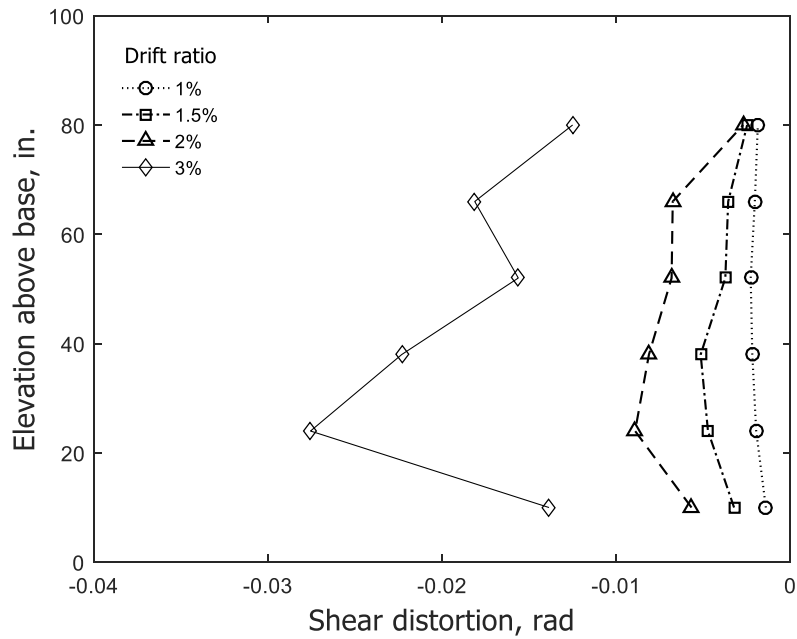


(b) Stem in tension

Figure 293 – Calculated shear distortion for T2 (data from optical markers, Columns 1 through 8) (1 in. = 25.4 mm)

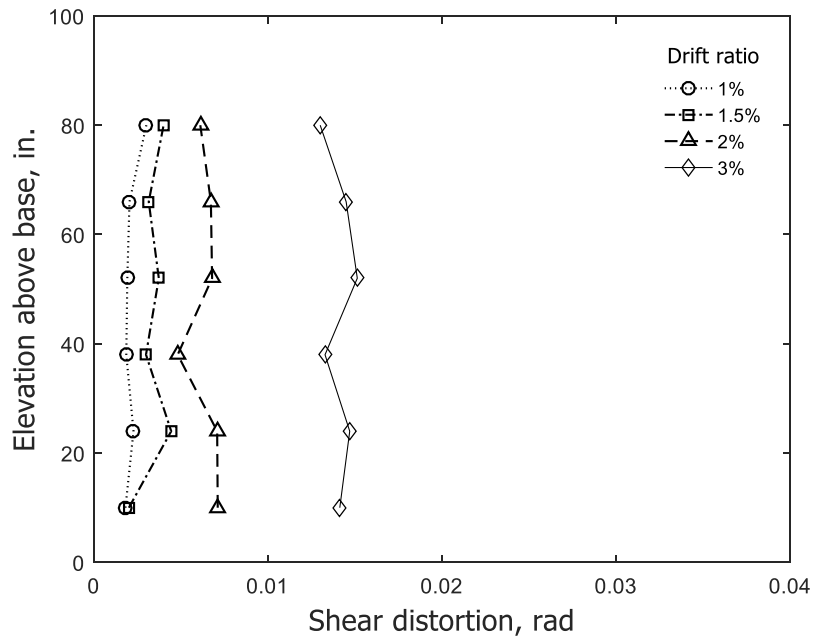


(a) Stem in compression

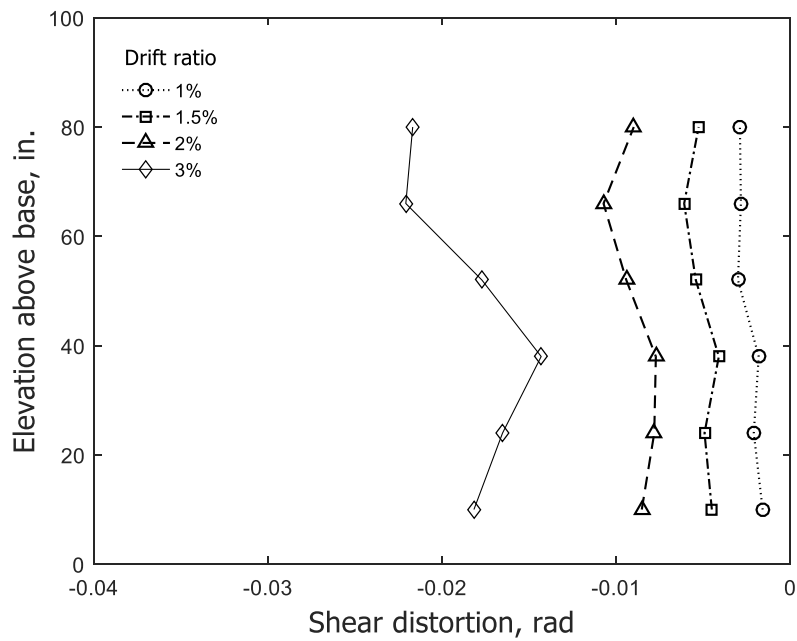


(b) Stem in tension

Figure 294 – Calculated shear distortion for T3 (data from optical markers, Columns 1 through 8) (1 in. = 25.4 mm)



(a) Stem in compression



(b) Stem in tension

Figure 295 – Calculated shear distortion for T4 (data from optical markers, Columns 1 through 8) (1 in. = 25.4 mm)

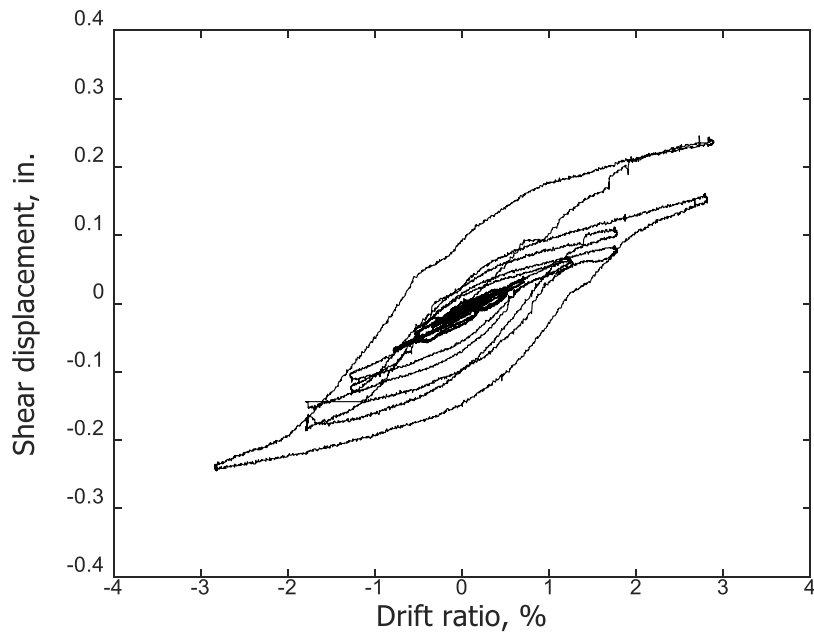


Figure 296 – Base shearing displacement of T1 based on data from optical markers, see Eq. 18
(1 in. = 25.4 mm)

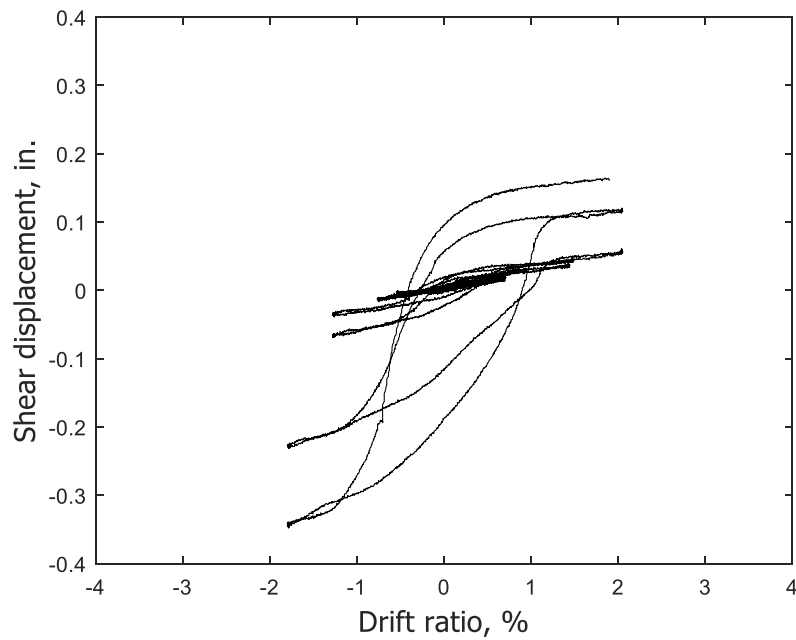


Figure 297 – Base shearing displacement of T2 based on data from optical markers, see Eq. 18
(1 in. = 25.4 mm)

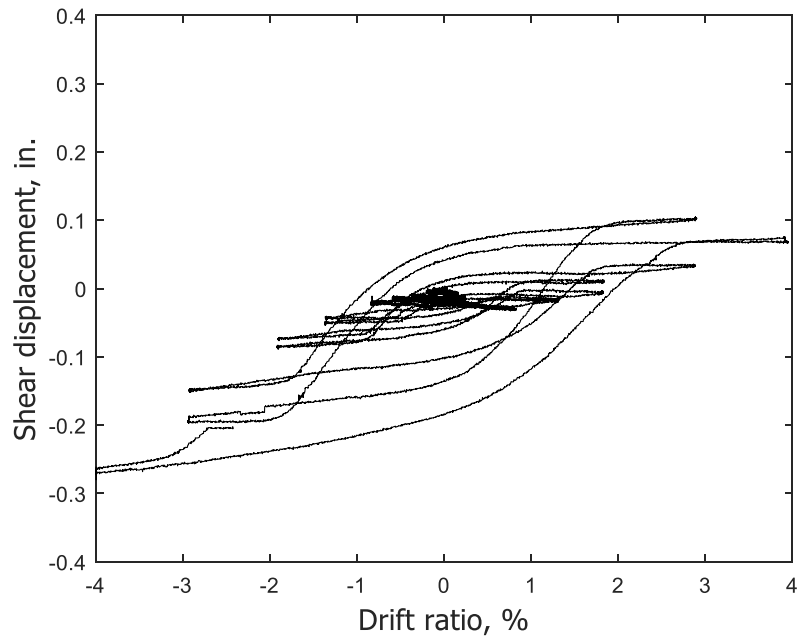


Figure 298 – Base shearing displacement of T3 based on data from optical markers, see Eq. 18
(1 in. = 25.4 mm)

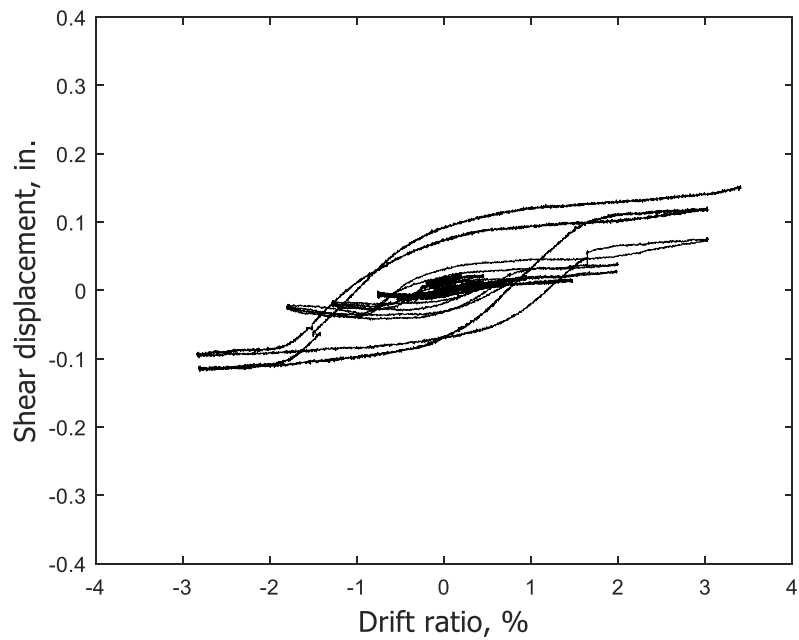
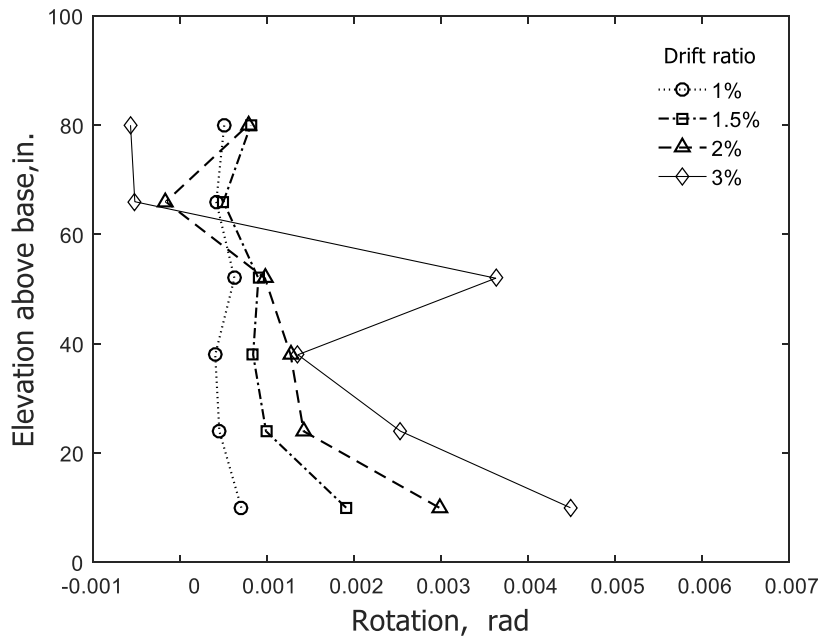
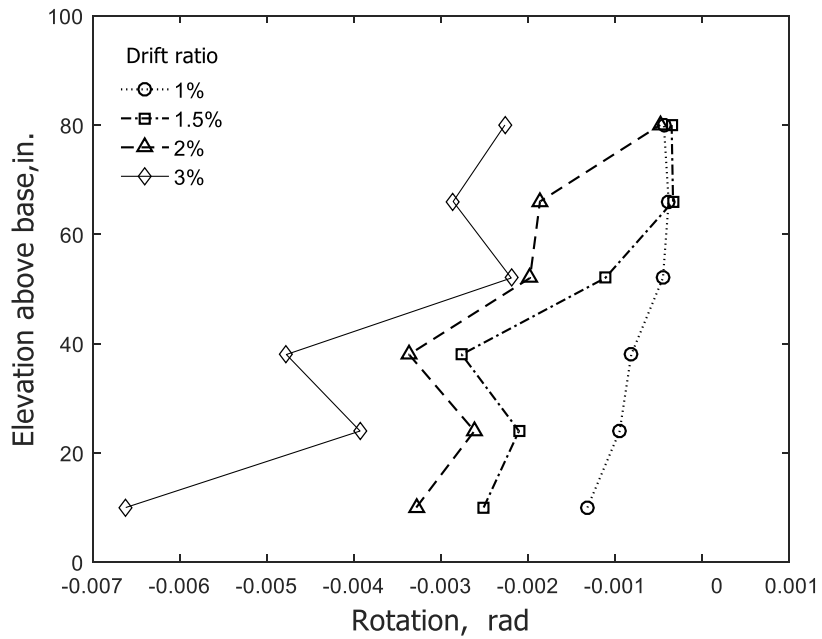


Figure 299 – Base shearing displacement of T4 based on data from optical markers, see Eq. 18
(1 in. = 25.4 mm)

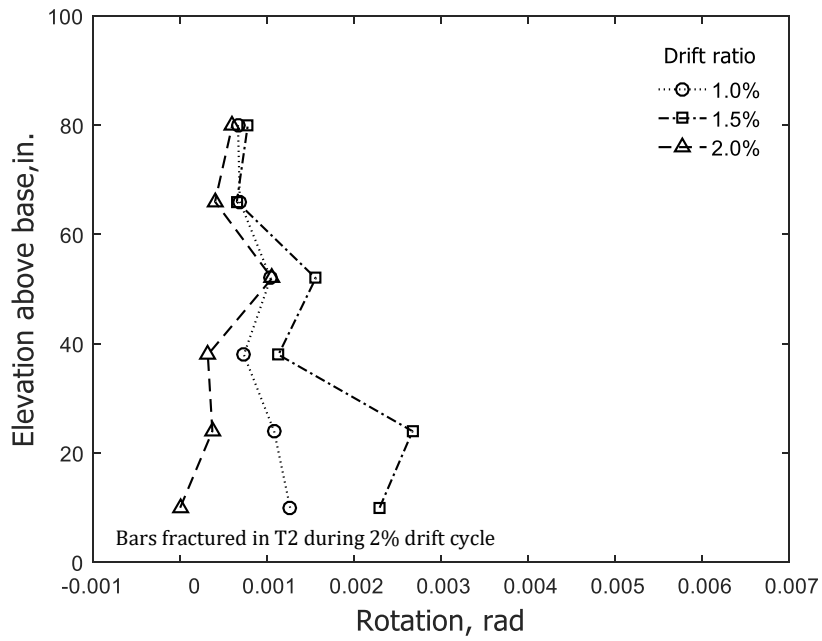


(a) Stem in compression

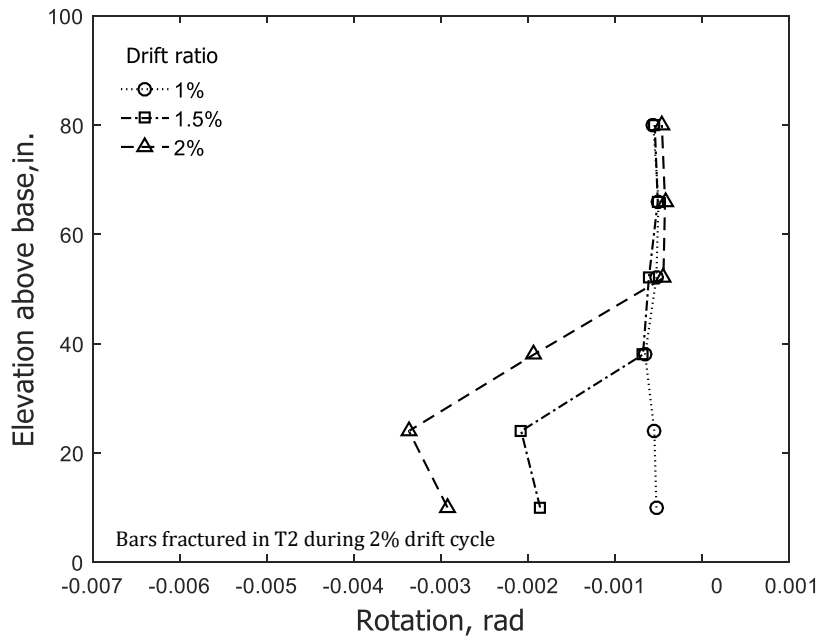


(b) Stem in tension

Figure 300 – Calculated flexural rotation for T1 (data from optical markers, Columns 1 and 8) (1 in. = 25.4 mm)

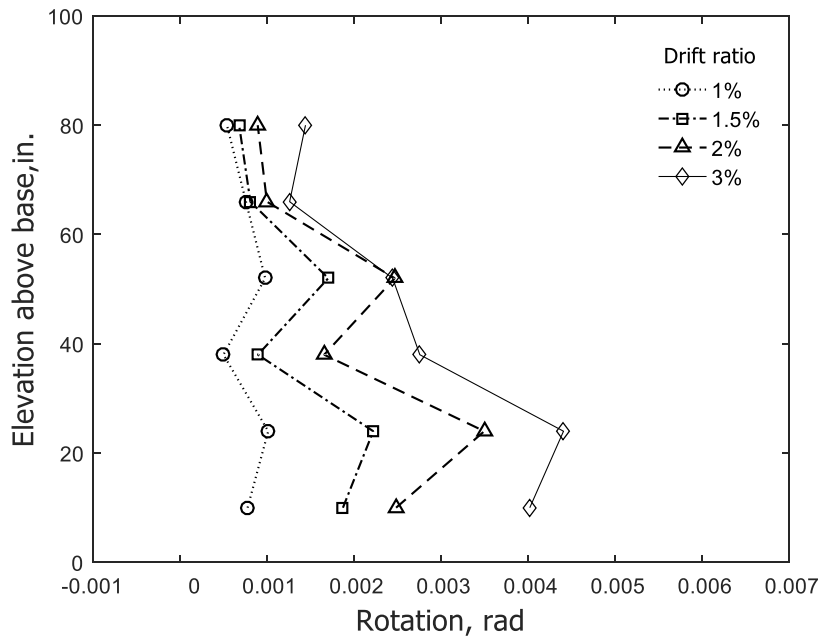


(a) Stem in compression

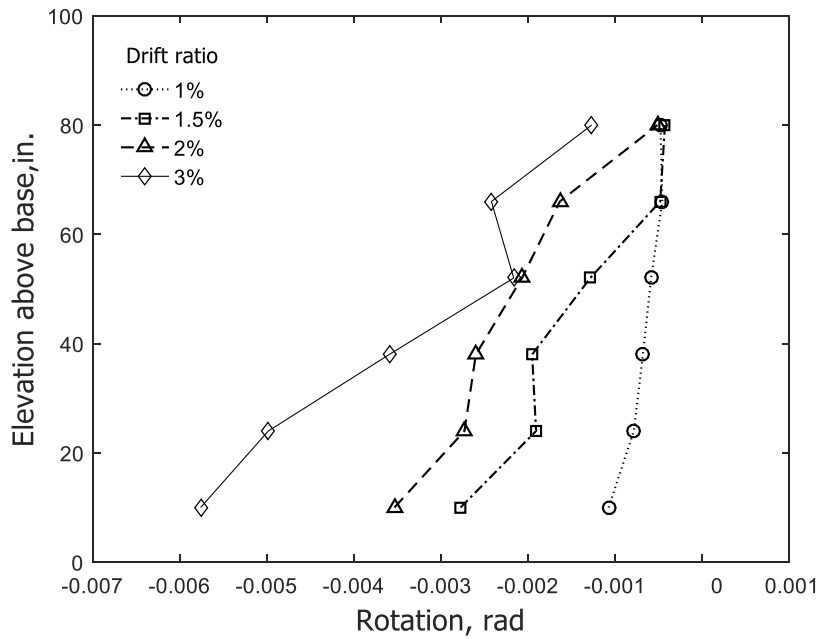


(b) Stem in tension

Figure 301 – Calculated flexural rotation for T2 (data from optical markers, Columns 1 and 8) (1 in. = 25.4 mm)

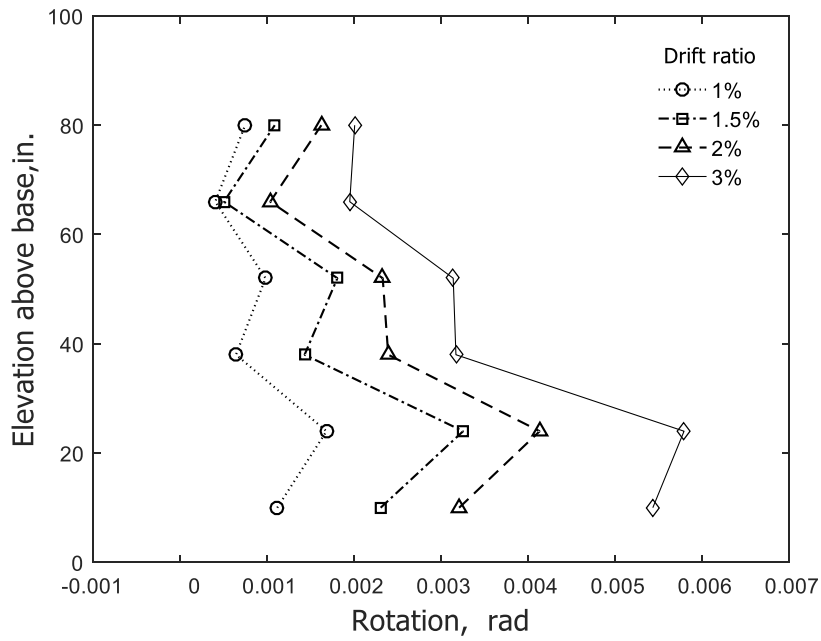


(a) Stem in compression

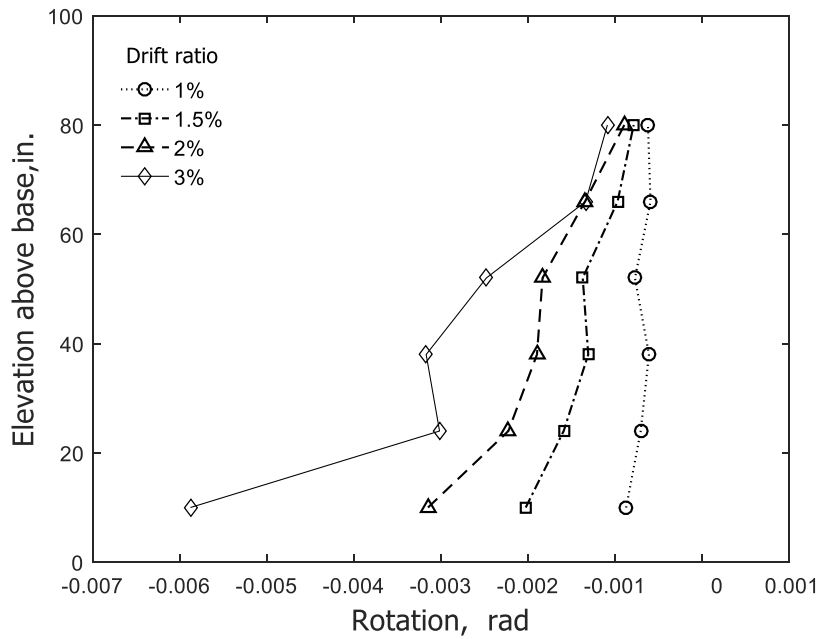


(b) Stem in tension

Figure 302 – Calculated flexural rotation for T3 (data from optical markers, Columns 1 and 8) (1 in. = 25.4 mm)



(a) Stem in compression



(b) Stem in tension

Figure 303 – Calculated flexural rotation for T4 (data from optical markers, Columns 1 and 8) (1 in. = 25.4 mm)

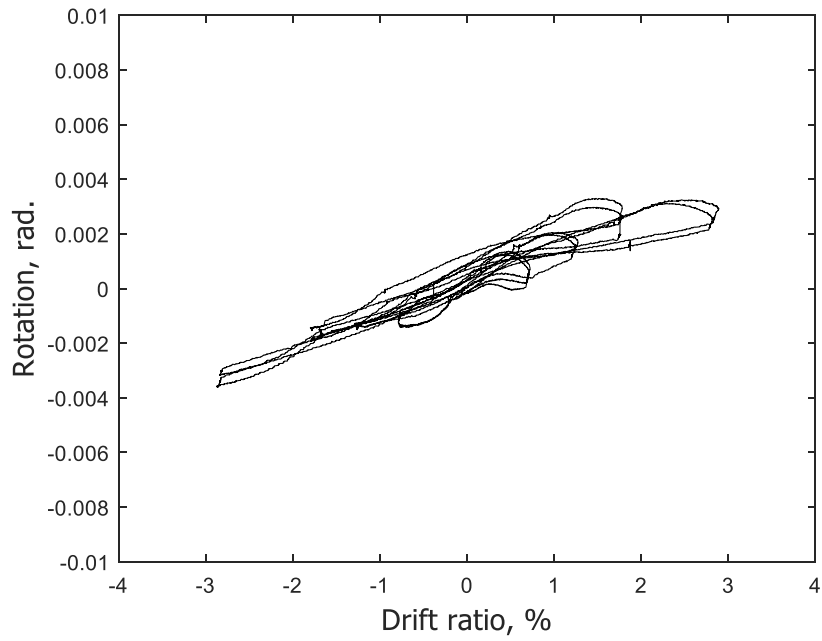


Figure 304 – Rotation due to base opening versus drift ratio for T1 (data from optical markers, see Eq. 16)

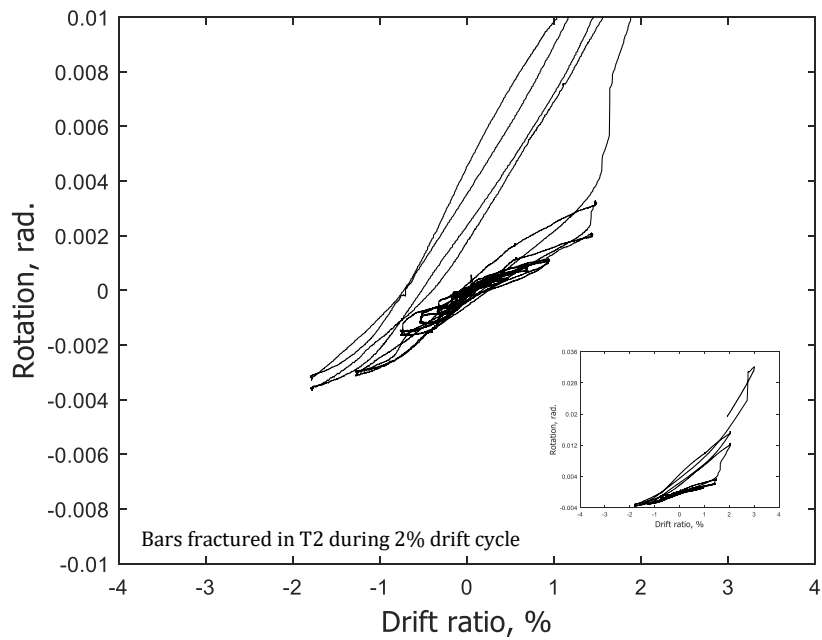


Figure 305 – Rotation due to base opening versus drift ratio for T2 (data from optical markers, see Eq. 16)

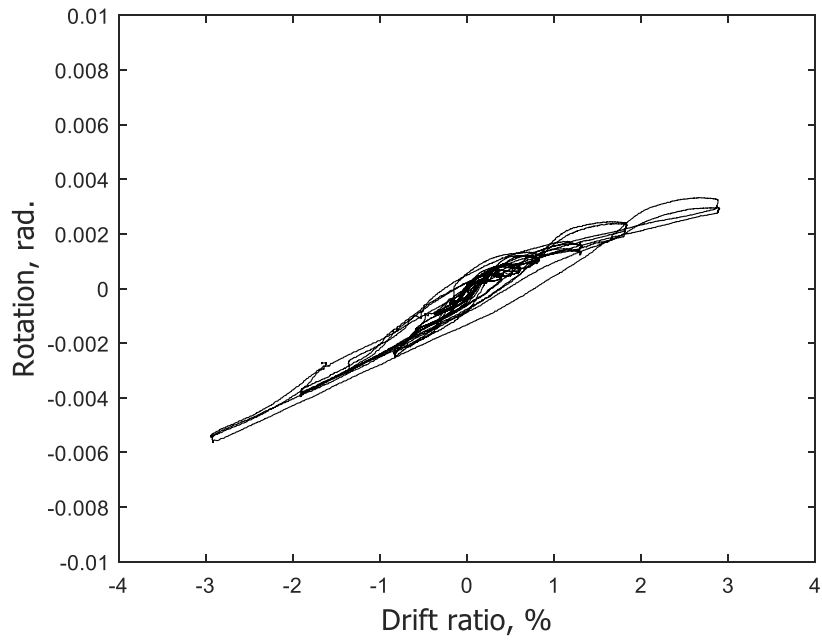


Figure 306 – Rotation due to base opening versus drift ratio for T3 (data from optical markers, see Eq. 16)

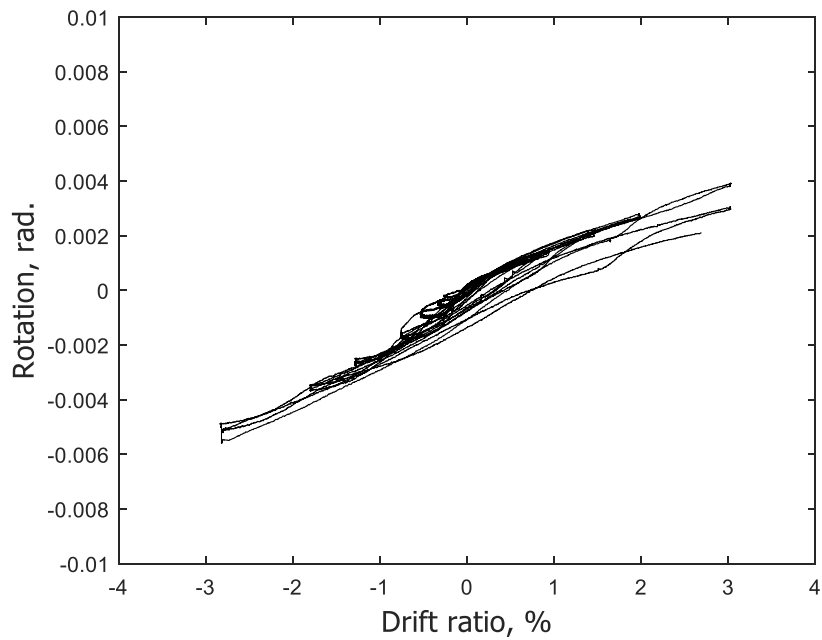
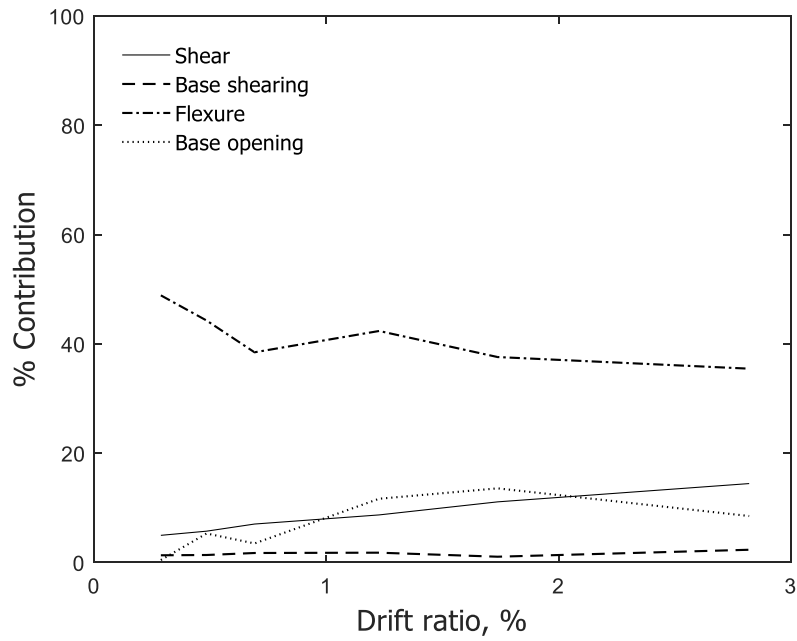
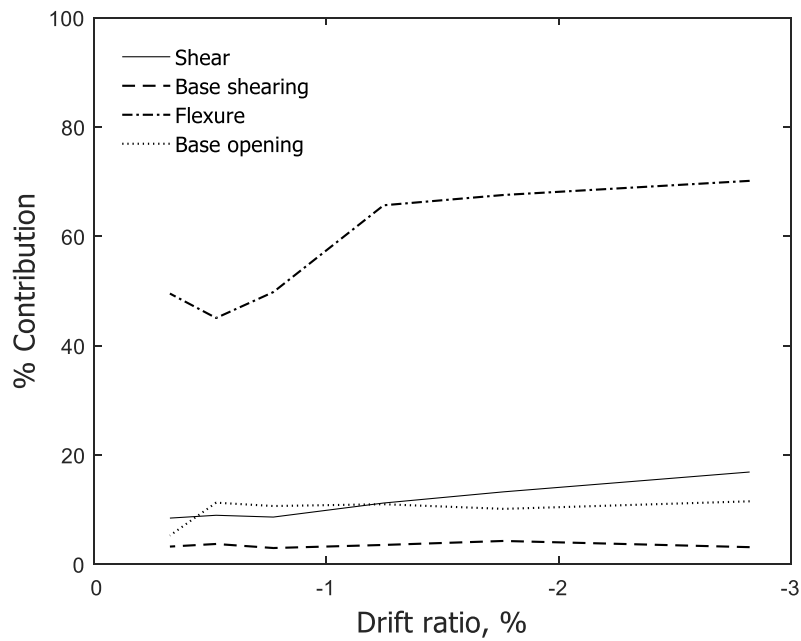


Figure 307 – Rotation due to base opening versus drift ratio for T4 (data from optical markers, see Eq. 16)

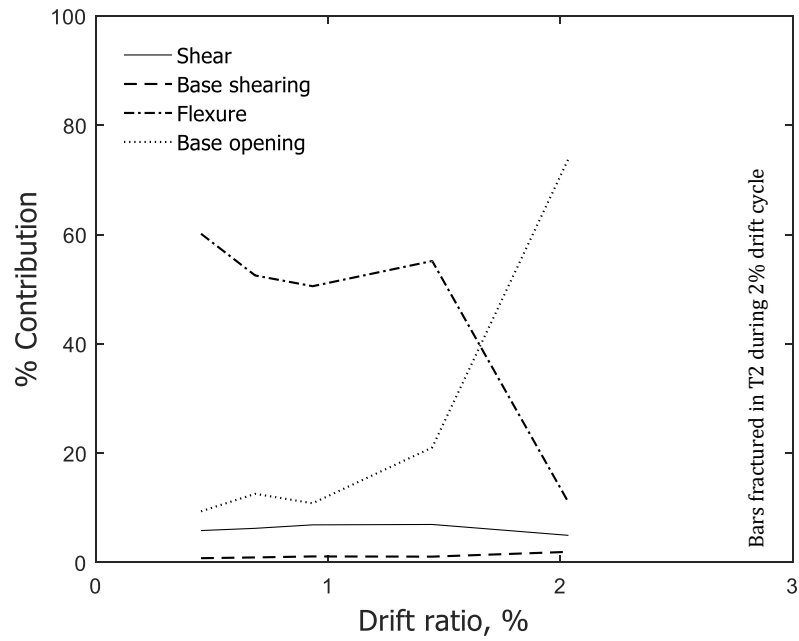


(a) Stem in compression

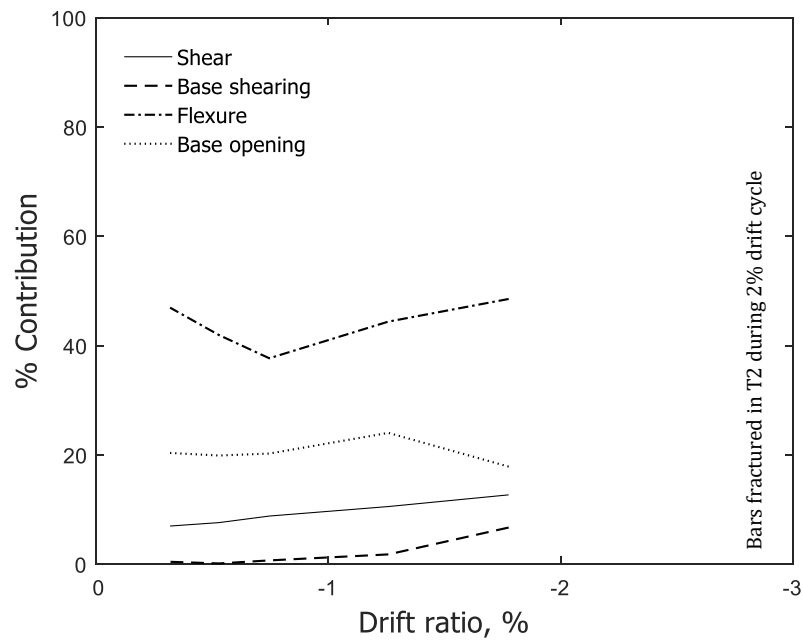


(b) Stem in tension

Figure 308 – Contribution of deformation components from bottom 87 in. (2210 mm) for T1

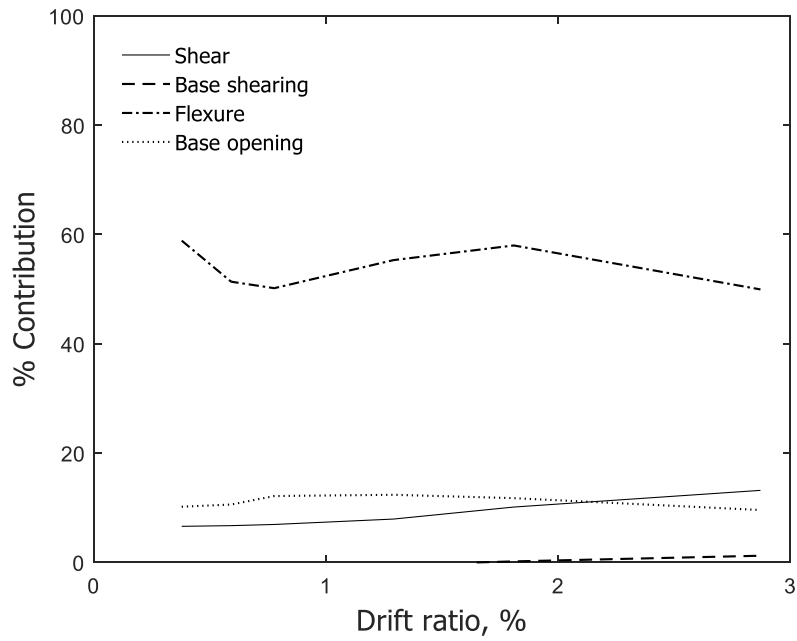


(a) Stem in compression

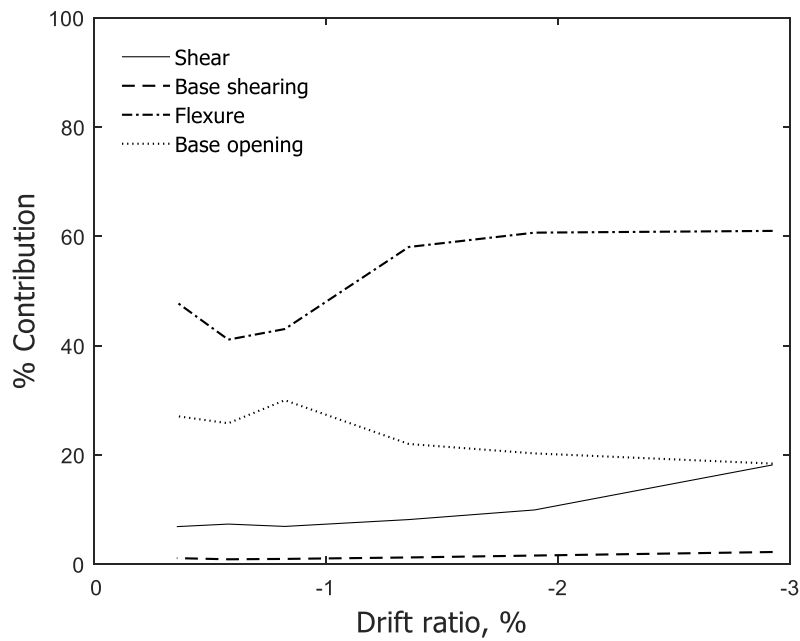


(b) Stem in tension

Figure 309 – Contribution of deformation components from bottom 87 in. (2210 mm) for T2

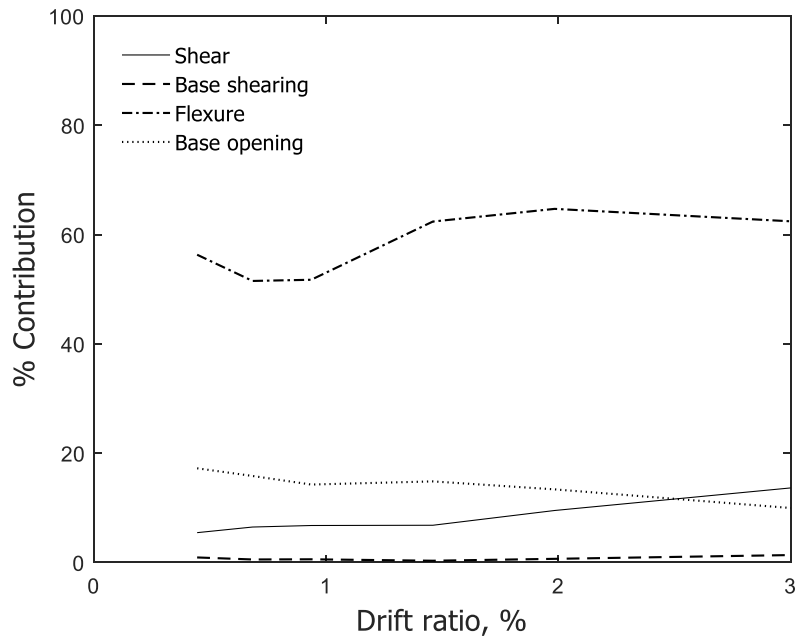


(a) Stem in compression

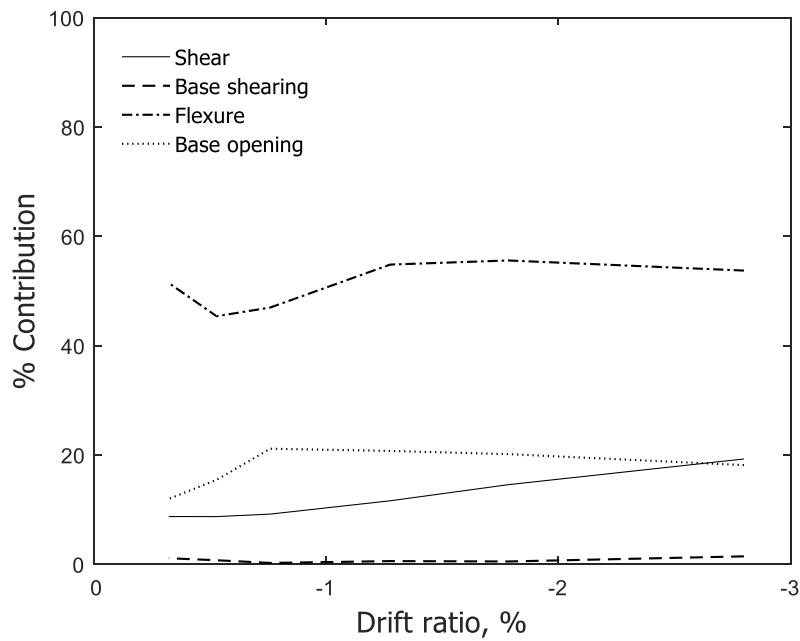


(b) Stem in tension

Figure 310 – Contribution of deformation components from bottom 87 in. (2210 mm) for T3

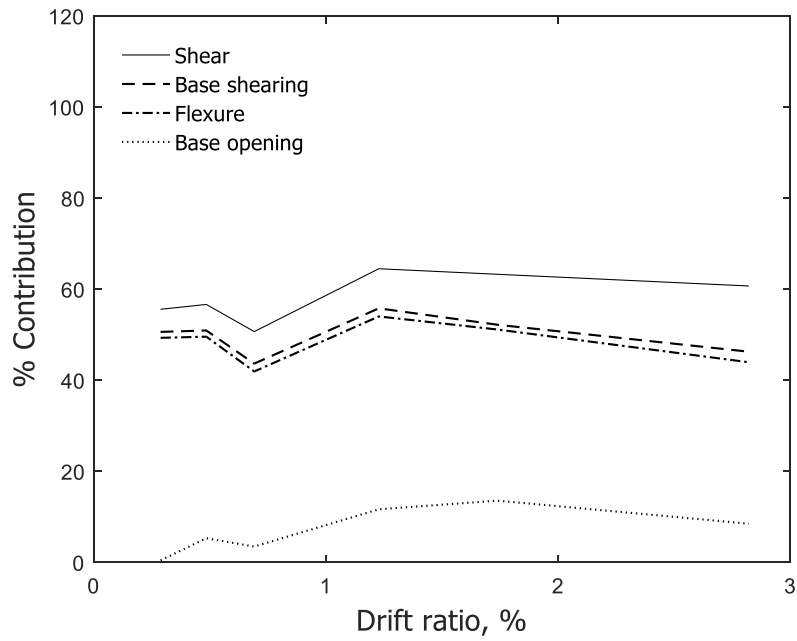


(a) Stem in compression

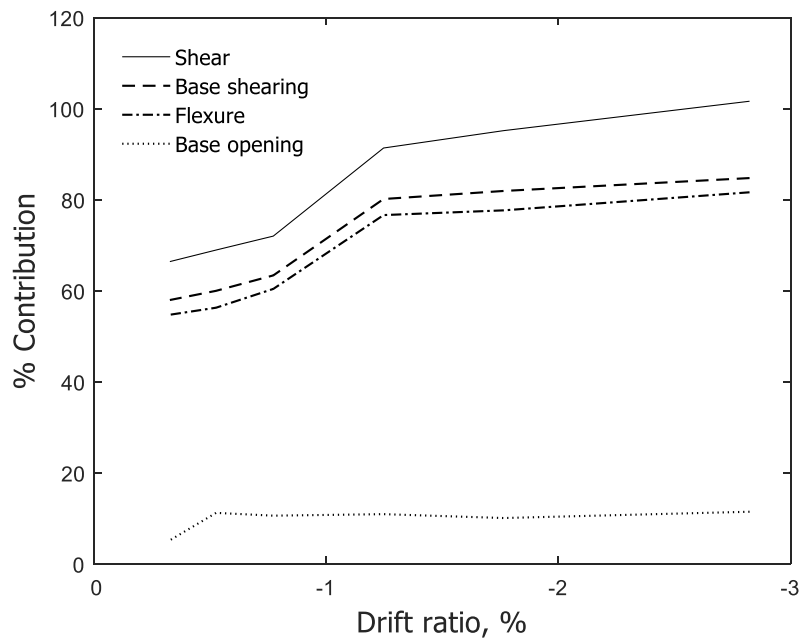


(b) Stem in tension

Figure 311 – Contribution of deformation components from bottom 87 in. (2210 mm) for T4

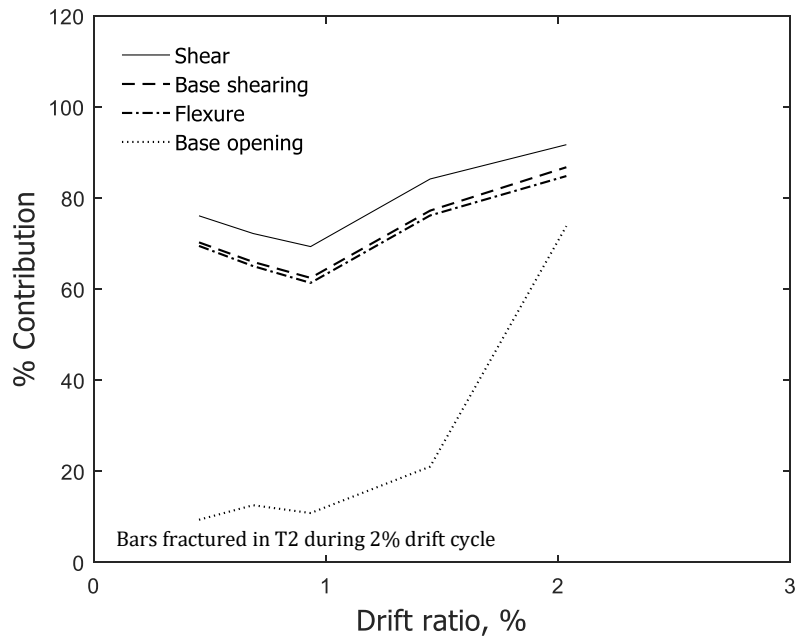


(a) Stem in compression

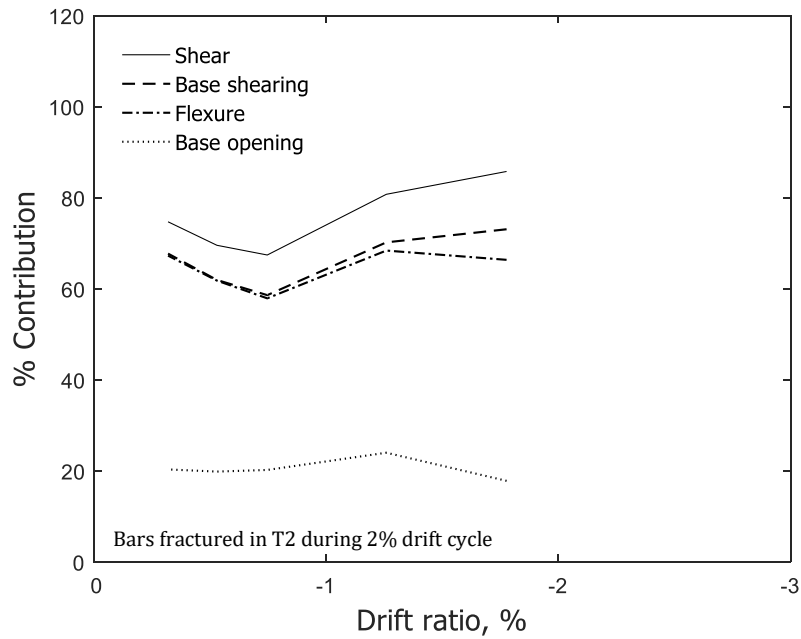


(b) Stem in tension

Figure 312 – Cumulative contribution of deformation components from bottom 87 in. (2210 mm) for T1

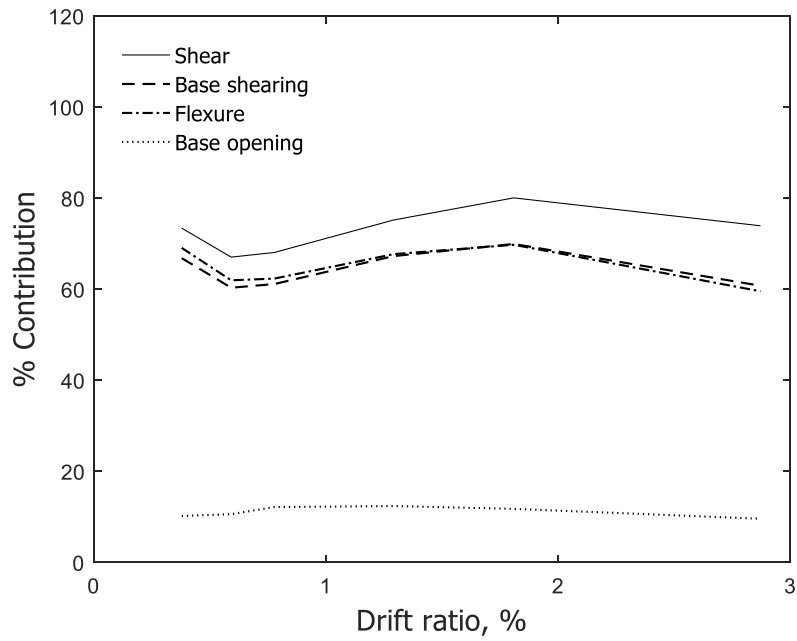


(a) Stem in compression

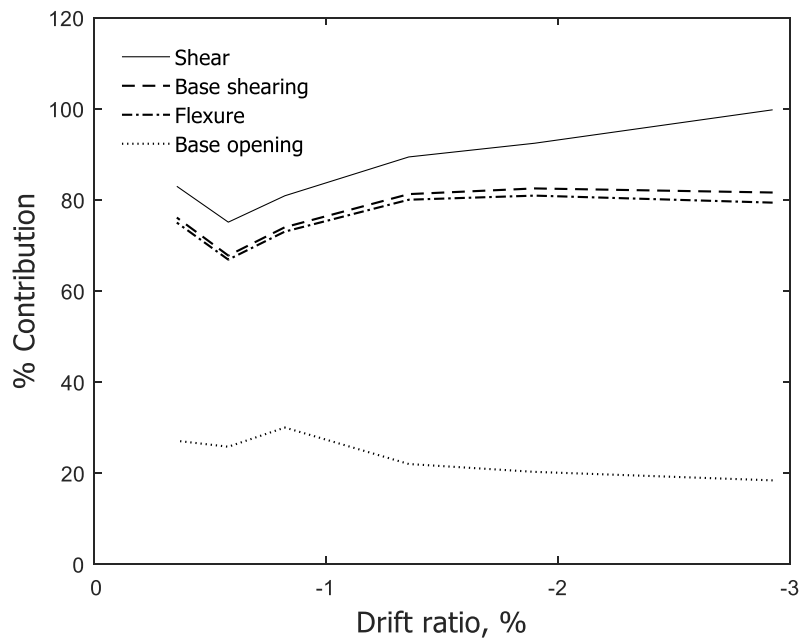


(b) Stem in tension

Figure 313 – Cumulative contribution of deformation components from bottom 87 in. (2210 mm) for T2

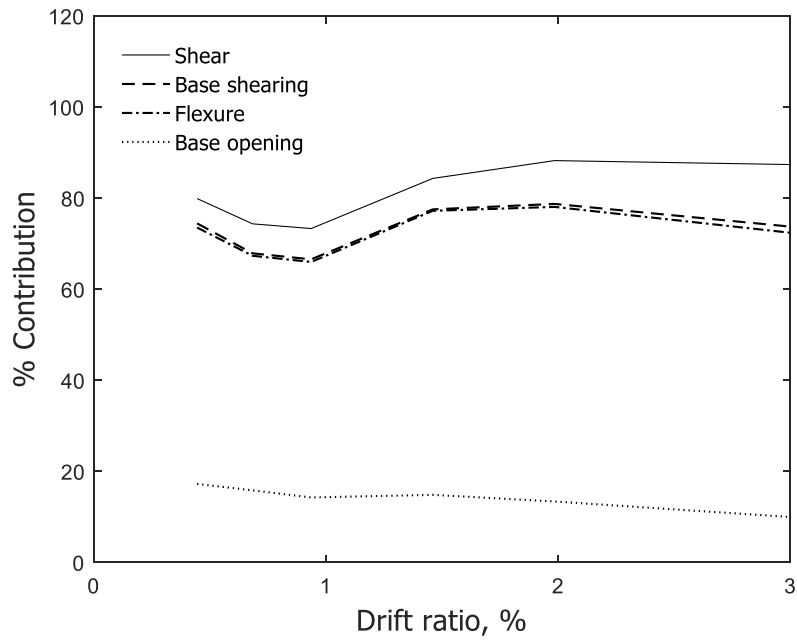


(a) Stem in compression

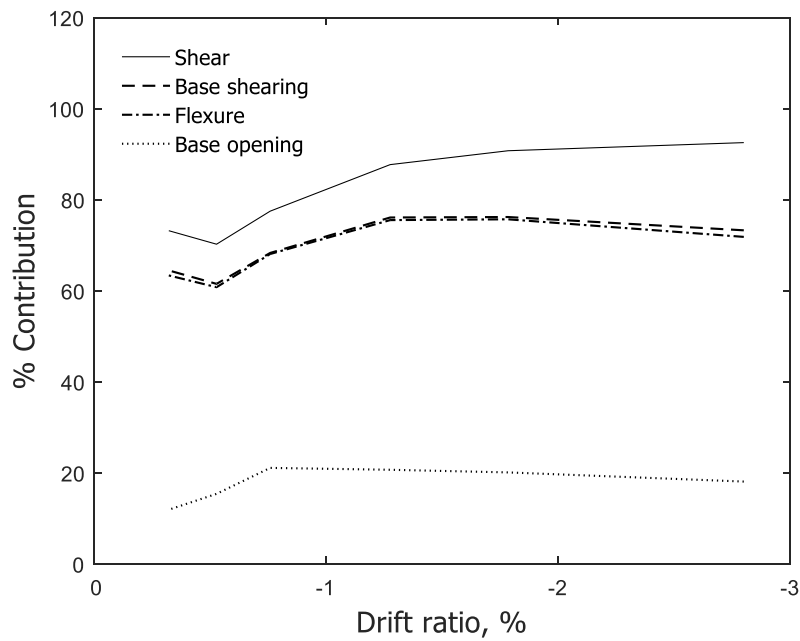


(b) Stem in tension

Figure 314 – Cumulative contribution of deformation components from bottom 87 in. (2210 mm) for T3



(a) Stem in compression



(b) Stem in tension

Figure 315 – Cumulative contribution of deformation components from bottom 87 in. (2210 mm) for T4

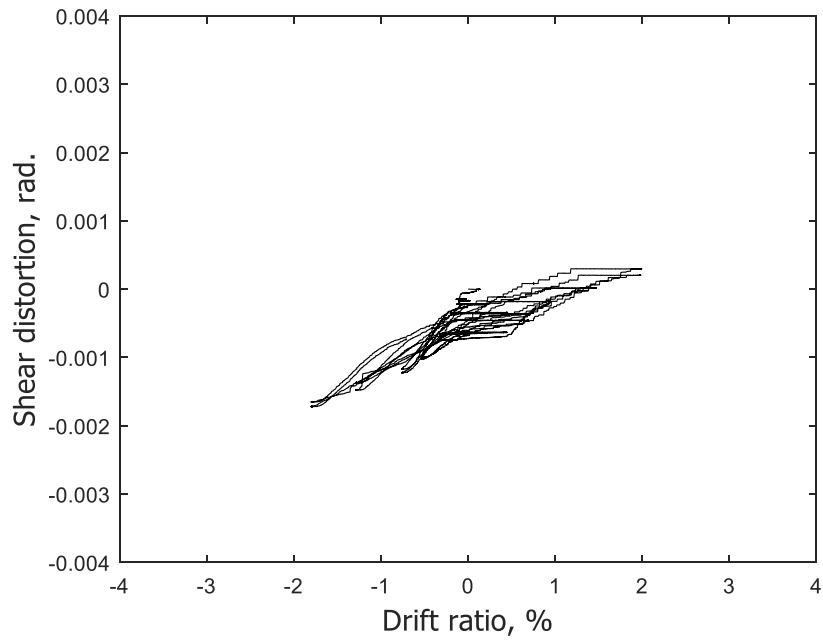


Figure 316 – Calculated shear distortion within top 200 in. (5080 mm) for T4 (data from potentiometers)

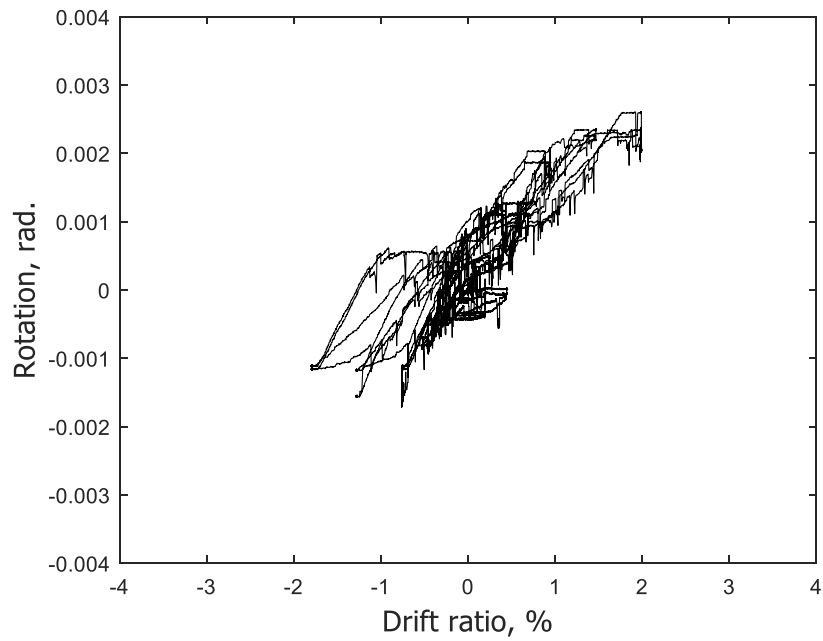
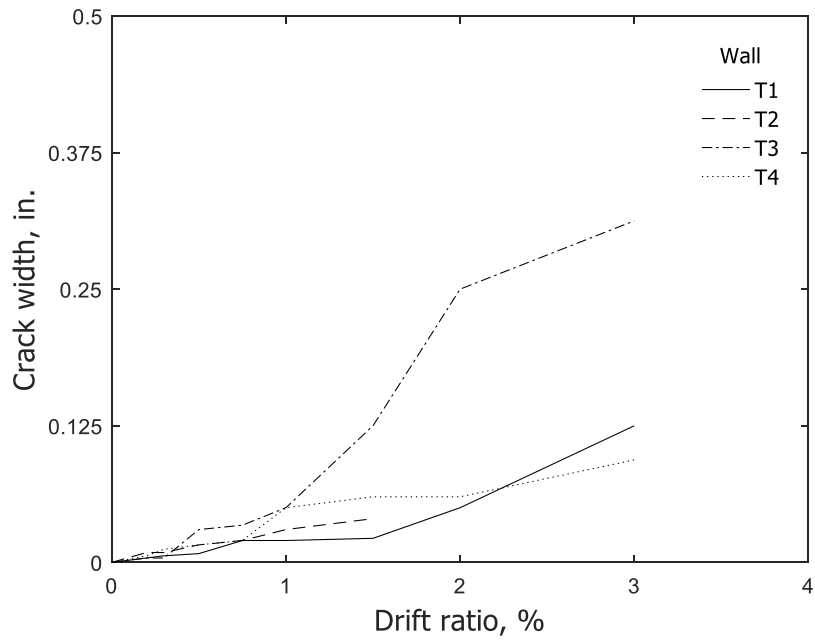
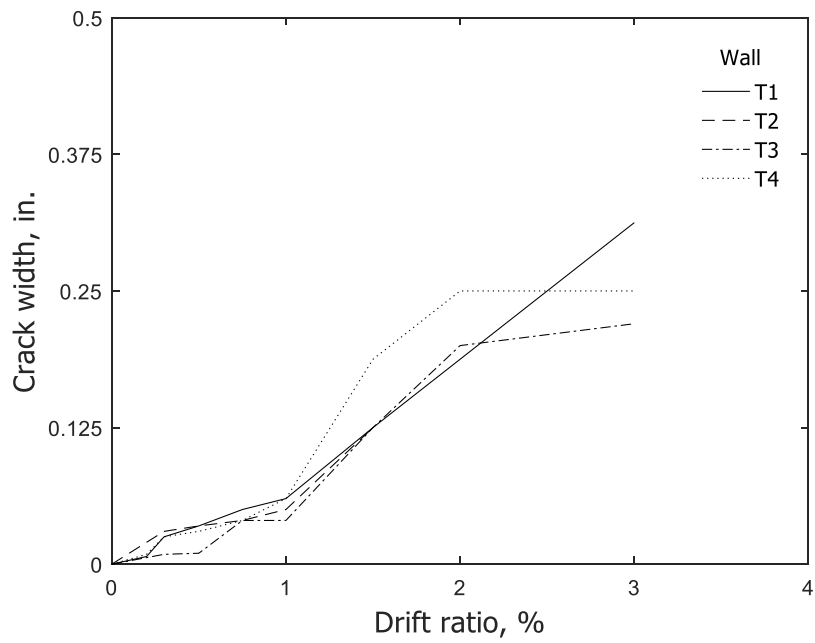


Figure 317 – Calculated flexural rotation within top 200 in. (5080 mm) for T4 (data from potentiometers)

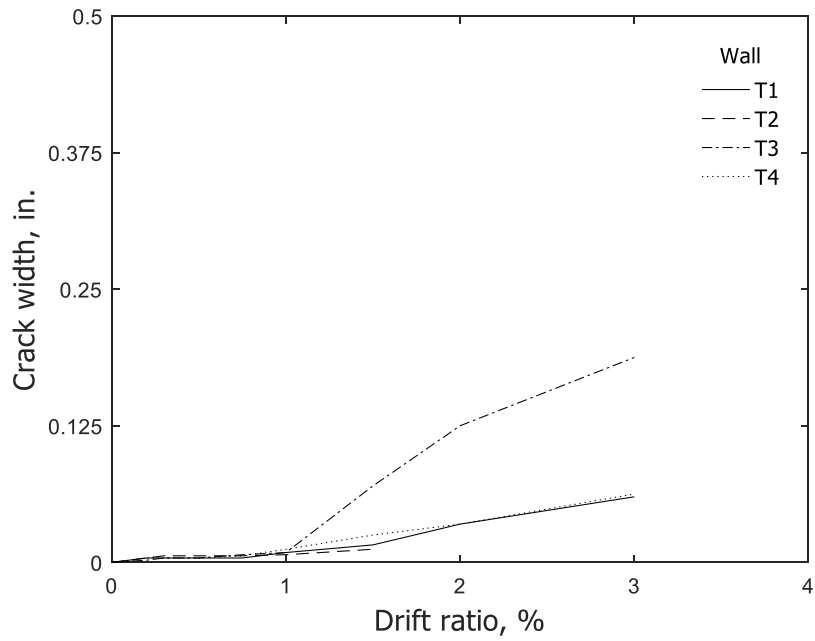


a) Confined flange

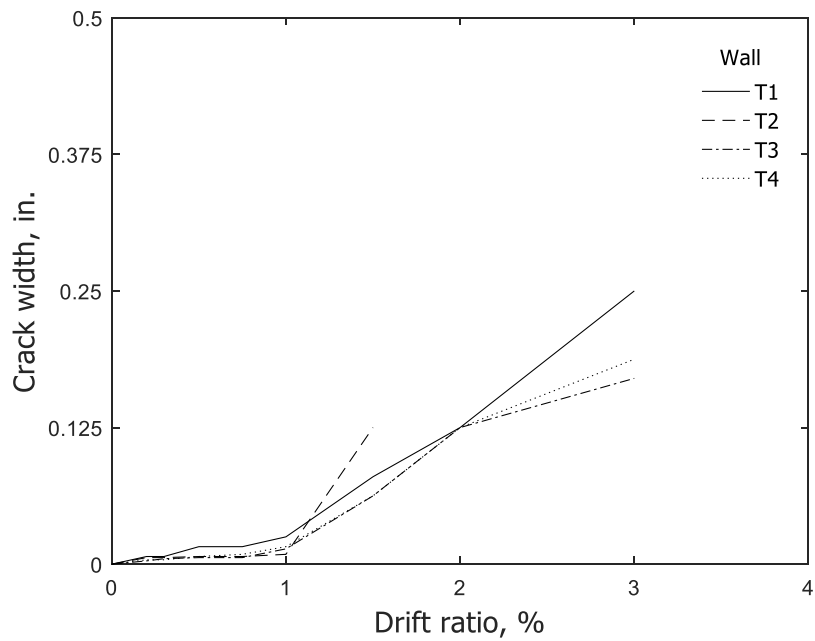


b) Unconfined flange

Figure 318 – Measured crack width at peak positive drift (stem in compression) versus drift ratio (1 in. = 25.4 mm)

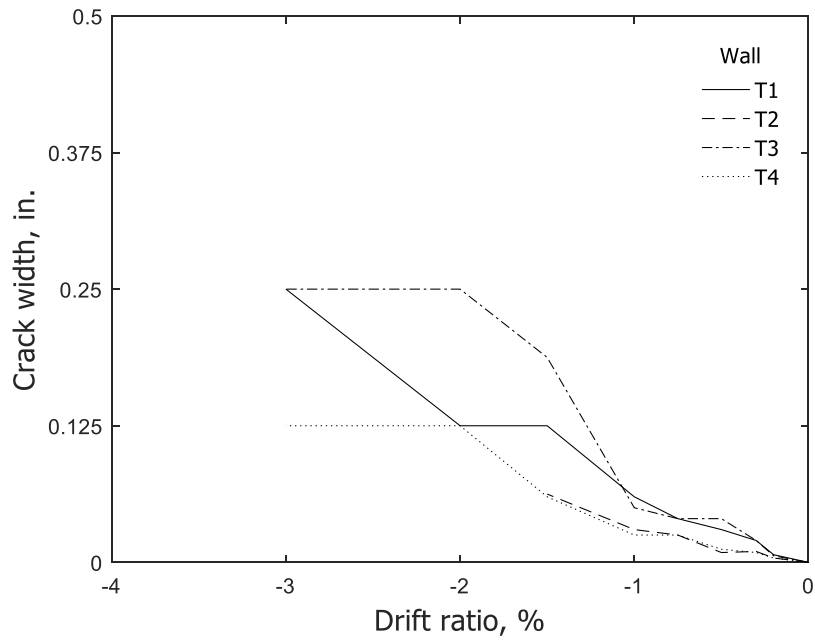


a) Confined flange

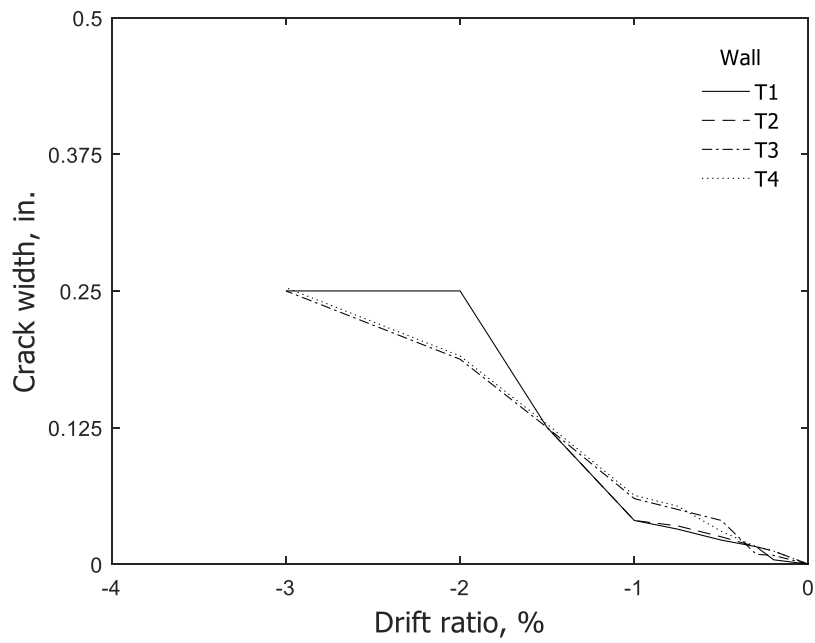


b) Unconfined flange

Figure 319 – Measured crack width at zero shear versus peak positive drift ratio attained (stem in compression) (1 in. = 25.4 mm)

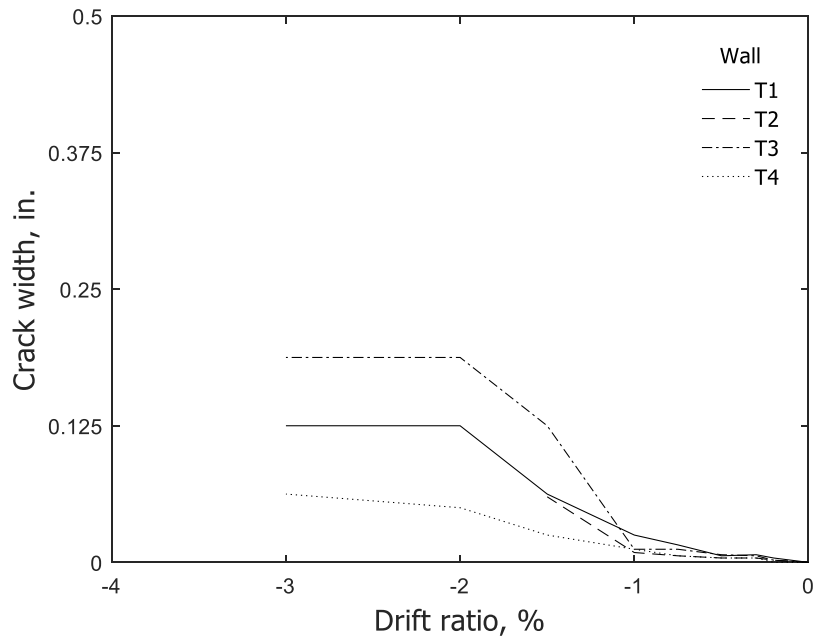


a) Confined stem

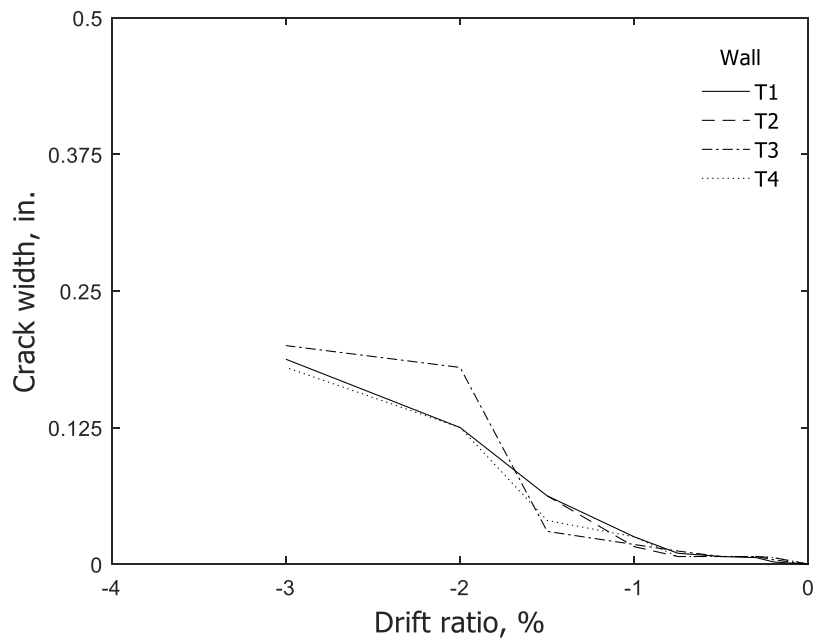


b) Unconfined stem

Figure 320 – Measured crack width at peak negative drift (stem in tension) versus drift ratio (1 in. = 25.4 mm)

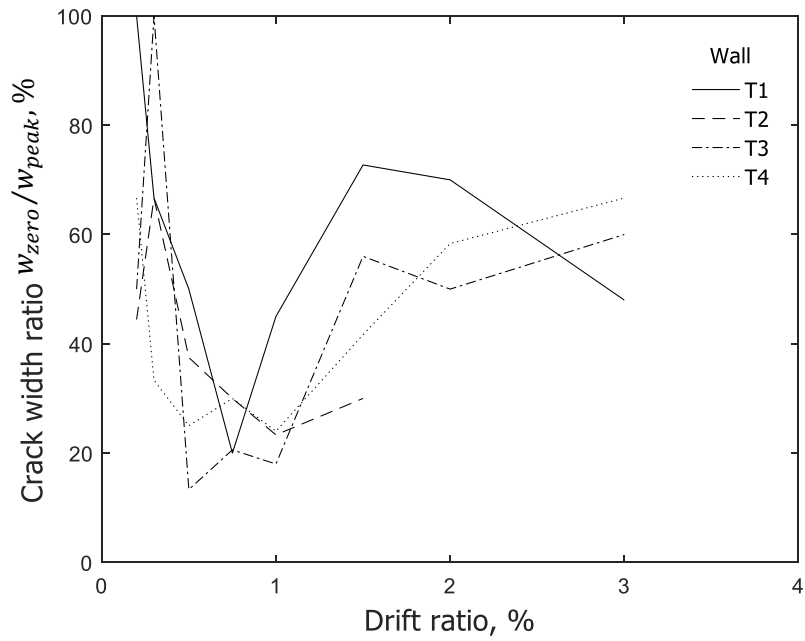


a) Confined stem

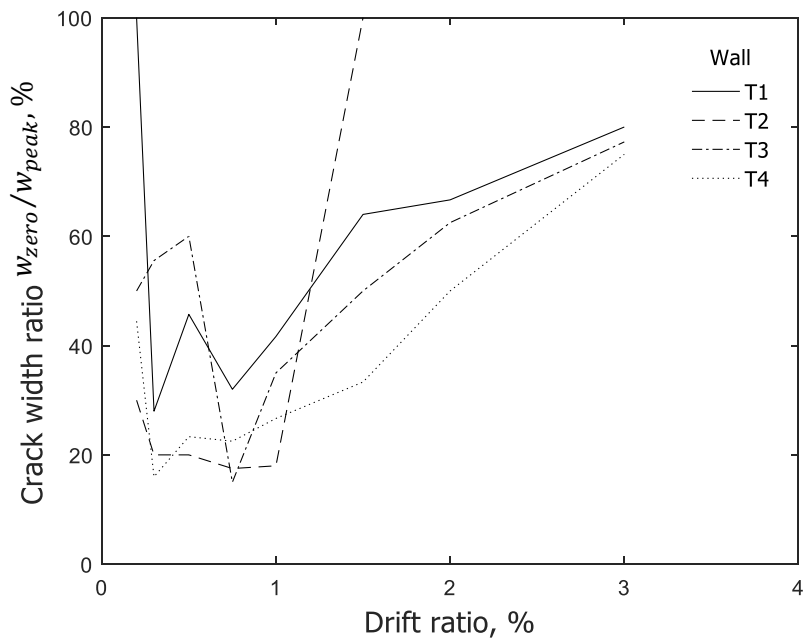


b) Unconfined stem

Figure 321 – Measured crack width at zero shear versus peak negative drift ratio attained (stem in tension) (1 in. = 25.4 mm)

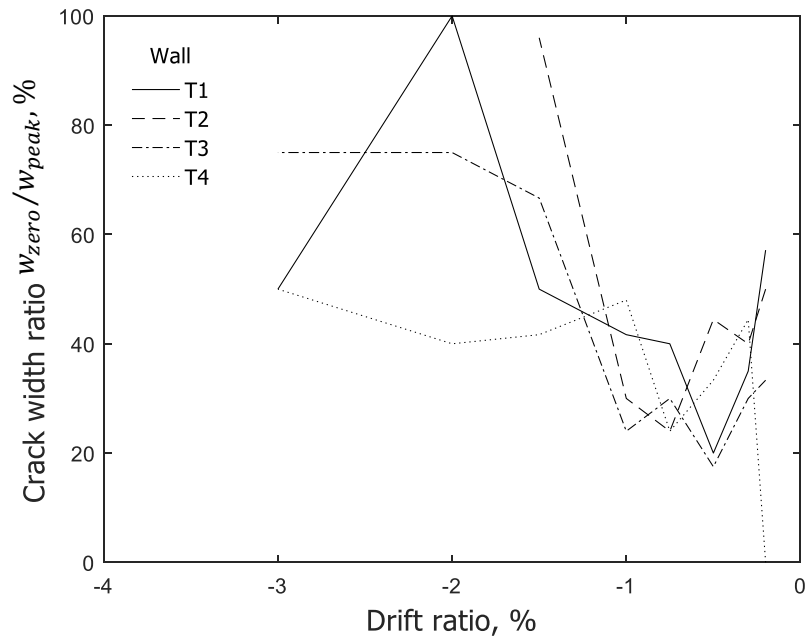


a) Confined flange

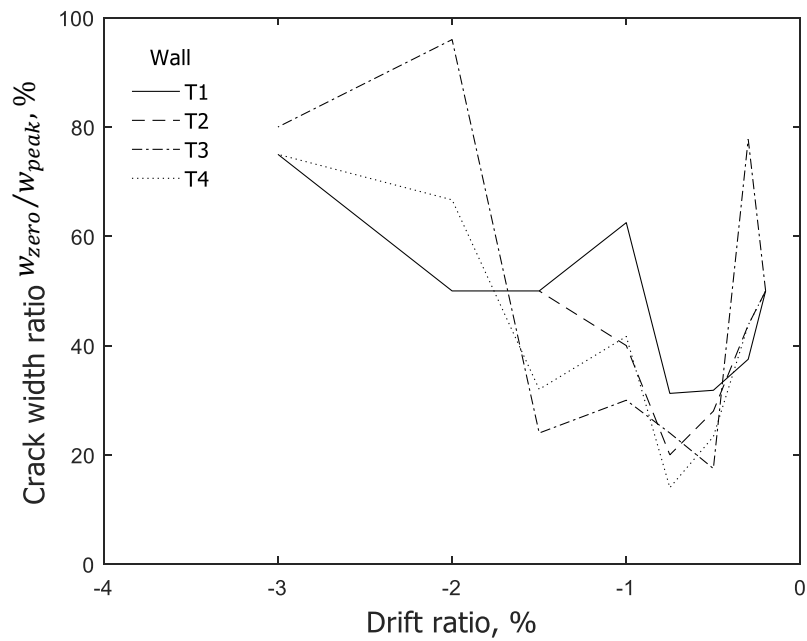


b) Unconfined flange

Figure 322 – Crack width ratio (w_{zero}/w_{peak}) versus drift ratio for positive loading direction (stem in compression)



a) Confined stem



b) Unconfined stem

Figure 323 – Crack width ratio (w_{zero}/w_{peak}) versus drift ratio for negative loading direction (stem in tension)

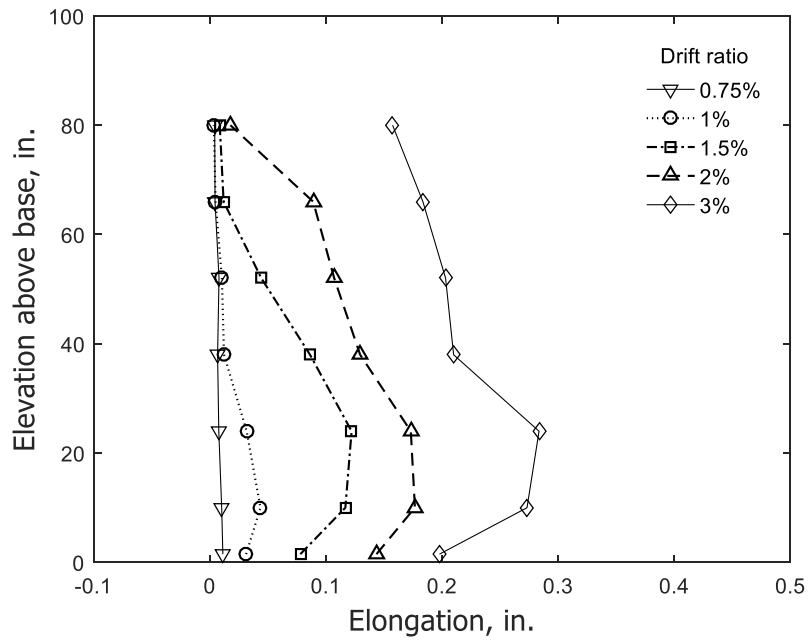


Figure 324 – Calculated elongation at zero shear for T1 (data from optical markers, Columns 1 through 8) (1 in. = 25.4 mm)

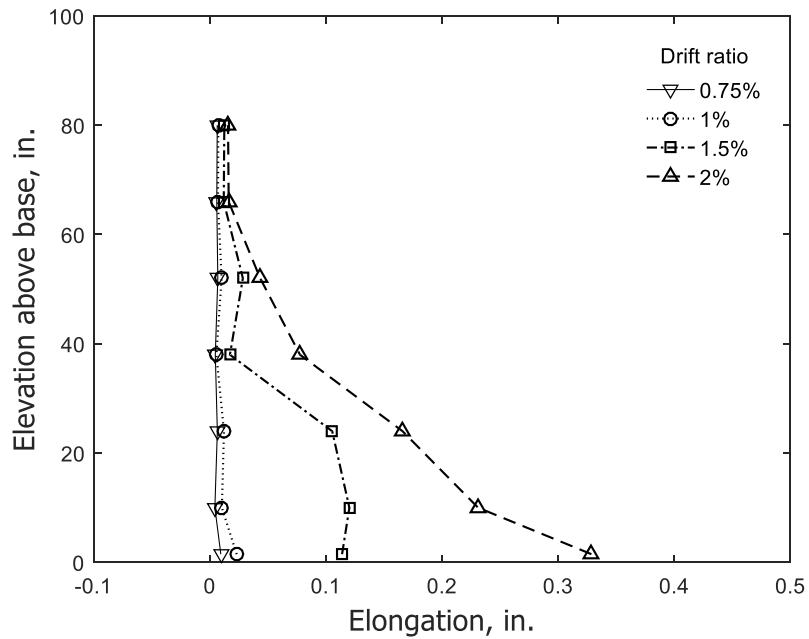


Figure 325 – Calculated elongation at zero shear for T2 (data from optical markers, Columns 1 through 8) (1 in. = 25.4 mm)

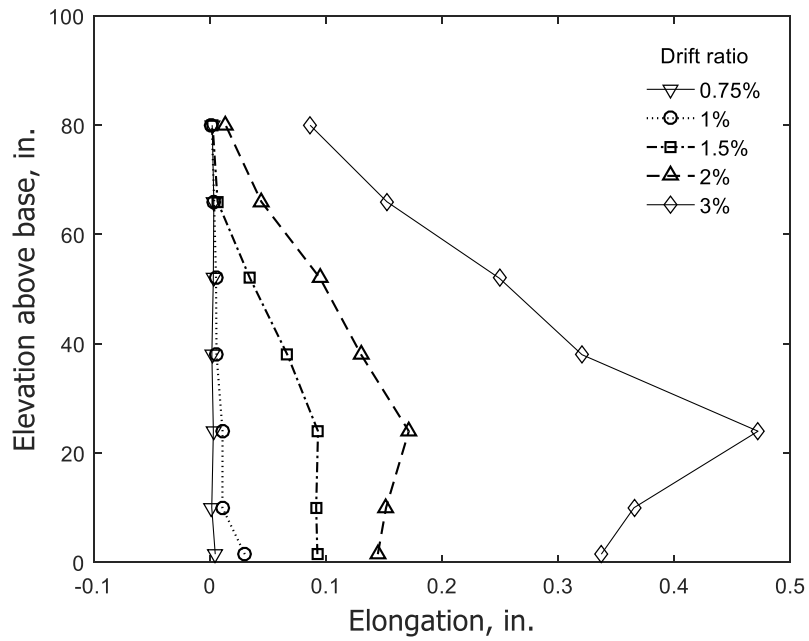


Figure 326 – Calculated elongation at zero shear for T3 (data from optical markers, Columns 1 through 8) (1 in. = 25.4 mm)

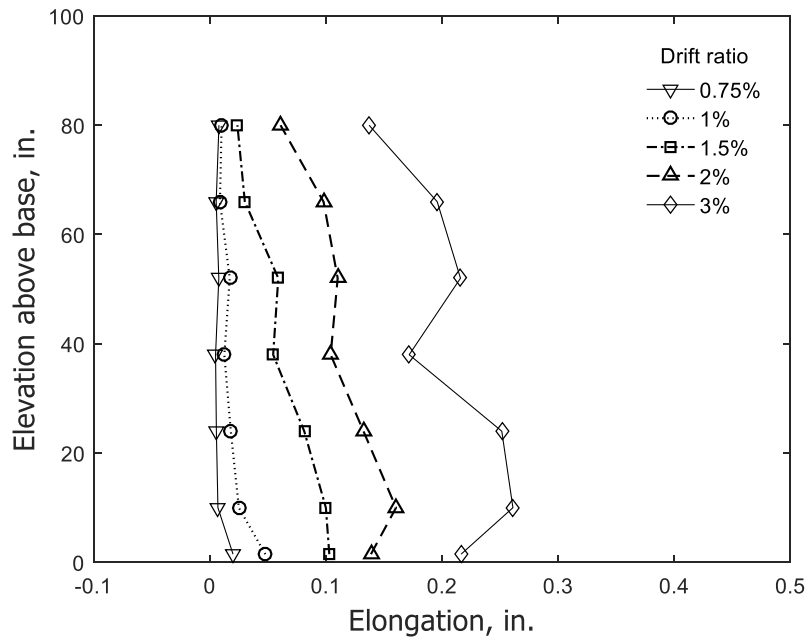


Figure 327 – Calculated elongation at zero shear for T4 (data from optical markers, Columns 1 through 8) (1 in. = 25.4 mm)

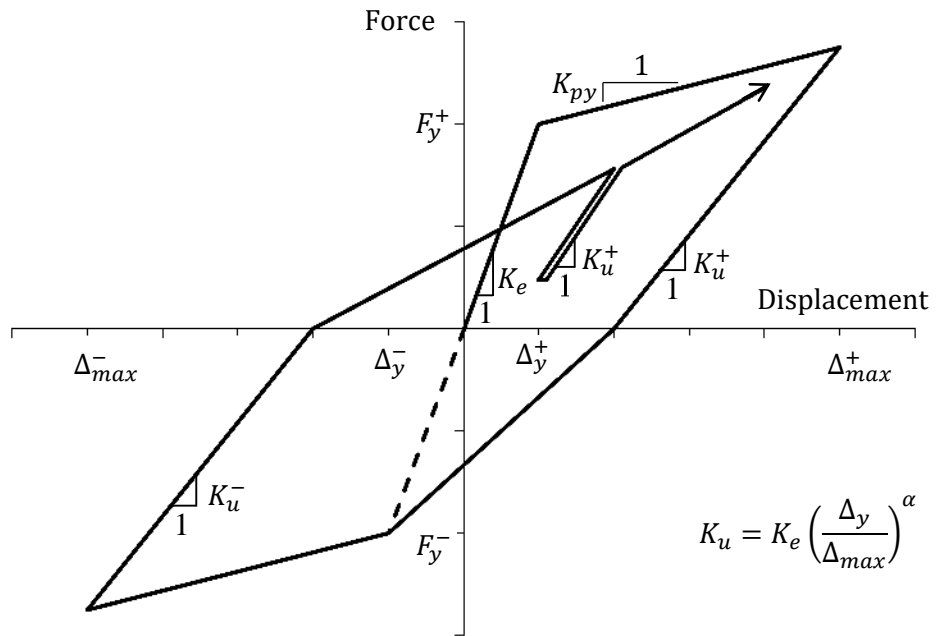


Figure 328 – Idealized force-displacement curve and hysteresis model

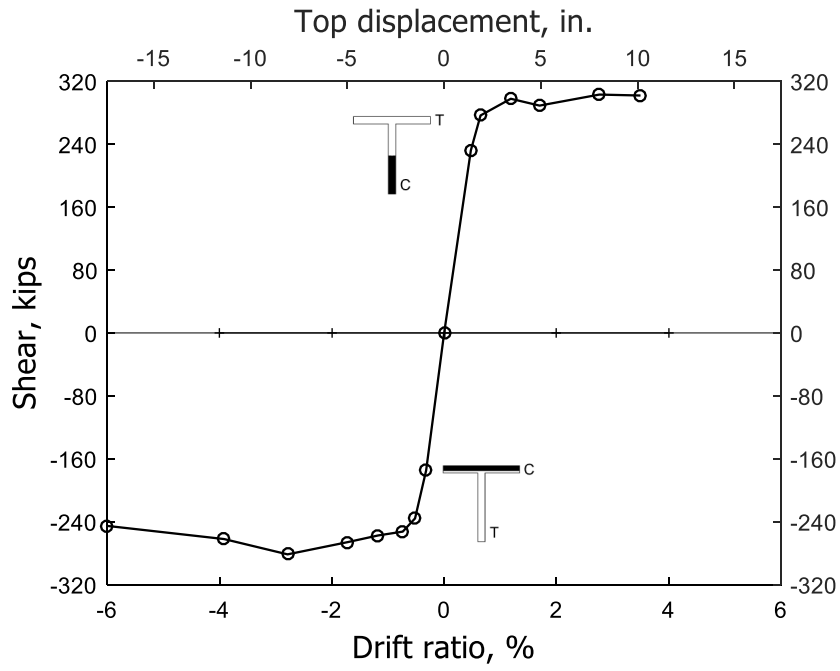


Figure 329 – Envelope of shear versus drift ratio for T1 (1 in. = 25.4 mm, 1 kip = 4.45 kN)

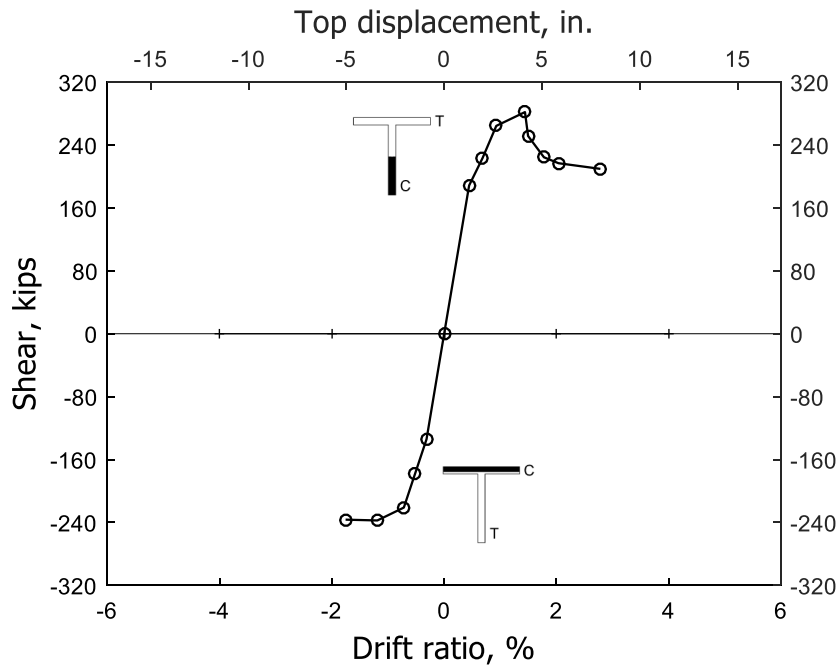


Figure 330 – Envelope of shear versus drift ratio for T2 (1 in. = 25.4 mm, 1 kip = 4.45 kN)

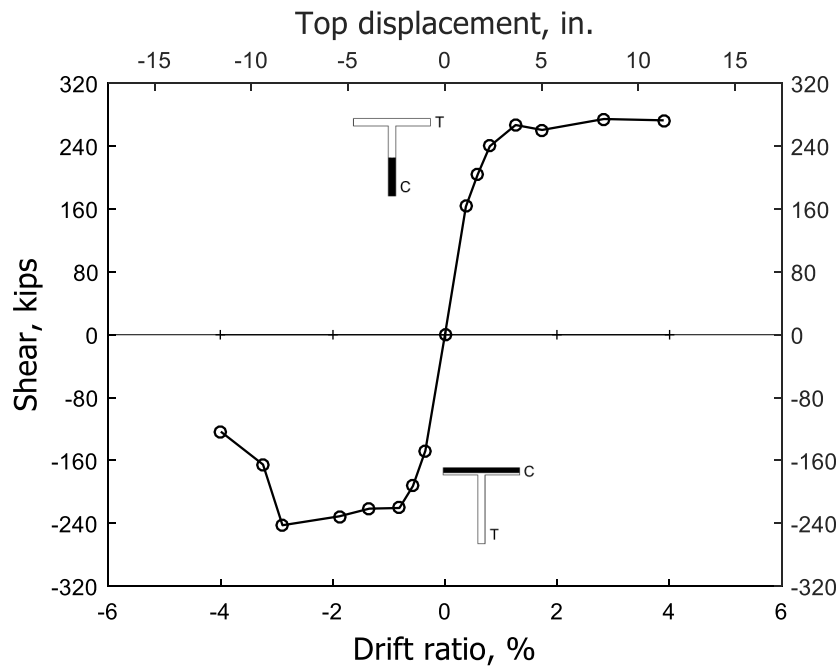


Figure 331 – Envelope of shear versus drift ratio for T3 (1 in. = 25.4 mm, 1 kip = 4.45 kN)

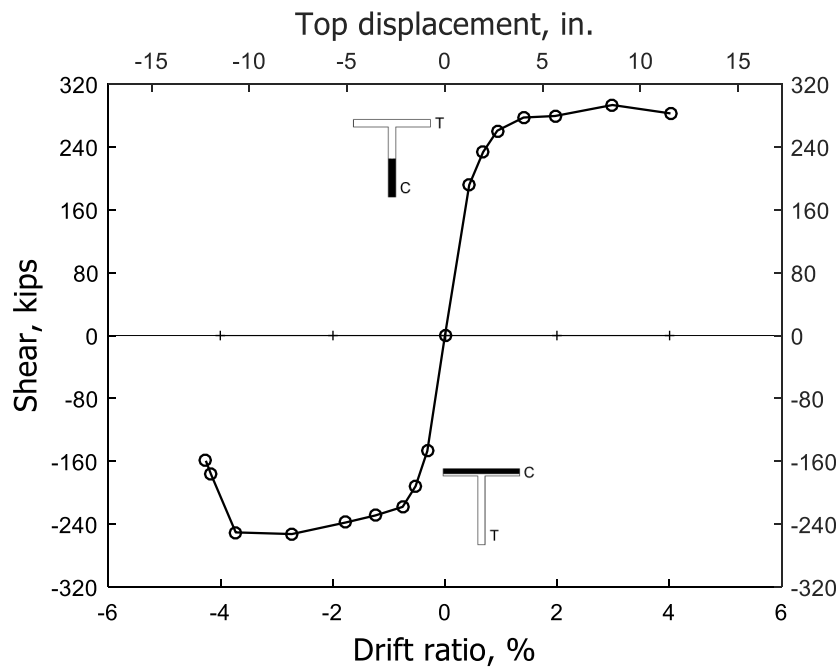


Figure 332 – Envelope of shear versus drift ratio for T4 (1 in. = 25.4 mm, 1 kip = 4.45 kN)

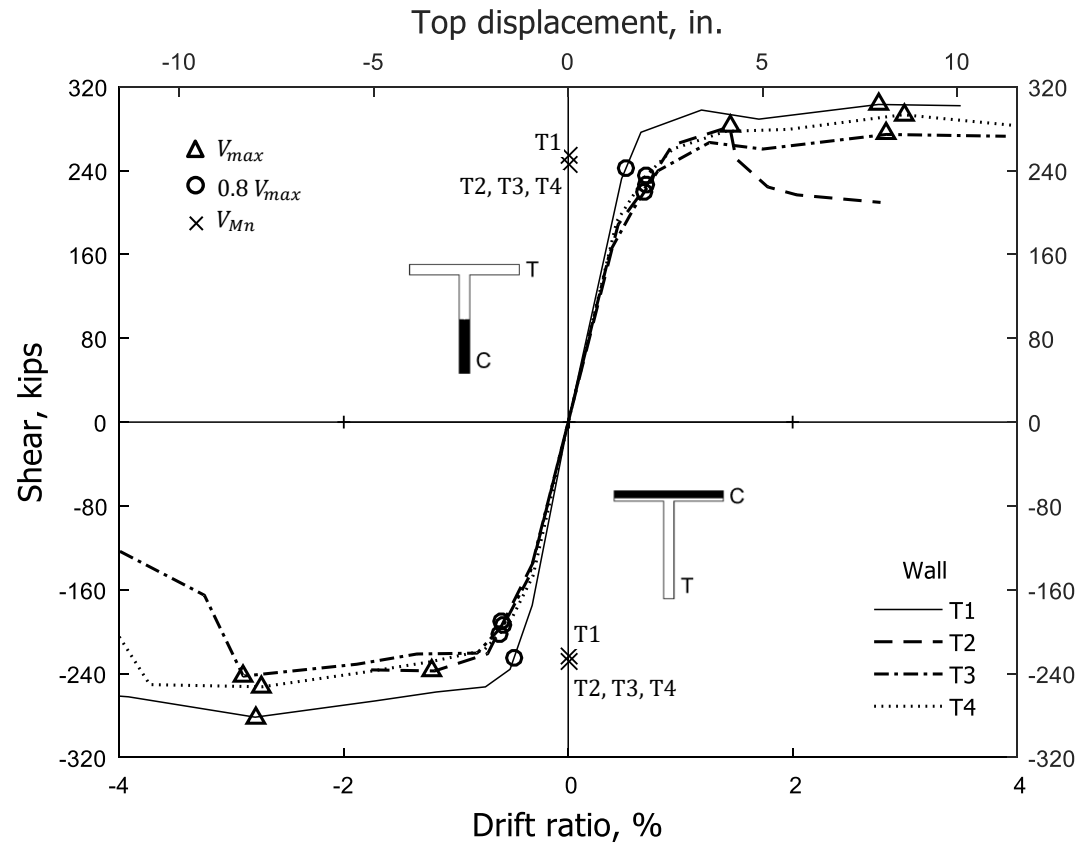


Figure 333 – Envelope of shear versus drift ratio (1 in. = 25.4 mm, 1 kip = 4.45 kN)

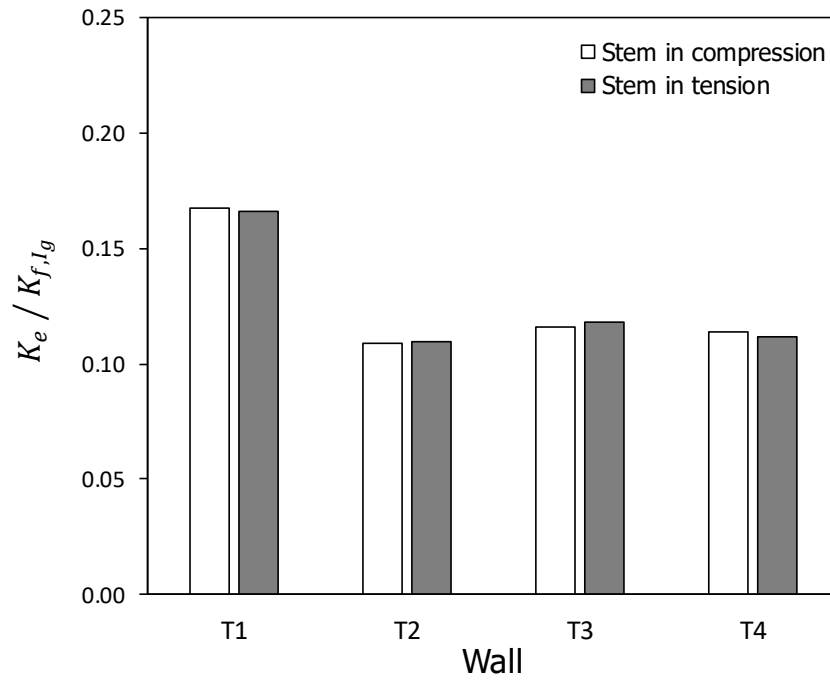


Figure 334 – Effective initial stiffness K_e normalized by flexural stiffness based on gross moment of inertia I_g

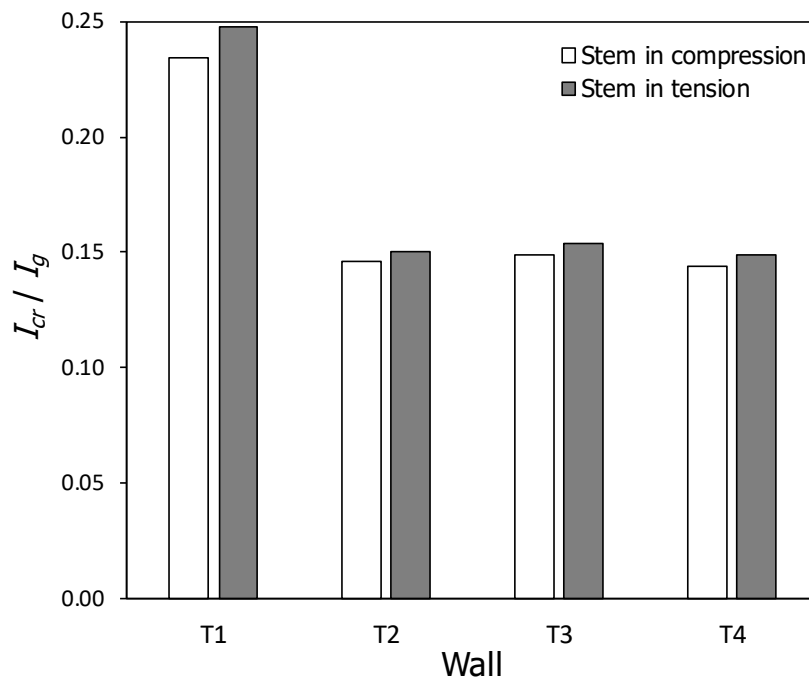


Figure 335 – Cracked moment of inertia I_{cr} normalized by gross moment of inertia I_g

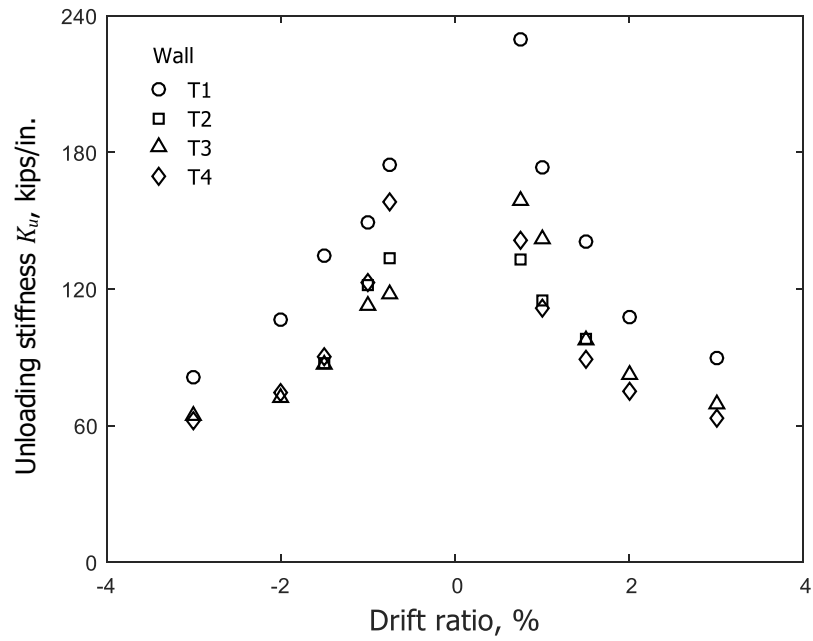


Figure 336 – Unloading stiffness versus drift ratio (1 in. = 25.4 mm, 1 kip = 4.45 kN)

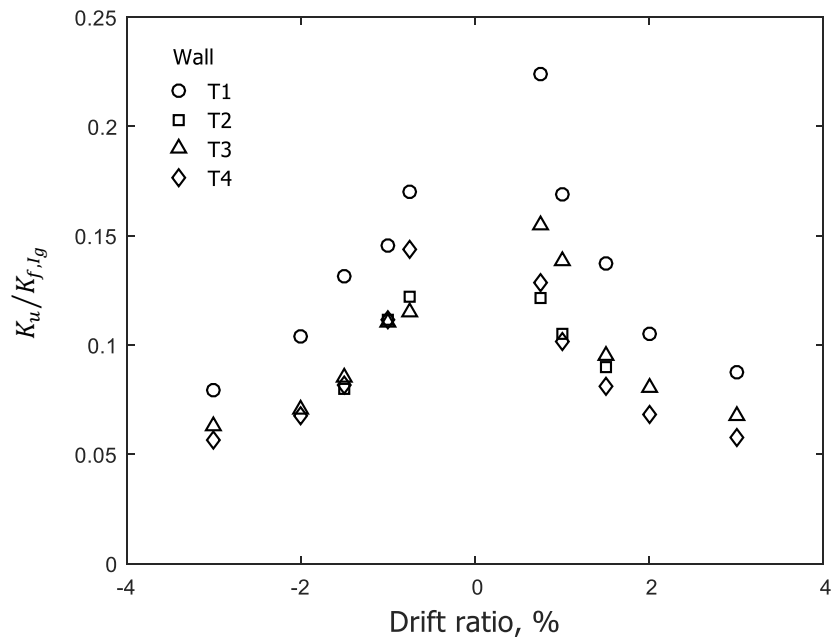
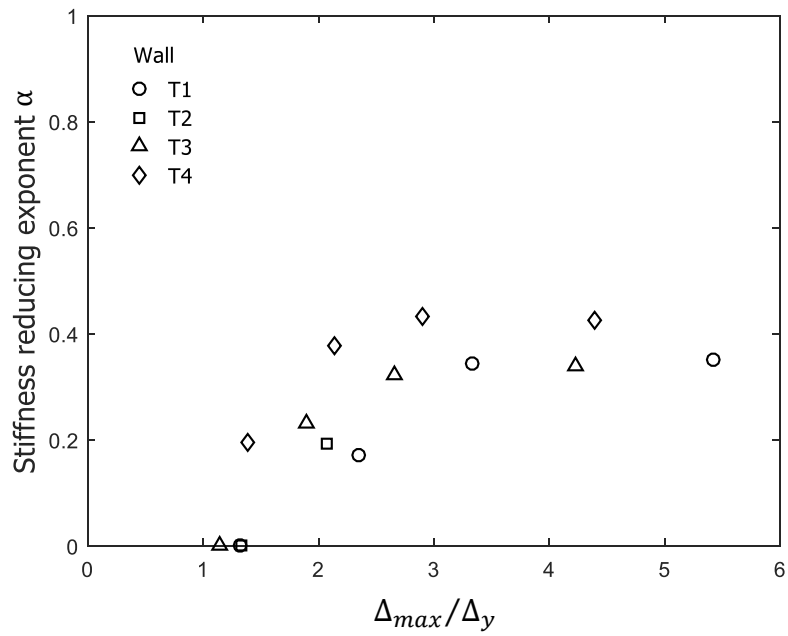
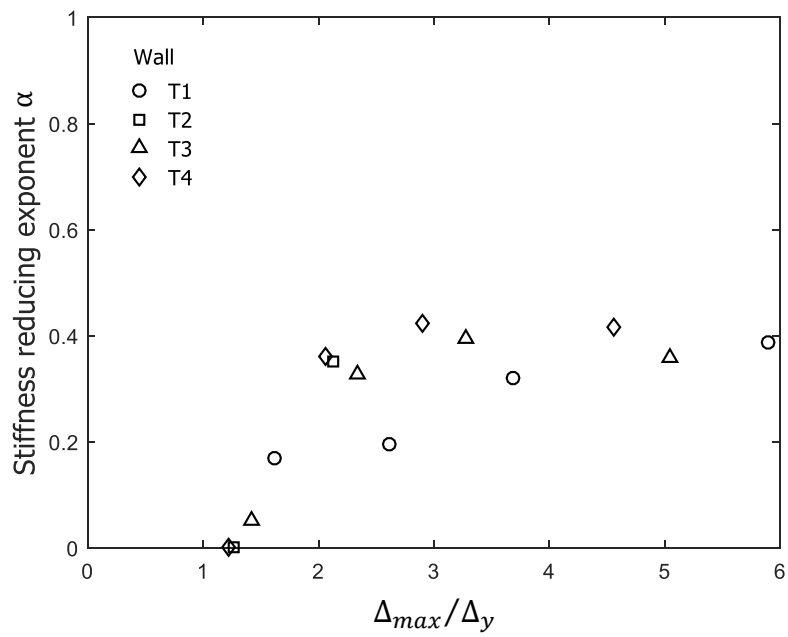


Figure 337 – Normalized unloading stiffness versus drift ratio



(a) Stem in compression



(b) Stem in tension

Figure 338 – Stiffness reducing exponent versus normalized displacement

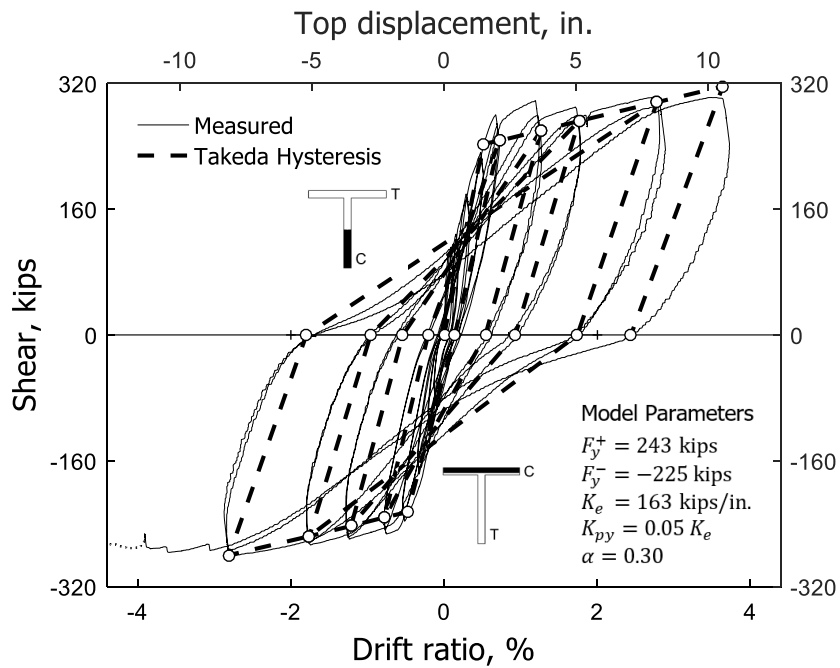


Figure 339 – Shear versus drift ratio for T1, Takeda hysteresis model vs. measured response (1 in. = 25.4 mm, 1 kip = 4.45 kN)

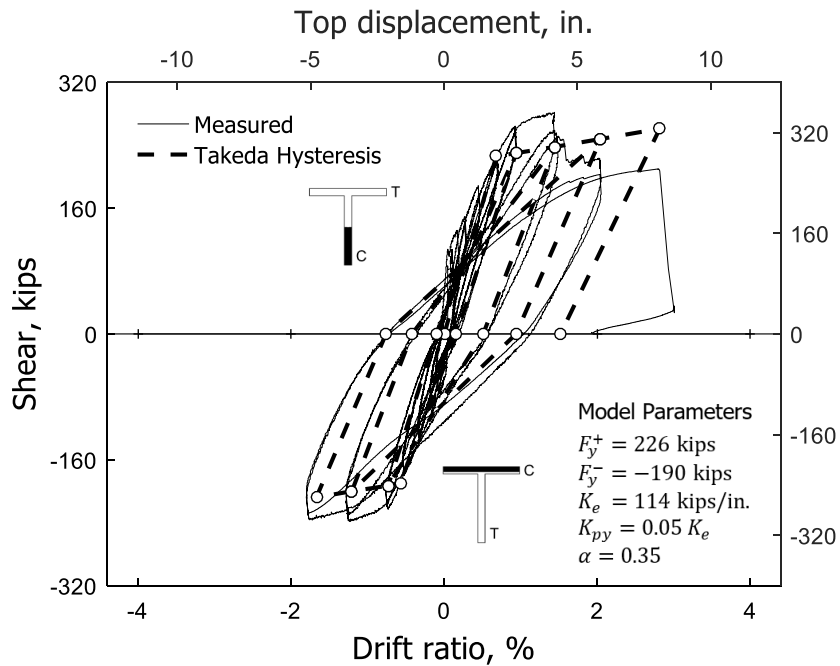


Figure 340 – Shear versus drift ratio for T2, Takeda hysteresis model vs. measured response (1 in. = 25.4 mm, 1 kip = 4.45 kN)

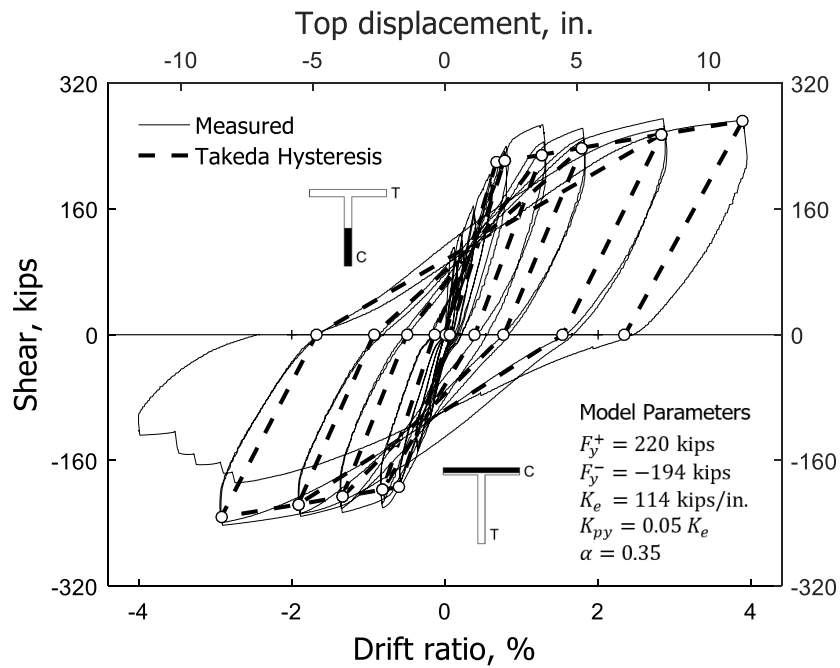


Figure 341 – Shear versus drift ratio for T3, Takeda hysteresis model vs. measured response (1 in. = 25.4 mm, 1 kip = 4.45 kN)

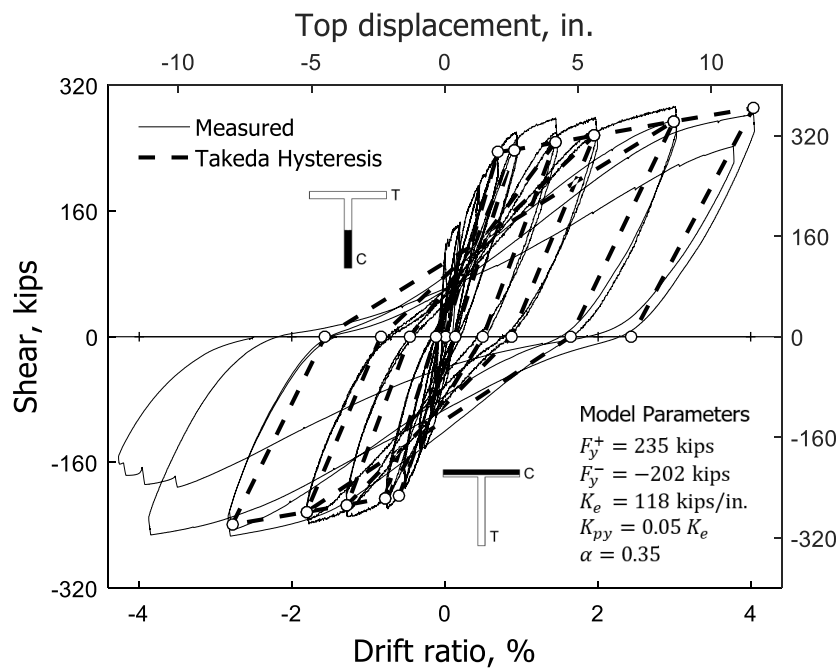


Figure 342 – Shear versus drift ratio for T4, Takeda hysteresis model vs. measured response (1 in. = 25.4 mm, 1 kip = 4.45 kN)

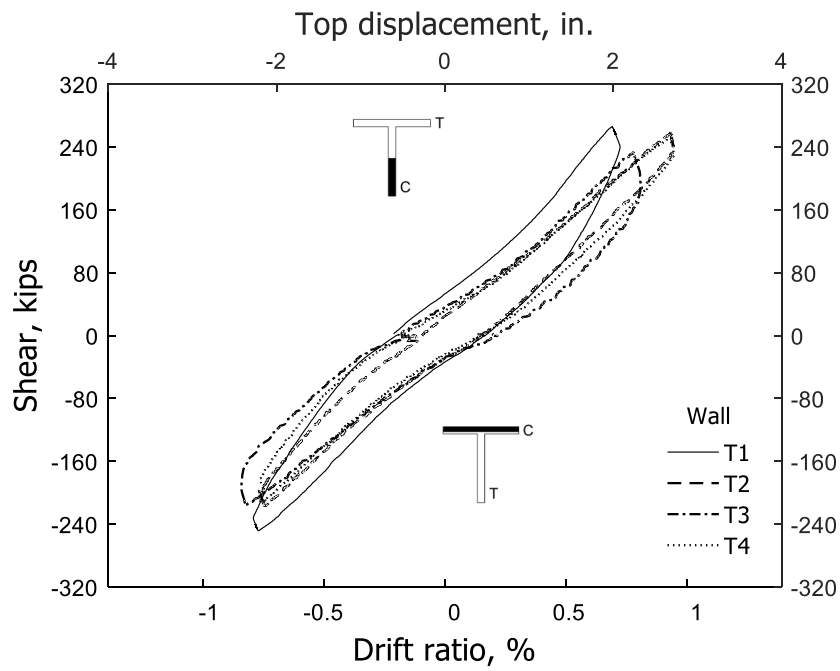


Figure 343 – Shear versus drift ratio during second cycle to 1% drift ratio (1 in. = 25.4 mm, 1 kip = 4.45 kN)

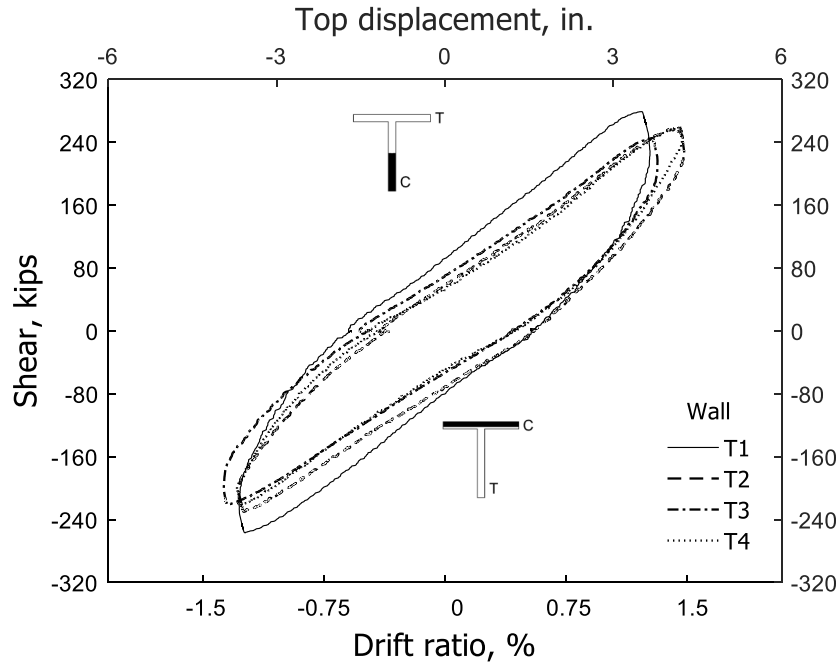


Figure 344 – Shear versus drift ratio during second cycle to 1.5% drift ratio (1 in. = 25.4 mm, 1 kip = 4.45 kN)

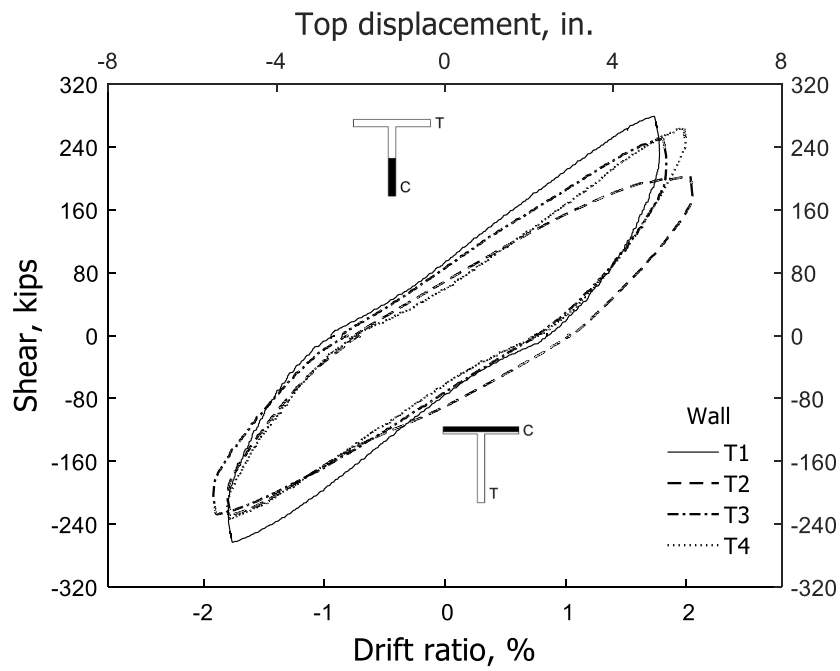


Figure 345 – Shear versus drift ratio during second cycle to 2% drift ratio (1 in. = 25.4 mm, 1 kip = 4.45 kN)

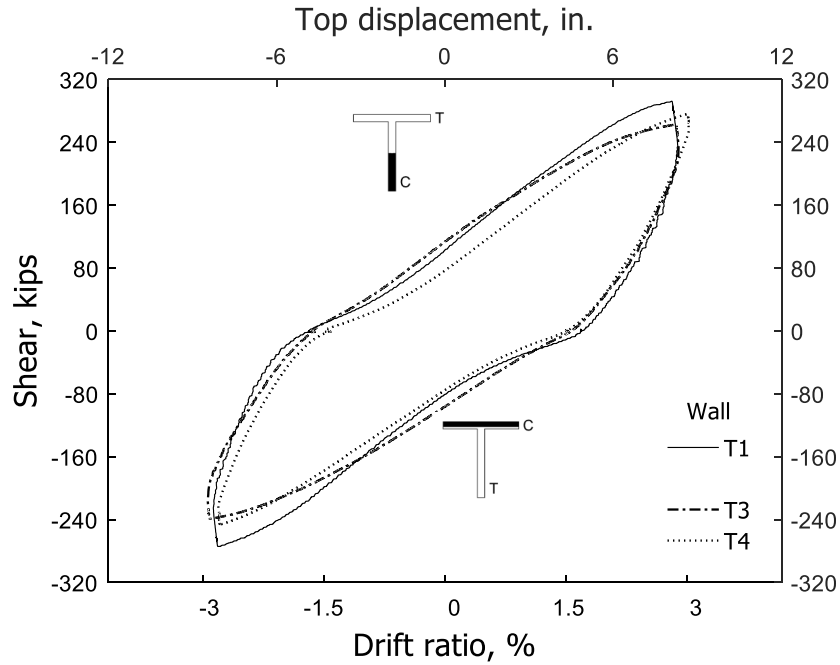
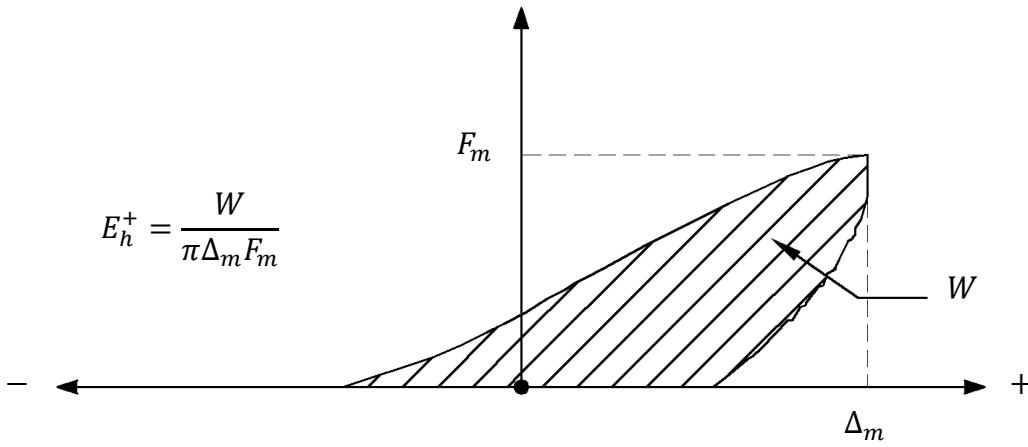
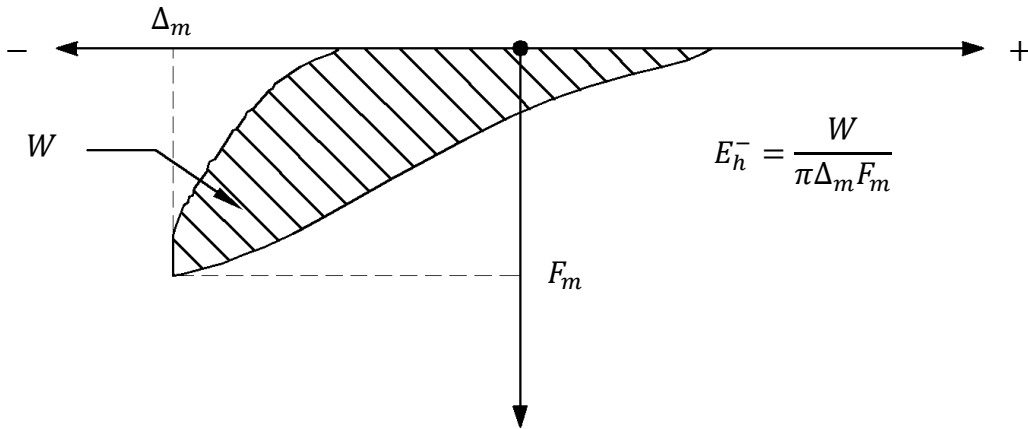


Figure 346 – Shear versus drift ratio during second cycle to 3% drift ratio (1 in. = 25.4 mm, 1 kip = 4.45 kN)

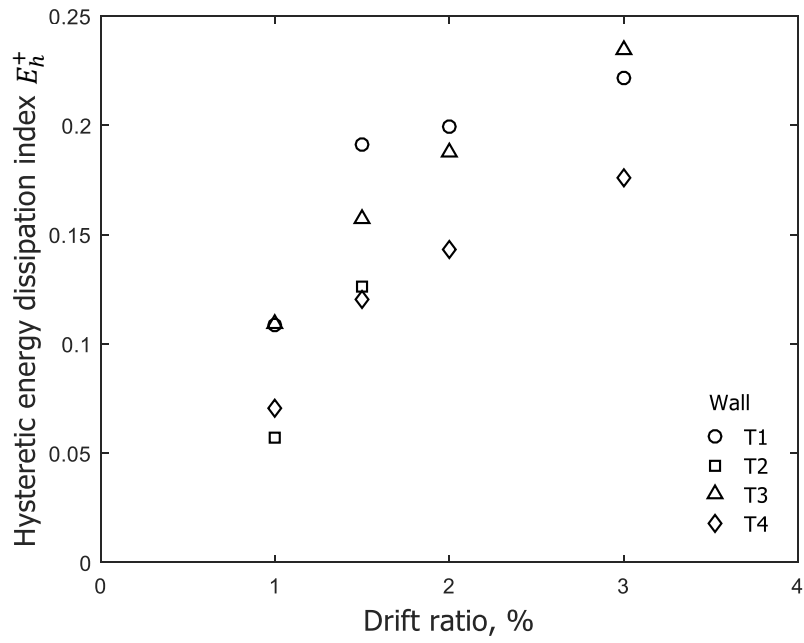


(a) Stem in compression

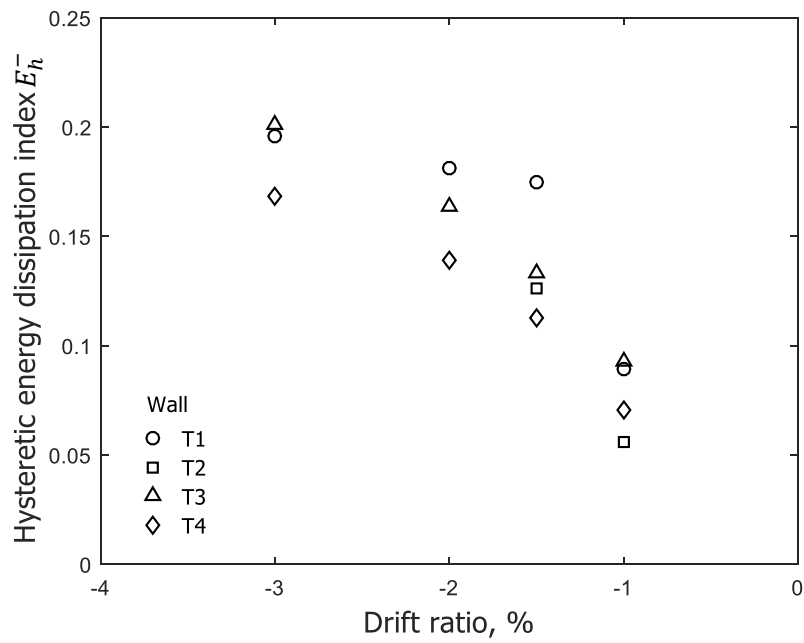


(b) Stem in tension

Figure 347 - Hysteretic energy dissipation index E_h

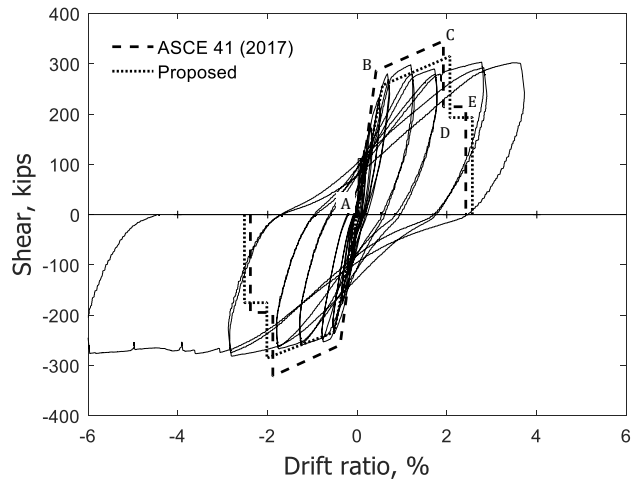


(a) Stem in compression

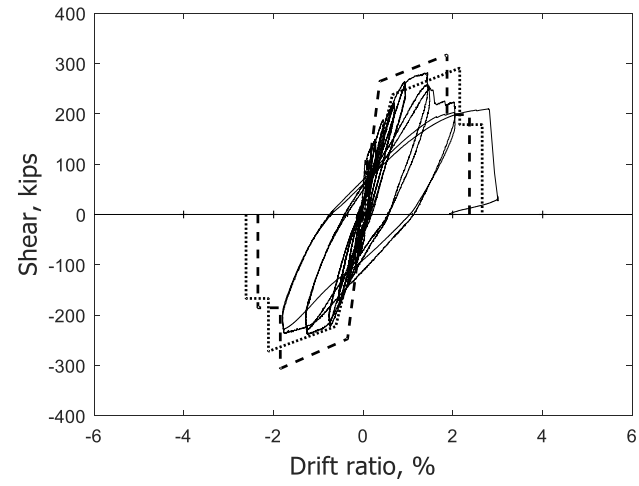


(b) Stem in tension

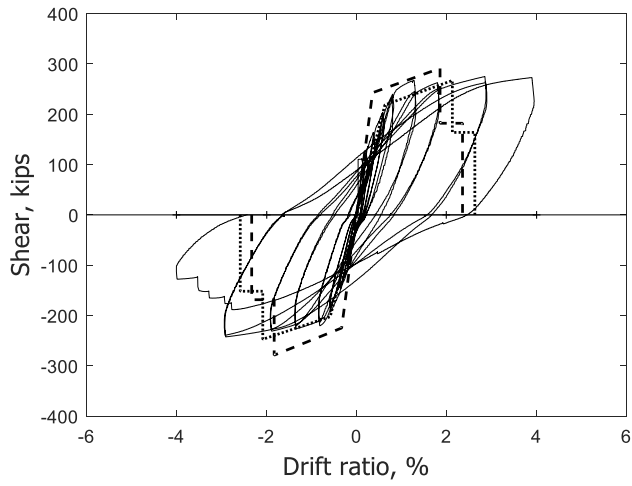
Figure 348 – Hysteretic energy dissipation index versus drift ratio



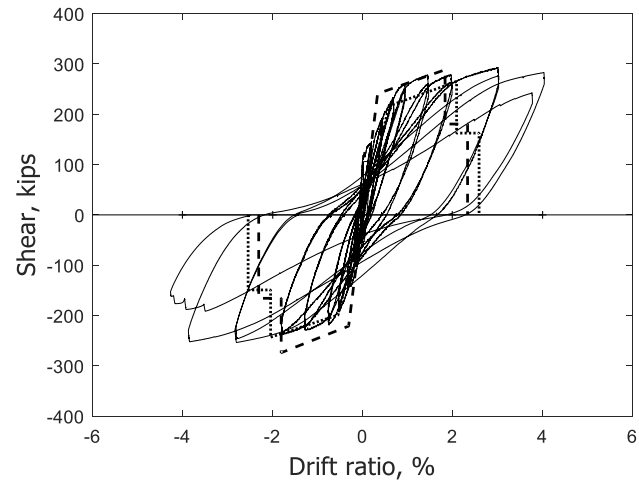
(a) T1



(b) T2



(c) T3



(d) T4

Figure 349 – Measured shear versus drift ratio compared with modeling parameters from Table 14 (1 kip = 4.45 kN)

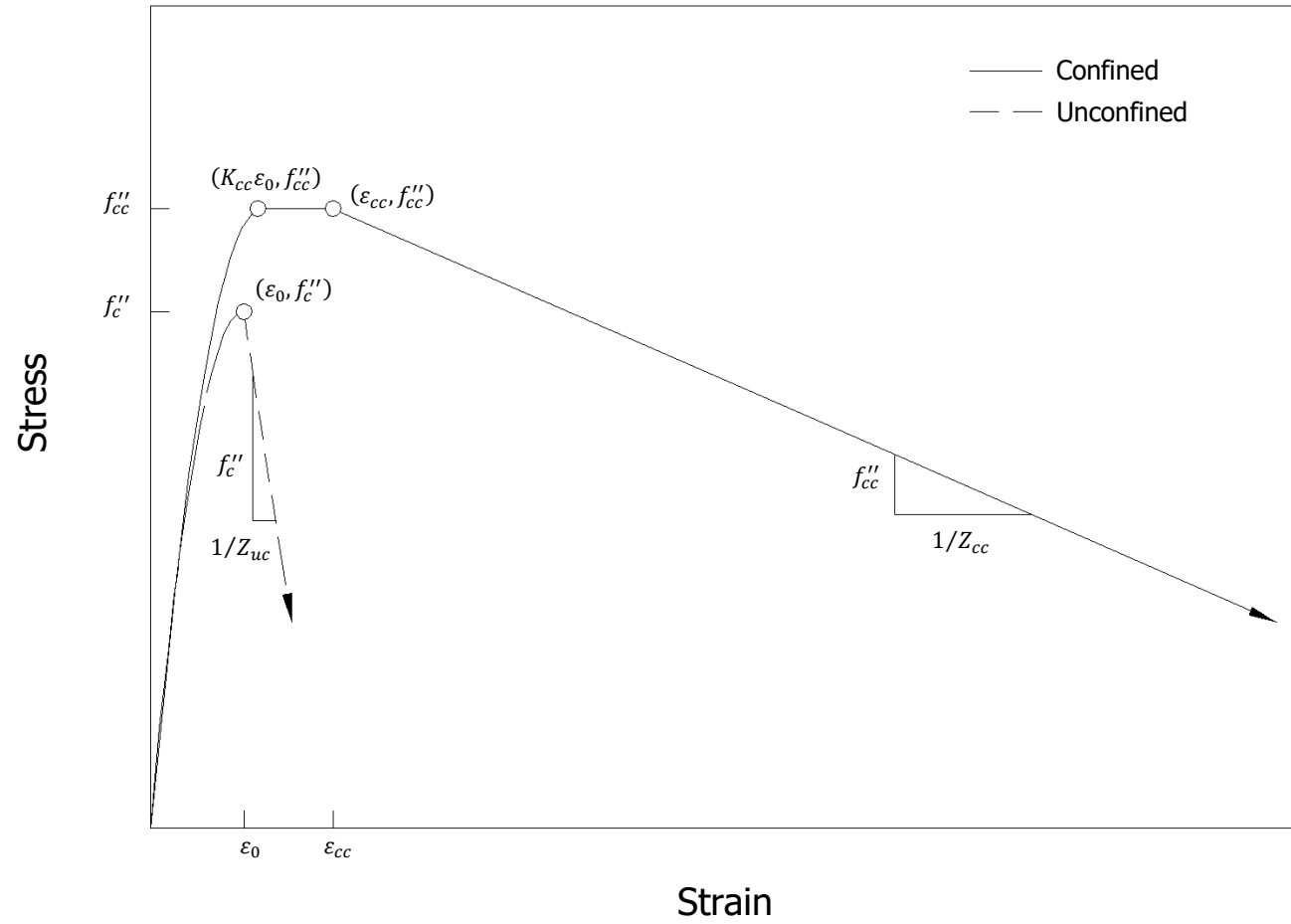
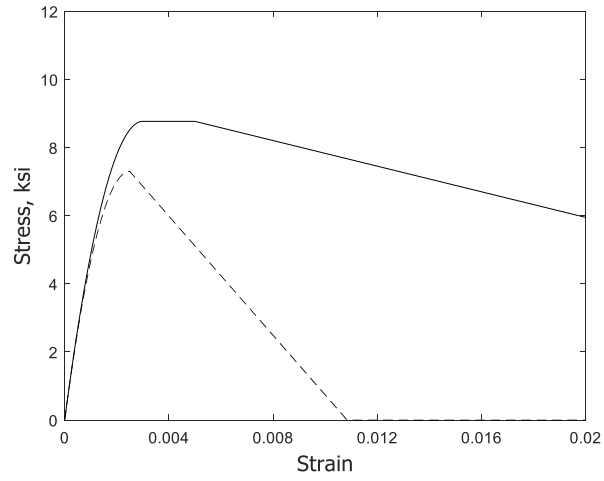
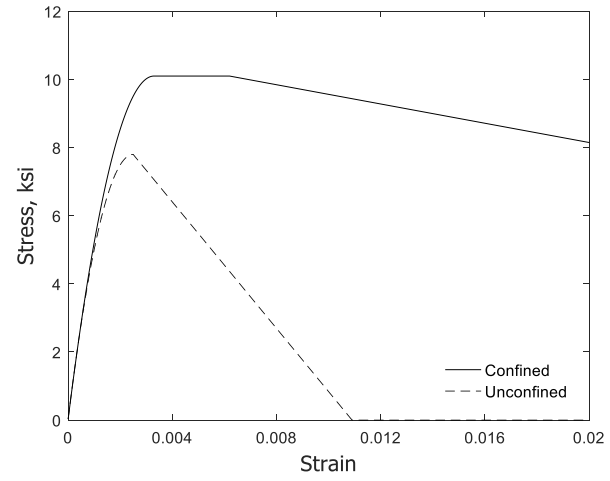


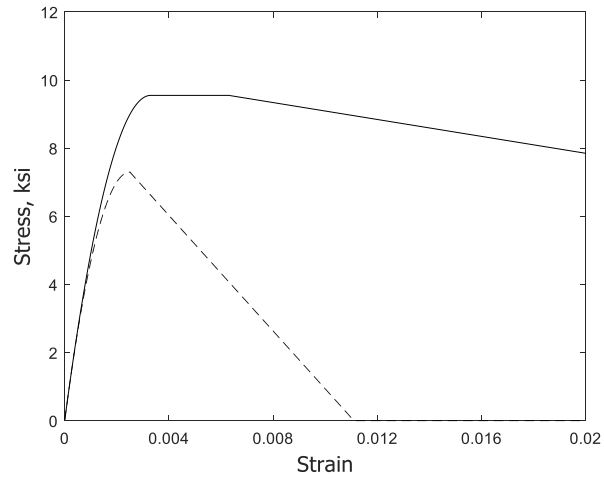
Figure 350 – Stress-strain relationships for concrete in compression



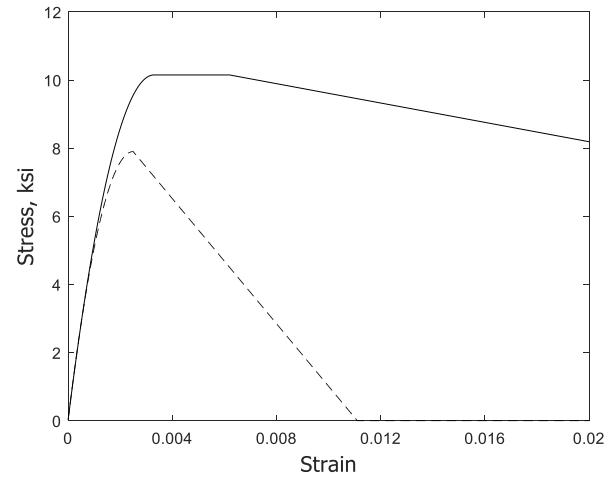
(a) T1



(b) T2



(c) T3



(d) T4

Figure 351 – Stress-strain relationships for confined and unconfined concrete in compression using parameter values from Table 15

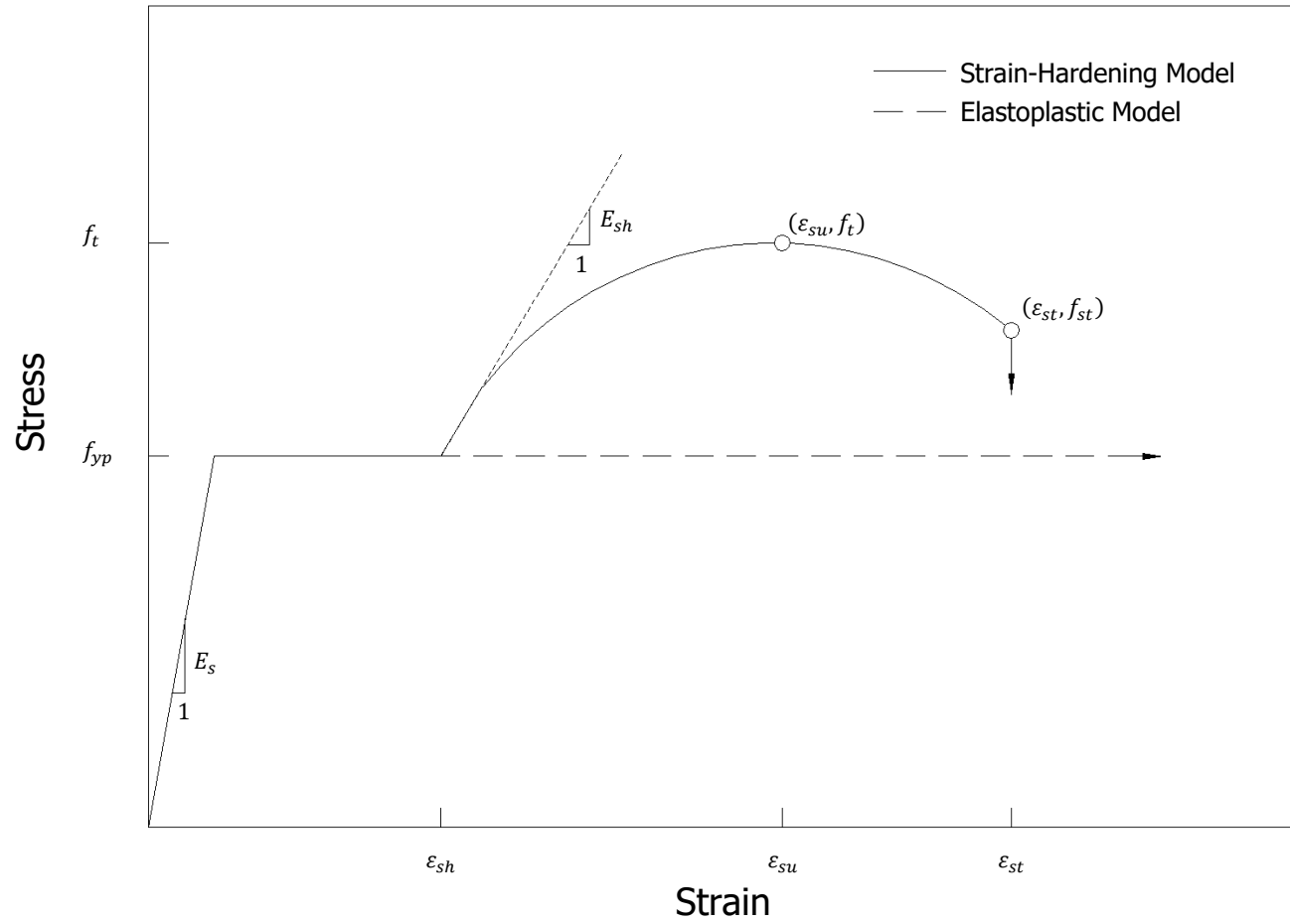
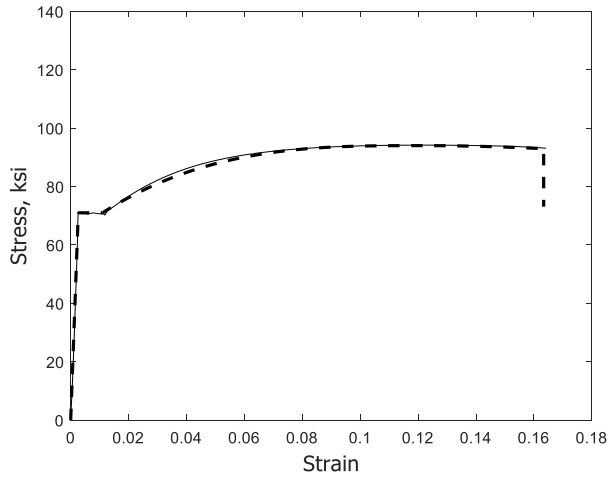
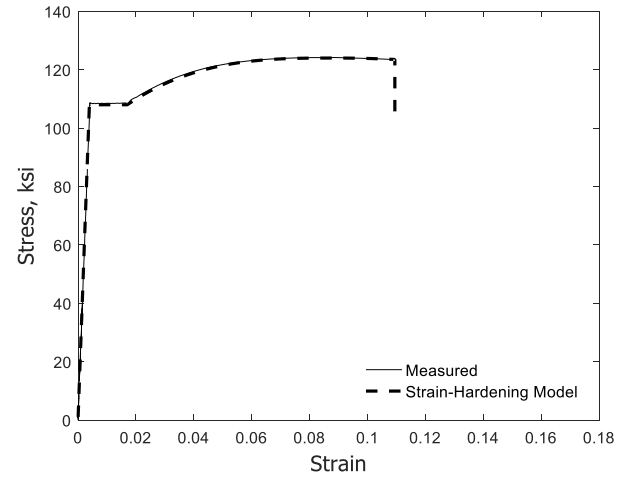


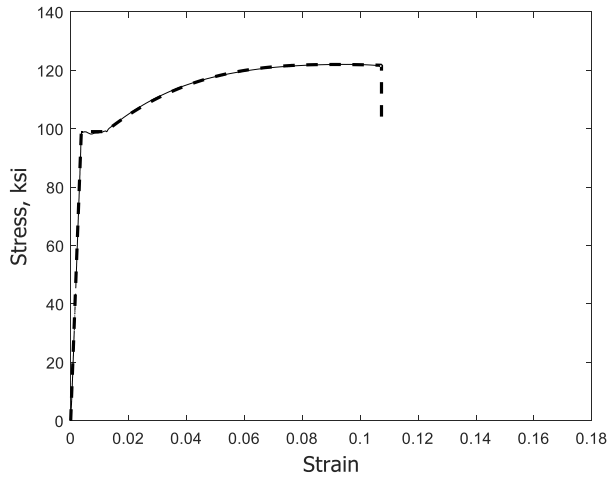
Figure 352 – Stress-strain relationships for steel



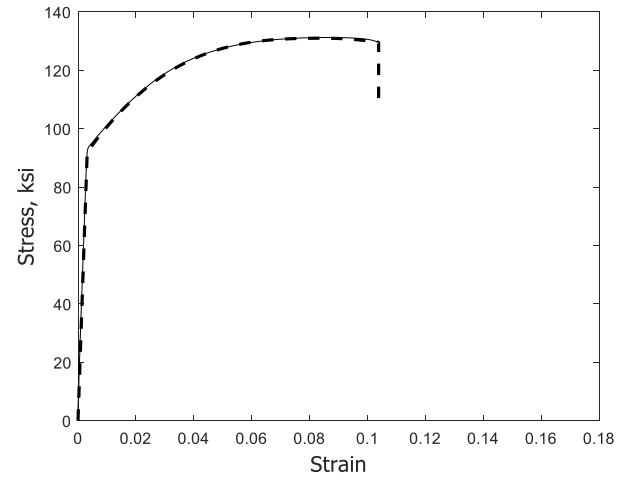
(a) T1



(b) T2

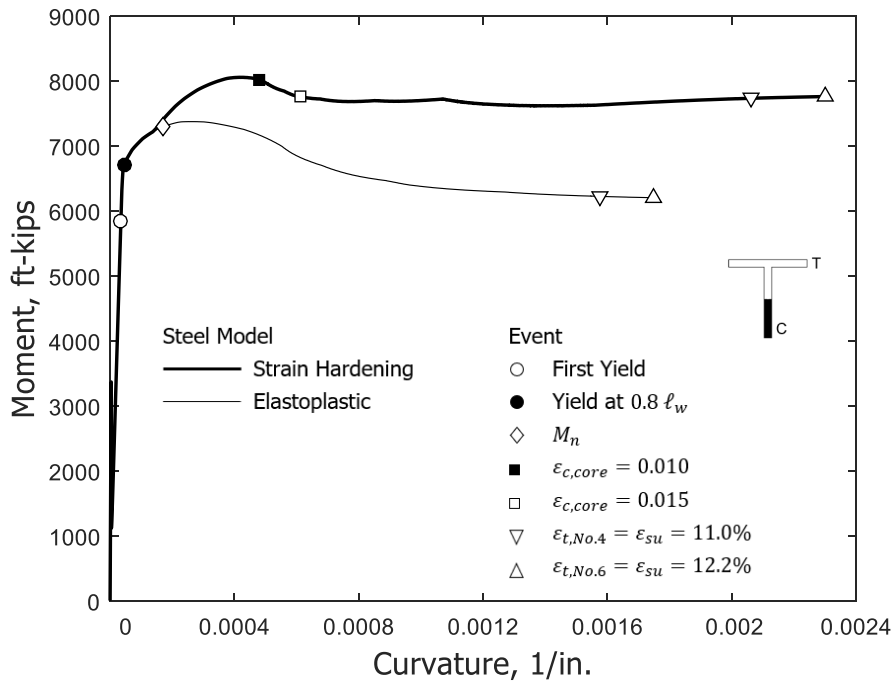


(c) T3

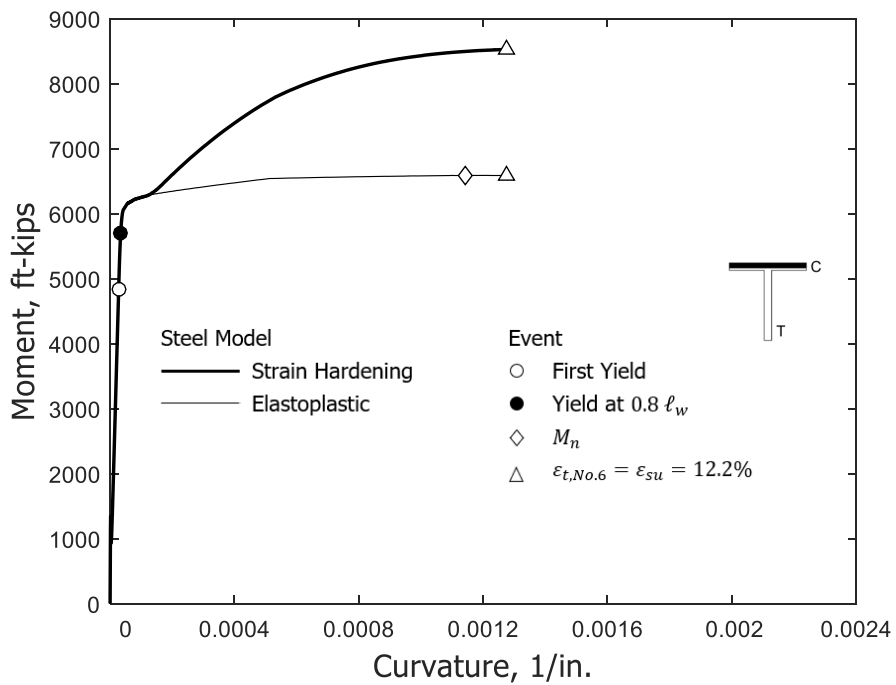


(d) T4

Figure 353 – Comparison of measured steel stress-strain relationships for No. 6 (19) bars with the calibrated strain-hardening model using parameter values from Table 16 (1ksi = 6.89 MPa)

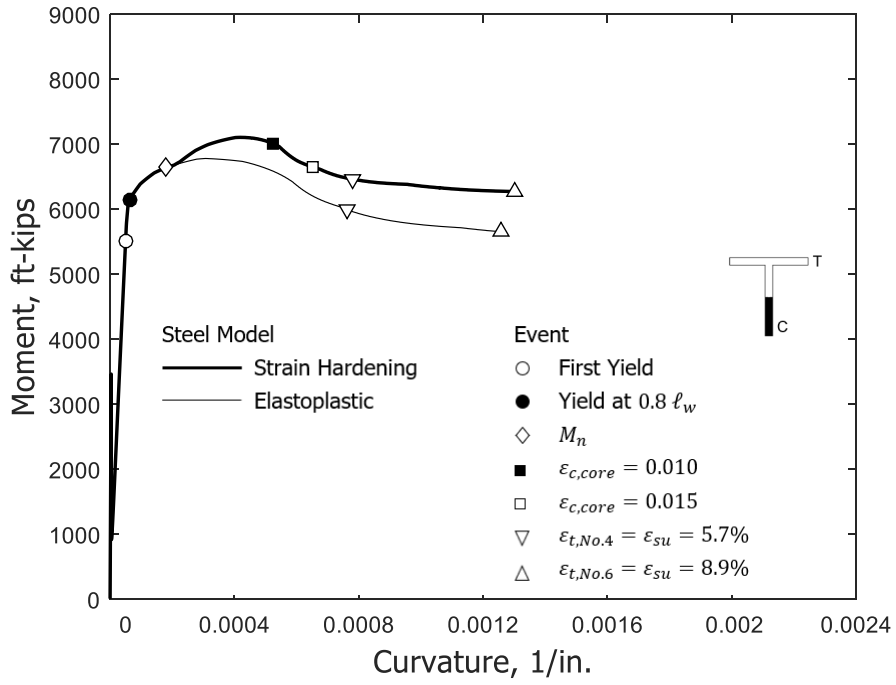


(a) Stem in compression

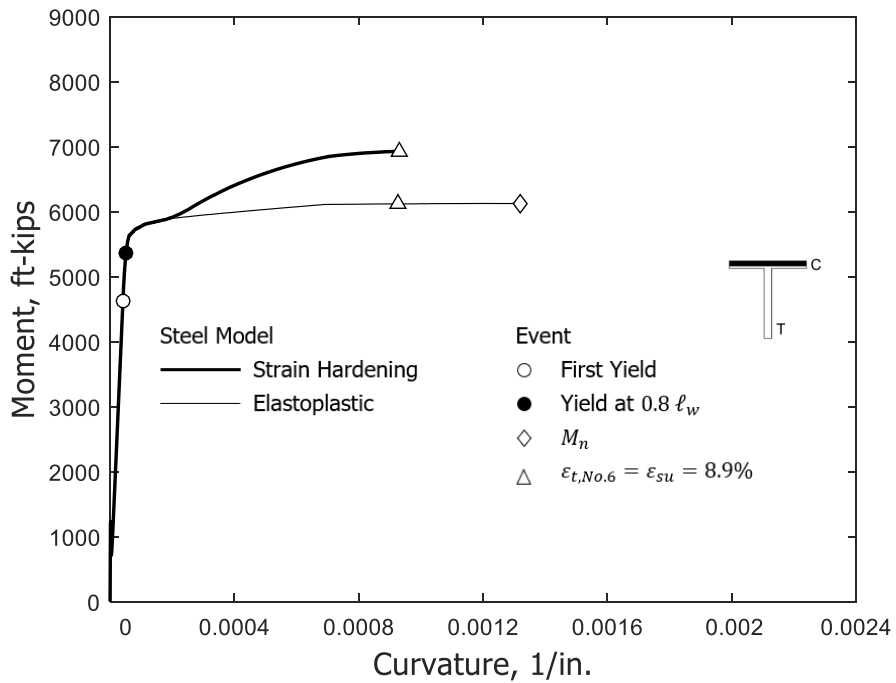


(b) Stem in tension

Figure 354 – Moment-curvature relationships for T1 (1 in. = 25.4 mm, 1 ft-kips = 1.36 m-kN)

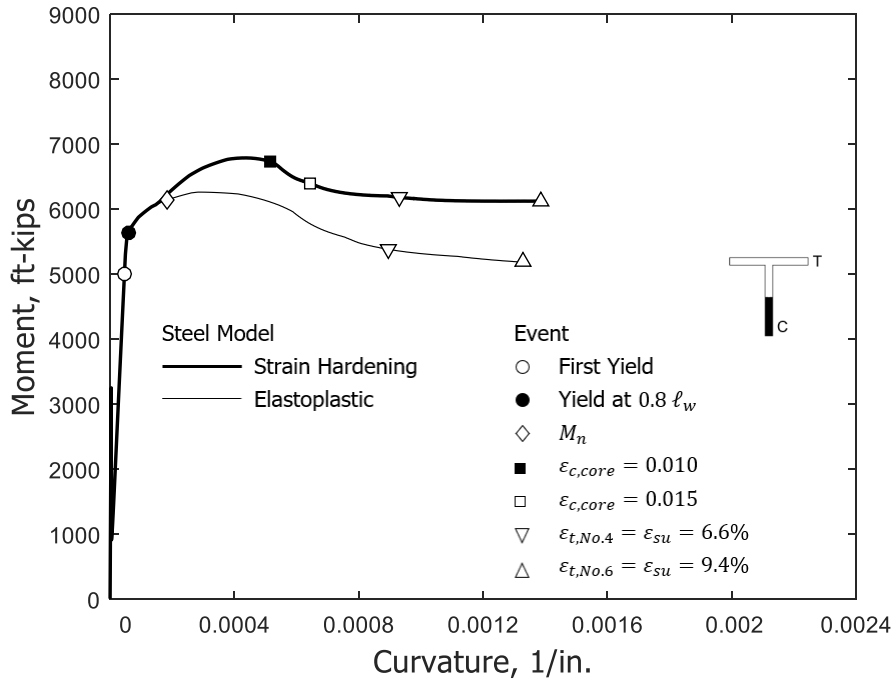


(a) Stem in compression

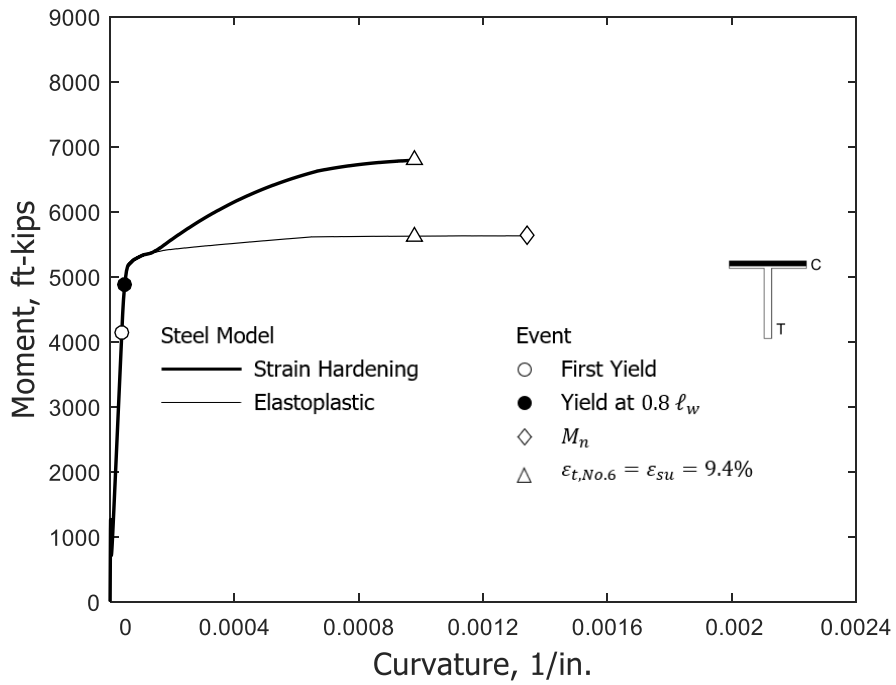


(b) Stem in tension

Figure 355 – Moment-curvature relationships for T2 (1 in. = 25.4 mm, 1 ft-kips = 1.36 m-kN)

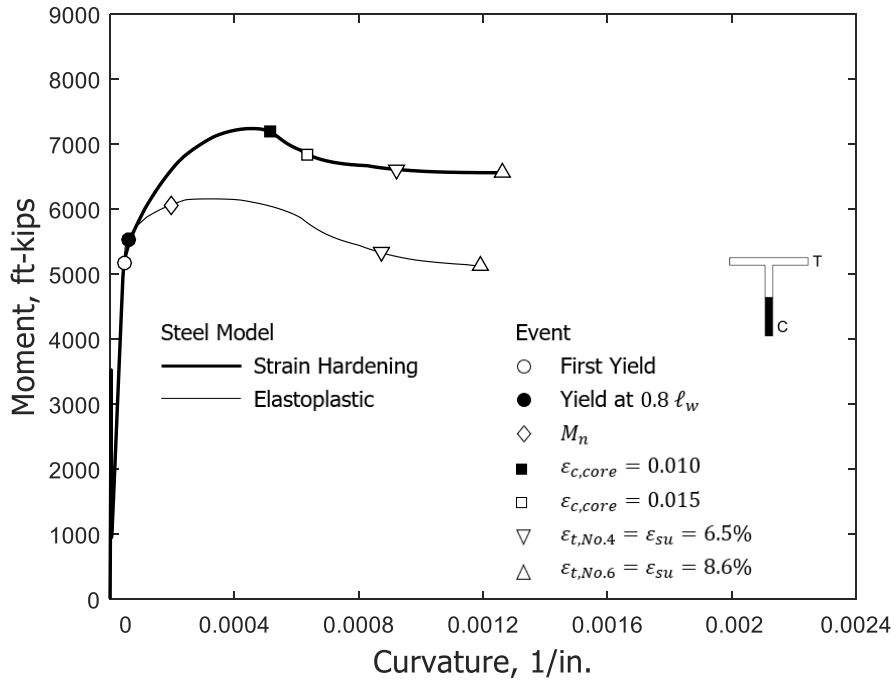


(a) Stem in compression

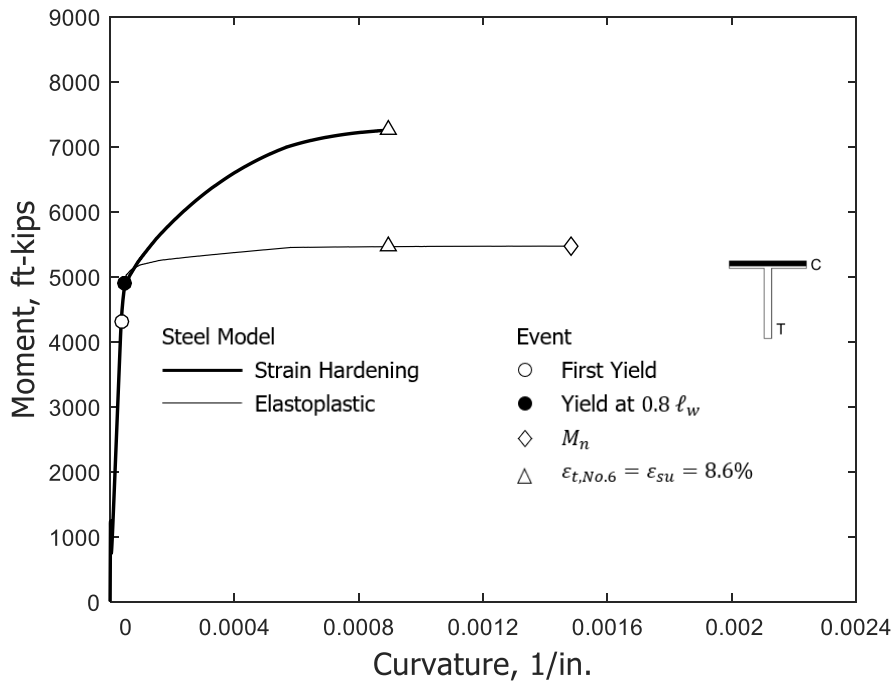


(b) Stem in tension

Figure 356 – Moment-curvature relationships for T3 (1 in. = 25.4 mm, 1 ft-kips = 1.36 m-kN)

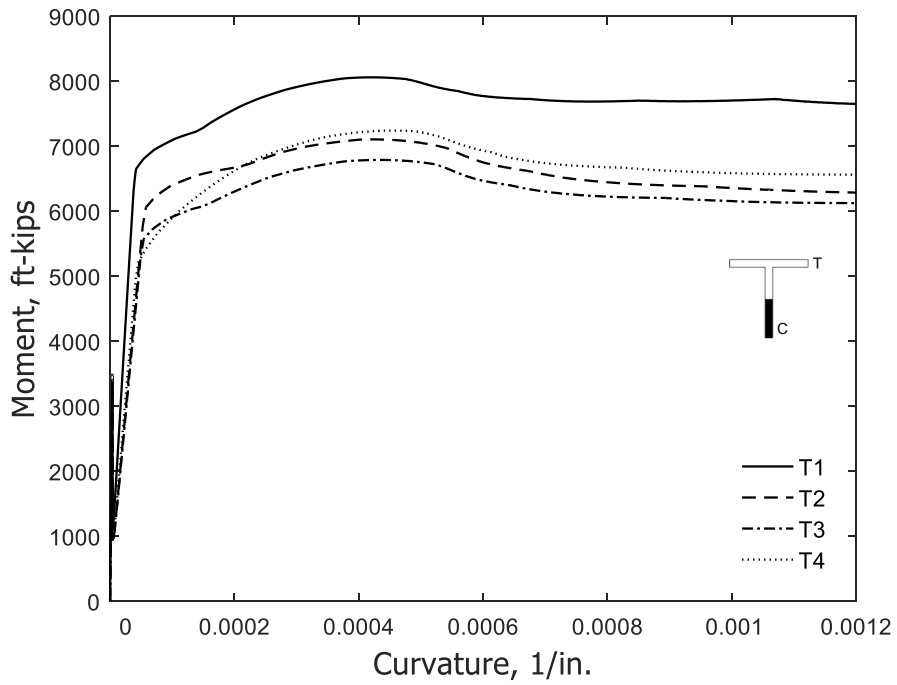


(a) Stem in compression

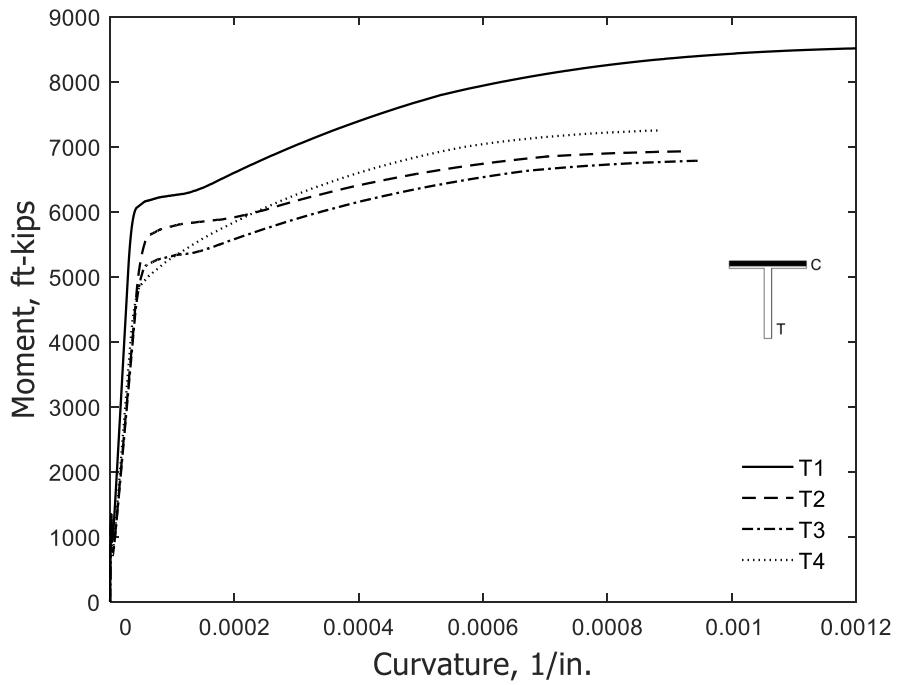


(b) Stem in tension

Figure 357 – Moment-curvature relationships for T4 (1 in. = 25.4 mm, 1 ft-kips = 1.36 m-kN)



(a) Stem in compression



(b) Stem in tension

Figure 358 – Moment-curvature relationships for all walls (1 in. = 25.4 mm, 1 ft-kips = 1.36 m-kN)

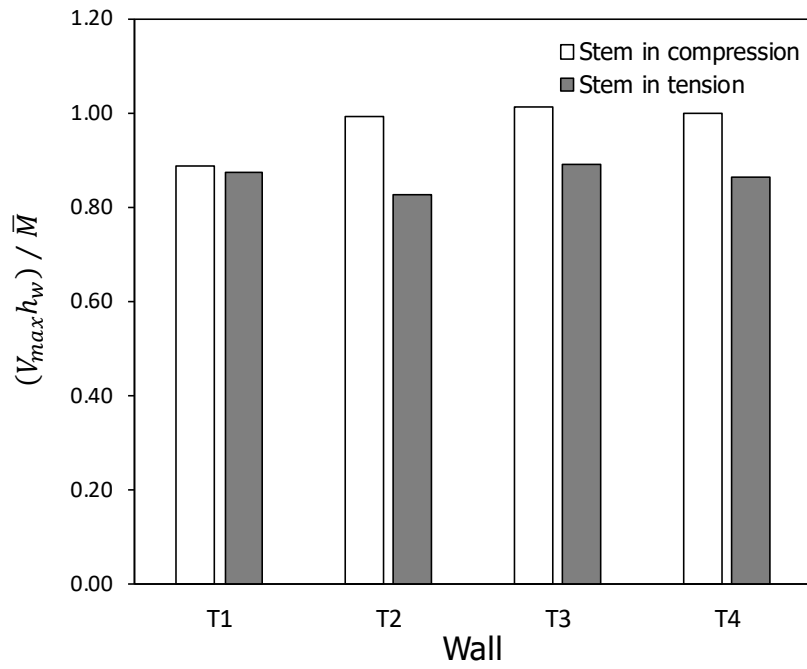


Figure 359 – Ratio of test to calculated maximum moment

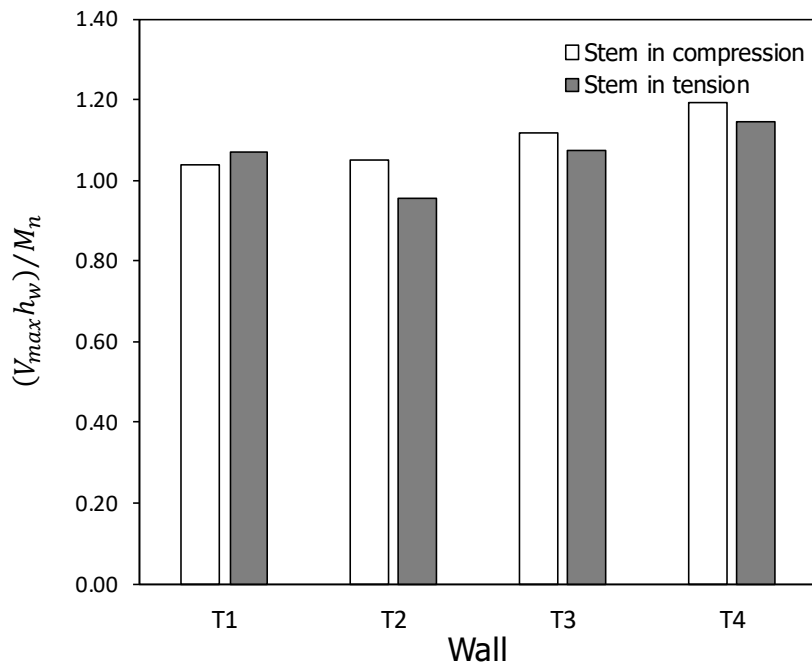
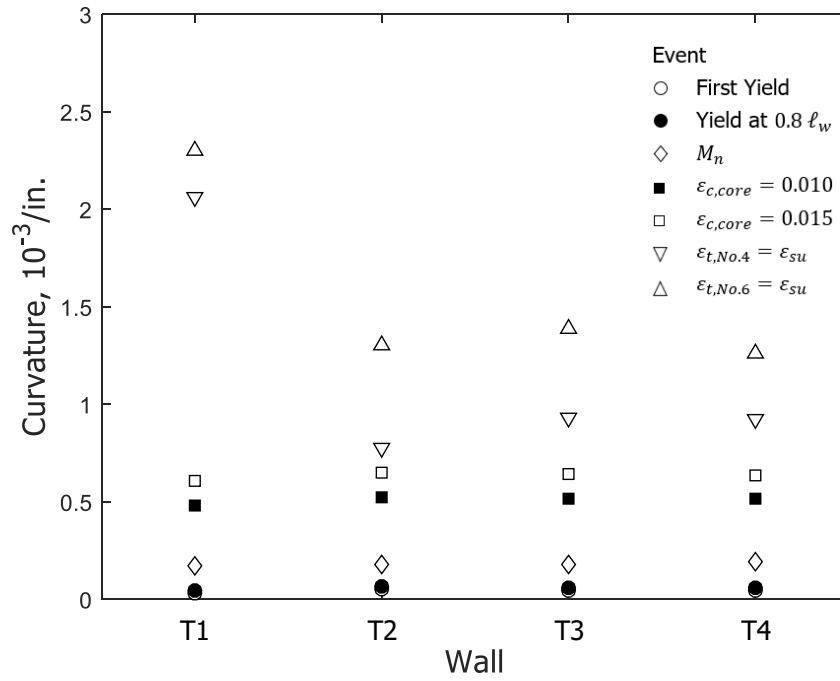
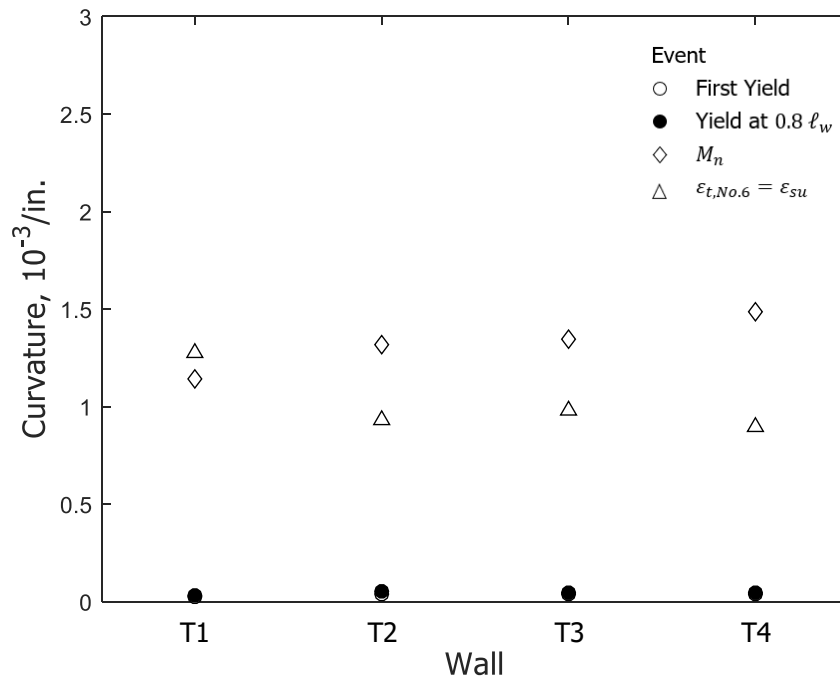


Figure 360 – Ratio of maximum moment from test to calculated nominal moment



(a) Stem in compression



(b) Stem in tension

Figure 361 – Curvature comparisons at relevant events for all walls (1 in. = 25.4 mm)

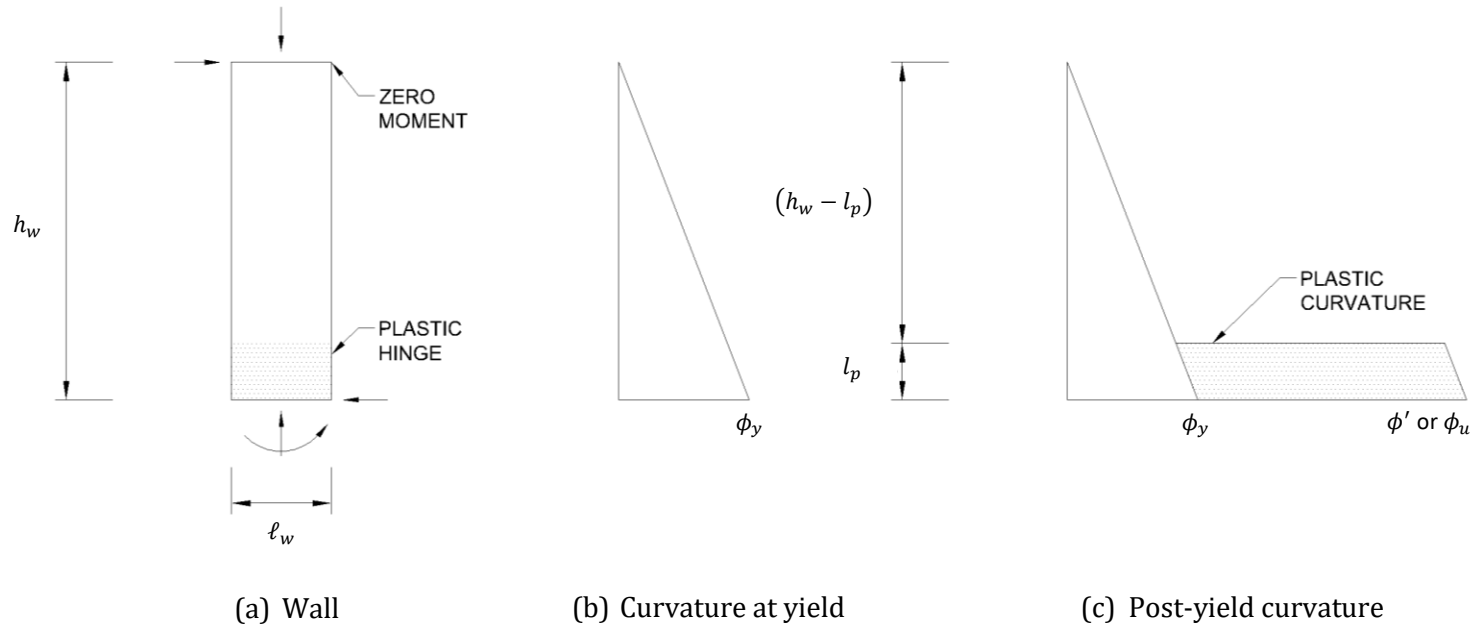
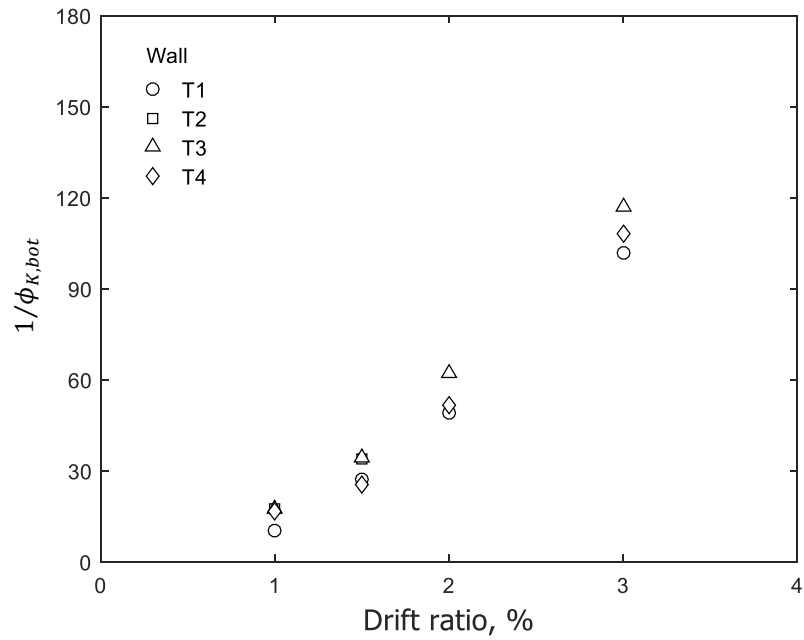
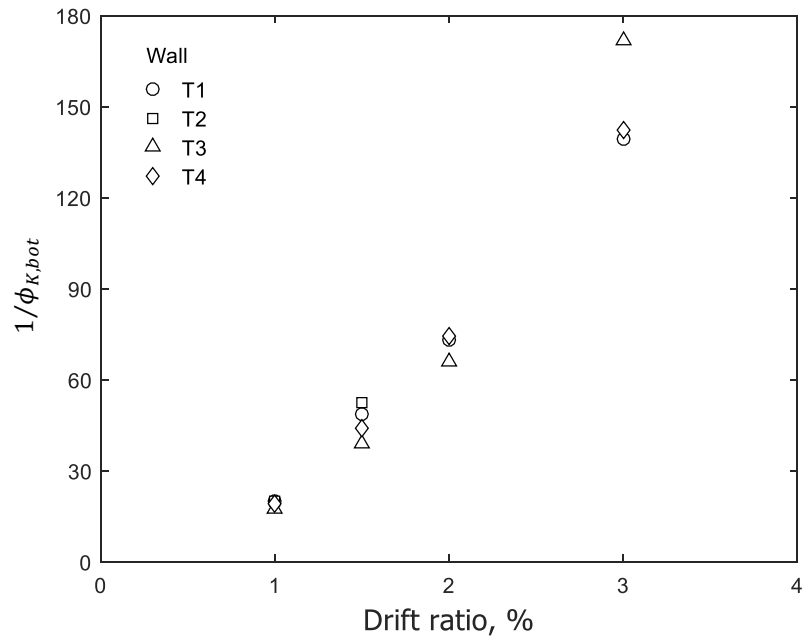


Figure 362 – Idealized curvature distribution for plastic hinge model



(a) Stem in compression



(b) Stem in tension

Figure 363 – Inverse of ϕ_k versus drift ratio for bottom 50 in. (1270 mm) of wall based on data from optical markers

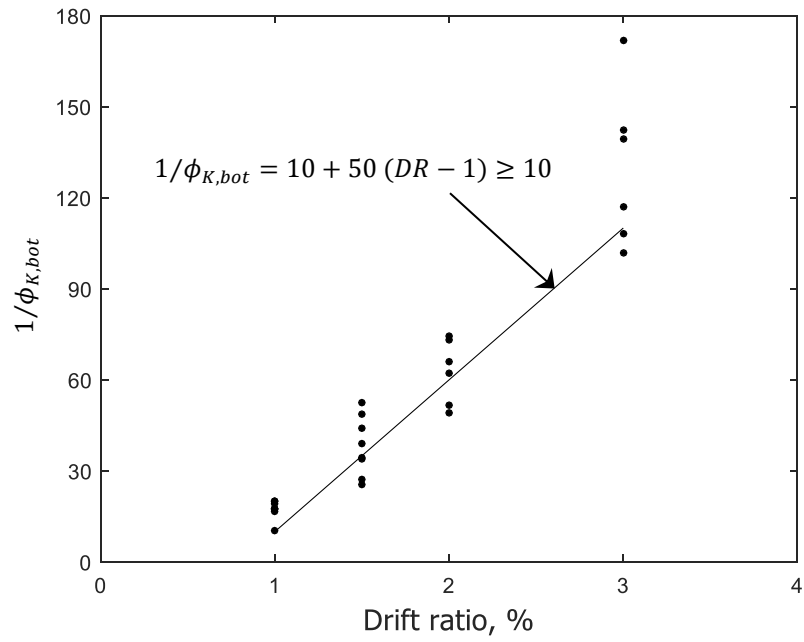


Figure 364 – Simplified trend for inverse of φ_K versus drift ratio for bottom 50 in. (1270 mm) of wall (data from Figure 363)

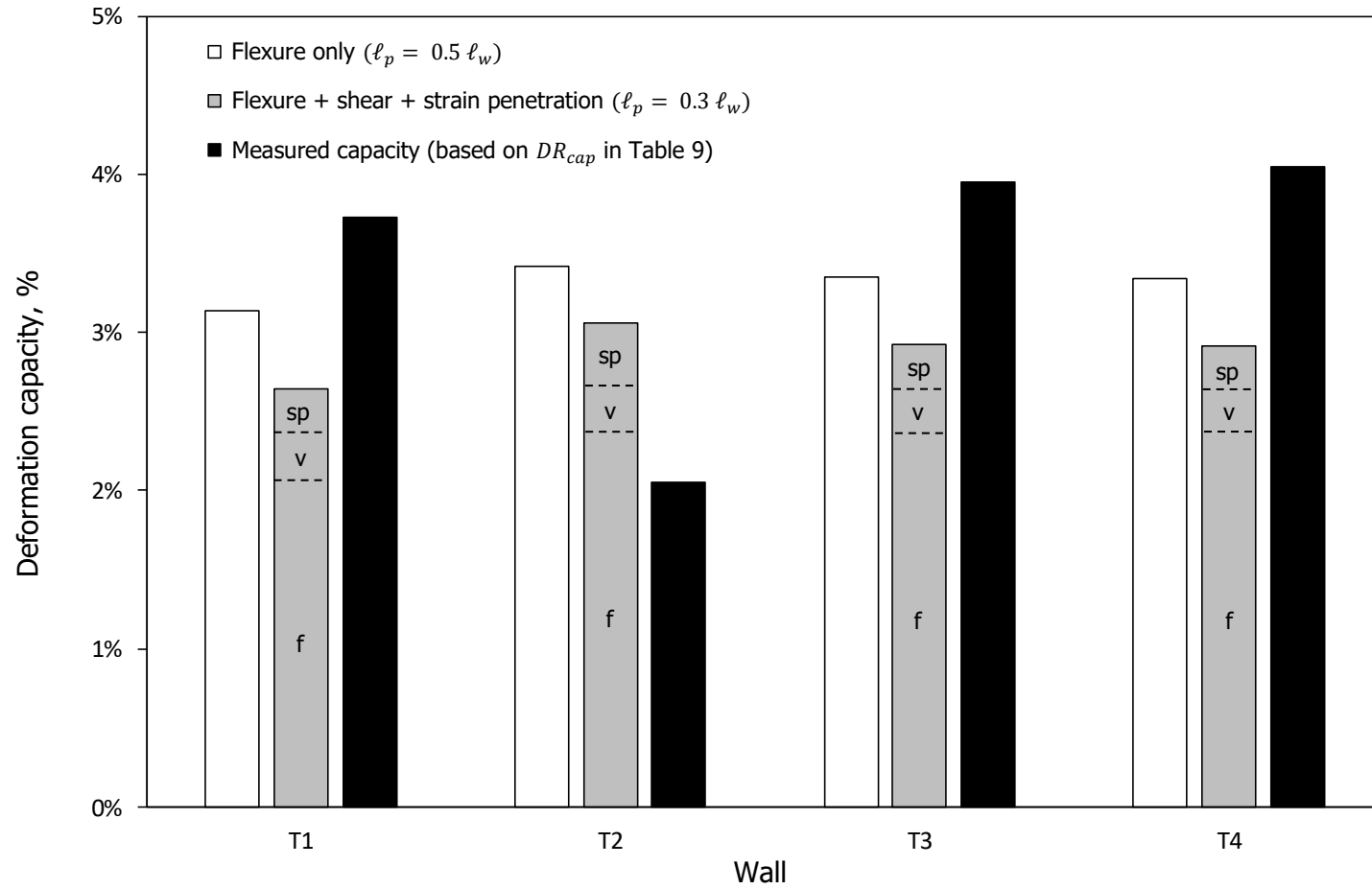


Figure 365 – Measured and calculated deformation capacities

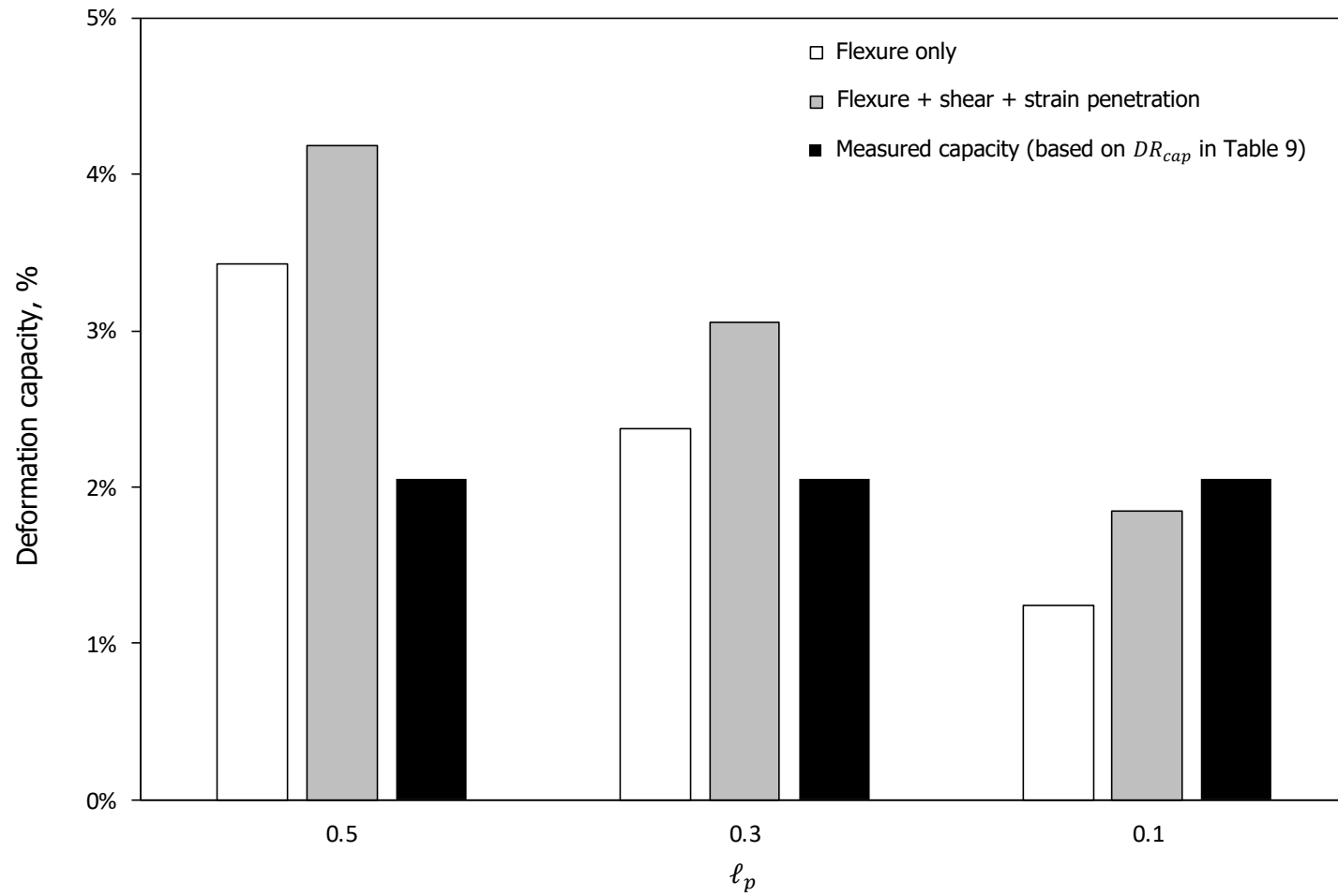


Figure 366 – Calculated deformation capacity for T2 using different values of ℓ_p

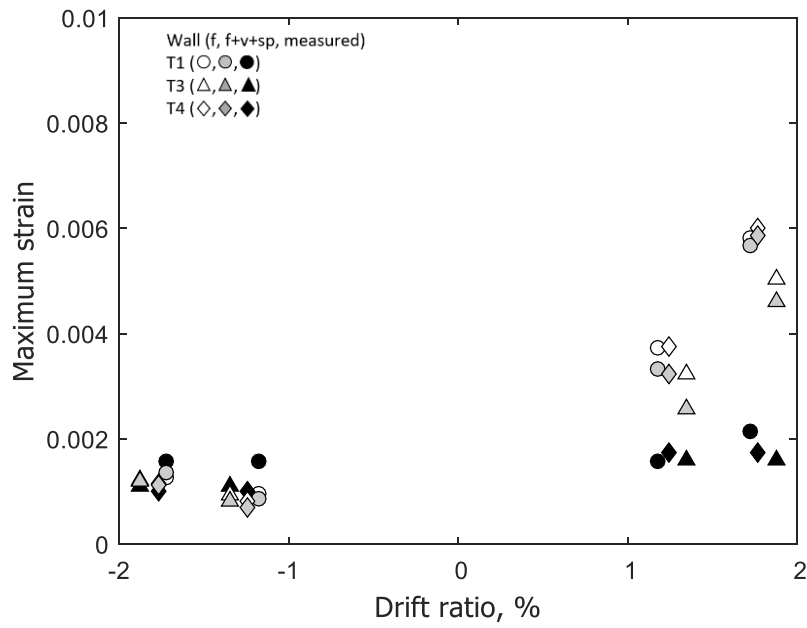


Figure 369 – Measured and calculated maximum compressive strain of concrete surface, 14-in. (356-mm) gauge length

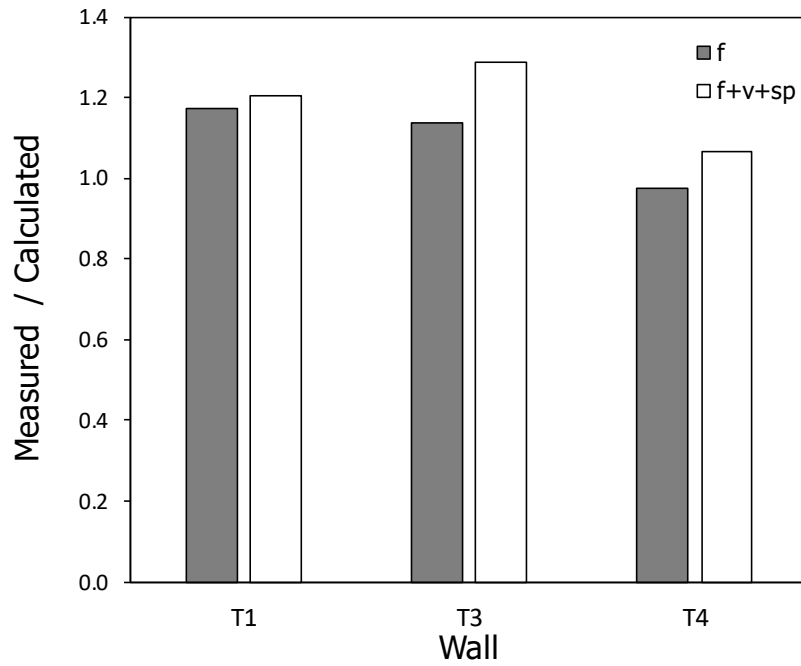


Figure 370 – Average of measured-to-calculated maximum tensile strain of reinforcement

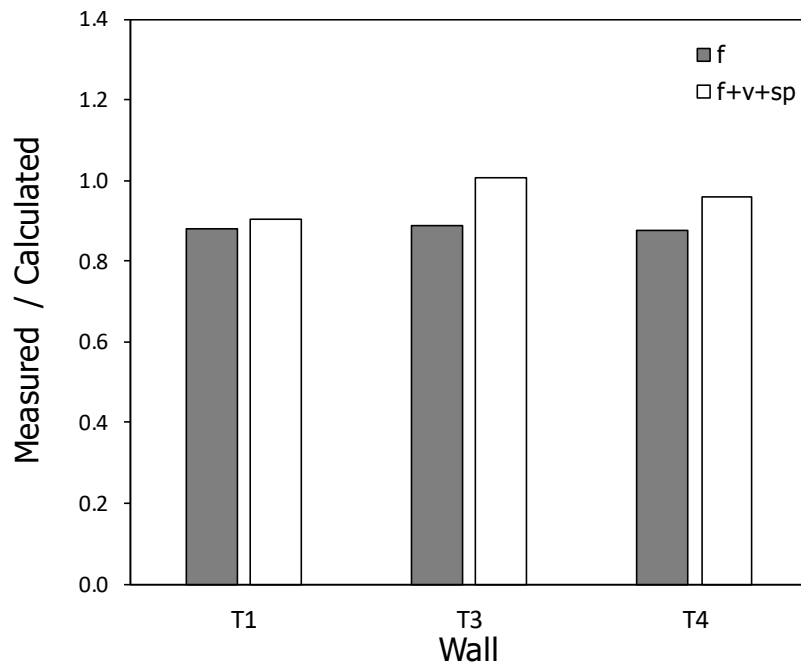


Figure 371 – Average of measured-to-calculated maximum tensile strain of concrete surface

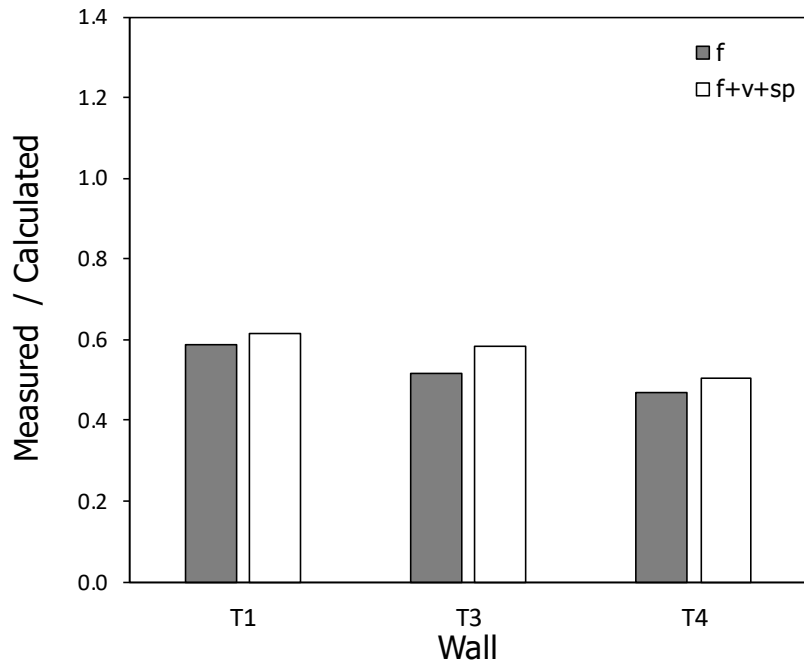


Figure 372 – Average of measured-to-calculated maximum compressive strain of concrete surface

APPENDIX A: NOTATION

A_{cv}	=	gross area of concrete section resisting shear ($t_w \ell_w$ for a T-shaped wall), in. ² (mm ²)
$A_{cv,eff}$	=	effective area of concrete section resisting shear ($\phi_k t_w \ell_w$ for a T-shaped wall), in. ² (mm ²)
A_g	=	gross area of concrete section, in. ² (mm ²)
A_s	=	area of reinforcement, in. ² (mm ²)
c	=	distance from extreme compression fiber to neutral axis, in. (mm)
CM	=	cementitious material, includes portland cement and mineral admixtures (fly ash, slag cement, and silica fume)
d_b	=	bar diameter, in. (mm)
d_t	=	distance from extreme compression fiber to extreme layer of longitudinal tension reinforcement, in. (mm)
d_1	=	length of the primary diagonal (from top left to bottom right) of a station, in. (mm) (Figure 290)
d_2	=	length of the secondary diagonal (from bottom left to top right) of a station, in. (mm) (Figure 290)
DR	=	drift (lateral displacement) divided by height (from base of wall to point of drift measurement), rad
e	=	elongation of flexural reinforcement due to strain penetration, in. (mm)
E_c	=	modulus of elasticity of concrete, ksi (MPa)
E_h	=	hysteretic energy dissipation index, Eq. 22
E_s	=	modulus of elasticity of reinforcement, ksi (MPa)
E_{sh}	=	initial strain-hardening modulus for reinforcement, ksi (MPa)
f'_c	=	specified compressive strength of concrete, ksi (MPa)
f''_c	=	peak compressive stress for unconfined concrete, ksi (MPa)
f''_{cc}	=	peak compressive stress for confined concrete, ksi (MPa)
f_{cm}	=	measured average compressive strength of concrete, ksi (MPa)
f_{cr}	=	critical buckling stress, ksi (MPa)

f_{ct}	=	measured average splitting tensile strength of concrete, psi (MPa)
f_r	=	modulus of rupture of concrete, ksi (MPa)
f_{st}	=	stress corresponding to strain ϵ_{st} at onset of fracture, ksi (MPa)
f_t	=	tensile strength of reinforcement, ksi (MPa)
f_y	=	yield strength of reinforcement, ksi (MPa)
f_{yh}	=	yield strength of confining reinforcement, ksi (MPa)
f_{yp}	=	reinforcement stress corresponding to the proportional limit, ksi (MPa)
F_m	=	force associated with Δ_m , kips (kN)
F_y	=	force associated with yield point, kips (kN)
G_c	=	shear modulus of concrete, taken as $E_c/2.4$, ksi (MPa)
h	=	height of lug, measured from the base of lug away from transition curve, in. (mm)
h_b	=	dimension at bottom side of station, in. (mm) (Figure 290)
h_i	=	height of Layer i , in. (mm) (Figures 30 and 31)
h_t	=	dimension at top side of station, in. (mm) (Figure 290)
h_y	=	height from base of wall to top horizontal potentiometers at elevation +290 in. (7370 mm) for T1, T3 and +287 in. (7290 mm) for T2, T4
$h_{y,i}$	=	distance from centroid of Layer i to top horizontal potentiometers at elevation +290 in. (7370 mm) for T1, T3 and +287 in. (7290 mm) for T2, T4
h_w	=	height from base of wall to point of load application, in. (mm)
i	=	counter or index, used to identify order or position
I_{cr}	=	moment of inertia of cracked transformed section using reinforcement data from Figure 13, in. ⁴ (mm ⁴)
I_{eff}	=	effective moment of inertia, in. ⁴ (mm ⁴)
I_g	=	moment of inertia of gross concrete section about centroidal axis, neglecting reinforcement, in. ⁴ (mm ⁴)
j	=	counter or index, used to identify order or position
k	=	counter or index, used to identify order or position
k	=	effective length factor, Chapter 3
K	=	secant stiffness, kips/in. (kN/m)

K_{cc}	=	ratio of confined to unconfined concrete compressive strength
K_e	=	secant stiffness at $V = V_{0.8} = 0.8 V_{max}$, kips/in. (kN/m)
K_f	=	stiffness associated with flexural deformation, kips/in. (kN/m)
K_{f,I_g}	=	stiffness associated with flexural deformation based on I_g , kips/in. (kN/m)
K_{py}	=	post-yield stiffness, kips/in. (kN/m)
K_{sp}	=	stiffness associated with strain penetration (below base of wall), kips/in. (kN/m)
K_t	=	stress concentration factor, ratio of the maximum elastic stress in the region of the notch to the nominal stress of the bar
K_u	=	unloading stiffness, kips/in. (kN/m)
K_v	=	stiffness associated with shear deformation, kips/in. (kN/m)
$K_{wall,calc}$	=	calculated stiffness of wall, kips/in. (kN/m)
$K_{wall,meas}$	=	measured stiffness of wall, kips/in. (kN/m)
ℓ_{cicj}	=	initial distance along x axis between markers at Columns i and j for a given row (or located at the same elevation), in. (mm) (Figures 30 and 31)
ℓ_d	=	development length or length of embedment required to develop the yield stress of reinforcement, in. (mm)
ℓ_j	=	width of station j , in. (mm) (Figures 30 and 31)
ℓ_p	=	plastic hinge length, in. (mm)
ℓ_w	=	length of wall section in direction of shear force, in. (mm)
\bar{M}	=	maximum moment from moment-curvature analysis, ft-kips (m-kN)
M_n	=	nominal flexural strength calculated for concrete compressive strain of 0.003 and elastoplastic reinforcement (following ACI 318 ^[6]), ft-kips (m-kN)
M_y	=	moment corresponding to flexural yielding, ft-kips (m-kN)
n_ℓ	=	number of layers bounded by optical markers (Figures 30 and 31))
n_s	=	number of stations bounded by optical markers (Figures 30 and 31)
P	=	axial load at the base of wall, kips (kN)
r	=	lug base radius (radius of the circular transition curve), in. (mm)
t_w	=	thickness of wall stem, in. (mm)
u	=	uniform bond stress associated with ℓ_d , psi (MPa)

v_c	=	nominal shear stress attributed to the concrete, psi (MPa)
v_ℓ	=	dimension at left side of a station, in. (mm) (Figure 290)
v_{max}	=	shear stress corresponding to V_{max} , psi (MPa)
v_n	=	nominal shear stress, psi (MPa)
v_r	=	dimension at right side of a station, in. (mm) (Figure 290)
v_s	=	nominal shear stress attributed to the transverse reinforcement, psi (MPa)
V	=	shear force applied at the top of the wall, kips (kN)
V_m	=	shear associated with Δ_m , kips (kN)
V_{max}	=	maximum measured shear force per loading direction, kips (kN)
V_{Mn}	=	shear corresponding to M_n for a nominal shear span of 25 ft., kips (kN)
V_n	=	nominal shear strength, kips (kN)
V_{peak}	=	shear at peak drift, kips (kN)
V_u	=	shear corresponding to limiting curvature ϕ_u , kips (kN)
V_y	=	shear corresponding to yield curvature ϕ_y , kips (kN)
w_{peak}	=	crack width measured at peak drift during second excursion to a target drift, in. (mm)
w_{zero}	=	crack width measured at zero applied shear after second excursion to a target drift, in. (mm)
W	=	hysteretic energy dissipated during half cycle of loading, in.-kips (m-kN)
X	=	coordinate of reinforcement layer (see Figure 13), in. (mm)
X_{cg}	=	coordinate of centroidal axis of gross section, neglecting reinforcement, in. (mm)
$X_{cg,cr}$	=	distance from extreme compression fiber to neutral axis depth of cracked section transformed to concrete, in. (mm)
y_{Ricj}	=	displacement of a marker (at Row i Column j) along y axis, in. (mm) (Figures 30 and 31)
Z_{cc}	=	parameter defining the slope of the linear post-peak branch for confined concrete
Z_{uc}	=	parameter defining the slope of the linear post-peak branch for unconfined concrete

α	=	stiffness reducing exponent
α_{sp}	=	strain penetration amplification factor
β_ℓ	=	fraction of ℓ_d
β_u	=	fraction of u
β_y	=	fraction of f_y
γ_i	=	average shear distortion for Layer i , rad
$\gamma'_{i,j}$	=	shear distortion in Layer i at station j , rad
δ_{base}	=	horizontal displacement of the base block, in. (mm)
δ_{top}	=	horizontal displacement measured by top horizontal potentiometers at elevation +290 in. (7370 mm) for T1, T3 and +287 in. (7290 mm) for T2, T4
Δ_{bo}	=	component of drift due to flexural deformation and strain penetration measured between base block optical markers and first row of markers, in. (mm) (Figures 30 and 31)
Δ_{bs}	=	shear component of drift (due to base shearing) measured between base block optical markers and first row of markers, in. (mm) (Figures 30 through 32)
Δ_f	=	drift (lateral displacement) due to flexural deformation, in. (mm)
$\Delta_{f,p}$	=	displacement corresponding to plastic curvature, Eq. 26, in. (mm)
$\Delta_{f,y}$	=	displacement corresponding to yield curvature, Eq. 25, in. (mm)
Δ_m	=	peak displacement during a loading cycle, in. (mm)
Δ_{max}	=	previously attained maximum displacement in a direction of loading, in. (mm)
Δ_{peak}	=	maximum drift attained in a loading direction during a given cycle, in. (mm)
Δ_{sp}	=	drift (lateral displacement) due to strain penetration, in. (mm) (Table 12)
Δ_v	=	drift (lateral displacement) due to shear deformation, in. (mm)
Δ_X	=	average horizontal displacement of a row of markers, in. (mm)
Δ_y	=	notional yield displacement, in. (mm)
Δ_0	=	measured drift corresponding to zero shear (unloading from Δ_{peak}), in. (mm)
ε_0	=	strain corresponding to peak stress of unconfined concrete
ε_{cc}	=	maximum strain corresponding to peak stress for confined concrete
$\varepsilon_{c,core}$	=	maximum strain in the confined concrete

ε_{sf}	=	measured fracture elongation of reinforcement
ε_{sh}	=	post-yield reinforcement strain where strain hardening begins
ε_{st}	=	strain at onset of reinforcement fracture
ε_{su}	=	uniform elongation of reinforcement or strain corresponding to f_t
θ_{base}	=	rotation of the base block about an axis normal to the plane of the wall stem
θ_{bo}	=	base opening rotation due to flexural deformation and strain penetration measured between base block optical markers and first row of markers (Figures 30 and 31), rad
θ_i	=	rotation due to flexural deformation for Layer i , rad
λ	=	number of bar diameters over which the yield strain of reinforcement is assumed to occur uniformly, $\lambda = \ell_d / (2d_b)$
ρ_ℓ	=	ratio of area of distributed longitudinal reinforcement to gross concrete area normal to that reinforcement
ρ_s	=	ratio of volume of confining reinforcement to volume of confined concrete, measured out-to-out of confining reinforcement
ρ_t	=	ratio of area of distributed transverse reinforcement to gross concrete area normal to that reinforcement
ϕ'	=	post-yield curvature associated with a target displacement, based on Eq. 31 (considering deformations due to flexure, shear, and strain penetration) or Eq. 33 (considering only deformations due to flexure)
ϕ_K	=	ratio of effective shear stiffness to uncracked stiffness
ϕ_y	=	yield curvature associated with the tensile yield strain of reinforcement occurring at a distance $0.8 \ell_w$ from the extreme compression fiber, 1/in. (1/mm)
ϕ_u	=	ultimate curvature corresponding to maximum controlling strain, 1/in. (1/mm)
ψ	=	distortion due to expansion (see Figure 291), rad

APPENDIX B: POST-YIELD STRAIN PENETRATION

Reinforcing bars subjected to tension at the base of a reinforced concrete wall can undergo large strain demands that penetrate into the support. Bar strains along the embedded length are associated with bar elongation and reinforcement slip, which manifest as a rotation at the wall base that contributes to the total lateral displacement at the top of the wall.

In this appendix, a model is proposed for estimating the contribution of reinforcement slip (due to strain penetration) to lateral displacement of a reinforced concrete wall responding in the inelastic range.

Assuming a uniform bond stress u acts on a reinforcing bar of diameter d_b along the development length ℓ_d , the total bond force to develop the yield stress f_y is given by

$$\ell_d \pi d_b u = \frac{\pi d_b^2}{4} f_y \quad \text{Eq. B.1}$$

which simplifies to

$$\frac{\ell_d}{d_b} = \frac{f_y}{4u} \quad \text{Eq. B.2}$$

Sezen and Moehle^[70] proposed a model with a stepped bond stress along the embedded length of the reinforcing bar, as shown in Figure B.1. Based on this model, for a bar to develop a post-yield stress of $(1+\beta_y)f_y$ requires an embedment length of $(1+\beta_\ell)\ell_d$. It is assumed that a uniform bond stress u acts over the length ℓ_d where the bar has not yielded and a reduced bond stress $\beta_u u$ acts over the length $\beta_\ell \ell_d$ where the bar has yielded. A relationship between β_ℓ , β_u , and β_y is derived by substituting these assumptions into Eq. B.2 to obtain

$$\beta_\ell \frac{\ell_d}{d_b} = \frac{\beta_y f_y}{\beta_u 4u} \quad \text{Eq. B.3}$$

where ℓ_d/d_b from Eq. B.2 provides

$$\beta_\ell = \frac{\beta_y}{\beta_u} \quad \text{Eq. B.4}$$

The elongation e due to strain penetration of a yielding bar, as shown in Figure B.1 (at the top of the base block), is obtained by integrating the bar strain diagram over the length $\ell_d + \beta_\ell \ell_d$, resulting in

$$e = \frac{\varepsilon_y}{2} \ell_d + \left(\frac{\varepsilon_s + \varepsilon_y}{2} \right) \beta_\ell \ell_d \quad \text{Eq. B.5}$$

Eq. B.5 was derived assuming zero slip at the unloaded end of the bar. To simplify Eq. B.5, ℓ_d is expressed as a function of d_b using

$$\ell_d = 2 \lambda d_b \quad \text{Eq. B.6}$$

where λ represents the number of bar diameters over which the yield strain of reinforcement is assumed to occur uniformly. Substituting Eq. B.6 into Eq. B.5 provides

$$e = \lambda d_b \varepsilon_y \left[1 + \beta_\ell \left(1 + \frac{\varepsilon_s}{\varepsilon_y} \right) \right] \quad \text{Eq. B.7}$$

The rotation at the wall base due to strain penetration is calculated using Eq. B.8 based on the elongation divided by the distance from the bar to the neutral axis depth ($d_t - c$).

$$\theta_{sp} = \frac{e}{d_t - c} = \lambda d_b \frac{\varepsilon_y}{d_t - c} \left[1 + \beta_\ell \left(1 + \frac{\varepsilon_s}{\varepsilon_y} \right) \right] \quad \text{Eq. B.8}$$

from which the displacement at a distance h_w from the support is obtained using

$$\Delta_{sp} = \lambda d_b \phi_y \left[1 + \beta_\ell \left(1 + \frac{\varepsilon_s}{\varepsilon_y} \right) \right] h_w \quad \text{Eq. B.9}$$

where $\varepsilon_y/(d_t - c)$ is taken as an approximate measure of the yield curvature ϕ_y . Eq. B.9 is further simplified using

$$\Delta_{sp} = \alpha_{sp} \lambda d_b \phi_y h_w \quad \text{Eq. B.10}$$

where

$$\alpha_{sp} = \left[1 + \beta_\ell \left(1 + \frac{\varepsilon_s}{\varepsilon_y} \right) \right] \quad \text{Eq. B.11}$$

Eq. B.10 only applies where $\varepsilon_s > \varepsilon_y$ and bar slip at the unloaded end of the bar is negligible. For the condition of $\varepsilon_s = \varepsilon_y$, $\beta_\ell = 0$ (given that ℓ_d is the required embedment length to develop f_y , see Figure B.1) resulting in $\alpha_{sp} = 1$ per Eq. B.11. Therefore, Eq. B.10 can be expressed as a function of the deformation due to strain penetration at yield $\Delta_{sp,y}$, using

$$\Delta_{sp} = \alpha_{sp} \Delta_{sp,y} \quad \text{Eq. B.12}$$

where $\Delta_{sp,y}$ is defined by

$$\Delta_{sp,y} = \lambda d_b \phi_y h_w \quad \text{Eq. B.13}$$

and α_{sp} represents the amplification factor of $\Delta_{sp,y}$ to obtain Δ_{sp} in Eq. B.12. The definition of deformation due to strain penetration at yield in Eq. B.13 is consistent with the definition of deformation due to strain penetration presented in Table 12.

The sensitivity of β_ℓ to parameters β_u and β_y is shown in Figure B.2. Values of $\beta_y = 0.25$ (corresponding to a stress of $1.25f_y$) and β_u between 0.5 and 1.0 provide values of β_ℓ between 0.5 and 0.25, respectively. In this study, $\beta_u = 0.75$ was adopted, which for $\beta_y = 0.25$ provides $\beta_\ell = 0.33$.

It is important to note that to develop $1.25f_y$ based on ACI 408^[7], the development length needs to increase by approximately 1.4 for $f_y = 60$ ksi (414 MPa) and 1.3 for $f_y = 100$ ksi (690 MPa). The development length equations in ACI 408^[7] have been shown to work for high-strength reinforcement subjected to post-yield stresses of up to 155 ksi (1070 MPa).^[47]

For an indication of the range of values to expect for α_{sp} , Table B.1 shows calculated data for T1 and T4 with Grade 60 (420) and Grade 100 (690) reinforcement, respectively, at strains of 0.02, 0.03, 0.04, and 0.05. Values of β_y were assumed to vary from 0.1 to 0.25 for strains between 0.02 and 0.05. A value of $\beta_u = 0.75$ was assumed constant for the values of β_y considered. The data in Table B.1 are plotted in Figure B.3 with a low-bound estimate of α_{sp} given by

$$\alpha_{sp} = 2 DR$$

Eq. B.14

where the drift ratio DR (in percent) is limited to values between 1 and 2. Figure B.3 shows that values of α_{sp} are in the range between 2 and 9 for drift ratios between 1 and 3%.

Table B.1 – Strain penetration amplification factor α_{sp} based on Eq. B.12^a

ε_s	β_y^b	β_u	β_ℓ	DR^c		α_{sp}^d		α_{sp}/DR^c	
				T1	T4	T1	T4	T1	T4
0.02	0.10	0.75	0.13	1.14	0.89	2.24	1.94	1.96	2.18
0.03	0.15	0.75	0.20	1.71	1.33	3.69	3.01	2.15	2.26
0.04	0.20	0.75	0.27	2.29	1.78	5.69	4.49	2.49	2.53
0.05	0.25	0.75	0.33	2.86	2.22	8.24	6.37	2.88	2.87

^aFor notation and definitions see APPENDIX A: NOTATION.

^bBased on a strain-hardening modulus of $5f_y$ for strains between 0.02 and 0.05.

^cDrift ratio (in percent) defined from $\varepsilon_s \cong 1.75 DR$ for T1 (based on negative loading direction in Figure 113) and $\varepsilon_s \cong 2.25 DR$ for T4 (based on negative loading direction in Figure 112). Negative loading direction corresponds to stem in tension.

^dAmplification factor for strain penetration, $\alpha_{sp} = 1 + \beta_\ell \left(1 + \varepsilon_s/\varepsilon_y\right)$, where $\varepsilon_y = 0.00241$ for T1 and $\varepsilon_y = 0.00331$ for T4.

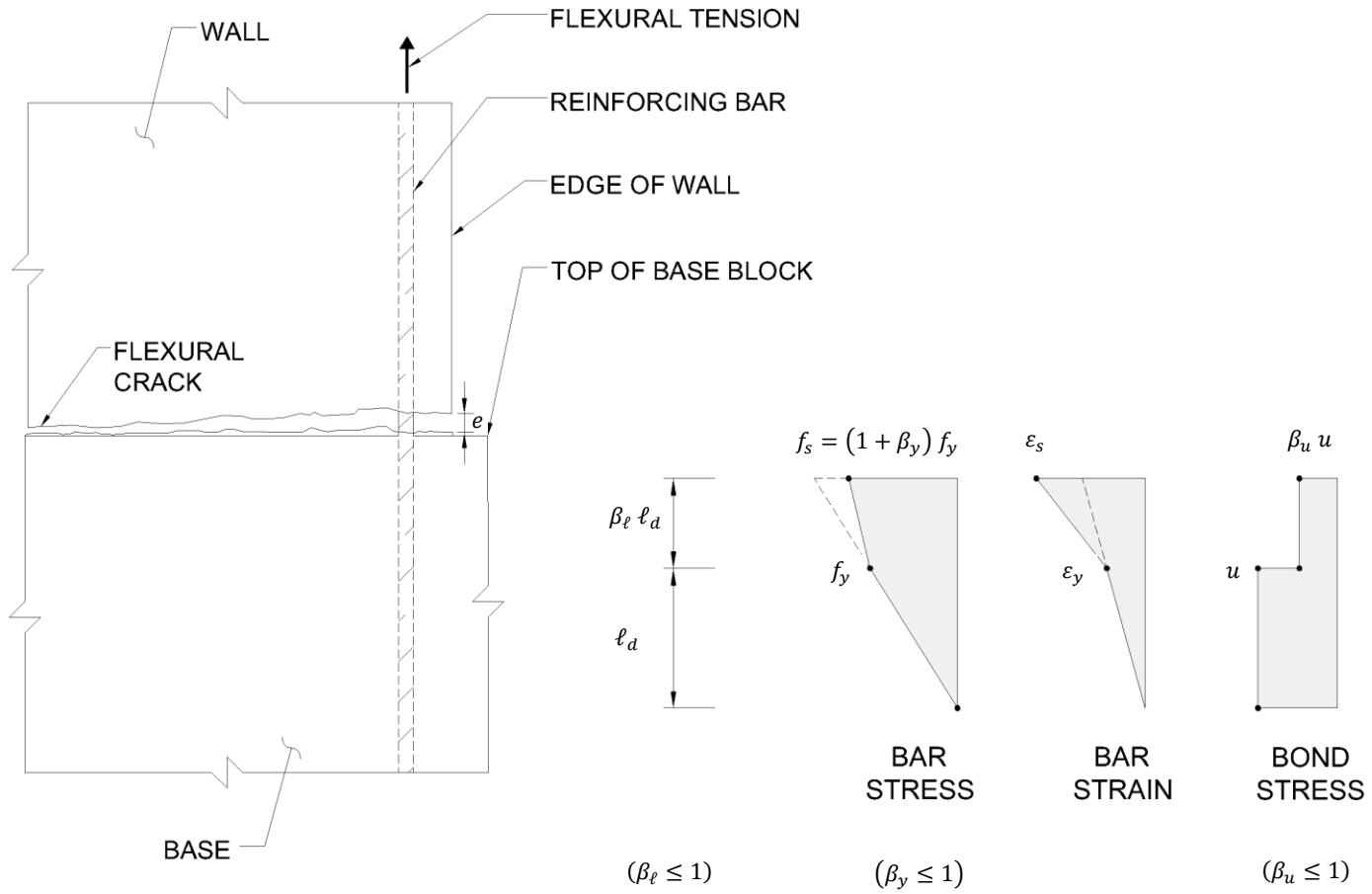


Figure B.1 – Post-yield strain penetration assumptions

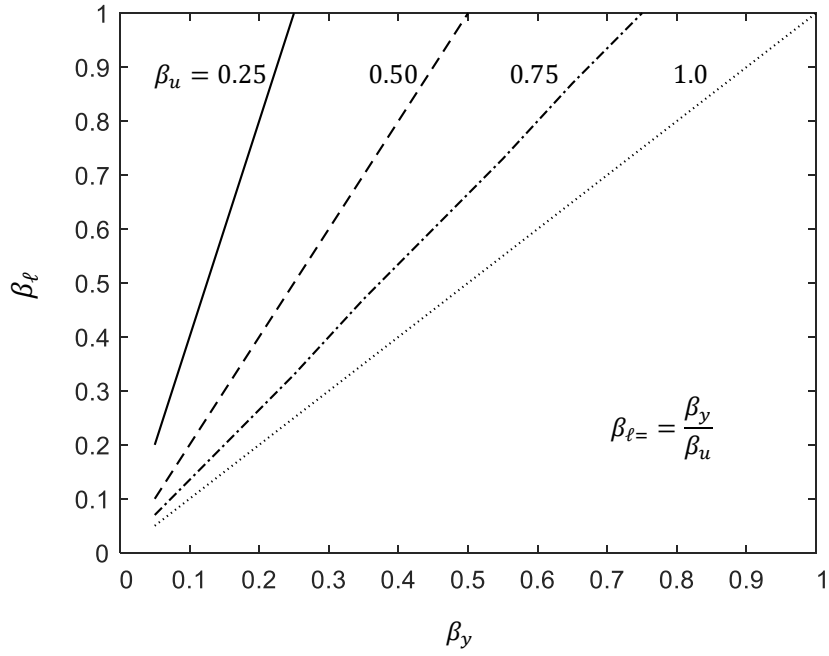


Figure B.2 – Influence of β_u and β_y on β_ℓ

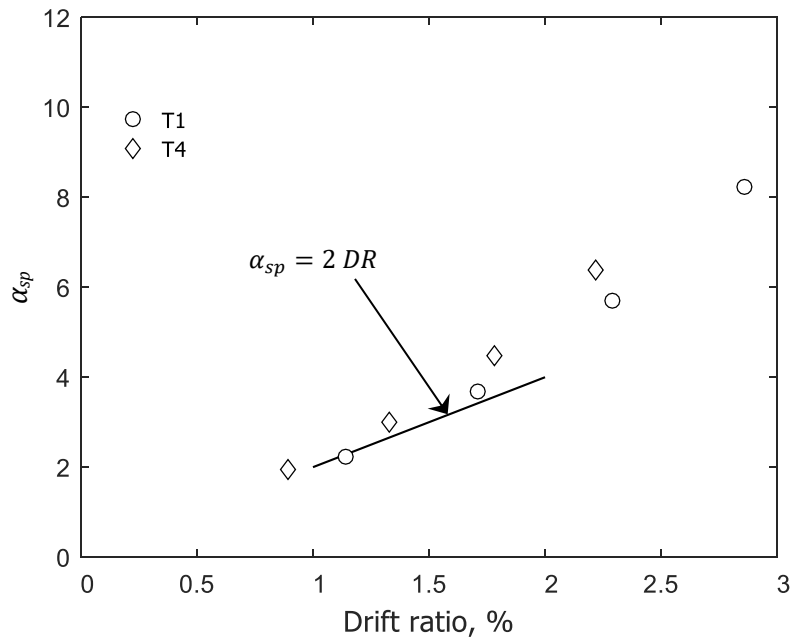


Figure B.3 – Strain penetration amplification factor α_{sp} versus drift ratio, based on Table B.1

